QST-M-8

QST Takasaki Annual Report 2016

Takasaki Advanced Radiation Research Institute

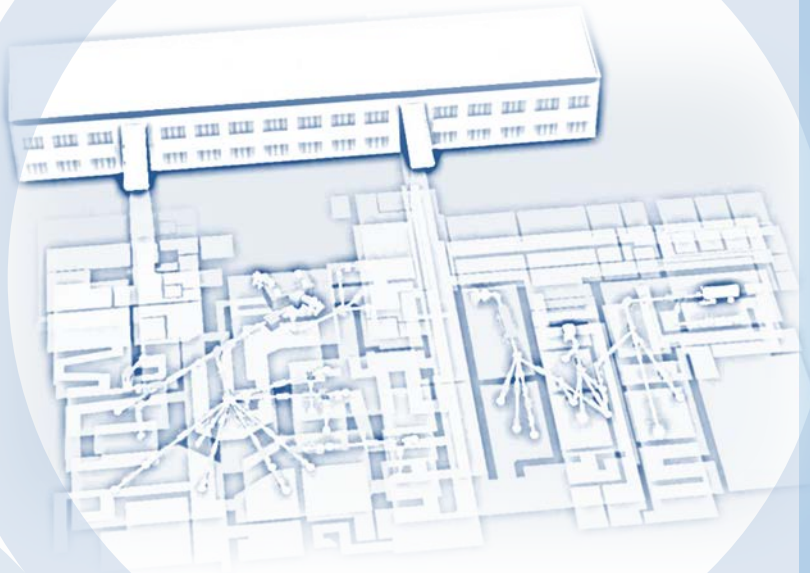

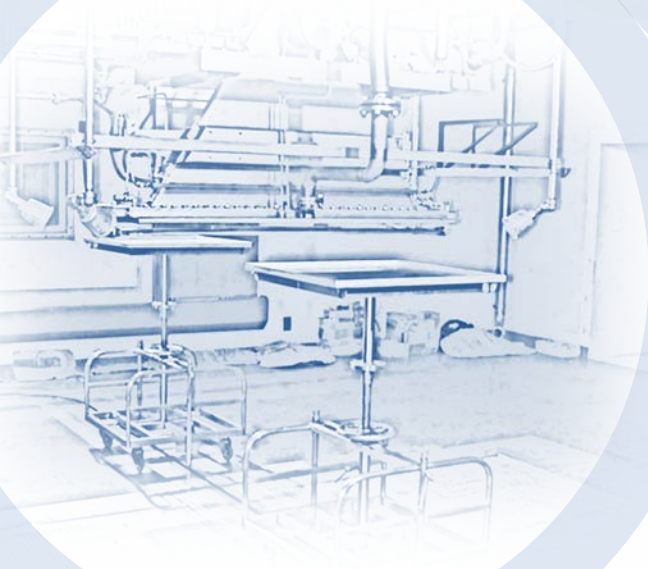

National Institutes for Quantum and

Radiological Science and Technology

Preface

Hisayoshi Itoh

Director General
Takasaki Advanced Radiation Research Institute
Quantum Beam Science Research Directorate
National Institutes for Quantum and Radiological Science and Technology

National Institutes for Quantum and Radiological Science and Technology (QST) was established in April of 2016 by integrating the National Institute of Radiological Sciences (NIRS) and some institutes promoting quantum beam science research and nuclear fusion research in the Japan Atomic Energy Agency (JAEA). The QST has three R&D directorates, *i.e.*, Quantum Beam Science Research Directorate (QuBS), Radiological Science Research and Development Directorate, and Fusion Energy Research and Development Directorate. In the QuBS, in which two research institutes of Takasaki Advanced Radiation Research Institute (TARRI) and Kansai Photon Science Institute (KPSI) are involved, we are intensively performing fundamental and applied research in a wide range of fields like materials science, life science, and quantum beam technology, using advanced beam facilities. Every institute has two research sites, *i.e.*, Takasaki and Tokai sites of TARRI, and Kizu and Harima sites of KPSI. Typical beam facilities we used are Takasaki Ion Accelerators for Advanced Radiation Application (TIARA) at the Takasaki site, Japan Proton Accelerator Research Complex (J-PARC) at the Tokai site, Japan-Kansai Advanced Relativistic Engineering Laser System (J-KAREN) at Kizu site, and highly sophisticated beamlines of Super Photon Ring-8 GeV (SPring-8) at Harima site.

In the TARRI, we have 17 Research Projects making quantum beam science R&Ds with TIARA, 2 MeV electron accelerator, ^{60}Co gamma-ray irradiation facilities, etc., for contributing to the progress of science and technology as well as the promotion of industry. Especially for strongly promoting alliance with industries, the Advanced Functional Polymer Materials Group has been launched under QST innovation hub program to develop next generation graft-polymer materials with combined use of quantum beam processing and analysis techniques as well as materials informatics. We are also performing R&D of advanced ion beam technology at the Beam Engineering Section of the Department of Advanced Radiation Technology. In addition, our beam facilities are open to industry, academia, and governmental research institutes, and the beam time is allocated for users based on the evaluation of their R&D programs.

This Annual Report covers the research activities at the TARRI primarily for the fiscal year 2016 (FY 2016). This report consists of two parts, Part I and Part II. In Part I, the recent activities of all Research Projects of TARRI are described and Part II presents the recent R&D results obtained by using quantum beam facilities of the TARRI. This part is composed of 130 research papers in the fields of materials

science, life science, and advanced quantum beam technology, and 8 status reports on operation/ maintenance of the quantum beam facilities. It should be noted as a typical topic in the field of materials science that regular arrays of shallow nitrogen-vacancy centers in diamond have been successfully fabricated for their quantum sensing applications by using low energy ion implantation and electron beam lithography. In the life science field, the feasibility of the proton beam imaging using a pinhole X-ray camera was evaluated experimentally and theoretically to realize precise dose control for particle therapies, showing that the beam trajectory was clearly imaged by secondary electron bremsstrahlung observation. As for the advanced quantum beam technology, a highly intense MeV C_{60} ion beam has been developed with continuous improvement of the negative C_{60} ion source for the TIARA 3 MV tandem accelerator, and found to be useful for fabricating porous nanostructures in the surface of GaSb semiconductors. For details of all R&Ds performed at the TARRI, please refer to the main text of this Annual Report.

Concerning the status of quantum beam facilities, three electrostatic accelerators of TIARA were operated steadily and safely as well as MeV-electron and ^{60}Co gamma-ray irradiation facilities. A serious layer short was found in the main coils of the TIARA AVF cyclotron in December 2016. We now operate the cyclotron with lower magnetic excitation using the normal part of the coils and are preparing to replace the whole coils for restoration.

Finally, we extend gratitude to both our domestic and foreign colleagues for their cooperation, support, and encouragement for our quantum beam science R&Ds as well as technological advance in the facilities of TARRI.

Facilities

Charged particle beams and RI facilities

Takasaki Ion Accelerators for Advanced Radiation Application (TIARA) consisting of four ion accelerators, an electron accelerator, and gamma irradiation facilities are available to researchers in QST and other organizations for R&D activities on new functional and environmentally friendly materials, biotechnology, radiation effects of materials, and quantum beam analysis. We are developing microbeams, single ion hits and uniform wide-area irradiation technique at the cyclotron. In addition, technical developments of three dimensional in-air PIXE analysis and production/acceleration of cluster ion beam such as C_{60} fullerene at the electrostatic accelerators are in progress.

Takasaki Ion Accelerators for Advanced Radiation Application: TIARA

TIARA buildings

Cyclotron

Tandem accelerator

Single-ended accelerator

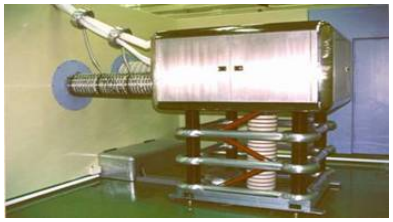

Ion implanter

Typical available ions

Accelerator	Ion	Energy (MeV)
AVF Cyclotron (K=110MeV)	H	10～ 90
	He	20～107
	C	75～320
	Ne	75～350
	Ar	150～520
	Fe	200～400
	Kr	210～520
	Xe	324～560
	Os	490
Tandem Accelerator (3 MV)	H	0.8～ 6.0
	C	0.8～18.0
	Ni	0.8～18.0
	Au	0.8～18.0
	C60	0.8～6.0
Single-ended Accelerator (3 MV)	H	0.4～ 3.0
	D	0.4～ 3.0
	He	0.4～ 3.0
	e^-	0.4～ 3.0
Ion Implanter (400 kV)	H	0.02～0.38
	Ar	0.02～0.38
	Bi	0.02～0.37
	C_{60}	0.02～0.36

Energy-element range covered with four accelerators

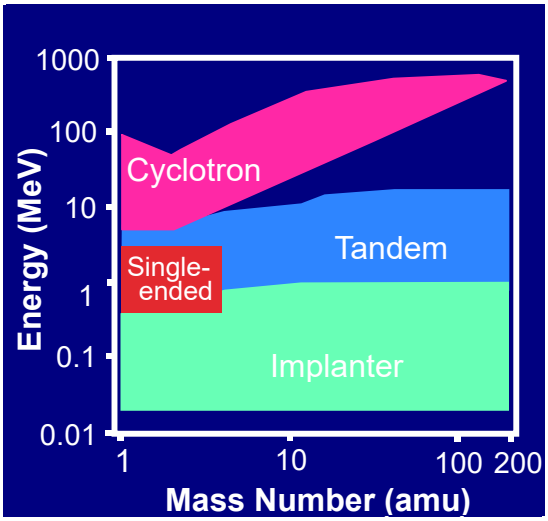

Cobalt-60 gamma-ray and electron beam irradiation facilities

Gamma-ray irradiation facility building

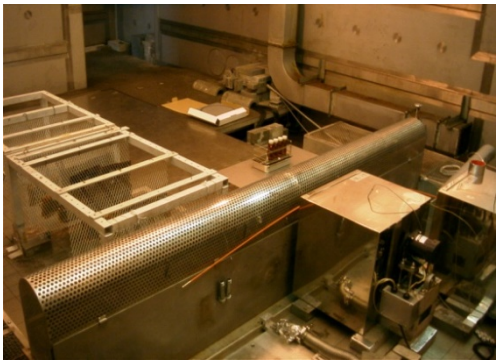

Gamma-ray irradiation room

Electron accelerator
(0.5～2.0 MeV 0.1～30 mA)

Electron irradiation room with conveyor system

Specification

Apr.2017

Name of facility	Cobalt-60 activity(PBq)	Number of rooms	Purpose
Co No.1 bld.	11.1	3	Radiation-resistance test Radiation effects on polymers
Co No.2 bld.	9.5	3	R & D on functional organic materials, dosimetry
Food Irrad.	3.3	2	Radiation effects on biological substance and semiconductors

Dose-rate range

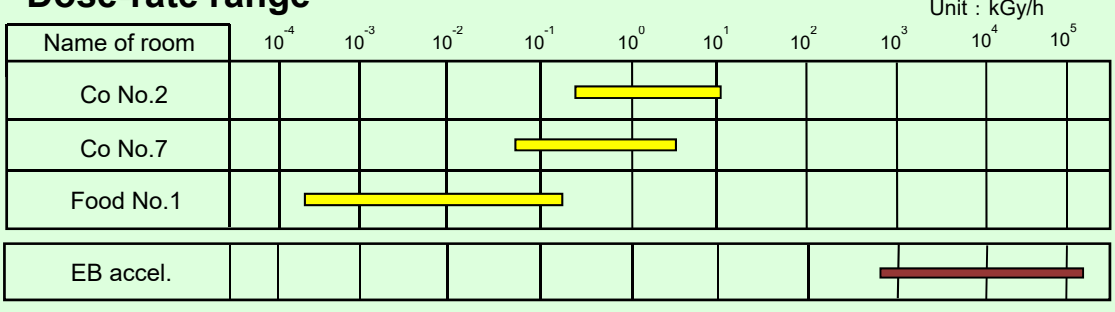

Contents

Part Ⅰ

Part II

Part I

Part Ⅰ

1. Materials Science

P1-1 Functional Polymer Research Project

Leader : Yasunari Maekawa

Project “Functional Polymer Research” has been developing the functional polymer materials for high performance fuel cells and hydrogen collection systems by using quantum beams such as electron beams, γ-rays and ion beams. We have synthesized the proton- and anion-conducting electrolyte membranes (PEM and AEM) and the hydrogen permselective membranes. We report herein two recent developments: PEMs based on poly(ether ether keton) (PEEK)/nanosilica hybrid films and AEMs based on poly(ethylene-co-tetrafluoroethylene) (ETFE) for hydrogen- and hydrated hydrazine-fuel cells applied in automobiles {1-16~19 in Part II}.

Silica-containing PEEK-PEMs prepared by radiation-induced graft polymerization [1]

Recent main concerns for PEMs are higher proton conductivity at low relative humidity (RH) and superior mechanical properties under humid conditions because these properties affect the power generation efficiency and the durability under extreme operating conditions in fuel cell systems. To improve the properties, recently, an incorporation of inorganic fillers into polymer matrix has attracted attention.

Silica-containing PEEK-PEMs were prepared by radiation-induced graft polymerization to PEEK films that contain 3 and 5 wt% dispersed nanosilica (PEM-Si3 and -Si5, respectively). The prepared PEM-Si3 and -Si5 showed slightly higher water uptakes compared with that of the silica-free PEMs. PEM-Si3 with an ion exchange capacity (IEC) of 3.30 mmol/g exhibited the highest water uptake among all samples. As shown in Fig. 1, a tensile strength (TS) of the PEM-Si3 exhibited 16.4 MPa under 100% RH at 80 ºC, which was 1.27 and 1.64 times greater than those of the silica-free PEM and Nafion 212, respectively. Thus, it was confirmed that the nanosilicas improved the mechanical properties of the PEMs.

The membrane electrolyte assembly (MEA) fabricated by using the PEM-Si3 with IEC of 3.30 mmol/g showed maximum power densities of 738 and 612 mW/cm^2 at 1,431 and 1,391 mA/cm^2 under 100% and 30% RH, which were 11% and 7% higher than those based on silica-free PEM, respectively.

Ion channels in ETFE-based AEMs {1-17}

In the previous study, we reported the development of ETFE-based AEMs with the graft chains consisting of imidazolium and styrene [2, 3]. The AEMs prepared by using 2-metyl-N-methyl-4-vinylimidazole and styrene exhibited well-balanced properties of high ion conductivity (> 100 mS/cm) and good alkaline stability. In order to reveal the structure required for the high performance, a specific AEM (denoted as AEM91, with 2-methyl imidazolium/styrene ratio = 6/4, a grafting degree of 91%, and ion exchange capacity of 1.82 meq/g) was analyzed by using small-angle neutron scattering (SANS) method.

As the results of SANS, a scattering maximum at q_1 = 0.2 - 0.3 nm^{-1} was observed in ETFE membrane, grafted-ETFE, and swollen AEM. The peak is due to typical crystalline lamellar structure with a d-spacing (= $2\pi/q_1$) of 20 - 34 nm. The increase in the d-spacing with grafting indicated that the lamellar stacks were expanded by the incorporation of the graft chains and water in the amorphous domains, as illustrated in Fig. 2. Furthermore, by the contrast variation SANS measurements on AEM91 equilibrated in mixtures of H_2O and D_2O with different volume fractions, it was revealed that the nanoscale ion channels were formed in hydrophilic phase composed of the entire grafts and water. The well-connected ion channels would be the key reason for the high ion conductivity of ETFE-based AEM.

References

[1] T. Hamada *et al.*, Int. J. Hydrogen Energy, **41**, 18624 (2016).
[2] K. Yoshimura *et al.*, J. Electrochem. Soc., **161**, F889 (2014).
[3] Y. Zhao *et al.*, Soft Matter, **12**, 1567 (2016).

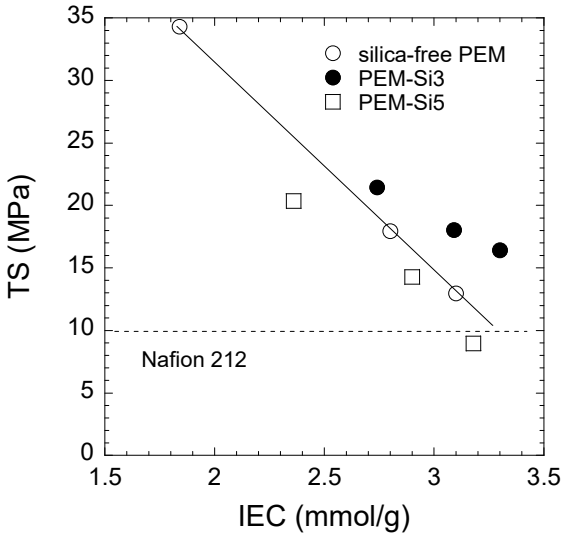

Fig. 1. TS of PEMs with different IECs and nanosilica contents and a silica-free PEM under 100% RH at 80 ºC.

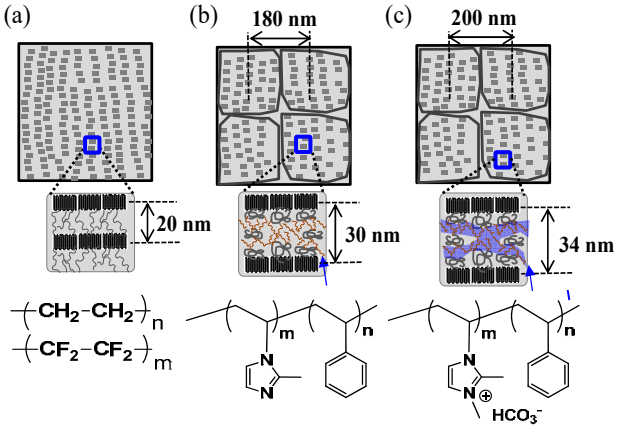

Fig. 2. Schematic illustrations of the morphology of (a) ETFE membrane, (b) grafted-ETFE, and (c) fully water-swollen AEM.

P1-2 Advanced Catalyst Research Project

Leader : Tetsuya Yamaki

We have been developing catalytic materials for next-generation energy devices for future hydrogen society by effective use of ion and electron beams. The advantage of our overarching research strategy is that these quantum beams can lead to high-energy defect creation, active-site formation via non-equilibrium chemical reactions, and micro-to-nano fabrication, which have a great potential to facilitate the development of novel functional materials through innovative interdisciplinary methodologies. This report deals with applications of the charged-particle beams to nanomaterials science for oxygen reduction reaction (ORR) catalysts in secondary batteries and fuel cells {1-06~14, 20~22 in Part II}.

Non- and low-platinum electrocatalysts prepared by irradiation with keV-ion and electron beams [1, 2], {1-10, 12, 13, 20~22}

Non- or low-platinum (Pt) ORR electrocatalysts are needed to lower the device cost. We have confirmed high controllability of impurity doping and defect formation; therefore, our advanced methods using low-energy keV ions as well as electron beams were pursued for the preparation of carbon-based non-Pt catalysts and highly-active Pt nanoparticles (NPs).

Quite recently, Pt NPs supported on the glassy carbon (GC) substrate pre-irradiated with Ar^+ have been found to exhibit strong electronic interactions with carbon atoms at the interface [1]. This unique interactions induced by the ion irradiation could affect the ORR activity of the Pt NPs by tuning their electronic structures. Thus, we investigated the effect of the Ar^+ irradiation on the ORR activity of the supported Pt NPs.

A 1-cm^2 GC substrate was irradiated with 380 keV Ar^+ at a fluence of up to 1.0×10^{16} ions/cm^2 and then heated at 400 ºC in an N_2 atmosphere for 1 h. Pt NPs were deposited at a weight of 5.7×10^{-6} g by RF magnetron sputtering on the pre-irradiated and non-irradiated GC substrates.

We measured the specific ORR activity of the Pt NPs on the GC substrates irradiated with Ar^+ at different fluences and on the non-irradiated substrate (zero fluence). The kinetic current was obtained by the linear sweep voltammetry curves and Koutecky-Levich theories. The kinetic current density, i_k, was then calculated using electrochemical surface area and represented in Fig. 1. The i_k at 0.85 V/RHE (reversible hydrogen electrode) became higher with an increase in the Ar^+ fluence. Strikingly, the pre-irradiated GC support was found to enhance the specific activity of the Pt NPs by 2.5 times. X-ray absorption fine structure measurements in combination with theoretical calculations are now in progress to examine the GC-Pt NPs interfacial structures.

New nano-sized materials prepared by swift-heavy-ion technology and their applicability [3], {1-06~09, 11, 14}

An MeV-GeV heavy-ion beam gives one-dimensional polymer nanostructures through its high energy deposition within a limited cylindrical area along the path, *i.e.*, an ion track. Crosslinking reactions occur in the ion track, yielding a nanowire by subsequent development to remove the non-crosslinked parts (referred to as a single-particle nanofabrication technique), while degradation reactions occur to afford a straight nanopore after preferential dissolution of the ion track (referred to as a track etching technique). We have recently developed a variety of new nanomaterials [4-6] such as ion-conductive membranes and biological sensors.

Hydrogel nanowires based on poly (vinylpyrrolidone) (PVP) and *N,N'*-methylenebis(acrylamide) (MBA) were prepared by the single-particle nanofabrication technique. The radius and length of the nanowires were controlled by varying the amount of the MBA crosslinker and film thickness. The swelling ratios in aqueous environments were measured along the nanowire radius and length. Interestingly, as shown in Fig. 2, there seemed to be a significant difference between the two directions. This anisotropic swelling would be because the nanowires had inhomogeneous crosslinking points due to the local energy distribution within the ion track. The high size-controllability enables us to expect potentially new applications in the ORR catalytic systems.

References

[1] T. Kimata *et al.*, Surf. Coat. Technol., **306**, 123 (2016).
[2] K. Kakitani *et al.*, Radiat. Ind., **141**, 29 (2016).
[3] S. Tsukuda *et al.*, J. Polym. Sci. B, Polym. Phys., **54**, 1950 (2016).
[4] M. Higa *et al.*, Bull. Soc. Sea Water Sci. Jpn., **71**, 37 (2017).
[5] A. Horio *et al.*, Nanoscale, **8**, 14925 (2016).
[6] T. Wasin *et al.*, ACS Sens., **1**, 766 (2016).

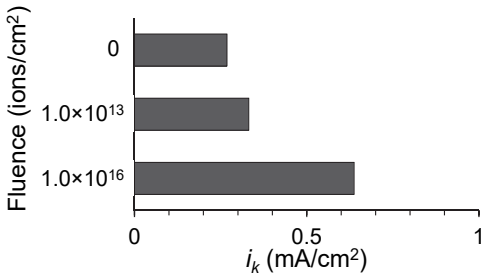

Fig. 1. The i_k at 0.85 V/RHE of Pt NPs on the the GC substrates irradiated with Ar^+ at different fluences and on the non-irradiated substrate.

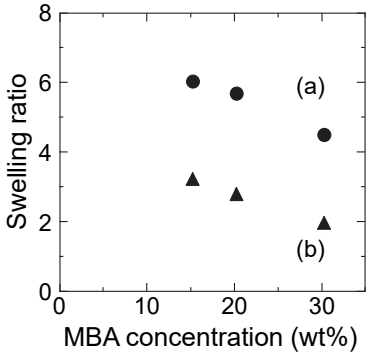

Fig. 2. The swelling ratio of the PVP/MBA nanowires at different crosslinker concentrations. This is plotted in (a) the radius and (b) length directions.

P1-3 Positron Nano-Science Research Project

Leader : Atsuo Kawasuso

The aim of the project “Positron Nano-Science Research” is to develop new and potential positron beam technologies for the advanced solid state physics. So far, we have been developing (i) the spin-polarized surface positronium spectroscopy that is substantially useful for detecting spin-polarization of electrons at the first surface layer, (ii) the spin-polarized positron annihilation spectroscopy in strong magnetic field for detecting vacancy-induced magnetism and (iii) the low-energy positron diffraction for the structural analysis of heavy metal surfaces. In this report, we pick up the achievements of themes (i) and (iii).

Spin-polarized surface positronium spectroscopy [1]

Evaluation of spin polarization at the first surface layer is very important in the studies of spin-Hall systems, the Rashba systems and the topological insulators. This is also true for the induced spin polarization in two-dimensional materials such as graphene. However, ordinary tools like angle-resolved photoemission spectroscopy and magneto-optical effect spectroscopy hardly discriminate the spin polarization at the first surface layer. In this respect, spin-polarized surface positronium spectroscopy is a promising method.

We have been actually demonstrating that even a simple measurement of three-gamma annihilation of surface positronium using a Ge detector can detect the surface spin polarization in some spin-Hall systems. A similar work is also on-going in the induced spin polarization of graphene from ferromagnetic substrates.

To further evaluate energy dependence of spin polarization especially at the Fermi level, we are developing a spin-polarized positronium time-of-flight (SP-PsTOF) system. In 2016, we finished the construction of a timing system required for TOF measurement. Figure 1 shows the Ps lifetime spectra obtained for a test sample (silica aerogel (SP-15)). The long-lived component (142 ns) corresponds to Ps self-annihilation. Thus, the timing system is successfully operated and hence we confirm the feasibility to SP-PsTOF measurement.

Low-energy positron diffraction [2]

Low-energy positron diffraction (LEPD) is the positron counterpart of low-energy electron diffraction (LEED). The first LEPD experiment was reported by the Brandeis group in 1980. They developed a LEPD system with an RI-based slow-positron beam and demonstrated that the LEPD showed better agreement between theoretical and experimental diffraction intensity profiles compared to LEED. Later theoretical works revealed that LEPD combined advantages of no forward focusing resulting in lower chance of multiple scattering and simple smooth scattering factor because of the weak relativistic effects due to the repulsive force from the core and no exchange interaction with material electrons. These advantages are of great significance for atomic structure analysis especially on high-Z materials. Low-energy positron diffraction also has an advantage of high surface sensitivity due to a short mean-free path. Despite these promising properties, however, any LEPD experimental research had not followed the pioneering works at Brandeis University from 1980s to mid-1990s.

Recently, we have developed a LEPD experiment system with a linac-based slow-positron beam at the Slow Positron Facility of the Institute of Materials Structure Science, KEK (High Energy Accelerator Research Organization).

Positrons are magnetically guided to the LEPD experiment station, and released into a nonmagnetic space. Then a brightness-enhancement unit is effectively used to achieve a brightness enhanced beam with an energy of 50-500 eV. We introduced microchannel plates (MCP) and a delay line detector (DLD) as a position-sensitive detector for obtaining a diffraction pattern.

With the newly developed LEPD experiment system, we have succeeded in obtaining a Ge(001)-(2×1) LEPD pattern at 140 eV (Fig. 2).

References

[1] M. Maekawa *et al.*, J. Phys. Conf. Ser., **791**, 012009 (2017).
[2] K. Wada *et al.*, to be submitted to e-Journal of Surface Science and Nanotechnology.

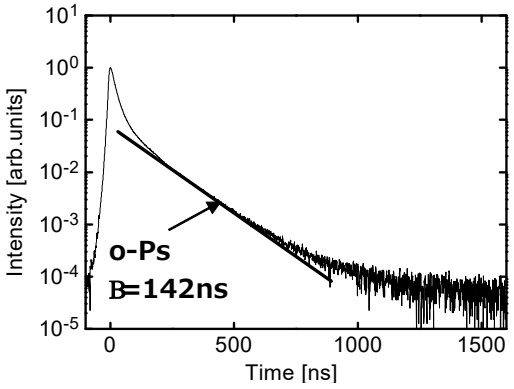

Fig. 1. Ps annihilation lifetime spectrum obtained from the silica aerogel (SP-15) at incident positron energy of 500 eV.

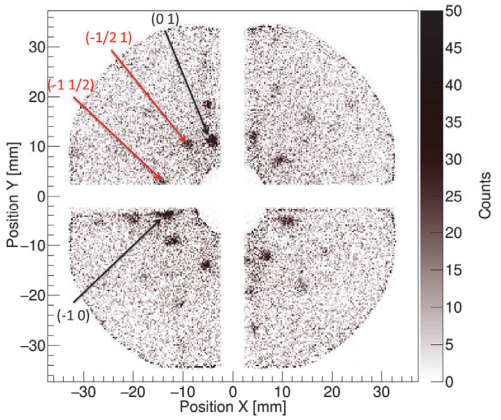

Fig. 2. A low-energy positron diffraction (LEPD) pattern from Ge(001)-(2×1) at 140 eV. In addition to the fundamental spot (0 1), the fractional order spots (-1/2 1) and (-1 1/2) are also observed.

P1-4 Semiconductor Analysis and Radiation Effects Research Project

Leader: Takeshi Ohshima

Technologies based on quantum effects, *i.e.* quantum computation, quantum information and quantum sensing, change our life to be more comfortable, safer and more secure. In order to realize those technologies, single photon sources (SPSs) operating with robust and steady are indispensable. We study defect engineering using ion and electron beams for the creation of SPSs in wide bandgap semiconductors such as diamond and silicon carbide (SiC). In addition, when semiconductor devices are irradiated with radiations such as ions, electrons and gamma-rays, degradation and malfunctions occur in electronic devices. We also study radiation response of semiconductor devices to reveal the radiation degradation/malfunction mechanisms and in addition, establish radiation resistant technologies for development of long lifetime and highly reliable semiconductor devices that can be used in high radiation environments such as space, nuclear and accelerator facilities {1-1~5, 26, 28 in Part II}.

Creation of silicon vacancy (V_{Si}) in SiC by proton beam writing (PBW)

Si vacancy (V_{Si}) in SiC is known as SPS acting at room temperature (RT) [1]. Since its spin can be manipulated by applying microwave, V_{Si} in SiC is expected to be applied to quantum spintronics, quantum sensing and quantum photonics applications operating at RT [2, 3]. Especially, since the luminescence from V_{Si} is around 900 nm, V_{Si} is suitable for quantum sensor for biological and medical applications. Ion irradiation is one of the most useful tools to create luminescent defects in materials. Especially, proton bean writing (PBW) is expected to be a powerful tool to create SPSs in certain locations. However, the creation of crystal defects which act as SPS in SiC using PBW has not yet been clarified. We therefore study creation of V_{Si}s in SiC by PBW [4]. Figure 1 shows confocal photoluminescence map for high purity semi-insulating (HPSI) SiC partially irradiated with 1.7 MeV-protons (PBW) at RT. Bright spots are observed from points irradiated with protons. The spectra of the bright spots show a PL peak around 900 nm, which corresponds to PL spectra for V_{Si}. The result obtained in this study suggests that V_{Si} can be created at a certain location by PBW.

Suppression of gamma-ray radiation degradation of SiC metal-oxide-semiconductor field effect transistors (MOSFETs) by humidity

Recently, it is required to develop electronic devices used in harsh radiation environments, such as nuclear and accelerator facilities. For decommissioning of nuclear reactors in Tokyo Electric Power Company Fukushima Daiichi Nuclear Power Station, it is necessary to realize electronic devices with extremely high radiation resistance (MGy order). SiC is expected to be applied for high radiation resistant electronics as well as power devices with outstanding excellent characteristics [5]. In this study, radiation response of vertical structure power 4H SiC MOSFETs was investigated [6]. The MOSFETs were irradiated with gamma-rays in either steam condition (with humidity) or N_2 atmosphere (without humidity) at 150 ºC. Figure 2 shows the change in threshold voltage (V_T) for the MOSFETs due to irradiation. The values of V_T were estimated from the value at the intersection between the gate voltage (V_G)-axis and the line extrapolated from the curve of the square root of drain current vs. V_G in the saturation region. The shift of V_T due to irradiation was suppressed by irradiation at elevated temperature (150 ºC). Furthermore, the shift of V_T for MOSFETs irradiated with humidity is smaller than that for ones irradiated without humidity. This suggests that the degradation of SiC MOSFETs can be suppressed by irradiation at elevated temperature with humidity.

References

[1] M. Widmann *et al.*, Nature Materials, **14**, 164 (2015).
[2] M. Niethammer *et al.*, Phys. Rev. Appl., **6**, 034001 (2016).
[3] M. Radulaski *et al.*, Nano Lett., **17**, 1782 (2017).
[4] T. Ohshima *et al.*, Mater. Sci. Forum, **897**, 223 (2017).
[5] T. Ohshima *et al.*, Jpn. J. Appl. Phys., **55,** 01AD01 (2016).
[6] A. Takeyama *et al.*, Jpn. J. Appl. Phys., **55**, 104101 (2016).

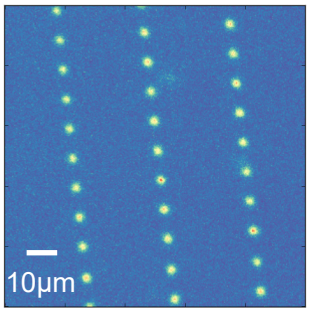

Fig. 1. Photoluminescence map obtained from HPSI SiC partially irradiated with 1.7 MeV protons (PBW) at RT.

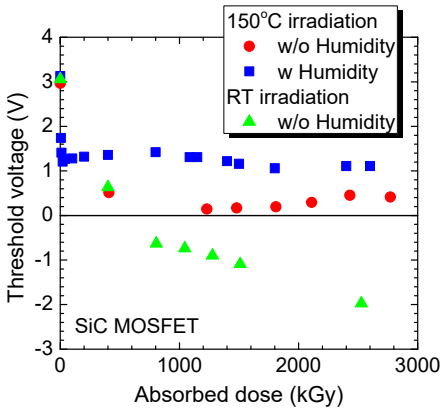

Fig. 2. Change in V_T for SiC MOSFETs due to irradiation. Circles and squares indicate the results obtained for MOSFETs irradiated at 150 ºC without and with humidity, respectively. For comparison, results obtained from MOSFET irradiated at RT are plotted in the figure (triangles).

P1-5 Biocompatible Materials Research Project

Leader : Mitsumasa Taguchi

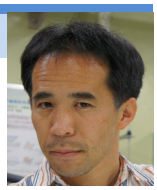

The research objective of Project "Biocompatible Materials Research" is to investigate the functional materials in the medical field using biocompatible polymers mainly based on the radiation-induced crosslinking and polymerization techniques. The obtained materials can be utilized for the functional bio-devices in regenerative medicine and advanced cancer therapy.

Fabrication of thermo-responsive cell culture sheet by pre-irradiation grafting technique

Functional cell-sheet, which makes the control of cell adhesion and detachment without a proteolytic enzyme, is a key tool for the regenerative medicine. Poly(ethylene - *co*-tetrafluoroethylene) (ETFE) sheet was used as a base matrix and irradiated with 200 kV electron beams up to 150 kGy under N_2 atmosphere at room temperature [1]. The irradiated ETFE sheets were then exposed to air for 30 min and grafted in 40 wt.% *N*-isopropylacrylamide / 2-propanol solution at 80 ºC for 2, 4, 6, 18 and 24 hours, respectively. The grafted sheets were washed by an ultrasonic water bath for 60 minutes. HeLa cells (BioResource Center, RIKEN, Wako, Japan) were cultured in minimum essential medium eagle, supplemented with 10% fetal bovine serum and 1% penicillin/streptomycin/L-glutamine. HeLa cells were maintained in a cell culture incubator at 37 ºC in humidified atmosphere with 5% CO_2.

HeLa cells adhered and proliferated on poly (*N*-isopropylacrylamide) (PNIPAAm) grafted ETFE sheets at 37 ºC (Fig. 1 (left)) but not on non-treated ETFE. The adhered HeLa cells were detached from the surface when temperature was reduced to below transition temperature of PNIPAAm at 20 ºC as shown in Fig. 1 (right). Cell detaching rate (*CDR*) was calculated from the following equation,

$$CDR\ [\%] = (N_A - N_D) / N_A \times 100 \qquad (1)$$

where N_A is the number of adhered HeLa cells in a surface unit area of the fabricated sheet at 37 ºC and N_D is the number of remained HeLa cells after thermal treatment at 20 ºC. CDR value gradually increased with the grafting periods and reached at 77% for 24 h grafting. The water contact angle at 20 ºC also decreased, indicating grafting degree increased, with the grafting period. It is concluded that cell adhesion and detachment are controlled by the grafting degree of PNIPAAm.

Radiation-induced chemical reactions in hydroxypropyl cellulose hydrogel

In the previous study, we reported the hydrogel dosimeters for cancer radiation therapy [2]. The dosimeter consists of radiation-crosslinked hydroxypropyl cellulose (HPC) gel matrix, 2-hydroxyethyl methacrylate, polyethylene glycol dimethacrylate, tetrakis(hydroxymethyl)phosphonium chloride and water. HPC hydrogel is transparent, contains much water, and prevent diffusion of small particle produced by the irradiation for the evaluation of the dose distribution. As aforementioned, HPC hydrogel has some advantages as base matrix for dosimeters. Chemical reactions happened in the hydrogel are considered to be the same as those in water, however, basic parameters, such as initial yields and rate constants of reactive species, are not clear so far.

A study on pulse radiolysis of HPC hydrogel was carried out in order to directly observe the behaviors of reactive species [3]. The HPC hydrogel was irradiated with 5.9-6.1 MeV pulsed electron at pulse width of 10 ps. Transient absorbances were recorded by a streak camera system and a pulse-probe system for qulitative and quantitative analyses, respectively.

Figure 2 shows fast kinetics of hydrated electron (e^-_{aq}) in pure water and HPC hydrogel. There is a slight difference in the beginning part (< 200 ps) of the kinetics in these matrix although whole kinetics over 3.8 ns are almost identical as shown in the inset. The slightly higher initial yield in HPC hydrogel is thought to be due to direct ionization of HPC. The rapid disappearance of the additional amount indicates that electrons ejected by the direct ionization rapidly react with holes on HPC or on surrounding water molecules in hydration layer or with HPC itself.

Rate constants of reactive species, hydroxyl radical (•OH) and e^-_{aq}, with the repitition unit of HPC were determined to be 4.5×10^9 and 1.8×10^7 $M^{-1}s^{-1}$, respectively. These values are reasonable in considering of the rate constants of glucose, backbone unit of HPC, in water.

References

[1] Y. Yamahara *et al.*, Radiat. Phys. Chem., in press.
[2] A. Hiroki *et al.*, Nucl. Instrum. Meth. B, **365**, 583 (2015).
[3] S. Yamashita *et al.*, Radiat. Res., **186**, 650-58 (2016).

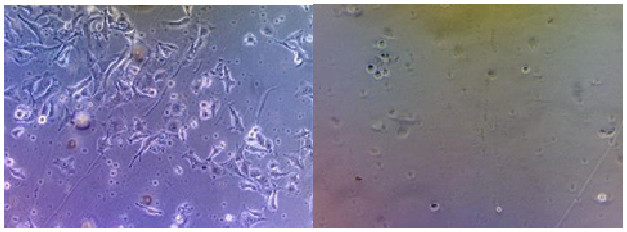

Fig. 1. Thermo-responsivity of HeLa cell adhesion on ETFE sheets grafted with *N*-isopropylacrylamide for 24 h; (left) HeLa cells cultured for 6 h on the sheet, (right) HeLa cells remained on the sheet after thermo-treatment for 2 h at 20 ºC.

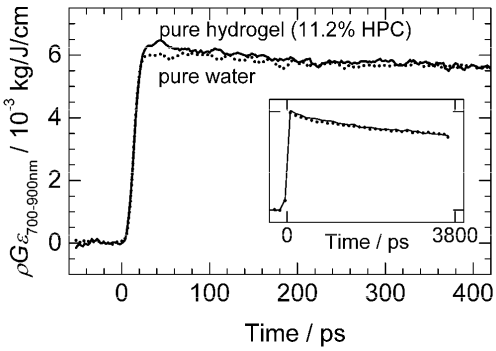

Fig. 2. Fast kinetics of e^-_{aq} in pure water and HPC hydrogel under air observed with the pulse-probe system. Inset shows longer kinetics over 3.8 ns with the same system.

P1-6 Environmental Polymer Research Project

Leader : Noriaki Seko

Project “Environmental Polymer Research” has been developing the functional polymer materials for high performance adsorption materials by radiation induced graft polymerization technique using such as electron beams, γ-rays. Fibrous metal adsorbents obtained by this technique can be used for recovering particularly low concentration metals. Also, we have been developing the surface treatment technique of a polymer substrate {1-50~54 in Part II}.

Arsenic (V) removal by radiation-induced emulsion grafted adsorbent [1]

Arsenic (As) is a naturally occurring substance in the earth, and it very widely distributes in the environment more often as arsenic sulfide or as metallic arsenates and arsenides. Most of the As produced commercially accumulates as a by-product in the melting of non-ferrous metal ores containing Cu, Ni, Pb, Ag and Co. Being inorganic, pentavalent arsenic (As(V)) is the most common species present in well-oxygenated surface waters. The most commonly used removal techniques for As(V) from aqueous matrixes are: (1) coagulation processes; (2) desalting technique; (3) ionexchange; (4) adsorption technique. Many types of adsorbents have been investigated for the removal of As(V) from aqueous effluents. But conventional adsorbents had a slow adsorption rate, and were difficult to adsorb low-concentration As(V) efficiently. Therefore, we have been developed a new method to make more effective adsorbents for As(V) removal. Such a novel nonwoven fabric adsorbent having 4-vinylpyridine (VP) functional groups was prepared by using radiation-induced emulsion graft polymerization method and grafting 4-vinylpyridine monomer onto a polyethylene-coated polypropylene nonwoven fabric(NF) in aqueous emulsion solution. The grafting conditions of VP monomer onto NF were optimized, and 150% of the degree of grafting (Dg) of VP was prepared using 30 kGy pre-irradiation dose, 5% VP monomer concentration and 0.5% (w/w) Tween20 in aqueous emulsion solution. The grafted VP chains were then quaternized in dimethyl sulfate solution for the preparation of As adsorbent (As-ad). As-ads were evaluated in batch adsorption experiments for As(V) ions by studying the pH, contact time, and initial As(V) ion concentration parameters. Results showed that As-ad has high adsorption performances and experimental adsorption capacity was 98 mg-As(V)/g-As-ad at pH 7.

Radiation-induced emulsion grafting with RAFT polymerization [2]

Radiation-induced graft polymerization (RIGP) method has advantages such as simplicity, control over the process, and adjustment of the material composition and structure. Most RIGP processes proceed via free radical mechanism. Free radical polymerization does not offer a complete control on the molecular weight and molecular structure of the polymer chains. It has been established that chain transfer agents (CTA) has profound effects in free radical polymerization processes. Developments in the field of chain transfer polymerizations include the use of conventional transfer agents, catalytic transfer agents based on cobalt complexes, degenerative transfer, and chain transfer by reversible addition-fragmentation (RAFT). The aim of this purpose is to study the graft polymerization of emulsified glycidyl methacrylate (GMA) onto electron beam irradiated polyethylene/polypropylene (PE/PP) nonwoven fabric in the presence of the RAFT agent 4-cyano-4-((phenylcarbonothioyl)thio)pentanoic acid (CPPA). It also discusses the effects of various experimental parameters to the degree of grafting (Dg). CPPA has a carboxylic group which allows good solubility in aqueous solutions, and it has been shown to control the polymerization of methacrylate monomers, such as 2-(dimethylamino)ethyl methacrylate and oligo(ethylene glycol)methacrylate, in aqueous media with addition of small amount of organic solvent. To the best of our knowledge, this is the first study that explores the effect of adding chain transfer agent in the graft polymerization of an emulsified monomer from an electron beam-irradiated olefin polymer. In a first trial experiment, GMA in emulsion phase was successfully graft polymerized from PE/PP by the combination of the RAFT technique and electron beam-induced initiation, leading to the oxirane group functionalization of the olefinic fibers. The RAFT agent CPPA was used, and the graft polymerization was carried out in a mixture that contained more than 90% water. The combination of CPPA-mediated process and grafting in emulsion state allowed the synthesis of PE/PP grafted polymers with tunable Dg over time. The presence of dithiobenzoate-capped PGMA homopolymers in the reaction medium as suggested by the NMR results supports the proposed reactions for the RAFT-mediated graft polymerization of GMA from pre-irradiated PE/PP backbone polymer. The gel permeation chromatography data showed that the PGMA homopolymers, which approximates the properties of the grafted chains, had reasonable distribution of molecular weights (PDI <1.8) (Table 1). The calculated Dg from the RAFT-mediated graft polymerization increased with increasing absorbed dose and grafting time. However, the Dg tended to decrease with increment in monomer and CPPA concentrations. The reactive pendant oxirane group of GMA provides versatility to the PE/PP-g-PGMA which can be useful for different specialty applications.

References

[1] P. A. Kavakli *et al.*, Radiat. Phys. Chem., **127**, 13 (2016).
[2] J. F. Madrid *et al.*, Colloid Polym. Sci., **295**, 1007 (2017).

Table 1
GPC data for free PGMA from grafting of GMA of PE/PP.

Reaction time (h)	Dg (%)	Conversion (%)	$M_{n,GPC}$	PDI
1	98	9.8	6,000	1.53
3	182	24.6	11,00	1.80

Adsorbed dose: 20 kGy, CMA conc.: 3%, GMA to RAFT molar ratio: 400/1.

P1-7 Element Separation and Analysis Research Project

Leader: Hironori Ohba

Quantum beams are versatile sources for materials processing. Our project explores basic process of the laser-matter interaction to separate elements from radioactive waste, and performs remote analysis of elements in an aqueous solution by laser irradiation. For element separation, we applied the separation using laser-induced particle formation technique for recovery of precious metals from high-level radioactive waste. For element analysis, laser-induced breakdown spectroscopy with a unique liquid jet has been applied. The recent results of our project are introduced as follows.

Separation of palladium from high-level radioactive waste by laser-induced particle formation

The separation using laser-induced particle formation is a novel technique to separate precious metals, PMs (PM=Au, Pt, Pd and so on), from industrial wastewater [1]. In this technique, the separation is performed by irradiation of a pulsed ultraviolet (UV) laser to the wastewater, which leads to photo-reduction of the PM^{n+} ions into PM^0 neutrals, because energy of the UV laser (> 3.5 eV) is well beyond reduction potential of PMs (for example, the standard electrode potential of the reduction $Pd^{2+} + 2e^- \rightarrow Pd(s)$ is + 0.987 V). The PM^0 neutrals spontaneously form metal-particles, which is recovered by filtration. The energy of the UV laser that needs to reduce the PM^{n+} ions is correlated with the reduction potential of the PMs. Thus, by arranging the energy of the UV laser, we can select the PM species that is recovered by the laser induced particle formation.

Advantage of the separation using laser-induced particle formation is brief and quick operation. Such technique is required in the metal separation from the solution containing radioactive element. Thus, we applied the separation using laser-induced particle formation for recovery of Pd from high-level radioactive waste (HLW) [2]. As shown in Table 1, the HLW includes various kinds of elements: actinides (Am, Np, Pr, Cm. Ru, U), lanthanides (Nd, Sm, La), PMs (Pd, Ru, Rh) and so on. However, the laser-induced particle formation succeeded in selectively separating the Pd metal with high efficiency (91.4%) without recovering the radioactive elements. This result suggests availability of the laser-induced particle formation for the separation of PMs in the HLW.

Analysis of zirconium in aqueous solution using laser-induced breakdown spectroscopy technique

In the post-accident Tokyo Electric Power Company Fukushima Dai-ichi Nuclear Power Plant (F1-NPP), the reactors have been filled with water injected for urgent cooling which contains seawater and a part of nuclear fuel debris. It is indispensable to know the content of zirconium in the contaminated water from the viewpoint of the accident analysis for the decommissioning of the nuclear power plant. In the context of the F1-NPP decommissioning process, laser-induced breakdown spectroscopy (LIBS) has many advantages. The purpose of the present work is to demonstrate the on-line monitoring capability of the LIBS coupled with the ultra-thin liquid jet sampling method [3]. The study focuses on zirconium in aqueous solution, considering that it is a major element in the F1-NPP fuel debris that has been subject to only a few LIBS studies in the past.

Using a zirconium mono-element aqueous solution, two regions of interest with many high intensity zirconium lines have been observed around 350 nm in the case of the ionic lines and 478 nm in the case of atomic lines. The best analytical conditions for zirconium are different depending on the analysis of ionic lines or atomic lines. Figure 1 shows relationship between emission-light intensity area and the concentration of zirconium in aqueous $ZrO(NO_3)_2 \cdot 2H_2O$ solution for ionic line of 349.62 nm (Calibration curve). The curve showed good liearlity and correlation. A low limit-of-detection of about 4 mg/L for ionic lines could be obtained, showing that LIBS coupled with the ultra-thin liquid jet sampling technique is a promising alternative for more complex solutions found in the F1-NPP, namely mixtures containing zirconium [4].

References

[1] M. Saeki *et al*., J. Photochem. Photobiol. A, **299**, 189-93 (2015).
[2] S. Asai *et al*., Anal. Chem., **88**, 12227-33 (2016).
[3] H. Ohba *et al*., Optics Express, **22**, 24478-90 (2014).
[4] A. Ruas *et al*., Spectrochim. Acta B **131**, 99-106 (2017).

Table 1
Recovery efficiency (%) of elements contained in HLW by laser-induced particle formation.

Pd	**91.4±0.5**	Mo	<0.01	Ru	0.03
Am	<0.01	Nd	0.03	Sm	<0.01
Ba	0.10	Np	<0.01	Sr	0.26
Ce	0.08	Pr	0.05	Tc	0.45
Cm	<0.01	Pu	<0.01	U	<0.01
Cs	0.03	Rb	0.07	Zr	0.02
La	0.05	Rh	0.05		

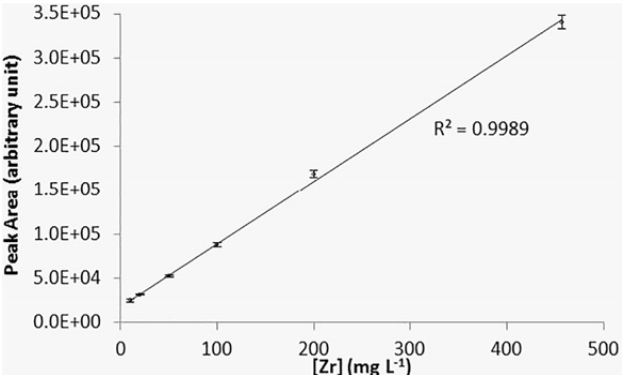

Fig. 1. Relationship between emission-light intensity area and the concentration of zirconium atoms in aqueous $ZrO(NO_3)_2 \cdot 2H_2O$ solution (calibration curve).

Part Ⅰ

2. Life Science

P2-1 Ion Beam Mutagenesis Research Project

Leader : Yutaka Oono

The long-term objective of our project is to develop applications of quantum beam technology in a wide range of applied biological fields including sustainable agriculture and environmental conservation through creating valuable genetic resources of plants and microorganisms. For this purpose, we have been trying to undestand mechanism of mutagenesis and establish efficient ion-beam mutagenesis techniques {2-11, 18~21 in Part II}. Detailed analyses of obtained mutants in model organisms such as yeast, *Chlamydomonas*, and rice enable to identify novel genes that link to important biological functions and can shed light on life's mysteries {2-10, 13~14, 25}. We also try to generate new valuable plants and microbes by ion beam under collaboration with academic or industrial research organizations {2-12, 15~17, 22, 24}. To reveal molecular biological basis of radio resistant organisms is another major interest of the project {2-23}.

The best ionizing radiation to induce large mutant sectors in plants but little loss of genetic information

In the process of ion-beam breeding for plants that reproduce by vegetative propagation, pieces of leaves, petals, callus (a batch of undifferentiated plant cells), or buds are targets of the ion-beam irradiation, followed by re-generating whole plants from the pieces of tissue by tissue culture techniques. The regenerated plant is thought of as a chimera that consists of sectors of mutated tissues and non-mutated tissues. A horticultural method, cutting is often applied to increase population of desired mutated cells and obtain a mutant clone consisting of only mutated cells. Therefore, the size of the sector is very important for effective detection of mutants. Larger mutant sectors are preferred to easily remove undesired non-mutated cells. Hase et al. established an excellent experiment system, using model plant *Arabidopsis thaliana*, in which sectors of mutated cells are visually detected [1]. The *Arabidopsis GLABRA1* gene (*GL1*) that required for hair formation on a leaf surface is used in this work. A disruption of the *GL1* gene leads to hair loss on leaves (Fig. 1). Arabidopsis seeds having single copy of the *GL1* gene are irradiated with different ionizing radiations; 15.8 MeV/u neon ions, 17.3 MeV/u carbon ions, and ^{60}Co gamma rays with doses causing the same effect on survival reduction, then frequency and size of hair-less sectors were examined in the seedlings. As shown in Table 1, although frequency of emergence of mutant sectors was the same regardless of the properties of ionizing radiations, neon and carbon ions induced large sectors at higher rate than gamma rays. DNA analyses around the *GL1* gene in the mutated sectors revealed that fraction of large DNA deletions (> several kbp) was less in carbon than neon ions. These results suggest that ion beams with moderate linear energy transfer (LET) values (carbon ions) are most effective for induce mutant sectors with less causing extensive genetic damage.

Analysis of an ion-beam mutant revealed mode of action of a herbicide, 2,4-D on cytoskeletal structure

2,4-Dichlorophenoxyacetic acid (2,4-D), a functional analogue of plant hormone auxin, is used as a herbicide as well as an exogenous source of auxin in plant tissue culture. Previous identification and analyses of *Arabidopsis* ion-beam mutant (*aar1-1*) have demonstrated a small acidic protein (SMAP1) functions to facilitate the 2,4-D-induced root growth inhibition. Whereas, another line of experiments has suggested that 2,4-D inhibits root growth through disrupting cytoskeletal structure, actin. Thus, SMAP1 and actin are two major components for modulating 2,4-D response. In the current work [2], under the collaboration with Iwate University, we revealed SMAP1 functions positively to facilitate the 2,4-D induced de-polymerization of actin (Fig. 2). Furthermore, we found that components of ubiquitin proteasome pathway (a cellular system for protein degradation) also function in the disrupting effects of 2,4-D on actin. Genetic analyses using *Arabidpsis* mutants suggested that SMAP1 and the ubiquitin proteasome pathway act synergistically and function as positive modulators for 2,4-D-induced alteration of actin in a root cell.

References

[1] Y. Hase *et al.*, Nucl. Instrum. Meth. Phys. Res., B, **391**, 14 (2017).
[2] M. Takahashi *et al.*, Plant J., **89**, 940 (2017).

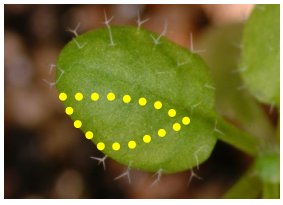

Fig. 1. A radiation-induced hair-less sector (surrounded by yellow dots) on an *Arabidopsis* leaf.

Table 1
Frequency and size of the sectors and occurrence of DNA deletions around the *GL1* gene.

	neon ions	carbon ions	gamma rays
Mean LET (keV/μm)	352	113	0.2
Frequency of emergence of mutant sectors (%)	2.8	2.7	3.0
Fraction of large sectors (%)	29.0	25.0	7.9
Fraction of sectors with large DNA deletions (%)	25.8	9.4	2.6

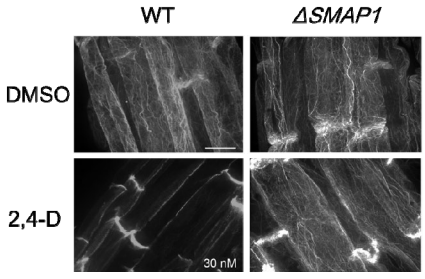

Fig. 2. Effects of 2,4-D on intracellular actin organization of wild type (WT) and the SMAP1-inactivated plant (*ΔSMAP1*). The figure shows epidermal cells of roots treated with or without 30 nM 2,4-D in DMSO. Actin filaments, visualized as white fibres in the cells, are disappeared by the 2,4-D treatment in WT but not in *ΔSMAP1*. The bar indicates 10 μm.

P2-2 Microbeam Radiation Biology Research Project

Leader : Tomoo Funayama

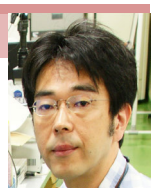

Project “Microbeam Radiation Biology” has developed a technology to irradiate biological samples locally using heavy ion microbeam system of TIARA, and is promoting analysis of biological effect of heavy ion hits. Microbeam is a radiation that miniaturizing the irradiation field below the cell size, and enables to irradiate a specific region of a biological sample under a microscope view. This unique irradiation method makes possible to induce a radiation damage on only targeted region of biological specimen. Furthermore, by targeting a part of the cell with extremely precise microbeam, it is possible to clarify the biological phenomenon which cannot be elucidated by conventional broad field irradiation such as the response of single ion hit on individual intra-cellular organella. The goal of our research is to advance a technology for applying microbeam irradiation to wide range of biological target and establish “Microbeam biology” beyond conventional radiation research.

Development of heavy-ion microbeam system of QST-Takasaki for wide range of biological research [1]

Unevenness of microdosimetric energy distribution by low fluence heavy-ion radiation prevents precise analysis of single heavy-ion hit on individual cells. To overcome this problem, we developed a system for target-irradiating individual cells, and established a method for irradiating cultured cells using collimating heavy-ion microbeam system [2]. Using this method, we demonstrated that single ion hit of high-LET argon ion on nucleus completely inhibited proliferation of CHO-K1 cells [3]. During a process of these research and development, we become feel strongly that microbeam has great possibilities for life science research. Therefore, we start to put into the place our vision by applying microbeam local irradiation on not only a cell but also cultured cell population and individuals in which various cells function organically.

In a mixture population of irradiated and non-irradiated cells, a biological phenomenon, which are called “bystander effects”, are induced on non-hit cells based on transduction of irradiated signal from hit cell. Microbeam, which can target and irradiate specific cells of the population, is a useful tool for analyzing bystander effect. However, to clarify the whole picture of the response, we need to analyze all cells individually in the bystander population over the long term after the irradiation. Therefore, we developed offline live-cell imaging system for long-term analysis of microbeam irradiated cell populations. The system can obtain live time-lapse fluorescent image of individual cells without harmful effect of fluorescent observation using high sensitivity CMOS camera and LED excitation light. Using the system, we became able to carry out the comprehensive analysis of dynamics of the entire bystander cell population over a long duration.

Targeting irradiation of individual organisms requires longer projectile range and variable size of beam spots. Therefore, we developed a microaperture of 60 μm in diameter, which fit a body width of nematode *C. elegans* and also suitable for irradiating local part of medaka-fish fry. New microaperture has more than 350 μm thickness of metal disc with pinhole that extract heavy-ion beam into air, therefore, it can collimate higher energy carbon ion ($^{12}C^{6+}$ 320 MeV) with 2.1 mm projectile range in water. Using this microaperture, we became able to irradiate a part of nematode and medaka fish fry, and analyze the effect on whole body response.

By these technological advancements of microbeam irradiation, potential subjects of life science research using heavy-ion microbeam of TIARA become expanding. By further expanding of utilization of microbeam irradiation, we will aim for the realization of multirole microbeam system that cannot be realized by microbeams in other institutions.

Utilization of polypropylene film dish for analyzing heavy-Ion hit effect of irradiated cells {2-01 in Part II}

In order to analyze the biological effect of heavy-ion hit on individual cells irradiated precisely with focusing heavy-ion microbeam, there needs a cell sample preparation that enables to observe hit effects over a long times.

To develop a method of cell preparation that enables long-term post incubation of irradiated cells, we examined a possibility to adopt a polypropylene film of 3 μm thick as an attaching surface for the cells. A dish for testing cell growth ability on polypropylene film was constructed by adhering film to a ring-shaped acrylic frame. After washing and sterilization, the dish was treated with vacuum plasma to change hydrophilicity of the film for examine an effect of hydrophilicity of cell attaching surface.

As an evaluation index of long-term culture on the film, we measured cell growth ability of HeLa cells. HeLa cells were irradiated with gamma-ray, inoculated in film dish, and the number of grown cells was counted in every 24 hours up to 3 days. As a control, commercial cell dishes with and without tissue culture treatment was also examined.

Initial attachment ability of the cells did not show significant differences among tested 4 type of cell dish. Growth on polypropylene film dish became lower than that on commercial dishes, however, a treatment with vacuum plasma improved restricted growth in some extent. Because cultured cells were difficult to attach on a hydrophilic surface, a lower growth ability on film dish will be caused by a hydrophobicity of polypropylene film. Vacuum plasma is known to improve hydrophilicity of material surface. The improvement of cell growth on plasma treated film may be a result of improved hydrophilicity of polypropylene film surface.

Growth curves of irradiated cells showed almost similar trend with non-irradiated cells. However, irradiated cells could not grow at all in polypropylene film dish without plasma treatment. From there result, we concluded that to utilize polypropylene film as a cell attachment surface for microbeam irradiation, improvement of hydrophilicity by vacuum plasma treatment will be necessary.

References

[1] T. Funayama *et al.*, Radiat. Biol. Res. Comm. **51**, 336 (2016). (in Japanese).
[2] T. Funayama *et al.*, J. Radiat. Res., **49**, 71 (2008).
[3] T. Funayama *et al.*, Radiat. Res., **163**, 241 (2005).

P2-3 Medical Radioisotope Application Research Project

Leader : Noriko S. Ishioka

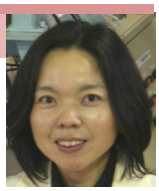

The research objective of our project is to develop the radiopharmaceuticals labelled with useful radioisotopes for cancer diagnosis and therapy. Our project focuses on research of the radioisotope drug delivery system (RI-DDS) using bioactive compounds such as antibodies and peptides in order to make the most of the ability of radioisotopes. We also search for novel molecular targets that enable effective diagnosis or therapy with radiopharmaceuticals {2-40~41 in Part II}.

Efficacy of system L amino acid transporter 1 inhibition as a therapeutic target in esophageal squamous cell carcinoma [1]

Esophageal cancer is one of the most common cancers and highly lethal. Early detection of esophageal cancer is difficult because patients rarely experience subjective symptoms in the early stages of the cancer. In addition, as esophageal cancer easily metastasizes, patients often have advanced or metastatic disease on admission. Patients with unresectable disease are usually treated with chemotherapy. However, common chemotherapeutic agents are not curative, and then the prognosis after treatment remains dismal. Therefore, it is important to establish novel molecular targets for improvement of therapeutic efficacy in esophageal cancer.

Amino acid transporters are essential for not only normal cells but also growth and survival of cancer. System L amino acid transporter 1 (LAT1) is highly expressed in various primary human cancers, and LAT1 expression has a close relationship with cell proliferation, angiogenesis and cell cycle regulator in human tumor tissues. The high expression of LAT1 could be an independent prognostic marker in prostate, breast, pancreatic, lung, tongue, and biliary tract cancer. Therefore, the possibility of molecular-targeted therapy focused on LAT1 inhibition has been investigated in many cancers. Recently we have found that LAT1 is closely related to the expression of CD98, growth, angiogenesis, and glycolysis in surgically resected human esophageal cancer, and expression of LAT1 could be an independent prognostic marker. However, the therapeutic efficacy of LAT1 inhibition against esophageal cancer remains unclear. In this study, we undertook both *in vitro* and *in vivo* studies to investigate the suppressive effects of LAT1 inhibition on the growth of esophageal cancer.

Both LAT1 and CD98, which covalently associates to LAT1 on the cell membrane, were expressed in human esophageal cancer cell lines KYSE30 and KYSE150. Quantitative polymerase chain reaction analysis showed that the expression of LAT1 was much higher than other subtypes of LAT. A selective inhibitor of LAT, 2-aminobicyclo-(2,2,1)-heptane-2-carboxylic acid (BCH), significantly suppressed cellular uptake of a LAT1 substrate, L-^{14}C-leucine. These results indicate that BCH could inhibit LAT1-dependent amino acid uptake in these esophageal cancer cells. BCH suppressed cell proliferation in a dose-dependent manner. In addition BCH inhibited phosphorylation of mammalian target of rapamycin, eukaryotic translation initiation factor 4E-binding protein 1 and 70 kDa ribosomal protein S6 kinase protein, and induced cell cycle arrest at G1 phase. These results suggest that LAT1 inhibition suppresses cell proliferation through inhibiting both mTOR signaling and cell cycle progression. BCH additively enhanced the growth inhibitory effects of standard chemotherapeutic agents for esophageal cancer, 5-fluorouracil and cisplatin. In tumor-bearing mice, daily treatment with BCH significantly delayed tumor growth (Fig. 1A), and weight loss, an indicator of toxicity, was not observed (Fig. 1B). BCH also decreased glucose metabolism (Figs. 1C and D). These results suggest that LAT1 inhibition potentially suppresses esophageal cancer growth *in vivo*. Therefore, we conclude that LAT1 can be a novel promising target for esophageal cancer therapy.

Reference

[1] Y. Ohshima *et al.*, Cancer Sci., **107**, 1499 (2016).

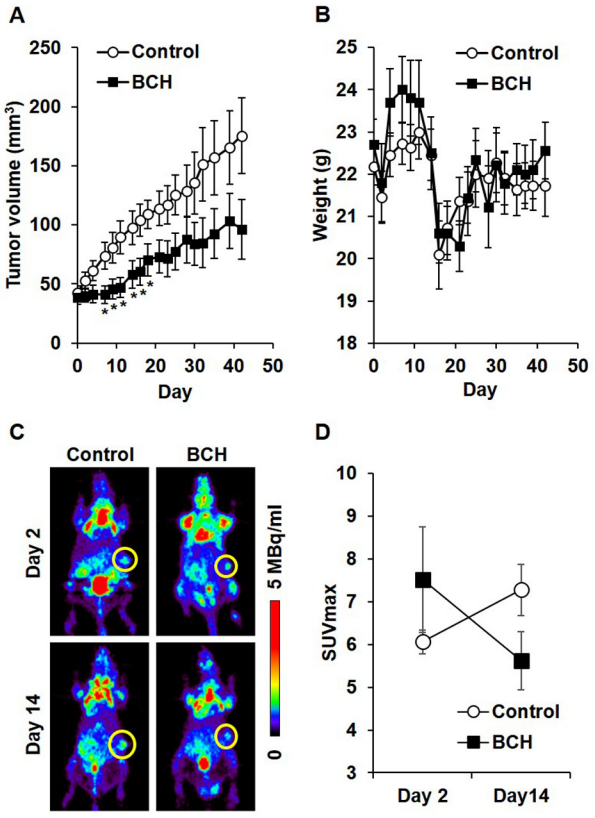

Fig. 1. Antitumor effect of BCH on KYSE150 tumor-xenograft model. (A) Growth curves of KYSE150 tumor after treatment with saline or BCH (sample number (n) =10). *Statistically significant difference from control (P<0.05). (B) Body weight of KYSE150 tumor-bearing mice after treatment with saline or BCH (n=10). (C) Representative coronal section of ^{18}F-fluorodeoxyglucose-positron emission tomography (^{18}F-FDG-PET) images of KYSE150-bearing mice at 2 h after ^{18}F-FDG injection. PET imaging was carried out at indicated days after the day of grouping. Yellow circle shows the tumor. The calibration bar is shown to the right of images. (D) Maximum standardized uptake value of ^{18}F-FDG-PET images at day 2 and day 14 after the day of grouping (n=4).

P2-4 Accelerator-Neutron-Generated Radioisotope Research Project

Leader : Kazuyuki Hashimoto

In our project, we have proposed a new system for the generation of medical radioisotopes for cancer diagnosis and therapy such as ^{99}Mo ($T_{1/2}$ = 66 h), ^{90}Y ($T_{1/2}$ = 64 h), ^{67}Cu ($T_{1/2}$ = 61.8 h), and ^{64}Cu ($T_{1/2}$ = 12.7 h) with accelerator neutrons for domestic production of medical radioisotopes [1]. The neutrons were obtained by the ^{nat}C(*d*,*n*) or ^{nat}Be(*d*,*n*) reaction using 40 - 50 MeV deuterons provided from the TIARA cyclotron. A method for separation and purification of aimed radioisotope from the target materials and radioactive impurities has also been developed. It was shown that the quality of ^{67}Cu produced by accelerator neutrons was sufficient for the biodistribution study {2-40 in Part II}.

Thermochromatographic separation of ^{99m}Tc from ^{100}MoO$_3$ irradiated by accelerator neutrons

Technetium-99m ($T_{1/2}$ = 6 h) has been most widely used in nuclear medicine diagnostic procedures. Molybdenum-99, the mother radionuclide of ^{99m}Tc, has been produced using a limited number of aging research reactors worldwide for many years. Conventional production of ^{99}Mo, a fission product of ^{235}U, however, has 4 orders of magnitude larger specific activity than ^{99}Mo produced via ^{100}Mo(n,2n)^{99}Mo reaction using accelerator driven neutrons. Separation of ^{99m}Tc from ^{99}Mo produced by accelerator driven neutrons therefore requires a system to process a large mass of sample ^{100}MoO$_3$ to compensate for the low specific activity of ^{99}Mo, while keeping the same radiochemical/chemical quality.

Thermochromatographic separation has the following advantages for processing ^{99}Mo with a low specific activity.
1) Processing a large mass (>100 g) of MoO$_3$
2) Minimum level of chemical contamination
3) High and consecutive production yield

Technetium-99m separation is conducted in a three zone tubular furnace containing quartz tubes, where three platinum boats to hold MoO$_3$ are placed inside, as shown in Fig. 1. A maximum temperature of the furnace zone was set at around 830 ºC to melt the irradiated MoO$_3$ samples. ^{99m}Tc probably in the form of oxide is vaporized at this temperature and released from the molten MoO$_3$. The furnace temperatures of the other two zones were lower to make a temperature gradient within the travelling pass of vaporized ^{99m}Tc and eventually ^{99m}Tc oxide deposits separated from ^{99}Mo. The deposition of ^{99m}Tc is focused by a crumpled gold wire placed within a targeted region (Fig. 1b). The deposited and the remained within the sample are monitored by CdZnTe detector (Fig.1e) in real time. Some of the vaporized MoO$_3$ and ^{99m}Tc oxide was condensed in separate regions at around 500 ºC and 300 ºC respectively. Moist oxygen gas was used to enhance oxidation of ^{99m}Tc and separation efficiency.

As shown in Fig. 1, the deposited ^{99m}Tc was washed with 0.1 M NaOH solution, which was then passed through a cation exchange cartridge (Dionex OnGuard II-H, Thermo Fisher Scientific, Inc.) connected with an alumina cartridge (Sep-Pak Alumina A Plus Light, Walters, USA). The cartridges were washed with ultrapure water and a few millilitres of physiological saline solution were loaded onto the alumina cartridge to obtain the condensed ^{99m}TcO$_4^-$ solution in a vial. The quality of the final ^{99m}Tc (Na^{99m}TcO$_4$) was demonstrated to be compatible to a commercially available product [2].

Recovery efficiency of enriched ^{100}MoO$_3$ irradiated by accelerator neutrons [3]

If ^{99}Mo is commercially produced throughout the year using accelerator, the amount of ^{100}MoO$_3$ raw material required for irradiation (minimum 100 g at a time) would rise to over 2 kg a month, costing 100 million yen (*e.g.* 50,000 yen/g) every month. Even if 90% is recycled (10% is compensated), the financial loss would be equivalent to the selling price of 500 Ci (18.5 TBq) ^{99}Mo (～20,000 yen/Ci-^{99}Mo). Recycling the used ^{100}MoO$_3$ is therefore absolutely essential in terms of economic efficiency.

Over 90% of ^{100}MoO$_3$ after separating ^{99m}Tc from were found in the crucibles (sample holder). The reminder which is vaporized and left the crucible can be trapped as a crystal deposit within the thermochromatographic separation system (Fig.1a and b). The distribution of these ^{100}MoO$_3$ crystals were investigated after ^{99m}Tc separation and the ^{100}MoO$_3$ was recovered using a simple washing with water under ultrasonciation. Of the 117 g original sample 99% was recovered using this method, without changing the chemical form of ^{100}MoO$_3$ nor being contaminated by any chemicals.

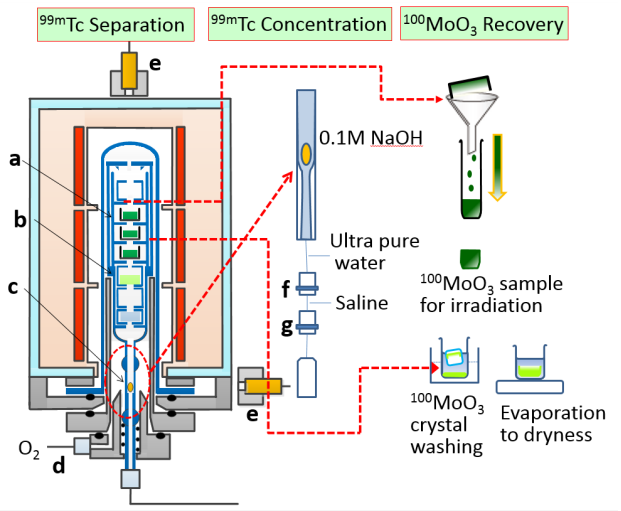

Fig. 1. Schematic diagram of thermochromatographic ^{99m}Tc separation, purification and ^{100}MoO$_3$ recovery: ^{100}MoO$_3$ sample (a), ^{100}MoO$_3$ crystal (b), gold wire for ^{99m}Tc deposition (c), moist oxygen inlet (d), CdZnTe detector (e), cation exchange column (f) and alumina column (g).

References

[1] Y. Nagai *et al.*, J. Phys. Soc. Jpn. **82**, 064201 (2013).
[2] Y. Nagai *et al.*, J. Phys. Soc. Jpn. **86**, 053202 (2017).
[3] M. Kawabata *et al.*, J. Phys. Soc. Jpn. **86**, 053201 (2017).

P2-5 Radiotracer Imaging Research Project

Leader : Naoki Kawachi

The aim of our project is to precisely measure, visualize, and characterize the biological processes of organs, using radioisotopes (RI) and imaging apparatus. We will establish systematized techniques for live-imaging using radiotracers, nuclear imaging apparatus, and kinetic analytical methods for understanding the transport function related to agriculture and medicine within living systems {2-37~39 in Part II}.

Imaging of radiocesium kinetics in a living plant based on a Cherenkov light imaging technology [1]

Radionuclide-based imaging strategies have elucidated the physiology invisible from the outside of a living plant by visualizing elemental kinetics using synthesized radionuclide tracers. After the nuclear disaster of Fukushima Daiichi nuclear power plant in 2011, high-resolution images of radiocesium (^{137}Cs) distribution are required to study cesium kinetics in plants. However, it is difficult to achieve a spatial resolution of the order of millimeters or sub-millimeters because the high-energy gamma photons penetrate the collimator of the gamma camera, or require scintillators of at least 1 mm size to detect the photons.

A Cherenkov light imaging method can visualize fine distributions of radionuclides emitting beta particles using an optical camera. The spatial resolution of a Cherenkov light imaging for radionuclide of ^{137}Cs was investigated [2]. It was shown that the method had a very high resolution, for instance, less than 220 μm for a 100 μm diameter ^{137}Cs point source placed 10 mm away from the lens surface of a CCD camera. Thus, unlike autoradiography, Cherenkov light imaging is able to image the distribution of radioisotopes in intact plants with a higher spatial resolution than other noninvasive plant imaging methods [3]. In this study, we have developed an imaging system that allows us to study radiocesium movement in live plants. Furthermore, we investigated the usability of this method to research plant physiologies with the other radionuclides of essential elements.

Our system comprised a highly sensitive cooled charge coupled device (CCD) camera (Hamamatsu Photonics, ORCA2-ER) and a bright lens (Xenon, F-number: 0.95, lens diameter: 25 mm) placed in a black box. The linearity of the sensitivity to the point source intensity was investigated with several ^{137}Cs point sources (with radioactivities of 10, 20, 50, 100, 200, 500, 1,000, and 2,000 kBq) and an acquisition time of 600 s. Besides, to demonstrate the use of this system for radiocesium detection in plants, an imaging experiment was performed with a live soybean plant over 7 days. First, the root of a 13-day-old soybean was dipped into 17 mL of a solution containing 10 MBq of ^{137}Cs, with no potassium. After one day, the solution was replaced with a potassium solution with no ^{137}Cs.

Image intensities in counts per second, acquired using the Cherenkov light imaging system, are plotted against the point source activity in Fig. 1. Figure 2 shows the ^{137}Cs distribution in the soybean plant. These high-resolution serial images indicate that ^{137}Cs was transported into the shoot and accumulated at the node.

The results of the two experiments described above lead us to conclude that Cherenkov light imaging may be a promising method for studying the kinetics of not only radiocesium but also other radioisotopes of essential elements in living plants.

References

[1] K. Kurita *et al.*, J. Nucl. Sci. Tech., **54**, 662 (2017).
[2] S. Yamamoto *et al.*, Nucl. Instrum. Meth. Phys. Res. A, **777**, 102 (2015).
[3] N. Kawachi *et al.*, J. Environ. Radioact., **151**, 461 (2016).

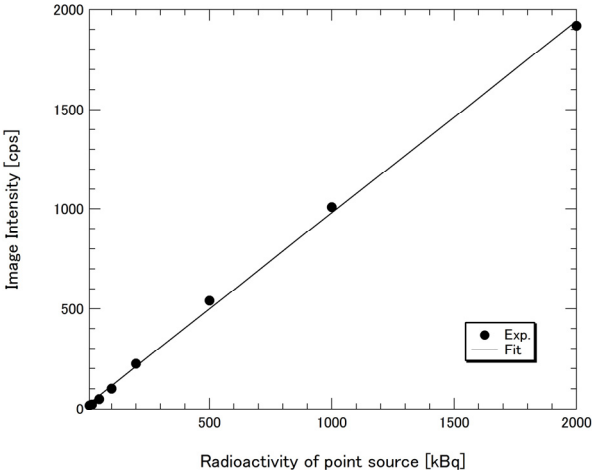

Fig. 1. Results of a performance test to evaluate the linearity of the Cherenkov light imaging system for a ^{137}Cs source. The data show linearity based on a correlation of $r^2 = 0.9987$ between the activity of the point source and the image intensity.

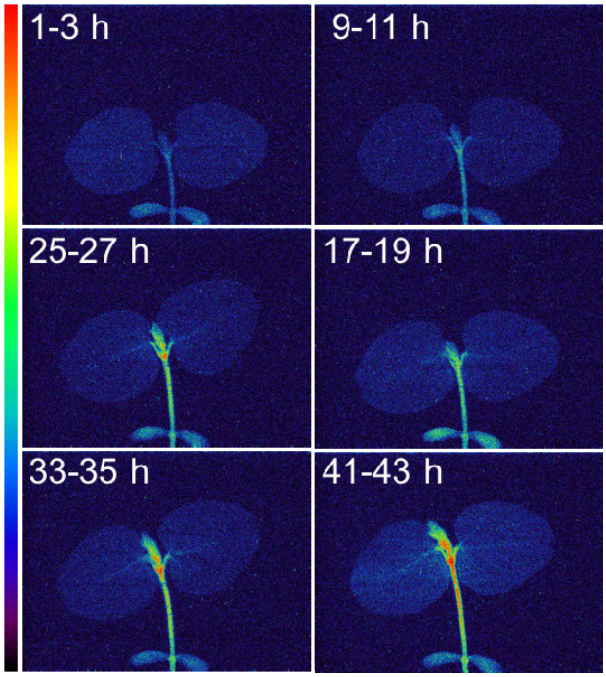

Fig. 2. Serial images of ^{137}Cs dynamics in a live soybean plant after feeding ^{137}Cs into the hydroponic culture.

P2-6 Radiation and Biomolecular Science Research Project

Leader : Akinari Yokoya

The objective of our project is to elucidate the radiation effect of living systems from molecular to cellular level using various advanced radiation sources. Theoretical approaches are also applied for mathematical modeling molecular and cellular responses to irradiation using computer simulation techniques. It is one of the unique characters of our group that both experimental and theoretical researchers cooperate closely to promote our projects. This allows us to understand the complex radiobiological phenomena from the physical point of view of "Systems Biology".

Efficiency of radiation-induced base lesion excision and the order of enzymatic treatment

To understand the enzymatical processes of clustered DNA damage, we investigated whether initial base excision repair processes at clustered DNA damage sites comprising multiple base lesions affect subsequent excision processes via the formation of additional strand breaks by glycosylase and apurinic/apyrimidinic (AP) endonuclease base excision enzymes [1]. Plasmid DNA (pUC18) as a model DNA molecule was exposed to high-linear-energy-transfer (LET) ionizing radiation (He^{2+} or C^{6+} ions) or low-LET ionizing radiation (X-rays) under various conditions to produce varied radical-scavenging effects. pUC18 was then sequentially or simultaneously treated with two bacterial base excision enzymes (glycosylases), namely, endonuclease III (Nth), and formamidopyrimidine-DNA glycosylase (Fpg), which convert pyrimidine (or abasic (AP) site) and purine (or AP site) lesions to single-strand breaks (SSBs), respectively. Yields of additional SSBs or double-strand breaks (DSBs) as digestion products were measured after changing the order of enzymatic treatments. There were few differences among the enzymatic treatments (Fig. 1), indicating that the treatment order did not affect the final yields of additional SSBs or DSBs formed by glycosylase activities. This suggests that the base lesion clusters induced by high- or low-LET radiation appear three or more base pairs apart, and are promptly converted to a DSB by glycosylase, regardless of the order of treatment.

Role of dynamic behavior of secondary electrons in DNA damage localization mechanism

To clarify the formation of radiation damage in DNA, particularly the clustering mechanism of lesions, the dynamic behavior of low-energy secondary electrons produced by ionizing radiation in water was studied by using a dynamic Monte Carlo code that considers the Coulombic force between electrons and their parent cations. The calculated time evolution of the mean energy, total track length, and mean traveling distance of the electrons indicated that the prehydration of the electrons occurs competitively with thermalization on a timescale of hundreds of femtoseconds. The decelerating electrons are gradually attracted to their parent cations by Coulombic force within hundreds of femtoseconds, and finally about 12.6% electrons are distributed within 2 nm of the cations. The collision fraction for ionization and electronic excitation within 1 nm of the cation was estimated to be about 40%. If these electrons are decelerated in a living cell, they may cause highly localized lesions around a cation in a DNA molecule through additional dissociative electron transfer (DET) as well as ionization and electronic excitation (EXC), possibly resulting in cell death or mutation.

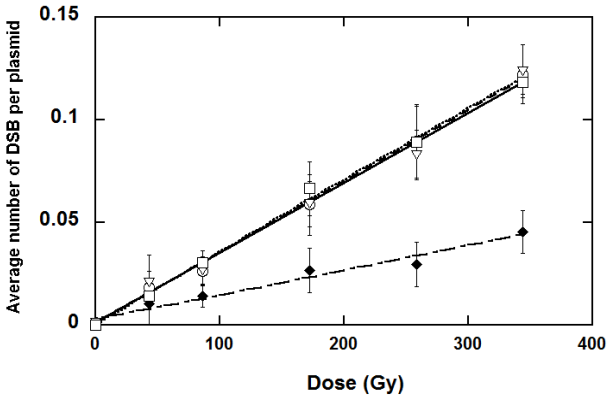

Fig. 1. Dependence on radiation dose of the number of DSBs determined from the fraction of the linear form of DNA after exposure of pUC18 plasmid DNA solution (10 mM Tris) to C ions (60 keV/μm) at 5.6 ºC following post-irradiation incubation for 30 min at 37 ºC in the absence of enzymes (◆), or treated first with Nth followed by Fpg (○), or first with Fpg and then Nth (□), or simultaneously with both Nth and Fpg (▽). The straight lines were drawn by the least squares method. The vertical error bars show ± SD for the values determined from three independent experiments.

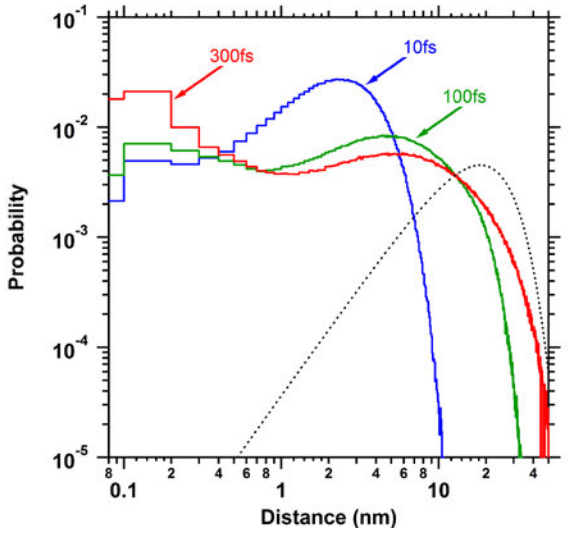

Fig. 2. Temporal evolution of spatial probability distributions of secondary electrons as a function of distance from ionization site. Dotted line shows the results obtained at 7 eV from a previous method by Ritchie et al. (1994).

References

[1] I. Shiraishi *et al.*, J. Radiat. Biol., 9**3**, 295 (2016).
[2] T. Kai *et al.*, J. Phys. Chem. A, **120**, 8228 (2016).

P2-7 Biomolecular Function Research Project

Leader : Motoyasu Adachi

Protein molecules play fundamental roles in biological system and exhibit unique functions on molecular recognitions, chemical reactions and energy transfer. Our research project has been focused on developments of the molecular design based on protein functional analysis using neutron, X-ray diffractions and ultra-short pulse laser. Firstly, we introduce our basic research concept (Fig. 1) and then activities regarding to two protein functional analyses to obtain useful knowledge for molecular engineering and application for industry and human health.

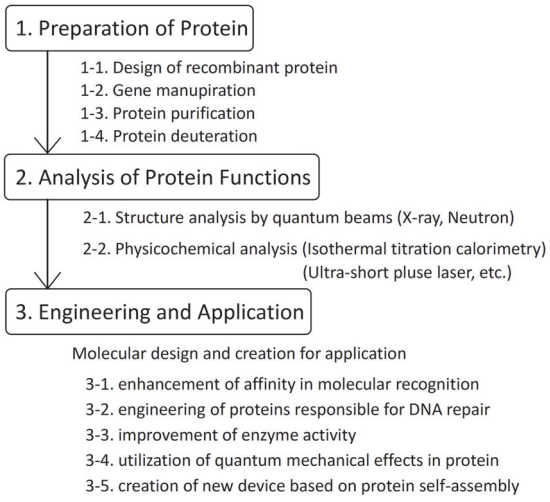

Fig. 1. Research concept of our project.

An insight into the thermodynamic characteristics of human thrombopoietin complexation with TN1 antibody [1]

Antidody is representative protein on molecular recognition. The TN1 antibody can regulate the function of human thrombopoietin (hTPO) that primarily stimulates megakaryocytopoiesis and platelet production. We analyzed thermodynamic characteristics of TN1 antibody–hTPO complexation by isothermal titration calorimetry using an antigen-binding fragment (Fab) from the TN1 antibody. Fab includes the antigen-binding site (molecular recognition site). To clarify the mechanism by which hTPO is recognized by TN1-Fab, the conformation of free TN1-Fab was determined to a resolution of 2.0 Å using X-ray crystallography and compared with the hTPO-bound form of TN1-Fab determined by a previous study [2]. This structural comparison revealed that the conformation of TN1-Fab does not substantially change after hTPO binding and a set of 15 water molecules is released from the antigen-binding site of TN1-Fab upon hTPO complexation. Interestingly, the heat capacity change measured by isothermal titration calorimetry differed significantly from calculations based upon the X-ray structure data of the hTPO-bound and unbound forms of TN1-Fab, suggesting that hTPO undergoes an induced-fit conformational change combined with significant desolvation upon TN1-Fab binding. The results shed light on the structural biology associated with neutralizing antibody recognition, and will contribute to molecular design for antibody on industry (3-1 in Fig. 1).

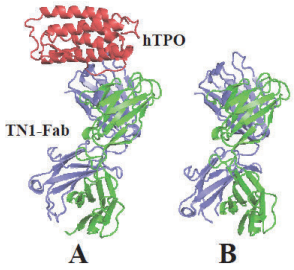

Fig. 2. Comparison of crystal structures between TN1-Fab and its complex with hTPO.

Structure analysis of human single nucleotide polymorphisms in cytochrome P450 2C9 [3]

P450 protein is the major enzyme family in human drug metabolism. Single nucleotide polymorphisms (SNP) in human cytochrome P450 (CYP) enzymes are important contributors to inter-individual variability in drug response and metabolism leading to drug-drug interactions and adverse reactions. CYP2C9 is a major xenobiotic metabolizing enzyme responsible for the clearance of over 15% of drugs, and polymorphisms in CYP2C9 has resulted in significantly altered catalytic activities. Despite the abundant structural and functional information available regarding CYPs in multiple species, the structural basis of SNPs is still lacking. The crystal structures of the CYP2C9 wild-type (WT) and CYP2C9 variants, I359L (*3) and A477T (*30), complexed with anti-hypertensive drug losartan demonstrated binding of three molecules of losartan to the WT and *30, and two to the *3 complex. In *3 variant, the effect of I359L located far away from the active site is transduced on several secondary structural elements, and remarkably influenced the orientations of important residue sidechains near the active site and the access channel. Furthermore, the T477 substitution in *30 variant formed hydrogen bond with the sidechain of Q214, which significantly reoriented from its interaction with the access channel losartan in the WT complex. The structures yield insight into the implications of genetic polymorphisms and provide useful framework to understand precision medicine (3-1 in Fig.1).

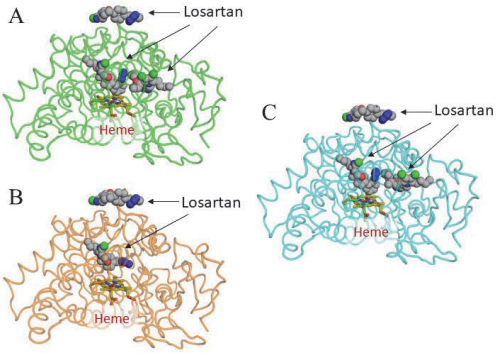

Fig. 3. Losartan complexes of CYP2C9 WT(A), *3(B) and *30(C).

References

[1] S. Arai *et al.*, Protein Sci., **25**, 1786 (2016).
[2] M. D. Feese *et al.*, PNAS, **101**, 1816 (2004).
[3] M. B. Shah *et al.*, to be published.

P2-8 Biomolecular Structure and Dynamics Research Project

Leader : Taro Tamada

The relationship between protein structure and dynamics is important for ultimate understanding of protein functions. Project “Biomoleular Structure and Dynamics Research” aims to contribute to a wide range of biological and life sciences by performing research and development of molecular imaging method using neutrons, along with other quantum beams like X-rays and computer simulations. In this report, we describe our latest activities for protein structure and dynamics.

Elucidation of the electronic properties in the electron transfer protein of photosynthetic bacterium [1]

High-potential iron-sulfur protein (HiPIP) functions as an electron carrier, which transfers electrons from the proton pump (cytochrome bc_1) to the photoelectric transducing protein (reaction center) in photosynthetic purple bacteria. HiPIP possesses the Fe_4S_4 cluster which shows +2/+3 redox states in the electron transfer reaction. Therefore, information about valence electrons is important for understanding the function of HiPIP.

To reveal the distribution of valence electron densities, the crystal structure of HiPIP from purple photosynthetic bacterium *Thermochromatium tepidum* was determined to 0.48 Å resolution. This is one of the highest resolution data sets in the Protein Data Bank, and it allowed us to perform structure refinement including contribution of valence electron densities with multipolar atomic model. Fe 3*d* and S 3*p* electron densities are clearly observed around the atoms of $Fe_4S_4(Cys\text{-}S\gamma)_4$ (Fig. 1(a)). In some Fe-S bonds, the Fe 3*d* electron density points towards the S 3*p* electron density (Fig. 1(b)). The 3*d*-3*p* overlaps are smaller for shorter Fe-S bonds, while the overlaps are larger for longer Fe-S bonds. The charge density analysis in HiPIP also visualizes the interactions between $Fe_4S_4(Cys\text{-}S\gamma)_4$ and the protein environment. Valence electron densities of S atoms identify the hydrogen bonds with the surrounding amino acids. Detailed views of interactions between the cluster and surrounding ligands imply that the FE1 atom together with FE2, S4 and Cys43-Sγ atoms are crucial for storing electronic charges in the reduced HiPIP.

Distinct behaviour of hydration water around F-actin and myosin S1 [2]

Various biological functions related to cell motility are driven by the interaction between the partner proteins, actin and myosin. Elucidation of this interaction is important for understanding these cellular functions. Flexibility of F-actin (polymerized form of actin) and myosin has been suggested to play an important role in this interaction. F-actin indeed shows enhanced fluctuations compared to myosin, and thereby facilitating binding of the myosin head to F-actin. Such behaviour of the proteins should be coupled to that of hydration water. To obtain insights into the role of hydration water in this interaction, dynamic behaviour of hydration water around F-actin and myosin was investigated by carrying out the quasielastic neutron scattering (QENS) experiments of solutions of F-actin and myosin S1 using the spectrometer, BL02 (DNA), at the MLF/J-PARC.

Figures 2(a) and (b) show examples of the QENS spectra of water around F-actin and myosin S1 (the proteolytic fragment of the myosin head containing the interaction region). Analysis of these spectra showed that translational diffusion of hydration water around F-actin is enhanced compared to that around myosin S1 (Fig. 2(c)), but rotational correlation time is reduced in hydration water around F-actin than that around in myosin S1 (Fig. 2(d)). These results suggest that whereas S1 has the typical hydration water, mobility of which is reduced compared to that of bulk water, F-actin has the unique hydration water, mobility of which is close to that of bulk water rather than the typical hydration water. This distinct behaviour of hydration water around F-actin should lower viscosity around F-actin, and thereby making F-actin fluctuate rapidly. This concerted action of F-actin and its hydration water would make F-actin explore the conformational space frequently, which facilitates the adjustment of its conformations for the binding of various actin-binding proteins including S1 to F-actin.

References

[1] Y. Hirano *et al.*, Nature, **534**, 281 (2016).
[2] T. Matsuo *et al.*, Biochem. Biophys. Rep., **6**, 220 (2016).

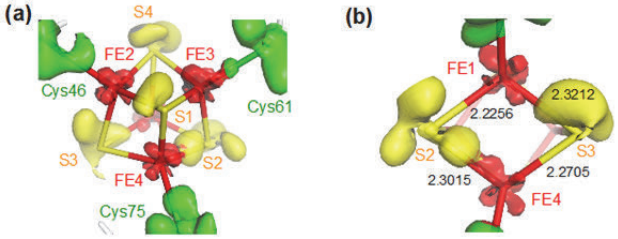

Fig. 1. Distribution of valence electron densities of $Fe_4S_4(Cys\text{-}S\gamma)_4$ in HiPIP. (a) Three dimensional representations of valance electron densities. The valence electron densities of Fe, S and Cys-Sγ atoms are shown as red, yellow and green isosurfaces contoured at the level of +0.2 e/Å^3. (b) A close-up view of the plane of FE1-S3-FE4-S2. Bond lengths are indicated in the figure.

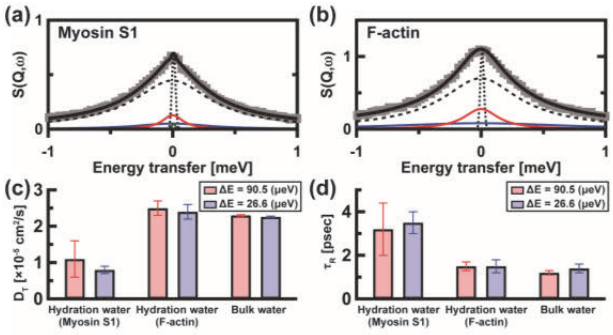

Fig. 2. The QENS spectra of water around (a) F-actin and (b) myosin S1, at Q = 1.7 Å^{-1} and at the energy resolution (ΔE) of 26.6 μeV. (c) The translational diffusion coefficients, and (d) the rotational correlation times, of hydration water around F-actin and myosin S1, and bulk water, obtained at two energy resolutions.

Part Ⅰ

3. Advanced Quantum-Beam Technology

P3-1 Laser Compton Scatterring γ-ray Research Project

Leader : Ryoichi Hajima

The research objective of LCS γ-ray Research Project is developing the technologies of high-brilliance γ-ray generation and exploring its scientific and industrial applications such as nuclear physics, nuclear astrophysics and non-destructive measurement of nuclear material. The γ-ray source is based on laser Compton scattering (LCS), which enables one to generate energy-tunable mono-energetic γ-rays. In the research project, we are developing critical components for electron accelerators to achieve small-emittance and high-average current beams, γ-ray optics and a Monte Carlo simulation code.

Branching and fragmentation of dipole strength in ^{181}Ta in the region of the scissors mode [1]

Non-destructive detection of fissile material can be realized using a combination of LCS γ-rays and nuclear resonance fluorescence (NRF), isotope-specific fingerprints [2]. Fissile isotopes, ^{235}U and ^{239}Pu, irradiated with 2-3 MeV γ-rays show transition to an excited state having an oscillation of the protons against the neutrons in a scissors like fashion. This is called the scissors mode. In recent measurements, transition strengths of the scissors mode were observed that were double that expected from theory and systematics well established from measurements on the excitation channel, that is, using NRF.

In order to resolve the discrepancy of transition strength in the scissors mode, we conducted a transmission NRF measurement on ^{181}Ta, which is a deformed odd-mass nuclide similar to the fissile isotopes. The measurement was made at the HIγS (High Intensity Gamma-ray Source) facility in Durham, NC, which provides a quasi mono-energetic γ-ray beam. We measured energy spectrum of γ-rays scattered from a Ta target with inserting an absorber at the upstream of the incident γ-ray beam path. Two absorbers, Ta and Pb, were used to distinguish resonant and non-resonant absorption in the upstream target.

Figure 1 shows scattered γ-ray spectra with and without an upstream absorber in different colors. Combining the results from the absorption and the NRF measurements, we found that the scissors mode in ^{181}Ta shows de-excitation through fragmented branching channels, which accounts for the discrepancy of transition strength in the theory and experiments. Furthermore, significant branching of the scissors mode, if similarly found in odd-mass fissile isotopes, could lead to enhanced sensitivity in detection and assay applications using transmission NRF.

Proposal for selective isotope transmutation of long-lived fission products using quasi-monochromatic γ-ray beams [3]

A new selective isotope transmutation method using photonuclear reactions with quasi-monochromatic γ-ray beams was proposed. This method is applicable, in principle, to transmutation of long-lived fission product (LLFP) such as ^{93}Zr, ^{107}Pd, or ^{79}Se, which dominate total activity of high-level radioactive waste to be managed in geological disposal. Our proposal is based on the fact that the particle threshold energy of these LLFP in photo-nuclear reaction is lower than those of stable isotopes of the same chemical element. Therefore, this method has the excellent advantage that LLFPs cannot, in principle, be produced newly even if the target materials include stable isotopes in addition to LLFPs.

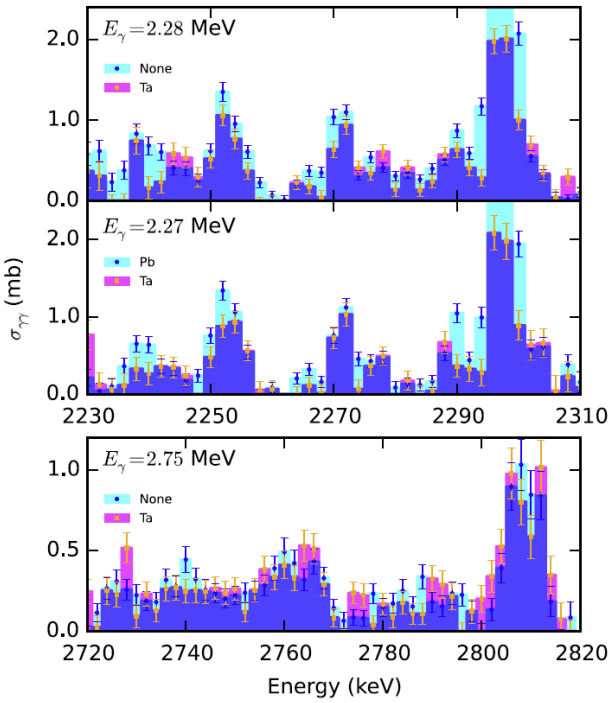

Fig. 1. The elastic cross section $\sigma_{\gamma\gamma}$ measured for a Ta target irradiated with a LCS γ-ray beam at HIγS. Cyan (blue circles) represents the no upstream absorber (or Pb absorber) spectrum. Magenta (orange squares) represents the Ta absorber spectrum. Resonant absorption (cyan above blue; blue indicates overlap of cyan and magenta) is evident at each beam energy.

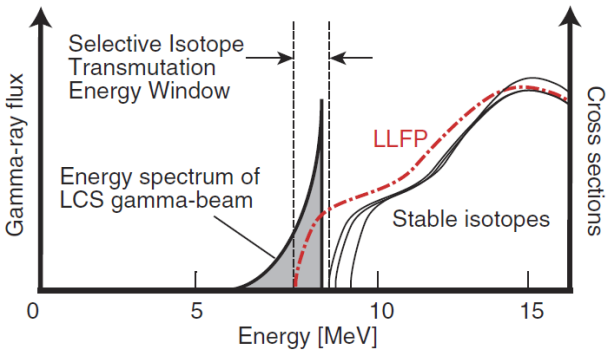

Fig. 2. Schematic view of nuclear transmutation for LLFP without isotope separation. The particle threshold of an LLFP is lower than those of stable isotopes for some elements such as Zr, Pd, and Se. If a target consisting of stable isotopes and LLFPs is irradiated with a γ-ray beam with an energy in the selective isotope transmutation energy window, the only LLPFs are selectively transmuted to stable or short-lived unstable isotopes.

Figure 2 shows a schematic view of the proposed transmutation. Since LCS γ-ray has a sharp cut off at the side of the maximum energy and its energy width is tunable, LCS γ-ray is suitable for selective transmutation of LLFP with keeping stable isotopes as they are.

High voltage threshold for stable operation in a dc electron gun [4]

A high-voltage electron gun is an essential device to generate a small-emittance electron beam. We developed a 500-kV dc electron gun equipped with a photocathode for the next-generation photon sources such as high-flux LCS γ-ray and high-power EUV FELs [5].

Recently we observed a new insight in threshold for stable operation in the dc electron gun. The high-voltage (HV) hold-off time without any discharge is longer than many hours for operation below the threshold, while it is roughly 10 min above the threshold. The HV threshold corresponds to the minimum voltage where discharge ceases. The threshold increases with the number of discharges during HV conditioning of the gun. Above the threshold, the amount of gas desorption per discharge increases linearly with the voltage difference from the threshold.

Figure 3 shows the HV hold-off time as a function of HV measured at the end of the conditioning. The hold-off time is longer than 4 h at 500 kV, while it is of the order of 10 min above 505 kV. The hold-off time is 2 h at 505 kV, which corresponds to the minimum discharge stop voltage at the end of HV conditioning. The signals of vacuum and radiation in Fig. 3 (b) and (c) do not suggest any signature of discharges during the hold-off time. Therefore, the minimum discharge stop voltage corresponds to the threshold voltage where the voltage hold-off performance changes dramatically

The present experimental observations can be explained by an avalanche discharge model based on the interplay between electron stimulated desorption (ESD) from the anode surface and subsequent secondary electron emission from the cathode by the impact of ionic components of the ESD molecules or atoms.

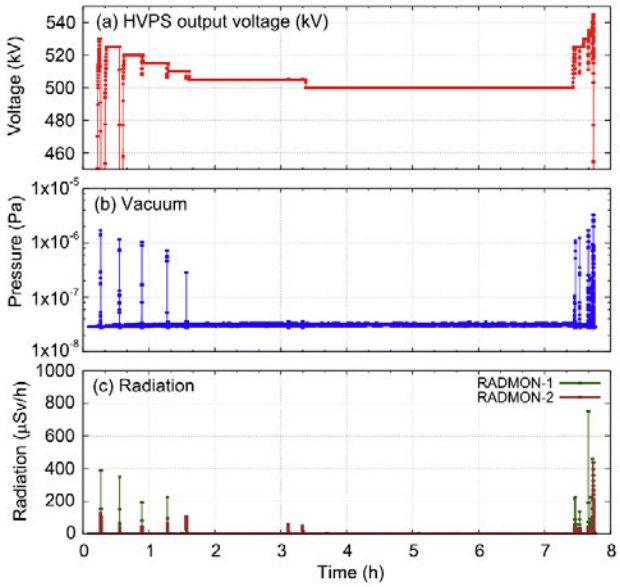

Fig. 3. Voltage hold-off test for various voltages. (a) HVPS output voltage (kV), (b) vacuum, and (c) radiation.

Enhanced diffraction of MeV γ-rays by mosaic crystals [6]

If diffractive optical devices that act as monochromators for γ-rays with energies of several MeV become available in the next-generation γ-ray sources, it would contribute to improvement of fundamental science and various applications. For this purpose, we are developing new-generation of γ-ray optics.

The diffraction of γ-rays by mosaic Si crystals in a transmission Laue geometry was measured using a high-flux ^{60}Co source at Facility of Radiation Standards, JAEA. The measured diffraction intensities at 1.17 and 1.33 MeV using 40- and 80-mm-thick mosaic crystals were enhanced by a factor of approximately 8.6 compared with those of the perfect Si crystal of 2-mm thickness. The integrated reflectivity is well described in statistical dynamical theory by taking into account γ-ray absorption inside the crystals. This result demonstrates that a mosaic crystal with a thickness of several centimeters is effective as an optical device for LCS γ -ray beams with a relatively wide divergence.

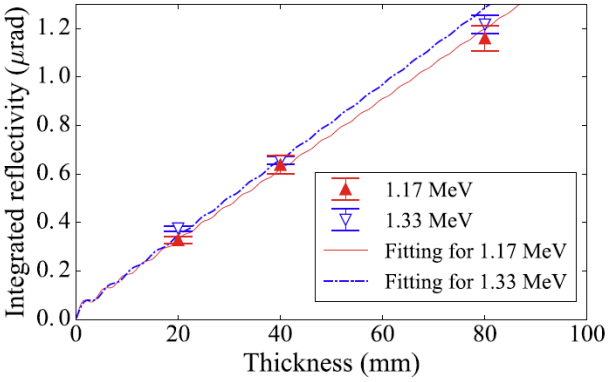

Fig. 4. Thickness dependence of the integrated reflectivity. The triangle symbols show the experimental integrated reflectivity. The solid and dot-dashed lines show the integrated reflectivity calculated by statistical dynamical theory of scattering for 1.17 and 1.33 MeV, respectively.

References

[1] C. T. Angell *et al.*, Phys. Rev. Lett., **117**, 142501 (2016).
[2] R. Hajima *et al.*, J. Nucl. Sci. Tech., **45**, 441 (2008).
[3] T. Hayakawa *et al.*, J. Nucl. Sci. Tech., **53**, 2064 (2016).
[4] M. Yamamoto and N. Nishimori, App. Phys. Lett., **109**, 014103 (2016).
[5] N. Nishimori *et al.*, Appl. Phys. Lett., **102**, 234103 (2013).
[6] S. Matsuba *et al.*, Jpn. J. App. Phys., **55**, 112402 (2016).

P3-2 Beam Engineering Section

Manager : Yasuyuki Ishii

The research objectives in our section are many kinds of development of accelerator related techniques which include ion beam irradiation techniques and ion beam analyses. Each member has been engaging in individual researches more than one. In the recent and remarkable studies, the spectrum changes of ion beam induced luminescence from organics were observed during microbeam irradiation and a beam diameter by decreasing the divergence angle of an incident beam was reduced in a compact ion microbeam system producing several-hundred-keV beam {3-01, 05~24, 27~29, 31 in Part II}.

Observation of changes in spectra of ion beam induced luminescence from organic targets during focused microbeam irradiation [1]

The ion beam induced luminescence (IBIL) analysis with ion microbeam is developed to obtain the information of chemical compositions, as well as elementary distribution, in a sample by combining IBIL and micro-PIXE and/or micro-PIGE.

In this study, continuous IBIL spectroscopy, induced by a 3 MeV proton microbeam, from several inorganic microscopic and standard organic targets was recorded by introducing a high-sensitivity spectrometer (CCD spectrometer) to visualize the decay and generation of spectra peaks. As an example of the decay, Fig. 1 shows three-dimensional images of IBIL spectra from a thin-layered polycyclic aromatic hydrocarbon (PAH) target with beam fluence of up to 1.5×10^{15} ions/cm^2. In these

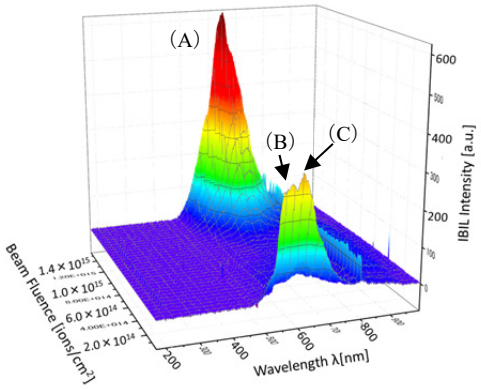

Fig. 1. Three-dimensional illustration of changes in a PAH target during 3 MeV proton irradiation. IBIL spectra from PAH benzo[a]pyrene were continuously recorded during proton microbeam irradiation.

spectra, initial IBIL peaks (A) quickly decay during irradiation. Decay at wavelengths around 540 nm and 610 nm (B) can be attributed to the degradation of the chemical structure of benzo[a]pyrene. Other strong IBIL peaks can be observed at wavelengths of 640 and 670 nm (C). These peaks were unexpected, and might be due to the generation of new chemical compositions during beam irradiation. These results suggest that the generation of new peaks in IBIL spectra is a result of chemical reactions triggered by intense beam irradiation. In this experimental case, PAH has various chemical compositions with different structures, chemical composition may change by the deposited energy from the beam.

These results also suggest that IBIL analysis enable us to obtain the chemical composite information of organic targets in short time before dissolving them by ion beam irradiation.

Reduction of beam diameter by adjusting the divergence angle of incident beam in compact ion microbeam system producing several-hundred-keV beam [2]

Ion microbeams ranging from several hundred keV to several MeV (hereafter, microbeam) are a powerful tool for ion beam analyses and microfabrication. These microbeams are produced by a large system, whose length is more than 4 m; this is problematic, as this makes installation of the system in average sized laboratories in universities and industrial facilities difficult. A more compact ion microbeam system would resolve this issue.

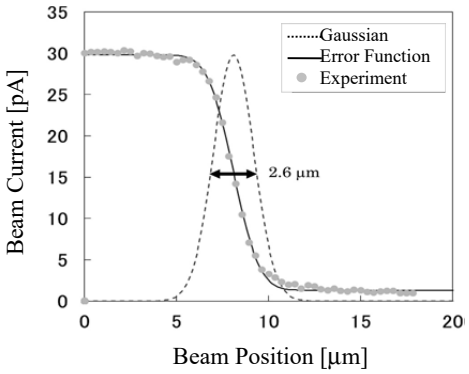

Fig. 2. Beam diameter measurement at 120 keV hydrogen ion beam.

A $1 \times 1 \times 2$ m^3 compact ion microbeam system of several hundreds keV comprising the three-stage acceleration lens and a duoplasmatron-type ion source has been developed as a prototype for a MV compact ion microbeam system within the size of $2 \times 2 \times 3$ m^3. In a preliminary study, the beam diameter was reduced from 17 μm to 5.8 μm by minimizing the residual gas pressure (5.3×10^{-5} Pa), which caused a beam halo. In the present studies, an incident beam with a small divergence angle was founded to be effective in enhancing the demagnification of the lens because demagnification is inversely proportional to the divergence angle of an acceleration lens. The divergence angle at a minimum was obtained at the distance of 10 mm. The positions of extraction electrodes in the ion source were adjusted on the basis of calculated results of beam transport.

The beam size was measured by a beam size measurement device applied to a knife-edge method under applying the distance in the ion source. The experimental results showed that a hydrogen beam with a diameter of 2.6 μm was formed at 120 keV as seen in Fig. 2.

References

[1] W. Kada *et al.*, Nucl. Instrum. Meth. Phys. Res. B, **404**, 100-05 (2017).
[2] Y. Ishii *et al.*, *ibid.*, 65-68 (2017).

Part II

Prat II

1. Materials Science

1 - 01 Quantification of Interface Traps with γ-ray, X-ray, and e^--Beams for Devices with Low Internal Power Dissipation

K. Hirose [a, b], S. Toguchi [b], D. Kobayashi [a, b], T. Makino [c] and T. Ohshima [c]

[a] Institute of Space and Astronautical Science, JAXA,
[b] Department of Electrical Engineering and Information System, The University of Tokyo,
[c] Department of Advanced Functional Materials Research, TARRI, QST

Wide band gap semiconductor materials such as SiC have been drawing attention because of their possible benefits superior to conventional Si. One of the benefits is their expected higher tolerance to electric break down. Such tolerance is attractive to develop lower heat dissipation devices, which are demanded for sustainable use of natural resources. One of the hurdles in the development is a severe increase in resistance under dielectric materials [1]. These materials are necessary to make device structures such as control gates, as designed, but their interfaces still have high density of traps, which cause the increase in resistance and that in internal power dissipation.

SiO_2 is widely used as a dielectric material in SiC devices. It is said that SiO_2 usually contains SiH and the release of H^+ due to radiation may increase interface traps. It is also expected that the influence of H^+ is magnified in the lower dose rate irradiation. However, their quantitative relationship was not experimentally demonstrated even in the classical SiO_2/Si stacks. We have hence developed a method and identified it in a SiO_2/Si stack [2], which was used for the first tested material instead for advanced SiC stacks.

Si chips with 3-, 5-, and 9-nm-thick SiO_2 over-layers were used. These SiO_2 layers were thermally grown on p- and n-type Si substrates in dry O_2 atmosphere and received a heat treatment at 350 ºC for 5 h in H_2 atmosphere. The densities of interface traps and SiH groups were evaluated with X-ray photoelectron spectroscopy (XPS) [3], in which VG ESCALAB 220i-XL with a monochromatic source of Al-Kα 1,486.6 eV was used and the binding energy of $Si2p_{3/2}$ was monitored as a function of the time of X-ray irradiation. Its time- or dose-dependent shift provides a charge balance equation at the SiO_2/Si interface among the oxide trap charge, interface trap charge, and surface space charge. This balance equation can be solved, providing each charge density. The influence of radiation-induced H^+ was studied using the ^{60}Co γ-ray irradiation facility. Some of the chips received the total dose of 100×10^3 rad(SiO^2) in different dose rates of 30 and 0.1 rad(SiO_2)/s. After the γ-ray irradiation, the density of interface traps was quantified through the XPS analysis and compared with the value before the γ-ray irradiation. The number of SiH groups was then quantified from the other samples that received an e^--beam with 14 eV in the XPS apparatus. It is known that OH groups in SiO_2 easily capture e^- and turn to negative oxide trap charge. Its density can be also quantified through the same XPS analysis. Its revealed density was then converted into that of SiH groups through their established ratio reported in the literature [4].

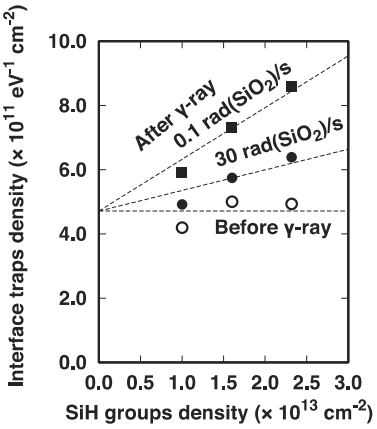

Fig. 1. Measured interface traps densities as a function of the density of SiH groups.

Figure 1 shows the measured density of the interface traps plotted as a function of the density of SiH groups. Before the γ-ray irradiation, the revealed interface traps densities are almost constant and independent on the density of SiH groups, as expected. After the γ-ray irradiation, increases in interface traps densities are observed, as is conventionally observed. In addition, it has been experimentally demonstrated for the first time that each dose rate condition conforms to a straight-line relationship and its slope is dependent on the dose rate. We also confirmed that this straight-line relationship is in line with an analytical model developed with a direct collision theory simply describing the H^+ release [2]. This confirmation supports the direct H^+ release mechanism suggested in simulation studies [5]. In summary, this study has developed a method and identified the quantitative relationship between the increase in interface traps and the number of SiH in SiO_2 film. Continuing this study will provide useful information on the traps of the interface of the SiO_2 dielectric with SiC and others.

References

[1] D. M. Fleetwood *et al.* (Edited), Defects Microelectron. Mater. & Dev., CRC Press (2009).
[2] S. Toguchi *et al.*, RADECS (2017), to be presented.
[3] K. Hirose *et al.*, Prog. Surf. Sci., **82**, 3-54 (2007).
[4] K. Beckmann *et al.*, J. Electrochem. Soc., **118**, 614-19 (1971).
[5] H. P. Hjalmarson *et al.*, IEEE Trans. Nucl. Sci., **50**, 1901-09 (2003).

1 - 02 An Evaluation of Single Event Effect by Heavy Ion Irradiation on Atom Switch Memory and Field Programmable Gate Array

K. Takeuchi [a)], M. Tada [b)], T. Sakamoto [b)], H. Shindo [a)], S. Kuboyama [a)], A. Takeyama [c)], T. Ohshima [c)] and K. Suzuki [a)]

[a)] Research and Development Directorate, JAXA,
[b)] System Platform Research Laboratories, NEC Corp.,
[c)] Department of Advanced Functional Materials Research, TARRI, QST

"Normally-off computing" featuring a next generation non-volatile memory, which enables to shut the power down whenever not being used, is one of the most promising methodologies to reduce the power consumption in large scale integrated circuit (LSI) and electronic devices [1]. In this work, we investigate a radiation tolerance of the new memory to achieve "Normally-off computing" in aerospace. NanoBridge (a.k.a. atom switch) as the nonvolatile memory/switch is subject to be irradiated in a radiation facility, and single event upset (SEU) cross-section against high linear energy transfer (LET) heavy ion was evaluated.

The radiation tolerance of both atom switch read only memory (ROM) and complementary atom switch (CAS) field programmable gate array (FPGA) were evaluated by using the Takasaki Ion Accelerators for Advanced Radiation Application (TIARA) in the National Institutes for Quantum and Radiological Science and Technology (QST). Atom switch ROM and CAS FPGA were initially developed by Low-power Electronics Association & Project (LEAP) and now NEC continues to develop them as NanoBridge®. The chips were irradiated by Xe ion. The LET of Xe was calculated to be 68.9 MeV/(mg/cm^2) at Si surface [2]. Irradiation and test conditions are described in Tables 1 and 2.

No SEU was observed through experiment. Atom switch was programmed for either ON or OFF state and validated before and after the radiation test by LSI tester. Since actual cell area of atom switch is 1.5×10^{-11} cm^2, about 19 or 1,376 particles were expected to hit somewhere in atom switches on ROM or FPGA respectively. Figure 1 shows estimated SEU cross section against Xe ion which has 69.8 MeV/(mg/cm^2) in LET. In-house Cf-252 data [3] was also plotted in 30 MeV/(mg/cm^2) in Fig. 1. It was revealed that SEU cross sections against heavy ions are much smaller than the atom switch cell itself irrespective of voltage conditions or cell states.

Table 1
Irradiation conditions.

Ion	$^{129}Xe^{25+}$
Net Energy [MeV]	389
LET at Si surface [MeV/(mg/cm^2)]	68.9
Range in Si [μm]	35.0
Total fluence [p/cm^2]	10^7

Table 2
Test conditions.

Item	Atom switch	
	ROM	FPGA
# of Atom switch	131 kbit	9.175 Mbit
Voltage applied to each cell during irradiation	0 V except read-out timing	continuously applied
Data	"0" & "1" in half	Buffer chain circuit
Expected # of ion hits for a fluence of 10^7 [p/cm^2]	19	1376
Cell area [cm^2]	1.5×10^{-11}	

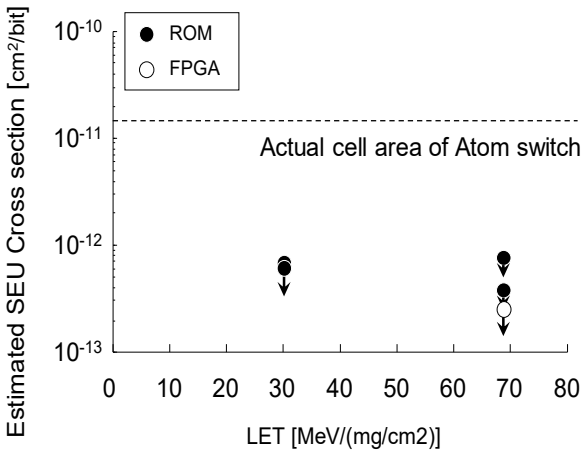

Fig. 1. Estimated SEU cross section.

References

[1] K. Ando, FED Journal, **12**, (4), 89-95 (2001).
[2] http://www.srim.org/.
[3] K. Takeuchi *et al.*, Poster material, MEWS28, (2015/10).

1 - 03 Radiation Degradation Characteristics of InGaP, GaAs and InGaAs Solar Cells Irradiated with 1 MeV Electrons

M. Imaizumi [a)], Y. Shibata [a)], T. Nakamura [a)], T. Sumita [a)], S-I. Sato [b)] and T. Ohshima [b)]

[a)] Research and Development Directorate, JAXA,
[b)] Department of Advanced Functional Materials Research, TARRI, QST

The inverted metamorphic (IMM) triple-junction (3J) solar cells formed of $In_{0.5}Ga_{0.5}P/GaAs/In_{0.2}Ga_{0.8}As$ material system have received considerable attention and are being developed as next-generation space solar cells owing to their higher conversion efficiency compared with the currently-used conventional $In_{0.5}Ga_{0.5}P/GaAs/Ge$ triple-junction space solar cells. To design a 3J solar cell for space applications, one has to understand the radiation degradation characteristics of each subcell in a designated 3J structure. In the design consideration of IMM-3J space cells, the degradation characteristics of the InGaP and GaAs subcells are well understood, while that of the InGaAs subcell is not. In this study, we compared the effects of radiation on the output characteristics of InGaAs single-junction (1J) solar cells with those of InGaP and GaAs 1J solar cells [1].

Three material types of 1J solar cells, namely, $In_{0.5}Ga_{0.5}P$, GaAs, and $In_{0.2}Ga_{0.8}As$ cells were prepared for this study. The cell layers were grown onto GaAs (100) substrates by metal-organic vapor phase epitaxy (MOVPE). The 1J cells were irradiated with 1 MeV electrons which create radiation defects uniformly in the whole cell layers. The light current-voltage characteristics (LIV) under simulated solar light (AM0, 1sun) and the external quantum efficiency (EQE) measurements were performed before and after the 1 MeV electron irradiation. Figure 1 depicts the changes in LIV and EQE of the three 1J cells as results of the electron irradiation. The solar cell output parameters, *i.e.*, the short-circuit current (Isc), the open-circuit voltage (Voc) and the maximum power (Pmax), were determined from the LIV characteristics.

For the LIV, the InGaAs cells obviously show greater degradation in Isc than the InGaP and GaAs cells. This tells us that a greater margin of current output is necessary for InGaAs bottom cells when designing the IMM-3J cell structure. On the other hand, the GaAs cell exhibits greater degradation in Voc than the InGaP and InGaAs cells. This is thought to be due to high quality of the GaAs before irradiation, which is confirmed from the smallest difference between bandgap and Voc among the three 1J cells.

For the EQE, in all the cases, the EQE in the longer wavelength region, which represents light absorption in the deeper locations of the cells, showed significant degradations. On the other hand, the EQE in the shorter wavelength region, which corresponds to light absorption in the shallower regions of the cells, does not show apparent degradation. This fact indicates that the degradation in EQE observed in all the 1J cells was principally caused by the decrease in minority-carrier diffusion length. In addition, it implies that the irradiations did not induce substantial increase of the front-surface carrier recombination velocity.

Reference

[1] M. Imaizumi *et al.*, Progr. Photovoltaics Res. Appl., **25**, 137-205 (2017).

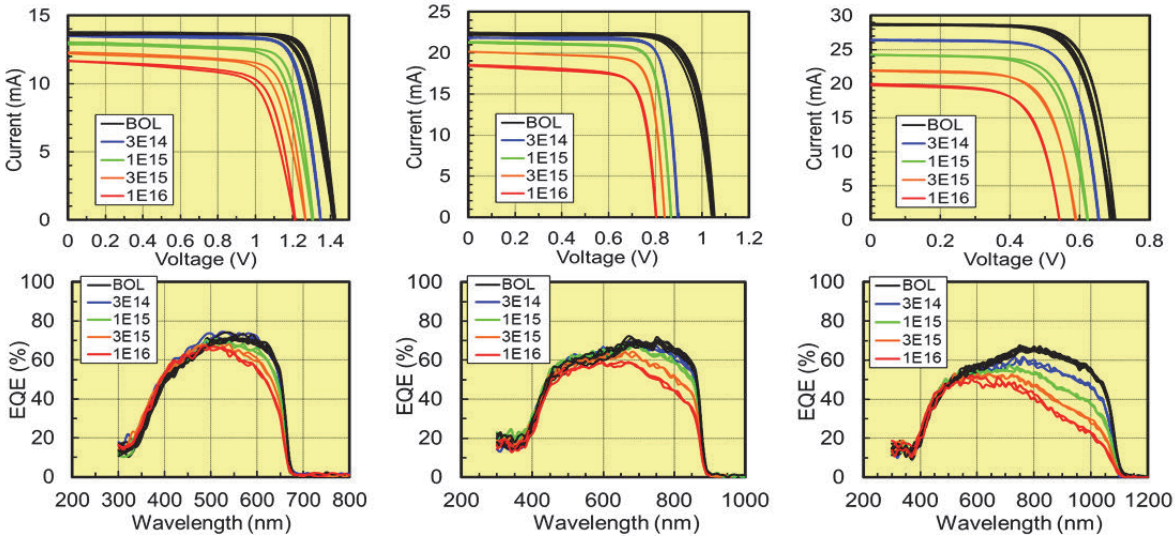

(a) InGaP (In=50%) cell (b) GaAs cell (c) InGaAs (In=20%) cell

Fig. 1. Change in the light current-voltage (LIV) characteristics and the external quantum efficiency (EQE) of InGaP, GaAs and InGaAs single-junction solar cells due to 1 MeV electron irradiation. The numbers in legends are the fluences (BOL: initial).

1 - 04 Development of Fluorescent Nuclear Track Detector Based on Diamond Crystal

S. Onoda [a)], M. Haruyama [a, b)], K. Tatsumi [a, b)], W. Kada [b)], O. Hanaizumi [b)] and T. Ohshima [c)]

[a)] Department of Advanced Functional Materials Research, TARRI, QST,
[b)] Faculty of Science and Technology, Gunma University

For several decades, Plastic Nuclear Track Detector (PNTD) has been applied to the fields of radiation detector for nuclear and high-energy physics, detection of cosmic rays, dosimetry, etc. The various charged particles and neutrons are detectable. To apply the PNTD to wide variety of fields, the optimization of the sensitivity for wide range of Linear energy transfer (LET) is required. Utilizing variety of plastic materials, the sensitivity has improved immensely over the decades.

In more recent years, Landauer, Inc. proposed a novel Fluorescent Nuclear Track Detector (FNTD) based on the single crystal of aluminium oxide (Al_2O_3) doped with carbon and magnesium [1]. When an ion traverses Al_2O_3:C, Mg, a large number of electrons is created by ionization process. The electrons are captured by F_2^{2+}(2Mg) centers, which are known as an aggregate defect containing two oxygen vacancies compensated by two magnesium ions. As a result of electron capturing process, the F_2^{+}(2Mg) centers are created along an ion track. When 635 nm laser is illuminated, 750 nm emission from F_2^{+}(2Mg) is detected by using a laser scanning Confocal Fluorescence Microscope (CFM). Then accurate image of ion track can be observed. The spatial resolution is dramatically improved by use of FNTD compared with PNTD.

Since the materials for FNTD are limited, exploration of a new FNTD material is important. In this study, we propose that the diamond is potentially more adequate for FNTD than the existing material from the point of view of spatial resolution.

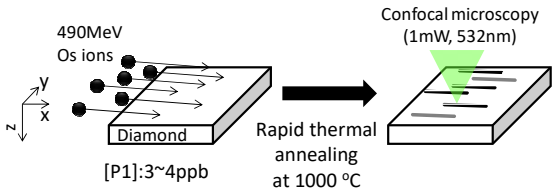

Fig. 1. Schematic of the experimental procedure.

The sample used in the experiments was non-commercial type-IIa high-pressure high-temperature (HPHT) diamond supplied by Sumitomo Electric Industries. The average concentration of substitutional nitrogen donors was 3 - 4 ppb. To introduce vacancies in diamond, we used the AVF cyclotron. The sample was irradiated by 490 MeV osmium (Os) ions at room temperature. The irradiation fluence was fixed at 5×10^6 ions/cm^2. As shown in Fig. 1, the uniform ion beam was slightly tilted with an angle from 5º to 10º. After ion irradiation, high temperature annealing was performed at 1,000 ºC to convert the substitutional nitrogen atoms and vacancies to Nitrogen-Vacancy (NV) centers. Finally, to observe the ion track, we used a home-built CFM system with a 532 nm excitation laser. For efficient photon collection, we used an objective lens with a large numerical aperture of 0.95. Fluorescent light from NV center passed through pinhole (25 µm in diameter). Reflected excitation light was rejected by long pass filter with the cut off wavelength of 647 nm. The fluorescent lights from NV center were detected by avalanche photo diode (model: COUNT-100C, Laser Components). When the laser power was 1 mW, the typical count rate from a single NV center was 50 kcounts/s.

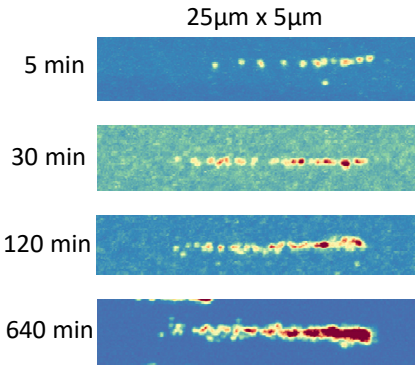

Fig. 2. Typical CFM images after annealing.

Figure 2 shows typical CFM images of the 490 MeV Os ion track after annealing at 1,000 ºC for 5 and 640 min in vacuum. Trail-like emissions are successfully detected. Although not shown here, we successfully observe the ion track in both HPHT and CVD diamonds. We therefore conclude that a diamond containing nitrogen impurity is able to be used for FNTD. To further improve the sensitivity, the optimization of nitrogen concentration is important.

Acknowledgements

The present work is a collaboration with Dr. Tokuyuki Teraji (NIMS), Prof. Junichi Isoya (Tsukuba Univ.). This work was supported by JSPS KAKENHI (Grant Numbers 26420877). We thank Dr. L. P. McGuinness (Ulm Univ.) and Prof. F. Jelezko (Ulm Univ.) for their help in building the CFM setup at QST. HPHT crystals were supplied from Sumitomo Electric Industries.

Reference

[1] G. M. Akselrod *et al.*, Nucl. Instrum. Meth. Phys. Res. B, **247**, 295 (2006).

1 - 05 Fabrication of Array of Shallow Single NV Centers in Diamond for Quantum Sensing Applications

J. Isoya [a)], T. Umeda [b)], S. Onoda [c)] and T. Ohshima [c)]

[a)] Research Center for Knowledge Communities, University of Tsukuba,
[b)] Faculty of Pure and Applied Science, University of Tsukuba,
[c)] Department of Advanced Functional Materials Research, TARRI, QST

Quantum sensing based on the principles of quantum mechanics potentially realizes high sensitivity and high selectivity beyond classical limit. Single electron spin associated with single nitrogen-vacancy (NV) center has unique properties at room temperature such as optical initialization/readout, coherent-manipulation by microwave pulses, and long coherence time. A NV center formed at near-surface is used as quantum sensor of detecting NMR signals of molecules placed on the diamond surface with the nanoscale spatial resolution [1 - 3].

We have fabricated regular array of shallow single NV centers by low energy nitrogen ion implantation (2.5 keV, 1×10^{12} cm^{-2}) via resist mask (PMMA, thickness ~200 nm) with the regular arrays of nanoholes (diameter: 20 nm) fabricated by EB (electron-beam) lithography technique. We used high purity ^{12}C-enriched (99.95%) CVD layers grown on type-Ib substrates. Subsequent annealing (1,000 ºC, 2 h) was applied after removing the resist mask. NV centers fabricated were characterized by pulsed ODMR (optically detected magnetic resonance) using laser-scanned confocal fluorescence microscopy (CFM).

The CFM image (xy-scan) of a part of the implantation area is shown in Fig. 1(a). The fluorescence spots in the regular array exhibited PL (photoluminescence) and ODMR spectra characteristic of NV centers. The alpha numeric characters (here, b55) consisting of dense NV centers which originated from patterned holes in the mask serve as address markers.

The number of NV centers per spot was estimated from the fluorescence intensity divided by the photon counting rate of a single NV center. A site of a single NV center was confirmed by the second-order photon auto-correlation function measurement. The Poisson distribution with the average = 1.40 obtained by fitting of 118 implantation spots indicates that nearly 40% spots contain a single NV center (Fig. 1(b)). Among the implantation sites, 70% have at least one NV center and 30% have no NV-center.

The depth of NV center was measured by using dynamical decoupling noise spectroscopy using XY8-k pulse sequence [1]. This sequence works as narrow band-pass filter to extract noise spectrum of frequency range selected by the pulse separation. The ^{1}H-NMR signal of immersion oil extracted from the noise spectrum serves to determine the depth of each of single NV centers. The depths determined for 23 NV centers are shown in Fig. 2. The horizontal positions are determined by the diameter (20 nm) of nanoholes and the straggling (Δr= 1.6 nm by SRIM simulation). The depth distribution (2-12 nm) is determined by straggling and ion channeling. Thus, we have achieved three-dimensional localization of NV centers. In using a single NV center as quantum sensor of detecting NMR signals, the depth (d) determines the detection volume ($\propto$ d^3). With the regularly arrayed positions together with the address markers, the position of each implantation spot is well-defined, allowing easy, reproducible access to the desired single NV position.

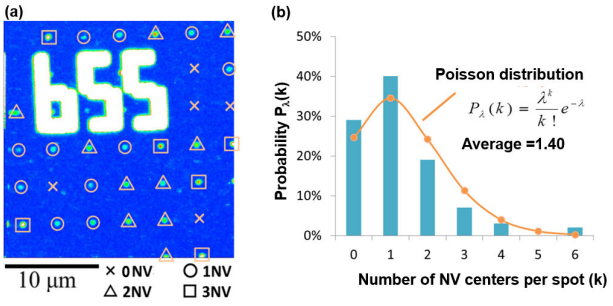

Fig. 1. Regular array of fluorescence spots in the CFM image (xy-scan). (b) Fitting of a Poisson distribution of the number of NV centers per spot.

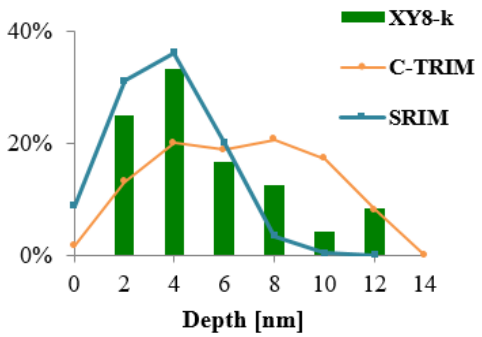

Fig. 2. The histogram of the depth of the NV centers measured from ^{1}H-NMR signal of immersion oil using XY8-k pulse sequence. The depth distributions estimated by SRIM and C-TRIM (3° tilted), respectively are also shown.

Acknowledgements

The present work is a collaboration with Dr. Tokuyuki Teraji (NIMS), Prof. Takashi Tanii (Waseda University) and Prof. Fedor. Jelezko (University of Ulm).

References

[1] T. Staudacher *et al.*, Science **339**, 561 (2013).
[2] H. J. Mamin *et al.*, Science **339**, 557 (2013).
[3] S. J. DevVience *et al.*, Nature Nanotech. **10**, 129 (2015).

1 - 06 Preparation of Carbonized Layer on Polyimide Ion-track Membranes Using Ar-ion Implantation

H. Koshikawa [a)], Y. Sato [b)], S. Yamamoto [a)], M. Sugimoto [a)], S. Sawada [a)] and T. Yamaki [a, b)]

[a)] Department of Advanced Functional Materials Research, TARRI, QST,
[b)] Graduate School of Science and Technology, Gunma University

Chemical etching of the polymer films irradiated with heavy ions leads to the formation of ion-track membranes with pores of different sizes and shapes. Quite recently, conically-shaped pores have successfully been prepared as template for metallic nanocones. The Pt nanocones were obtained by (i) sputter deposition of a thin Pt layer on a pore wall and (ii) electroplating of Pt within the pores [1]. We still have great difficulty in preparing the nanocones especially in a high aspect ratio (length/width) probably because the sputtered cathode layer cannot reach all the area of the template surface.

It is well-known that the near-surface region of polyimide (PI) can easily be carbonized by an ion implantation method [2]. The resulting carbonized surface layer, mainly composed of the graphitic carbon [2], was electrically conductive and expected to work as the electrode alternative to the sputtered Pt layer. In this study, therefore, we investigated the formation of the conductive layer on PI ion-track membranes by the Ar-ion implantation for the electroplating.

Three stacked PI films (Kapton) with thicknesses of 12 (topmost), 25 (middle) and 25 μm (lowermost) were irradiated with 560 MeV ^{129}Xe ions at a fluence of 3.0×10^7 ions/cm^2 at the AVF cyclotron of TIARA. The lowermost film, inside which the bombarding ions are found to stop according to the SRIM calculation, was etched in a sodium hypochlorite solution at 60 ºC for 1.0 h. This led to the formation of non-penetrating conical pores. Ions of 100 keV Ar were implanted in the PI ion-track membranes from their open-pore side. The irradiation was done at fluences of 3.8×10^{15} to 7.7×10^{16} ions/cm^2 in an IA chamber at the TIARA ion implanter. The surface and cross-section of the samples were observed by field emission scanning electron microscopy (FE-SEM). The surface resistivity was measured by a four-point probe method. The thickness of the carbonized layer was estimated to be 200 nm by the SRIM code.

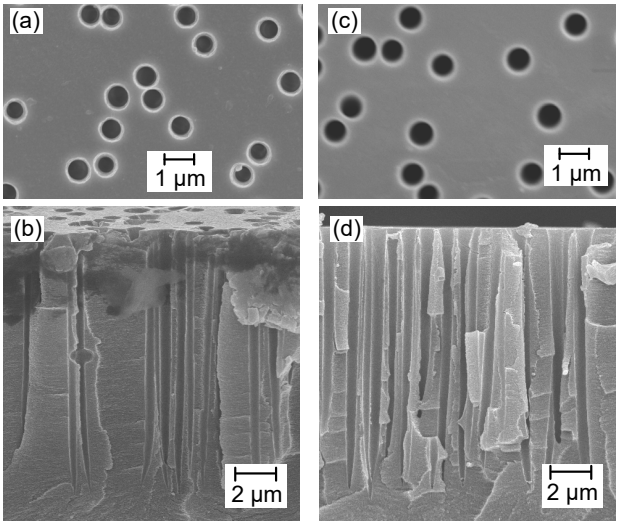

Fig. 1. FE-SEM images of (a) the surface and (b) cross-section of the as-prepared PI ion-track membrane. Images (c) and (d) are for the same membrane after the implantation (7.7×10^{16} ions/cm^2).

Figures 1 (a) and (b) show the FE-SEM images of the obtained ion-track membrane before the implantation. These can confirm the formation of non-penetrating conical pores with a surface diameter of 830 ± 30 nm and a depth of 13 μm. Figures 1 (c) and (d) present the FE-SEM images of the same membrane after the implantation at a fluence of 7.7×10^{16} ions/cm^2. The surface diameter slightly increased to 940 ± 10 nm while the depth was almost unchanged. Our Rutherford backscattering analysis (no result shown) indicated that the ion implantation increased the number density of carbon. Thus, the larger pore diameter can be related to the densification of the surface layers during the course of the carbonization.

Figure 2 shows the surface resistivity of the PI ion-track membranes as a function of fluence. As the fluence increased, the surface resistivity of the carbonized layer decreased, reaching the lowest value of 1.4 MΩ/cm^2 at 7.7×10^{16} ions/cm^2.

In conclusion, the Ar-ion implantation of the PI ion-track membranes led to the formation of the conductive layer on their surface. The application to the electroplating cathode is now under investigation.

References

[1] H. Koshikawa *et al*., 26th Annu. Meet. MRS-J, D3-P21-016 (2016).

[2] T. Terai *et al*., Nucl. Instrum. Meth. Phys. Res. B, **166-67**, 627-31 (2000).

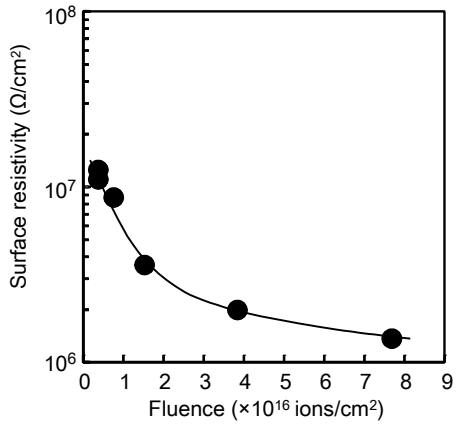

Fig. 2. The surface resistivity of the PI ion-track membranes as a function of fluence.

1 - 07 Platinum Nanocones Electrodeposited in Ion-track Membranes of Different Materials

Y. Sato [a)], H. Koshikawa [b)], S. Yamamoto [b)], M. Sugimoto [b)], S. Sawada [b)] and T. Yamaki [a, b)]

[a)] Graduate School of Science and Technology, Gunma University,
[b)] Department of Advanced Functional Materials Research, TARRI, QST

One-dimensional (1D) nanostructures directly integrated with a conducting substrate have several structural advantages. (i) The open space among the nanostructures has efficient mass transfer; (ii) the large surface areas accelerate the surface reaction [1]. Especially, the conical shape enhanced mechanical stability because it has not only the fine tip but also large base. Polymer-based ion-track membranes have been used as templates for the 1D nanostructures of metals and semiconductors. Control over the irradiation and etching conditions, and selection of membrane materials enabled the production of various membranes with the pores of predefined geometries, sizes and aspect ratios [2]. In this work, therefore, we prepared Pt nanocones using polycarbonate (PC) and polyethylene terephthalate (PET) ion-track membranes as templates.

Films of PC and PET with a thickness of 50 μm were irradiated with 150 MeV ^{40}Ar ions at a fluence of 3.0×10^7 ions/cm^2 at TIARA. The films which the bombarding ions did not penetrate were etched in a 4.0 M NaOH solution at 60 ºC for 5 - 40 min, leading to the non-penetrating conical pores. The pore-open side of these ion-track membranes was coated with a thin Pt layer by vapor deposition to make a cathode for electrodeposition. Pt nanocones were electrodeposited in the conical pores by applying a voltage of 5.0 V for 3 min in a commercial platinum electrolyte (PRECIOUSFAB Pt3000) at 60 ºC. The obtained samples were observed with scanning electron microscopy (SEM).

According to the SEM observations, the pore diameter linearly increased with etching times. The growth rates of the pore diameter were 26 nm/min for PC and 57 nm/min for PET, meaning controllability of the pore diameters.

Figure 1 shows the cross-sectional SEM images of the obtained pores. The PC films etched for 30 min had a base diameter of 540 nm and a length of 3.8 μm. The aspect ratio, defined as a ratio of the depth to base diameter, was calculated to be 6.8. On the other hand, the PET films etched for 20 min exhibited a base diameter of 1,040 nm and a length of 2.5 μm; thus, the aspect ratio was 2.4. The roughness of the pore wall was larger for PET films than for PC probably because PET is a semi-crystalline polymer, that is, a mixture of the crystalline and amorphous domains with different etch rates [3].

Figure 2 shows the SEM images of the Pt nanocones obtained from the etched pores shown in Fig. 1. The shapes and sizes of the Pt nanocones seemed to correspond exactly to those of the template pores. The selected-area electron diffraction pattern exhibited concentric rings, indicative of the polycrystalline structures of the Pt nanocones.

In conclusion, the shapes and sizes of the Pt nanocones prepared by the combination of vapor-deposition and electrodeposition methods corresponded to the geometry of the template pores. The ion-track membranes of PC gave the smooth surface of the nanocones while, in contrast, the ion-track membrane of semi-crystalline PET provided the rough surface.

References

[1] Y. Li *et al.*, Adv. Mater., **22**, 1926-29 (2010).
[2] M. E. T. Molares, Beilstein J. Nanotechnol., **3**, 860-83 (2012).
[3] H. Mukaibo *et al.*, small, **5**, 2474-79 (2009).

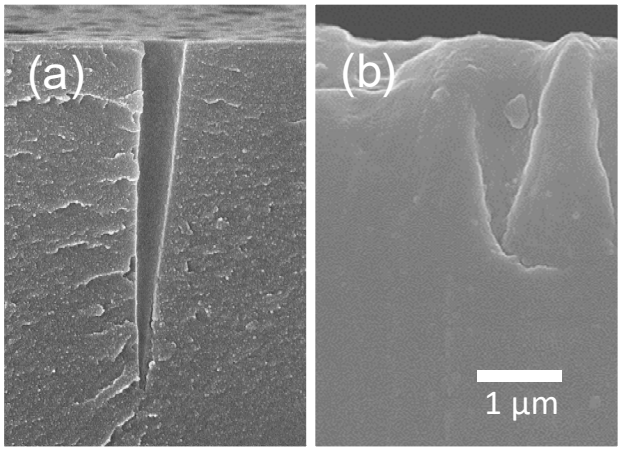

Fig. 1. SEM images of the cross-section of the pores obtained by etching in a 4.0 M NaOH solution from the different membrane materials: (a) PC and (b) PET.

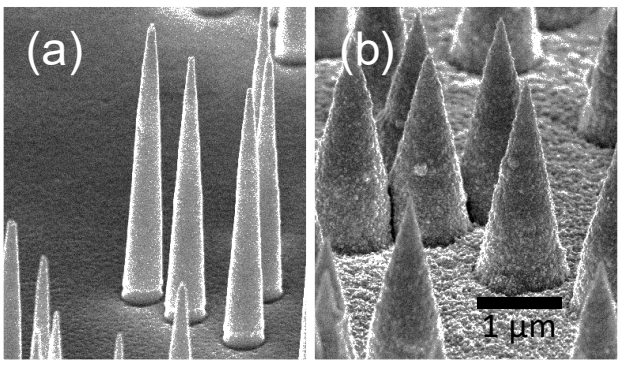

Fig. 2. SEM images of the Pt nanocones obtained from the etched pores shown in Fig. 1.

1 - 08 Prediction of Scintillation Light Yield Based on Sub-micrometer Radiation Transport Calculation and Förster Effect

T. Ogawa [a], T. Yamaki [b] and T. Sato [a]

[a] Environment and Radiation Sciences Division, NSEC, JAEA,
[b] Department of Advanced Functional Materials Research, TARRI, QST

Scintillators are the materials which convert the energy of radiation to photons. They are widely used for scientific experiments, medicine, and radiation control. The light yield of scintillators is in principle proportional to the deposited energy but often suppressed by a quenching effect depending on the energy deposition density of the incoming radiation. It is likely that the quenching effect is attributed to the Förster effect. When the Förster effect occurs, the excitation energy of the excited molecule is absorbed by one of the neighboring molecules and the absorbed energy is dissipated by non-radiative de-excitation. So far, strength of the quenching effect and its dependence on the incident particle species and energies was empirically known [1] but it was pinpointed that such an empirical parameterization was inadequate for high-LET particles [2]. In this study, excitation of fluorescent molecules was calculated based on the radiation track-structure calculation in sub-micrometer scale and Förster effect between the excited fluorescent molecules to finally obtain the scintillation light yield considering the quenching effect. The calculation was done for the most typical scintillation material NE-102A.

Energy deposition in the scintillator crystal by the incident radiation was calculated by a track-structure calculation code RITRACKS [3]. Among energy deposition reactions calculated by RITRACKS, those depositing energies larger than 10 eV were assumed to result in one excited fluorescent molecule. The intensity of the Förster effect was calculated afterwards. Probability that the excitation energy of one molecule is transferred to another excited molecule is written as $1/(1+(r/R_f)^6)$, where r is the distance between the molecules, and R_f is the parameter specific to NE-102A. The energy transfer probability between all the molecule-pairs was calculated. If the energy is transferred to another excited molecule, one of the molecules goes to the ground state and the other turns to the original excitation state after dissipating the received excitation energy as phonons. Finally, the light yield was assumed to be proportional to the number of remaining excited molecules.

The scintillation light yield owing to irradiation by electrons and protons was calculated in a wide energy range and compared with literature data [4] in Fig. 1. Under all the conditions, the scintillator was thick enough to fully stop the incident radiation, and therefore the incident energy agrees with the deposited energy. In the case of electron-incidence, energy deposition is spatially dispersed; therefore quenching is weak. On the other hand, energy deposition by protons is so dense that light emission is suppressed by quenching. In particular, in the energy range from 0 to 3 MeV, the light yield is suppressed by a factor of 1/3 to 1/10. In contrast, at higher energies, the light yield by protons is almost proportional to the deposited energy. These trends calculated by our model are in good agreement with the literature data.

References

1) J. B. Birks, Proc. Phys. Soc. A, **64**, 874 (1951).
2) N. Matsufuji *et al.*, Nucl. Instrum. Meth. Phys. Res. A, **437,** 346-53 (1999).
3) I. Plante *et al.*, New J. Phys., **10**, 125020 (2008).
4) G. V. O'Rielly, *et al.*, Nucl. Instrum. Meth. Phys. Res. A, **368,** 745 (1996).

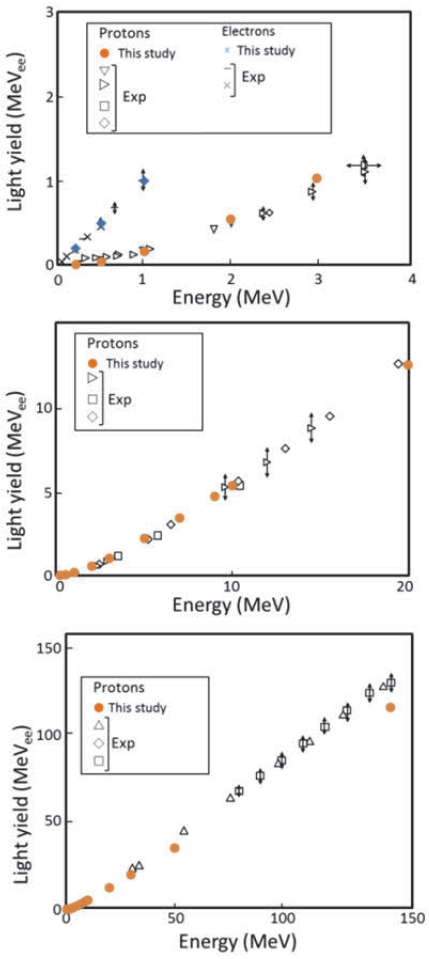

Fig. 1. Scintillation light yield of NE-102A scintillator exposed to electrons or protons. Vertical axis is the light yield normalized for 1 MeV electron.

1 - 09 Preparation of Nano-structure Controlled Ion-exchange Membranes by Ion Beams and Their Application to Seawater Concentration

T. Yamaki [a)], M. Goto [b)], S. Sawada [a)], H. Koshikawa [a)], A. Kitamura [c)] and M. Higa [d)]

[a)] Department of Advanced Functional Materials Research, TARRI, QST,
[b)] Graduate School of Science and Engineering, Yamaguchi University,
[c)] Fuels and Materials Engineering Division, NSEC, JAEA,
[d)] Graduate School of Sciences and Technology for Innovation, Yamaguchi University

Until recently, many researchers have been developing better ion-exchange electrodialysis membranes for applications to a seawater concentration process. The present study deals with the preparation of nano-structure-controlled cation- and anion-exchange membranes (CEMs and AEMs) by a so-called ion-track grafting technique [1, 2]. This new technique involves irradiation of a polymer substrate with an MeV-GeV heavy-ion beam and the graft polymerization into the resulting latent tracks. If the ion-exchange groups are introduced only into the nano-sized cylindrical tracks, the surrounding substrate matrix without any modifications is expected to mechanically prevent any excess swelling, thereby improving ion transport properties.

A 25-μm-thick poly(ethylene-*co*-tetrafluoroethylene) (ETFE) film was irradiated with a 560 MeV ^{129}Xe ion beam at fluences of 3.0×10^8 and 1.0×10^9 ions/cm^2. The irradiated ETFE films were immersed in grafting solutions of ethyl *p*-styrenesulfonate (EtSS) (solvent: 1, 4-dioxane) and chloromethyl styrene (CMS) (solvent: pure water or toluene) and then afforded to hydrolysis and quaternization of the grafted chains for the preparation of CEMs and AEMs, respectively. Not only the EtSS and CMS grafting reactions but also the following hydrolysis and quaternization proceeded quantitatively, resulting in the preparation of the CEMs and AEMs with controlled ion exchange capacities up to 2.0 - 2.5 mmol/g.

Figure 1 shows the relationship between the water uptake and membrane resistance for our nano-structure controlled CEMs prepared at the different fluences. Both the water uptake and resistance were lower for our ion-track grafted CEMs than for the conventional γ-ray-grafted membranes, and strikingly the transport number was also comparable to that of a commercially-available membrane (results not shown). Figure 2 shows the experimental data for our AEMs, also demonstrating the lower water uptake and resistance than the commercially-available membrane. These results above would be because local and high-density energy deposition due to the ion beam enabled us to control the membrane structure in a nanometer scale.

The track diameter was theoretically estimated to be ca. 250 nm, and the volume percentage of the tracks was only 14% at a fluence of 3.0×10^8 ions/cm^2. A key for success here is to achieve high graft levels in as small a number of tracks as possible.

Acknowledgement

This work was partially supported by the Salt Science Research Foundation No. 1521 and 1623.

References

1) M. Higa *et al.*, Bull. Soc. Sea Water Sci. Jpn., **71**, 37-38 (2017).
2) T. Yamaki *et al.*, J. Power Sources, **195**, 5848-55 (2010).

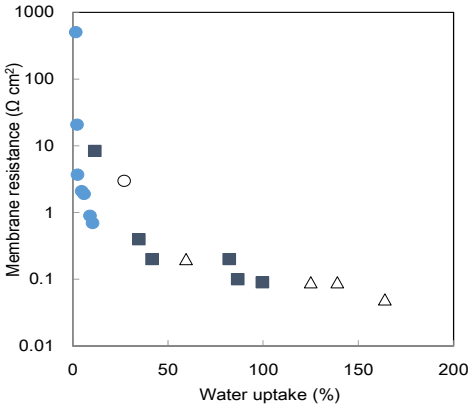

Fig. 1. Relationship between the water uptake and membrane resistance for our nano-structure controlled CEMs prepared at different fluences of 3.0×10^8 (●) and 1.0×10^9 ions/cm^2 (■). The data are compared with those of the conventional CEMs prepared by γ-ray grafting (△) and a commercially-available Neosepta CMX membrane (○).

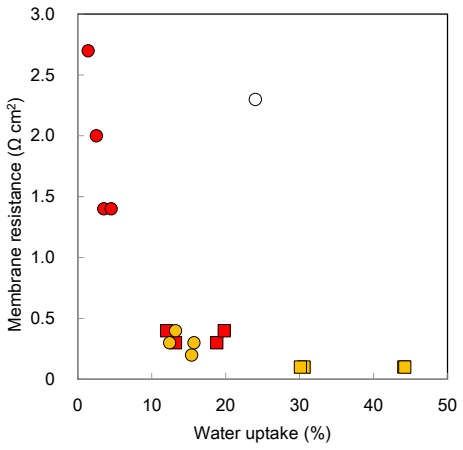

Fig. 2. Relationship between the water uptake and membrane resistance for our nano-structure controlled AEMs prepared by the CMS grafting in toluene (●, ■) and water (●, ■) solvents and at different fluences of 3.0×10^8 (●, ●) and 1.0×10^9 ions/cm^2 (■, ■). The data are compared with those of a commercially-available Neosepta AMX membrane (○).

1 - 10 How Does Ion-beam-irradiated Carbon Support Improve the Activity of Platinum Nanoparticle Catalysts ?

K. Kakitani [a, b], T. Kimata [b], T. Yamaki [a], S. Yamamoto [a], T. Taguchi [a], D. Matsumura [c], I. Shimoyama [c], A. Iwase [d], T. Kobayashi [e] and T. Terai [b]

[a] Department of Advanced Functional Materials Research, TARRI, QST,
[b] Department of Nuclear Engineering and Management, The University of Tokyo,
[c] Energy and Environment Materials Science Division, MSRC, JAEA,
[d] Department of Materials Science, Osaka Prefecture University,
[e] Neutron Beam Technology Team, RIKEN

Carbon-supported platinum nanoparticles (Pt NPs) are used as electrocatalysts of polymer electrolyte fuel cells (PEFCs). Since the sluggish kinetics of the oxygen reduction reaction (ORR) at the cathode is one of the serious challenges for wide commercialization of PEFCs, it is strongly required to improve the ORR activity of the Pt NPs. Quite recently, we have prepared the Pt NPs on the glassy carbon (GC) substrate pre-irradiated with energetic Ar ions and found them about 2.5 times more active for the ORR than those on the non-irradiated one [1]. However, this enhancement has not yet been explained mechanistically. One possibility is that the chemical state of the Pt NPs would be affected by the ion-beam-irradiated carbon support [2]. Therefore, the present study deals with the X-ray absorption near edge structure (XANES) measurements to investigate how the catalytic activity was improved by the chemical state.

A GC substrate was irradiated with 380 keV Ar ions at the fluence of 1.0×10^{16} ions/cm^2 in an IA chamber at the TIARA ion implanter and then heated at 400 ºC in an N_2 atmosphere for 1 h to remove surface contaminations originating from water. Then the Pt NPs were prepared by RF magnetron sputter deposition on the pre-irradiated and non-irradiated GC substrates. The mean size of the Pt NPs prepared in the same manner was reported to be about 5 nm [1]. The X-ray absorption data at the Pt M_3 edge were measured in the total electron yield mode using the synchrotron radiation on the beamline 27A of the Photon Factory of the High Energy Accelerator Research Organization.

Figure 1 shows the XANES spectra of the Pt NPs on the irradiated and non-irradiated GC substrates after normalization and background subtraction. The intensity of the peak in the vicinity of the threshold in the XANES (also called white-line) was lower on the irradiated GC substrate. The white-line intensity generally gets lower as the Pt 5d orbital is more filled. Thus, the result indicates that more electrons were populated in the Pt 5d orbital on the irradiated GC substrate than on the non-irradiated one. We consider here that the Pt NPs on the irradiated GC substrate could be less oxidized [3]; in other words, the Pt-carbon support interaction formed by the pre-irradiated GC substrate possibly suppresses the formation of Pt oxide. It is accepted that this chemical-state change of the Pt NPs increases the kinetics of the rate-limiting step of the ORR (the removal of adsorbed O and OH species from the Pt NPs). Therefore, the suppression of the Pt oxidation resulting from the Ar^+-irradiation of the carbon support would account for the high ORR activity.

Theoretical calculations based on the density functional theory are now in progress to investigate the relationship between the ion-beam-irradiated carbon support and the suppression of the Pt-NP oxidation [4].

Acknowledgement

This work was partly performed under the NIMS-RIKEN-JAEA-QST Cooperative Research Program on Quantum Beam Science and Technology.

References

[1] K. Kakitani *et al.*, Housyasen To Sangyou, **141**, 29-32 (2016) [in Japanese].
[2] T. Kimata *et al.*, Surf. Coat. Tech., **306**, 123-26 (2016).
[3] T. Yamamoto *et al.*, BUNSEKI KAGAKU, **62**, 555-63 (2013).
[4] K. Kakitani *et al.*, Abst. ECSJ 2016 84th Spring Meet., 1D25 (2017).

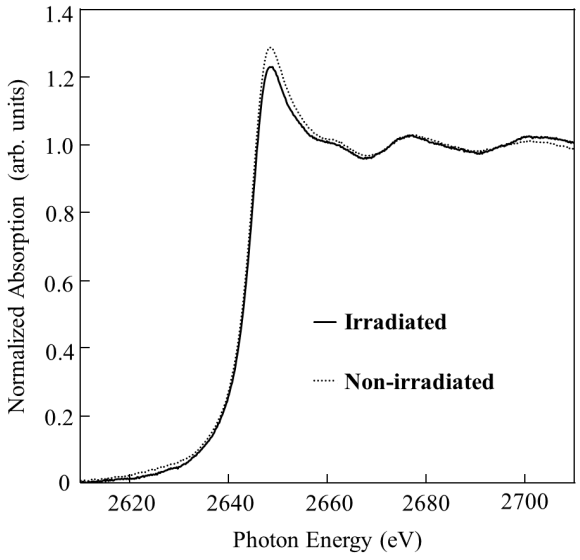

Fig. 1. Pt M_3 edge XANES spectra of the Pt NPs on the irradiated and non-irradiated GC substrates.

1 - 11 Ion Track Etching of PVDF Films Irradiated with Fast C_{60}^{+} Cluster Ions

A. Kitamura [a)], T. Yamaki [b)], A. Chiba [c)] and A. Usui [d)]

[a)] Fuels and Materials Engineering Division, NSEC, JAEA,
[b)] Department of Advanced Functional Materials Research, TARRI, QST,
[c)] Department of Advanced Radiation Technology, TARRI, QST,
[d)] Health and Safety Department, ORDC, JAEA

Poly(vinylidene-fluoride) (PVDF) is useful for various membrane applications to microfiltration, gas separation or water desalination because of its high chemical resistance. We previously reported a new ion-track-etching technique for PVDF involving the irradiation with a uniform beam in an oxygen atmosphere at an LB course of the TIARA cyclotron [1]. Compared to the conventional method using the irradiation in a vacuum, the size of the etchable tracks was found to increase significantly. Our focus here is on the irradiation with carbon cluster ions because they can deposit very dense energy into their tracks [2, 3]. We investigated the track-etched surface of PVDF films irradiated with C_{60}^{+} cluster ions, comparing the data with C^{+} monoatomic ions.

Commercially-available PVDF films (25 μm in thickness) were irradiated with 6 MeV C_{60}^{+} cluster ions using the TC course of a 3 MeV tandem ion accelerator of TIARA. The energy of the each carbon ion is 100 keV/atom; thus, for comparison, the PVDF films were also irradiated with 100 keV C^{+} ions using the 400 keV ion implanter of TIARA. The fluence was fixed at 3.0×10^{7} ions/cm^{2}. According to a calculation using a SRIM code, the range and LET of 100 keV C^{+} ions in PVDF was 350 nm and 280 eV/nm, respectively. The LET of the C_{60}^{+} cluster ion, an aggregate of 60 carbon atoms, was estimated to be 17 keV/nm by the following formula: 280 × 60. The irradiated films were etched in an aqueous KOH solution at a concentration of 9 M at 80 ºC without stirring. The etching time was in a range from 48 h to 72 h. The etched samples were washed with water and dried at 40 ºC. The surface was observed using a scanning electron microscope (SEM) and an atomic force microscope (AFM). The surface diameter of track-etched pores was measured by using an image processing program.

Figure 1 shows SEM and AFM surface images of track-etched PVDF films irradiated with 6 MeV C_{60}^{+} cluster ions and with 100 keV C^{+} ions after alkaline etching for 72 h. The surface irradiated with C_{60}^{+} cluster ions apparently possessed flat-bottomed pores (Fig. 1a) with an average diameter and depth of approximately 400 and 250 nm, respectively. On the other hand, track-etched pores were also formed on the surface irradiated with C^{+} ions, but their morphology was irregular or obscure (Fig. 1b).

Figure 2 shows the surface diameter of track-etched pores as a function of etching time. In the irradiation with the C_{60}^{+} cluster ions, the diameter increased with increasing the etching time (Fig. 2a). The tracks of the 100 keV C^{+} ions seemed to be hardly developed by the etching when the time was shorter than 72 h. The average diameter at 72 h was measured as about 100 nm with a large experimental error.

In conclusion, the C_{60}^{+} cluster ions irradiation caused a large size of etchable tracks on the PVDF surface. The result could represent the effect of local and simultaneous collision by the aggregated ions.

References

[1] A. Kitamura *et al.*, JAEA Takasaki Annu. Rep. 2014, JAEA-Review 2015-022,137 (2016).
[2] H. Dammak *et al.*, Phys. Rev. Lett. 74, 1135 (1995).
[3] A. Chiba *et al.*, Nucl. Instrum. Meth. Phys. Res. B, **269**, 824 (2011).
[4] W. Wesch *et al.*, Ion Beam Modification of Solids, 366 (2016).

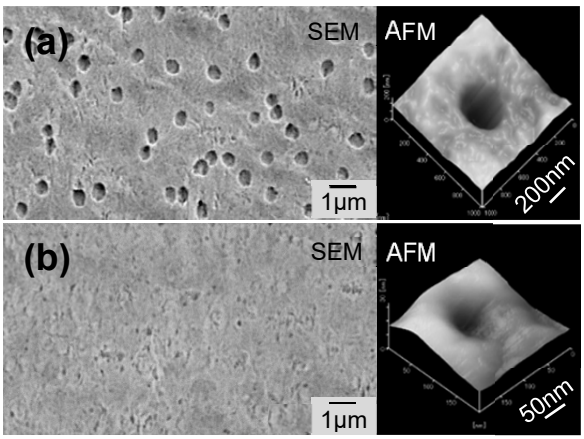

Fig. 1. SEM and AFM images of track-etched PVDF films irradiated (a) with 6 MeV C_{60}^{+} cluster ions and (b) with 100 keV C^{+} ions. The etching time was 72 h.

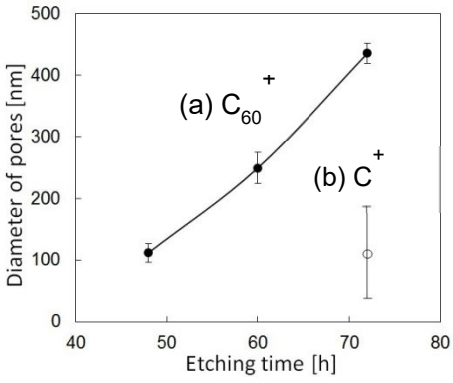

Fig. 2. Diameter of track-etched pores as a function of etching time for the PVDF films irradiated (a) with 6 MeV C_{60}^{+} cluster ions and (b) with 100 keV C^{+} ions.

1 - 12 Electro-electrodialysis Performance of Radiation-grafted Cation-exchange Membranes with Different Graft Chains

N. Tanaka [a)], S. Sawada [b)], T. Yamaki [b)], K. Onuki [a)] and S. Kubo [a)]

[a)] Hydrogen Application Research and Development Division, NHARC, JAEA,
[b)] Department of Advanced Functional Materials Research, TARRI, QST

Thermochemical water-splitting Iodine-Sulfur (IS) process [1] is known to be a promising method for hydrogen production. In the IS process, a new cation-exchange membrane prepared by the radiation-induced graft polymerization has been applied to the electro-electrodialysis (EED) for enriching hydrogen iodide (HI) in an HI-I_2-H_2O mixture (HIx) solution [2, 3]. The membrane properties should be improved for the efficient HI concentration. The concentration performance in the EED can be represented by indexes such as transport number of protons (t_+) and water permeation factor (β). Our previous study [4] suggested that I_2 affinity of the grafted polymer affected the membrane permeation for the HI concentration. In the present study, therefore, we introduced different chemical structures in the cation-exchange membrane using a methyl acrylate (MA) monomer, while we previously prepared the membranes using the styrene (St) monomer. The t_+ and β indexes were also evaluated experimentally for the sulfonated MA- and St-grafted poly(ethylene-*co*-tetrafluoroethylene) (ETFE) membranes.

The membranes were prepared by pre-irradiation of the ETFE film with γ-rays, the graft polymerization of MA or St, and sulfonation. The resulting membranes are referred to as ETFE-MA and ETFE-St, and their ion exchange capacity (IEC) ranged 0.6 - 1.0 and 1.1 - 1.6 mmol/g, respectively. The t_+ and β values were measured using a filter-press type EED cell [2], to which a direct current of 200 mA/cm^2 was supplied for 4 hours at 313 K. The feeding HIx solution contained HI = 10 mol/kg and I_2 = 10 mol/kg.

Figure 1 shows the variation of t_+ as a function of IEC. The t_+ value of ETFE-MA decreased with an increase in IEC; interestingly, it seemed to become close to that of ETFE-St at IEC > 0.8 mmol/g. This result suggests that the permeation mechanism of proton would be similar to each other. Figure 2 shows the variation of β as a function of IEC. The β value of ETFE-MA has little change and was in the range of 1.0 to 1.5 . On the other hand, that of ETFE-St increased with an increase of IEC.

After HI concentration tests of ETEE-MA and -St membranes, a change of color derived from I_2 was observed on the surface of both membranes, suggesting that the I_2 affinity of both membranes is similar to each other, irrespective of kinds of the monomer. In ETFE-St membrane, it is suggested that electro-donor complex is formed between I_2 and benzene ring in St [4]. Considering this, although ETFE-MA does not have the benzene ring, it is predicted that other chemical bonds in the sulfonated MA unit react with I_2.

Through this attempt, we did not observe the different performance between ETFE-MA and –St; however, these results of MA could not necessarily reject the effectiveness of MA for HI concentration. We need the further investigation about the permeation mechanism of the HI concentration using MA.

References

[1] S. Kubo *et al.*, Nucl. Eng. Des. **233**, 355 (2004).
[2] N. Tanaka *et al.*, J. Membr. Sci. **411-12**, 99 (2012).
[3] T. Yamaki *et al.*, Polymer **45**, 6569 (2004).
[4] N. Tanaka *et al.*, J. Membr. Sci. **456**, 31 (2014).

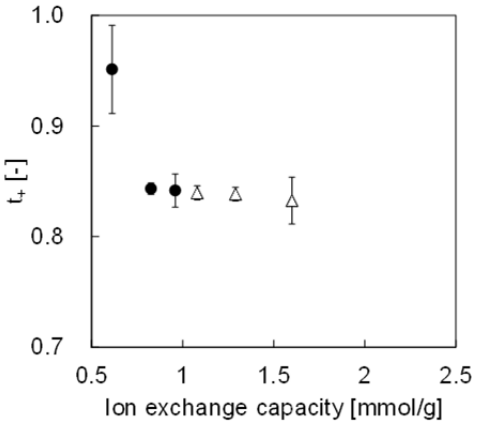

Fig. 1. Ion exchange capacity dependence of the transport number, t_+ (●: ETFE-MA, △: ETFE-St).

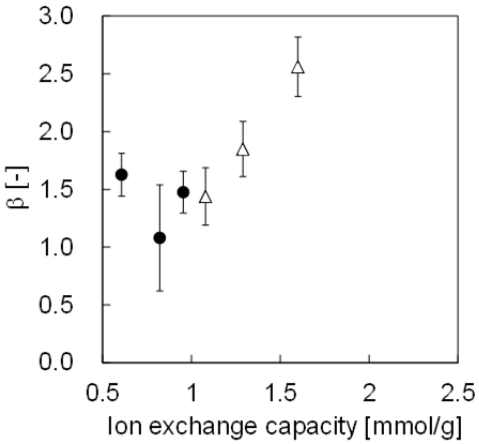

Fig. 2. Ion exchange capacity dependence of the water permeation factor, β (●: ETFE-MA, △: ETFE-St).

1 - 13 Durability of Cation Exchange Membranes for the Membrane Bunsen Reaction in the Hydrogen Production IS Process

T. Kimura [a)], M. Nomura [a)], S. Sawada [b)], T. Yamaki [b)], N. Tanaka [c)] and S. Kubo [c)]

[a)] Department of Applied Chemistry, Shibaura Institute of Technology,
[b)] Department of Advanced Functional Materials Research, TARRI, QST,
[c)] Hydrogen Application Research and Development Unit, NHRC, JAEA

The thermochemical water splitting Iodine-Sulfur (IS) process which uses I_2 and SO_2 as catalyst is a promising hydrogen production method [1]. The Bunsen reaction ($I_2 + SO_2 + H_2O \rightarrow 2HI + H_2SO_4$) is one of the key steps in the IS process. To reduce the amount of circulated I_2, the Bunsen reaction was examined by an electrochemical cell using a cation exchange membrane (CEM) as separator [2]. This so-called membrane Bunsen reaction produces HI and H_2SO_4 in the cathode and anode sides, respectively. We have successfully operated the membrane Bunsen reaction employing new CEMs, which were prepared by a radiation-graft polymerization method [3-5]. Since the operation period was only 3 h, the CEM stability for longer time was not clear. In this study, therefore, the acid durability of the radiation-grafted CEM was investigated for up to 1,000 h.

A 50-μm-thick poly(ethylene-*co*-tetrafluoroethylene) substrate film was irradiated in argon with γ-rays in a ^{60}Co irradiation facility. The irradiation time was 1.5 h at a dose rate of 10 kGy h^{-1}. The irradiated film was immersed in a toluene solution of styrene and divinylbenzene (DVB) at 60 ºC for 1-10 h. Then, for sulfonation, the grafted film was immersed in a chlorosulfonic acid solution at 50 ºC for 6 h. The ion exchange capacity (IEC) of the CEMs was evaluated by a titration method using an aqueous NaOH solution (0.01 mol kg^{-1}).

The proton conductivity of the CEM was measured by a two-probe AC impedance technique. The water permeance was measured by a pervaporation method. For the stability test, the DVB-crosslinked CEM was immersed in a 90% H_2SO_4 aqueous solution at room temperature. The IEC change ratio (R) was calculated as follows:

$$R = 100 \times (IEC_1 - IEC_0) / IEC_0, \qquad (1)$$

where IEC_0 and IEC_1 are the IECs before and after the H_2SO_4 immersion, respectively.

The IEC of the CEMs was controlled between 0.9 and 2.2 mmol g^{-1} by varying the grafting time from 1 to 10 h. This indicates that each unit of the grafted polystyrene was successfully sulfonated. The radiation-grafted CEM at an IEC of 1.9 mmol g^{-1} exhibited a proton conductivity comparable to that of Nafion 212 membrane (the commercially-available CEM). Furthermore, it revealed a 40% decrease in the water permeance. We strongly expect that a combination of the sufficient proton conductivity and low water permeance would be quite suitable for highly efficient membrane Bunsen reactions.

Figure 1 shows the R value as a function of the H_2SO_4 immersion time. The IEC slightly decreased during the course of immersion, and R reached only -4.7 % at 1,000 h. It follows from this result that the radiation-grafted CEM has sufficient chemical stability under the strong acid condition. A slight IEC reduction indicates degradation of only a small part of the CEM. The detailed degradation mechanism will be discussed in our future work.

In conclusion, the radiation grafted CEM was almost stable for 1,000 h in the H_2SO_4 immersion test, demonstrating the feasibility to continue the membrane Bunsen reaction for a long time.

Acknowledgement

This work was partially supported by Council for Science, Technology and Innovation (CSTI), Cross-ministerial Strategic Innovation Promotion Program (SIP), “energy carrier” (Funding agency: JST).

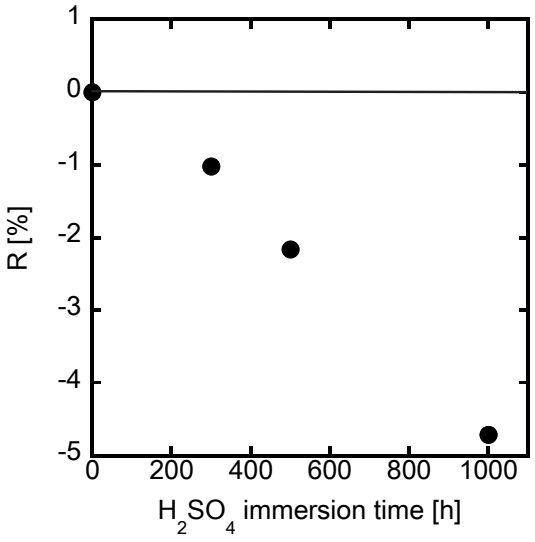

Fig. 1. The R value as a function of H_2SO_4 immersion time.

References

[1] S. Kasahara *et al.*, J. Chem. Eng. Jpn., **36**, 887-99 (2003).
[2] M. Nomura *et al.*, AIChE J., **50**, 1991-98 (2004).
[3] T. Yamaki, J. Power Sources, **195**, 5848-55 (2010).
[4] M. Nomura *et al.*, QST Takasaki Annu. Rep. 2015, **QST-M-2**, 45 (2017).
[5] http://www.jst.go.jp/pr/announce/20170302/.

1 - 14 Design and Fabrication of Near-perfect Optical Absorbers Having Micro-structured Surface Using Etched Ion Tracks

K. Amemiya [a)], H. Koshikawa [b)], T. Yamaki [b)], H. Shitomi [a)] and T. Zama [a)]

[a)] National Metrology Institute of Japan, AIST,
[b)] Department of Advanced Functional Materials Research, TARRI, QST

The novel broadband ultralow reflectance optical absorber having micro-structured surface using etched ion tracks has been developed. Poly allyl diglycol carbonate (CR-39) plastic plates were irradiated with energetic heavy ion beam from AVF cyclotron of TIARA; then the samples were etched in NaOH solution to fabricate micro-structures on their surface, followed by black layer coating. Some of the fabricated optical absorbers exhibited low reflectance of 0.2%~0.4% in UV–VIS, < 2% in NIR respectively, while also exhibiting good mechanical durability.

黒色材料は、太陽熱エネルギー吸収体、熱型光センサの吸収体、高放射率黒体、迷光防止など、幅広い用途がある。紫外域～赤外域にわたり 99.9%もの吸収率を誇る平板型極低反射黒体には、配向カーボンナノチューブ（VACNT）[1, 2]やニッケル-リン（NiP）ブラック[3, 4]がある。VACNT はカーボンナノチューブ（CNT）フォレストが低面密度に配向していて、実効屈折率が 1 に近くなることで表面反射が抑えられているのに対し、NiP ブラックでは入射光が表面のマイクロ構造中で多重反射するうちに吸収が促進され、正味の反射率が低減されている。しかし、いずれも機械的にもろく、取扱いの困難なため広く普及するには至っていない。

筆者らはこれまでに、理論計算を通じて、NiP ブラックの反射率が表面マイクロ構造の鋭さ（アスペクト比）及び光吸収層の厚みに依存することを明らかにしてきた[4]。この知見に基づき、本研究では光吸収性を高められる表面マイクロ構造を機械的にロバストな基板上に狙った通りに形成することで、新規な極低反射光吸収体の開発を目指している。表面マイクロ構造形成にイオントラックエッチング法[5]を用いると、吸収させたい光の波長に合わせてピット構造を容易に最適化できるという利点がある。

前年度までに、時間領域差分法（FDTD 法[6]）計算により、0.1%級の極低反射率を達成できる条件［ピット構造アスペクト比>3、ピット開口径≧入射光波長、黒色材層はアモルファスカーボン（DLC）で厚さ>1 μm］が得られていた[7]。この条件を満たす構造を形成するため、まず CR-39 樹脂基板に TIARA AVF サイクロトロンからの $^{40}Ar^{14+}$ビーム 520 MeV を照射した。試料を化学エッチングしたのち、表面を DLC で黒色コートすることで、光吸収体を作成した。黒色層厚が反射率に与える影響を調べるため、DLC 厚は 1 μm, 2 μm, 3 μm のものを作製した。各試料の分光反射率は分光光度計（PerkinElmer LAMBDA 900）により計測した。その結果を Fig. 1 に示す。紫外～可視域ではいずれも反射率<1%、近赤外域でも反射率≦2%という低い値が得られた。DLC は平坦面の場合、表面反射率が約 16%にもなるので、表面マイクロ加工により大幅に反射率が低減したことになる。黒色コーティング厚が増加するにつれ、波長約 600 nm - 1,500 nm においては反射率が低減したが、それ以下の短波長域においては反射率に増加傾向が見られた。これはコーティングが厚いと表面の微細構造がなまっていき、入射光が微細構造内に十分導光しなくなるためと考えられる（波長約 600 - 1,500 nm では、DLC 層の吸収係数があまり高くないこともあり、傾向が逆転しているものと考えられる）。また、本光吸収体の機械的強度を調べるため、エアブロー試験、及びテープ貼付・引き剥し試験も行ったが、試験前後の分光反射率の差は 0.1%程度以内で一致していることがわかり、従来の極低反射素材（NiP ブラック、VACNT ブラック）にない耐性も確認できた。

本研究は東京大学大学院工学系研究科原子力専攻の原子力機構施設利用総合共同研究制度、量子科学技術研究開発機構の施設共用制度により実施された。ここに感謝の意を表す。

References

[1] Z. P. Yang *et al.*, Nano Lett. **8**, 446-51 (2008).
[2] K. Mizuno *et al.*, Proc. Natl. Acad. Sci. U.S.A. **106**, 6044-47 (2009).
[3] S. Kodama *et al.*, IEEE Trans. Instrum. Meas. **39**, 230-32 (1990).
[4] K. Amemiya *et al.*, Appl. Opt. **51**, 6917-25 (2012).
[5] S. Kodaira *et al.*, Radiat. Meas. **46**, 1782-85 (2011).
[6] A. F. Oskooi *et al.*, Comput. Phys. Commun. **181**, 687-702 (2010).
[7] K. Amemiya *et al.*, Nucl. Instrum. Meth. Phys. Res. B **356-57**, 154-59 (2015).

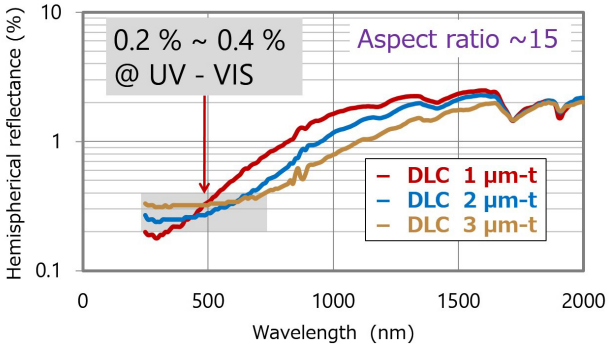

Fig. 1. Black-layer-thickness dependence of the spectral hemispherical reflectance of the developed optical absorber.

1 - 15 Formation Mechanism of (111)-oriented $Ti_{1-x}Al_xN$ Thin Films on Monocrystalline AlN by Reactive CVD

Y. Kasukabe [a, b], H. Shimoda [b], S. Yamamoto [c] and M. Yoshikawa [c]

[a] Global Learning Center, Tohoku University, [b] Department of Metallurgy, Tohoku University, [c] Department of Advanced Functional Materials Research, TARRI, QST

Films of $Ti_{1-x}Al_xN$ have been known as the material which exhibits superior mechanical and thermal properties, and those are widely used as coatings for industrial applications such as cutting tools. Irrespective of those attracting performance, little is studied on the growth mechanism as well as the chemical process. In this work, $Ti_{1-x}Al_xN$ thin films have been prepared by reactive Chemical Vapor Deposition (CVD) and analyzed by Field Emission Gun Scanning Electron Microscopy (FEG-SEM), Transmitting Electron Microscope (TEM) [1], and X-ray Diffraction (XRD).

Recently, it has been reported that $Ti_{1-x}Al_xN$ films have been grown by use of the titanium tetra chloride, $TiCl_4$, and c-plane (0001) monocrystalline hexagonal aluminium nitride, AlN, precursors [2]. The AlN has been prepared at 1,500 ºC with the gas mixture of NH_3 and $AlCl_3$ on c-plane (0001) monocrystalline hexagonal sapphire. During the $Ti_{1-x}Al_xN$ growth, hydrogen gas is supplied in order to promote the reactivity. The growth has been performed at various temperatures between 800 ºC and 1,200 ºC on the 100-nm-thick monocrystalline AlN on sapphire.

If there are no mechanical constraints in the films grown on monocrystalline AlN substrates at 800 - 1,200 ºC, the relationship between contents of Ti and lattice parameters is expected to have a linear behavior (as known as Vegard's law), as shown by a linear line (a)-(b) in Fig. 1, which summarizes some previous experimental results [3] and present results. It has been found from these results that according to this Vegard's law, the contents of Ti in $Ti_{1-x}Al_xN$ increase in accordance with the substrate temperature. Figure 2 shows the surface morphologies of $Ti_{1-x}Al_xN$ layers deposited at (a) 800 ºC, (b) 900 ºC, (c) 1,000 ºC and (d) 1,200 ºC on monocrystalline AlN substrates. At temperatures lower than 1,000 ºC, surface morphologies appear to be smooth. As the temperature is raised, the grain size appears to become larger, but there is almost no substantial change between 800 ºC and 1,000 ºC (Figs. 2 (a) – (c)). However, the surface morphology deposited at 1,200 ºC (Fig 2(d)) is quite different form the others. The grains are much smaller than those fabricated at less than 1,000 ºC, and some of them seem to grow in a columnar shape. It can be considered that this difference results from the reactivity between $TiCl_4$ and condensed AlN. Generally, as temperature is raised, reaction rate increases. If the reaction rate increases in this system, it can be expected that $TiCl_4$ and AlN react as soon as $TiCl_4$ reaches the AlN surface, leading to grow in a columnar shape. In other words, surface diffusion is limited. In contrast, at temperature lower than 1,000 ºC, it can be considered that reaction rate is not as high compared to the system at 1,200 ºC, therefore, sufficient time to diffuse on the surface exists, leading to an increase of surface flatness.

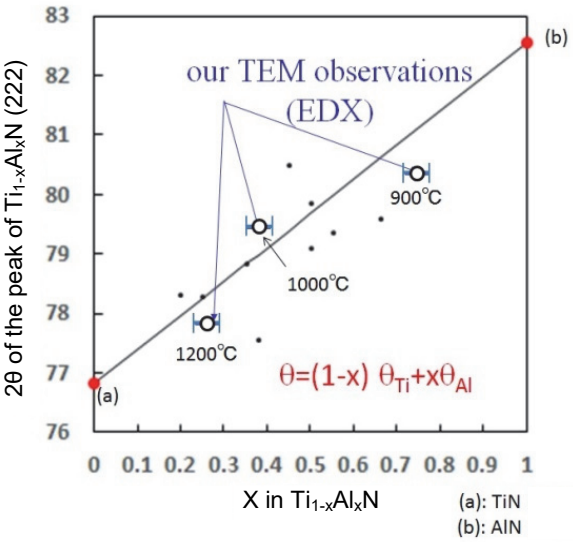

Fig. 1. The position of the peaks corresponding to cubic $Ti_{1-x}Al_xN$ (222) in X-ray diffraction pattern.

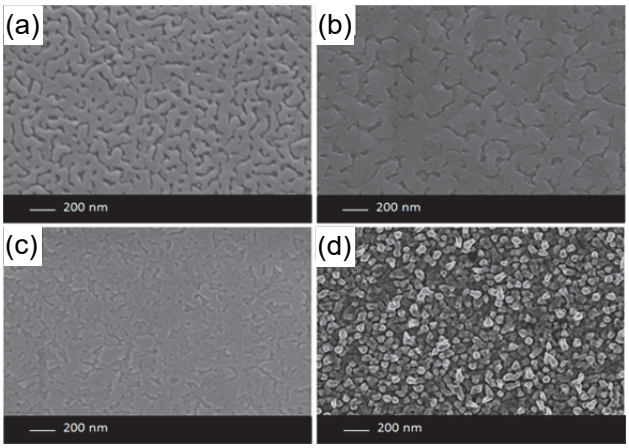

Fig. 2. Surface morphologies of the layers fabricated on monocrystalline AlN at (a) 800 ºC, (b) 900 ºC, (c) 1,000 ºC and (d) 1,200 ºC observed by FEG-SEM.

References

[1] H. Abe *et al.*, JAERI-Res. 96-047, 1 (1996).
[2] R. Boichot *et al.*, Surf. Coat. Tech. **205**, 1294 (2010).
[3] P. H. Mayrhofer *et al.,* J. Appl. Phys., **100**, 9490 (2006).

1 - 16 Development of Hydrogen Permselective Membranes by Radiation-induced Graft Polymerization into Porous PVDF Membranes

S. Hasegawa, A. Hiroki and Y. Maekawa

Department of Advanced Functional Material Research, TARRI, QST

An establishment of non-electric power hydrogen collection system is required to utilize effectively hydrogen gas. For developing the non-electric power hydrogen collection system, a combination of hydrogen permselective membranes with hydrogen storage materials has been proposed. The hydrogen permselective membranes play an important role for a separation of hydrogen from air or oxygen consisting of water. In this work, the hydrogen permselective membranes based on porous polyvinylidene fluoride (PVDF) were prepared by using radiation-induced graft polymerization technique [1]. To control the permeability, the porosity of the membranes and the type of graft chains that interact with gas molecules were adjusted.

According to the process as shown in Fig. 1, graft polymerization was carried out with commercially available porous PVDF membrane (MERCK MILLIPORE GVWP09050, pore size 0.22 μm, 110 μm thickness). The PVDF membranes γ-irradiated with 20 or 60 kGy were immersed into vinyl acetate (VAc) or chloromethylstyrene (CMS) at 60 or 70 ºC, respectively. Grafting degrees (*GDs*) of VAc and CMS in the porous PVDF are shown in Table 1. The *GDs* of VAc-grafted PVDF increased with the reaction time, and reached 54% at 24 hours. The VAc-grafted PVDF was saponified with 1.0 M NaOH in methanol solution at 50 ºC for 1 hour to obtain the grafted chains of poly(vinyl alcohol) (VA). The *GD* of CMS-grafted PVDF reached 165% at only 1 hour.

The porosity of porous PVDF (ca. 58%) decreased up to 41% at 165% of the *GD*. Permeabilities of hydrogen, oxygen, and water vapor were controlled by adjusting the *GDs* of these grafted membranes, which exhibited in the range of 10^{-6} to 10^{-11} mol/(m^2 sec Pa) (Table 1). The highest permeation ratios of H_2/O_2 in the CMS- and VA-grafted membranes were 0.9 and 1.2, respectively. Highest permeation ratios of H_2/H_2O in the CMS- and VA-grafted membranes were 33 and 120, respectively. The CMS-grafted membrane would exhibit hydrogen permselectivity due to an affinity for hydrogen molecules. On the other hand, in the VA-grafted membrane, the permeation of water vapor would be inhibited by the interaction between the hydrophilic hydroxyl groups and water molecules.

Reference

[1] S. Hasegawa *et al.*, Polymer **54**, 2895-900 (2013).

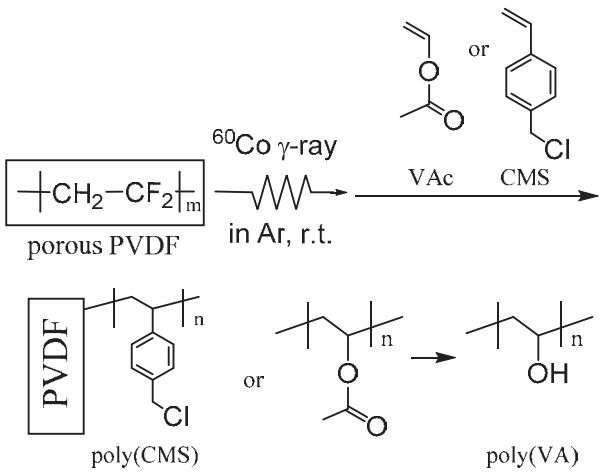

Fig. 1. Synthetic scheme of gas selectivity membranes by radiation-induced graft polymerizations.

Table 1

Permeability and permeation ratio with CMS- and VA-grafted porous PVDF membranes after hot press treatment.

Graft Chains	Reaction Time(h)	GD(%)	Porosity (%)	Permeability ×10^{-7} mol/sec・m^2・Pa			H_2/H_2O	H_2/O_2
				H_2	O_2	H_2O		
-	-	0	58	2.6	1.4(N_2)	5.2	0.5	1.9(N_2)
CMS	1	165	41	66	71	2.0	33	0.9
VA	2	16	62	40	40	7.7	5.1	1.0
VA	5	30	50	38	32	3.2	4.5	1.2
VA	24	54	47	53	48	1.2	120	1.1

1 - 17 Using Small Angle Scattering Method to Reveal the Required Structure for Anion Exchange Fuel Cell Membranes with High Performance

Y. Zhao [a)], K. Yoshimura [a)], A. Hiroki [a)], Y. Kishiyama [b)], H. Shishitani [b)], S. Yamaguchi [b)], H. Tanaka [b)] and Y. Maekawa [a)]

[a)] Department of Advanced Functional Materials Research, TARRI, QST,
[b)] Daihatsu Motor CO. LTD.

In recent years, anion-exchange membranes (AEMs) are being treated as an alternative to proton-exchange membranes (PEMs) in energy conversion devices, due to the advantage of saving expensive platinum catalysts. Compared to the plenty studies on PEMs, neither the molecular design nor the property understanding is sufficient for developing AEMs capable of practical fuel cell applications. Therefore, it is crucial to thoroughly study the current AEMs in terms of their microstructures, ion conductivity, mechanical and alkaline stabilities. Recently, our group developed a new series of AEMs by radiation-induced grafting method, where imidazolium and styrene monomers were grafted into poly(ethylene-co-tetrafluoroethylene) (ETFE) base films γ-irradiated with a dose of 80 kGy at room temperature, followed by alkylation and ion exchange reaction [1]. These AEMs exhibit well-balanced properties of high ion conductivity (> 100 mS/cm) and good stability. It is believed that the good properties are controlled by the structure of membranes. In this work, we focus on a specific AEM (denoted as AEM91, with 2-methyl imidazolium / styrene ratio = 6 / 4, a grafting degree of 91%, and ion exchange capacity of 1.82 meq/g), and aim to reveal the structure required for the high performance, by using small-angle neutron scattering (SANS) method.

Figure 1 shows SANS intensity profiles, $I(q)$, of pristine ETFE membrane (profile 1), dry grafted-ETFE membrane (profile 2), dry AEM91 (profile 3) and AEM91 equilibrated in D_2O (profile 4) as a function of scattering vector q. A

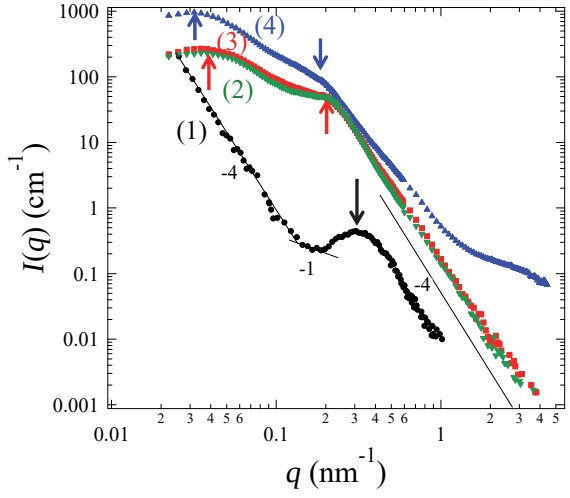

Fig. 1. SANS profiles measured for (1) pristine ETFE membrane, (2) grafted-ETFE, (3) dry AEM, and (4) fully D_2O swollen AEM.

scattering maximum at $q_1 = 0.2 - 0.3$ nm^{-1} is observed in each profile, indicating the typical crystalline lamellar structure with a d-spacing (= $2\pi/q_1$) of 20 - 34 nm as illustrated in Fig. 2.

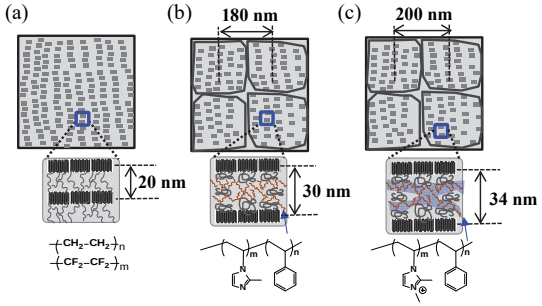

Fig. 2. Schematic illustrations of the morphology of (a) ETFE membrane, (b) grafted-ETFE, and (c) fully water-swollen AEM.

The peak around $q_1 = 0.2 - 0.3$ nm^{-1} shifted towards low-q range upon grafting. This indicates that the lamellar stacks were expanded by the incorporation of the graft chains and water in the amorphous domains. The other maximum peak observed for grafted membrane and AEM91 at $q_2 \sim 0.03 - 0.04$ nm^{-1}, is due to the existence of grains of crystallites with a mean distance of 180 - 200 nm. Profiles 2 and 3 are similar, indicating the morphology is determined in the grafting process but not the alkylation. These findings by SANS method confirm the semi-crystalline feature of AEM91 is conserved from the original ETFE membranes, which is the key reason for its high mechanical stability.

Furthermore, contrast variation SANS measurements, which performed on AEM91 equilibrated in mixtures of H_2O and D_2O with different volume fractions, show that the hydrophilic phase is composed of the entire grafts and water [2]. Therefore, the well-connected ion channels are easily formed in the hydrophilic phase of AEM91, which is the key reason for its high ion conductivity in water. Thus, the relationship between property and structure is characterized by the following 3-phase system: phase 1) crystalline phase offers good mechanical properties; phase 2) amorphous ETFE phase offers a matrix to embed conducting regions; phase 3) well-connected ion channels in hydrophilic phase promotes the anion conductivity.

References

[1] K. Yoshimura *et al.*, J. Electrochem. Soc. **161**(9) F889-93 (2014).
[2] Y. Zhao *et al.*, Soft Matter, **12**, 1567-78 (2016).

1 - 18 Preparation of Novel Bipolar Membranes by an Asymmetric Radiation Grafting Method

S. Sawada and Y. Maekawa

Department of Advanced Functional Materials Research, TARRI, QST

A new type of fuel cell comprising a bipolar membrane (BPM) that possesses both the cation exchange layer (CEL) and the anion exchange layer (AEL) has been recently proposed [1]. In this BPM fuel cell, hydrogen supplied to the anode is split into protons that diffuse in a CEL, while oxygen supplied to the cathode is reduced into hydroxyl ions that diffuse in an AEL. Protons and hydroxyl ions react together at the CEL/AEL boundary to yield water to keep the membrane hydration state. This so-called self-humidification eliminates the demand of an external humidifier, promising considerable size and cost down of a fuel cell system. Besides, less-expensive non-platinum metals can be used for the cathode catalyst, since the oxygen reduction reaction is inherently facile in alkaline environments.

The development of the BPM, the most critical component in a fuel cell system, has been conducted worldwide. The conventional BPM is prepared by combining the individual cation exchange membrane (CEM) and anion exchange membrane (AEM). One drawback of this BPM is the CEM/AEM interface is subject to peeling off during fuel cell operation to reduce output power. To solve this problem, we prepared a novel monolithic BPM by asymmetric radiation grafting of different monomers from both sides of the base film. All graft chains comprising the CEL and AEL are covalently bonded to the base-polymers in the film; namely, the CEL/AEL interface in principle avoids the peeing off. Consequently, this BPM is expected to enable long-term stable fuel cell operation.

A base poly(ethylene-*co*-tetrafluoroethylene) (ETFE) film was γ-irradiated with 15 kGy, and located at the center of a two-compartment cell. As shown in Fig. 1, an aqueous solution of sodium *p*-styrenesulfonate (SSS) and acrylic acid (AA) was injected into the left compartment, while a xylene solution of chloromethylstyrene (CMS) was injected into the right one. The cell was kept at 60 ºC for 6 h for the SSS/AA and CMS grafting from the different sides. After the grafting, the film was immersed in toluene for 6 h and in purified water for 6 h to remove any remaining monomers and homopolymers. The film was dried in a vacuum oven at 50 ºC. The degree of grafting (DOG) was calculated by:

$$DOG = 100 \times (W_1 - W_0) / W_0,$$

where W_0 and W_1 are the film weight before and after the grafting, respectively. The grafted film was immersed in an aqueous solution of trimethylamine for 8 h to give the quaternary ammonium salt group in the CMS unit. The structure of the BPM was analyzed by a scanning electron microscope (SEM) coupled with energy dispersive X-ray spectrometry (EDX).

The DOG of the asymmetric grafted film was 51%. In the BPM prepared from this grafted film, the ion exchange capacities of the sulfonic acid, carboxy, and quaternary ammonium salt groups were evaluated to be 0.24, 0.67, and 1.0 mmol/g, respectively. In the SEM-EDX analysis, the distribution of sulfur and chlorine across the transverse plane of the surface of the BPM was examined. The CEL and AEL are the sulfur- and chlorine-containing regions because sulfur and chlorine are included only in the sulfonic acid groups and quaternary ammonium salt groups, respectively. The CEL and AEL formed in the BPM clearly separated from each other. In the previous similar study on the preparation of the BPM by asymmetric grafting of styrene and 1-vinylimidazole into the ETFE film and subsequent sulfonation and alkylation, the obtained membrane did not have a clear CEL/AEL boundary [2]. Thus, the BPM prepared in this study is the first example to have the distinct CEL/AEL layers in a monolithic film.

The thickness of the CEL and AEL is 19 and 48 μm, respectively. This thickness difference in the both layers can be explained by taking into account the speed of the grafting reaction. Hydrophobic CMS monomer can smoothly penetrate the hydrophobic ETFE film to be grafted. In contrast, the penetration and grafting of the hydrophilic SSS/AA monomer should be relatively slowed down because of the low monomer/film affinity.

Our future work is to investigate the effect of the experimental condition (types of base films, monomers and solvents, temperature and time of grafting reaction) on the BPM structure and properties. Moreover, power generation test of the fuel cell employing our novel BPM will be performed.

References

[1] S. Peng *et al.*, J. Power Sources, **299**, 273-79 (2015).
[2] Y. Guan *et al.*, J. Power Sources, **327**, 265-72 (2016).

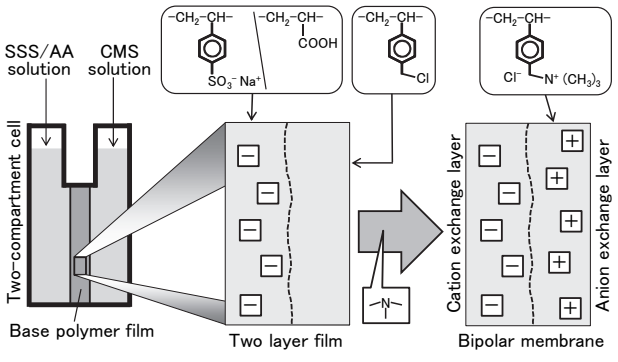

Fig. 1. Procedure of the preparation of the BPM.

1 - 19 Synthesis and Characterization of Aniline-containing Anion-conducting Polymer Electrolyte Membranes by Radiation-induced Graft Polymerization

T. Hamada, K. Yoshimura, A. Hiroki and Y. Maekawa

Department of Advanced Functional Materials Research, TARRI, QST

For the preparation of anion-conducting polymer electrolyte membrane (AEM) with high alkaline stability, graft-type AEMs with aniline groups were synthesized through radiation-induced graft polymerization of *N,N*-dimethylaminostyrene (DMASt) on poly(ethylene-co-tetrafluoroethylene) (ETFE), followed by *N*-methylation and ion-exchange reactions (Scheme 1).

DMASt was synthesized according to the literature (a yield of 70%) [1]. ETFE membranes were pre-irradiated with a dose of 30 kGy, and subsequently, the membranes were immersed in DMASt solution at 60 ºC or 80 ºC to obtain poly(dimethylaminostyrene)-grafted ETFE (ETFE-DMASt) membranes with grafting degrees (GDs) of 12-80% (Table 1). The GDs of ETFE-DMASt graft-polymerized at 80 ºC increased rapidly up to 8 hours of grafting time, and then it reached plateau at about 40%. In contrast, the GDs at 60 ºC gradually increased with increasing time and reached 80% after 48 hours. In this system, the radicals were quickly consumed due to the annihilation and chain transfer at high temperature.

ETFE-DMASt membranes were *N*-methylated with iodomethane to obtain poly(trimethylaminostyrene iodide)-grafted ETFEs. The iodide form was then converted to the corresponding chloride form in 1 M HCl solution. Finally, the chloride form of the membrane was converted to the hydroxide form following immersion in 1 M KOH solution to obtain the poly(trimethylaminostyrene hydroxide)-grafted ETFEs (ETFE-TMASt/OH) with ion-exchange capacities (IEC) of 0.67 - 1.86 mmol/g. The ETFE-TMASt/OH with IEC of 0.67 - 1.86 mmol/g showed conductivities of 53 - 213 mS/cm at 60 ºC and water uptakes of 18 - 118%.

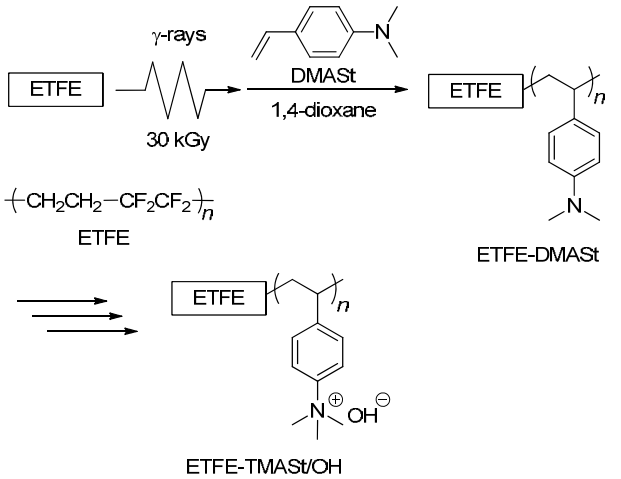

Scheme 1. Preparation scheme for ETFE-TMASt/OH.

The alkaline stability of ETFE-TMASt/OH with IEC of 1.59 mmol/g was evaluated by monitoring the change in their conductivities in 1 M KOH at 80 ºC; the conductivities were plotted as a function of immersion time in Fig. 1. The conductivity of ETFE-TMASt/OH with 1.59 mmol/g maintained 46% level of the initial value even up to 168 h. ETFE-TMASt/OH exhibited excellent alkaline stability in comparison with poly(vinylbenzyltrimethylammonium hydroxide)-grafted ETFE that decomposed into some pieces after 72 hours in 1 M KOH at 80 ºC.

Reference

[1] S. Mallakpour *et al.*, J. Poly. Sci.: Part A: Poly. Chem., **27**, 125-38 (1989).

Table 1
GDs of DMASt into ETFE at 60 ºC and 80 ºC.

No.	Time (h)	Dose (kGy)	Solvent	GD (%)	
				60 ºC	80 ºC
1	1	30	1,4-dioxane	16	12
2	8	30	1,4-dioxane	34	31
3	18	30	1,4-dioxane	51	27
4	36	30	1,4-dioxane	71	39
5	48	30	1,4-dioxane	80	42

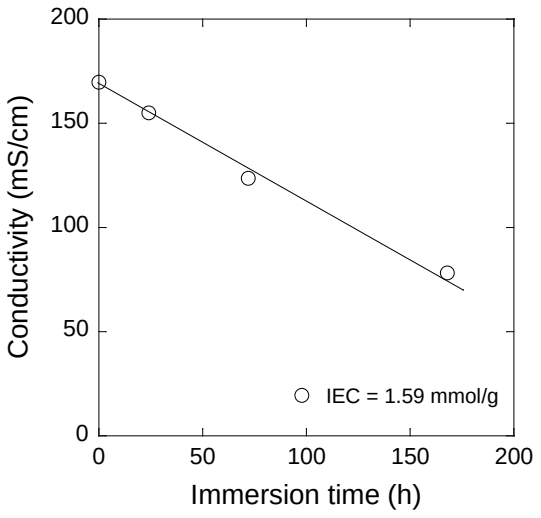

Fig. 1. Changes in the conductivities of ETFE-TMASt/OH in 1 M KOH at 80 ºC, plotted as a function of immersion time.

1 - 20 Preparation of Nitrogen-doped Carbon-based Catalysts by Electron-beam Irradiation Method: Effect of NH_3 Concentration in Irradiation Atmosphere

Y. Kanuma [a)], A. Idesaki [b)], M. Sugimoto [b)], S. Yamamoto [b)], H. Koshikawa [b)] and T. Yamaki [a, b)]

[a)] Chemistry and Chemical Biology, Gunma University,
[b)] Department of Advanced Functional Materials Research, TARRI, QST

Nitrogen-doped (N-doped) carbon-based catalysts have attracted much attention as platinum-alternative materials for fuel cell applications due to their promising oxygen reduction reaction (ORR) activity [1]. We are interested in the electron-beam (EB) irradiation methods for the preparation of N-doped carbon-based catalysts. Quite recently, we have prepared N-doped carbon by heating aromatic polymer precursors in an ammonia (NH_3) atmosphere under the EB irradiation. The EB irradiation enhanced the doped-N content through the radiolytic formation of reactive N species such as NH_2 and NH radicals and thus improved the ORR activity [2]. In most cases, the N concentration was one of the critical factors for the ORR activity of the carbon-based catalyst [3]. Therefore, there has been a strong motivation for us to develop techniques for controlling the N contents. This study deals with the effect of the NH_3 concentration during the EB irradiation on the N doping.

A precursor was a phenolic resin (Gunei Chemical, PSK-2320) or its mixture with 5% cobalt(II) chloride ($CoCl_2$). This was irradiated with 2 MeV EB at a dose of up to 6 MGy in 0.1, 1.0, 10 and 100% NH_3 at 500 ºC. The irradiated powder was then subjected to carbonization at 800 ºC for 1 h in N_2. The resulting samples were characterized by transmission electron microscopy (TEM), X-ray diffraction (XRD) and X-ray photoelectron spectroscopy (XPS). The electrocatalytic activity was tested by the linear sweep voltammetry (LSV) with a rotating disk electrode (RDE). The catalyst powder was dispersed in a mixture of a Nafion solution, ethanol and water and applied onto the surface of a glassy carbon electrode. The LSV was carried out in a KOH solution saturated with N_2 (N_2-LSV) or with O_2 (O_2-LSV). The net ORR voltammograms were obtained by subtracting the N_2-LSV from the O_2-LSV [4]. To make a quantitative comparison of the ORR activity, we took the current density at 0.7 V vs. RHE ($I_{0.7V}$).

Figure 1 shows the TEM image of N-doped carbon-based catalysts prepared in 100% NH_3. All the prepared samples apparently had amorphous and layered structures. Thus, a crystallization of a carbon structure would not be affected by the NH_3 concentration. Figure 2 shows the N 1s XPS spectra of the carbon-based catalysts prepared at the different NH_3 concentrations. The spectra were commonly composed of the two main signals: quaternary-N (Q-N) and pyridic-N (Py-N). According to quantitative analysis of the XPS data, the N/C ratio increased along with an increase in the NH_3 concentration. Interestingly, the $I_{0.7V}$ was found to reach a maximum of 0.8 mA/cm^2 at 100% of NH_3 concentration. This result suggests that the high N/C ratio caused the number of the active sites to increase, leading to the high ORR activity.

In summary, varying the NH_3 concentration in the EB irradiation atmosphere made it possible to control the N content in the carbon-based catalysts and finally improve their ORR activity.

References

[1] J. Ozaki *et al.*, Electrochem., **83**, 319-25 (2015).
[2] M. Sugimoto *et al.*, QST Takasaki Annu. Rep. 2015, **QST-M-2**, 52 (2017).
[3] Q. Wei *et al.*, Catalysts, **5**, 1574-602 (2015).
[4] Y. Nabae *et al.*, Catal. Sci. Tech., **4**, 1400-06 (2014).

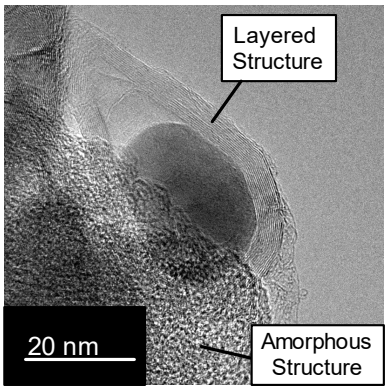

Fig. 1. TEM image of N-doped carbon-based catalysts prepared in 100% NH_3.

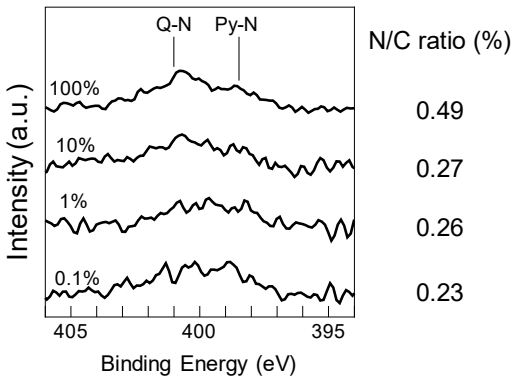

Fig. 2. N 1s XPS spectra and N/C ratios of the carbon-based catalysts prepared at the different NH_3 concentrations.

1 - 21 Utilization of Ion Implantation for Synthesis of Nitrogen-doped Carbon Material with Catalytic Activity (2)

A. Idesaki, M. Sugimoto, S. Yamamoto and T. Yamaki

Department of Advanced Functional Materials Research, TARRI, QST

Nitrogen-doped (N-doped) carbon materials which exhibit the catalytic activity for an oxygen reduction reaction (ORR), $O_2 + 4H^+ + 4e^- \rightarrow 2H_2O$, have been considered as platinum-alternative catalyst in the cathode of proton exchange membrane fuel cells. In many cases, the N-doped carbon materials are synthesized from precursor polymers and their blends because of controllability of compositions by selecting starting materials. However, most of them exhibited low catalytic performance, and thus a new synthesis method to increase the number of active sites must be pursued. Therefore, for the first time, an ion implantation technique has been used for preparing ORR-active carbon materials from a precursor polymer [1].

The ion implantation technique has been widely used for controlling electrical properties of semiconductors and modifying ceramic and polymer surfaces because it has advantages of (1) easy doping of various heteroatoms and (2) high energy deposition at a surface. In the surface modification of polymer materials, a relatively-low energy ion beam (up to several hundred keV) is irradiated for improvement in wear resistance, electrical conductivity, and so on. This technique is based on reactions of crosslinking, decomposition, and ultimately carbonization of macromolecules due to high energy deposition. On the other hand, few researchers have attempted the heteroatom doping in the polymer by the ion implantation. Our expectation in this study is that the N-doping as well as carbonization reactions can be achieved in the N^+-implanted polymer.

We previously chose polyimide as the polymer precursor and obtained the N-doped carbon material by the N^+ ion implantation and subsequent pyrolysis at 800 ºC [1]. This sample exhibited the ORR activity, but the contribution of the doped N ions was not clear because polyimide contains N elements in its structure and left some N residue. Thus, an N-free phenolic resin was irradiated with 50 keV N^+ ions at a fluence of 1×10^{15} ions/cm^2 at room temperature in a vacuum using a 400 kV ion implanter at TIARA. The irradiated film was pyrolyzed at 800 ºC in a nitrogen atmosphere. Finally, the ORR activity was evaluated by a cyclic voltammetry method and compared between the implanted and non-implanted samples.

Figure 1 shows the ORR activity of obtained carbon materials with and without the N^+ ion implantation. Each of the arrows in the figure represents the potential at which the current under the O_2-saturated condition started to deviate from that under the N_2-saturated condition (background current) and is referred to as an ORR potential. Note here that a higher potential indicates higher ORR activity; conventional platinum-catalysts exhibit the ORR potential of around 0.9 V vs RHE. The ORR potential was found at 0.5 V vs RHE for the non-implanted sample; in contrast, it reached 0.7 V vs RHE for the implanted sample. This enhancement suggests that implanted N elements could be incorporated and function as catalytic active sites. The obtained ORR potential was slightly lower than that of the N-doped carbon materials reported in other literatures (0.7-0.8 V vs RHE); therefore, the conditions of the implantation and pyrolysis should be optimized for better catalytic performance.

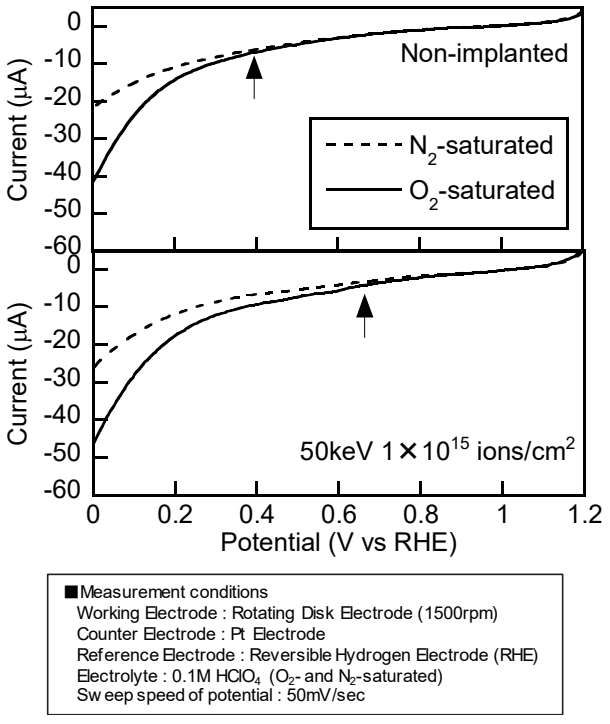

Fig. 1. ORR activity of the obtained carbon material with and without the N^+ ion implantation.

Acknowledgement

This work was partly supported by JSPS KAKENHI Grant Number 15K04736.

Reference

[1] A. Idesaki *et al.*, QST Takasaki Annu. Rep. 2015, **QST-M-2**, 53 (2016).

1 - 22 Preparation of Orientation-controlled CeO_2 Films on Sapphire Substrates by Sputtering

S. Yamamoto, M. Sugimoto, T. Hakoda, H. Koshikawa and T. Yamaki

Department of Advanced Functional Materials Research, TARRI, QST

Cerium dioxide (CeO_2) is an interesting support material and a promoter for noble metals in catalyst. In recent years, CeO_2 supported platinum catalysts has been developed for low content of Pt in cathode of polymer membrane fuel cells. Epitaxial CeO_2 films grown on $SrTiO_3$ (001) substrates as a model catalyst have been used to investigate the catalytic activity improvement caused by interface structure between Pt and CeO_2 [1]. To investigate its mechanistic effect on catalytic behavior from a standpoint of the interface structure with noble metals, orientation-controlled CeO_2 films were desired. Moreover, epitaxial CeO_2 films have been extensively studied for fundamental understanding of their properties. In this work, we investigated the effect of the deposition temperature and post-annealing on the epitaxial growth of CeO_2 films on c- and r-plane sapphire substrates.

The epitaxial CeO_2 films were grown by rf magnetron sputtering carried out using a sintered CeO_2 target in an Ar and O_2 gas mixture. The single-crystal sapphire substrates of c- and r-planes were used. The substrate temperature varied from 150 to 500 ºC during the deposition. The post-annealing treatment was carried out at various temperatures ranging from 400 to 1,000 ºC in air for 1 hour using an electric furnace. The deposited films with a thickness of 17 nm were characterized by X-ray diffraction (XRD), and Rutherford backscattering spectroscopy (RBS)/channeling using a 2.0 MeV $^4He^+$ beam.

Figure 1 shows the θ-2θ XRD patterns for the CeO_2 films deposited on (a) the c-plane and (b) r-plane sapphire substrates. The films were deposited at T_{dep} = 150 and 500 ºC and then annealed at 1,000 ºC. It was found that CeO_2 (001) films were formed by deposition at 150 ºC and post-annealing even though growth of CeO_2 (111) films was predicted with considering of energetically and thermodynamically stable plane compared to that of the (001) plane and the crystal symmetry of the c-plane sapphire substrates. The results suggest that (001) and (111) oriented CeO_2 films were selectively prepared on sapphire substrates of the same plane orientation by a suitable choice of the deposition and the post-annealing temperatures.

The minimum yield χmin value, the ratio between the random and the axially aligned yield in RBS/channeling measurements, gives a measure to evaluate the degree of disorder in crystalline solids. The χmin value in the CeO_2<001> aligned spectrum was 0.24 in the peak of the Ce component in the CeO_2 film, which suggests that imperfections exist in the CeO_2 film. The χmin value of the CeO_2 (001) film on the r-plane sapphire substrate deposited at 150 ºC and the annealed 1,000 ºC was 0.37. The RBS results suggested the level of crystallinity of the CeO_2 film was low compared to that of epitaxial CeO_2 films on sapphire substrates prepared by PLD [2]. Thus, to improve the crystallinity of the CeO_2 films, further optimization of deposition and post-annealing conditions was necessary.

References

[1] K. Fugane *et al.*, Appl. Mater. Interfaces **7**, 2698-707 (2015).

[2] F. Wang *et al.*, Thin Solid Films, **227**, 200-04 (1993).

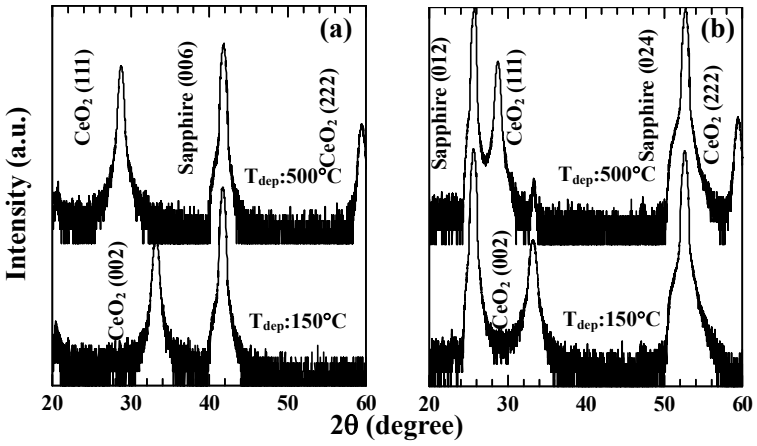

Fig. 1. θ-2θ XRD patterns of the CeO_2 films deposited on (a) the c-plane and (b) r-plane sapphire substrates. The films were deposited at 150 and 500 °C and then annealed at 1,000 °C in air.

1 - 23 Fiber-optic Remote Laser-induced Breakdown Spectroscopy in Environment of High-Dose Radiation (1)

H. Ohba [a)], M. Saeki [a)], K. Tamura [a)], T. Taguchi [a)] and S. Yamamoto [b)]

[a)] Tokai Quantum Beam Science Center, TARRI, QST,
[b)] Department of Advanced Functional Materials Research, TARRI, QST

Decommissioning of TEPCO Fukushima Daiichi nuclear power plant (F1-NPP) needs information on post-accident environment inside nuclear reactor core. In the F1-NPP, molten fuel debris (mixture of melted fuel core (U), fuel cladding (Zr) and construction materials (Fe)) might be submerged in water inside the reactor core. There is not enough space for inspecting the reactor core, because many pipes for water and electric supply occupy the inside space. Moreover, a high radiation field hinders people's access. Thus, a remote sensing technique that is available in a narrow space is crucial for the inspection of the F1-NPP.

For the internal survey of the damaged reactor core in F1-NPP, combining the imaging observation and a laser-induced breakdown spectroscopy (LIBS) analysis provides more rich information, because it is difficult to distinguish the kind of material of the debris only by imaging. Information concerning the kind of material helps us to select the cutting technique of the debris during the decommissioning process. For this purpose, we have proposed a fiber-optic probe LIBS, and confirm that the light transmission of the employed fiber optics is not degraded by the radiation exposure in near infrared region, which is used for the laser and emission transmission. In addition to the radiation resistivity, we have demonstrated underwater LIBS using simulated debris [1]. However, it is unknown how the LIBS emission is observed in an environment of high-dose radiation. In the present work, we investigate laser-produced plasma in the fiber-optic probe LIBS under high radiation dose rates using the ^{60}Co gamma irradiation facility number-1 at QST Takasaki.

Laser-induced breakdown plasma from a Zr alloy target was generated by an irradiation of focused Nd:YAG laser beam (1,064 nm, 7 ns, 5 Hz) through a 30 m fiber-optic cable of high-OH type. The laser energy was set to 7.5 mJ at the target. Emission spectra were acquired using an Echelle spectrograph ($\lambda/\Delta\lambda$ > 50,000) equipped with an EMCCD (1 μs Delay time, 1 μs Exposure time) at the laser shots of 100. The dose rates were varied from 0 kGy/h to 12 kGy/h by changing the distance between ^{60}Co source and the probe head. We performed the LIBS in air, under radiation dose in air, and under radiation dose with nitrogen gas flow.

The fiber-optic cable transmits emission light at near infrared and some visible wavelength region even under high radiation dose. In the LIBS with nitrogen gas flow, ionic lines (Zr II) are enhanced in visible region. Intensity of the ionic lines shows positive dependence on the radiation dose. Figure 1 shows the comparison of Zr II/Zr I ratio at wavelength range of 480 ~ 540 nm. Gamma-ray irradiation decomposes nitrogen molecules and excites dissociated nitrogen atoms. So, the ionization of Zr atoms may take place during laser ablation due to collision between excited nitrogen atoms and laser-produced excited Zr atoms. We estimated the plasma temperature derived from Boltzmann plot of Zr atoms at near infrared wavelength region (780 ~ 840 nm). As shown in Fig. 2, there was no correlation between the plasma temperature and the radiation dose rate. It means that the intensity ratio of elements is not affected by the radiation. This result suggests the LIBS enable us to perform quantitative analysis even under the high-radiation field.

Reference

[1] M. Saeki *et al.*, J. Nucl. Sci. Tech., **51**, 930-38 (2014).

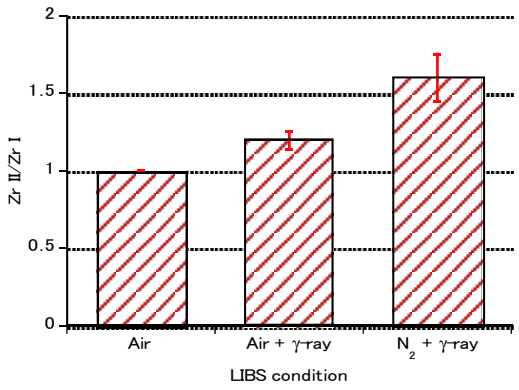

Fig. 1. Comparison of ionic lines (Zr II) to atomic lines (Zr I) ratio at dose rate of 12 kGy/h. The value was normalized at 0 kGy/h in air.

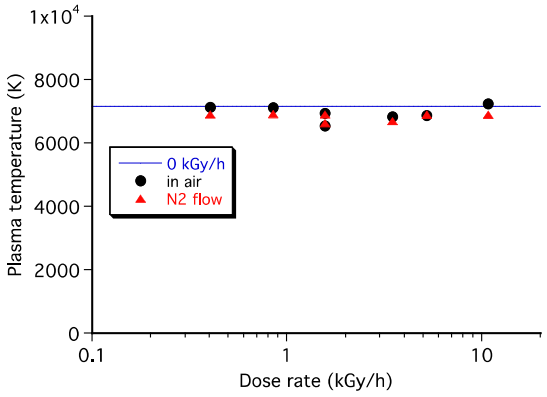

Fig. 2. Dependence of plasma temperature on radiation dose rate.

1 - 24 Configuration Change Analysis of Ion-irradiated SiC Nanotube Using In-situ TEM Observation

T. Taguchi [a)], S. Yamamoto [b)] and H. Ohba [a)]

[a)] Tokai Quantum Beam Science Center, TARRI, QST,
[b)] Department of Advanced Functional Materials Research, TARRI, QST

Since the discovery of carbon nanotubes (CNTs) in 1991, many researchers have synthesized a lot of new one-dimensional nanostructured materials such as nanotubes, nanorods and nanowhiskers for potential applications. Some of them have reported that many nanomaterials such as TiC, NbC, BN, SiO_2 and GaN nanostructures are fabricated from CNTs as the template. SiC is well known as not only wide-band-gap semiconducting material for high temperature and high power use but also high temperature structural materials. Therefore, SiC offers exciting opportunities in electronic devices and in structural materials at high temperature. We have reported that polycrystalline single-phase SiC nanotubes were synthesized [1, 2]. Furthermore, the amorphous SiC nanotubes were also successfully synthesized by the ion irradiation of the polycrystalline SiC nanotubes at under 100 ºC [3]. However, the effect of ion irradiation on configuration change of SiC nanotube has not been known yet. In the present study, we investigated the configuration change of SiC nanotube during the ion irradiation by using in-situ transmission electron microscopy (TEM) observation technique.

Carbon nanotubes (GSI Creos Corporation, Tokyo, Japan) are used as the template. The C-SiC coaxial nanotubes are synthesized by heating CNTs with Si powder (The Nilaco Corporation, Tokyo, Japan) at 1,200 ºC for 100 h in a vacuum. And then single-phase SiC nanotubes were formed by the heat treatment of C-SiC coaxial nanotubes at 600 ºC for 2 h in air. The molybdenum grid holder, which deposits the SiC nanotubes, are irradiated with 200 keV Si^+ ions from 400 kV ion implanter at room temperature in TEM (Model JEM-4000FX, JEOL Ltd., Akishima, Japan) operating at 400 kV. In-situ TEM observation of SiC nanotube under Si^+ ions irradiation is carried out. The ion fluence is up to 4.3×10^{20} ions/m^2, and the corresponding irradiation damage is calculated by SRIM 2008 to be 24.1 dpa.

Figure 1 shows the change ratio of outer and inner diameters of SiC nanotube evaluated from the TEM images of in-situ TEM observation. The outer diameter of SiC nanotube decreases to less than ha/lf with increasing the ion fluence. On the other hand, the inner diameter of SiC nanotube increases up to the ion fluence of 2.9×10^{19} m^{-2}, after then it decreases. According to the selected area electron diffraction taken form in-situ TEM observation of SiC nanotube, we confirmed that the SiC crystals were completely amorphized when the ion fluence exceeded this value. The outer diameter increase would be depended on the volume swelling by amorphization of SiC crystals. Under the ion irradiation, the ionization effect and the knocking silicon and carbon atoms out of the tube lattice cause a contraction of SiC nanotube. This phenomenon has been also observed in SiO_2 nanotubes and multi-walled CNTs under electron irradiation. The TEM images reveal that the thickness of SiC wall increases with increasing the ion fluence. These results suggest that the outer and inner diameters and wall thickness of SiC nanotube can be controlled by the ion irradiation fluence. Furthermore, the increase of ion irradiation causes an inner diameter narrowing, which ultimately transforms the nanotube into the nanowire.

References

[1] T. Taguchi *et al.*, J. Am. Ceram. Soc, **88**, 459-61 (2005).
[2] T. Taguchi *et al.*, Physica E, **28**, 431-38 (2005).
[3] T. Taguchi *et al.*, Carbon, **95**, 279-85 (2015).

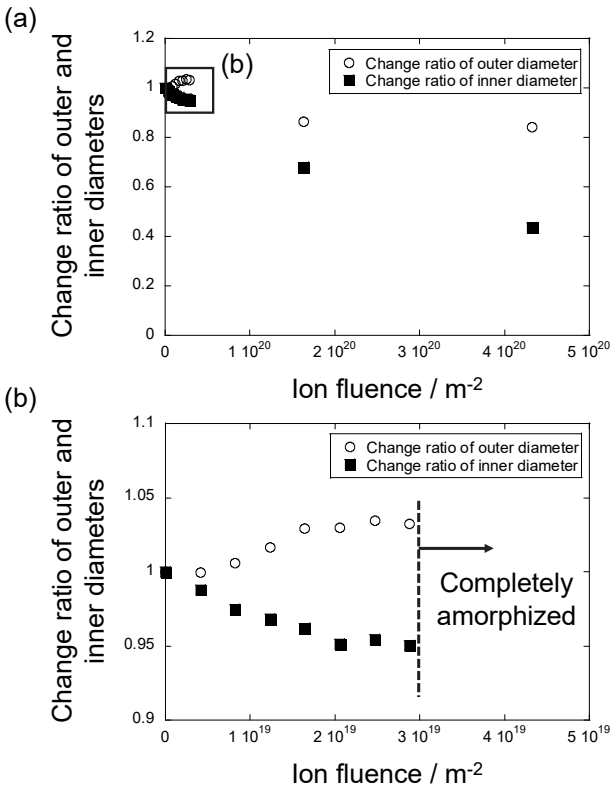

Fig. 1. Change ratio of outer and inner diameters of SiC nanotube evaluated from the TEM images of in-situ TEM observation. (b) An enlargement of the rectangle in (a). The ranges of ion fluence are up to (a) 5×10^{20} and (b) 5×10^{19} m^{-2}.

1 - 25 Electrical Properties of CNTFET with Al_2O_3 Passivation Layer for Gamma Irradiation

S. Ishii [a], T. Hamano [b] and T. Hirao [c]

[a] Department of Physics, Tokyo Denki University,
[b] Department of Accelerator and Medical Physics, NIRS, QST,
[c] Ryoei Technica Corporation

Carbon nanotube (CNT) is a nanosized material composed of only carbon atoms, and thus, it is very light and has an extremely small size. Moreover, it has high carrier mobility as well as superior mechanical strength. These characteristics make CNTs of potential value for use in a variety of applications, notably in CNT field-effect transistors (CNTFET). CNTFETs use CNTs as conduction channels exhibiting higher speed response than that of conventional Si-based devices, and therefore, CNTFETs are being studied extensively as potential electrical devices for the next generation. Furthermore, CNTs have recently been reported to exhibit radiation tolerance that opens up possibilities for applications, such as in aerospace technology and radiation treatment [1]. However, the electrical properties of CNTFETs under irradiation environment have not been studied extensively. In order to use CNTFET as a radiation tolerant device, a crucial factor is to prevent irradiation-induced damage of the device. In this study, we have investigated the availability of passivation technique for CNTFETs and evaluated the electrical characteristics of the passivated devices. The device properties of a CNTFET with Al_2O_3 passivation layer were characterized before, during, and after gamma irradiation.

The CNTFET sample was fabricated on an SiO_2/p+-Si substrate using microfabrication. First, the back gate electrode was patterned using Ti/Au thin film metal on the surface of the substrate via photolithography using electron beam evaporation. The Al_2O_3 gate insulator with a thickness of 300 nm was then deposited on the gate electrode using atomic layer deposition (ALD). After an aqueous solution of CNT was dispersed on the Al_2O_3 layer, the source-drain metal electrodes were patterned on them using the same technique as described for patterning the gate electrode. Finally, a CNT network channel was formed by removing the CNTs outside the channel region via oxygen plasma etching, and the device surface was passivated using Al_2O_3 layer with a thickness of 100 nm via ALD.

The device was irradiated with gamma rays in a metal vacuum chamber under a pressure of 10^{-2} Pa at QST, Takasaki. The dose rate was determined to be 5.78 kGy/h from results of dose measurement using a PMMA dosimeter, and the irradiation was performed for 1 h. The drain current-gate voltage (I_D-V_{GS}) characteristics of the test device were measured using an 8252 digital electrometer (ADCMT, JAPAN). The measurements were performed at the beginning and end of the irradiation, as well as before and after the experiment. Between each measurement, the value of V_{GS} was maintained at -20 V.

Figure 1 shows the I_D-V_{GS} characteristics of the device at a drain voltage (V_{DS}) = -1 V for each measurement. V_{GS} was swept from -20 to +20 V, and then back to -20 V. The device exhibited typical ambipolar behavior. The on and off currents were observed to remain constant at the initial

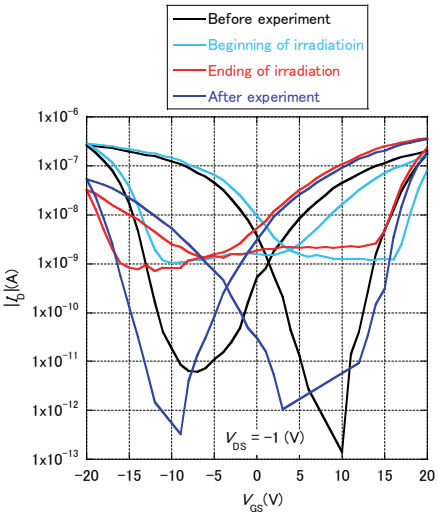

Fig. 1. I_D-V_{GS} characteristics of CNTFET at V_{DS} = -1 V.

current level proving that passivation using Al_2O_3 layer effectively protects the device from irradiation. However, the off current increased by two orders of magnitude during irradiation and a shift of the threshold voltage was observed that might be attributed to the generation of charges trapped in the oxide layer during irradiation, as seen in previous studies [2]. However, the oxide layer was used for passivation as opposed to a gate insulator, and thus the effect of trapped charges is expected to be complicated. The distribution of the charges trapped in the devices requires further investigation.

Al_2O_3 passivation is effective for the protection of CNTFET from gamma ray irradiation, although the device characteristics are observed to change during irradiation. These changes would cause serious errors when the integrated circuit is fabricated using a number of CNTFETs. Thus, our next goal is to understand the charge trap distribution mechanism.

References

[1] C. D. Cress *et al.*, IEEE Trans. Nucl. Sci., **57**, 3040-45 (2010).
[2] S. Ishii *et al.*, Physica E, **86**, 297-302 (2017).

1 - 26 Electrochemical Hydrogen Absorbing Properties of Surface on LaNi Based Alloys by O^+ Irradiation

H. Abe [a], S. Tokuhira [b] and H. Uchida [b]

[a] Department of Advanced Functional Materials Research, TARRI, QST,
[b] Faculty of Engineering, Tokai University

Metallic hydrogen absorption reaction starts from adhesion of a hydrogen molecule and a reaction such as dissociation and absorption in a metal surface. According to the hydrogen absorption reaction by the electrochemical reaction, a water molecule dissociates in hydrogen and hydroxyl on the alloy surface, and hydrogen invades the alloy inside and diffuse. However, because residual gas (mainly H_2O) forms an oxidation film, a hydroxylated film on the alloy surface in the atmosphere and a vacuum, the dissociation of hydrogen and the water molecules is inhibited, and an initial hydriding rate decreases. Therefore, the state of the alloy surface is an important factor of the initial hydriding rate. The alkaline pretreatment of the alloy surface using LiOH, NaOH or KOH was found to accelerates the rate of the initial activation [1, 2]. Alkaline atoms in the surface oxide lower the work function of electron of the surface, and this facilitates the rate of dissociation of H_2 or H_2O molecules, resulting in the acceleration of hydrogen absorption. In addition, the surface modification of materials, ion irradiation was found to be a quite useful method [3]. Then, ion irradiation onto the surface of a metal effectively induces defects such as vacancies, dislocations and micro-cracks in the surface region of the materials.

In this study, we applied oxygen ion (O^+) irradiation to surface modifications of the electrode of the Ni-MH battery. And the effect O^+ irradiation on the initial hydriding rate of LaNi based alloys was investigated in electrochemical process.

A powder sample of a $LaNi_{4.6}Al_{0.4}$ alloy was used. The particle size was smaller than 38 μm in diameter. The alloy powder was mixed with a copper (Cu) powder at a ratio of the alloy to Cu 1 : 3 in weight. The mixed powder was pressed at 8 t/cm^2 to form a pellet with a size of 12.3 mmϕ and 1.3 mm thickness as an electrode for electrochemical hydriding measurement. O^+ irradiation onto the surface for a sample was made at energies of 100 keV, 350 keV, 3 MeV and 12 MeV, and doses of 2×10^{16} cm^{-2}, 2×10^{16} cm^{-2}, 3×10^{16} cm^{-2} and 1×10^{16} cm^{-2} respectively, using a 400 kV ion implanter for energy of keV order and a 3 MV tandem accelerator for MeV order. The initial hydriding rate was measured in electrochemical process where a pellet sample was used as a cathode, and $Ni(OH)_2$ as an anode. An Hg/HgO electrode was used as a reference electrode in an open cell. The initial hydriding rate of the sample was measured in a 6 M-KOH using the open cell at constant voltage -0.93 V and at 298 K.

The curves of the hydriding reaction rate by $LaNi_{4.6}Al_{0.4}$ alloy irradiated at doses of from 1×10^{16} to 3×10^{16} cm^{-2} of an O^+ are shown in Fig. 1. The ordinate indicates the ratio of absorbed hydrogen atom to $LaNi_{4.6}Al_{0.4}$ alloys (H/M) and the abscissa is the time of onset of charge by an electrochemical effect. With increasing O^+ beam energies up to 12 MeV, the reaction rate and H/M value at 120 minutes were decreased. It turned out that the reaction rate by the irradiation energy lower than high energy becomes fast. At the irradiation energy of 100 keV which was the highest as for the effect in comparison with un-irradiated sample, 7 times of a H/M value improved. As mentioned above, the hydriding rate and the hydrogen absorption curve shows ion irradiation energy dependence.

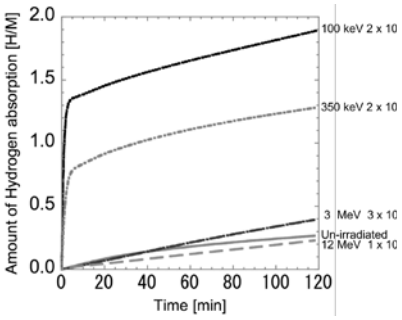

Fig. 1. Hydriding curve of samples irradiated by O^+ at energy of 100 keV to 12 MeV.

Figure 2 shows the relation between the irradiation energy of $LaNi_{4.6}Al_{0.4}$ and the initial hydriding rate after O^+ irradiation. The initial hydriding rate decreases with increasing irradiation energy. The initial hydriding rate of an un-irradiated is 3.52×10^{-3} min^{-1} as described by a dotted line. At the irradiation energy of 100 keV which was the highest as for the effect in comparison with un-irradiated sample, 95 times as initial hydriding reaction rate improved. When the ion irradiation introduced defects, it turned out that the initial hydriding rate was improved. The La in the alloy tends to form stable oxides, however, H_2 molecules can dissociate on the oxides with high reactivity. In this study, we confirmed the formation of La oxide layers after the irradiations. In the initial state of the hydriding process, the hydrogen is trapped by the defects and it is surmised that initial hydriding rate becomes fast.

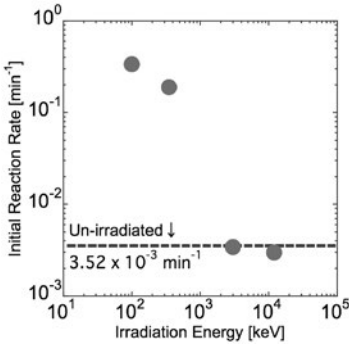

Fig. 2. The relation between the irradiation energy and the initial hydriding rate.

References

[1] H. Uchida *et al.*, J. Alloy. Comp., **253-54**, 525-28 (1997).
[2] H. Uchida *et al.*, J. Alloy. Comp., **253-54**, 547-49 (1997).
[3] H. Abe *et al.*, Nucl. Instrum. Meth. Phys. Res. B, **206**, 224-27 (2003).

1 - 27 Positron Annihilation Study of Ion-Beam Synthesized β-$FeSi_2$

A. Yabuuchi [a)], A. Kinomura [a)], M. Maekawa [b)] and A. Kawasuso [b)]

[a)] Research Reactor Institute, Kyoto University,
[b)] Department of Advanced Functional Materials Research, TARRI, QST

Beta(β)-$FeSi_2$, having a band gap corresponding to the infrared region of the 1.5 μm band, is expected as infrared-light receiving/emitting devices since it does not contain rare metals or harmful elements and has an excellent optical absorption coefficient [1]. The ion-beam synthesis (IBS) technique, which is forming β-$FeSi_2$ in the surface layer of the Si substrate by annealing after implanting Fe ions into Si, is well compatible with the Si-LSI process. Thus, it attracts attention as a technique for realizing the LSI internal optical wiring, however, further enhancement of the emission intensity is demanded. The emission intensity of IBS β-$FeSi_2$ is reported to be enhanced with Al-doping in contrast with Mn-doping [2]. The enhancement of the emission intensity by Al-doping is considered to be caused by filling Si vacancies which acts as nonradiative recombination centers with Al atoms, however, the direct evidence of reducing Si vacancies by Al-doping is still not shown. In this report, the IBS β-$FeSi_2$s were characterized by using a slow positron beam.

High-resistivity FZ-Si(100) substrates were implanted with a maximum energy of 100 keV Fe^+ ions to a total dose of 1×10^{17} ions/cm^2 at room temperature. Mn^+ and Al^+ ions were additionally implanted as Mn-doped and Al-doped samples to a total dose of 5×10^{15} ions/cm^2 with a maximum energy of 100 keV and 50 keV, respectively. After the ion implantation, the substrates were annealed at 800 ºC for 2 hours in vacuum to synthesize the β-$FeSi_2$. According to the previous studies [1, 3], the β-$FeSi_2$ layer is reported to be formed with a thickness of 50 nm at the surface of the Si substrate under these implantation and annealing conditions. The Doppler broadening of annihilation radiation (DBAR) spectra were acquired for each sample at room temperature with varying incident positron energies. All the samples were treated with dilute hydrofluoric acid to remove the native oxide film before the positron annihilation measurements.

Figure 1 shows the peak intensity of DBAR spectra (S parameters) for the unimplanted FZ-Si and Fe^+-implanted Si (β-$FeSi_2$) sample as a function of incident positron energy. The solid lines are fitted using the VEPFIT code [4]. The S parameters of the Fe^+-implanted Si sample are lower than those of the original FZ-Si substrate in the incident-energy region of 2 - 4 keV which corresponds to the β-$FeSi_2$ layer. From this fact, we decide that the β-$FeSi_2$ layer was successfully synthesized with this annealing treatment.

Figure 2 also shows the peak intensity of DBAR spectra (S parameters) for the undoped, Mn-doped, and Al-doped IBS β-$FeSi_2$ samples as a function of incident positron energy. The incident-energy region of 2 - 4 keV in these samples also corresponds to the IBS β-$FeSi_2$ layer. The Al-doped β-$FeSi_2$ sample, which is reported to be enhanced the emission intensity, shows the largest S values in three samples. Interestingly, contrary to our initial expectation, this result suggests that more vacancies are introduced into the IBS β-$FeSi_2$ by the Al-doping. One possibility is that vacancy-Al defect complexes are formed in order to reduce a lattice strain induced around Al atoms which have a larger atomic radius than Si atoms.

References

[1] M. Sugiyama *et al.*, Thin Solid Films, **381**, 225 (2001).
[2] Y. Terai and Y. Maeda, Appl. Phys. Lett., **84**, 903 (2004).
[3] Y. Maeda *et al.*, Phys. Procedia, **11**, 83 (2011).
[4] A. van Veen *et al.*, AIP Conf. Proc., **218**, 171 (1991).

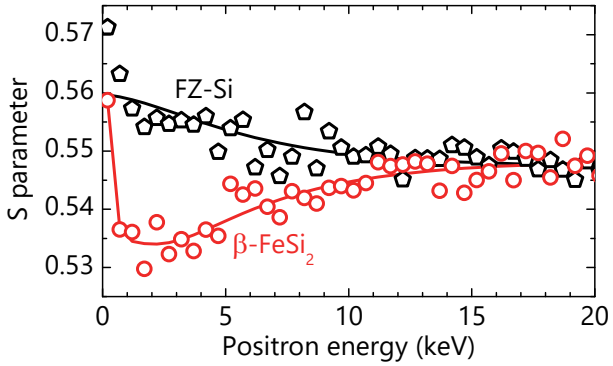

Fig. 1. S parameters for the FZ-Si substrate (open pentagons) and β-$FeSi_2$ synthesized sample (open circles) as a function of incident positron energy.

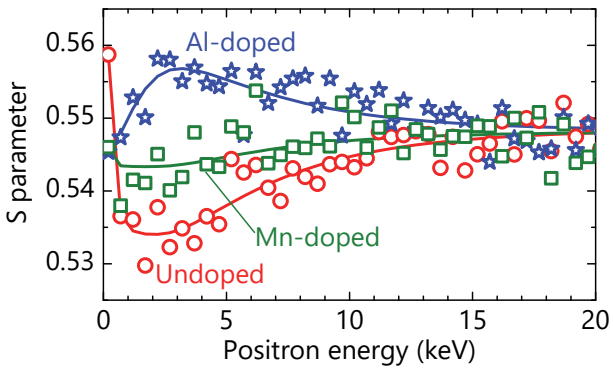

Fig. 2. S parameters for the undoped (open circles), Mn-doped (open squares), and Al-doped (open stars) β-$FeSi_2$ samples as a function of incident positron energy. The incident-energy region of 2 - 4 keV is corresponds to the IBS β-$FeSi_2$ layer.

1 - 28 Effect of Electron Beam Irradiation on the Luminescence Property of Titanium Oxide Powder

A. Takeyama and T. Ohshima

Department of Advanced Functional Materials Research, TARRI, QST

Isolated point defects formed in wide-gap oxide semiconductor materials are expected as an emission source of a single photon [1]. Since the energy level originated from the point defect is dependent on its charged state, to explore novel charged defects expected as a single photon source (SPS) has been intensively studied. In this viewpoint, studying relationship between the luminescence property and point defects formed in titanium oxide (TiO_2) is of interest. TiO_2 is one of common wide-gap oxides composed of transition metal of titanium and oxygen, and thus various charged defects easily introduce energy levels into the band gap.

Commercial TiO_2 powders (Anatase type) were irradiated by electron beam up to 62 MGy. An acceleration energy and beam current were 2 MeV and 6 mA, respectively. Irradiation was carried out in air at room temperature. After sandwiching each powder with quartz plates, photo luminescence (PL) spectrum was measured at room temperature. The excitation wavelength of 330 nm was chosen, by which electron at valence band is excited into conduction band. Diffuse reflectance spectrum was measured and a change of reflectance of powders is calculated by subtracting reflectance for irradiated powder from that for pristine one.

Figure 1 shows PL spectrum of powders. Sharp PL lines observed among 400 to 500 nm and at 660 nm are the secondary light of excitation source (Xenon lump). With increasing dose, luminescence intensity in the wavelength of 350 to around 450 nm increased. While, in other wavelength region, relatively small deference between irradiated and pristine powders was observed. In Fig. 2, area intensity of spectra observed in UV to visible (near UV) region is plotted against dose. The area intensity is calculated for spectra defined from 355 to 410 nm. The area intensity was maximized at 20 MGy, then slightly decreased in higher dose region.

Figure 3 shows a change of reflectance of irradiated powders plotted as a function of wavelength. Positive change indicates defects were introduced due to irradiation [2]. A peak observed at around 400 nm was assigned to singly positive charged interstitial Ti. Reflectance change at 490 and 587 nm were originated from singly and doubly positive charged O vacancy. The change is large in the order of 20, 50, 62 MGy over 490 nm, which is an opposite trend observed for area intensity in Fig. 2. This suggests that in high dose region, doubly charged oxygen vacancy was predominantly oxidized rather than formed. In addition, PL spectra observed in near UV region is mainly attributed to oxygen vacancies. In summary, we found a close relationship between the luminescence and charged defects in TiO_2 using electron beam irradiation.

References

[1] K. Chung *et al.*, Nanophotonics, **6**, 269-78 (2017).
[2] M. Mikhailov *et al.*, Nucl. Instrum. Meth. Phys. Res. B, **333**, 52-57 (2014).

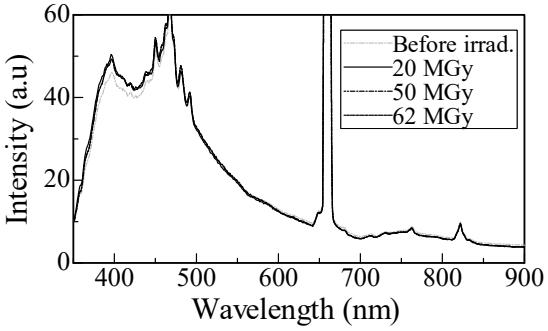

Fig. 1. PL spectra of TiO_2 powders. Pale grayish curve is for a pristine powder.

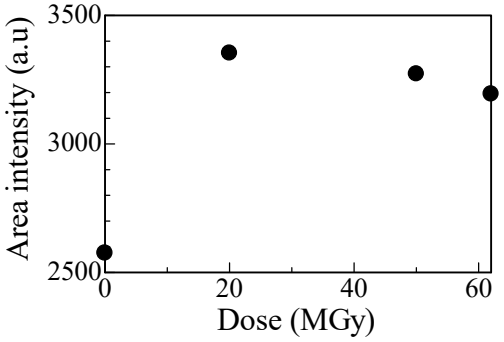

Fig. 2. Dose dependence of area intensity of near UV spectra.

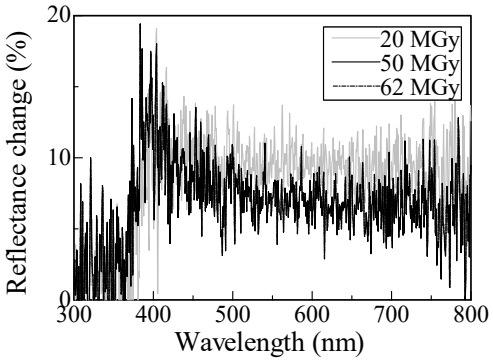

Fig. 3. Change of reflectance after irradiation. It is calculated by subtracting reflectance spectrum (%) for irradiated powders from that for pristine one.

1 - 29 Study on Irradiation-enhanced Precipitation in FeCu Alloy by Using Energetic Ion Irradiation and EXAFS Measurement

A. Iwase [a)], J. Kinari [a)], H. Kojima [a)], R. Mayumi [a)], Y. Saitoh [b)], Y. Okamoto [c)] and S. Semboshi [d)]

[a)] Department of Materials Science, Osaka Prefecture University,
[b)] Department of Advanced Radiation Technology, TARRI, QST,
[c)] Energy and Environment Materials Science Division, MSRC, JAEA,
[d)] Institute for Materials Research, Tohoku University

When supersaturated alloys are irradiated with energetic particles, the interaction between irradiation-produced lattice defects and solute atoms enhances the diffusion of solute atoms and precipitates of solute atoms are produced. This phenomenon is called “Radiation Enhanced Precipitation”. As the precipitates produced through the radiation enhanced precipitation are much smaller than those produced by the thermal aging, they act as effective obstacles against dislocation motions and cause the hardening and the embrittlement of alloys. Such hardening and embrittlement by the irradiation become a serious problem for reactor pressure vessel steels which have been exposed to high flux energetic neutrons for a long period. In the present study, Fe-0.6wt.%Cu binary alloy samples were used as a model alloy for the reactor pressure vessel alloys, and the effect of heavy ion irradiation on hardness was investigated. The structure of Cu precipitates was examined by using the EXAFS measurement.

We prepared samples of supersaturated Fe-0.6wt.%Cu alloy by quenching samples the temperature of which was 1,123 K into iced–water. Such solution-treated samples were irradiated with 16 eV Au ions at 523 K. The Au ion fluences were from 5×10^{12} /cm^2 to 5×10^{14} /cm^2. For comparison, some samples were irradiated with Au ions at room temperature. The change in hardness by the irradiation was measured by a Vickers hardness tester. To observe the local structure of Cu precipitates in Fe matrix, the EXAFS spectra were obtained around the Cu K absorption edge by using KEK photon factory.

Figure 1 show the Au ion fluence dependence of the Vickers hardness for the samples irradiated at 523 K and at room temperature. The hardness increase for the sample irradiated at 523 K is much larger than that for room temperature irradiation. As irradiation-produced defects diffuse more rapidly at elevated temperatures, the result confirms that the radiation enhanced precipitation dominates the increase in hardness. Figure 2 shows the EXAFS-FT spectrum for the sample irradiated at 523 K with the Au fluence of 1×10^{14} /cm^2. The spectrum for the unirradiated sample is also plotted. The spectrum for the unirradiated sample is quite similar to that for pure Fe, which means that Cu atoms are surrounded by Fe lattice with the BCC structure. The spectrum for the irradiated sample is similar to the lattice with the FCC structure.

This result suggests that the growth of Cu precipitates with the FCC structure occurs during the irradiation.

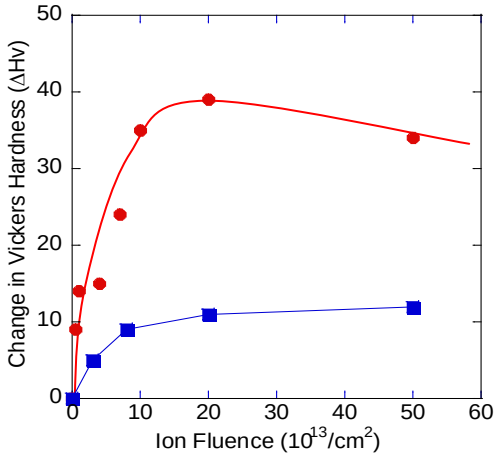

Fig. 1. Change in hardness as a function of 16 MeV Au ion fluence. Red) for the irradiation at 523 K, and blue) for the irradiation at room temperature.

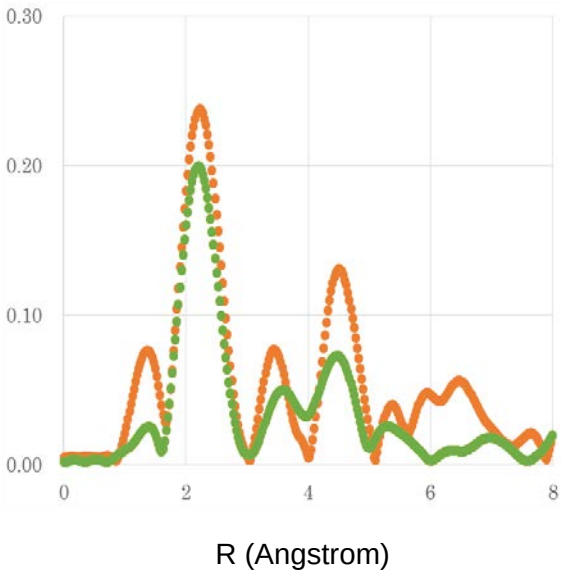

Fig. 2. EXAFS-FT spectra for unirradiated sample (orange) and for that irradiated with the fluence of 1×10^{14} /cm^2 (green).

1 - 30 Synergetic Effect of He, H and Displacement Damages on the Void Swelling of F82H

D. Hamaguchi [a)], M. Ando [a)] and H. Tanigawa [a)]

[a)] Department of Fusion Reactor Materials Research, Rokkasho, QST

Reduced activation ferritic/martensitic steels (RAFMs) such as F82H are the most promising candidates for the blanket structural materials in fusion reactor [1]. One of difficulties to predict the development of damages under fusion neutron irradiations is a lack of irradiation facility that can reproduce an irradiation conditions regarding fusion reactor environment. Therefore, we need to collect information on particular events that are expected to be specific under fusion neutron irradiations by using existing irradiation facilities. The unique feature of fusion neutron irradiation on ferritic steels is a high He and H transmutation gas production rate. Therefore, to understand the effect of He and H gas on the development of irradiation damages, complex beam ion irradiation experiments are essential. In this study, multiple ion irradiation experiments were carried out using TIARA complex irradiation facility to examine the synergetic effect of He and H with displacement damage of F82H.

The materials used in this study were F82H IEA, Mod3, and BA07. IEA is a standard version of F82H whereas Mod3, BA07 and BA12 were modified versions with slightly different compositions and the heat treatment conditions. The basic chemical composition of IEA and BA07 is Fe-8Cr-2W-0.2V-0.04Ta-0.1C whereas Mod3 have a higher Ta content of 0.1%. For heat treatment, IEA was normalized at 1,040 ºC for 0.63 h followed by a tempering at 750 ºC for 1h whereas other modified versions have normalizing temperature ranged from 1,080 - 1,020 ºC and tempering temperature of 740 ºC. The irradiations were carried out with 10.5 MeV Fe^{3+} ions with/without 1.05 MeV He^{+} and 0.38 MeV H^{+}. The irradiation was performed up to 20 dpa at the depth of 1.0 μm.

Figure 1 shows the cavity microstructure of F82H IEA irradiated with multiple ion-beams up to 20 dpa at the temperatures from 400 to 500 ºC. It should be noted that triple-beam refers to He, H and Fe multiple ion-beam and dual-beam refers to He and Fe multiple ion-beam. The cavities observed here could be distinguished into two types; rather large sized voids and tiny He bubbles. The high-density of cavity formation was even seen at the temperature of 400 ºC for the case of both dual and triple-beam irradiations, where no cavities were observed for the case of Fe single-beam irradiation. In addition, at 400 ºC, only tiny He bubbles were observed. It is also clear that the enhancement of cavity formations occurs by He or He + H co-implantation in all tested temperatures. The average size of the cavity increased as temperature arises, with the swelling peaks at around 450 ºC. Figure 2 shows the irradiation temperature dependence of the void swelling for the case of multiple and single beam irradiated F82H up to 20 dpa. It is clearly shown the swelling peaks at around 450 - 470 ºC. On the other hand, the density of the cavities for the case of triple-beam irradiations are tend to become higher compared to dual-beam irradiated cases. The effect of the production of H with He under displacement damages was not positively discussed so far because it was believed to be less effective since the diffusion of H is very rapid at high temperatures in Fe-based system. But the result clearly indicates the effect of H on the cavity formation; the study suggests the importance of continuous investigation on the effects of transmutational produced He and H in RAFMs. Moreover, since void swelling and irradiation creep have a strong correlation with each other, it is important to systematically understand the swelling behavior of RAFMs especially under high dose conditions. More investigations on further effect of He and H against swelling for higher doses are on going.

Reference

[1] H. Tanigawa *et al.*, J. Nucl. Mater. **417**, 9-15 (2011).

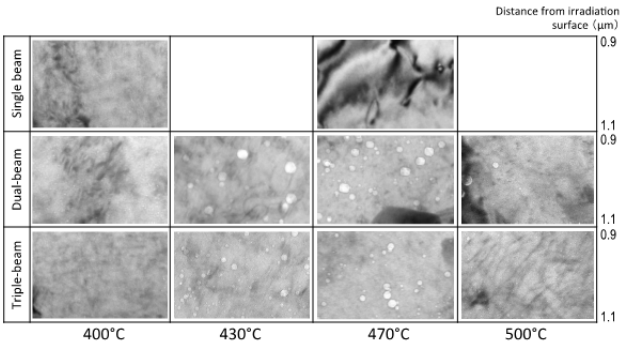

Fig. 1. Cavity microstructure of F82H-IEA irradiated with complex ion-beam up to 20 dpa at temperatures ranged from 400 to 500 ºC.

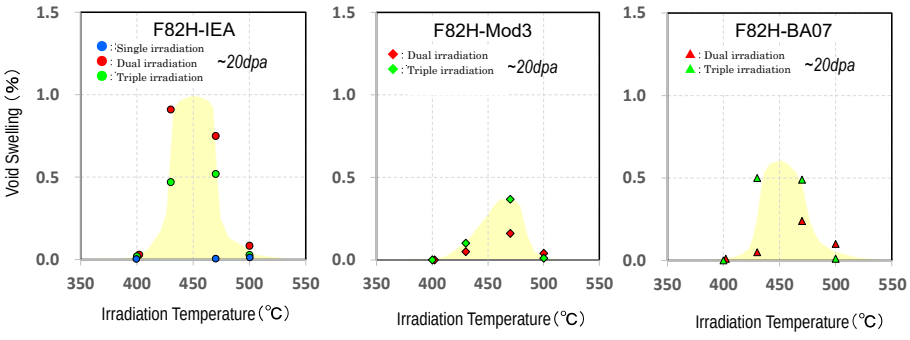

Fig. 2. Temperature dependence of the void swelling for F82H-IEA, Mod3 and BA07 after multiple ion irradiation up to 20 dpa.

1 - 31 Irradiation Effects of ADS Target Window Materials on Corrosion in Liquid Metal

N. Okubo and N. Ishikawa

Fuels and Materials Engineering Division, NSEC, JAEA

Japan atomic energy agency (JAEA) has been conducting research activities for developing the accelerator driven system (ADS) [1], which is expected to reduce and transmute radioactive wastes involved in spent fuels. The ADS adopts a liquid metal of LBE (lead-bismuth eutectic) as a coolant to remove the heat deposition from the high energy proton beam and a spallation target to produce high energy neutrons. In a future ADS plant, the target window, which is the most important safety boundary between a high vacuum accelerator and a fuel core, will be irradiated under LBE flow. Degradation of mechanical properties and corrosion/erosion of the materials after irradiation at relatively high temperature, *ex*. from 300 to 550 ºC in LBE, should be suppressed within a range permissible for the ADS design. The effect of oxygen concentration in LBE on material corrosion behavior has been studied from about 15 yeas ago [2], however, few studies for effect of irradiation on the corrosion is conducted so far. In this study, the effect of irradiation on the corrosion in LBE was experimentally simulated by using triple ion beam irradiation for ADS spallation condition and static LBE pod, prior to experiments in LBE loop in near future.

Irradiations of 10 MeV - Fe^{3+}, 1.05 MeV - He^{+} and 0.38 MeV - H^{+} ions were simultaneously conducted for T91 steels at 450 ºC in TIARA facility, QST. Depth distributions of He and H were broadened around 1 micron depth by using 800 nm thick aluminum energy degrader. Helium rate was about 15 appmHe/dpa. Hydrogen rate was about 110 appmH/dpa. By using special holder, by which tensile stress, about 200 MPa, was introduced in the surface of bend specimen, both of bend and flat (no-bend) specimen were aligned side by side and simultaneously irradiated at almost same beam condition. After irradiation, the specimen holder with two specimens was soaked in static LBE pod and started the corrosion test at 450 ºC for 1,000 h. Figure 1 is the specimen holder and the specimens after soaking. The specimens were cleaned up in silicone oil bath at 200 ºC to remove the surface LBE after the soaking and observed by SEM (Scanning Electron Microscope) to estimate surface corrosion morphology.

As a first step to extract only influence by the displacement damage, the T91 specimen was irradiated by self-ion of iron. Figure 2 shows SEM images of the flat specimen, which soaked in LBE for 1,000 h after irradiation at 450 ºC up to 10 dpa (displacement per atom). Left picture was taken from non-irradiation area and right one was from irradiation area. Energy dispersive X-ray spectrometry (EDS) results showed that plate type and needle type particles with relative large size from several hundred nm to a few μm were mainly composited from lead as shown by arrows in upper side. In the case of non-irradiation area a few hundred nm plate type of particles were observed while fine particles below a hundred nm with round shape were observed in the case of irradiation as shown by arrows in lower side. These particles were both composited from iron chromium oxide from EDS analyze. It is suggested that the irradiation influenced the size of oxide on the specimen surface after corrosion in LBE. The difference caused by the stress between bend and non-bend specimens was not observed in this study

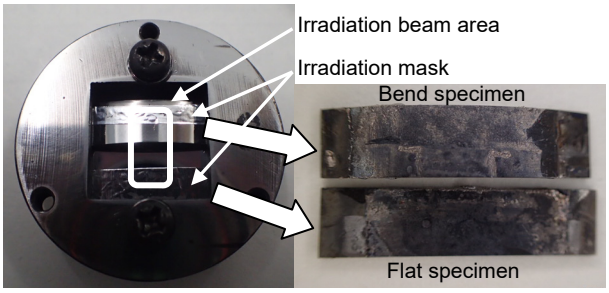

Fig. 1. Specimen holder (left) and specimen after soaking in LBE at 450 ºC (right). Upper is bend and lower is flat specimen.

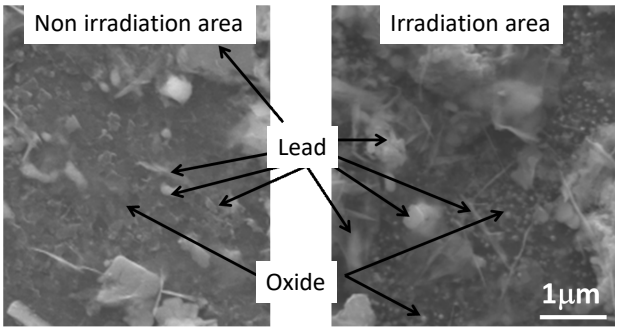

Fig. 2. SEM images of flat specimen soaked in LBE for 1,000 h at 450 ºC. Left is non irradiation and right is irradiation area.

References

[1] K. Tsujimoto *et al.*, J. Nucl. Sci. Tech., **44**, No.3, 483-90 (2007).

[2] K. Kikuchi *et al.*, JSME Int. J., series B, **47**, No.2, (2004).

1 - 32 Property Change of Oxygen Sensor Used in Liquid Metal under Gamma-ray Irradiation

N. Okubo [a)], A. Kitamura [a)], Y. Okuno [a)] and T. Taguchi [b)]

[a)] Fuels and Materials Engineering Division, NSEC, JAEA,
[b)] Tokai Quantum Beam Science Center, TARRI, QST

Japan atomic energy agency (JAEA) has been conducting research activities for developing the accelerator driven system (ADS) [1], which is expected to reduce and transmute radioactive wastes involved in spent fuels. The ADS adopts a liquid metal of LBE (lead-bismuth eutectic) as a coolant to remove the heat deposition from the high energy proton beam and a spallation target to produce high energy neutrons. In LBE, the corrosion behavior of some steels like austenitic and ferritic steels depends considerably on the oxygen concentration and temperature of LBE. The oxygen concentration control in LBE is one of most important R&Ds for estimating the component lifetime in ADS. The developing of oxygen sensor which can be used even in the liquid metal and relative low temperature (ex. 250 - 550 ºC) is most important issue for oxygen control in LBE. JAEA has developed air reference type of sensors, which electrolyte is made of YSZ (Yttria Stabilized Zirconia) [2]. In ADS, the oxygen sensors will be exposed by gamma-ray irradiation from activation of LBE under long time operation. In this report, some basic data of mechanical property for YSZ and EMF (electromotive force) for oxygen sensor will be shown to inspect the reliability of oxygen sensors after gamma-ray irradiation.

Three types of YSZ, in which yttria concentration was 3, 6 and 8 mol%, were irradiated at the gamma-ray dose rate of 1 kGy/h by using ^{60}Co gamma-ray source in Takasaki research center, QST. The specimen size is 40 mm length, 4 mm width and 3 mm height, based on the Japanese Industrial Standards, JIS-R1601. The 1 kGy/h corresponds to the activity of LBE after 1 year operation. The irradiation at 2 kGy/h was conducted also to simulate the maximum case of LBE activity. The irradiation time was 1,000 and 5,000 h. Heat treatment in air and soaking in LBE at both temperature of 450 ºC were conducted as referential experiments. After irradiation, 4 points bend tests were conducted at RT. The EMF of a prototype oxygen sensor was also measured in LBE before and after the irradiation.

Figure 1 shows bend strength for each specimen of 8Y-YSZ(ZR-8Y), as received, heat treated at 450 ºC for 1,000 h, gamma-ray irradiated at 1 kGy/h for 1,000 h, 2 kGy/h for 5,000 h and soaked in LBE at 450 ºC for 1,000 h. In the case of irradiation at 1 kGy/h for 1,000 h, the strength is not so much different with as-received specimen. In the case of high dose, 2 kGy/h for 5,000 h, the strength is almost same with as received and 1 kGy/h specimen. This means that in the case of 8Y-YSZ, there is no irradiation effect for mechanical property by gamma-ray even at high dose. In the case of specimen soaked in LBE, the strength increased significantly. Heat treatment at 450 ºC in air causes reduction of strength slightly, however, soaking in LBE increase the strength about 80 MPa. This suggests that the micro-cracks and/or pores on the surface are fulfilled by LBE, which causes suppression of crack initiation. It is noted that LBE penetration into grain boundary on the specimen surface was observed by optical microscope. The EMF before and after gamma-ray irradiation at 1 kGy/h for 1,000 h were measured in LBE as shown in Fig. 2. Upper line is before irradiation and bottom one is after the irradiation. Some continuous steps mean temperature change and constant EMF corresponds to saturation oxygen concentration at 450 ºC. The gamma-ray irradiation caused decreasing of EMF about 0.05 V. The prototype sensor used in this study included plastic connection part inside, which was not durable for gamma-ray. It may be caused as a degradation of the EMF value.

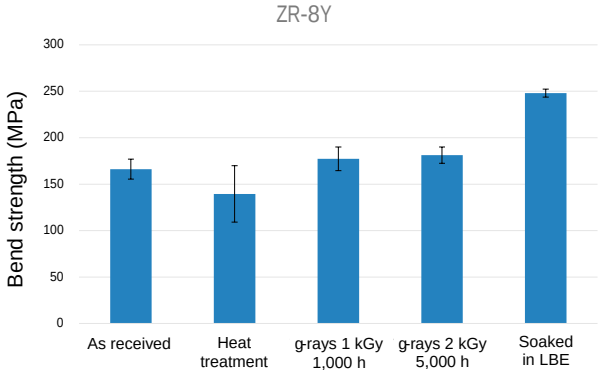

Fig. 1. Bend strength for ZR-8Y, as received, heat treated, gamma-ray irradiated and soaked in LBE specimens.

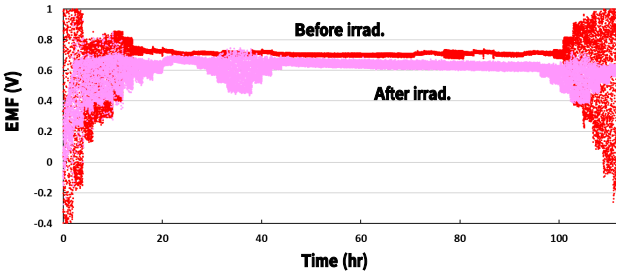

Fig. 2. EMF before and after gamma-ray irradiation at 1 kGy/h for 1,000 h.

References

[1] K. Tsujimoto *et al.*, J. Nucl. Sci. Tech. **44**, (3), 483-90 (2007).
[2] T. Sugawara *et al.*, JAEA-Tech. 2015-022 (2015).

1 - 33 Evaluation of Irradiation Resistance of ODS Ferritic Steel for Fast Reactor Application

T. Tanno, H. Oka, Y. Yano, S. Ohtsuka and T. Kaito

Fast Reactor Fuels and Materials Technology Development Department, AFRCC, JAEA

A high performance fuel cladding tube which has long lifetime, high temperature strength, and good irradiation resistance, is a key technology for fast reactors (FRs). In Japan Atomic Energy Agency (JAEA) we developed oxide dispersion strengthen (ODS) steels as the candidate materials. Particularly, tempered martensitic 9 chromium (Cr) and 11Cr-ODS steels are promising. Recently, the quality of them has gotten better by an applying improved powder metallurgy process which is called “full pre-alloy” process. This process uses only pre-alloyed metallic powder and yttria powder to prevent inclusions [1].

The high temperature strength corresponding to the durability of the ODS steels is provided by fine and dense oxide particles. Hence, the stability of dispersed oxide particles under the irradiation has to be evaluated to predict the durability of the ODS steel cladding tubes during the FR operation. The irradiation tests of ODS steels had been carried out [2, 3]. However, the new high-quality JAEA 9Cr and 11Cr-ODS steels have been never irradiated. Thus in this study, we aim to evaluate the irradiation behavior of the new JAEA-ODS steels in shorter time using the self-ion beam irradiation than that by neutron irradiation. The target dose is over 250 dpa which is the peak one at the end of the life of the advanced FR fuel.

The irradiation materials were the new JAEA 9Cr and 11Cr-ODS steels fabricated by the full pre-alloy process. They were annealed at 1,050 ºC followed by furnace slow cooling to obtain transformed ferrite structure which does not include the obstructive defects for microstructure observation. The small coupon specimens were cut from heat treated ODS steels for ion irradiation. In order to induce large amount of irradiation damage in short time, 10.5 MeV Fe^{3+} self-ion beam irradiation tests at 700 ºC have been carried out repeatedly using tandem accelerator in TIARA through a few years. Finally, the irradiation dose reached to 200 dpa. Microstructure observation using transmission electron microscopy (TEM) of the 9Cr-ODS steel was done to check the dispersion conditions of nano-sized oxide particles.

Figures 1(a) and (b) are the microstructure of the specimens unirradiated and irradiated to 200 dpa by Fe ion beam at 700 ºC, respectively. A number of nano-oxide particles can be confirmed in both images. It shows that a recoil dissolution of the nano-oxide particles by the ion irradiation up to 200 dpa was not significant.

Figure 2 shows the size distribution analysis of observed nano-sized oxide particles. The distribution profiles before and after irradiation are almost same. The average diameter and the number density of the particles are 5.2 nm and 3×10^{22} m^{-3}, respectively, for both specimens. Those show that the coarsening of the nano-sized oxide particles was slight, and the distribution condition of them remained as fabricated even though the material was exposed to the high-dose ion irradiation up to 200 dpa.

These results obtained in this work suggest that the nano-oxide particles dispersed in the 9Cr-ODS steel have good irradiation resistance. In addition, the strengthening by them will be able to support the good high temperature strength of the fuel cladding tubes up to high burn-up.

References

[1] T. Tanno *et al.*, J. Nucl. Mater. **455**, 480-85 (2014).
[2] S. Yamashita *et al.*, J. Nucl. Mater. **442**, 417-24 (2013).
[3] T. R. Allen *et al.*, J. Nucl. Mater. **375**, 26-37 (2008).

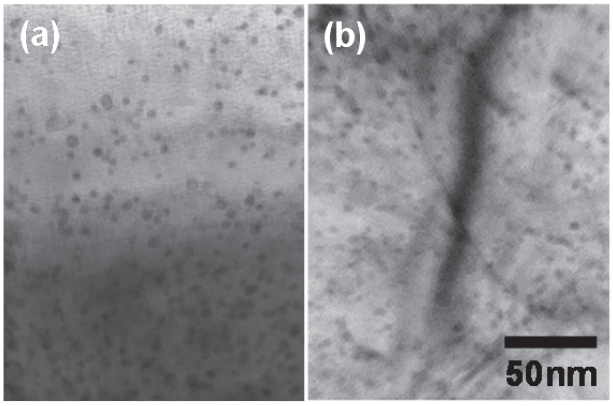

Fig. 1. TEM microstructure images of specimens (a) unirradiated, (b) irradiated to 200 dpa at 700 ºC.

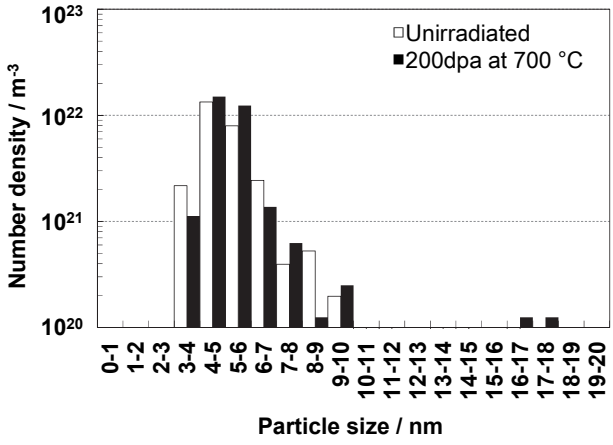

Fig. 2. Oxide particle size distribution before and after irradiation.

1 - 34 Ion Beam Induced Luminescence of CMPO-HDEHP/SiO_2-P Adsorbent

S. Watanabe [a)], Y. Katai [b)], H. Matsuura [b)], W. Kada [c)], M. Koka [d)], T. Satoh [e)] and T. Arai [f)]

[a)] Fast Reactor Fuels Cycle Technology Development Department, AFRC, JAEA,
[b)] Atomic Energy Research Laboratory, Tokyo City University,
[c)] Division of Electronics and Informatics, Faculty of Science and Technology, Gunma University,
[d)] Beam Operation Co. Ltd,
[e)] Department of Advanced Radiation Technology, TARRI, QST,
[f)] Department of Material Science and Engineering, Shibaura Institute of Technology

Partitioning and transmutation of minor actinides (MA(III); Am(III) and Cm(III)) in spent nuclear fuel is an important strategy for reduction in volume and radiotoxicity of the radioactive waste. Japan Atomic Energy Agency has been developing the extraction chromatography technology for separation of MA(III) from other fission products. In this technology, adsorbent is prepared by impregnating an extractant into styrene divinyl benzene copolymer coating around porous silica particle (referred as SiO_2-P), and MA(III) are recovered through adsorption and elution reactions inside the packed column. Currently, our research focuses on developments in an adsorbent with binary extractants system for simplification of the MA(III) recovery process. In the previous study, CMPO and HDEHP extractants are impregnated into an adsorbent (referred as CMPO-HDEHP/SiO_2-P), and MA(III) separation from trivalent lanthanides (Ln(III)) with the adsorbent was successfully achieved [1]. However, elution of remaining Ln(III) from the adsorbent was recognized to be indispensable for practical use of the adsorbent. In this study, chemical state of Eu(III) complex formed in the adsorbent was investigated by ion-beam induced luminescence (IBIL) and Extended X-ray Absorption Fine Structure (EXAFS) analyses in order to give fundamental information to design a promising Ln(III) elution condition.

CMPO-HDEHP/SiO_2-P, CMPO/SiO_2-P and HDEHP/SiO_2-P were prepared as the usual procedure, and Eu(III) was charged into them by column operation. IBIL measurements were carried out at light-ion microbeam line connected to a 3-MV single-ended accelerator in TIARA of QST. Three MeV H^+ beam was irradiated on the adsorbent, and luminescence was measured by UV-Vis spectrometer. Detail analytical conditions are described in ref [2]. Eu L_{III}-edge (6.98 keV) X-ray absorption spectra were collected at BL27B beamline of PF, KEK, Japan.

Major part of the IBIL spectra of the binary extractants system seemed to be superposition of those of CMPO/SiO_2 or HDEHP/SiO_2 as shown in Fig. 1. Intensities of those peaks rapidly decreased with increasing the irradiation time (see Fig. 2), therefore those peaks are considered to be attributed to luminescence from organic compounds *i.e.* complex of Eu(III) with CMPO or HDEHP. In the binary system, both CMPO and HDEHP should contribute to form complexes. Generally, CMPO and HDEHP work for Ln(III) extraction from high and low acidic medias, respectively. However, HDEHP also participate to extract Eu(III) from acidic solution to the binary system. Contributions of CMPO and HDEHP for Eu(III) extraction must be not only individual ones but also cooperative.

EXAFS analysis showed that the number of the nearest neighboring O atom around Eu(III) in the binary system is about 9 which is slightly smaller than that of CMPO system (*i.e.* 10-12) and is distinctly larger than that of HDEHP system (*i.e.* 6). These results also suggest the cooperative extraction of CMPO with HDEHP.

Based on these results, appropriate eluent for back-extraction of Ln(III) from complex with CMPO and HDEHP is currently under examination.

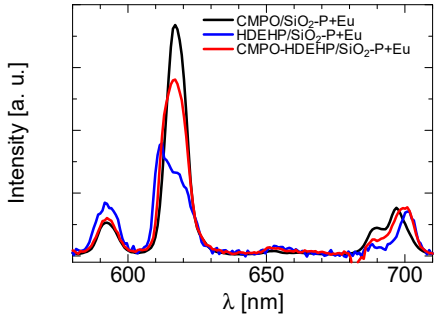

Fig. 1. The IBIL spectra of Eu(III) charged CMPO/SiO_2-P, CMPO-HDEHP/SiO_2-P and HDEHP/SiO_2-P adsorbents.

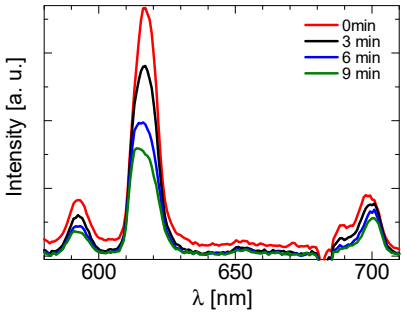

Fig. 2. Intensity of the IBIL spectrum from CMPO-HDEHP/SiO_2-P during irradiation

Acknowledgement

The EXAFS measurements were carried out under the proposal of 2016G557 of the PF, KEK.

References

[1] S. Watanabe *et al.*, Nucl. Instrum. Meth. B (2017) in press.
[2] W. Kada *et al.*, Nucl. Instrum. Meth. B, **318**, 42-46 (2014).

1 - 35 Application of Ferrite Process to Radioactive Waste -Study of Ferrite Product Stability by Micro-PIXE Analysis-

T. Abe [a)], T. Shimazaki [a)], T. Osugi [a)], N. Yamada [b)], Y. Yuri [b)] and T. Satoh [b)]

[a)] Nuclear Backend Technology Center, NFCEL, JAEA,
[b)] Department of Advanced Radiation Technology, TARRI, QST

Toxicity of radioactive wastes has focused on the risk only for exposing to radiation. Although, the radioactivity is decreased by radioactive decay, but the toxicity of hazardous metals contained in radioactive materials is not decreased. Accordingly, chemical toxicity of hazardous metals is as important as the toxicity of radiation. In this research, we focused on the chemical toxicity of the hazardous substances. We tried to develop a solidification technology that can stabilize radioactive substances and hazardous substances for a long time.

A ferrite process is one of the treatment methods for liquid waste containing hazardous metal ions. The ferrite process can treat various hazardous metal elements collectively. A hazardous metal ion is immobilized in the magnetite lattice of the formed ferrite. Therefore, the ferrite process can stably solidify hazardous metal ions. However, there are metal elements of various valences in liquid waste. The magnetite structure could cause change depending on the element to be treated. Thus, the valence may affect the immobilization performance of hazardous metal ions. However, previous studies of the ferrite process have not noted the valence of metal and structural stability. Ferrite is composed of a large amount of iron. Thus, the method of analyzing the trace components contained in the ferrite is limited. It is difficult to observe how coexisting elements in the ferrite reaction relate to the reaction. The Micro-PIXE analysis method allows a highly sensitive analysis and measurement of light elements. We attempted to measure coexisting elements, including sulfur(S) contained in raw materials, during ferrite reaction. In the present study, we tried to synthesize ferrite containing hazardous metals and clarify the change caused by the elements and valences.

The ferrite treatment was carried out under conditions of Table 1, to obtain the ferrite product. Concentration of Pb and Cr in solution after treatment was analyzed using ICP-AES. The crystal phase of ferrite was analyzed using X-ray diffractometer (XRD). Powder XRD analyses were performed using a Rigaku Ultima IV diffractometer with Cu radiation (50 kV, 40 mA). The composition of the ferrite was analyzed using Micro-PIXE. The Micro-PIXE analysis was carried out by H^+ beam with 3 MeV from the single-ended accelerator in TIARA.

Table 1
Conditions of the ferrite process.

Concentration of Pb and Cr in simulated liquid waste (ppm)	1000
pH	11
Temperature (°C)	70
Oxidizing air (L/min)	1.7
Reaction time (h)	2

Cr and Pb were not detected in solution after treatment. Therefore, Pb and Cr were effectively recovered from the simulated waste. Figure 1 shows that X-ray diffractograms of the ferrite product. The peak of magnetite was only observed. No peak of nitrate of Pb or Cr used as a starting material was observed. Moreover, no peak of other Pb and Cr compound was observed. Consequently, each ferrite containing Pb and Cr did not generate crystals other than the magnetite. According to a preceding study conducted under similar conditions, it was supposed that Cr and Ni,Cu,Co were encapsulated in the lattice of the ferrite [1]. Therefore, we considered that all products were crystalline substance. This result suggested that the Pb and Cr were solidified in the magnetite. Figure 2 shows that Micro-PIXE analysis result of the ferrite product. Fe and target elements were detected from both ferrites. On the other hand, S was detected only from Pb ferrite. S exists in both ferrites as sulfate before treatment. However, S exists only in Pb ferrite after ferrite treatment. Hence, these results suggested that the S may be involved in immobilization of the Pb.

This study, the analysis of difference in composition of ferrite was achieved by the Micro-PIXE analysis. In addition, it is found that the composition varies by changing the target element although the same magnetite structure consists.

Reference

[1] Y. Ishibashi *et al.*, Inorg. Mater., **5** (1998).

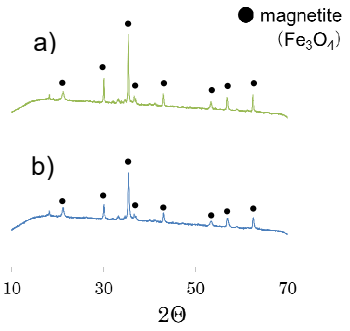

Fig. 1. X-ray diffraction of ferrite product. a) is Pb-containing ferrite, and b) is Cr-containing ferrite.

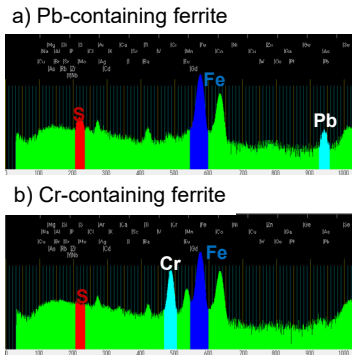

Fig. 2. Micro-PIXE diffraction of ferrite product. The blue area shows Fe, the red area shows S, and the white area shows each hazardous element of Pb and Cr.

1 - 36 Investigation of Hydrogen Gas Generation by Radiolysis for Cement-solidified Products of Used Adsorbents for Water Decontamination

J. Sato [a, b], H. Kikuchi [c], J. Kato [a, b], T. Sakakibara [a, b], R. Matsushima [a, b], F. Sato [a, d], J. Kojima [a, d] and O. Nakazawa [a, b]

[a] International Research Institute for Nuclear Decommissioning (IRID), [b] Nuclear Backend Technology Center, NFCEL, JAEA, [c] Inspection Development Company Ltd., [d] Tokai Reprocessing Technology Development Center, NFCEL, JAEA

Several kinds of used adsorbents, which contain large amounts of radionuclides, have been generated from the Multi Radionuclide Removal System (MRRS) in the Fukushima Daiichi Nuclear Power Station (1F NPS). The adsorbents are organic or inorganic materials and have not been solidified so far. Thus it is necessary to confirm feasibility of existing solidification techniques and to select some prospective techniques from among them toward an early accident resolution.

Cementation is one of the candidate techniques for solidification of the used adsorbents. The cement-solidified product contains free water, which is a major source of hydrogen gas generated by radiolysis. The accumulated hydrogen gas in storage would be a cause of fire/explosion. G-value of hydrogen gas generation is necessary to evaluate safety of storing/disposing of the actual cement-solidified body. In this study, the G-values were estimated using cement-solidified products of non-radioactive simulated adsorbents by ^{60}Co gamma-ray irradiation as in the previous study [1].

Fresh adsorbents were provided by Toshiba Co., Ltd. The adsorbents were titanate (TN), titanium oxide (TO), ferrocyanide (FC), chelate resin (CR) and resin adsorbent (RA), which are actually used in the MRRS to decontaminate accumulated water. To prepare simulated adsorbent, non-radioactive elements (Sr, Sb, Cs, Co and Ru) were adsorbed at 0.1 wt.% by contacting with aqueous solution. The TN and TO were dried by heating at 105 ºC. The FC, CR and RA were incinerated at 400~800 ºC to decompose cyanide or organic components. Each simulated adsorbent and cement material were mixed with prescribed water as shown in Table 1. Ordinary Portland cement (OPC) or Portland Blast-Furnace Slag Cement Type-B (BB) was used as cement material. The filling rate of simulated adsorbents was 40 wt.%. The 2 wt.% of water-reducing agent by cement weight was added for better workability. The mixture was filled into a container (φ13 × 50 mm), and cured at 20 ºC for 28 days. The solidified product was put into a glass ampule (φ18 × 150 mm), and was irradiated by ^{60}Co gamma-ray at 30 Gy/h for 100 h in the Food Irradiation Facility (TARRI, QST) as shown in Fig. 1. The concentration of hydrogen gas in the ampule was measured by gas chromatography. The total absorbed dose was measured by using a polymethylmethacrylate dosimeter, and the averaged value of five points close to the ampules was used as representative value. The G-value was calculated from the amount of hydrogen gas, cement-solidified product weight and total absorbed dose.

As a result, hydrogen gas was detected in all ampules. The calculated G-values were shown in Table 1. The data is fundamental to discuss feasibility of cementation as a solidification technique for the actual used adsorbents generated at the 1F NPS.

Acknowledgement

This work includes a part of the result from the subsidy program “Project of Decommissioning and Contaminated Water Management (R&D for treatment and disposal of solid radioactive waste)” by METI.

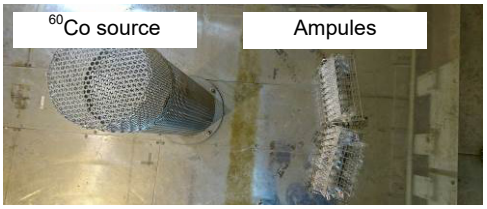

Fig. 1. Placement of glass ampules in the Food Irradiation Facility.

Table 1
Conditions of solidification and G-value of hydrogen.

Condition			G-value(H_2) (/100 eV) (n=3)
Adsorbent (element)	Cement material	Water/ Cement	
TN (Sr)	OPC	0.90	6.0×10^{-2}
	BB	0.90	4.9×10^{-2}
TO (Sb)	OPC	4.50	1.9×10^{-1}
	BB	4.50	1.7×10^{-1}
FC (Cs)	OPC	0.55	5.4×10^{-4}
	BB	0.55	3.3×10^{-4}
CR (Co)	OPC	0.80	3.7×10^{-2}
	BB	0.80	2.3×10^{-2}
RA (Ru)	OPC	0.45	2.2×10^{-2}
	BB	0.45	1.9×10^{-2}

Reference

[1] J. Sato *et al.,* QST Takasaki Annu. Rep. 2015, **QST-M-2**, 88 (2017).

1 - 37 Characterization of Phosphate Cement Irradiated by γ-ray During Dehydration

K. Irisawa [a], I. Kudo [b], T. Taniguchi [a], M. Namiki [a], T. Osugi [a] and O. Nakazawa [a]

[a] Nuclear Backend Technology Center, NFCEL, JAEA,
[b] ADVAN ENG. Co., Ltd.

Secondary wastes arising from the processing of contaminated water in the Fukushima Daiichi Nuclear Power Station have been stored with a large amount of liquid and seawater components. The risks of fire and explosion by radiolytic H_2 and leakage of radioactive wastes present during storage. To store them safely in the long term, risks for these secondary wastes should be reduced. Phosphate cement is expected to solidify the secondary wastes involving seawater components, and only requires water mainly for reasons of workability. A solidification technique with phosphate by dehydration is therefore being developed for the safe storage of the secondary wastes. The solidification technique showed feasibillity under non-irradiation [1]. However, the actual secondary wastes have high radioactivity. In this study, the developing solidification technique was carried out under ^{60}Co γ-ray irradiation. Radiolytic H_2 amounts were analyzed, and the characteristics of the phosphate cement were investigated.

The phosphate cement was synthesized by mixing 100 g of anhydrous calcium aluminate cement (Secar 51, Kerneos Ltd.), 40 g of sodium polyphosphate (Acros Organics Ltd.) and 35 g of de-ionized water by hand for 30 seconds and a mechanical mixer for 2 minutes at 2,500 rpm (L5MA high shear mixer, Silverson Ltd.). The phosphate cement was then placed in a made-to-order heater, and was dehydrated at 90 ºC and irradiated by 30 Gy/h of ^{60}Co γ-ray during 7 days (total 5 kGy) in the food irradiation facility. Radiolytic H_2 during irradiation was transported to a vacuum vial, and was analyzed by gas chromatography. After 7 days, the irradiation and dehydration were stopped, and the phosphate cement was analyzed by TG etc.

The $G(H_2)$ (molecule/100 eV) is calculated as follows

$$G(H_2) = \frac{M_{H2} \times N_A \times 1.6 \times 10^{-17}}{R \times w}$$

where M_{H2} is H_2 amount (mol), N_A is Avogadro constant (molecule/mol), R is absorbed dose (J/g) and w is the sample weight (g). The $G(H_2)$ for the phosphate cement after 1 day dehydration was approximately 0.14 and decreased with time (Fig. 1). The $G(H_2)$ after 7 day dehydration could not be detected. The $G(H_2)$ for the phosphate cement synthesized at 90 ºC under non-irradiation was also negligible, meaning it matched with the $G(H_2)$ after 7 day dehydration under the irradiation. This clarifies that the developing solidification technique can reduce the risks of fire and explosion by H_2 gas.

Figure 2 shows the DTG results for phosphate cement after 7 day irradiation. The DTG peak at 120 ºC is associated to weekly-bonding water with phosphate cement, and the water in the phosphate cement did not generate radiolytic H_2. The difference of DTG results for the phosphate cement synthesized between under non-irradiation [1] and irradiation during dehydration was not observed (Fig. 2). This indicates that ^{60}Co γ-ray irradiation during dehydration did not contribute to the formation of crystalline and amorphous phases for the phosphate cement.

The above results show that the developing solidification technique can be applied under the dose rate. The dehydrated phosphate cement would be useful as a matrix for a waste package which does not generate radiolytic H_2. The risks of fire and explosion by H_2 and leakages can be minimized by this technique. In the future, the characterization of phosphate cement involving simulated secondary wastes irradiated by ^{60}Co γ-ray during dehydration and influence of electron beam on radiolytic H_2 will be investigated, considering heating effect by their irradiation.

Reference

[1] K. Irisawa *et al.,* Proc. ICAPP 2017, No. 17618, [Fukui & Kyoto, Japan], (2017/04).

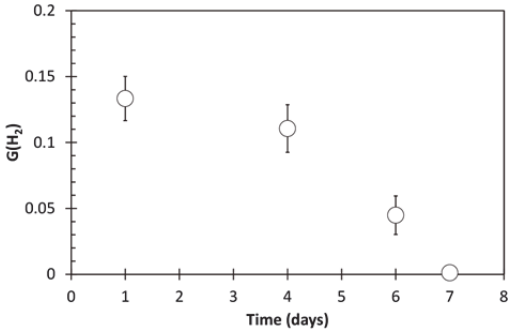

Fig. 1. The $G(H_2)$ for the phosphate cement during dehydration.

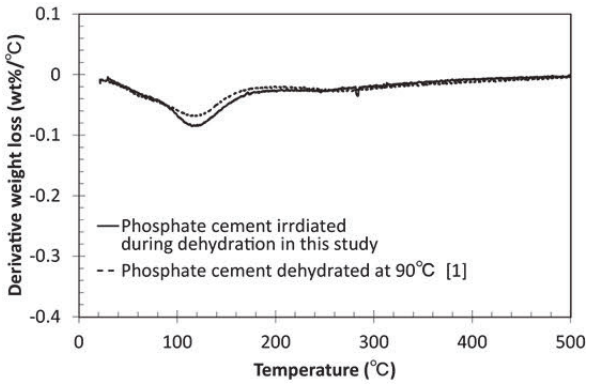

Fig. 2. The derivative weight loss (%/°C) of the phosphate cement as a function of temperature for the phosphate cement irradiated during hydration.

1 - 38 Effect of Damage Depth Profile on Hydrogen Isotopes Dynamics in W

Y. Oya, H. Fujita, S. Sakurada, Y. Uemura, K. Azuma, Q. Zhou, T. Miyazawa and T. Chikada

Graduate School of Science and Technology, Shizuoka University

Introduction

Tungsten (W) is the candidates for the plasma facing materials in future D-T fusion reactors like ITER due to its lower sputtering yield and higher melting point. During plasma operation, W will be exposed to energetic particles, such as hydrogen isotopes, impurity ions, and 14 MeV neutrons. It is known that the hydrogen isotope is trapped by the damages introduced by these energetic particles, leading to the enhancement of fuel retention. In previous study [1], it was found that hydrogen isotope retention was clearly controlled by damage concentration. In addition, It is important to understand how the damage distribution in W contributes on hydrogen isotope retention enhancement. Therefore, this study focuses on the effect of damage distribution controlled by heavy ion irradiation with various energy on D retention behavior in W.

Experimental

A disk-type polycrystalline W (10 mm^{φ} × 0.5 mm^{t}) purchased from A. L. M. T. Corp. Ltd were used. These samples were preheated at 1173 K for 30 minutes under ultrahigh vacuum (<10^{-6} Pa) to remove the impurities. Combination of 0.8 MeV Fe^{+} ion and 6 MeV Fe^{2+} ion was irradiated into the samples at room temperature with the damage concentrations of 0.01 - 0.1 dpa (displacement per atom) by 3 MV tandem accelerator, Takasaki Ion Accelerators for Advanced Radiation Application (TIARA) at National Institutes for Quantum and Radiological Science and Technology (QST). Thereafter, 1.0 keV D_2^{+} was implanted with the ion fluence of 1.0×10^{22} D^{+} m^{-2}, and the D desorption behaviors were evaluated by TDS measurements. In addition, 1.0 keV DT^{+} implantation was also performed with the ion fluence of 5.8 - 6.1 × 10^{20} DT^{+} m^{-2} at University of Toyama to evaluate the T depth distribution by β-ray-induced X-ray spectrometry (BIXS) measurement.

Result &Discussion

Figure 1 shows the D_2 TDS spectra for Fe ion irradiated W samples with various damage concentrations. The D_2 TDS spectra consisted of four major D desorption stages located at 400 K, 550 K, 650 K and 850 K which were attributed to the desorption of D adsorbed on the sample surface or trapped by dislocation loops, the desorption of D trapped by vacancies, vacancy clusters and voids, respectively [2-4]. TDS spectra showed that the retention of D adsorbed on the surface or trapped by dislocation loops was saturated with 0.01 dpa despite additional 0.8 MeV Fe ion irradiation. Furthermore, The D desorption at Peak 2 for multiple Fe ion irradiated W were higher than that for single Fe ion irradiated W, while the D desorption at Peak 3 for multiple Fe ion irradiated W were reduced. Figure 2 shows the results of BIXS measurements. It was found the both intensities of Ar (Kα) and W (Mα) characteristic X-rays for No. (1) and No. (2) were higher than that for No. (3), indicating that the T concentrations near the surface for No. (1) and No. (2) were higher than that for No. (3). These results indicated that D de-trapping from irradiation defects would be enhanced and the D desorption peak temperature could be shifted toward lower temperature side by dense damage introduction in shallow region.

References

[1] Y. Oya *et al.*, J. Nucl. Mater. **461**, 336-40 (2015).
[2] H. Eleveld *et al.*, J. Nucl. Mater. **191**, 433 (1992).
[3] H. Iwakiri *et al.*, J. Nucl. Mater. **307**, 135 (2002).
[4] G. N. Luo *et al.*, Fusion Eng. Des. **81**, 957 (2006).

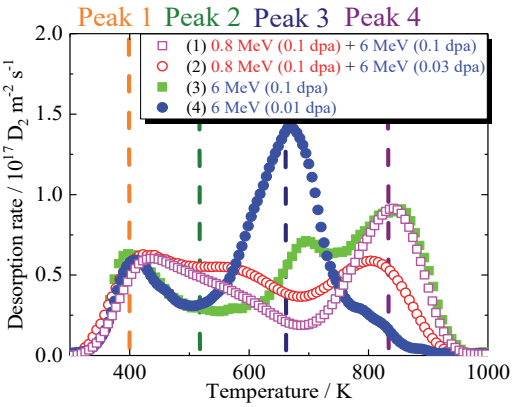

Fig. 1. D_2 TDS spectra for each Fe ion irradiated sample.

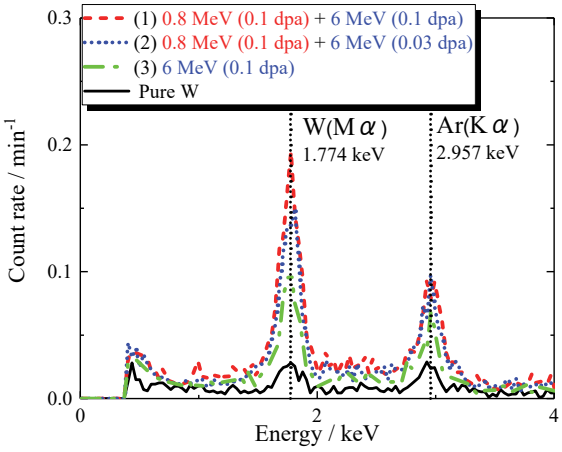

Fig. 2. The spectra of BIXS measurement results for Fe ion irradiated W and Pure W.

1 - 39 Effects on Displacement Damage on Electrical Properties of Silicon Carbide

T. Nozawa, K. Ozawa and H. Tanigawa

Department of Fusion Reactor Materials Research, RFI, QST

Silicon carbide (SiC) is a promising candidate material of liquid metal breeding blanket for a fusion DEMO reactor [1]. Toward practical application, the irradiation-induced change of the electrical conductivity of SiC is a potential concern, as well as other possible detrimental effects on the microstructure due to displacement damage, since these properties are readily affected by irradiation. Electrical resistivity measurements have therefore been conducted using some irradiation sources such as FNS and JRR-3 so far [2-5]. However, the damage levels and the primary knock-on atom (PKA) energy available for these facilities are insufficient for the DEMO component design. Accordingly, we adopted a new technique using a TEM thin disk specimen to evaluate the irradiation behavior of electrical resistivity by the high-energy Tandem accelerator irradiation [6].

The specimen configuration and the electric circuit for electrical conductivity measurement during high energy ion irradiation are shown in Fig. 1. The specimen applied is the standard high-purity and high-crystallinity CVD SiC. The diameter and thickness of the specimen were 3 mm and 50 μm, respectively. Thin film Pt electrodes were deposited on the specimen surfaces. To suppress the effect of leak current at the specimen surface sensitive to surface electron migration and carbon contamination during irradiation, the specimen with a guard ring is often applied to measure the electrical conductivity of ceramics. An irradiation area was selected by specimen mask to cover only the center electrode and monitored by both currents of center and guard ring. Specifically the AC impedance method was applied to evaluate the irradiation behavior in detail. Irradiation of 6.0 MeV Si^{2+} ions was conducted by the TIARA facility. No external heating was applied but considerable temperature increase by beam heating was measured. The irradiation temperature was approximately 648 K.

Figure 2 shows the AC impedance results before and after irradiation. The volume conductivity was preliminarily evaluated in this study. Note that the surface conductivity will be more emphasized in the future evaluation since the irradiation damage area was localized near the surface. As for the low frequency AC impedance data, there was almost no change of the shape of the impedance plot except for a slight difference identified at high frequency data. Figure 3 then summarized the dose dependence of the volume resistivity of CVD SiC by 6.0 MeV Si^{2+} single ion irradiation up to ~40 dpa at ~648 K. This is very rough sketch but it was speculated that no significant degradation of the volume resistivity was identified.

References

[1] P. Norajitra *et al.*, Fusion Eng. Des., **69**, 669-73 (2003).
[2] K. Noda *et al.*, Fusion Eng. Des., **29**, 448-54 (1995).
[3] T. Tanifuji *et al.*, J. Nucl. Mater., **253**, 156-66 (1998).
[4] T. Shikama *et al.*, J. Nucl. Mater., **367-370**, 995-1002 (2007).
[5] B. Tsuchiya *et al.*, J. Nucl. Mater., **367-370**, 1073-78 (2007).
[6] N. Okubo *et al.*, Nucl. Instrum. Meth. Phys. Res. B, **314**, 208-10 (2013).

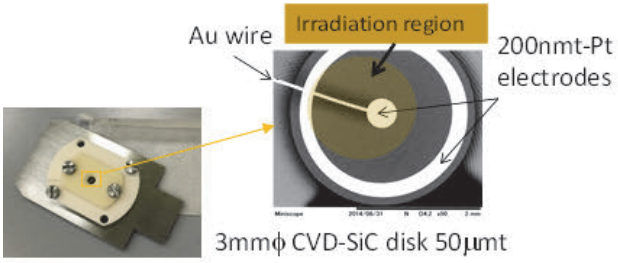

Fig. 1. Irradiation holder and specimen applied in this study.

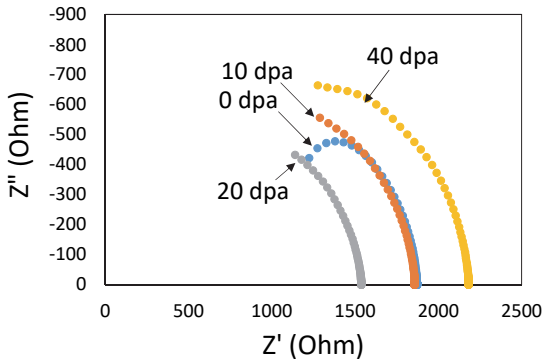

Fig. 2. Irradiation effect on volume resistivity of CVD SiC by the AC impedance method.

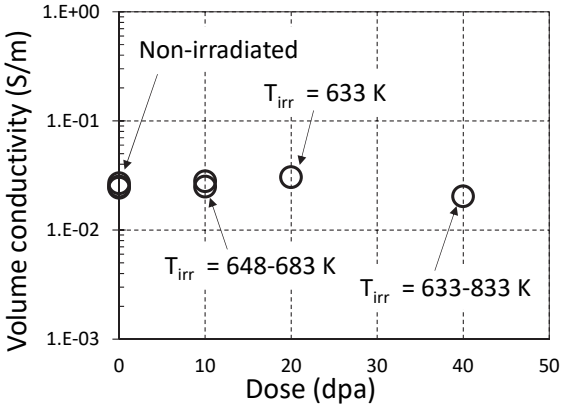

Fig. 3. Dose dependence of the volume resistivity of CVD SiC.

1 - 40 Irradiation Tests of Radiation Hard Components and Materials for ITER Blanket Remote Handling System

M. Saito, T. Maruyama, Y. Noguchi, M. Kazawa, K. Nakata and N. Takeda

Department of ITER Project, NFI, QST

1. Introduction

The ITER blanket remote handling system (BRHS) will replace the blanket first walls (FWs) and shield blocks in the vacuum vessel after plasma shutdown [1]. In addition, the BRHS will operate in a high radiation environment. The in-vessel components will be activated by neutrons and there is concern that the remote handling components will be irradiated by gamma rays and break down. The most important operation of the BRHS is the two-year maintenance campaign in which all 440 FWs will be replaced in an an environment having dose rate of 250 Gy/h. The ITER Project requires 1 MGy of radiation hardness for all BRHS parts, which corresponds to 180 days. The parts must be replaced every 180 days, which will decrease availability. Therefore a total dose of 5 MGy, corresponding to 2 years, was set as the target value to increase availability. The BRHS is composed of many parts and materials; in this study, in particular, the AC servo motors and nickel coating were investigated.

2. Experimentation

The radiation hardness of AC servo motors (supplied by Waco Giken Co., Ltd.) and nickel coated samples (supplied by Brother Co., Ltd.) was tested by irradiating Co-60 gamma rays at 2,100 Gy/h to 3,000 Gy/h and 1,100 Gy/h to 2,700 Gy/h, respectively, without humidity control at atmospheric pressure and at room temperature. Some of the nickel coated samples were irradiated with 50 g of dry silica gel (relative humidity: 2% to 3%) to confirm the effects of humidity.

3. Results

3.1 AC servo motor

In past tests, commercial motors were modified by replacing the lubricant with MORESCO GK-1, which is a commercial radiation hard lubricant, and replacing the electrical insulators with ones made of polyimide. These motors functioned at 8 MGy, however, at 10 MGy, the carbon steel bearings corroded and the motors ceased to operate. In this study, motors were modified by replacing some parts with stainless steel and irradiating them up to 10 MGy. After irradiation, static friction torque, brake torque, conduction resistance, insulation resistance and withstand voltage were measured. With the exception of conduction resistance, all values satisfied the acceptance criteria. Conduction resistance of all six motors increased at 8 MGy (shown in Fig. 1) and one motor was not operational. The malfunctioning motor was disassembled and it was found to have a degraded of rubber clamp of the motor cable. After retightening the clamp, its conduction resistance decreased and the motor become operational again. As a result, all motors operated normally at 10 MGy.

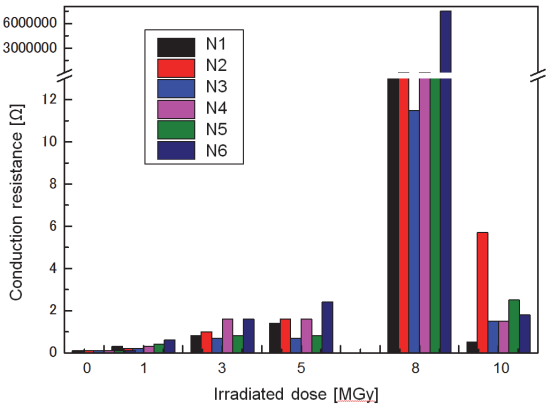

Fig. 1. Conduction resistance after irradiation.

3.2 Nickel coating

An increase in corrosion on the surface of the nickel-coated samples was observed as the irradiation increased, as shown in Fig. 2. A surface analysis was performed by using SEM-EDX to find what elements were present on the surface. Nickel and phosphorus, the main elements of nickel coating, along with carbon, oxygen, and iron were detected. However, sodium and sulfur were not detected, indicating that no coating solutions (NaH_2PO_3 and H_2SO_4) remained on the surface. Moreover, the chemical compounds were investigated by using XRD. After irradiation, a peak of nickel (iron) hydroxide was detected. The nickel-coated samples were also irradiated under a relative humidity of 2% to 3% by using silica gel. Consequently, corrosion was not observed on the surface. From these results, we concluded that the corrosion was caused by a combination of moisture and gamma irradiation.

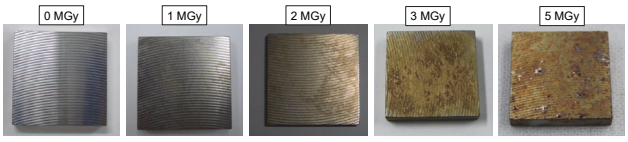

Fig. 2. The surface of nickel coated sample after irradiation.

4. Conclusion

Gamma ray irradiation tests were performed to confirm the radiation hardness of the ITER BRHS components. These tests allowed us to define most of the materials for the AC servo motors. The next step is to directly connect the motor cable to the body and operate the AC servo motors under irradiation.

The nickel coating corroded from irradiation. Judging from the results of the surface analysis and irradiation in dry air, this suggests that the nickel coating corroded because of the reaction of atmosphere and gamma irradiation.

Reference

[1] A. Tesini *et al.*, FED, **83**, 810-16 (2008).

1 - 41 Development of Luminescence Profile Monitor for High-Intensity Proton Accelerator Facility

S. Meigo [a], H. Matsuda [a], T. Yuyama [b] and Y. Yuri [b]

[a] Transmutation Division, J-PARC Center, JAEA,
[b] Department of Advanced Radiation Technology, TARRI, QST

In high power hadron accelerator facilities such as the spallation neutron source of J-PARC (JSNS) and the material test facility for ADS called TEF-T, the beam profile monitor is essential for stable accelerator operation. For a diagnosis of the intensity distribution of high-energy proton beams on the target, a one-dimensional multi-wire profile monitor was developed in J-PARC [1]. In addition, another method was also developed to observe the two-dimensional beam profile at the target using an imaging plate [2] because the two-dimensional information of the beam profile was important for reducing the peak current density at the target with nonlinear optics. The imaging plate technique is, however, only applicable to offline analysis giving the profile after beam irradiation. Therefore, we are developing a new profile monitor based on the luminescent material placed at the target. In this study, the degradation test of a luminescent material and the operation test of a new monitoring system were performed at the cyclotron facility in TIARA.

In the experiment, Desmarquest AF995R (Al_2O_3 99.5% and CrO_3 0.5%) with a thickness of 5 mm was irradiated with the 150-MeV $^{40}Ar^{15+}$ beam having a flat-shaped transverse intensity distribution. The luminescence of AF995R was observed with the spectrometer (Flame-NIR: Ocean Photonics). The spectrum is shown in the solid line in Fig. 1 for the first shot of the beam. The spectrum has a prominent peak at 694 nm with several unresolved shoulder peaks produced by the excitation state of Cr^{3+} [3]. After the irradiation of AF995R with the Ar beam of 75 nA for 2.3 h, it was found that the peak intensity decreased by 35% as shown in Fig. 2. In the first 0.2 h from the beginning, the intensity decreased rapidly. After the 0.2-h irradiation, the intensity decreased slowly and steadily, which can be fit well by a linear function as shown in the solid line in Fig. 2. The spectrum after the 2.3-h irradiation is also shown in the dotted line in Fig. 1. The intensity of the unresolved peak with a wavelength region shorter than the peak located at 694 nm less decreased than the intensity at the peak. Therefore, it appears that an optical filter cutting off long-wavelength light mitigates the influence of the degradation.

For the development of the profile monitor system, the image of the luminescence from the DRZ-High (Gd_2O_2S:Tb) was observed with the ordinary CCD camera through imaging fiber (FISR Fujikura) having high radiation hardness. Since the ordinary CCD camera is insensitive to the long-wavelength luminescence of AF995R, which is widely used as a beam profile monitor in many accelerator facilities, the DRZ-High that emits the short-wavelength luminescence was employed. As shown in Fig. 3, it is confirmed that the image of the profile of the beam can be clearly obtained with the present system.

References

[1] S. Meigo *et al.*, Proc. HB2016, WEPM2X01, [Malmo, Sweden] (2016).
[2] S. Meigo *et al.*, Proc. IBIC2012, MOPB68, [Tsukuba, Japan] (2012).
[3] S. Geschwind *et al.*, Phys. Rev. **137**, A1087 (1965).

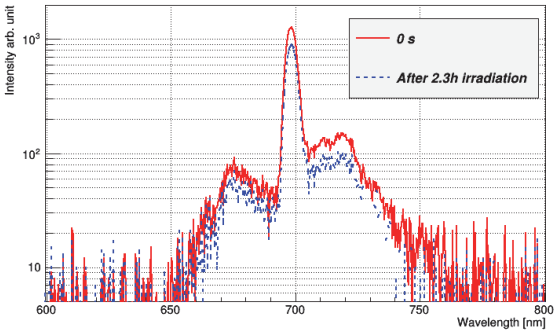

Fig. 1. Result of spectrum of luminescence of AF995R irradiated with $^{40}Ar^{15+}$ beam.

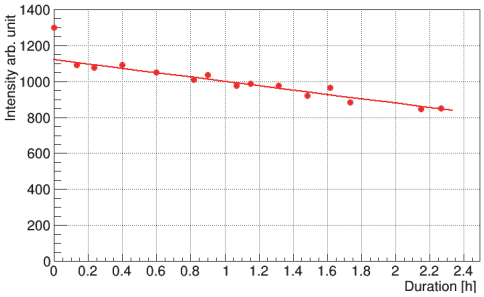

Fig. 2. Dependence of Intensity of luminescence at peak wavelength as function of beam irradiation duration.

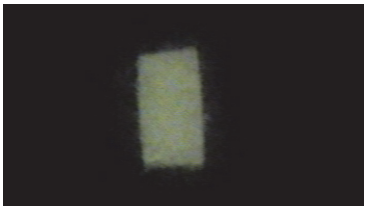

Fig. 3. Image of beam profile observed with the present fiber scope. The size of the flat beam was approximately 4 cm × 4 cm.

1 - 42 Development of Information Acquisition Device in Light Water Reactor under Specific Environment

T. Takeuchi [a)], N. Otsuka [a)], S. Tanaka [b)], O. Ozawa [b)], T. Shibagaki [b)], H. Komanome [b)] and K. Tsuchiya [a)]

[a)] Neutron Irradiation and Testing Reactor Center, ORDC, JAEA,
[b)] Ikegami Tsushinki Co., Ltd.

During the Fukushima Daiichi Nuclear disaster, almost all instruments for monitoring of plant situation were broken down. In response to these provisions, a research and development of a monitoring system for nuclear power plants (NPPs) situations during severe accidents have been addressed.

The developing system includes a radiation-resistant monitoring camera system and in-water wireless transmission system [1] as shown in Fig. 1. For both the systems, radiation resistance of the component parts had been revealed by gamma irradiation tests and adequate parts were selected for required system performance [2]. With the selected parts, the prototype models of the camera and transmission system were designed and fabricated in trial. Figure 2 shows the photographs of the trial prototype models of the radiation-resistant monitoring camera and in-water wireless transmission system.

The camera system was designed as separate type composed of lens/head and controller units. The output image signal of the lens/head unit in high-radiation environment is converted to optical signal and transferred by a 100-meter-long optical fiber to the camera controller unit in non-radiation environment. In the head unit, a part of the electric components with insufficient radiation resistance are inside of a radiation shielding wall. The transmission system was composed of a stand-alone transmitter with LED matrix as light signal generator and a receiver using a digital camera. In the transmitter, all the electric components except for the LED matrix are inside of a radiation shielding wall. Gamma irradiation tests were performed up to about 1 MGy with 3 kGy/h on both the systems. For the camera system, the lens/head with additional shielding walls was located in an irradiation room and image of a test chart was obtained and transferred to a monitor. For the transmission system, temperature data of a thermocouple set in an electric furnace was converted to light signal by the transmitter located in the irradiation room and the signal received by a digital camera was decoded to temperature value. The gamma irradiation tests indicated both the systems were workable even about 1 MGy radiation environment. The basic specifications of the developed systems are listed in Table 1.

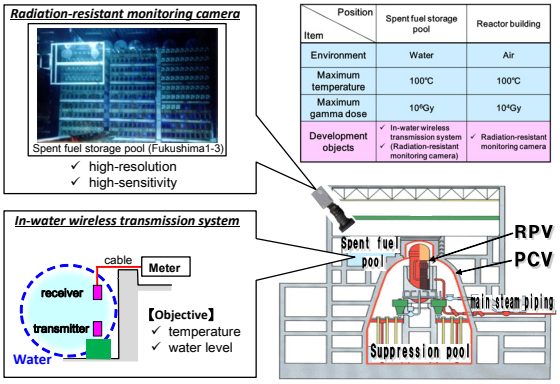

Fig. 1. Outline of the developing monitoring system.

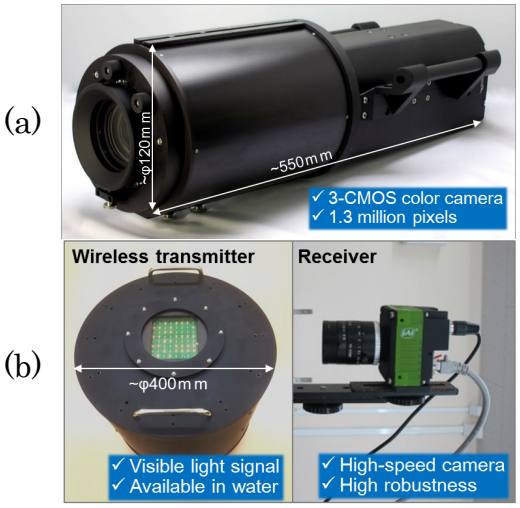

Fig. 2. Photographs of prototype models of the (a) radiation-resistant monitoring camera and (b) in-water wireless transmission system.

Table 1
Basic specifications of the camera and transmission systems.

	Parts	Type
Camera (Lens & Head)	Image sensor	2/3 inches, 1.3M pixels, CMOS×3
	Prizm	RGB
	Lens	motorized zoom (24 - 120mm)
	Sensitivity	F8/2000
	Overall size	W116mm×H179mm×D552mm
	Weight	~16kg

	Item	specification
Transmission system	Transceiver	Transmitter: LED matrix Receiver: digital camera
	Measuring object	temperature, pressure
	Output signal / resolution	0 - 5V / 8bit
	Sampling period	30 seconds
	Battery life time	100 hours

References

[1] K. Tsuchiya *et al.*, Proc. 13th Annu. Conf. Jpn. Soc. Maintenology, 375-78 (2016). [in Japanese]
[2] T. Takeuchi *et al.*, Proc. 2017 Int. Congr. Adv. Nucl. Pow., 17251 (2017).

1 - 43 Study on Hydrogen Generation from Cement Solidified Products Loading Low-radioactive Liquid Wastes at Tokai Reprocessing Plant

Y. Itoh, R. Matsushima and F. Satoh

Tokai Reprocessing Technology Development Center, NFCEL, JAEA

Cement solidification of Low-level radioactive Liquid Wastes (LLWs) generated from Tokai reprocessing plant is planned in Low-level radioactive Waste Treatment Facility (LWTF). The LLWs are categorized into “sodium carbonate effluent” with low radioactivity and “slurry effluent” with comparatively high radioactivity, which will be generated from the radionuclide separation process and the nitric acid ion decomposition process [1]. The sodium carbonate effluent is planned to solidify with BC cement (BC), which is a mixture of 70 wt.% BFS (Blast Furnace Slag) and 30 wt.% OPC (Ordinary Portland Cement). And also, the slurry effluent is planned to solidify with ‘Super Cement’ (SC), which is a commercial product of JGC Co. and is an alkali activated slag cement with various minor additives.

It is known that $G(H_2)$ value of a cement solidified product containing radionuclides varies with cement and effluent composition. In this study, we investigated hydrogen production from the cement solidified sample containing these effluents.

Irradiation samples were prepared by mixing simulated liquid waste and these cement, then filled into a container (ϕ13 mm × 50 mmH) at 20 ºC for 28 days. After curing, each sample was put into a vial container (50 mL) and was sealed with rubber septum. These samples were irradiated by Co-60 gamma-rays at about 2.5 kGy/h for 20 hours. After the gamma irradiation, the concentration of hydrogen gas generated in the vial was measured by gas chromatography.

Figures 1 and 2 show $G(H_2)$ values obtained from the slurry and the sodium carbonate loading samples.

The $G(H_2)$ values of the slurry loading samples were about 0.03 (/100 eV) regardless of the loading ratio, and they were around half of the $G(H_2)$ without slurry. It was supposed that the $G(H_2)$ decreased under the influence of the sodium nitrate in the slurry effluent because the nitrate ion reduces hydrogen production by gamma-ray irradiation [2].

For the sodium carbonate loading samples, the $G(H_2)$ for 10 wt.% loading sample was about 0.14 (/100 eV) which was around one-and-a-half of the $G(H_2)$ without sodium carbonate. However, the $G(H_2)$ for 20 wt.% and 30 wt.% loading samples were around half or less of the $G(H_2)$ without sodium carbonate. So, reaction products in these samples were measured by XRD analysis.

C-S-H and $CaCO_3$ were observed in the 10 wt.% loading samples, and Pirssonite (composite salt of Na_2CO_3 and $CaCO_3$) was observed in the 20 wt.% and 30 wt.% loading samples. The Pirssonite increased in response to the sodium carbonate loading ratio.

To investigate the influence of these salts (reaction products) on $G(H_2)$ value, we measured the $G(H_2)$ of Na_2CO_3 and $CaCO_3$ containing a little water by gamma-ray irradiation. As a result, we obtained that the $G(H_2)$ of Na_2CO_3 and $CaCO_3$ were about 0.02 (/100 eV) and 0.11 (/100 eV), respectively.

Therefore, it is suggested that 1) sodium carbonate fully reacts and forms $CaCO_3$ at low loading ratio (~10 wt.%) and promotes the generation of hydrogen; 2) sodium carbonate partially reacts and forms Pirssonite at high loading ratio (20 wt.%~30 wt.%) and hydrogen generation becomes lower than the previous case.

References

[1] A. Sugaya *et al.*, WM2011 Conf., 11078 (2011).

[2] N. Nakagiri, T. Miyata, J. Atom. Energy Soc. Jpn., **36,** 42 (1994).

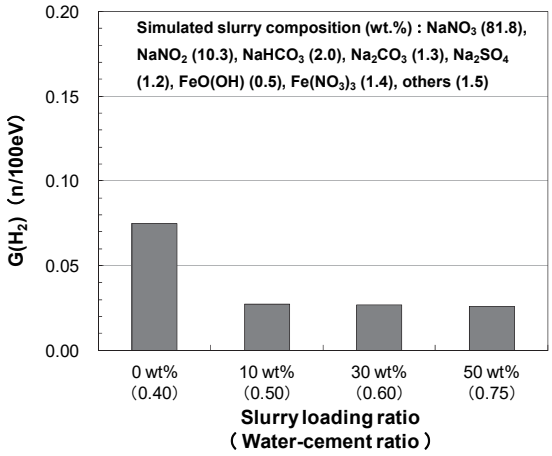

Fig. 1. Observed $G(H_2)$ values from slurry loading samples.

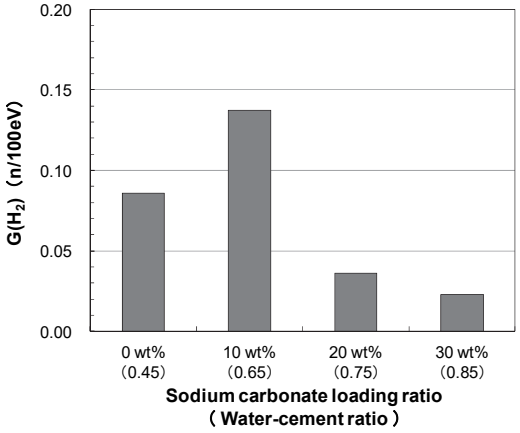

Fig. 2. Observed $G(H_2)$ values from sodium carbonate loading samples.

1 - 44 Radiolytic Hydrogen Absorption Behavior of Explosive Bonded Zr/Ta/R-SUS304ULC Joint

Y. Ishijima [a)], F. Ueno [a)] and H. Abe [b)]

[a)] Fuels and Materials Engineering Division, NSEC, JAEA,
[b)] Nuclear Safety Research Center, JAEA

In Japan, a commercial reprocessing plant is being test operated in the Rokkasyo reprocessing plant. The Purex process which uses nitric acid (HNO_3) for solvent has been adopted in the plant. In order to avoid severe corrosion in HNO_3 environment, some equipments in the plant have been made of zirconium (Zr) and reprocessing plant grade SUS304ULC (R-SUS304ULC). In order to connect these equipments, explosive bonded Zr/Ta/R-SUS304ULC joints are used.

However, it is well known that Zr and tantalum (Ta) has susceptibility of hydrogen embrittlement. In used nuclear fuel solution, radiolytic hydrogen atoms are always generated under irradiation. And it is considered that radiolytic hydrogen can diffuse into the metal and generate the hydride of metal. Therefore, there is a concern about the degradation of Zr/Ta/R-SUS304ULC joint by hydrogen embrittlement in long term operation.

In this study, we conducted radiolytic hydrogen absorption test by HNO_3 immresion test under gamma-ray irradiation.

Explosive bonded Zr/Ta/R-SUS304ULC plate was used as test material. Figure 1 shows the SEM micrograph of the test material at the Zr/Ta interface. Plate type specimens (10 × 10 × 1 mm) were used for radiolytic hydrogen absorption tests. Specimens were polished up to #1000 by SiC paper.

Radiolytic hydrogen absoption tests were carried out in 1 mol/L HNO_3. Dose rates from ^{60}Co source were chosen 7 kGy/h. Irradiation time was 1,000 h. After the irradiation, two dimensional secondary ion mass spectrometry (2D-SIMS) was carried out to evaluate the distribution of hydrogen absorption with quadrupole mass spectrometer (QMS). Evaluate area of 2D-SIMS was 250 × 250 μm. Zirconium, tantalum and hydrogen were selected as elements to evaluate the distributions.

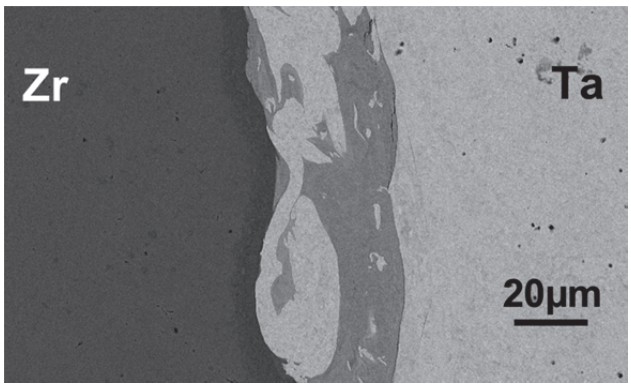

Fig. 1. SEM micrograph of the test material at the Zr/Ta interface.

Figure 2 shows that distributions of elements on test material by 2D-SIMS imaging. These images show that the hydrogen distribution almost matched the zirconium distribution on zirconium/tantalum interface. This result exhibits that the hydrogen is preferentially absorbed by zirconium as a zirconium hydride. Fromm et al. reported [1] that the passivity film on the tantalum reduces hydrogen adsorption. This is the reason that the hydrogen did not detected in the tantalum area.

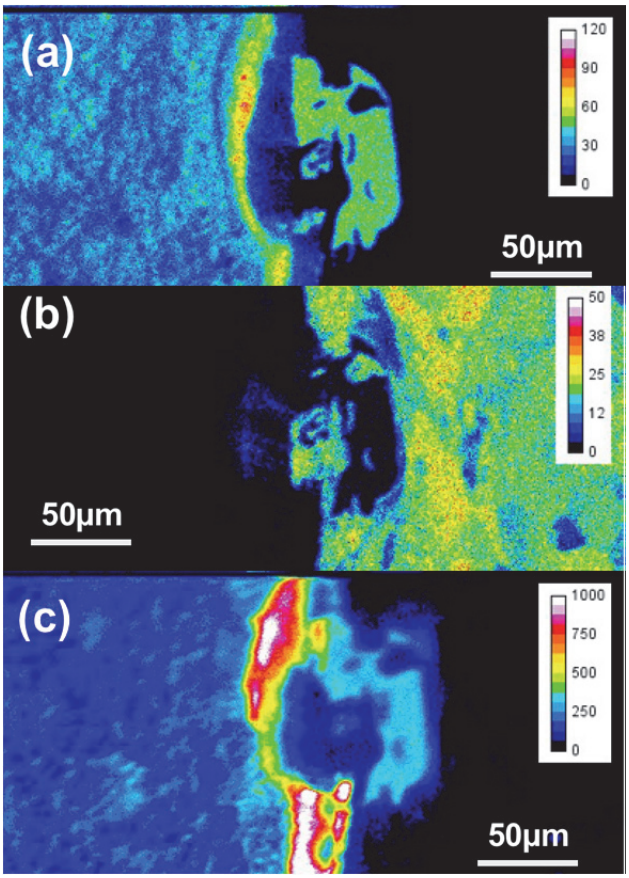

Fig. 2. Distribution of elements after gamma ray irradiation by 2D-SIMS imaging ((a) Zr, (b) Ta and (c) H).

Acknowledgements

Results from the commissioned research of the Nuclear Reguration Authrority are included in this study.

Refarence

[1] E. Fromm *et al.*, J. Less Common Met. **66,** 77-88 (1979).

1 - 45 Effects of the Inhibitors Against the Corrosion of Carbon Steel in the Diluted Seawater under Irradiation Conditions

T. Satoh, C. Kato, F. Ueno and M. Osaka

Fuels and Materials Engineering Division, NSEC, JAEA

In the Fukushima Daiichi Nuclear Power Station (1F), the seawater was injected into the reactor cores in the Unit 1, Unit 2 and Unit 3. The high dose of radiation has been continuing in the primary containment vessel (PCV) because of the molten fuel debris and the fission products. It is well known that H_2, H_2O_2, short life radicals, etc., are produced by water radiolysis [1]. The produced species are chemically active and it is considered that corrosion of the PCV is influenced by gamma-rays irradiation. The typical countermeasure against the corrosion of carbon steel (CS), which is the material of the PCV, is the injection of the corrosion inhibitors. To evaluate the availability of the corrosion inhibitors under irradiation condition, the corrosion test of the CS was performed in the diluted seawater containing corrosion inhibitors under gamma irradiation condition.

Sheet type specimens of 40 mm × 10 mm × 2 mm were machined from SGV480 (JIS G3118) for the PCV, and immersed in diluted artificial seawater (DASW), which contained 20 ppm of Cl^-, at 323 K (50 ºC). The dose rates were estimated as 4 k and 200 Gy/h, respectively. Sodium tungstate (Na_2WO_4), sodium molybdate (Na_2MoO_4), sodium nitrite ($NaNO_2$) and zinc chromate ($ZnCrO_4$) were selected as inhibitors. It was expected that the mixture of the inhibitors would be more effective than that used singly. Not only each inhibitor condition but also mixture of each inhibitor and sodium pentaborate ($Na_2B_{10}O_{16}$) was evaluated in this study to investigate the synergy effects of the inhibitors and $Na_2B_{10}O_{16}$. $Na_2B_{10}O_{16}$ is one of inhibitors investigated in the previous research [2]. The injected concentrations of inhibitors were listed in Table 1. The added concentration of $Na_2B_{10}O_{16}$ was 400 ppm as boron, in which the corrosion of CS couldn't be mitigated [2].

Table 1 Concentrations of injected inhibitors.

Inhibitor	Concentration
$NaNO_2$	400ppm
$ZnCrO_4$	50ppm
Na_2WO_4	1500ppm
Na_2MoO_4	3000ppm
Added $Na_2B_{10}O_{16}$ in the mixture conditions	400 ppm-boron

The obtained corrosion rates are shown in Fig. 1 with the corrosion rate of CS without inhibitors. The corrosion rates of CS exposed to DASW with inhibitors decreased about one order of magnitude except for Na_2MoO_4. On the other hand, the corrosion was enough mitigated in the mixture conditions of the inhibitors and $Na_2B_{10}O_{16}$. It was confirmed that the mixture of the inhibitor and $Na_2B_{10}O_{16}$ is one of effective countermeasures against the corrosion of CS under irradiation condition such as the PCV in 1F.

References

[1] Caër S. L., Water, 235-53 (2011).

[2] Sato *et al.*, Proc. 62th Zairyo to Kankyo Touron-kai, A-104, (2015) [in Japanese].

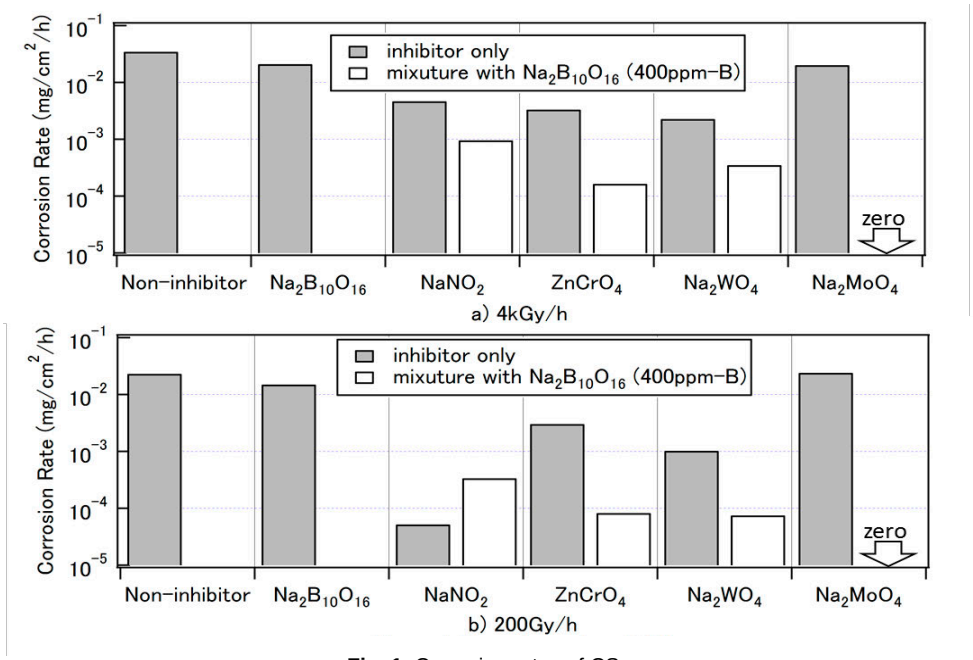

Fig. 1. Corrosion rates of CS.

1 - 46 Effect of Particle Size of the Zircaloy-4 Oxidation Product on the Hydrogen Generation in Water Radiolysis

Y. Matsumoto [a)], M. Inoue [b)], R. Nagaishi [b)], T. Suzuki [a)] and T. Ogawa [a, b)]

[a)] Nuclear System Safety Engineering, Nagaoka University of Technology,
[b)] Waste Management Division, CLADS, JAEA

After a severe accident of nuclear power plant, a debris contains various oxidation products of Zircaloy-4, used as a cladding material of nuclear fuel rod of LWR. These debris and nuclear fuel are now immersed in cooling water.

Under ionizing radiation fields, water is decomposed by the radiation to produce a volatile molecular product of hydrogen (H_2). When oxidation products such as ZrO_2 or UO_2 are present in water, the H_2 generation is well-known to be enhanced [1]. We have been investigated the enhancement by the oxidation products of Zircaloy-4 in water. In our previous study, the enhancements were observed with some kinds of the oxidation products [2, 3]. However, the enhancements are not understood while it seemed to depend on specific surface area or particle size because the oxidation products were prepared as various sized particles in previous study.

In this study, we prepared five different sized particles of the oxidation product of Zircaloy-4. We investigated the enhancement of H_2 generation by these particles.

Zircaloy-4 was heated in dry air at 1,100 ºC for 4 hours. After heated, we pulverized the oxidation product using an agate mortar and then the pulverized particles classified by stainless sieves. We measured the median diameter of particles through a wet method by using a laser scattering particle size distribution analyzer (HORIBA Ltd. LA-960). We also analyzed the phase composition of the oxidation product by using XRD.

Pure water and the oxidation product were put into a glass vial to prepare a constant 10 wt.% sample. The height of sample in the vial was set to be 1 cm. Co-60 gamma-ray irradiation to the prepared samples was carried out at QST Takasaki. The dosimetry was conducted by a chemical dosimeter of aqueous solution. After the irradiation, we measured H_2 gas concentration in the headspace of vial by using gas chromatograph. The observed yield of H_2, $G(H_2)$ (mol/J), was estimated from the generated H_2 amount, P (mol/g) and the absorbed dose of sample, D (J/g).

We obtained the 5 kinds of classified particles whose median diameters were 473, 245, 134, 63, 3 μm respectively (Fig. 1). The oxidation product was analyzed to be composed of monoclinic ZrO_2 (98 wt.%), tetragonal ZrO_2 (1 wt.%) and ZrN (1 wt.%).

Figure 2 shows the relationship between the $G(H_2)$ and the median particle diameter of the oxidation product. The $G(H_2)$ in the case of pure water only was 1.5×10^{-8} (mol/J) for comparison in this study. The H_2 generation by water radiolysis were enhanced by the particles. As the median diameter decreased, the $G(H_2)$ increased. Especially, the $G(H_2)$ was strongly increased for the particle with median diameter less than 100 μm.

According to our previous study, the oxidation products of Zircaloy-4 in dry air at high temperature possess small specific surface area [2, 3]. This means these oxidation products are almost non-porous. From these facts and results, it is considered that main factor of the increase of $G(H_2)$ with decreasing the median particle diameter of oxidation product of Zircaloy-4 is increase of total surface area of the particles in the 10 wt.% sample.

References

[1] N. G. Petrik *et al.*, J. Phys. Chem. B, **105**, 5935-44 (2001).
[2] Y. Matsumoto, T. M. D. Do, M. Inoue, R. Nagaishi, T. Ogawa, J. Nucl. Sci. Tech., **52**, 1303-07 (2015).
[3] Y. Matsumoto, T. M. D. Do, M. Inoue, R. Nagaishi, T. Ogawa, JAEA Takasaki Annu. Rep. 2014, JAEA-Review 2015-022, 166 (2016).

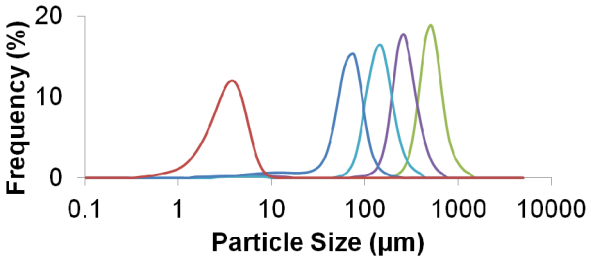

Fig. 1. Particle size distributions of 5 kinds of particles of the oxidation product.

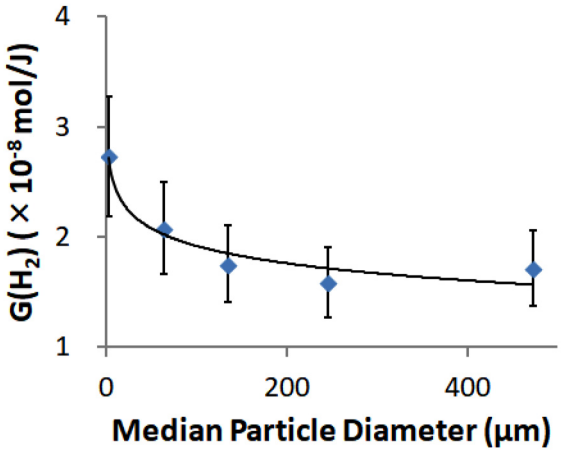

Fig. 2. Observed $G(H_2)$ vs. median particle diameter of the oxidation product.

1 - 47 Rust and Corrosion Mechanism of Carbon Steel in Dilute Chloride Solution at Low Dose Rates

T. Motooka [a, b)]

[a)] Fuels and Materials Engineering Division, NSEC, JAEA,
[b)] Waste Management Division, CLADS, JAEA

1. Introduction

Previous corrosion test of carbon steel in dilute artificial seawater under Co-60 γ-ray irradiation has indicated that corrosion rate was enhanced at absorbed dose rates: > 100 Gy/h [1] and rust color was changed from black to dark brown. In the pesent study, the corrosion mechanism of carbon steel under Co-60 γ-ray irradiation was investigated by identification of rust.

2. Experimental

Test specimen was cut out from carbon steel plate of SS400. The test solution is a diluted artificial seawater (concentration of Cl^- is 100 ppm). Hereafter called 1/200ASW. At room temperature (15 - 23 ºC), test specimen in a glass bottle filled with 1/200ASW was irradiated with γ-rays of Co-60 external radiation source for 160 h. Corrosion rates were calculated from weight loss measurements. After the irradiation, rust was identified by Raman spectroscopy and X-ray diffraction (XRD) methods.

3. Results and Discussion

3.1 Corrosion Rate

Figure 1 shows the relationship between corrosion rate and absorbed dose rates ranging from 50 to 500 Gy/h. Corrosion rate increased with increase of the dose rate. Remarkable increase was observed over 80 Gy/h. Corrosion rate exceeded 0.15 mm/y at 300 Gy/h.

3.2 Rust Analysis

Rust color on test specimen was changed with and without irradiation. Rust color was changed from black to dark brown. The rusts formed at dose rates of 0 - 550 Gy/h were analyzed by Raman spectroscopy and XRD. As shown in Fig. 2, Raman spectra of rusts brushed away from test specimen surface. Some peaks Iron oxide (Fe(II) and/or Fe(III) oxides) were observed without irradiation. Hematite (α-Fe_2O_3) peak is at 230, 295 and 410 cm^{-1}, FeOOH peak is at 255 and 720 cm^{-1} and Fe_2O_3 peak is at 670 cm^{-1}. At higher dose rates, only hematite (Fe(III) oxide) peaks was observed. Irradiation enhanced oxidation of dissolved iron ions during corrosion.

3.3 Corrosion mechanism

H_2O_2 which is one of radiolysis product can oxide iron ions. Including above the rust analysis, corrosion mechanism was considered as following reactions. Here, the symbol " ⟿ " indicates radiolysis.

Radiolysis of water:

H_2O ⟿ H_2O_2, e_{aq}^-, $^{\bullet}H$, H_2 etc.

Rust formation by radiation:

Fe ⟿ Fe_3O_4 ⟿ Fe_2O_3

Rust formation roots without irradiation:

$Fe \rightarrow Fe(OH)^+ \rightarrow Fe(OH)_2^+ \rightleftarrows$ γ-FeOOH $\rightarrow Fe_3O_4$, α-Fe_2O_3

$Fe \rightarrow Fe(OH)^+ \rightarrow [Fe_a^{2+}Fe_b^{3+}O_x(OH)_z]^{(2a+3b-2x-y)+} \rightarrow Fe_3O_4$

4. Conclusion

Co-60 γ-rays enhanced oxidation of iron ion from Fe(II) ion to Fe(III) ion. Rust formed under the irradiation had a higher oxidation state.

References

[1] T. Motooka, Proc. JSCE Mater. Environ. 2015, JSCE, A-307 (2015).
[2] http://www.fis.unipr.it/phevix/ramandb.php.

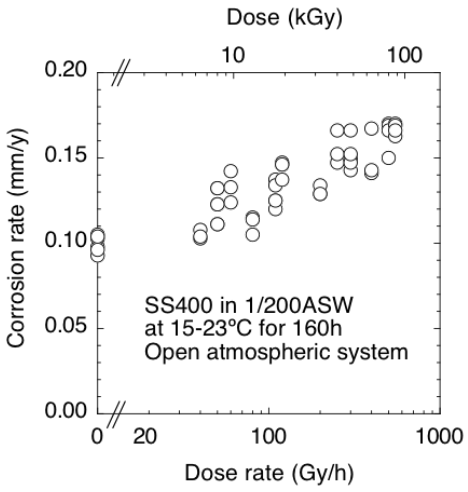

Fig. 1. Corrosion rate of carbon steel under γ-ray irradiations.

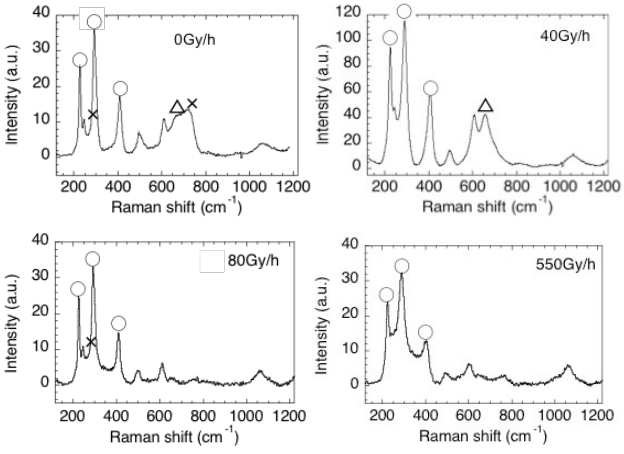

Fig. 2. Raman spectra of rust formed on carbon steel under γ-ray irradiation. ○ : α-Fe_2O_3 : 230, 295, 410 cm^{-1}, × : FeOOH : 255, 720 cm^{-1}, △ : Fe_3O_4 : 670 cm^{-1}.

1 - 48 Gamma Radiolysis of an Extractant for Minor Actinides, HONTA, in Dodecane Diluent

T. Toigawa, H. Suzuki, Y. Ban, S. Ishii and T. Matsumura

Nuclear Chemistry Division, NSEC, JAEA

Separation of minor actinide (MA) elements from high level liquid waste is one of the most important technical issues for the nuclear industry. Solvent extraction and extraction chromatography are promising methods for MA extraction [1]. Each method needs ligands for the selective extraction of MA. It is preferable for the extractant to have adequate radiation stability, because the MAs act as alpha or gamma emitters. To evaluate the radiation stability, it is essential to elucidate radiation effects on liquid-liquid or solid-liquid interfacial reaction. This study focuses on a potential MA extractant *N*,*N*,*N*',*N*',*N*'',*N*''-hexaoctyl-nitrilotriacetamide (HONTA) [2]. To evaluate the radiolytic stability of HONTA, its degradation yield and radiolytic products were investigated.

The radiation stability of HONTA was tested by using gamma-rays emitted from ^{60}Co at National Institutes for Quantum Radiological Science and Technology (QST, Japan). Samples were solution of HONTA in *n*-dodecane, and irradiated at 4 different dose rates for 16 h. Water equivalent absorbed doses of the samples were obtained to be 13.9, 29.7, 76.7, and 159 kGy. The irradiated samples were analyzed by gas chromatography using Shimadzu GCMS QP2010 equipped with a column of HP-1 (Agilent). Degradation products of HONTA were identified and concentrations of HONTA and of the degradation products were determined.

Absorbed dose dependence of the concentration of HONTA is shown in Fig. 1. The concentration of HONTA decreased with increasing absorbed dose. The obtained data were fitted by an exponential decay curve, in accordance with a previous study by Mincher and Curry [3]. The decay constant, so-called dose constant, was determined to be 2.8×10^{-6} Gy^{-1}. Also, the G-value for the degradation of HONTA was 0.37 μmol/J. These values were comparable or lower than those of other candidate MA extractants such as *N*,*N*,*N*',*N*'-tetraoctyl-diglycolamide (TODGA) [4] and octyl-phenyl-*N*,*N*'-diisobutyl-carbamoylmethylphosphine oxide (CMPO) [5]. However, the results also show an initial degradation of HONTA at a remarkable yield. The concentration of HONTA decreased by 24% at the absorbed dose of 13.9 kGy.

The main degradation products of HONTA were assigned to dioctylamine (DOA), dioctylformamide (DOFA), and dioctylacetamide (DOAA) based on both the retention times and the mass spectra. The assignment of these products indicates that DOA, DOFA, and DOAA were generated from ruptures of an amide bond, a carbon-carbon bond adjacent to the amide bond, and a carbon-amine bond of HONTA, respectively. The measured concentrations of these products are shown in Fig. 2 as a function of absorbed dose. The concentrations of DOA and DOAA increased with increasing absorbed dose. On the other hand, the concentration of DOFA rapidly increased at the beginning of the irradiation and thereafter no appreciable increase was observed. These results indicate that the initial decrease of HONTA corresponds to the generation of DOFA, while the following exponential decay of HONTA primarily generates DOA or DOAA. These findings suggest that the radiolysis of HONTA was ruled by different mechanisms depending on the absorbed dose.

References

[1] International Atomic Energy Agency, IAEA-TECDOC-1648 (2010).
[2] Y. Sasaki *et al.*, Chem. Lett., **42**, 91-92 (2013).
[3] B. J. Mincher and R. D. Curry, Appl. Radiat. Isot., **52**, 189-93 (2003).
[4] Y. Sugo *et al.*, Radiat. Phys. Chem., **76**, 794-800 (2007).
[5] S. P. Mezyk *et al.*, J. Radioanal. Nucl. Chem., **296**, 711-15 (2013).

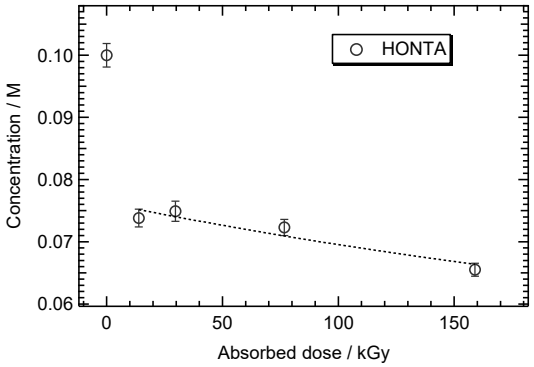

Fig. 1. Absorbed dose dependence of concentration of HONTA.

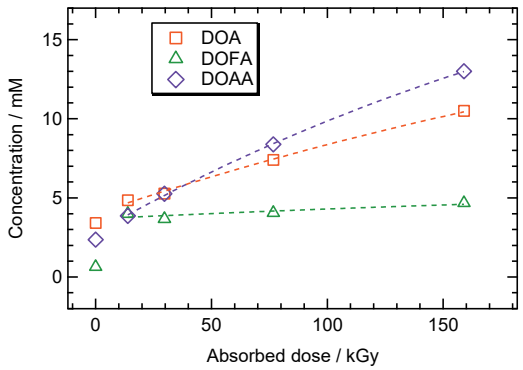

Fig. 2. Absorbed dose dependence of concentration of DOA, DOFA, and DOAA.

1 - 49 Radiation-induced Crosslinking of Polyamide11 in Presence of Triallylisocyanurate

N. Nagasawa [a)], T. Tago [b)], H. Kudo [b)] and M. Taguchi [a)]

[a)] Department of Advanced Functional Materials Research, TARRI, QST,
[b)] Graduate School of Engineering, The University of Tokyo

Bioplastic has become one of the most attractive materials in research on global environment protection because it can replace petrochemical plastics. Polyamide11 (PA11) derived from castor beans oil is a popular bioplastic, because of its advantageous properties such as superior thermal and chemical resistances, good flexibility, and good impact resistance. Hence, it is used in a large range of industrial fields such as injection molding, heavy duty automotive parts, cooling fans, wire connecters, and brake fluid reservoirs. However, in order to use PA11 in the field of aerospace, dimensional stability of electrical cable sheathing and hydraulic hoses at more melting point of PA11 (about 200 °C) is required for use. In this study, to improve the above-mentioned property of PA11, we investigated radiation-crosslinking with triallyl isocyanurate (TAIC) by electron beam (EB)-irradiation [1].

PA11 (trade name: Rilsan® B) and TAIC were provided by Arkema, Co. Ltd, France and Nippon Kasei Chemical Co., Ltd, Japan, respectively. PA11 and TAIC were mixed in a laboplastomill with a mixing speed of 20 rpm at 210 ºC for 10 min after preheating at 210 ºC for 5 min. The mixed sample was pre-pressed in a hot press at 210 ºC for 5 min and then pressed for another 5 min at a pressure of 14.7 MPa to form a sheet (150 mm × 150 mm, 1 mm thickness). The sample was then quenched by a cooling press for 5 min under the same pressure. For comparison, a neat PA11 film was prepared using the same procedure. The TAIC contents are expressed as a ratio of the mass of TAIC to the mass of the polymer. The PA11 films were irradiated by the EB released from an accelerator with the energy of 2 MeV and a beam current of 2 mA.

The gel content of the crosslinked samples was estimated by weighing the insoluble part of the crosslinked PA11 films after immersion in 98% formic acid and chloroform solution (50/50 v/v%) for 48 h at room temperature. The gels were formed for the irradiated pure PA11 film in vacuum, and gel fraction increased with the increasing dose. The gel fractions were about 9.7% at the irradiation dose of 200 kGy, and saturated to 76.2% at higher 750 kGy, although no gelation was observed at 190 kGy. Furthermore, for the PA11/TAIC film, the gel content increased significantly when the dose was lower than 200 kGy as shown in Fig. 1. The gel fraction of the PA11 /TAIC films, represented by the crosslinking density, increased with the increases in the TAIC content and the radiation dose. The gel fractions of PA11 mixed with 3 and 5 phr TAIC showed a similar dose dependence to that with 1 phr TAIC.

The thermal stability of the irradiated PA11 film without and with 3 phr TAIC was evaluated by measuring the deformation (elongation) of the sample using a thermal mechanical analyzer. The irradiated PA11 films with 3 phr TAIC at 10 - 200 kGy were found to be more stable at higher about 185 ºC (melting temperature) as shown in Fig. 2. The enhancement in the thermal stability is attributed to the higher crosslinking density. This could be also due to the presence of a cyclic unit of TAIC, which contributes to the thermal stability of the material.

The crosslinked PA11 film has many advantages such as high heat resistance as demonstrated above. It can be concluded that radiation-induced crosslinking is beneficial for expanding the applications of PA11.

Reference

[1] N. Nagasawa *et al.*, Polym. Degrad. Stab., **136**, 98-102 (2017).

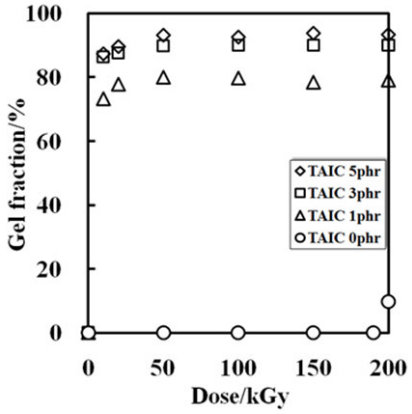

Fig. 1 Gel fraction of crosslinked PA11 in presence of TAIC after electron beam irradiation.

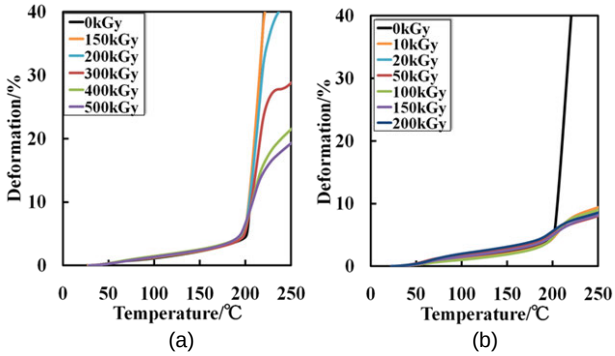

Fig. 2 Thermal mechanical analysis curves of EB-induced-crosslinked PA11 film (a) without and (b) with 3 phr TAIC.

1 - 50 Biodiesel Fuel Production from Mixed Oil Consisting of Triglyceride/Free Fatty Acid Using Radiation-grafted Fibrous Catalysts

Y. Ueki, S. Saiki, H. Hoshina and N. Seko

Department of Advanced Functional Materials Research, TARRI, QST

Waste cooking oils to be raw materials of a biodiesel fuel (BDF) contain two kinds of oil components such as triglycerides (TGs) and free fatty acids (FFAs). In our previous research, we developed two kinds of grafted fibrous catalyst for BDF production: one is an anionic grafted catalyst for transesterification of TGs and the other is a cationic grafted catalyst for esterification of FFAs [1 - 3]. The objective of this study is to decide the optimal procedure of the BDF production from mixed oil consisting of TGs and FFAs, by using the grafted catalysts.

The reaction solution was composed of 0.9 g of TGs, 0.3 g of FFAs, 9.2 g of ethanol and 5.0 g of *n*-decane, and 0.3 g each of anionic and cationic grafted catalysts was used, respectively. The all molar quantities of TGs, FFAs, OH^- of anionic grafted catalyst and H^+ of cationic grafted catalyst in this reaction system were fixed at 1 mmol. The BDF production was carried out at 70 ºC.

When the anionic grafted catalyst was used as the primary catalyst for BDF production from a mixed oil, the transesterification of TGs was stopped in just 30 minutes before reaching complete conversion of TGs, although a part of the TGs was converted into BDF. Over 80% of the initial TGs still remained. The reason for this incomplete transesterification of TGs that the anionic grafted catalyst not only functioned as a catalyst for TGs but also functioned as an adsorbent for FFAs. In this case, the electrostatically immobilized OH^- on the graft chain were reacted with FFAs (RCOOH), and then the OH^- were consumed in the production of water, as shown in the following equation:

$$RCOOH + S^+(OH^-) \rightarrow S^+(RCOO^-) + H_2O$$

where S is the grafted polymer. The FFAs-adsorbed anionic grafted catalyst was inactivated, because of consumption of OH^-. Additionally, as a result of trying BDF production from mixed oil by using together with anionic and cationic grafted catalysts, the TGs and the FFAs were incompletely converted into BDF. The reason for this incomplete conversion was as follows: the FFAs esterification speed using the cationic grafted catalyst was very slow, and, on the other hand, the FFAs adsorption speed to the anionic grafted catalyst was very fast. Consequently, the FFAs adsorption onto anionic grafted catalyst was preferentially progressed as compared with the FFAs esterification, even though the cationic grafted catalyst was present in the reaction solution.

So next, we attempted to produce BDF from mixed oil by sequentially using the cationic and anionic grafted catalysts, in the same manner as the conventional homogeneous catalyst method. As shown in Fig. 1 (A), when the cationic grafted catalyst was used as the primary catalyst, the FFAs was completely converted into BDF for about 15 hours, and the unreacted TGs remained as it is in the reaction solution. After reaching complete esterification of FFAs, the cationic grafted catalyst in the reaction solution was replaced with the anionic grafted catalyst functioned as the secondary catalyst. In the subsequent transesterification, the all remaining TGs was completely converted into BDF by the anionic grafted catalyst, without remaining any kind of oil components, as shown in Fig. 1 (B). Based on above results, it was found that the optimal procedure of the BDF production from mixed oil containing TGs and FFAs using the grafted catalysts was the sequential catalytic treatment using cationic and anionic grafted catalysts.

References

[1] Y. Ueki *et al*., Int. J. Org. Chem., **1**, 24-29 (2011).
[2] Y. Ueki *et al*., Int. J. Org. Chem., **4**, 91-105 (2014).
[3] Y. Ueki *et al*., QST Takasaki Annu. Rep. 2015, **QST-M-2**, 99 (2017).

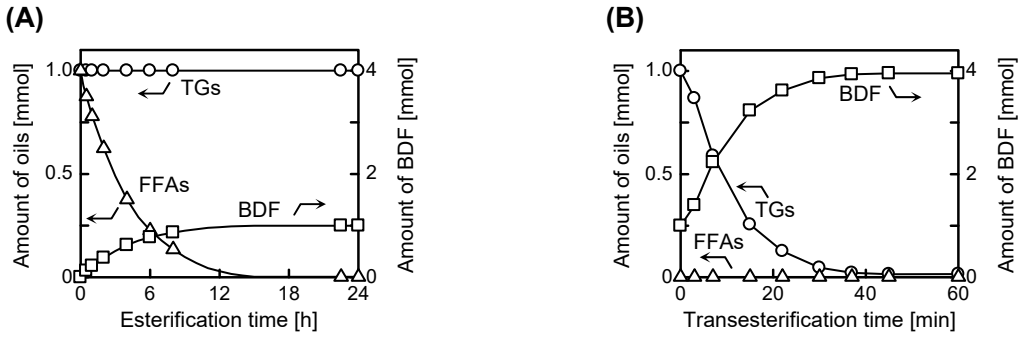

Fig. 1. BDF production from mixed oil through sequential (A) esterification using cationic grafted catalyst and (B) transesterification using anionic grafted catalyst. ○: TGs, △: FFAs, □: BDF.

1 - 51 Development of Novel Mass Production Method of Fibrous Grafted Adsorbent

H. Hoshina [a)], N. Kasai [a)], T. Shibata [b)], J. Chen [a)], Y. Ueki [a)], S. Saiki [a)], N. Hayashi [c)] and N. Seko [a)]

[a)] Department of Advanced Functional Materials Research, TARRI, QST,
[b)] Sector of Fukushima Research and Development, JAEA,
[c)] Graduate School of Science and Technology, Gunma University

An adsorbent synthesized by radiation induced graft polymerization using non-woven fabric as a trunk material can effectively remove and recover metals with low concentration from water media [1]. In order to put the adsorbent into practical use, it is necessary to establish a mass production method of the adsorbent [2]. A continuous pre-irradiation grafting system was invented to synthesize non-woven fabric grafted adsorbent in quantities efficiently (Fig. 1). The system was consisted of a carrier device, a low energy accelerator and a grafting reaction tank. By adapting this system, it is possible to carry out an irradiation process and a polymerization process continuously under nitrogen atmosphere. In this study, the mass production method of adsorbent was investigated by using the continuous pre-irradiation grafting system.

A roll nonwoven fabric of width 30 cm was set to the carrier device, which was deliver to the low energy accelerator at a speed of 100 m/s and was irradiated at absorbed dose of 200 kGy. The irradiated fabric was soaked into a deaerated glycidyl methacrylate (GMA) solution containing tween20 as a surfactant in the grafting reaction tank. The concentration of GMA and tween20 in the monomer solution was 10% and 1%, respectively. The reaction temperature was maintained in the reaction tank at 40 ºC. The rolled fabric in the reaction tank was rotated in the GMA solution for 5 minutes. To evaluate the distribution of the degree of grafting (Dg), nonwoven fabric pieces cut into 3 cm × 8 cm were affixed to a long nonwoven fabric at intervals of 2.5 meters. The Dg was determined by the following equation:

$$Dg\ [\%] = 100[(W_1 - W_0)/W_0]$$

where W_0 and W_1 were the weights of nonwoven fabric pieces before and after grafting, respectively. After grafting, the residual GMA and homopolymer were removed by washing with purified water and methanol.

The distribution of the Dg in a grafted long nonwoven fabric was shown in Fig. 2. Although various kinds of functional groups could be introduced into the GMA grafted fabric by chemical modification easily, more than 100% of Dg was required to show enough performance as an adsorbent. The grafted nonwoven fabric had the highest Dg of 179% at around 15 meters, and the minimum Dg was 124% at 0 meter. The Dg of all sampled nonwoven fabric pieces were higher than 100%, that was satisfied the requirement for the practical use. These results established that the GMA grafted nonwoven fabric could be produced efficiently in large-scale through the use of continuous pre-irradiation grafting system.

References

[1] T. Shibata *et al.*, Radiat. Phys. Chem., **119**, 247-52 (2016).
[2] H. Hoshina *et al.*, Radiat. Phys. Chem., **81**, 1033-35 (2012).

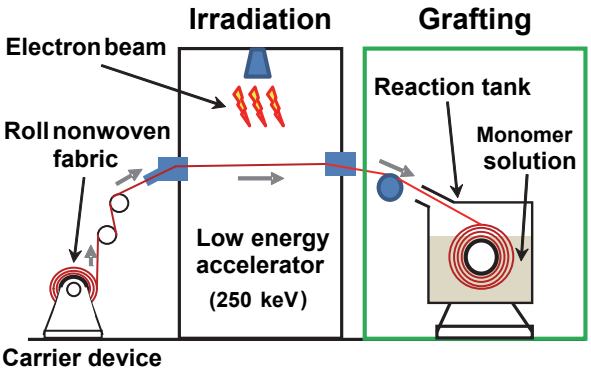

Fig. 1. Mass production of non-woven fibrous grafted adsorbent using continuous pre-irradiation grafting system.

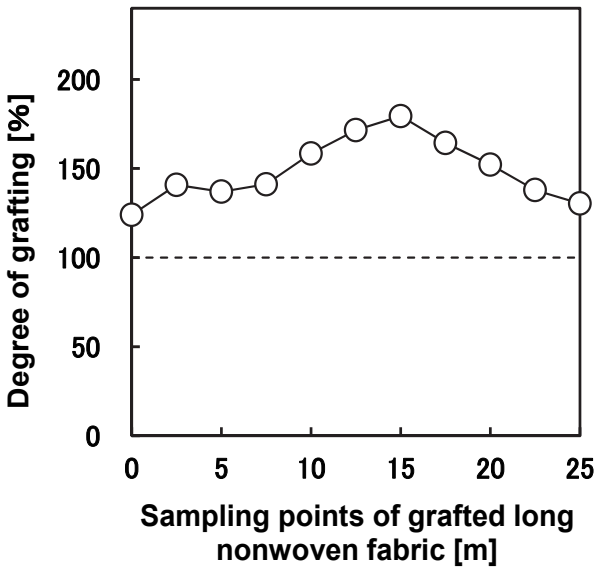

Fig. 2. The distribution of the Dg in a grafted long nonwoven fabric synthesized using continuous pre-irradiation grafting system.

1 - 52 Surface Modification of PA66 by Radiation Grafting

T. Makabe [a)], H. Saito [a)], H. Sando [a)], N. Mizote [a)], Y. Ueki [b)] and N. Seko [b)]

[a)] Mitsuba R&D Center, Mitsuba Corporation,
[b)] Department of Advanced Functional Materials Research, TARRI, QST

Butyl Methacrylate, which was a lipophilic monomer, was grafted on a surface of polyamide 66 (PA66) substrate by pre-irradiation grafting technique using a low-energy electron beam accelerator. The lipophilicity of the surface-modified PA66 substrate increased with increasing grafting time. The surface-modified PA66 substrate after 0.5 h of grafting exhibited a smaller contact angle with respect to olefin oil than the un-modified PA66 substrate. The surface roughness of the surface-modified PA66 substrate increased compared to the un-modified PA66 substrate. Consequently, it was found that the optimal grafting time for a PA66 substrate was 0.5 h.

我々はこれまでに放射線グラフト重合法を用いて、樹脂の表面改質に関する研究に取り組み、親油性を付与した表面改質樹脂の開発に成功した[1]。本研究では、摺動用樹脂材の油潤滑性の向上を狙いとして、電子線グラフト重合により樹脂表面に親油性モノマーをグラフトし、その反応時間と表面状態の関係を調査した。

樹脂基材として、ポリアミド 66（PA66）シートを用いた。無酸素条件下において、PA66 シートに低エネルギー電子加速器を用いて電子線を照射した（加速電圧: 250 kV, 電流: 2.3 mA, 吸収線量: 200 kGy）。その後、電子線照射した PA66 シートを親油性モノマーであるメタクリル酸ブチルを含むモノマー溶液と接触させることにより、エマルショングラフト重合を実施した。その際、モノマー溶液の組成比は、モノマー5 wt.%、水 94.5 wt.%、界面活性剤（Tween20）0.5 wt.%とし、反応温度は 40 °C とした。また、グラフト重合反応時間は、最大 12 時間とした。これらの調製したサンプルを用いて、FT-IR 測定、オレフィン油に対する接触角測定、共焦点顕微鏡による表面粗さ（Sa）の測定を行った。

Figure 1 に未処理および表面改質 PA66 シートの FT-IR スペクトルを示す。FT-IR は、ゲルマニウムプリズムを用いた ATR 法にて測定した。表面改質 PA66 シートには、1,730 cm^{-1} にメタクリル酸ブチルに由来するカルボニルのピークが認められた。この結果により、グラフト重合反応によりメタクリル酸ブチルを PA66 シート表面に導入可能であることがわかった。また、反応時間の増加に伴い、カルボニルのピークが増加していることからも、グラフト重合反応時間の増加によりグラフト重合が進行することがわかった。

Figure 2 はグラフト重合反応時間が及ぼす表面改質 PA66 シートの接触角および Sa の関係を示したものである。表面改質 PA66 シートの接触角は、0.5 時間の反応時間において低下するものの、1 時間以上の反応時間では、あまり大きな変化はない傾向を示した。また、表面粗さは、反応時間の増加に伴い増加した。この表面粗さの増加は、反応時間の増加に伴いメタクリル酸ブチルモノマー間の反応が進行し、ホモポリマーが発生し、それらのホモポリマーが樹脂表面へ付着したことによるものと考えられる。

以上の結果から、PA66 シートへの表面改質手法としては、表面粗さの影響が少ない短時間でのグラフト重合が有効であり、モノマーとしてメタクリル酸ブチルを用いることにより PA66 シート表面に親油性を付与することが可能であることがわかった。

今後、表面粗さ変化が少ないグラフト重合条件である反応時間 0.5 時間で親油性を付与した PA66 シートにて摩擦係数を測定し、摺動用樹脂材としての有効性を確認する。

Reference

[1] T. Makabe *et al.*, QST Takasaki Annu. Rep. 2015, **QST-M-2**, 102 (2017).

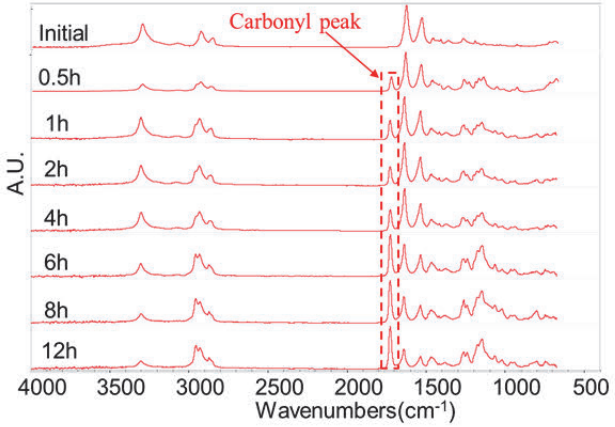

Fig. 1. FT-IR spectra of surface-modified PA66 substrate in the different reaction times.

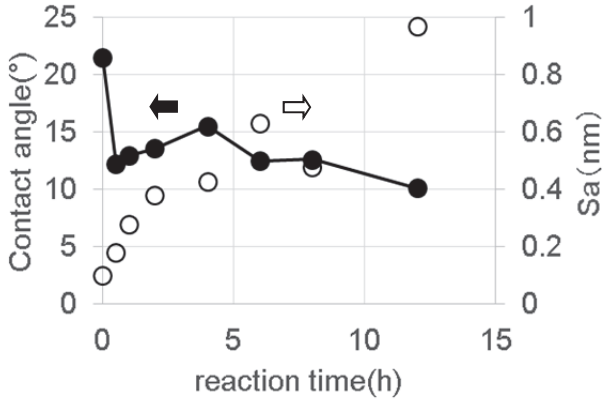

Fig. 2. Variation in contact angle and surface roughness with reaction time.

1 - 53 Development of Radiation-grafted Fibrous Adsorbent for Trivalent and Hexavalent Chromium Removal

N. Hayashi [a)], Y. Ueki [b)], J. Chen [b)] and N. Seko [b)]

[a)] Education Program of Materials and Bioscience,
Graduate School of Science and Technology, Gunma University,
[b)] Department of Advanced Functional Materials Research, TARRI, QST

Chromium is an excellent metal used for plating, alloy, and leather tanning. Its toxicity depends on an ion valence, however, hexavalent chromium (Cr(VI)) may cause lung cancer in people for having strong oxidation power [1]. In order to treat the wastewater containing toxic Cr(VI), a coagulation sedimentation method is normally applied [2]. However, this method needs complicated processes and generates a large amount of watery sludge. In addition, there are concerns about soil and groundwater contamination at industrial waste final disposal sites. Therefore, development of a new environmentally friendly treatment method is required.

Radiation-induced graft polymerization (RIGP) is a unique technique for functionalizing of conventional polymer with various forms maintaining polymer's original properties [3]. In this paper, two types of adsorbent for trivalent chromium (Cr(III)) and Cr(VI) separation were synthesized by RIGP, and the adsorption behavior was researched.

In order to prepare adsorbents, polyethylene nonwoven fabric (NF) was irradiated by electron beam under a nitrogen atmosphere at a dry ice temperature. The total dose was 100 kGy for preparing amide-type adsorbent. Irradiated NF was put into a glass ampoule and contacted with the deoxidized monomer solution (acrylonitrile / methacrylic acid / dimethyl sulfoxide) under vacuum condition. Graft copolymerization was done at 40 ºC in water bath. After grafting, the grafted fabric was immersed in the 3 wt.% hydroxylammonium solution at 80 ºC.

To synthesize amine-type adsorbent, NF was irradiated by the same way. The total dose was 50 kGy. Monomer emulsion, which was composed of 3 wt.% 4-chloro-methylstyrene (CMS), 0.3 wt.% Tween20 and 96.7 wt.% purified water, was prepared by homogenizing mixture, and removed dissolved oxygen by supplying nitrogen gas into the CMS emulsion. RIGP was carried out by immersing the irradiated NF into CMS emulsion at 40 ºC. After RIGP, the grafted NF was dried under reduced pressure. The degree of grafting (Dg) was defined as rate of increase weight of NF before and after grafting reaction. Grafted NF for amine-type adsorbent was contacted with 0.25 M trimethylamine ethanol solution at 60 ºC. The Dg of amide-type and amine-type were 110% and 169%, respectively. The ligand density of amide-type was 4.2 mmol/g-adsorbent, and that of amine-type was 3.6 mmol/g-adsorbent.

Adsorption performances of amide-type and amine-type adsorbents depending on the pH were examined. The adsorbent (20 mg) was put into bottle filled with 45 mL solution containing chromium ions of 100 ppb. As a result, the highest distribution coefficient (a value of dividing the amount of metal trapped in the adsorbent by the amount of metal remaining in the solution) of amide-type and amine-type were 9.3×10^3 for Cr(III) and 7.5×10^5 for Cr(VI) at pH 5, respectively.

To evaluate the adsorption capacities of two adsorbents, column mode adsorption tests were carried out with 7 mm inner diameter of the column. Total volume of packed adsorbent in the column was adjusted to 0.1 cm^3. The test solution was adjusted to chromium concentration 10 ppm at pH 5, and flowed into the column at 600 h^{-1} of space velocity. The results were shown in Fig. 1 as breakthrough curves. The breakthrough curve means the relation of bed volume (BV) and leaking ratio (C/C_0) where C_0 and C mean chromium ion concentration before and after passing the column. Amide-type adsorbent had high affinity for Cr(III) and amine-type adsorbent had a high affinity and capacity for Cr(VI) at pH 5. Adsorption capacity at breakthrough point were 25 g-(Cr(III))/kg-(amide-type adsorbent) and 120 g-Cr(VI)/kg-(amine-type adsorbent).

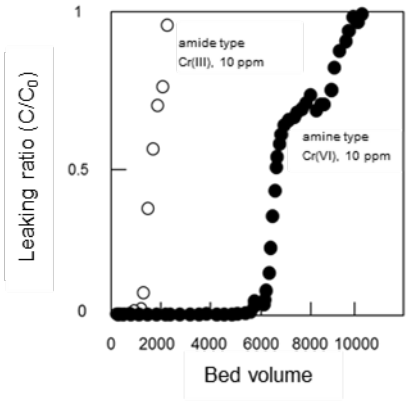

Fig. 1. Breakthrough curves of Cr(III) adsorption onto amide-type adsorbent and Cr(VI) adsorption onto amine-type adsorbent.

References

[1] H. Horiguchi, "Pollution and Poison/Dangerous Materials Inorganic", SANKYO SHUPPAN Co., Ltd., 378-82 (1971).
[2] T. Kanchi, Hiroshima Prefectural Western Ind. Tech. Cent. Res. Rep., **54**, 49-52 (2011).
[3] N. H. Mohamed *et al.*, Radiat. Phys. Chem., **82**, 63-68 (2013).

1 - 54 Polymerization in ETFE films and in Chloromethylstyrene Solution under Gamma Ray Simultaneous Irradiation

J. Chen and N. Seko

Department of Advanced Functional Materials Research, TARRI, QST

To suppress homopolymerization in the monomer solution and to precisely control the grafting process as much as possible, we tried to introduce reversible addition fragmentation chain transfer (RAFT) polymerization into the simultaneous irradiation grafting system. For this purpose, a RAFT agent, 2-cyano-2-propyl benzodithioate (CPB), was added to the simultaneous irradiation grafting systems, where the ethylene-tetrafluoroethylene copolymer (ETFE) film was completely immersed in the chloromethylstyrene (CMS) monomer solution for γ-ray irradiation under nitrogen gas environment at room temperature. The grafted ETFE films were treated in xylene at 120 ºC for more than 44 h. The extracted materials from the grafted materials and the homopolymer in the monomer solution were analyzed using GPC and NMR instruments.

Figure 1 shows the GPC and NMR results of the extracted materials obtained from the samples with a degree of grafting of 67.6%. The NMR results indicated that only the poly(CMS) were detached from the grafted ETFE films and dissolved in the xylene solvent during the immersion. The GPC curves for the samples at 44, 92 and 132 h immersion times were very similar to each other, indicating that the detached poly(CMS) was stable in hot xylene and did not deteriorate during immersion.

The degree of grafting and homopolymerization increased with increasing irradiation dose, and decreased with increasing the concentration of RAFT agent. The number average molecular weight (Mn) and polymer dispersity index (PDI) of the poly(CMS) extracted from the grafted films and homopolymerized in the solution were shown in Table 1, where the grafting was carried out with a total dose in the range of 16 - 88 kGy, and the dose rate was fixed at 1.0 kGy/h. The mole ratio of RAFT agent to CMS monomer was 1/72. The extracted poly(CMS) from grafted films showed a narrow Mn range of 7,700 - 9,400 and a PDI quite higher than 1.0, indicating that the conventional radical polymerization still plays an important role in the interior of the ETFE films. On the contrary, the Mn of the homopolymer in the solution increased with increase in irradiation dose, and the PDI was very close to 1.0, showed a typical RAFT polymerization in the monomer solution.

Furthermore, although the poly(CMS)s in the interior of ETFE films and in solution graft were polymerized in the same reactor, the Mn of the poly(CMS) in the ETFE films was quite higher than that in the solution. As shown in Table 1, the Mn of the poly(CMS) in the ETFE films was higher than 7,700, while that in the solution was less than 2,200. The former was more than three times higher than the latter. Therefore, the polymerizations in the monomer solution and in the ETFE films were different from each other. In the monomer solution, the growing chains were easily terminated by the surrounding molecules or other radicals. In the ETFE films, the propagating radicals were fixed in the crystalline micro-particles, and were relatively stable.

In conclusion, by addition of RAFT agent, the grafting and homopolymerization were considerably suppressed, and the RAFT polymerization in the ETFE films and in monomer solution occurred more dominantly. The molecular weight of the poly(CMS) polymerized in the films was several times higher than that polymerized in the solution.

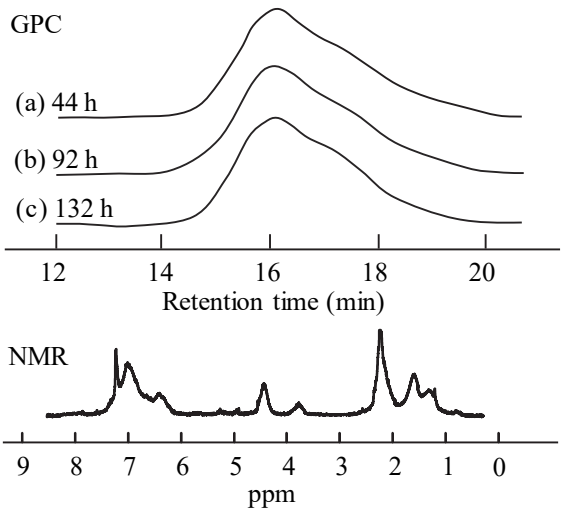

Fig. 1. GPC and NMR results of the dissolved materials in the xylene solution in which the ETFE-g-poly(CMS) film was immersed.

Table 1
Mn and PDI of the poly(CMS) in the interior of ETFE films and in monomer solution.

Dose	In ETFE films		In solution	
(kGy)	Mn	PDI	Mn	PDI
16	9400	2.1	760	1.1
30	8600	1.8	1200	1.1
50	7700	1.6	1400	1.2
66	7800	1.7	1600	1.3
88	7700	1.5	2200	1.3

Part II

2. Life Science

2 - 01 Target Irradiation of Individual Cells Using Focusing Heavy-ion Microbeam of QST-Takasaki (VII): Utilization of Polypropylene Film Dish for Analyzing Heavy-ion Hit Effect of Irradiated Cells

T. Funayama and S. Tabei

Department of Radiation-Applied Biology Research, TARRI, QST

Heavy-ion have been utilized for various application such as ion beam breeding and heavy-ion cancer therapy. However a mechanism underlying its specific biological effect has not well been analyzed. To examine single hit effect of heavy-ion is important to elucidate cellular response of heavy-ion radiation. Therefore, we have developed heavy-ion microbeam system in QST-Takasaki, and established a method for target-irradiating individual cells with defined number of heavy-ions [1].

To examine a biological effect of irradiated cells, the cells must be observed in duration of post irradiation incubation. However, our current preparation of cell sample is specialized for observing radiation effects of immediate after irradiation, therefore, we need to develop new cell preparation that enables long-term post incubation of irradiated cells. As microbeam irradiation of defined number of ions requires thin target, we adopted a polypropylene film of 3 μm thick as an attaching surface for the cells. In this study, we examined a cell growth of irradiated cells on polypropylene film for validating a possibility for analyzing the radiation effect of the cells.

A polypropylene film dish for testing cell growth ability was constructed by adhering film to a ring-shaped acrylic frame. The dishes were well washed and sterilized with 70% ethanol. To examine an effect of hydrophilicity of cell attaching surface, vacuum plasma treatment that improve hydrophilicity of polypropylene film was carried out to. To examine cell growth ability, HeLa cells were irradiated with gamma-ray, inoculated in cell dish, and the number of grown cells were counted in every 24 hours up to 3 days. As a control, commercial cell dish with / without tissue culture treatment was also examined.

As shown in Fig. 1, cellular growth became different with different types of cell dish. Growth on polypropylene film dish became lower than that on commercial dishes, however, a treatment with vacuum plasma improved restricted growth in some extent. This might be caused by an improved hydrophilicity of the film. Growth curves of irradiated cells showed almost similar trend with non-irradiated cells (Fig. 2). However, irradiated cells could not grow at all in polypropylene film dish without plasma treatment (Fig. 2c). Therefore, to utilize polypropylene film as a cell attachment surface for microbeam irradiation, improvement of hydrophilicity by vacuum plasma treatment will be necessary.

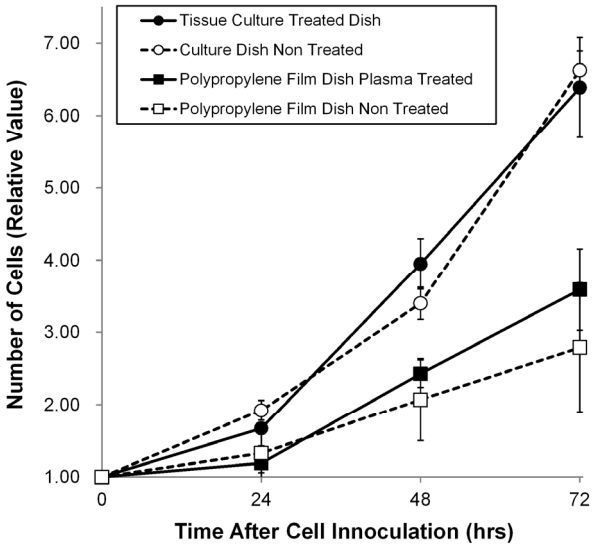

Fig. 1. Comparison of cell growth of non-irradiated cell in different types of cell dish. A vacuum plasma treatment of polypropylene film increased growth of cell on hydrophobic surface.

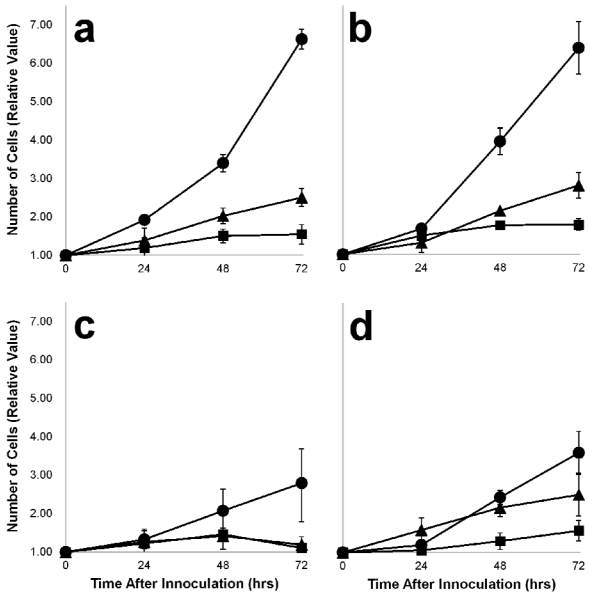

Fig. 2. Growth curve of gamma-ray irradiated HeLa cell in different culture dish. a. tissue culture treated dish, b. culture dish non-treated, c. polypropylene film dish non-treated, d. polypropylene film dish plasma treated. The cells were irradiated with gamma-ray of 0 Gy (circle), 4 Gy (triangle), 8 Gy (square), thereafter the growth curve of the cell were measured.

Reference

[1] T. Funayama *et al.*, J. Radiat. Res. **49**, 71-82 (2008).

2 - 02 Apoptosis Was Markedly Induced in Human Neural Stem Cells but not in Glioblastoma Cells after Gamma-ray and Carbon-ion Irradiation

Y. Yokota [a)], Y. Wada [b)] and T. Funayama [a)]

[a)] Department of Radiation-Applied Biology Research, TARRI, QST,
[b)] Graduate School of Medicine, Gunma University

Human neural stem cells (NSCs) have been reported to proliferate and differentiate into neurons and glial cells not only in fetal but also in adulthood brain. Survivors of cranial irradiation for primary or metastatic malignant brain tumors often suffer from long-term side effects such as mental retardation and reduced lerning ability. This is because NSCs are severely damaged and neurogenesis is inhibited after radiotherapy. Radiation protection of NSCs during cranial irradiation is thus needed to keep the quality of life in patients. Increasing bodies of evidence have been shown that human NSCs are quite sensitive to X-ray and gamma-ray irradiation [1]. However, there is a limited piece of knowledge on biological responses of NSCs after heavy-ion irradiation [2]. We reported last year that human NSCs were more sensitive to heavy-ion irradiation than glioblastoma cells, and, that interphase death was related to growth inhibition after irradiation in NSCs but not in glioblastoma cells [3]. This year we report frequent apotpsis induction in NSCs after carbon-ion irradiation.

NSCs derived from human H9 embryonic stem cells and A-172 cells derived from human glioblastoma were irradiated with gamma-rays (^{60}Co, LET = 0.2 keV/μm) at the Cobalt 60 Irradiation Facilities and with carbon-ion beam ($^{12}C^{5+}$, 18.3 MeV/n, LET = 108 keV/μm) at the HY1 port of TIARA. After irradiation, cells were cultured for 72 h, and then, stained with annexin V, that specifically binds with apoptotic cells, to detect apoptosis induction. The percentages of apoptotic cells were measured by flow cytometry.

Figure 1 shows representative results of the flow cytometry 72 h after irradiation. Annexin-V positive cells markedly increased in NSCs but not in A-172 cells after carbon-ion irradiation of 2 Gy. Figure 2 shows dose responses of the apoptosis induction rates 72 h after irradiation. The percentages of apoptotic cells increased after gamma-ray and carbon-ion irradiation in both of NSCs and A-172 cells. However, the percentages of apoptotic calls were higher in NSCs than in A-172 cells. Our results suggest that frequent apoptosis induction in human NSCs is related to their high radiosensitivity as found in our previous report [3]. Inhibition of apoptosis induction may alleviate damage of NSCs and long-term side effects after cranial irradiation. Now we are investigating bromodeoxyuridine incorporation and cell cycle distribution to elucidate the mechanisms underlying different radiosensitivities between NSCs and glioblastoma cells.

References

[1] V. N. Ivanov *et al.*, Apoptosis, **19**, 399 (2014).
[2] M. Isono *et al.*, J. Radiat. Res. **56**, 856 (2015).
[3] Y. Yokota *et al.*, QST Takasaki Annu. Rep. 2015, **QST-M-2**, 110 (2017).

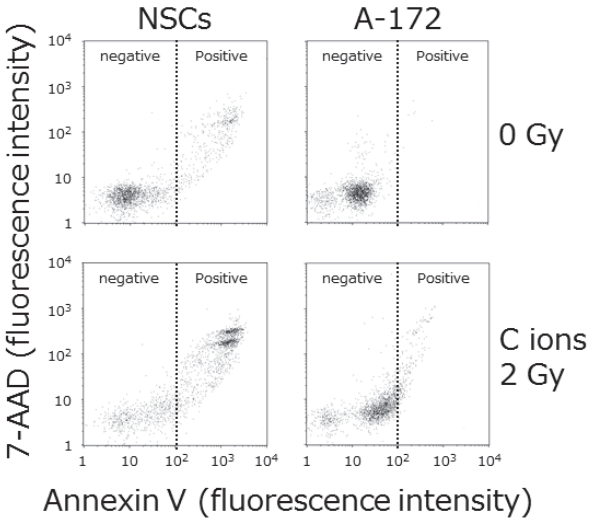

Fig. 1. Representative results of the flow cytometry 72 h after irradiation. Annexin-V positive cells markedly increased in NSCs (left lower) but not in A-172 cells (right lower) after carbon-ion irradiation of 2 Gy.

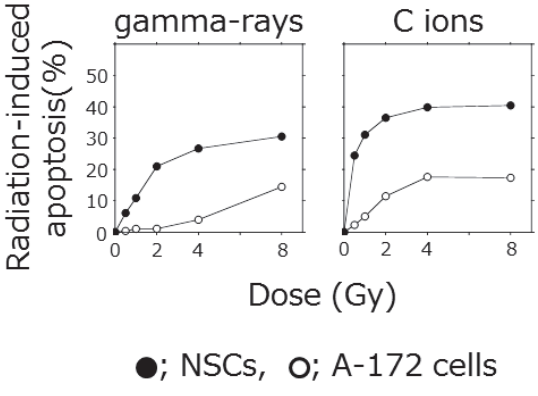

Fig. 2. Dose responses of the apoptosis induction rates 72 h after irradiation. NSCs (closed circle) and A-172 cells (open circle) were irradiated with 0 to 8 Gy of gamma-rays (left) or carbon ions (right). Data are the mean of 3 or more independent beam times. The percentages of radiation-induced apoptosis were much more in NSCs than in A-172 cells.

2 - 03 Epigenetic Modifier as a Potential Radiosensitizer for Heavy-ion Therapy on Malignancy (V)

K. Saito [a, b, c], T. Funayama [b, c], Y. Yokota [b], Y. Kobayashi [b, c] and T. Murakami [a]

[a] Faculty of Pharmacy, Takasaki University of Health and Welfare,
[b] Department of Radiation-Applied Biology Research, TARRI, QST,
[c] Graduate School of Medicine, Gunma University

Refractory tumors accumulate epigenetic abnormalities, which often cause the resistance to various therapeutic options. While the high linear energy transfer (LET) heavy-ion radiation provides more pronounced therapeutic effects than the low-LET radiation (*e.g.*, γ-ray), it is necessary to develop promising sensitizers for the enhanced radiation therapy. Herein we demonstrate that the use of histone deacetylase inhibitors (HDACi) could sensitize refractory tumor cells well for the heavy-ion therapy.

B16F10 murine melanoma cells were treated with several HDACis and followed by irradiations. The clonogenic survival assay [1, 2], annexin-V staining [3], cell cycle analysis [3], Western blotting [4] and immunofluorescence microscopy observation were performed. Results showed that some HDACis significantly enhanced antitumor effects in heavy-ion irradiated cells [5]. In combination with irradiation, those HDACis abrogated the G2/M arrest and increased much early apoptotic events, leading to the decreased clonogenicity. Moreover, these radiosensitizing effects of HDACi were much higher in heavy-ion irradiated cells but lower phosphorylation of H2AX, a marker for DNA damage, than in γ-ray irradiated cells. Foci size of γH2AX in γ-ray irradiated cells became bigger by pretreatment with HDACis, although foci size of γH2AX in heavy-ion irradiated cells was almost unchanged by pretreatment with HDACis (Fig. 1).

Thus, we propose that the pretreatment of HDACi may provide clinical efficacy to refractory cancer patients in combination with heavy-ion therapy.

Materials and methods

Cells and cell culture, Radiation exposure

See our previous description [1].

Treatment

Cells in exponential growth were seeded at a density 1×10^5 cells per 35 mm culture dish 20 - 24 h before irradiation. Cells were treated with investigational or comparator HDACi for 16 h and then irradiated. The concentration of HDACi was selected that required to reduce colony formation by 10% alone and the irradiation dose was selected D_{10}.

Immunofluorescence Microscopy Observation

After HDACi and radiation exposure, the cells were incubated for 0.75 h. Cells were fixed with 4% paraformaldehyde in PBS for 15 min and permeabilized with methanol for overnight at -20 ºC. Primary antibodies of γH2AX (Millipore; 1 : 100) and 53BP1 (Millipore; 1 : 100) were diluted in PBS/1% bovine serum albumin (BSA) and 5% goat serum and applied for an hour at room temperature. After removal of the primary antibodies and washing, samples were incubated for 45 min with the secondary antibodies (anti-mouse IgG goat pAB Alexa 488 (Molecular Probes; 1 : 200) and anti-rabbit IgG goat pAB Alexa 568 (Molecular Probes; 1 : 200)) in PBS/1% BSA and 5% goat serum, and washed three times with PBS. Coverslips were then mounted in ProLong Diamond Antifade Mountant with DAPI (Thermo Fisher Scientific Inc, US). The immunostained samples were imaged using fluorescence microscope.

References

[1] K. Saito *et al.*, JAEA Takasaki Annu. Rep. 2012, JAEA-Review 2013-059, 80 (2014).
[2] K. Saito *et al.*, JAEA Takasaki Annu. Rep. 2013, JAEA-Review 2014-050, 83 (2015).
[3] K. Saito *et al.*, JAEA Takasaki Annu. Rep. 2014, JAEA-Review 2015-022, 75 (2016).
[4] K. Saito *et al.*, QST Takasaki Annu. Rep. 2015, **QST-M-2**, 115 (2017).
[5] K. Saito *et al.*, Biol. Pharm. Bull. **40**, 844-51 (2017).

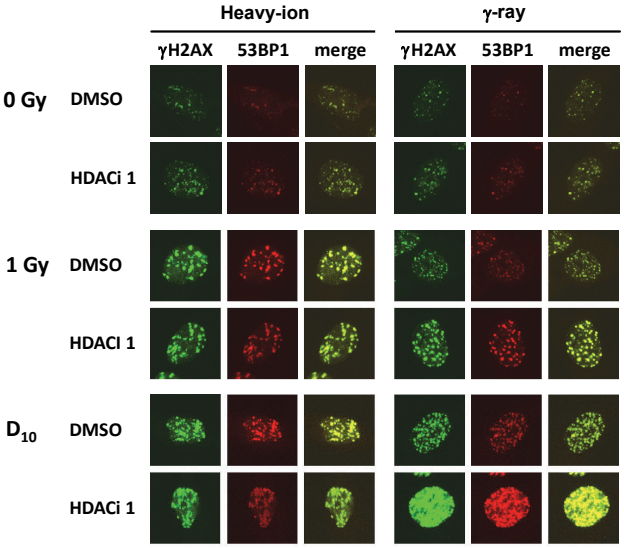

Fig. 1. Immunofluorescence microscopy of γH2AX and 53BP1.

2 - 04 Analysis of Biological Effect on the 3D Cultured Tissue Induced by Heavy-ion Microbeam Irradiation

M. Tomita [a)], H. Matsumoto [b)], K. Otsuka [a)], Y. Yokota [c)], M. Suzuki [c)], Y. Kobayashi [c)] and T. Funayama [c)]

[a)] Radiation Safety Research Center, Central Research Institute of Electric Power Industry,
[b)] Faculty of Medical Sciences, University of Fukui,
[c)] Department of Radiation-Applied Biology Research, TARRI, QST

A radiation-induced bystander response is generally known as a cellular response induced in non-irradiated cells by receiving bystander signaling factors released from directly irradiated cells within a tissue [1]. The heterogeneity of the absorbed dose within the irradiated tissue is more relevant for high-LET heavy ions than for low-LET photons. Therefore, directly irradiated and non-irradiated cells are co-existing within the tissue exposed to the low fluence of high-LET heavy ions. In this study, we aim to clarify a role of bystander response to sustain the homeostasis of tissue irradiated with high-LET heavy ions. We have established a method of irradiating a 3D cultured human epidermis with microbeams and of measuring the viable cell rates.

Figure 1 shows highly differentiated human epidermis model, the LabCyte EPI-MODEL24 (Japan Tissue Engineering CO., Ltd., Aichi, Japan), and the epidermal cells cultured for 3 days using the EPI-KIT. Human epidermal cells cultured for 3 days consisted of basal and spinous layers. The 3D cultured tissues were irradiated with 1 - 10 Gy of 260 MeV $^{20}Ne^{7+}$ broadbeams or 15 particles of 260 MeV $^{20}Ne^{7+}$ microbeams at 61 points (100 μm interval) in a straight line.

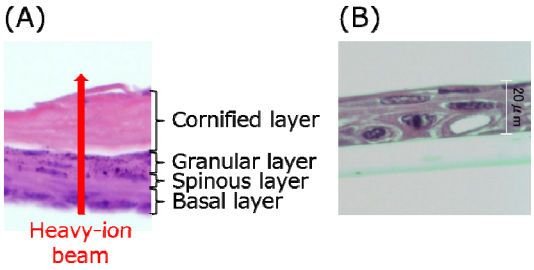

Fig. 1. Hematoxylin and eosin (HE) stained human epidermis model. (A) LabCyte EPI-MODEL24. (B) Human epidermal cells cultured for 3 days using the EPI-KIT.

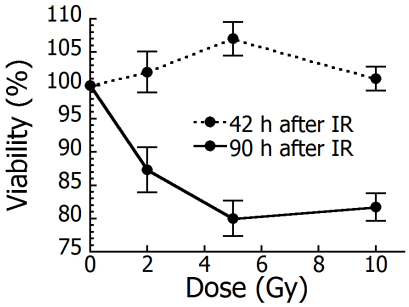

Fig. 2. Dose response of cell viability of the LabCyte EPI-MODEL24 after Ne-ion broadbeam irradiation.

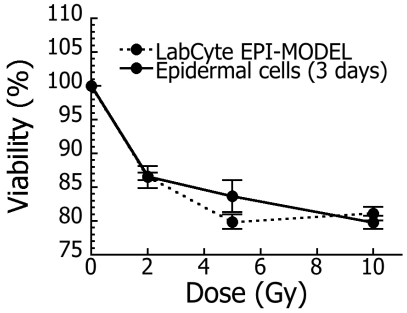

Fig. 3. Dose response of cell viability of the 3D cultured tissues 90 h after Ne-ion broadbeam irradiation.

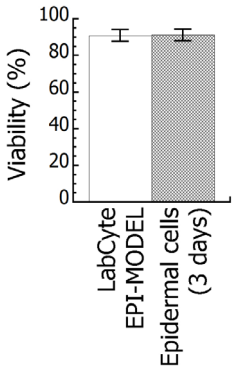

Fig. 4. Ratio of viable cells of the 3D cultured tissues 90 h after Ne-ion microbeam irradiation.

Figure 2 shows the dose response of cell viability of the LabCyte EPI-MODEL24 irradiated with Ne-ion broadbeams. Cell viability was assessed by an MTT assay. The viability was not changed 42 h after irradiation, whereas it decreased significantly 90 h.

Next, the cell viability of the highly differentiated and differentiating epidermis was measured 90 h after broadbeam irradiation. Figure 3 shows the progress of results reflecting new data. The dose response of viability of the epidermal cells cultured for 3 days was similar to that of the LabCyte EPI-MODEL24. Figure 4 shows the cell viability 90 h after microbeam irradiation. The viability was approximately 90% and was not also significantly different by differentiation.

Those results suggest that the differentiative basal and spinous cells in the 3D cultured epidermis mainly respond to high-LET heavy ions and bystander signals.

Reference

[1] M. Tomita and M. Maeda, J. Radiat. Res, **56**, 205-19 (2015).

2 - 05 Bystander Mutagenic Effect via Secreted Factor(s) in Normal Human Fibroblasts Induced by Heavy ions

M. Suzuki [a)], T. Funayama [b)], Y. Yokota [b)], M. Suzuki [b)] and Y. Kobayashi [b)]

[a)] Department of Basic Medical Sciences for Radiation Damages, NIRS, QST,
[b)] Department of Radiation-Applied Biology Research, TARRI, QST

We reported the secreted-factor induced bystander lethal effect using C-, Ne- and Ar-ion microbeams [1, 2]. Our data clearly showed that the bystander lethal effects were induced by the different mechanisms between C- and Ar-ion-irradiated cells. It was dominant via the gap-junction mediated cell-cell communication by C ions and was dominant via the secreted factor, which was scavenged by ascorbic acid, to culture medium from the irradiated cells by Ar ions. This year we focused on the time course of bystander mutagenic effect via gap-junction mediated cell-cell communication in normal human fibroblasts irradiated with C-, Ne-, and Ar-ion microbeams.

Normal human skin fibroblasts were obtained from Riken Bio Resource (Cell No. RCB0222). Approximately 6×10^5 exponentially growing cells were inoculated into each microbeam dish 2 days before irradiation. Half of the sample dishes were treated with a specific inhibitor of gap-junction mediated cell-cell communication (40 μM of γ-isomer of hexachloro-cyclohexane) from 3 h before irradiation to the defined times of post-irradiation incubation. Irradiations were carried out using the 256 (16 × 16)-cross-stripe method described in previous report [3] using C ions ($^{12}C^{5+}$, 220 MeV), Ne ions ($^{20}Ne^{7+}$, 260 MeV) and Ar ions ($^{40}Ar^{13+}$, 460 MeV) at the HZ1 port in the TIARA. The beam size of each ion microbeam was 20 μm in diameter and the irradiations in each point were performed to deliver 8 ions for carbon, 2 ions for neon and single ion for argon, respectively. The values of linear energy transfer (LET) at the sample position were estimated to be 103 keV/μm for C ions, 380 keV/μm for Ne ions and 1,260 keV/μm for Ar ions. After irradiations, sample dishes were incubated for the each defined time of 0.5 h, 3 h and 24 h in a CO_2 incubator at 37 ºC, and then assayed gene mutation at *HPRT* (Hypoxanthine-guanine phosphoribosyltransferase) locus mapped on the X chromosome, which was detected by the incidence of 6-thioguanine resistant clones.

Figure 1 shows the results of the time course of mutation frequencies. The mutation frequency in cells irradiated with carbon-ion microbeams (IR) is 8 - 6 times higher than those of unirradiated control at 0.5 h and 3 h, but no mutation is observed in cells treated with the gap-junction inhibitor (L+IR). The frequencies, however, are 4 times higher at 24 h and are almost the same between IR and L+IR. On the other hand, no differences among control, IR and L+IR are observed in cells irradiated with Ne- and Ar-ion microbeams at 0.5 h and 3 h, but the frequencies of IR and L+IR are 3 - 5 times higher at 24 h. In our 256-cross-stripe irradiation method, we estimate that the percent of heavy-ion direct hit cells is around 0.036% of all cells on the dish. The obtained results show a higher mutation frequency in cells irradiated with microbeams than that of expected frequency, assuming no bystander effect. The data suggest that mutation is induced in cells unirradiated with heavy ions directly by bystander effect and the pathway of the induced bystander effect by C ions at 0.5 h and 3 h is via gap-junction mediated cell-cell communication. Also, the bystander mutagenic effects by C, Ne and Ar ions at 24 h, which are independent on the presence of the gap-junction inhibitor, is via different pathway(s) of cell-cell communication.

There is clear evidence that the bystander mutagenic effects were induced with different mechanisms, depending on ion species and times after irradiation.

References

[1] M. Suzuki *et al*., JAEA Takasaki Ann. Rep. 2014, JAEA-Review 2015-022, 70 (2016).
[2] M. Suzuki *et al*., QST Takasaki Ann. Rep. 2015, **QST-M-2**, 118 (2017).
[3] M. Suzuki *et al*., JAEA Takasaki Ann. Rep. 2006, JAEA-Review 2007-060,107 (2008).

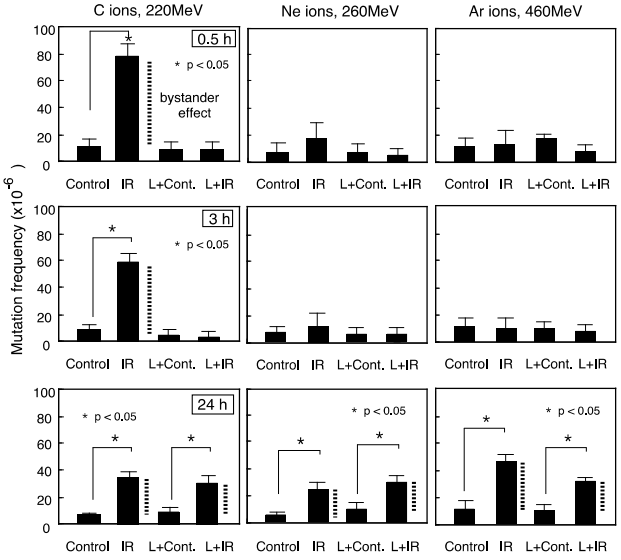

Fig. 1. The time course of mutation frequencies in cells irradiated with C-, Ne- and Ar-ion microbeams at 0.5 h, 3 h and 24 h after irradiations. The data showed the average and the standard error of 4 indipendent experiments. Control : microbeam-uniradiated samples, IR: microbeam-irradiated samples, L+Cont.: microbeam-uniradiated samples treated with the gap-junction inhibitor, L+IR: microbeam-iradiated samples treated with the gap-junction inhibitor.

2 - 06 Application of ESR Method for Frozen Raw Bovine Livers under Practical Irradiation Condition

M. Kikuchi and T. Funayama

Department of Radiation-Applied Biology Research, TARRI, QST

To prevent food-borne illness in Japan, after the outside of raw meat had been roasted and then the cooked parts were trimmed off, the steak tartare must be prepared from only the inside meat in restaurants. However, since pathogenic bacteria such as some *E. coli* were found inside raw bovine livers where any tested disinfection is not effective, the sale of raw bovine livers to eat as "liver-sashimi", as it is called "GYU-REBA-SASHI" in Japanese, has been prohibited since July 1, 2012. Providing for the radiation exposure that can be used to kill bacteria in the sealed food packages without heating, two detection methods have been developed to distinguish raw livers that have been disinfected by radiation [1, 2]. In the previous study, free radicals in the livers irradiated in chilled condition (~0 ºC) were detected using electron spin resonance spectroscopy (ESR) [2]. However, g-irradiation of the bovine livers might be carried out in frozen condition (below -15 ºC). In this study, the livers irradiated in dry-ice were investigated for the radical detection after practical preparations of ESR specimens.

Since radiation-induced radicals are highly reactive species in ambient temperature, most of them are diminished within 1 s after the irradiation. Prior to irradiation, when raw bovine livers were frozen, the radicals can be more stable in the frozen condition but there may be difficulty to cut out liver specimens for ESR measurement. Therefore, to prepare ESR specimens easily, narrow plastic straw was used. Raw bovine livers were first stuffed into the straws at the ambient temperature, then frozen and irradiated in dry-ice. After the irradiation, whole straws containing the liver were put into ESR tubes. Immediately, ESR measurements were carried out at liquid nitrogen temperature. As shown in Fig. 1 and Fig. 2, ten dose-responsible peaks were found on differential spectra. When bovine livers chilled on ice were irradiated, linear responses increasing left and right side peak intensities were observed [2]. To confirm whether similar signal responses observed in the livers that were exposed in dry-ice and stored in -80 ºC for 7 days, samplings were carried out from the thawed livers using plastic straws. The ESR spectra indicated that the dose-responsible side peaks were still observable in the livers (Fig. 3).

In conclusion, ESR can be used as the detection method of the raw bovine livers which were irradiated in the frozen condition. The ESR measurement at liquid nitrogen temperature is suitable for the screening of the irradiated bovine livers because of its quick and easy sample preparation.

References

[1] M. Kikuchi *et al.*, FOOD IRRADIATION, JAPAN, **50(1)**, 3-8 (2015).

[2] M. Kikuchi *et al.*, FOOD IRRADIATION, JAPAN, **50(1)**, 9-12 (2015).

[3] M. Kikuchi, FOOD IRRADIATION, JAPAN, **51(1)**, 3-10 (2016).

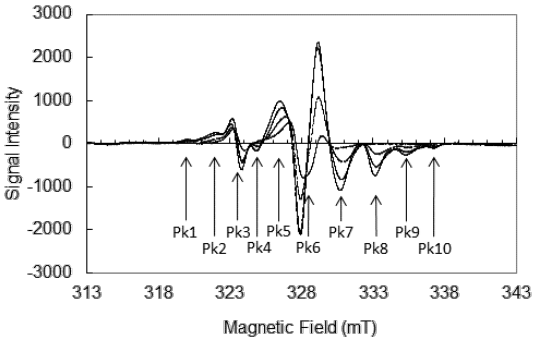

Fig. 1. ESR spectra of irradiated bovine livers obtained as differential spectra, subtracting a polypropylene straw from bovine livers within the straw at the same irradiation doses.

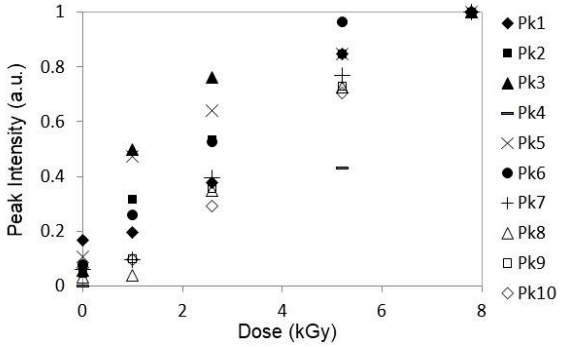

Fig. 2. Dose responses of each peak obtained from the differential spectra shown in Fig. 1.

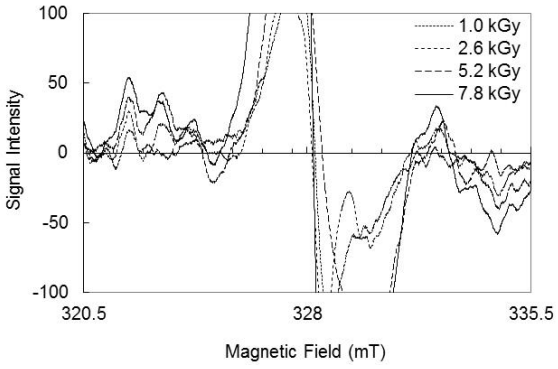

Fig. 3. ESR spectra of thawed livers obtained as differential spectra, subtracting the spectrum of non-irradiated liver from those of irradiated ones.

2 - 07 Observation of Oxidative Damage in DNA Sheet Generated Along Ion Beam Track

A. Ito [a)], F. Ouchi [a)], T. Ushiroda [a)], R. Hirayama [b)], Y. Furusawa [b)], Y. Yokota [c)] and T. Funayama [c)]

[a)] School of Engineering, Tokai University,
[b)] Department of Basic Medical Sciences for Radiation Damages, NIRS, QST,
[c)] Department of Radiation-Applied Biology Research, TARRI, QST

The track structure of heavy ions is generally recognized to consist of a core region with high ionization density and a penumbra region, where secondary electrons mainly contribute to energy deposition, with relatively low LET nature. The biological effects of heavy ions should be characterized by such a track structure of energy deposition. In our previous study, we reported significant yield of oxidative DNA base damage, 8-hydroxydeoxyguanosine (8-OHdG) produced via a reaction with OH radicals, upon irradiation of heavy ions to guanine solution by using HPLC system in coupled with an electrochemical detector [1]. We thought that 8-OHdG could be used as an indicator of the penumbra area in combination with an immuno-staining method using a fluorescence antibody against 8-OHdG. The penumbra area would be expected to extend over the size in the order of micrometer [2], which is within the spatial resolution of optical fluorescence microscope.

The observation of 8-OHdG distribution using an immuno-staining method was carried out for DNA-lipid complex sheet (abbreviated as DNA sheet) with insoluble nature in water, which has been developed by Tanaka and Okahata [3]. We made the DNA sheet on a cover glass by applying a capillary phenomenon in a very narrow gap between cover glass and Teflon® sheet to the chloroform solution of the DNA-lipid complex. In the TARRI report published last year, we described fluorescence dots by irradiating DNA sheet set vertically to ion beams, and confirmed that the dots result from ion beams [4].

In the present study, to observe DNA damage along a beam path, ion beams were irradiated to DNA sheet on a cover glass which was fixed vertically in order to set the sheet in parallel with vertical ion beam path. DNA sheet attached to a cover glass was covered with Mylar sheet to hold water on the surface of the DNA sheet.

Figure 1 shows the result for 20 MeV proton beam with an LET of 2.77 keV/mm. Left panel images demonstrated the generation of 8-OHdG along a beam path successfully. Five images were combined to keep track of a whole path. It was confirmed that the oxidative damage was produced upon high LET radiation along a beam path, providing an experimental evidence for the presence of penumbra region with low LET nature. The damage production seems to be almost continuous, but a few discontinuous regions were also noted. The width of the damage perpendicular to the beam path was estimated below 10 mm from a scale bar. The right panel shows DAPI staining images of the same sample as that of the left panel. Since DAPI is a specific staining agent of nucleic acids, the uniform staining assures that the DNA sheet is nearly uniform.

Although several ion beams in addition to proton were irradiated including C, Ne and Ar, we have not been able to observe such an image showing linearly generated damage, probably due to the very low probability to impinge on very thin film in a parallel direction. Increase of irradiation dose should be tried in future experiments.

Acknowledgement

We thank Drs. M. Mitarai and K. Iohara, Central Research Institute of Maruha Nichiro Cooperation, for their courteous supply of DNA sample.

References

[1] R. Hirayama *et al.*, Radiat. Phys. Chem. **78**, 1207-10 (2009).
[2] A. Chatterjee and H. J. Schaefer, Radiat. Environ. Biophys. **13**, 215-27 (1976).
[3] K. Tanaka and Y. Okahata, J. Am. Chem. Soc., **118**, 10679-83 (1996).
[4] A. Ito *et al.*, JAEA Takasaki Annual Rep. 2014, JAEA-Review 2015-022, 78 (2016).

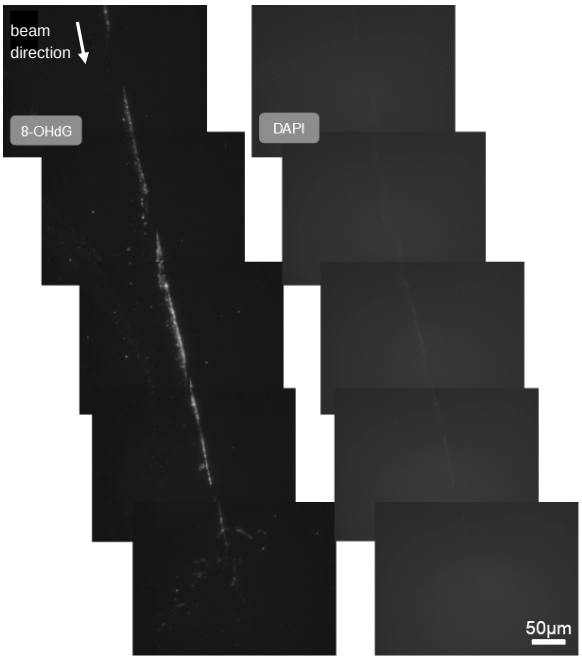

Fig. 1. Generation of 8-OHdG along proton beam path (left panel). Right panel: DAPI staining to confirm DNA uniformity.

2 - 08 Detection of Initiator Caspase, Bm Dronc Protein in the Heavy-ion Irradiated Silkworm Egg During Early Development

M. Iwamoto [a)], D. Ueda [a)], T. Funayama [b)], Y. Yokota [b)], M. Suzuki [b)], T. Sakashita [b)], Y. Kobayashi [b)] and K. Shirai [a)]

[a)] Faculty of Textile Science and Technology, Shinshu University,
[b)] Department of Radiation-Applied Biology Research, TARRI, QST

When the silkworm (*Bombyx mori*) eggs at just fertilization were irradiated with 10 Gy of carbon ions ($^{12}C^{5+}$; 220 MeV), the eggs restarted its development after about 2 hours delay. However, the eggs would have the unrepaired damages in the DNA. At 12 to 14 hours after oviposition (cellularization of the dividing nuclei), the eggs carried out the apoptotic cell death.

Inducing apoptosis in response to DNA damage is quite important to eliminate unfavorable mutations in the genome. The purposes of our studies are to make clear the molecular mechanisms that enables restart of the developments of the heavy-ion irradiated silkworm eggs without repairing the damages and that suppress the apoptotic cell death of the eggs until cellularization.

Last year, we investigated the amount of transcripts of the genes concerned with checkpoint and apoptosis induction. Then, we revealed the transcripts of all 4 apoptosis related genes were detected in the silkworm eggs. However, the amounts of the transcripts seemed to be insufficient. In comparison *Actin A3* mRNA, the levels of apoptosis related 4 genes were quite low, especially the amount of the initiator caspase, *Bm Dronc* mRNA (< 0.5%). Those results suggest one of the reasons that the heavy ion irradiated silkworm eggs at early development cannot detect apoptotic cell death.

However, the proteins (or factors) that already exist in the eggs would induce apoptotic cell death. So, we addressed the detection of Bm-Dronc protein in the silkworm eggs at early development by using anti Bm Dronc antiserum. We also investigated the activation of Bm Dronc protein in the heavy-ion irradiated eggs. The antiserum against Bm Dronc protein was kind gift from Dr. M. Ikeda (Nagoya University).

The bands of Bm Dronc were detected in the non-irradiated eggs at the early development (Fig. 1). The bands are more clearly detected at the lane of eggs than that of larval tissues (silk gland, Midgut, epidermal cells) (Data was not shown). These results indicate the silkworm egg have Bm Dronc sufficiently to induce apoptosis, although the mRNA in the egg is not abundant.

In *Drosophila*, the first 13 syncytial nuclear divisions are maternally controlled [1]. So we investigated the Bm Dronc in the eggs at just oviposited. As a result, Bm Dronc bands were revealed in the unfertilized eggs (Data was not shown). Therefore the Dronc protein in the silkworm eggs would be maternal protein.

In the cellar blastoderm stage, the nuclei of heavy-ion irradiated eggs are TUNEL positive. This indicates that the damaged nuclei are eliminated by apoptosis. Generally, caspase are activated by limited break. So we try to detect the activated fragment (active form) of Bm Dronc in the irradiated eggs at the cellular blastoderm stage (Fig. 2). But the activated fragments of Bm Dronc were not detected (arrow). The reasons that why could not detect the activated fragment were unknown. But we could not detect the fragment in the larval midgut and silk gland at metamorphosis. These tissues also indicated the apoptotic cell death.

In the studies, we detected the initiator caspase in the eggs. The suppression mechanisms of apoptosis induction are unknown. Now we consider the localization of the protein to be the clue of the question.

Reference

[1] S. Pushpavalli *et al*., BMC Molec. Biol. **14**:1 (2013).

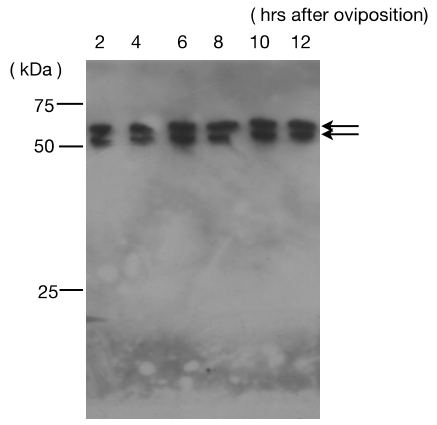

Fig. 1. Detection of Bm-Dronc protein in the non-irradiated eggs during early development. Arrows indicate Bm Dronc Proteins.

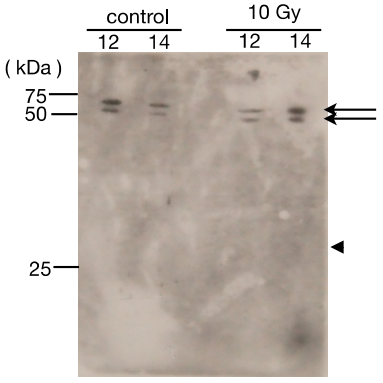

Fig. 2. Detection of the active fragments of Bm-Dronc in the heavy-ion irradiated eggs. Arrows indicate Bm Dronc proteins. Arrowhead indicates the position of active form.

2 - 09 Establishment of Irradiation Protocol of Carbon-ion Microbeam to Adult Japanese Medaka, *Oryzias latipes*

T. Asaka [a)], K. Nagata [a)], T. Yasuda [a)], K. Ohashi [a)], M. Kamahori [a)], M. Suzuki [b)], Y. Yokota [b)], H. Ikeda [b)], T. Sakashita [b)], T. Funayama [b)], Y. Kobayashi [b)], S. Oda [a)] and H. Mitani [a)]

[a)] Department of Integrated Biosciences, The University of Tokyo,
[b)] Department of Radiation-Applied Biology Research, TARRI, QST

Radiotherapy is widely used in cancer treatment. In addition to inducing effects in the irradiated area, irradiation may induce effects on neighboring cells in the tissues close to and distant from the irradiated area [1, 2]. Japanese medaka, *Oryzias latipes*, is a small teleost fish and a model organism for evaluating the radiation effects. Recently, we applied 15 Gy of low-energy carbon-ion ($^{12}C^{6+}$, 26.7 MeV/u) irradiation to adult medaka to a depth of approximately 2.2 mm from the body surface using TIARA and evaluated the histological alterations induced by irradiation through the whole body serial section [3]. In this study, we made a specific method to irradiate the kidney or testis using a shield or targeted irradiation system in TIARA and examined the effect of the irradiation on number of blood cells and tissue abnormality.

In the broadbeam experiment, 5 mm thick acrylic plate with 2 - 3 mm diameter hole was used as a shield so that the target organs; kidney or testis, was directly irradiated by carbon-ion beam (Fig. 1A). After the irradiation, the number of blood cells was counted, followed by chemical fixation with Davidson's solution, and histological analysis of tissue sections. The dorsal irradiated fish and irradiated fish with shield, which was expected to be irradiated the kidneys on both lobes showed decrease in the number of blood cell (Fig. 1B). The reduction was small in the group irradiated on one side of the kidney. In the histological analysis, nucleated blood cells were absent from the dorsal region of the kidney in the dorsal irradiated fish. These results suggested the broadbeam irradiation of carbon-ion was successful and these data reflected the precise localization of the injuries caused by carbon-beam irradiation. Especially, the irradiation caused direct damages in haematopoietic cells in the kidney, which in fish is a haematopoietic organ.

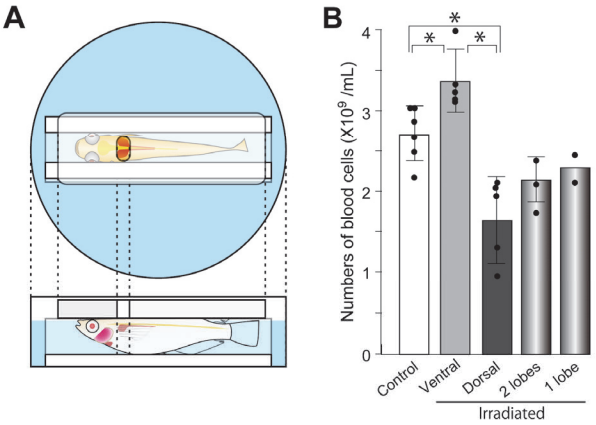

Fig. 1. Carbon ion irradiation with shield. A: Diagram of the shielded irradiation to 2 lobes of the kidney. B: Number of the blood cells 7 or 8 days after the irradiation. Asterisks indicate statistical significance ($p<0.05$).

In the microbeam experiment, we used a ø250 μm micro aperture and managed targeted carbon-ion irradiation of 15 and 2 Gy in the confined areas of the kidney and testis, respectively. The position of the kidney or testis was determined visually (Figs. 2A and B). After the irradiation, to evaluate whether the target was properly irradiated, we performed histological analyses of those tissue sections. The blood cells were reduced in the irradiated kidney and abnormal differentiation was observed in the testis in the limited area supposed to be irradiated (Figs. 2C and 2D), suggesting that the influence of irradiation was appeared around the irradiated area.

In this study, we established the targeted irradiation system using broad- and microbeam of TIARA. As the next step, we will carry out further experiment to analyze the cellular effect in the tissue by local irradiation *in vivo*.

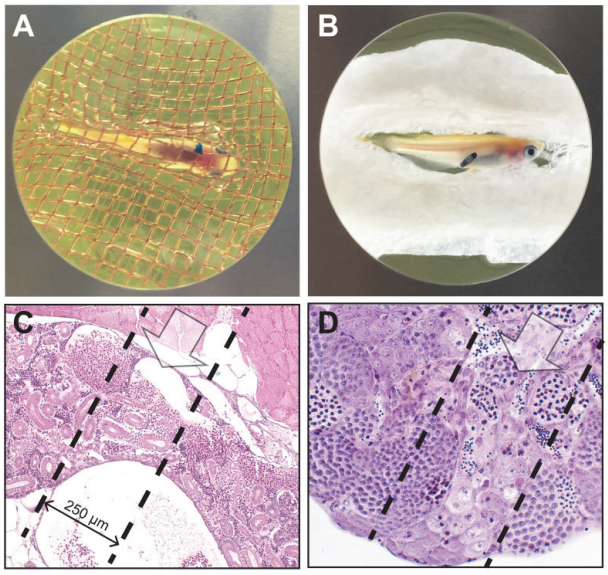

Fig. 2. Microbeam experiment. Adult medaka was mounted in a petri dish for the kidney (A) and testis (B) irradiation. Blue or black marks indicate the target organs. The limited area (between dashed lines) supposed to be irradiated in the kidney (C) and testis (D) showed specific and abnormal phenotype.

References

[1] S. C. Formenti *et al.*, Lancet. Oncol. **10**, 718 (2009).
[2] B. J. Blyth *et al.*, Radiat. Res. **176**, 139 (2011).
[3] K. Nagata *et al.*, Sci. Rep. **6**, 28691 (2016).

2 - 10 Screening of Rice Mutants to Sophisticate Ion-beam Breeding Technology for Next Generation Agriculture

Y. Oono [a)], Y. Hase [a)], S. Nozawa [a)], K. Satoh [a)] and H. Kato [b)]

[a)] Department of Radiation-Applied Biology Research, TARRI, QST,
[b)] Radiation Breeding Division, Institute of Crop Science,
National Agriculture and Food Research Organization (NARO)

We have been conducting a research for “Technologies for creating next-generation agriculture, forestry and fisheries” in the Strategic Innovation Promotion Program (SIP) led by the Cabinet Office. Our role in this program is to gnerate rice mutants with valuable phenotype by ion beams, identify causal genes of the mutants, and provide target DNA sequences for genome editing to agricultual scientific community. Another purpose of our work is to understand property of ion-beam-induced mutations in genomic level. Genomic DNA of ion-beam-induced mutants will be subjected to next generation sequencing (NGS) and characteristics of induced mutations such as number of mutations, type of substitutions, and frequency and size of deletions or insertions will be investigated. The results will be compared with the data obtained in other research institutes having radiation facilities [RIKEN Nishina Center, Radiation Breeding Division of The National Agriculture and Food Research Organization (RBD, NARO), and The Wakasa Wan Energy Research Center] to find out differences and similalities of mutagenic effects among different radiation sources.

A rice cultiver Nipponbare whose whole genome sequence has been available in public is used in this work. As reported previously, we had grown approximetry 2,000 M2 lines generated from the seeds irradiated with 40 Gy of carbon ions (surface LET = 76 keV/μm) and succesfully identifed several mutant candidates in a green house at TARRI, QST [1].

We also cultivated M2 lines in a paddy field of RBD, NARO (Hitachiomiya, Ibaraki, Japan), selected mutant candidates such as early heading date and dwarf mutants, and harvested their M3 seeds (Fig. 1). Then, the M3 lines were grown in the same paddy field. Among them, the mutant phenotype of early heading date was comfirmed in 4 lines (Table 1). Furhermore, all panicles of approximately 1,830 M2 plants grown in the paddy field were individually collected and high-yield mutant candidates were screened by weighing the batch of panicles of each plant (Fig. 2).

NGS analyses such as exome and whole genome sequencing for these confirmed mutants as well as mutant candiates are in progress and property of mutation induced by ion beams will be characterized. Meanwhile, several mutant candidates were crossed with Nipponbare (wild type) to generate F2 lines for investigating genetic link between mutatant phenotype and mutations in the mutant genome. This would help idetification of causal genes of the mutants.

This work was supported by Cabinet Office, Government of Japan, Cross-ministerial Strategic Innovation Promotion Program (SIP), “Technologies for creating next-generation agriculture, forestry and fisheries” (funding agency: Bio-oriented Technology Research Advancement Institution, NARO).

Reference

[1] Y. Oono *et al.*, QST Takasaki Ann. Rep. 2015, **QST-M-2**, 127 (2017).

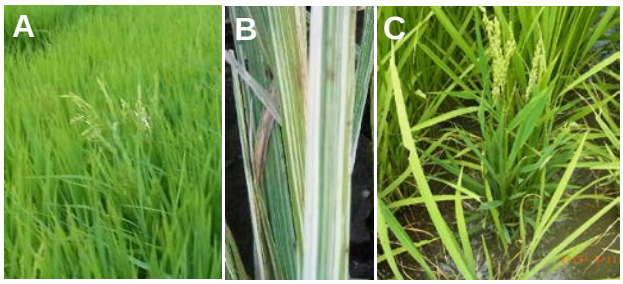

Fig. 1. Mutant candidates of early heading date (A), stripe leaves (B), and dwarf (C) obtained in the paddy field.

Table 1
Comparison of 4 early-heading-date mutants with Nipponbare control.

Line	Heading date*	Days earlier than control	Additional phenotype
Nipponbare	Aug. 14	-	
786-5	Jul. 28	17	wide leaves
IRB3484-9	Jul. 28	17	semi dwarf
IRB3517-3	Aug. 3	11	
IRB3528-4	Aug. 8	6	

* Heading date was recorded in the paddy field in 2016.

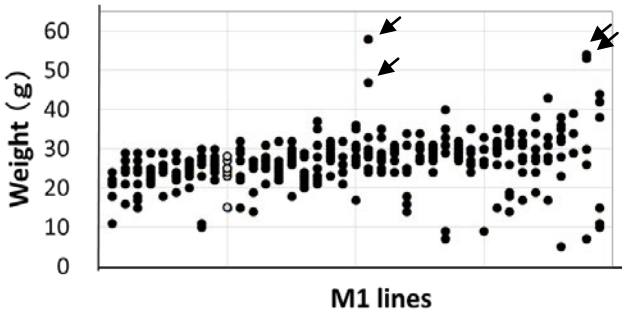

Fig. 2. Screening of high-yield mutant candidates. Batches of all panicles from M2 plants were individually weighed. Values of siblings originated from the same M1 plants were plotted on the same horizontal position. Candidates are indicated by arrows. Gray circles are Nipponbare control.

2 - 11 Analysis of Radiation-induced Mutation by Focusing on Plant Pigment Synthesis Genes

S. Hirata [a, b], S. Kitamura [b], K. Satoh [b], I. Narumi [a] and Y. Oono [b]

[a] Faculty of Life Sciences, Toyo University,
[b] Department of Radiation-Applied Biology Research, TARRI, QST

Ion beams are useful tools to induce mutations in plants and produce valuable varieties. By analyzing characteristics of ion-beam-induced mutations, we could systematically understand what type of mutation is induced under certain conditions and what is the best condition to obtain mutants efficiently. In this work, we focused on plant pigment (anthocyanin) synthesis genes and developed an experimental system to investigate the characteristics of mutations induced by ion-beams. Two anthocyanin synthesis genes (*TT4* and *TT8*) [1], former is expressed constitutively in whole developmental stage but the latter is expressed specifically in reproductive developmental stage, are chosen as targets of the experiment in order to address the relationship between gene expression and mutation frequency.

From an ion-beam-re-irradiated population of an ion-beam induced mutant (*banyuls* (*ban*) [2]) whose immature seeds are red, plants that give white or green immature seeds were screened. Among them, *tt4* and *tt8* mutants in *ban* background were identified. An F1 plant obtained by crossing these two mutants is a heterozygote of wild-type and mutated genes for both *TT4* and *TT8* loci, resulting in having red immature seeds. When a mutation occurs in wild-type *TT4* or *TT8* gene by irradiation of the F1 plants, produced immature seeds become white or green because of loss of heterozygosity (LOH) [3] (Fig. 1). Through LOH, we could easily isolate mutated tissues by color change in immature seeds. In addition, after completely drying the seeds in which LOH has occurred, it is possible to discriminate which gene is mutated, *TT4* or *TT8* by observing seed color (Fig. 2).

F1 seeds were aseptically seeded on MS medium and kept at 4 ºC for 4 days. Then, seeds were incubated at 22 ºC for 24 hours under light conditions to promote germination. After additional 24-hour incubation, the seedlings were irradiated with carbon ion beams ($^{12}C^{5+}$, 220 MeV, 15 Gy) in TIARA. The irradiated seedlings were transplanted to soil, and grown in an incubation room (18 h light / 6 h dark condition). At 7 days after flowering, siliques formed in inflorescence stems were dissected and color of the immature seeds was investigated to see whether LOH was occurred (Fig. 1). In addition, by observing the color of the dried seeds, mutated gene (*tt4* or *tt8*) was scored.

Result obtained with 3,471 stocks of irradiated F1 plants is shown in Table 1. We found 20 LOH events. From the observation of these dried seeds, the seed color of one plant showed the same color as *tt4* mutant, and the remaining 19 plants showed the same seed color as *tt8* mutant. No mutation was detected by investigating 348 non-irradiated plants. The result suggests that, in our experimental system, *TT8* gene is more mutable than *TT4* gene and that the frequency of LOH is largely different by the gene. One possible reason for explaining the difference of the frequency of LOH between *TT4* and *TT8* gene is that it depends on size of the target gene. *TT8* gene is about 2.6 times larger than *TT4* gene; genomic sequence of *TT4* is 1,789 bp, whereas, *TT8* is 4,643 bp. However, difference of the size of the gene is not enough to explain the 19-times difference of the frequency. Further investigations such as increasing sample number and confirming mutation at the nucleotide sequence level are necessary.

In this work, we succeeded in developing an experimental system that can easily detect mutated tissues by visual inspection. Using the experimental system, we could investigate factors that would affect mutation frequency (for example, growing condition, irradiation timing, and gene expression status). By accumulating evidences with this system, we believe we can find the best conditions to obtain expected mutants with high frequency.

References

[1] N. Nesi *et al.,* Plant Cell **12**, 1863-78 (2000).
[2] S. Kitamura *et al.*, Plant Mol. Biol. **90**, 7-18 (2016).
[3] Y. Hase *et al.,* Nucl. Instrum. Meth. Phys. Res. B, **391**, 14-19 (2017).

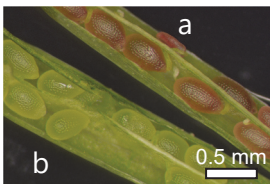

Fig. 1. Color of immature seeds of F1 plants. The red color of the non-mutated seeds (a) is disappeared in the mutated seeds (b) because of LOH.

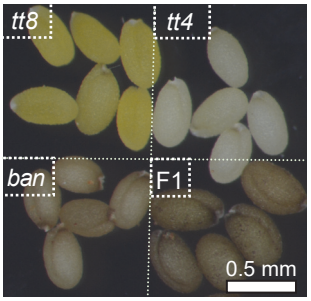

Fig. 2. Color of completely dried seeds. The *tt4*, *tt8*, their parent *ban,* and F1 seeds are white, yellow, red-brown, and red-brown color, respesctively.

Table 1
Screening of *tt* mutations on F1 plants.

	number of stocks		
	surveyed	*tt4* type	*tt8* type
Unirradiated plants	348	0	0
Irradiated plants	3471	1	19

2 - 12 Breeding of the Oil-producing Algae by Heavy Ion beam Irradiation

H. Araie [a, c], Y. Hase [b], Y. Oono [b], I. Suzuki [a] and Y. Shiraiwa [a]

[a] Faculty of Life and Environmental Sciences, University of Tsukuba,
[b] Department of Radiation-Applied Biology Research, TARRI, QST,
[c] Department of Biosciences, College of Science and Engineering, Kanto Gakuin University

Biofuel production using algae is attracting attention as a next generation energy candidate because (1) oil productivity of algae per unit area is higher than that of land plants and (2) biofuel from algae does not compete with food production. In this study, we focused on unique neutral lipid called alkenones that are shown in Fig. 1 since that are thought as one of the sources of fossil fuels. Alkenones are produced by only five marine haptophyte species. As material, we selected one of alkenone producing haptophytes, *Tisochrysis lutea*. *T. lutea* is easy to cultivate and shows higher alkenone productivity. In recent, use of alkenones as jet fuel has been proposed since alkenones generate hydrocarbons by butenolysis [1].

However, in order to advance the algae biomass industry, it is necessary to improve existing oil producing algae by mutation for making useful mutants such as strain with high growth rate or oil high accumulated strain. In general, chemical treatment, UV irradiation and heavy ion beam irradiation are used as mutagen since obtained mutants can be used in open system as non-GMO. Until now, highly oil producing algae mutants are obtained by heavy ion beam irradiation [2, 3]. So we also focused on heavy ion beam irradiation and tried to develop ion beam utilization technology that contributes to the creation of useful mutant strains.

Previously, we reported the way of cultivation on the agar plate for heavy ion beam irradiation and dose-dependent for colony formation with 0 ~ 320 Gy of carbon ions (26.7 MeV/u). We also reported alkenone productivity of mutants obtained by 0, 20 or 80 Gy irradiation. Here, we report screening of high biomass producing mutants and alkenone productivity of mutants obtained by secondly 80 Gy irradiation to highly alkenone producing mutant obtained by 80 Gy irradiation.

High biomass producing mutants were evaluated with both growth speed and maximum density. We cultivated 3,950 strains with 96-well plate and checked time course of change in optical density by plate reader. For selection, we picked up strains involved in top 15% of both growth speed and maximum density. As the results of three times experiments, we obtained 351 strains. In these strains, we picked up 77 strains that were obtained from more than two of three experiments. Table 1 shows list of 77 strains with irradiation energy and acquisition rate. From these results, heavy ion beam irradiation didn't show large effect for biomass improvement. Figure 2 shows histogram of alkenone productivity. Parent mutant (green arrow) that was obtained by 80 Gy irradiation was used for 80 Gy irradiation again (blue). As a result, 8 of 69 mutants showed higher alkenone productivity than parent mutant. In this case, mutation rate was 12% and increase of alkenone productivity was only 1.1 times higher. So we concluded that 80 Gy irradiation is not suitable for second time irradiation.

References

[1] G. W. O'Neil *et al.*, Energy & Fuels **29**, 922-30 (2015).
[2] S. Ota *et al.*, Biotechnology for Biofuels **9**, 13 (2016).
[3] K. Yamada *et al.*, Sci. Rep., **6**, 26327 (2016).

Table 1
Screening results of high biomass producing mutants.

Irradiation dose (Gy)	Number of strains	Acquisition rate (%)
0	15	3.5
5	5	1.7
10	3	0.9
15	4	2.8
20	26	4.0
30	0	0.0
40	11	2.9
60	4	1.5
80	9	5.5

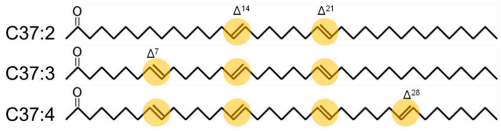

Fig. 1. Alkenone structures. Carbon number of these alkenones is 37 and they have two to four *trans*-type double bonds and keto group at a certain position.

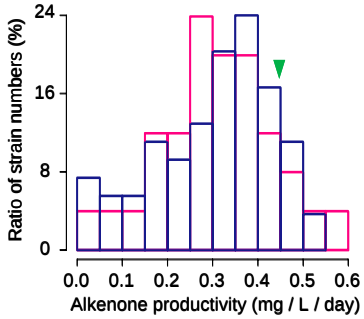

Fig. 2. Histogram of alkenone productivity. Alkenone productivity of 32 strains from mutants obtained by by 80 Gy irradiation (pink) and 69 strains from mutants obtained by by 80 Gy irradiation to highly alkenone producing mutant (parent mutant) obtained by 80 Gy irradiation (blue) were analyzed. Green arrow shows parent mutant level.

2 - 13 Characterization of *Sinorhizobium* Mutants Showing High Salt Tolerant Using the Ion Beam Mutation Breeding

Y. Maruyama [a)], N. Tomooka [b)], K. Satoh [c)], Y. Oono [c)] and T. Yokoyama [d)]

[a)] Graduate school of Agriculture, Tokyo University of Agriculture and Technology,
[b)] Genetic Resources Center, National Agriculture and Food Research Organization,
[c)] Department of Radiation-Applied Biology Research, TARRI,
[d)] Institute of Agriculture, Tokyo University of Agriculture and Technology

Vigna marina is one of wild legumes, which called as Hamaazuki, are distributed at the vicinity of the coast from tropical to sub-tropical regions and *Vigna marina* can grow at 400 mM NaCl condition. Furthermore, we found that the root nodules on *Vigna marina* have a symbiotic relationship with rhizobia that related to the genus *Sinorhizobium* having high stress tolerance (500 mM NaCl, 45 ºC, pH 10.5) [1]. Above both symbiotic partners showed extremely high salt tolerance, however, *Vigna marina* cannot develop root nodules with *Sinorhizobium* at over 80 mM NaCl conditions. In this study, to improve symbiotic performance of *Vigna marina* with *Sinorhizobium* under high salt conditions, we attempted to enhanced salt tolerant ability using ion beam mutation breeding based on the previous our study [2].

Sinorhizobium bacterial cells were irradiated with carbon ion-beams ($^{12}C^{5+}$, 220 MeV, 121.8 keV/μm) accelerated by an AVF cyclotron at TIARA, TARRI, QST. The optimum irradiation dose of the carbon ion beam to obtain survival ratio at 0.01% in *Sinorhizobium* cells was the range from 300 to 400 Gy. After irradiated bacterial cells were rescued by Yeast-Mannitol (YM) broth (0.05% yeast extract, 0.5% mannitol, 0.05% K_2PO_4, 0.02% $MgSO_4$, 0.01% NaCl; pH 6.8), The cell suspensions (50 μL) were dropped on YM agar (solidified with 1.5% agar) plates with 6% NaCl and were incubated for 3 weeks. After the 3 weeks incubation, to detect the survival cells, the drops were transfer to the fresh YM agar. Then, the survived cells were verified their salt tolerant abilities in terms of growth rates on YM agar with different NaCl conditions from 0 to 10% for 3 weeks. The high salt tolerant mutants were further tested in terms of nitrogen fixation and root nodulation abilities by plant tests using *Vigna marina*.

So far, we could obtain 5 mutants such as No. 3, No. 7, No. 13, No. 27 and No. 45 having high NaCl tolerant which can survive at 7.5% NaCl concentration. Of the 5 mutants, 2 mutants of No.7 and 45 could survive at 8% salt containing media, however remaining 3 mutants could not survive at the condition for 3 weeks (Fig. 1). Root nodules obtained from *Vigna marina* inoculated by No.7 showed the highest nitrogen fixation activity (Fig. 2). Furthermore, dry weight of *Vigna marina* inoculated by those mutants showed higher growth rate than that inoculated by wild type (Fig. 3). Especially, in case of No.7 mutant, root and shoot weights of Vigna marina inoculated by the mutant clearly showed the highest increase rate in the tested plants.

References

[1] N. Tomooka *et al.*, Proc. 14th NIAS Int. Workshop Genetic Resources, 11 (2011).
[2] K. Takeda *et al.*, JAEA Takasaki Annu. Rep. 2012, JAEA-Review 2013-059, 114 (2014).

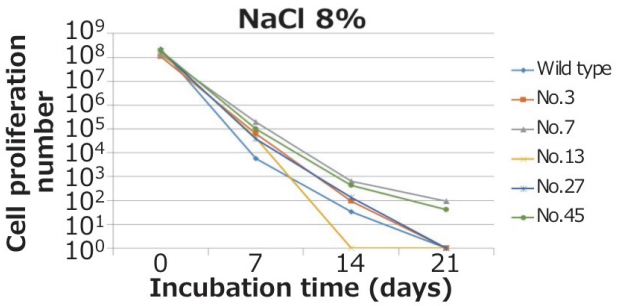

Fig. 1. Cell proliferation number under 8% NaCl condition.

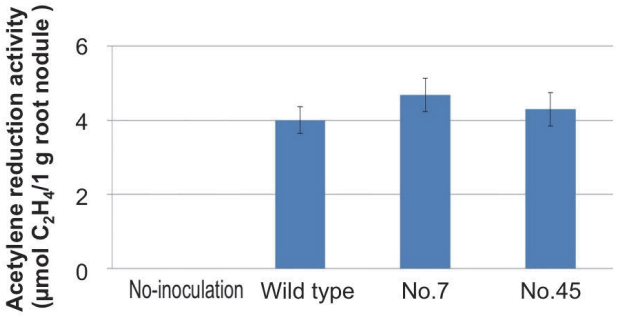

Fig. 2. Nitrogen fixation activities in combination among *Vigna marina* and different strains.

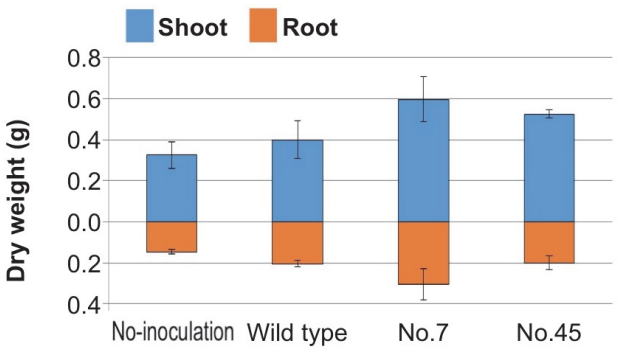

Fig. 3. Dry weight of Vigna marina inoculated by different strains.

2 - 14 Screening of Mutants Generated by Heavy Ion Beam for Identification of Genes Involved in Bacterial Interaction

M. Yanagisawa [a)], S. Asamizu [a)], Y. Sugai [a)], K. Satoh [b)], Y. Oono [b)] and H. Onaka [a)]

[a)] Graduate School of Agricultural and Life Sciences, The University of Tokyo,
[b)] Department of Radiation-Applied Biology Research, TARRI, QST

Actinomycetes are filamentous, gram-positive bacteria that are prominent producers of bioactive natural metabolites, which can serve as drug candidates. Recent genome analyses of actinomycetes revealed previously unrecognized “cryptic” gene clusters, indicating that actinomycetes have huge potential to produce more diverse secondary metabolites. We have studied the bacterial interaction-induced production of secondary metabolites by actinomycetes, and have shown that *Tsukamurella pulmonis* TP-B0596 (Tp) has the ability to induce the production of secondary metabolites by *Streptomyces* species that are only produced in combined culture [1]. To date, six classes, and 19 new compounds have been isolated using our “combined-culture” method with various *Streptomyces* spp. and Tp [2]. The aim of this study was to elucidate the genetic factor(s) that are involved in the activation of signaling pathways of secondary metabolism within actinomycetes. Clarification of this mechanism could lead to the generation of novel genetic tools to discover new drug compounds.

We used *Streptomyces coelicolor* A3(2) (Sco) as our model actinomycete, since it produces a distinctive red pigment (RED) on direct physical contact with live Tp [1,3]. In this study, we aimed to generate a mutant library of Sco to screen for mutants that had lost the ability to produce RED upon Tp induction. Little was known about the effects of heavy ion beam irradiation on actinomycete spores; therefore, we first examined the survival rates at a series of ascending irradiation doses (10, 50, 100, 200, 500 and 1,000 Gy). Spores of Sco (approx. 7×10^7) were fixed on mixed cellulose ester membranes and irradiated by heavy ion beam ($^{12}C^{5+}$, 220 MeV), using the AVF cyclotron at TIARA. The survival rate was determined by colony forming units (cfu) compared with that of a non-irradiated control (n=3). We observed a dose-dependent decrease in survival rates, as determined by viable cfu counts (Fig. 1).

Initially, we tested approximately 6,000 colonies from 1,000 Gy irradiated spores (survival rate: 1.8%) for the screening of mutants; however, the phenotype of obtained mutants showed undesired growth deficiency and morphological differentiation, indicating multiple genomic DNA mutations. Subsequently, we tested approximately 150,000 colonies from 200 Gy irradiated spores (survival rate: 13%). We screened for mutants by mixing the spores with the Tp culture on an agar plate. Using this combined-culture method, we were able to isolate 131 mutants that did not produce RED upon Tp induction. Twenty-nine mutants were excluded because they did not show growth on minimal medium and a further 40 mutants were excluded because they exhibited defective in morphological differentiation. From the remaining 62 mutants, we found that 8 mutants were able to produce RED induced by osmotic stress, but not by Tp induction (Fig. 2). We are now sequencing the genomes of the mutants to determine the site(s) of mutation in order to identify the gene(s) responsible for the activation of RED by Sco upon interaction with Tp.

References

[1] H. Onaka *et al.*, Appl. Environ. Microbiol., **77 (2)**, 400-06 (2011).
[2] H. Onaka, J. Antibiot., (2017).
[3] S. Asamizu *et al.*, Plos One, **10**, e0142372 (2015).

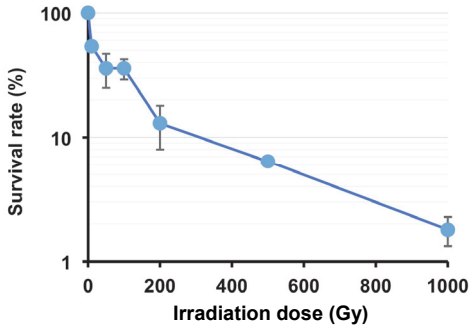

Fig. 1. Survival rates of *Streptomyces coelicolor* A3(2) spores to carbon ion beams.

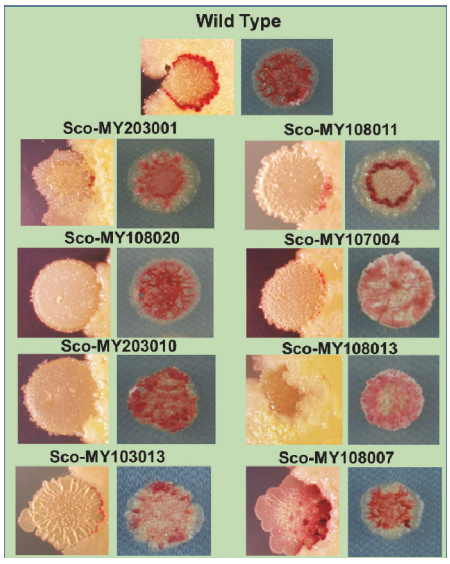

Fig. 2. Phenotype of the 8 selected Sco mutants, showing the different interaction with *Tsukamurella pulmonis* TP-B0596 (Tp) compared with wild type (left), and the production of Sco distinctive red pigment (RED) under osmotic stress (right).

2 - 15 Improvement of Autumn-flowering Spray-type Chrysanthemum Cultivar 'Kyura Syusa' by Ion Beam Irradiation

M. Tamari [a)], Y. Tanokashira [a)], M. Nishi [a)], F. Tojima [a)] and Y. Hase [b)]

[a)] Kagoshima Prefectural Institute for Agricultural Development,
[b)] Department of Radiation-Applied Biology Research, TARRI, QST

In order to confer an early flowering trait to the autumn-flowering chrysanthemum cultivar 'Kyura Syusa', more than 11,000 plants regenerated from the carbon-ion-irradiated leaf tissues were screened. Finally, three strains were selected, which flower earlier than the parental cultivar under low temperature condition and also have good agricultural traits equivalent to or better than the parental cultivar.

2016 年に品種登録された「きゅらシューサー」(Fig. 1)は、交配によって作出された純白色の鹿児島県育成の秋スプレーギクである。花の商品性が高く草丈伸長性に優れ、台風や高温など過酷な南西諸島の母株栽培環境でも採穂が良好であり、沖永良部地区を中心に急速に栽培が増加しているが、本土施設栽培では低温期の栽培において開花が遅れるなどの改善点がある。我々は、秋輪ギク「新神」へのイオンビーム再照射により低温開花性を付与した「立神」「冬馬」を 2015 年に育成した[1]。この事例を元に「きゅらシューサー」に低温開花性が付与された変異体の作出を 2015 年から開始しており、ここではこれまでの育成経過について報告する。

不定芽再生培地(MS 培地：IAA 5 mg/L，BA 1 mg/L, sucrose 3%, gellangum 0.3%, pH 5.8)を入れたシャーレに無菌植物の葉片(2 mm × 4 mm)を並べ、320 MeV 炭素イオンビームを照射し、再生した不定芽を培養瓶(ホルモン無添加 MS 培地)に継代培養した。十分に生育した個体をバーミキュライト培土で順化・発根させ、ほ場で 40 日間母株養成した。採穂した穂を 5 ºC の冷蔵庫で 3 週間冷蔵した。照射線量毎の個体再生率(照射後の 1 葉片から再生した不定芽数／無照射培養 1 葉片から再生した不定芽数)は 0.5 ～ 3 Gy では顕著な差は見られなかったが、5 Gy では 0.4 に低下した(Fig. 2)。

2015 年 10 月及び 12 月に、鹿児島県農業開発総合センター徳之島支場の露地電照ほ場に 2 月開花作型で 4,906 個体、3 月開花作型で 6,197 個体を定植した。3 月開花作型の電照消灯から開花までの到花日数は、56 日 ～ 77 日以上と分散した(Fig. 3)。到花日数別個体割合は照射線量が高くなる程ばらつく傾向を示し、特に開花が遅れる割合が増加した。今回試験した計 11,103 個体から、「きゅらシューサー」の平均到花日数 62 日(3 月開花作型)より到花日数が短く(59 日以下)、奇形が見られなかった 90 個体を選抜した(Table 1)。照射線量毎の選抜個体数を見ると 0.5 Gy では 3 個体と最も少なく、3 Gy では 42 個体と最も多くなった。

選抜した 90 個体は、徳之島支場において 2016 年に夏場の母株萌芽性と露地電照栽培 12 月・2 月開花作型で生育開花特性を確認し、「きゅらシューサー」より開花が早く、生育特性も同等かそれ以上の 3 系統を選抜した。このことからイオンビーム照射による秋輪ギクの特性改良の手法を応用することで、秋スプレーギクでも低温開花性の付与が可能であることが確認された。

更に特性の優れた個体を獲得するため、今後も変異体の選抜を継続する予定である(2016 年 5,670 個体、2017 年約 9,000 個体予定)。選抜した系統は、鹿児島県農業開発総合センター花き部(指宿市)での施設電照栽培でも栽培特性を確認し、全国で広く栽培できる純白色秋スプレーギク品種の作出を目指す。

Reference

[1] Tamari *et al.*, JAEA Takasaki Annu. Rep. **2014**, JAEA-Review 2015-022, 130 (2016).

Fig.1. Chrysanthemum Variety 'Kyura Shusa'.

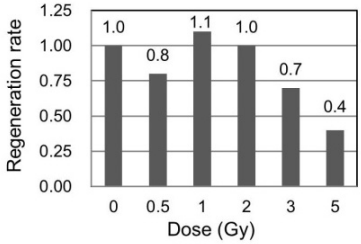

Fig.2. Regeneration rate from irradiated leaf tissue.

Table 1
Result of the screening of early flowering plants.

Dose (Gy)	Flowering in February		Flowering in March		Total
	No. of plants examined	No. of selected plants	No. of plants examined	No. of selected plants	No. of selected plants
0.5	1,296	0	1,242	3	3
1	1,317	4	1,688	5	9
2	985	6	1,539	14	20
3	1,004	19	1,058	23	42
5	not tested	not tested	554	8	8
0	304	8	116	0	8
Total	4,906	37	6,197	53	90

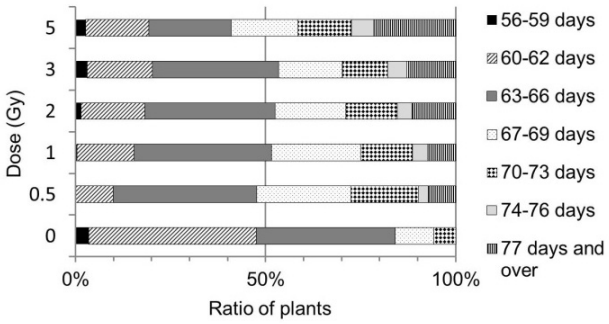

Fig.3. Ratio of the flowering period (Data of the flowering in March).

2 - 16 Ion Beam Breeding of Rice for the Mutation Breeding Project of the Forum for Nuclear Cooperation in Asia (FNCA)

A. Tanaka [a)], S. Nozawa [a)], Y. Hase [b)], Y. Oono [b)], A. Koike [c)] and A. Takano [c)]

[a)] Research Planning and Promotion Office, QuBS, QST,
[b)] Department of Radiation-Applied Biology Research, TARRI, QST,
[c)] Nuclear Safety Research Association

The Forum for Nuclear Cooperation in Asia (FNCA) is a framework for the peaceful use of atomic energy led by the Cabinet Office/ MEXT of the government of Japan. At present, ten countries are engaged in the project "Mutation Breeding of Rice for Sustainable Agriculture (2013-2017)" under the Mutation Breeding Project of the FNCA. Ion beams and gamma rays have been utilized to mutagenize the rice seeds to obtain mutant varieties that meet the demands of the participating countries [1].

Hulled dry seeds of rice varieties were exposed to 320 MeV carbon ions at TIARA with individual optimal doses to induce mutation. After irradiation, seeds were sent back to the participating countries and investigated for mutation induction. As for the appropriate population size for mutation induction, we assume that at least several seeds from each 5 panicles from each 1,000 M1 plants (5,000 initial mutated cells) should be harvested in order to expect a good result.

The representative achievement and economic benefit are shown in Table 1 [2]. In Bangladesh, BINA dhan 14 was registered as a new variety and have been cultivated for farmer with the help of agriculture extension in the different area of Bangladesh. In Malaysia, drought tolerant and disease resistant mutant lines were obtained from mutagenized population of MR219. In Vietnam, several mutant lines including, high yield, lodging resistant, disease resistant (bacterial leaf blight), salt tolerant were obtained.

Usefulness of Ion beam breeding has been recognized in Asian countries [3]. However, accelerator facilities available for ion beam breeding and the shared use system of them are very limited. At the 2014 workshop of the Regional Co-operative Agreement for Research, Development and Training Related to Nuclear Science and Technology for Asia and the Pacific (RCA), demanding paper for the use of ion beams in Asian countries was submitted to the International Atomic Energy Agency (IAEA). Dissemination of ion beam breeding technology is desired to stimulate sustainable agriculture to cope with global climate change and environmental destruction.

References

[1] A. Tanaka *et al.*, JAEA Takasaki Annu. Rep. **2014**, JAEA-Review 2015-022, 96 (2016).
[2] A. Tanaka *et al*., Proc. 1st QST Takasaki Symp., 105 (2017).
[3] A. Tanaka *et al*., J. Radiat. Res., **51**, 223-33 (2010).

Table 1
Representative mutants (varieties) and economic benefit (December 2015).

Country	Mutagen	New Variety and Mutant Line	Mutant traits	Economic Benefit *
Bangladesh	Ion beams	・New variety BINA dhan14 ・A mutant line from BRRI dhan29	Photo insensitive, Early flowering, High yield	1,800 million USD / year
China	Gamma-rays, Ion beams	・Mutants from GS79	Photo insensitive, Early flowering (hybrid rice)	
Indonesia	Gamma-rays, Ion beams	・Three mutant lines (one of them will be registered in 2018)	High yield, Early flowering	40 million USD / year for one variety
Japan	Gamma-rays, Ion beams	・Several mutant lines	High yield, Early flowering, Disease resistance	
Korea	Gamma-rays	・New variety Tocomi-1 ・New variety Wonhae-2	High tocopherol content, Salt tolerant	1 million USD / year for each variety
Malaysia	Gamma-rays, Ion beams	・Several mutant lines including MR219-4 and MR219-9	Drought tolerant, Disease resistant, Suitable for diabetic patients	90 million USD / year (Drought tolerant)
Mongolia	Gamma-rays	・Four mutant lines (wheat) (one of them will be registered in 2016)	Early flowering, Drought tolerant	Additional profit 82.9 USD/ha
The Philippines	Gamma-rays	・Six mutant lines from two varieties	High yield under organic farming	
Thailand	Gamma-rays	・Several mutant lines	Aromatic, High quality, Submergence tolerant	300 million USD / year
Vietnam	Gamma-rays, Ion beams	・Several mutant lines from four varieties	Early flowering, High quality, High yield	24.5 million USD / year 1.6 million USD / year

* Estimation by the person in charge in each country.

2 - 17 Determination of Ion Beam Irradiation Conditions for Callus of Tulip -the Second Report-

S. Ikegawa [a)], K. Shoji [a)], Y. Hase [b)] and S. Nozawa [c)]

[a)] Toyama prefectural Agricultural, Forestry & Fisheries Research Center,
[b)] Department of Radiation-Applied Biology Research, TARRI, QST,
[c)] Research Planning and Promotion Office, QuBS, QST

For obtaining a novel mutant from tulip plant by ion beam irradiation, we determined effective mutagenesis conditions for callus derived from flower stalk of tulip cv. "Yumenomurasaki". In this report, we investigated adequate dose and period of irradiation from the rate of growth of regenerated shoots after irradiation to calli, using 320 MeV carbon ion (320 C) or 107 MeV helium ion (107 He). As a result, 0.5 Gy of 320 C or 1.5 - 2.0 Gy of 107 He was thought to be adequate for inducing mutations.

富山県では、チューリップの培養技術を活用し、効率的な突然変異誘発技術の開発を目指している。2015年1月から高崎量子応用研究所においてチューリップの花茎由来カルス（未分化細胞塊）へのイオンビーム照射を実施し、照射後は、再分化および小球根誘導により変異集団を育成している。

本研究では、富山県育成品種「夢の紫」の花茎由来カルスに320 MeVの $^{12}C^{6+}$ イオンビーム（320 C）、または107 MeVの $^{4}He^{2+}$ イオンビーム（107 He）を照射（1つのカルスに対し1回のみ照射）し、照射後の生育状況により、適正なイオンビームの種類と照射量および照射時期について検討した（Table 1）。

照射の影響については、照射済み個体総数に対する、シュート長が50 mm以上に伸びた個体数（50 mm未満では次世代小球根が得られにくいため）の割合を指標値として用いた。なお、照射後にシュート長が50 mm以上に伸長するまで、早いもので3ヶ月、遅いもので2年以上が必要である。

また、試験区名は、高崎への輸送も照射も行わずに富山県で育成を続けた区を「対照」、輸送は行うが照射を行わない区を「0（ゼロ）Gy」とした。

まず、適正なイオンビームの種類と照射量について、実験Ⅰ～Ⅳにおける、照射イオン種および照射量別の指標値により検討した（Fig. 1(A)）。なお、図に記載のない照射区は指標値0である。対照の指標値は約13%、0 Gyは約14%であったのに対し、107 He, 1 Gyでは約16%と対照および0 Gyとほぼ同等であり、照射の影響をほとんど受けていないと考えられた。しかし、320 C, 0.5 Gy、107 He, 1.5および2 Gyの指標値は、約3%と照射によるダメージが強いことが窺える。これらの結果から、チューリップカルスへの適性照射量は320 C, 0.5 Gy、107He, 1.5～2 Gyと考えられた。これは、前報[1]で個体残存率を指標とした結果と同様である。

次に、適正な照射時期を検討した（Fig. 1(B)）。通常、チューリップの花茎由来カルスは、6月に掘り取った球根を夏以降に低温処理し、12月以降に置床した後、約1ヶ月で照射可能となる。また、カルス形成は12月から3月までに置床したもので良好となるため、花茎由来カルスへの照射が可能な時期は、1月から4月までと考えられる。これまでの4回の実験はいずれもこの期間中に照射を行っており、照射可能時期の中でも適正な照射時期を検討するため、各実験期の対照および0 Gyの指標値を比較した。その結果、いずれも1月末に照射した実験ⅠとⅢでは高く、4月下旬照射の実験Ⅱでは対照区の指標値が0となるなどかなり低い。このことから、照射時期は1月末が最も適していると考えられた。

また、照射サンプルの輸送時の温度変化の懸念や、一部のカルスで培地からの「はがれ」が生じたため、照射のための輸送（温度指定なしの宅配便）の影響を検討した。実験Ⅰ～Ⅳの対照と0 Gyの指標値の平均を比較すると、ほぼ同程度であることから（Fig. 1(B)）、サンプル輸送は、その後のカルスの生育に大きな影響を及ぼさないと考えられた。

実験Ⅰ～Ⅳの照射済みカルスから、再分化誘導、シュート育成、小球根形成誘導を行った結果、これまでに320 C照射で15個、107 He照射で19個の小球根を得た。得られた小球根は、培地または培養土へ植え付け、育成を進めている。

Reference

[1] S. Ikegawa *et al.*, QST Takasaki Annu. Rep. 2015, **QST-M-2**, 131 (2017).

Table 1
Irradiation conditions.

Experiment No.	Irradiation Date	320 C Dose (Gy)	107 He Dose (Gy)
Ⅰ	2015. 1.27	0、0.5、1、1.5、2、4、6、8、10、50	0、1、2、3、4、8、12、16、20、100
Ⅱ	2015. 4.22	0、0.5、0.75、1、1.5、2、50	0、1、1.5、2、3、4、100
Ⅲ	2016. 1.27	0、0.5	0、2
Ⅳ	2016. 3.09	0、0.5	0、2

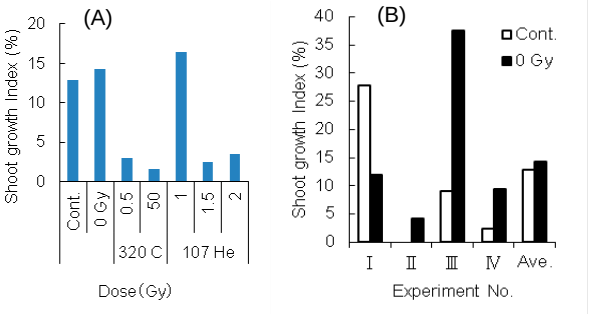

Fig. 1. Comparison of shoot growth index among (A) the irradiation doses and (B) the different experiments.

2 - 18 Study on the Genetic Consequence of Low Dose Rate Gamma Irradiation in Plants

Y. Hase [a)], H. Seito [b)] and Y. Oono [a)]

[a)] Department of Radiation-Applied Biology Research, TARRI, QST,
[b)] Department of Advanced Radiation Technology, TARRI, QST

Introduction

Effects of low dose rate gamma rays have been pointed out in native trees around the Fukushima Daiichi Nuclear Power Plant [1]. A significant increase of morphological change in native Japanese fir was observed in the next year of the power plant accident in March 2011, and gradually decreased in the following years. This suggested that those morphological changes are due to low dose-rate gamma rays. However, the dose assessment is difficult in the field and many factors other than gamma rays might be involved. Therefore, in parallel with those fieldwork, studies under controlled environment is required to consider the effects of low dose rate gamma rays in plants. Furthermore, little is known about the genetic consequence at the molecular level not only in plants but in other organisms. This study is aimed to determine the genetic consequence in plants grown under low dose rate gamma environment. Here, the irradiation damage in terms of plant morphology and the effect on seed fertility were examined using model plant *Arabidopsis thaliana*.

Materials and methods

Wild type *Arabidopsis* plants were grown in the first irradiation room at the Food Irradiation Facility from 7th day after sowing until flower stems start to grow. This period is usually around 2 weeks. Seeds were sown in a plant box (60 W × 60 D × 100 H mm) filled with rock wool and culture soil. The irradiation room was kept around 22 ºC and the plant box was illuminated with fluorescent light bulbs (around 70 μmol/m^{-2} s at the surface of the soil) under 16-h light / 8-h dark photoperiod. Control plants were grown in a growth room under the same temperature, light intensity and photoperiod. Dose rate of gamma rays were measured using an ionization chamber (C-110, Applied Engineering) or a scintillation survey meter (TCS-166, Hitachi-Aloca Medical). The fertility was determined as a ratio of the fertilized ovules to the total number of ovules in a silique.

Results and discussion

All plants did not grow at 10 Gy/h and withered within 10 days after starting irradiation. At 1 Gy/h, abnormal leaf shape such as shrinkage was evident. Pigment accumulation, which is a common response to various stresses in plants, was also observed at 1 Gy/h. Seed fertility decreased by ~50% at 1 Gy/h and by ~20% at 0.5 Gy/h compared to the control plants (Table 1, Fig. 1). No significant irradiation effect was observed in plant morphology and seed fertility at 0.1 Gy/h or less. These facts suggest that the gamma environment with the dose rate of 0.1 Gy/h or less does not cause significant effect on plant growth during vegetative growth stage.

In order to determine the genetic consequence of low dose rate gamma environment, *Arabidopsis* plants were grown with the dose rate of 0.5 Gy/h, 0.1 Gy/h, 0.6 mGy/h and 4.2 μGy/h for five successive generations. Whole genome resequencing will be done using the harvested seeds from successively irradiated plant population.

Reference

[1] Y. Watanabe *et al.*, Sci. Rep., **5**, 13232 (2015).

Table 1
Observed irradiation damage in *Arabidopsis* plants grown in gamma environment with different dose rates.

Dose rate (mGy/h)	Irradiation damage
10,000	Lethal
1,000	Fertility ~50% of control, Growth reduction, Abnormal leaf shape, Pigment accumulation
500	Fertility ~20% of control, Growth reduction, Abnormal leaf shape
100	None
0.6	None
0.004	None

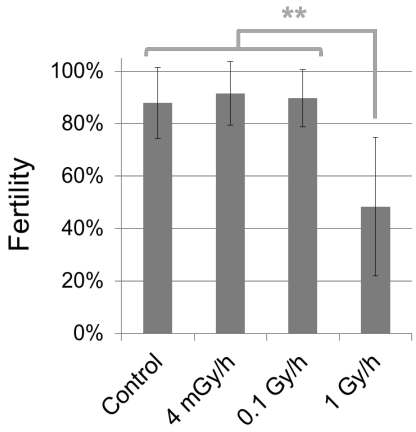

Fig. 1. Fertility of *Arabidopsis* plants grown in gamma environment with different dose rates. Data represents mean ± standard deviation of 24~30 siliques collected from 8~10 plants for each treatment. Asterisks indicate significant difference (*t*-test, $p < 0.01$).

2 - 19 Molecular Analysis of Carbon and Neon Ion Induced Mutations in Budding Yeast *S. cerevisiae*

Y. Matuo [a)], Y. Izumi [a)], A. N. Sakamoto [b)], Y. Hase [b)] and K. Shimizu [c)]

[a)] Research Institute of Nuclear Engineering, University of Fukui,
[b)] Department of Radiation-Applied Biology Research, TARRI, QST,
[c)] Radioisotope Research Center, Osaka University

Our research group has been studying ion-beam induced mutations in budding yeast S288c (*RAD*$^+$), as a model of eukaryote cell [1]. We showed that high-LET (107 keV/μm) carbon ion-beam was more mutagenic than low-LET gamma rays. A remarkable feature of yeast mutations induced by the carbon ions was that the mutations were located at a hotspot near the linker regions of nucleosomes in *URA3* gene, whereas mutations induced by gamma-rays were located uniformly through the marker gene. Also, we established a novel method to estimate radiation dose by the quantitative polymerase chain reaction (qPCR) [2, 3]. In the study, we further investigated the biological effects of high-LET Neon ion beam on lethality and mutagenicity of yeast cells and compared it with our previous results by carbon ion beam (LET: 13 - 107 keV/μm). *S. cerevisiae* S288c haploid cells were grown in YPD medium, transferred onto membrane filters and irradiated with Neon ions (LET: 317 keV/μm) with the dose of 1 - 200 Gy at TIARA. After irradiation, the membrane filters were incubated on YPD plates at 30 ºC for two days. Cell survival was measured by counting the number of single colonies. The membranes were then transferred onto the 5-fluoroorotic acid (5-FOA) selection plates and cultured for 5 days at 30 ºC, after which the number of *ura*3$^-$ colonies were counted.

In preceding studies, the yeast cells were irradiated with carbon ions (220 MeV, LET: 107 keV/μm) at TIARA or irradiated with carbon ions (290 MeV, LET: 13 to 75 keV/μm) at HIMAC-NIRS.

The survival of yeast cells irradiated with ion beams of various LETs were shown in Fig. 1. Cell survival decreased as an increase in the dose in each ion. At the same dose, the higher LET beam provided the higher lethality. The mutation frequency, expressed as a ratio of *ura3*$^-$ cells to total cells, increased and peaked at 100 Gy and decreased thereafter (Fig. 2). However, the high-LET neon ion (LET: 317 keV/μm) was not significantly effective than high-LET carbon ion (LET: 107 keV/μm) on lethality and mutagenicity. This tendency may be related to an "overkill" phenomenon. As the LET of the radiation increases, the RBE also increases. After reaching a maximum, the RBE for radiation with a LET above 100 - 200 keV/μm decreases due to "overkill" [4]. We are planning to accumulate the associated data, as well as investigating the effect of the ion beam of low LET such as a proton.

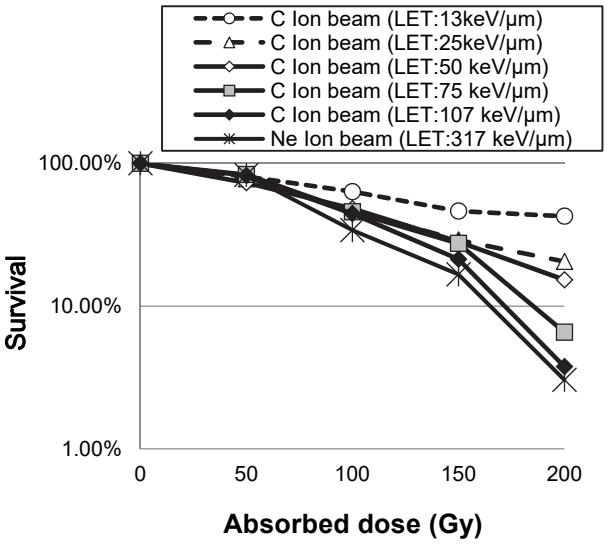

Fig. 1. Survival rates for yeast strain S288 after irradiation with carbon and neon ion beams.

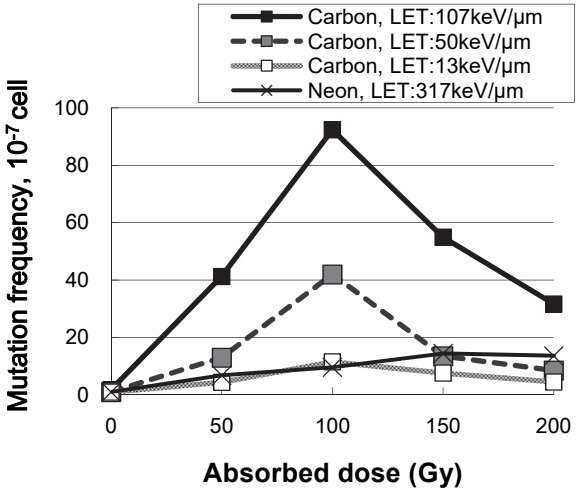

Fig. 2. Mutation frequency in the yeast strain S288c induced by carbon and neon ion beams.

References

[1] Y. Matuo *et al*., Mutat. Res., **602**, 7-13 (2006).
[2] Y. Matuo *et al*., Radiat. Meas., **55**, 93-95 (2013).
[3] Y. Matuo *et al*., JAEA Takasaki Annu. Rep. 2011, JAEA-Review 2012-046, 105 (2013).
[4] Y. Furusawa *et al*., Radiat. Res., **154**, 485-96 (2000).

2 - 20 Biological Effects of Cluster Ion Beams in *Bacillus subtilis*

Y. Hase [a)], K. Satoh [a)], A. Chiba [b)], Y. Hirano [b)] and K. Narumi [b)]

[a)] Department of Radiation-Applied Biology Research, TARRI, QST,
[b)] Department of Advanced Radiation Technology, TARRI, QST

Introduction

Cluster ion beams are characterized by their high-density energy deposition, and thus, the cluster ion-specific irradiation effects have been observed in the field of material science [1]. The cluster ion beams may also have a unique irradiation effects in biological materials, however, hardly applied so far. This study is aimed to establish the irradiation method of cluster ions in bacteria and consider the cluster ion-specific effects by comparing the irradiation effects of cluster and monomer ion beams.

Sample preparation

Spore suspension solution of *Bacillus subtilis* (subspecies subtilis 168) was prepared in sterile water by a conventional procedure with slight modification [2]. Aliquots (4 μL) of spore suspension (2×10^5 spores in total) were dropped onto small pieces of silicon wafer (approximately 10 mm × 10 mm). After freezing at -80°C for 30 min, the samples were freeze-dried for 30 min using a freeze drier (FDU-2200, EYELA). The diameter of spore spots was confirmed to be less than 4 mm. The samples were put on ice for approximately 5 minutes until water vapor begins to condense on the surface. Then, the samples were air-dried and kept in a humidified box until irradiation. We found this dew condensation and air-dry process enabled the spores spread in almost monolayer on the surface of the silicon wafer (Fig. 1). All samples were prepared on the day before irradiation.

Effect of cluster ion beams on spore survival

The samples were exposed to cluster ion beams from the 3 MV tandem accelerator at TARRI. The ion beams used here were as follows:

1 MeV/u: 6 MeV C_6 and 1 MeV C,
2 MeV/u: 6 MeV C_3, 4 MeV C_2 and 2 MeV C,
3 MeV/u: 6 MeV C_2 and 3 MeV C.

The beam size was adjusted to 5 mm in diameter. The beam current was measured by the Faraday cup equipped with the irradiation chamber at the TC beam line. After irradiation, spores on the silicon wafer were recovered by pipetting several times with PBT buffer (10 mM sodium phosphate buffer pH 7.0 containing 0.1% Tween 20). The recovery rate was >90% in two independent experiments. Colony forming units (CFU) were determined by the dilution plate method. The surviving fraction was shown as a ratio of the number of CFU of the irradiated samples to the number of CFU of mock-irradiated samples. The samples were generally kept in a vacuum condition for 2 to 3 hours during pre-vacuuming and irradiation process. The vacuum environment was confirmed not to affect the colony forming ability.

The surviving fraction linearly decreased as the fluence increased in a semi-logarithmic graph (Fig. 2). Irradiation with the fluence of 5×10^9 p/cm^2 was lethal for all types of ion beams. The cluster ion beams were slightly less effective on survival reduction than monomer ion beams with unknown reasons. This tendency was observed for all three combinations of cluster and monomer ion beams with the same energy per unit. Further experiments are required to confirm the reproducibility of the results.

References

[1] A. Chiba *et al*., Nucl. Instrum. Meth. Phys. Res. B, **315**, 81-84 (2013).
[2] W. L. Nicholson and P. Setlow, *In* C. R. Harwood and S. M. Cutting (ed), Molecular Biological Methods for *Bacillus*., 391-450 (1990).

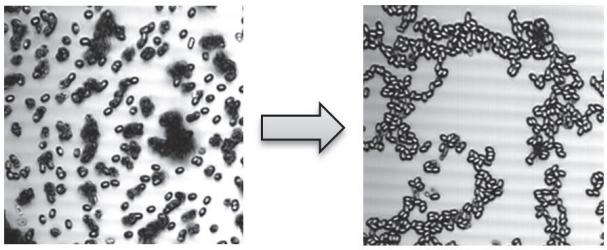

Fig. 1. Spread of spores in monolayer on a surface of silicon wafer by a dew condensation treatment. Left and right picture shows before and after treatment, respectively. The thickness of spore is approximately 1 μm.

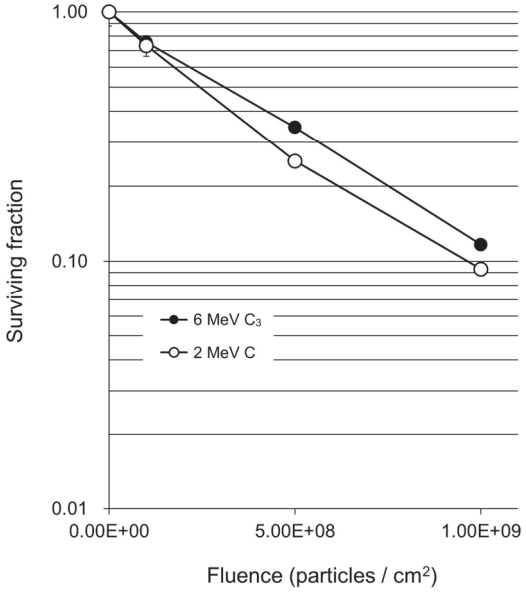

Fig. 2. Effect of cluster and monomer ion beams with the same energy per unit on the survival of spores in *Bacillus subtilis*.

2 - 21 The Lethal Effect of Ion Beams and Gamma Rays on *Bacillus subtilis* Spores

N. H. P. Uyen [a)], M. Furuta [a)], K. Satoh [b)] and Y. Oono [b)]

[a)] Quantum Radiation Engineering, Graduate School of Osaka Prefecture University,
[b)] Department of Radiation-Applied Biology Research, TARRI, QST

Introduction

Ionizing radiation induces DNA damages including single-strand breaks (SSBs) and double-strand breaks (DSBs) and generates reactive oxygen species (ROS) by water radiolysis within cells. ROS also induces DNA strand breaks. DSB is a particularly serious form of DNA damage and causing mitotic failure and cell death [1]. Ion beams have a high linear energy transfer (LET, keV/μm) and give DNA damage containing DSBs locally (clustered damage) than gamma rays do. The relative biological effectiveness (RBE) is dependent on the LET in mammalian cells, plants and *Escherichia coli* and exhibits a peak at a range about 100 to 200 keV/μm [2].

While *Bacillus subtilis* is known as Gram-positive, rod-shape, aerobic, spore-forming bacterium that is naturally found in soil, the spore is resistant to environmental factors such as heat, desiccation, chemical and radiation. Although the relationship between LET and RBE for gamma ray and carbon-ion beam irradiations on *B. subtilis* vegetative cells were reported [3], this relationship on the spore of *B. subtilis* is poorly understood. In this study, we investigate lethal effects and relationship between LET and RBE for gamma rays and different LET ion beams on the *B. subtilis* spores.

Experimental procedures

The spores of *Bacillus subtilis* 168 (*trpC2*) were prepared by inoculating the vegetative cells onto Schaeffer's sporulation medium [4] at 37 ºC for 4 days. Spores were harvested and treated sequentially with 1 mg/ml lysozyme and 1% SDS. Subsequently, spores were washed in sterilized water and resuspended in a solution containing protective agents at the concentration of 10^9 colony forming unit (CFU)/mL. Aliquots (1 μL) of the spore suspensions were dropped onto the sterilized cellulose membrane and dried. Dried spores were irradiated four kind of ion beams ($^4He^{2+}$ [50 MeV; 19.4 keV/μm], $^{12}C^{5+}$ [220 MeV; 121.8 keV/μm], $^{20}Ne^{8+}$ [350 MeV; 440.8 keV/μm] and $^{40}Ar^{13+}$ [460 MeV; 1,649.6 keV/μm]) accelerated by an AVF cyclotron at TIARA, TARRI, QST or with ^{60}Co gamma rays (0.2 keV/μm) at Osaka Prefecture University. The irradiation doses were 1, 2, 4, 6 kGy. Irradiated spores were recovered from the membrane, diluted and spreaded onto Luria Bertani agar, Miller (LB-M agar), and incubated at 37 ºC for 2 days.

The surviving fraction was determined by calculating the number of surviving colonies divided by the total number of viable colonies. The RBE was calculated from the equation: RBE = D_{10} of gamma rays (Gy) / D_{10} of the ion beam (Gy), where D_{10} is the dose quantity necessary for decreasing the survival fraction to 10%.

Results and discussion

Figure 1 shows dose response of the survival fraction of *B. subtilis* spores. The spores exhibited sensitivities to gamma rays and four kinds of ion beams depending on radiation dose. The $^{12}C^{5+}$ ion-irradiated spores showed the most sensitive than those of other radiations. As shown in Fig. 2, *B. subtilis* spores exhibited the dependence of LET on RBE. The spore killing efficiency was estimated to be in the order $^{12}C^{5+} > {}^{20}Ne^{8+} > {}^{4}He^{2+} > {}^{60}Co > {}^{40}Ar^{13+}$. The RBE value of $^{12}C^{5+}$ ion beams was 3.03, suggesting that $^{12}C^{5+}$ ion beams had the most lethal effects for *B. subtilis* spores. These results are consistent with the previous reports [2]. In future analysis, we will investigate the mutagenic effects to different LET radiations.

References

[1] C. F. Dunne, Br. J. Hosp. Med., **74**, 166-69 (1999).
[2] A. Tanaka *et al.*, J. Radiat. Res., **51**, 223-33 (2010).
[3] K. Satoh *et al.*, QST Takasaki Annu. Rep. 2015, **QST-M-2**, 135 (2017).
[4] P. Schaeffer *et al.*, Proc. Natl. Acad. Sci. USA, **54**, 704-11 (1965).

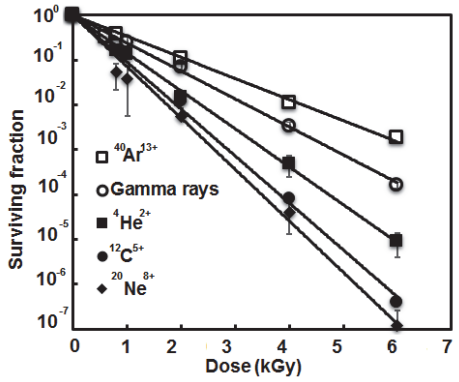

Fig. 1. Survival curves to gamma rays and different ion beam radiations.

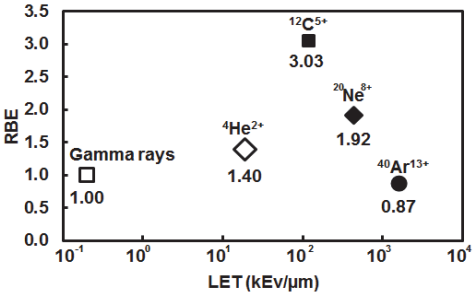

Fig. 2. The relationship between LET and RBE in *B. subtilis* spores.

2 - 22 Low Cesium-accumulating Mutants of *Rhodococcus Erythropolis* CS98 Generated by Ion Beam Breeding

K. Satoh [a)], S. Ozawa [b)], H. Hayashi [b)] and Y. Oono [a)]

[a)] Department of Radiation-Applied Biology Research, TARRI, QST,
[b)] Faculty of Engineering, Maebashi Institute of Technology

Introduction

Bioremediation uses biological organisms to solve an environmental problem, which draws attention as a technology with a low environmental burden compared with physical and chemical technologies. Microorganisms were often used for developing a technology to remove and recover contaminated environments. *Rhodococcus erythropolis* CS98 was isolated from soil as a cesium (Cs)-accumulating bacteria [1]. However, the mechanisms of Cs-accumulation in *R. erythropolis* CS98 are still incompletely understood. In this study, we tried to generate mutants that altered Cs-accumulating ability by ion beam breeding technology.

Experimental procedures

R. erythropolis CS98 was kindly provided by Dr. N. Tomioka (National Institute for Environmental Studies, Japan). *R. erythropolis* CS98 cells were cultivated at 30 ºC for 20 h in TGY broth with agitation. Cells were harvested and washed with 10 mM sodium phosphate buffer (PB). Cells were resuspend in 1% skim-milk/1.5% sodium glutamate solution. Aliquots (0.1 mL) of the cell suspensions were adhered onto cellulose membrane, frozen at - 80 ºC for 60 min and dried *in vacuo*. Freeze-dried cells were irradiated with carbon ion beam ($^{12}C^{5+}$, 220 MeV, 121.8 keV/μm) accelerated by an AVF cyclotron at TIARA, or with ^{60}Co gamma rays (0.2 keV/μm) at Food Irradiation Facility, TARRI, QST. Irradiated cells were cultivated at 30 ºC for 20 h in TGY broth with agitation to fix mutations. The mutagenized cells were harvested, diluted appropriately with 10 mM PB, spread onto either TGY agar or TGY agar supplemented with rifampicin (10 μg/mL), and incubated at 30 ºC for 5 days.

The cell growth of *R. erythropolis* CS98 was affected according to the high Cs concentration (over 10 mM) [2]. Candidates of altered Cs-accumulating mutants were screened from the mutagenized cells using the cell growth under the high Cs concentration as an index. Candidates were cultivated at 30 ºC for 20 h in TGY broth (10 mL), added 0.5 mM and cultivated for another 20 h with agitation. Cells were harvested, frozen and dried *in vacuo*. Freeze-dried cells were subjected to acid digestion with 6.5 M HNO_3 (2 mL) at 110 ºC for 1 h and 140 ºC for 1 h, drying at 80 ºC for 20 h and finally resuspended in 0.1 M HNO_3 (1 mL). The Cs concentration in the cell was measured with an atomic absorption spectrometer.

Results and discussion

The freeze-dried cells exhibited a higher resistance to gamma-irradiation than the wet cells, indicating that the effect of water radiolysis was relieved under the freeze-dried condition. From this result, the freeze-dried cells were used for ion beam irradiation. The cells exhibited sensitivities to carbon ion beams depending on radiation dose (Fig. 1). The rifampicin resistant (Rif^R) mutant frequency increased depending on radiation dose (Fig. 1). The highest Rif^R mutant frequency was observed at a dose range that give 10^{-1} to 10^{-2} of surviving fraction, like other microorganisms [3, 4].

We screened 7 candidates, that were exhibited Cs-resistant than the parental strain CS98, from the mutagenized cells. And we measured the intracellular Cs concentration in the candidates. As a result, all the candidates had lower intracellular Cs concentration than that of the parental strain, and in particular 2 candidates were over 1/5-fold lower (Fig. 2). Furthermore, it is expected that important insight on the Cs-accumulating mechanisms in *R. erythropolis* be obtained by the genomic analysis of the generated low Cs-accumulating mutants.

References

[1] N. Tomioka *et al.*, Appl. Environ. Microbiol., **58**, 1019-23 (1992).
[2] N. Tomioka *et al.*, Appl. Environ. Microbiol., **60**, 2227-31 (1994).
[3] Y. Toyoshima *et al.*, Mutat. Res., **740**, 43-49 (2012).
[4] K. Satoh *et al.*, JAEA Takasaki Annu. Rep. 2011, JAEA-Review 2012-046, 103 (2012).

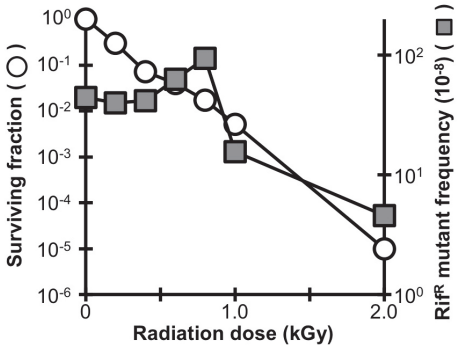

Fig. 1. Survival curve and Rif^R mutant frequency.

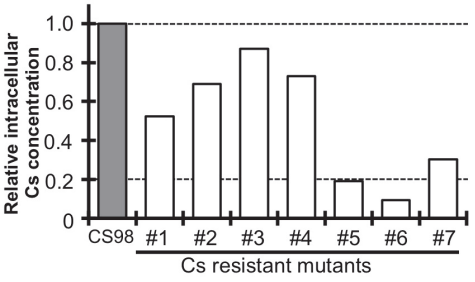

Fig. 2. Relative intracellular Cs concentration in *R. erythropolis*.

2 - 23 Effect of *dnaE2* Knockout and Overexpression in the Radioresistant Bacterium *Deinococcus grandis*

K. Omoso [a)], K. Satoh [b)], Y. Oono [b)] and I. Narumi [a, c)]

[a)] Graduate School of Life Sciences, Toyo University,
[b)] Department of Radiation-Applied Biology Research, TARRI, QST,
[c)] Department of Life Sciences, Toyo University

Deinococcus grandis, formerly *Deinobacter grandis*, is a Gram-negative, red-pigmented, radioresistant, rod-shaped bacterium isolated from freshwater fish in Japan [1]. Recently, we determined the draft genome sequence of *D. grandis* [2]. The genome analysis revealed that *D. grandis* possesses two *lexA-imuB-dnaE2* cassettes which are gene clusters related to error-prone DNA repair [3]. LexA, the gene product of *lexA*, binds to palindromic operator sites of regulated genes and represses their expression. ImuB, the gene product of *imuB*, is an apparently inactive paralog of the DNA polymerase V catalytic subunit UmuC. DnaE2, the gene product of *dnaE2*, is an alternative and catalytically active paralog of DNA polymerase III α-subunit [4]. In the *D. grandis* genome, one *lexA-imuB-dnaE2* cassette was located in chromosome II, and another *lexA-imuB-dnaE2* cassette was located in chromosome III. No *lexA-imuB-dnaE2* cassette is found in the most studied radioresistant bacterium *Deinococcus radiodurans*. Therefore, we are interested in the role of the *lexA-imuB-dnaE2* cassettes in *D. grandis*. In this study, we examined phenotypic changes in sensitivity to ultraviolet-C (UVC) and γ-rays in a *dnaE2* knockout strain and a *dnaE2* overexpression strain compared to wild type strain (WT).

A $dnaE2_{c2}$ (*dnaE2* paralog located in chromosome II) knockout stain (XDE2) was generated by the double crossover-mediated insertion mutagenesis technique using the chloramphenicol acetyltransferase gene as a marker. A $dnaE2_{c2}$ overexpression strain (OXE2) was generated by inserting the *D. radiodurans groE* minimal promoter upstream of $dnaE2_{c2}$ in a similar manner.

Figure 1 shows the mutation rates of WT, XDE2 and OXE2 measured by the fluctuation analysis using the Ma-Sandri-Sarkar maximum likelihood method [5]. Decrease in mutation rate was observed in XDE2 following UVC irradiation compared to WT, suggesting that $dnaE2_{c2}$ is involved in UVC-induced mutagenesis. On the other hand, OXE2 exhibited high mutation rates both in mock-irradiated and UVC-irradiated conditions, indicating that the intracellular overexpression of $dnaE2_{c2}$ results in the induction of spontaneous mutation.

Figure 2 shows sensitivity of WT, XDE2 and OXE2 to UVC and γ-rays. Surviving fraction was measured by the drop plate method [6]. OXE2 exhibited significant resistance to UVC compared to WT and XDE2. On the other hand, γ-ray sensitivity was comparable among all strains tested. These results suggest that $DnaE2_{c2}$ is involved in repair of UVC-induced DNA damage in an overexpressed condition. Underlying mechanisms of DNA repair by DnaE2 remain to be investigated.

References

[1] H. Oyaizu *et al.*, Int. J. Syst. Bacteriol., **37**, 62-67 (1987).
[2] K. Satoh *et al.*, Genome Announc., **4**, e01631-15 (2016).
[3] I. Erill *et al.*, Nucleic Acids Res., **34**, 66-77 (2006).
[4] L. Aravind *et al*., Biology Direct, **8**, article 20 (2013).
[5] B. M. Hall *et al*., Bioinformatics, **25**, 1564-65 (2009).
[6] C. Chen *et al*., J. Microbiol. Meth., **55**, 475-79 (2003).

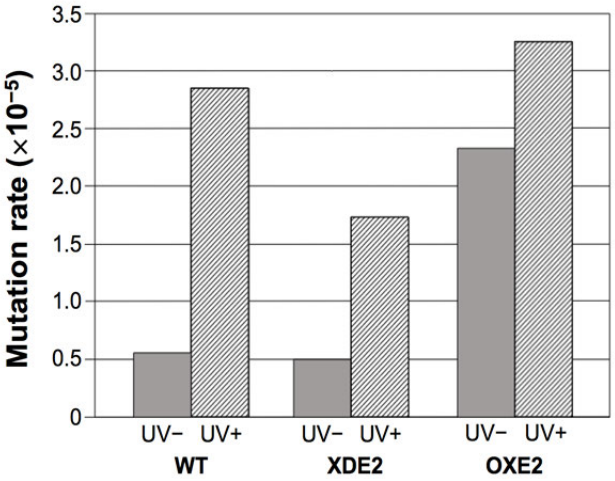

Fig. 1. Mutation rate of *D. grandis* strains WT, XDE2, and OXE2. UV−: mock-irradiated cell; UV+: UVC-irradiated cell. Resistance to the aminoglycoside bacteriocidal antibiotic, kanamycin, was used as the indicator of mutation.

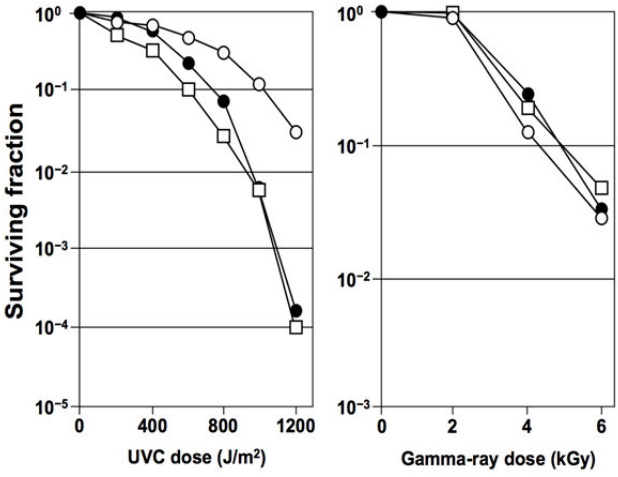

Fig. 2. Sensitivity of *D. grandis* strains WT (closed circles), XDE2 (open squares), and OXE2 (open circles) to UVC (left panel) and γ-rays (right panel).

2 - 24 Investigation of Conditions to Isolate Non-urea Producing Gunma Sake Yeasts which are Suitable for Export

T. Masubuchi [a)], K. Satoh [b)] and Y. Oono [b)]

[a)] Gunma Industrial Technology Center,
[b)] Department of Radiation-Applied Biology Research, TARRI, QST

Japanese sake is traditional liquor fermented from water, rice, and koji by yeast. Recently, export volume of Japanese sake has been gradually increased, because Europeans and Americans recognized Japanese sake as rice wine. Especially, they like local Japanese sake fermented from local rice and local yeasts. Gunma sake yeasts have been bred for producing local sake in Gunma prefecture. However, it is considered that the countries regulating volume of ethyl carbamate in Japanese sake would be also increased. Ethyl carbamate is classified the group 2A “probably the cause of cancer” by International Agency for Research on Cancer (IARC). Therefore, to reduce the volume of ethyl carbamate in Japanese sake, we attempted to breed Gunma sake yeasts that do not produce urea as a precursor of ethyl carbamate. In this year, we investigated conditions to isolate non-urea producing mutants from Gunma sake yeast KAZE2 by ion-beam irradiation.

The media compositions used in this study were shown in Table 1. In the yeast cells, arginine is hydrolyzed to ornithine and urea by arginase. Thus, researchers had used canavanine, analog of arginine, to obtain arginine transporter or arginase inactivate mutants. Kitamoto *et al*. reports that non-urea producing yeasts can be isolated from canavanine, arginine, and ornithine (CAO) medium [1]. The arginase-inactivated mutants, as non-urea producing mutants, grow on ornithine (Orn) medium, but not on arginine (Arg) medium [1].

KAZE2 was statically pre-incubated in YM5 medium (0.3% yeast extract, 0.3% malts extract, 0.5% peptone, and 5% glucose) at 30 ºC for 4 days. Cells were harvested, washed with sterilized saline (0.9% NaCl) and adhered on cellulose acetate membrane (0.22 nm). After freeze-dried treatment, cells were irradiated with carbon ion beams ($^{12}C^{5+}$, 220 MeV, 50 - 300 Gy) accelerated by the AVF cyclotron of TIARA, TARRI, QST. Then, cells were resuspended in sterilized saline and spread on CAO medium. After 1 week incubation at 30 ºC, colonies grown on CAO medium were replicated on Orn and Arg media. Unfortunately, all candidates grew both media, meaning all of them were not non-urea producing mutants.

Next, we used Kyokai No. 901 (K901) and K1901 as negative and positive controls, respectively. However, non-urea producing yeast strain, K1901 also grew Arg medium. According to advice from Niigata Prefectural Sake Research Institute, K1901 was treated to nitrogen starvation condition by incubated in nitrogen free medium for 2 days. By this treatment, K1901 grew on CAO and Orn media, but not on Arg medium.

Table 1
Compositions of media used in this study.

	CAO	Arg	Orn	Nitrogen free
YNB w/o AA & AS* (g/L)	1.7	1.7	1.7	1.7
arginine-HCl (mg/L)	210	210	-	-
ornithine-HCl (mg/L)	840	-	840	-
canavanine (mg/L)	10 - 30	-	-	-
Glucose (g/L)	20	20	20	20
Agar (g/L)	20	20	20	-

* Yeast nitrogen medium without amino acid & ammonium sulfate.

So, we retried to isolate non-urea producing mutants from KAZE2 by the improved method. After ion-beam irradiation, cells were treated to nitrogen starvation condition described above and spread on CAO medium. However, all candidates grown on CAO medium grew Arg medium. These results suggested that the concentration of canavanine in CAO medium (10 mg/L) was not enough to suppress growth of false-positive colonies of KAZE2. Thus, we increase the concentration of canavanine from 10 mg/L to 30 mg/L in CAO medium. After 3 weeks incubation on CAO medium containing 30 mg/L of canavanine, 5 large colonies were replicated on Arg and Orn media. From 5 candidates, only 1 colony did not grow on Arg medium.

In this study, we tried to isolate non-urea producing yeasts from Gunma sake yeast KAZE2 in order to reduce ethyl carbamate in Japanese sake. By the method of Kitamoto *et al.* [1], false-positive colonies of KAZE2 cannot be suppressed to grow on CAO medium. Thus, we investigated and found conditions to isolate non-urea producing mutants from KAZE2 by ion-beam irradiation described above.

Acknowledgement

We thank to Dr. Keigo Sato of Niigata Prefectural Sake Research Institute for technical advice.

Reference

[1] K. Kitamoto *et al.*, J. Brewing Soc. Jpn., **87**, 598-601 (1992).

2 - 25 Mutational Breeding of Salt-resistant *Chlamydomonas* sp. Strains Reveals Salinity Stress-activated Starch-to-lipid Biosynthesis Switching

Y. Kato [a)], S.-H. Ho [a)], C. Ogino [a)], T. Hasunuma [a)], K. Satoh [b)], Y. Oono [b)] and A. Kondo [a)]

[a)] Graduate School of Science, Technology and Innovation, Kobe University,
[b)] Department of Radiation-Applied Biology Research, TARRI, QST

High salinity stimulates lipid accumulation in the green microalga *Chlamydomonas* sp. JSC4 by activating a starch-to-lipid biosynthesis switching mechanism, but also negatively affects microalgal biomass production [1 - 3]. The aim of this study was to improve JSC4 algal biomass production under high salinity conditions by breeding a salt-resistant strain. Heavy ion beam-coupled mutagenesis and evolutionary engineering were performed using JSC4 as the parent strain. Microalgal cells seeded on agar plates were irradiated with 50 Gy of the carbon ion beams ($^{12}C^{5+}$, 220 MeV), which were accelerated by an AVF cyclotron at TIARA, QST. After long-term and continuous cultivation with high salinity, the salt-resistant strain (KHI) that grow well even in the presence of 7% sea salt was successfully obtained [4].

Figure 1 shows time-course profiles of algal biomass production under salinity conditions. Under 3% sea salt, the biomass production of the KHI at the Day 9 was 5.74 g/L, which was higher than that of JSC4 (5.05 g/L). Under 7% sea salt, the maximum biomass productions of the KHI was 4.08 g/L, while JSC4 showed almost no biomass production.

Figure 2 shows time-course profiles of starch and lipid contents. Starch content was determined with HPLC after a hot acid hydrolysis procedure (Fig. 2a). The KHI showed higher starch content than JSC4; the starch contents of JSC4 and KHI under 3% sea salt at the Day 9 were 18.3% and 30.3%, respectively. Lipid content was measured by quantifying fatty acid methyl esters using GC-MS (Fig. 2b). The maximum lipid content of the KHI under 3% sea salt was 32.8%, which is lower to that of JSC4 (46.2%). The maximum lipid content of the KHI under 7% sea salt was 34.7%, which are higher than the values under 3% sea salt. As JSC4 did not produce enough biomass for analysis, starch and lipid content could not be measured under 7% sea salt.

Figure 3 shows cellular particle sizes determined by microscopic image analyses. The salt induced aggregation and hypertrophy was relieved in the KHI. The mean sizes of JSC4 cell particles were 14.8 and 26.8 μm under 3% and 7% sea salt, respectively. On the other hand, the mean particle sizes of the KHI were 11.7 and 18.6 μm under 3% and 7%, respectively. The morphological analysis indicated that the cellular salt stress response was minimized in the salt-resistant microalga.

These results suggest that high salinity stress, not the salinity condition itself, is important for activating lipid accumulation mechanisms in microalgae.

References

[1] S.-H. Ho *et al*., Biotechnol. Biofuels, **7**, 97 (2014).
[2] S.-H. Ho *et al*., Biotechnol. Biofuels, **8**, 48 (2015).
[3] S.-H. Ho *et al*., Sci. Rep., **7**, 45471 (2017).
[4] Y. Kato *et al*., Bioresour. Tech. In press (2017).

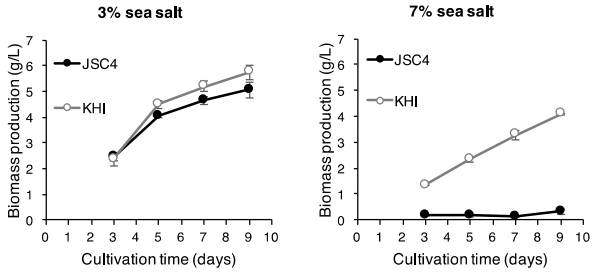

Fig. 1. Time-course profiles of biomass production.

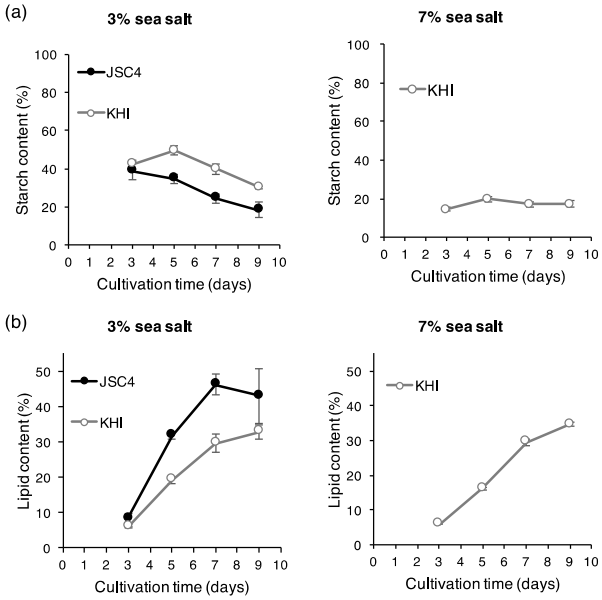

Fig. 2. Time-course profiles of starch (a) and lipid (b) content.

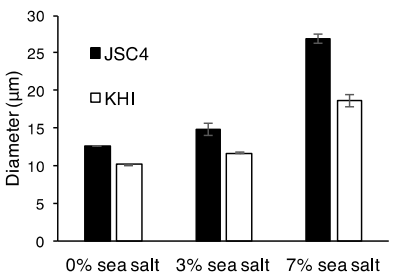

Fig. 3. Cell morphology under salinity conditions.

2 - 26 Evaluation of Radiation Effects Focusing on Body Posture in *Caenorhabditis elegans*

M. Suzuki [a)], N. Murakami [a)], S. Yanase [b)], Y. Yokota [a)] and T. Funayama [a)]

[a)] Department of Radiation-Applied Biology Research, TARRI, QST,
[b)] Faculty of Sports and Health Science, Daito Bunka University

We have investigated radiation effects regarding muscular movements in the nematode *Caenorhabditis elegans*. We have so far shown that whole-body irradiation with gammma-rays significantly reduce locomotion in a dose-dependent manner [1], in which we had evaluated locomotion by counting body bends/ 20 s [2].

On the other hand, recently we found out that the body posture of irradiated animals might be changed as well as body bends. In the present study, to evaluate the radiation effects in more detail, we therefore proposed a novel standard focusing on the body posture.

Wild-type adult animals were used in all experiments. Fifty or more animals placed on an agar plate spread with a bacterial lawn were irradiated with ^{60}Co gamma rays (1,000 Gy or 1,500 Gy) at the ^{60}Co irradiation facilities of QST-Takasaki. Immediately after irradiation, locomotion of ten animals were video-recorded at each irradiation experiment. To evaluate body posture, we proposed 'bending rate' denoted as follows: Bending rate [%] = 100 × straight length between head and tail [mm] (a in Fig. 1)/ body length [mm] (b in Fig. 1). We derived this value by image processing from the movie of each animal.

As shown in Figures 2A and 2B, there was no difference between the body posture of animals irradiated with 1,000 Gy and that of non-irradiated control animals. Averages of them were 82.0% for 0 Gy and 84.1% for 1,000 Gy, respectively. On the other hand, animals with abnormal posture, such as stretching (around 100%) and curling (~40%), increased in the animals irradiated with 1,500 Gy (Fig. 2C), and the average of the bending rate was 75.1%. These results indicate that our novel evaluation standard is effective to detect qualitative differences of locomotion. The sequel experiments, in which we use some kinds of mutants and heavy ions, regarding changes of the body posture are in progress.

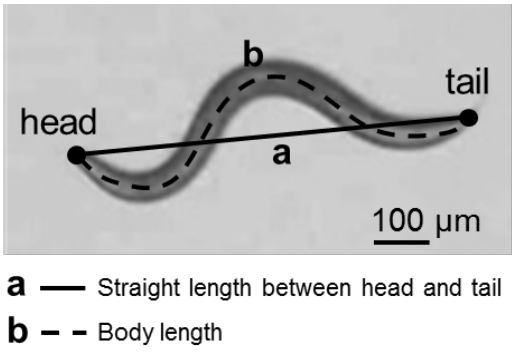

Fig. 1. Wild-type adult *C. elegans.* The quantitative data regarding the body size, straight length between head and tail (a) and body length (b), were derived by image processing and used for evaluation of posture.

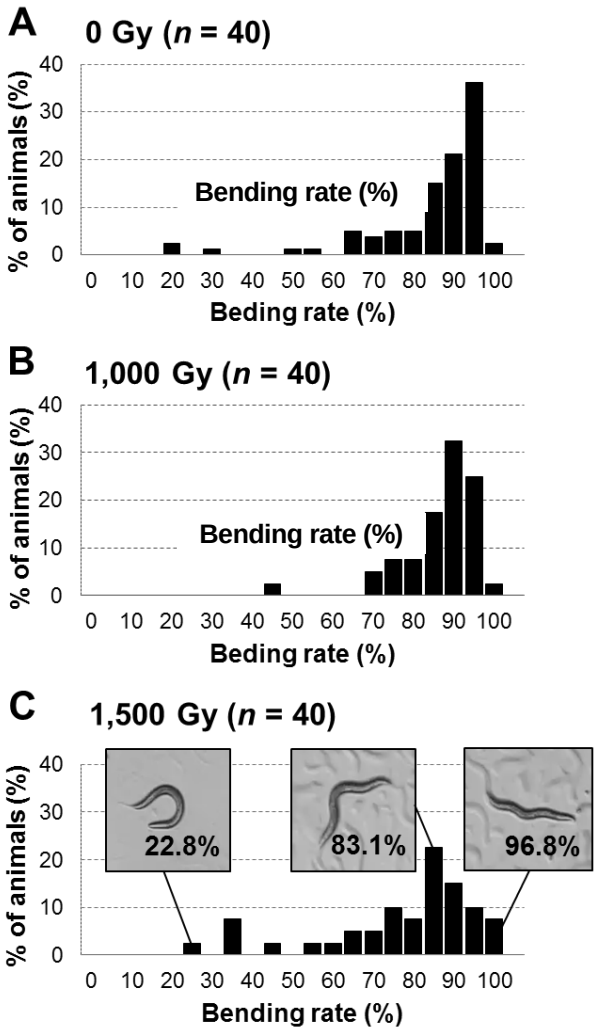

Fig. 2. Histogram of the body posture (bending rate) in the *C. elegens* immediately after gamma-ray irradiation.
(A) Non-irradiated control animals; (B) animals irradiated with 1,000 Gy of gamma rays; (C) animals irradiated with 1,500 Gy of gamma rays. Animals in boxes show typical body posture with low, normal, and high value of the bending rate, respectively.

References

[1] M. Suzuki *et al.*, J. Radiat. Res. **50**, 119-25 (2009).
[2] E. R. Sawin *et al.*, Neuron **26**, 619-31 (2000).

2 - 27 Effects of Hyperoxia and ^{60}Co γ-ray Irradiation on Lifespan in the Nematode *C. elegans*

S. Yanase [a)], M. Suzuki [b)] and T. Sakashita [b)]

[a)] Daito Bunka University School of Sports & Health Science
[b)] Department of Radiation-Applied Biology, TARRI, QST

In a model organism, the nematode *C. elegans*, intermittent preexposure to hyperoxia induces various adaptive responses such as lifespan extension and increased radioresistance to low linear energy transfer (LET) radiation [1, 2]. Previously, we have shown that insulin/insulin-like growth factor-1 (ins/IGF-1) signaling, which is associated with normal aging, plays an important role in lifespan extension induced by hyperoxia. However, marked extension of lifespan in the wild-type N2, which is characterized by the inactive ins/IGF-1 signaling, has not been observed following the intermittent exposure to hyperoxia [3].

Here, we studied the biological effects of radiation and hyperoxia in the wild-type. Figure 1 shows the airtight chamber used to expose the animals to oxygen and ^{60}Co γ-ray irradiation. Four or five-day-old wild-type animals placed on plates in the chamber were exposed to 95% oxygen for 8 h and irradiated with a 500 Gy γ-ray dose (at 33.4 Gy/min). After exposure, the animals were removed from the chamber and lifespans and mitochondrial superoxide radical ($\cdot O_2^-$) levels were recorded.

Table 1 shows the effect of hyperoxia and γ-ray irradiation on the lifespan of wild-type N2. Exposure to only hyperoxia for 8 h did not affect either the mean or maximum lifespan at 20 ºC; however, a combination of hyperoxia and γ-ray irradiation significantly increased the mean lifespan in the wild-type compared to that of animals treated with only γ-ray irradiation. Note that only γ-ray irradiation (500 Gy) does not affect the lifespan in wild-type *C. elegans* [4]. Surprisingly, treatment with temporal exposure to hyperoxia and γ-ray irradiation resulted lifespan extension (approximately 10-14%) in wild-type N2 compared with animals treated with only γ-ray irradiation. In general, oxygen enhances radiobiological damage (the so-called oxygen effect in radiation biology). According to our finding, however, oxygen with γ-ray irradiation seemed to induce beneficial effects in *C. elegans*, such as adaptive responses.

Here we aimed to determine the cause of lifespan extension in the wild-type N2 treated with temporal hyperoxia and γ-ray irradiation. Figure 2 shows the mitochondrial and cytosolic $\cdot O_2^-$ levels in wild-type N2 animals treated with or without hyperoxia and γ-ray irradiation. In the animals exposed to both hyperoxia and γ-ray irradiation, mitochondrial $\cdot O_2^-$ production levels were significantly reduced compared to those in animals treated with only γ-ray irradiation.

These results suggest that an interaction between oxygen and γ-ray irradiation induces a reduction in the production of mitochondrial $\cdot O_2^-$ and leads to lifespan extension as an adaptive response in *C. elegans*.

References

[1] S. Yanase *et al.*, Mutat. Res., **426**, 31-39 (1999).
[2] S. Yanase *et al.*, Mech. Ageing & Dev., **123**, 1579-87 (2002).
[3] S. Yanase *et al.*, J. Radiat. Res., **49**, 211-18 (2008).
[4] T. E. Johnson *et al.*, J. Geront., **43**, B137-41 (1988).

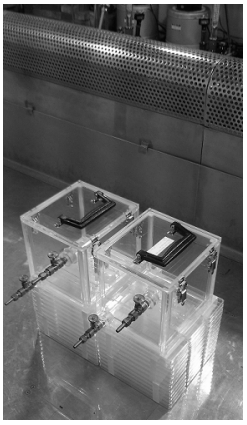

Fig. 1. Two airtight plastic chambers set in front of ^{60}Co γ-ray sources in the food irradiation building of TARRI. The chamber was ventilated with one atmosphere of 100% oxygen at a rate of 2 L/min to achieve a final concentration of 95%. Wild-type N2 animals on plates were exposed to 95% oxygen for 8 h and irradiated with a 500 Gy γ-ray dose in the chamber.

Table 1
Effect of hyperoxia and γ-ray irradiation on lifespan.

Strain (condition)	Mean lifespan (days ± S.D.)			Max. lifespan (days ± S.D.)
N2 (21% O_2)	26.3 ± 7.0	22.4 ± 7.3		42.0 ± 4.2
N2 (95% O_2)	25.3 ± 7.4	21.7 ± 8.3		41.0 ± 2.8*
N2 (21% O_2 + γ)	26.9 ± 7.8*	23.1 ± 9.4**	27.6 ± 9.1***	47.0 ± 3.5
N2 (95% O_2 + γ)	30.6 ± 7.8*	27.0 ± 9.8**	30.6 ± 9.7***	51.0 + 2.0*
	*P < 0.001, **P < 0.005, ***P < 0.05			*P < 0.05

A total of 100 worms were scored for each experiment. Results in mean of lifespan are indicated as means ±standard deviation (S.D.) from three independent experiments. Results in maximum of lifespan are expressed as means ± S.D. of three determinations. *P* values by *t*-test with a different superscripts in each column.

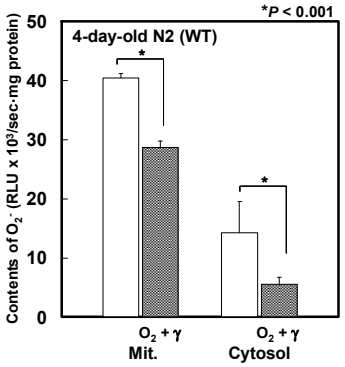

Fig. 2. Mitochondrial and cytosolic $\cdot O_2^-$ levels in wild-type animals treated with or without hyperoxia and γ-ray irradiation. Each unshaded left-hand column indicates the $\cdot O_2^-$ levels in animals treated with only γ-ray irradiation.

2 - 28 Estimation of Damage Localization in DNA Irradiated with $^{12}C^{5+}$ and ^{60}Co γ-rays in the Solid State

K. Akamatsu and N. Shikazono

Department of Quantum Beam Life Science, KPSI, QST

1. Introduction

Ionizing radiation-induced DNA damage can cause mutation and carcinogenesis. In particular, "clustered damage", that is a DNA region with two or more lesions within a few helical turns, is believed to be hardly repaired. This damage is considered to be induced around high-LET ionizing radiation tracks. However, detail of the damage is unknown. We have already developed a method for estimating localization of apurinic/apyrimidinic sites (APs) on DNA using Förster resonance energy transfer (FRET) occurring between different fluorescent dyes (Alexa350 and Alexa488) (*hetero*-FRET). The FRET efficiency (*E*) was calculated from Alexa350 fluorescence intensities before/after enzymatic digestion of the labeled DNA with APs [1]. We succeeded in estimating qualities of clustered APs produced in $^{4}He^{2+}$-, $^{12}C^{5+}$-, and ^{60}Coγ-irradiated dry DNA film to study "direct" radiation effects using the method [2]. However, there are some problems of the complex protocol and of the sensitivity due to the low extinction coefficient of Alexa350. We have, therefore, developed "*homo*-FRET" occurred between two or more Alexa488 molecules. We will obtain magnitude of FRET also from "fluorescence anisotropy" of *homo*-FRET between Alexa488 molecules. The new protocol using *homo*-FRET enables us to estimate DNA damage localization without any enzymes and improves sensitivity to detect a clustered damage.

2. Experiments

●*Sample preparation and irradiation*

PUC19 digested by Sma I was used (linear formed) for DNA samples to be irradiated. The DNA aqueous solution was dropped onto a glass plate, followed by drying in vacuum. Thickness of the dry DNA film was about 1 μm. The DNA film was irradiated with $^{12}C^{5+}$ (0.34 MeV/u, LET: ~760 keV/μm). Moreover, ^{60}Co γ-rays were also used as a standard radiation source at Kyoto University Research Reactor Institute.

●*Preparation of fluorophore-labeled irradiated DNA and FRET observation* [3]

The irradiated DNA (10 μL in water) and 10 μL of 100 mM Tris-HCl (pH 7.5) were mixed in a microtube. Two microliters of Alexa488/DMSO was added to the DNA solution and was incubated for 24 h at 35 ºC. The fluorophore-labeled DNA was purified by ethanol-precipitation followed by ultrafiltration. The fluorescence anisotropy was measured at 525 nm (ex. 470 nm).

The anisotropy, $< r >$, is defined as follows:

$$< r > = (I_{VV} - G \cdot I_{VH})/(I_{VV} + 2 \cdot G \cdot I_{VH})$$

where I_{VV} is the fluorescence intensity when the excitation and emission polarizers are both vertically oriented. I_{VH} is one when the excitation/emission polarizers are vertically/horizontally oriented. G is the grating factor defined as I_{HV}/I_{HH}.

3. Results and Discussion

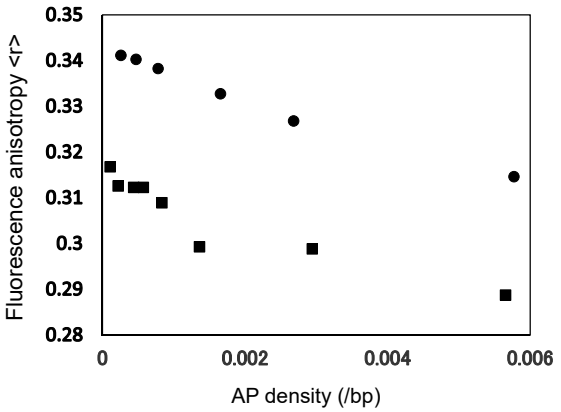

Fig. 1. Fluorescence anisotropy of AF488-labeled DNA irradiated with ^{60}Co γ-rays (●) and $^{12}C^{5+}$ (■) as a function of AP average density.

Figure 1 shows relationships between AP average density and fluorescence anisotropy for the C ion beams, and ^{60}Co γ-rays. As can be seen, anisotropy for C ions are clearly smaller than that for the γ-rays. The y-intercept of the relationship for C beam seems to be 0.315 ± 0.005. The anisotropy value can be converted into 5~6 nm (15~18 base pairs). This suggests that C ion beam near Bragg peak produces clustered AP lesions on a radiation track by direct radiation effects.

4. Acknowledgment

We would like to gratefully thank Dr. Takeshi Saito of Kyoto University Research Reactor Institute for supporting ^{60}Co γ-ray irradiation.

References

[1] K. Akamatsu, N. Shikazono, Anal. Biochem. **433**, 171-80 (2013).
[2] K. Akamatsu *et al.*, Radiat. Res., **183**, 105-13 (2015).
[3] K. Akamatsu, JAEA Takasaki Ann. Rep. 2008, JAEA-Review 2009-041, 63 (2009).
[4] L. W. Runnels, S. F. Scarlata, Biophys. J., **69,** 1569 (1995).

2 - 29 Visualization of Boron within Cultured Glioma Cells Using Micro Particle Induced Gamma-ray Emission

K. Nakai [a, b], K. Endo [a], T. Kurita [a], Y. Yamamoto [a], T. Yamamoto [a], F. Yoshida [a], A. Matsumura [a], N. Yamada [b], M. Koka [c] and T. Satoh [d]

[a] Department of Neurosurgery, Faculty of Medicine, University of Tsukuba,
[b] Department of Neuro-rehabilitation, Ibaraki prefectural University Hospital,
[c] Beam Operation Co., Ltd,
[d] Department of Advanced Radiation Technology, TARRI, QST

Boron neutron capture therapy (BNCT) has been expected as novel particle irradiation therapy for invasive malignant diseases [1]. Several clinical trials had undergone with reactor neutron source and revealed prolonged overall survival periods compared with standard therapy on some selected cases, such as malignant brain tumors and head and neck cancers. ^{10}B enriched boronophenylalanine have been used as a boron agents. The boron distribution is important elements of BNCT. Intra tumor boron concentrations are inferred from blood boron concentrations during patient irradiation. To determine intracellular boron concentration, we reported the possibility of using micro particle induced gamma-ray emission (micro-PIGE) [2, 3]. Though we could not visualize the boron distribution on previous study, we used high boron containing medium (800 μg ^{10}B/mL) this time and analyzed 2-dimentional intra cellular boron distribution of single cultured glioma cell.

Material and Methods

The U251 human glioma cell line were propagated in Dulbecco's modified Eagle's MEM with 10% fetal bovine serum and 10 mg/L penicillin-streptomycin. The cells were grown on the 4-μm-thick polycarbonate membrane that pretreated with poly-L-Lysine. Boron concentration of 800 μg ^{10}B/mL in the form of a fructose complex were used to increase its solubility in water. The cells were treated 2 h. 800 μg ^{10}B/mL containing PBS, then the cells were freeze-dried at -80 ºC. The samples were attached directly to the window at the end of the microbeam line at TIARA, and were irradiated by a 1.7-MeV proton microbeam in air for micro-PIXE/PIGE analysis, where the emitted X-rays and gamma rays from the samples were detected for acquiring elemental distributions. A nuclear reaction of ^{10}B(p, p' γ)^{7}Be was especially used to measure ^{10}B concentration. The gamma rays by this reaction were detected using a detector placed 5 mm behind the specimen in air. Concentrations of potassium and phosphorus, which were simultaneously detected with a detector placed in the vacuum, were measured using an X-ray detectors in vacuum.

These data were analyzed using an analyzing software PIXEana originally developed by TIARA, to draw a spectrum and two-dimensional element distribution images (Fig. 1).

Results

We successfully detected the boron in the cells. Previous reports revealed that boron atoms exist only on the surface of the cell membrane with less than two hours of f-BPA exposure. We need longer measurement periods in order to acquire more boron counts, but this is not possible because of the sample heating and break [3]. Thus, there is a limitation to the gain in high boron counts so far.

Conclusions

The results obtained in this study suggest that it is possible to detect boron in the cell by using PIGE after exposuring 800 μg ^{10}B/mL of f-BPA in the culture medium. Further investigation is needed for boron distribution imaging, but at least two hours of f-BPA exposure is required to create a boron distribution image by PIGE.

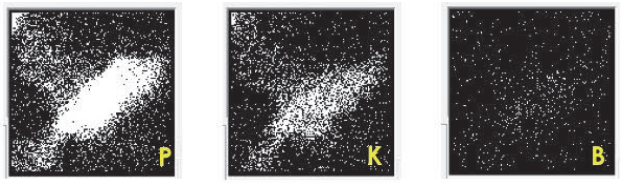

Fig. 1. U251 glioma cell were freeze dried after treatment of boron containing medium. The two dimension images show the existence of phosphorus, potassium, and boron distribution. Image size is 50 μm × 50 μm.

References

[1] T. Yamamoto, K.Nakai, *et al.*, Radiother. Oncol. **91**, 80-84 (2009).
[2] K. Endo *et al.*, Oncol. Res. **16**, 57-65 (2006).
[3] K. Nakai *et al.*, Appl. Radiat. Isot. **106**, 166-70 (2015).

2 - 30 Fluorine Distribution from Fluoride-containing Luting Materials to Dentin

K. Okuyama [a)], Y. Matsuda [b)], H. Yamamoto [c)], Y. Tamaki [a)], T. Saito [b)], M. Hayashi [c)], T. Satoh [d)] and M. Koka [e)]

[a)] School of Dentistry, Asahi University,
[b)] School of Dentistry, Health Sciences University of Hokkaido,
[c)] Graduate School of Dentistry, Osaka University,
[d)] Department of Advanced Radiation Technology, TARRI, QST,
[e)] Beam Operation Co., Ltd

Introduction

There are some kinds of dental luting materials(cements) in the market. Recently, some of them have a function of fluoride releasing from material because of preventing secondary caries after cementing with prosthetic appliances (crown or bridge). The purpose of this study is to evaluate distribution of fluorine from fluoride-containing luting materials to adjacent dentin by in-air micro PIXE/PIGE system at TIARA.

Materials and Methods

Extracted human teeth were used in this study. Each tooth crown was cut and grinded to expose a flat dentin surface. An acrylic resin plate (2 mm thickness) was cemented with four kinds of fluoride-containing luting materials (Fuji I: FO, Fuji Luting EX: FL, Clearfil SA Luting plus: SA, BeatiCem SA: BC) on the dentin surface. The specimen was embedded by epoxy resin and then the outer dentin surface including dentin-luting material-resin plate interface was exposed. The embedded specimen was sliced (about 500 μm thickness) and coated with sticky wax except for exposed dentin surface. Each sliced sample was carried out on pH cycling (pH:4.5 and 7.0; simulate oral condition) for 4w for preparing artificial carious dentin using an automatic pH-cycling system [1]. After pH cycling, calcium and fluorine distribution were analyzed by an in-air micro-PIXE/PIGE system with a 1.7-MeV $^{1}H^{+}$ microbeam at TIARA [2]. The outermost surface of the dentin was defined at the position containing 5% of the calcium concentration in intact dentin. For the comparison of fluorine uptake, the average fluorine concentration in each specimen was calculated at area of 100 μm from the defined surface.

Results

Figure 1 shows average concentration of uptake fluoride into dentin around each material at 100 μm depth area from superficial surface. FO and FL indicated high fluorine uptake.

Figure 2 shows the representative mapping images of calcium and fluorine on each material. Fluorine was distributed on dentin adjacent to materials and superficial area. FL and FO indicated high fluorine distribution.

Discussion

High concentration of fluorine was exhibited on FO and FL, because these two materials released large amounts of fluoride to water compared with SA and BC (unpublished data). Therefore, it is speculated that FO and FL were more effective in reducing the dental caries than other materials. However, FO was tended to have higher concentration than FL at PIGE analysis, though FL showed high amount of fluoride release than that of FO. This difference might be caused by the components of materials or pH value around materials.

Conclusion

Fluorine uptake is observed when fluoride-containing luting materials are used on dentin. The amount of fluorine distribution on dentin might be depend on amount of fluoride release from each material.

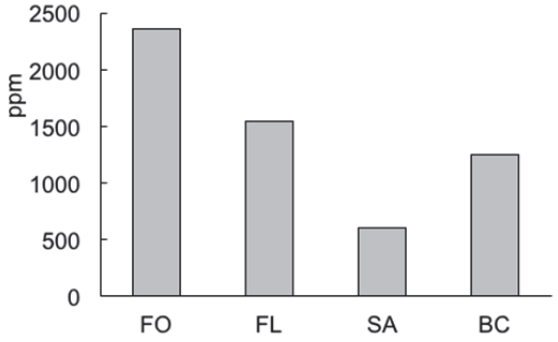

Fig. 1. Average concentration of distributed fluorine into dentin around each material at 100 μm depth area from superficial surface (ppm).

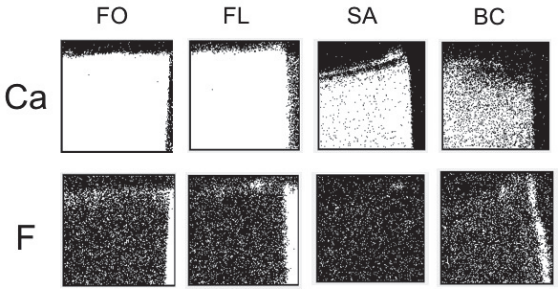

Fig. 2. Representative elemental PIXE/PIGE mapping images of each material. Upper images show calcium by PIXE. Middle images show fluorine by PIGE. White dots in the map represent PIXE(Ca)/PIGE(F) signals. Lower left image shows a schema of specimen, right image shows a CCD photo image of specimen mounted on PIXE/PIGE system.

References

[1] Y. Matsuda *et al.*, Dent. Mater. J. **24**, 280-85 (2006).
[2] H. Yamamoto *et al.*, Nucl. Instrum. Meth. Phys. Res. B **210**, 388-94 (2003).

2 - 31 Demineralize Prevention of Dentin With Fluoride Varnish via Automatic pH-cycling

Y. Matsuda [a)], K. Okuyama [b)], H. Yamamoto [c)], T. Saito [a)], Y. Tamaki [b)], M. Hayashi [c)], T. Satoh [d)] and M. Koka [e)]

[a)] School of Dentistry, Health Sciences University of Hokkaido,
[b)] School of Dentistry, Asahi University,
[c)] Graduate School of Dentistry, Osaka University,
[d)] Department of Advanced Radiation Technology, TARRI, QST,
[e)] Beam Operation Co., Ltd

Introduction

Fluoride varnishes are applied for preventing of dental caries. Recently, an experimented surface reaction-type pre-reacted glass-ionomer (S-PRG) filler has been developed. This material release such as sodium, boron, strontium, silica, aluminum, and fluorine. This study evaluated the demineralization preventing effect and distribution of fluorine of conventional fluoride varnish and S-PRG filler containing fluoride varnish on dentin surface via an automatic pH-cycling system, using Transversal Microradiography (TMR) method and in-air micro PIXE/PIGE system with a 3.0-MeV $^{1}H^{+}$ microbeam at TIARA.

Materials and Methods

Specimen preparation: 10 extracted human teeth were prepared. Four 200 μm thickness single-sections were obtained from each tooth. The polished surfaces, except the outer surface, were covered with wax. Two different conventional fluoride varnish (Enamel Pro® Varnish, Premier® (EP), Vanish™ 5% NaF White Varnish, 3M ESPE (WV)) and one fluoride varnish (S-PRG Varnish, SHOFU (S-PRG)) were applied on the root surface. No treated specimens were used as a control (Control). The pH-cycling system (pH 6.8 - 4.5) was carried out for four weeks in four beakers, which have ten specimens applied the same material, Control, EP, WV, and S-PRG. After pH-cycling [1], all specimens were taken TMR and integrated mineral loss (IML) were calculated from TMR images. Fluorine and calcium distributions of each specimen were evaluated using micro-PIGE/PIXE system at TIARA (Takasaki Ion Accelerators for Advanced Radiation Application, Takasaki JAPAN). The average fluorine concentration in each specimen was calculated at the area of 60 μm from the defined surface. Both data were analyzed by Kruskal–Wallis test ($p<0.05$).

Results

The IML of WV and S-PRG showed a significantly lower value than other two groups. For fluorine uptake, EP and S-PRG showed a significantly higher value than other two groups (Fig.1).

Discussion and Conclusion

In this study, EP and WV groups did not show both of demineralization prevent effect and fluorine uptake effect. Only, S-PRG filler contains fluoride varnish showed both of the demineralization preventing effect and provide fluoride to the dentin also. Therefore S-PRG filler which cloud release several ions will improve the fluorine uptake and the demineralization effect by fluoride varnish. These results suggested that several ions will affect fluorine uptake into the dentin and prevent the dentin demineralization. In addition, the effects of S-PRG filler other than fluoride release and inhibition of demineralization, such as antibacterial effects and protective effects against root dentin degradation applying S-PRG varnish should be investigated further.

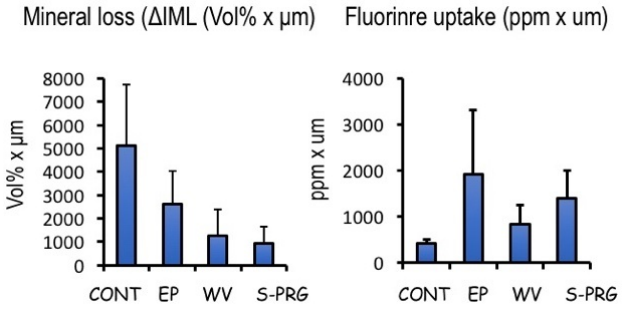

Fig. 1. The ΔIML for group WV and S-PRG significantly lower value comparing to that for CONT ($p<0.05$, Kruskal-Wallis test). There was no significant difference in ΔIML between group WV and S-PRG ($P > 0.05$). The F uptake for group EP and S-PRG had significantly higher value comparing to that for group WV and Cont ($p < 0.05$, Kruskal-Wallis test). There was no significant difference in fluorine uptake between group WV and CONT ($p>0.05$).

References

[1] Y. Matsuda *et al.*, Dent. Mater. J. **24**, 280-85 (2006).
[2] H. Yamamoto *et al.*, Nucl. Instrum. Meth. Phys. Res. B, **210**, 388-94 (2003).

2 - 32 Elemental and Immunohistochemical Analysis of the Lungs and Hilar Lymph Node in a Patient with Asbestos Exposure, A Pilot Study

Y. Koga [a)], T. Satoh [b)], K. Kaira [c)], M. Koka [e)], T. Hisada [a)] and K. Dobashi [d)]

[a)] Department of Medicine and Molecular Science, Graduate School of Medicine, Gunma University,
[b)] Department of Advanced Radiation Technology, TARRI, QST,
[c)] Department of Oncology Clinical Development, Graduate School of Medicine, Gunma University,
[d)] Graduate School of Health Science, Gunma University,
[e)] Beam Operation Co., Ltd

Studies have shown that inhaled mine dust, such as asbestos, can be translocated to various organs including the lymph nodes. However, little research has examined the concentration of these inhaled fibers in various organs or the mechanisms of their translocation. In this study, we compared the concentration of inhaled fibers in the lung parenchyma to the concentration in the hilar lymph node as well as to determine the elemental spatial distribution of the inhaled fibers in a patient with occupational asbestos exposure. Elemental analysis was performed by in-air micro-PIXE. Immunohistochemical analysis was performed using anti CD163 antibody. The analysis revealed that the amount of inhaled silicon was approximately 6 times higher in the lymph node than in the lungs. The immunohistochemical analysis showed localized agreement of the inhaled fibers with macrophages in the hilar lymph node. This study showed that in-air micro-PIXE could be useful for analyzing the elemental distribution and quantification of inhaled fibers in the human body.

はじめに

大気マイクロ PIXE（Particle Induced X-ray Emission）では、微量な肺組織を用いた元素分布の測定が可能である。そこで、肺内微粒子の分布メカニズムを検討するために、アスベスト吸入歴のある肺癌症例のパラフィン切片を用いて、肺内及び肺門部リンパ節の微粒子の分析を大気マイクロ PIXE により行った。また、同一のパラフィン切片を用いてマクロファージ表面マーカーの免疫染色を行い元素分布との関連性を検討した。

方法

肺切除検体のパラフィン切片にイオンマイクロビームを照射し、パラフィン切片内の元素分布を測定した。また、マクロファージの免疫組織染色には anti CD163 antibody を用いた。

大気マイクロ PIXE 分析は 3.0 MeV の水素イオンマイクロビームを用いて行った。ビーム径は約 1.0 μm、ビーム電流は 100 pA 以下であった。

結果

大気マイクロ PIXE 分析により、肺野より肺門部リンパ節のパラフィン切片から、約 6 倍の吸入されたシリカを検出した（Fig. 1）。また同じパラフィンブロックからのマクロファージの免疫染色でも、マクロファージの集積が肺門部リンパ節で高率に認められた（Fig. 2）[1]。

考察

大気マイクロ PIXE によって、同一組織検体のパラフィン切片を用いて患者の粉塵吸入の有無が推定でき、さらに免疫組織学検討を加えることによって、吸入された粉塵の生体内での移動メカニズムを解明する一助になる可能性が示唆された。

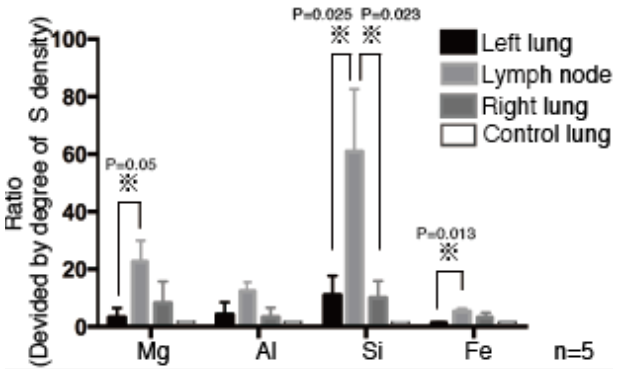

Fig. 1. Quantitative analysis of inhaled elements in the left and right lung parenchyma, lymph node, and control lung by in-air micro PIXE.

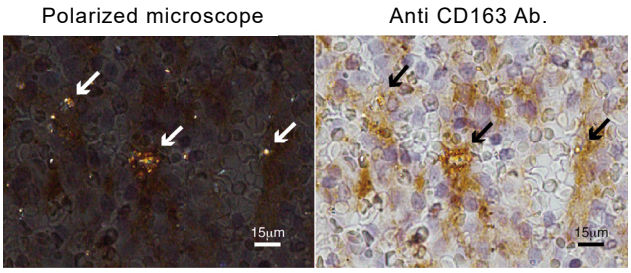

Fig. 2. High-power field images from the polarized microscope and the anti-CD163 staining of the hilar lymph node. White arrowheads indicate polarized elements. Black arrowheads indicate co-localized anti-CD163 antibodies.

Reference

[1] Y. Koga *et al.*, Environ. Health Prev. Med. **21**(6), 492-500 (2016).

2 - 33 Releasing of Carboplatin from Protamine-hyaluronic Acid Particles, Encapsulated in Lipid Nanocapsules

S. Harada [a)], T. Segawa [a)], S. Ehara [a)] and T. Satoh [b)]

[a)] Department of Radiology, School of Medicine, Iwate Medical University,
[b)] Department of Advanced Radiation Technology, TAARI, QST

Introduction

We have been developing drug delivery systems composed of nanoparticles that release anticancer drugs in response to radiation. First, tumors were treated with radiation, after which P-selectin antigen was induced in the irradiated tumor vessels. Second, nanoparticles labeled with P-selectin antibody were injected through the tail vein of mice. Third, particles accumulated in the tumor vessels through an antigen-antibody reaction. Fourth, the accumulated particles were irradiated and the anticancer drug was released into the tumor. The radiation and released anticancer drugs synergistically attack the tumor, increasing the anticancer effect. The localization of anticancer drugs reduced the adverse effects of the anticancer drugs. We previously generated particles by mixing solutions of protamine and hyaluronic acid, which bound electrostatically to produce fine particles (approximately 23 nm in diameter). However, when the particles were purified using a cellulose filter, the fine particles aggregated to form large particles (approximately 530 nm in diameter). Therefore, a new purification method is needed to prevent aggregation [1]. The coatsome is a lipid capsule that can encapsulate particles to prevent particle aggregation. In this study, we encapsulated particles into coatsomes and tested their ability to reduce particle size.

Materials and Method

First, 1.6 mg protamine and 1.28 mg hyaluronic acid were added to 2.0 mL of 1 mg/mL carboplatin (Pt containing anticancer drugs), and then reacted for 30 min at room temperature. Hyaluronic acid-protamine (HA-P) particles were generated by electrostatic interactions between protamine and hyaluronic acid. A 1.0-mL solution of these particles was mixed with a sample of coatsome 01-EL-1 (Nichiyu Corporation) and incubated for 15 min. Finally, encapsulated particles were centrifuged at 1,500 rpm for 20 min and then resuspended in 1.0 mL of distilled water. These particles were irradiated with 140-keV soft X-ray at a single dose of 10 Gy. The solution of particles was processed routinely and images were acquired using an in-air micro-PIXE camera with 3.0-MeV $^{1}H^{+}$ microbeam.

Results

The encapsulated nanoparticles were imaged using a micro PIXE camera, based on their Pt distribution (Fig. 1-A, B). The mean diameter of encapsulated particles was 342 ± 26 nm. Before irradiation, there were high points of Pt in the particles (Fig. 1-A). The number of high points of Pt was 26.2 ± 2.6 (mean ± SE) within 10 fields of a 12 × 12 μm-square area. After irradiation, the number of high points of Pt significantly decreased to 8.5 ± 6.7 (mean ± SE) as shown in Fig. 2.

These results indicate that the particles released carboplatin in response to radiation.

Discussion

By encapsulating HA-P particles into lipid capsules, particle sizes were slightly reduced, which prevent particles from being trapped into capillaries. The capsules released carboplatin in response to radiation. These features will lead to targeted delivery of carboplatin directed by radiation.

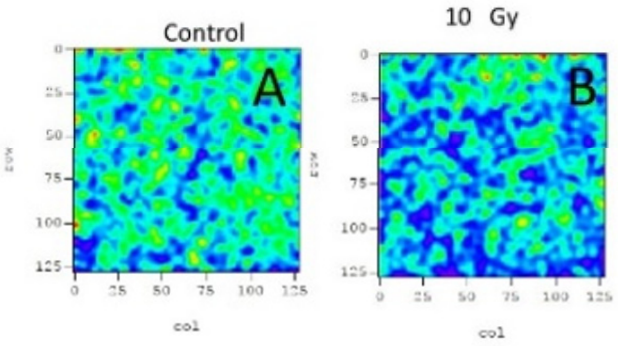

Fig. 1. Distribution of carboplatin, basing on Pt imaging. A: Before irradiation, B: After 10 Gy irradiation.

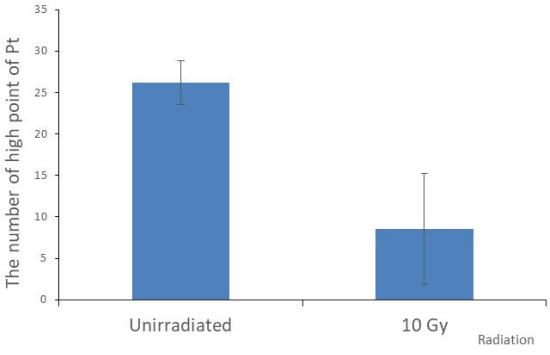

Fig. 2. The number of high points of Pt within 10 views of 12 × 12 μm-square area.

Reference

[1] S. Harada *et al.*, Int. J. PIXE **26**, 45-51 (2016).

2 - 34 Distribution Changes of Trace Elements in Rats Lung Microvascular Endothelial Cells Treated with Nicotine or Wakosil by In-Air Micro-PIXE Analysis

E. Sakurai [a, b], E. Sakurai [c], K. Yanai [b], S. Matsuyama [d], T. Hatakeyama [d], Y. Ueki [d], K. Ishii [d], M. Koka [e], T. Satoh [f] and T. Kamiya [g]

[a] Faculty of Pharmacy, Iwaki Meisei University,
[b] Department of Pharmacology, School of Medicine, Tohoku University,
[c] Faculty of Pharmaceutical Sciences, Tokushima Bunri University,
[d] Department of Quantum Science and Energy Engineering, Tohoku University,
[e] Beam Operation Co., Ltd,
[f] Department of Advanced Radiation Technology, TARRI, QST,
[g] Faculty of Science and Technology, Gunma University

Combination of seriously air pollutants and smoking have unknown risks to our health. Lung microvascular endothelial cells (LMECs) act as a barrier to protect from dangerous matter such as PM2.5 or nicotine. Kelly *et al.* was reported that Nicotine exposures triggered dose-dependent loss of endothelial barrier in cultured cell monolayers and rapidly increased lung inflammation and oxidative stress in mice [1]. Our previous reports showed that the amount of trace metal as components of superoxide dismutase (SOD) were increased in a time-dependent on mice LMECs treated with 0.2 mM nicotine [2]. These results suggest that the existence of SOD is an antioxidant-related enzyme in LMCs. It is well known that an air pollutants and smoking is the most risk factor for respiratory disorder. However, nobody knows the distributions of trace elements in LMECs by PM2.5 or nicotine. In this study, we succeed in culturing LMECs from mice and rats on the polycarbonate membrane, and analyzed them with an in-air micro-PIXE analyzer which can quantitatively measure the distribution of trace elements in the cells or tissue slices.

Three-weeks-old male SD rats purchased from Japan SLC. These SD rats were isolated using a modification of the technique described by Magee *et al.* [3]. The procedures of cell culture on collagen-coated polycarbonate film (2.54 cm^2) for microanalysis were described in previous reports [2]. The cells were first washed two times with 1 mL of Krebs buffer, and pre-incubated with 0.9 mL of Krebs buffer at 37 ºC for 5 min. Then, Krebs buffer containing 0.2 mM nicotine or 0.0047 mg wakosil® (silica gel as a model of PM2.5) were added to each film, and cells were incubated for 5 min. The cells on the 5-μm-thick polycarbonate films were washed 7 times with THAM buffer. The specimens were promptly dipped into 2-methylbutane and chilled with liquid nitrogen, and then freeze-dried overnight in the vacuum stage [2]. In-air micro-PIXE analysis of these samples was performed using 3-MeV $^1H^+$ microbeam at TIARA facility.

Figure 1 shows the trace elements images (50 × 50 μm^2) analyzed by micro-PIXE. The third row showed the image of rats LMCEs treated with 0.2 mM nicotine and wakosil. Sulfur was induced by stimulation of both materials. This phenomenon may indicate signal of an inflammation [4].

Comparison of the trace elements levels in the LMECs were shown in Fig. 2. Potassium level is usually existence higher inside the cells than outside of the cells. However, in the case of LMECs treated with nicotine and Wakosil, the levels of potassium were significantly degreased, and sulfur levels were extremely high with this case. These results suggest that nicotine maybe induce loss of lung endothelial barrier function.

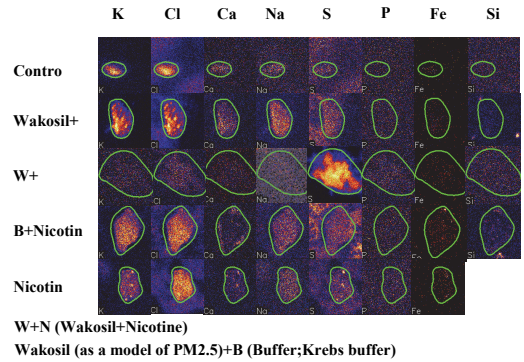

Fig. 1. Distributions images (50 μm × 50 μm) of potassium, chloride, calcium, sodium, sulfur, phosphorus, iron, silicon after addition of 0.2 mM nicotine or wakosil on rats LMECs.

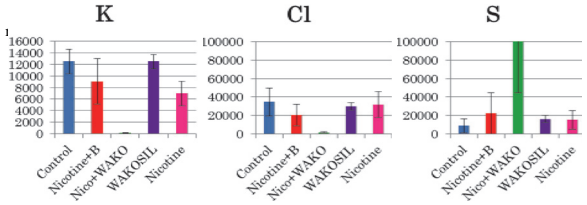

Fig. 2. A trace elements levels of potassium, chloride and sulfur in the LMECs treated with 0.2 mM nicotine or Wakosil for 5 min.

References

[1] S. Kelly *et al.*, Am. J. Physiol. Lung Cell Mol. Physiol., **309**, L175-87 (2015).
[2] E. Sakurai *et al.*, JAEA Takasaki Annu. Rep. 2014, JAEA-Review 2015-022, 82 (2016).
[3] E. Sakurai *et al.*, Am. J. Physiol. Lung Cell Mol. Physiol., **282**, L1192-7 (2002).
[4] E. Sakurai *et al.*, JAEA Takasaki Annu. Rep. 2006, JAEA-Review 2007-060, 182 (2008).

2 - 35 Analysis of Trace Elements in Multiple Myeloma Cell Line Using In-Air Micro-PIXE

T. Kasamatsu, T. Nagashima and H. Murakami

Graduate School of Health Sciences, Gunma University

After the induction of auto-hematopoietic stem cells transplantation and novel agents such as thalidomide and proteasome inhibitor, overall survival of multiple myeloma (MM) patients have improved from 3 to 5 years. However, the disease become resistant to chemotherapy and is incapable of being cured in most patients. To evaluate the influence of proteasome inhibitor (bortezomib), we analyzed the trace elemental changes in myeloma cell using in-air micro-PIXE method.

One human myeloma cell line, KMS-11, was used in this study. KMS-11 cell were grown in RPMI with 10% heat-inactivated fetal bovine serum, and antibiotics. These cells were treated with 0 nM, 20 nM and 50 nM bortezomib for 18 hours and with 50 μM melphalan, which are alkylating agents, for 18 hours. The cells were centrifuged by cytocentifuge for 500 rpm, 15 minutes on a 0.5 μm polycarbonate film after washing and resuspension in TRIS-HNO_3 (pH 7.4). The film was sunk into isopentane chilled with liquid nitrogen down to its melting point (-160 ºC), then lyophilized by vacuum evaporation at 1.3 Pa. A 3.0-MeV proton microbeam having 1 μm diameter were generated by the TARRI single-ended accelerator at the National Institutes for Quantum and Radiological Science and Technology, Takasaki, and was used for the in-air micro-PIXE analysis.

In an X-ray spectrm derived from KMS11, calcium yield was higher in 50 nM bortezomib treatment cells than 0 nM and 20 nM bortezomib and 50 μM melphalan treatment cells (Fig. 1). Other elemental yields were almost similar among four treatment groups.

We compered the distribution of P, S, Cl and Ca using elemental maps of KMS11 after treatment. The distribution of four elements was similar among 0 nM, 20 nM bortezomib treatment and 50 μM melphalan treatment. However, P form of 50 nM bortezomib treatment cells was fragmentary. Moreover, we observed that Ca distribution of 50 nM bortezomib treatment cells was accumulated in its nucleus (Fig. 2).

Bortezomib inhibits proteasome, and it lead to the cell death via cell endoplasmic reticulum stress (ER stress). The Ca ion is stored to the endoplasmic reticulum mainly in the cell, and Ca ion is emitted in cytoplasm by ER stress [1]. Subsequently, apoptotic instruction factors such as cytochrome C are released by mitochondria. Our result suggested that the change of Ca may affect the efficacy of bortezoomib in the MM cells.

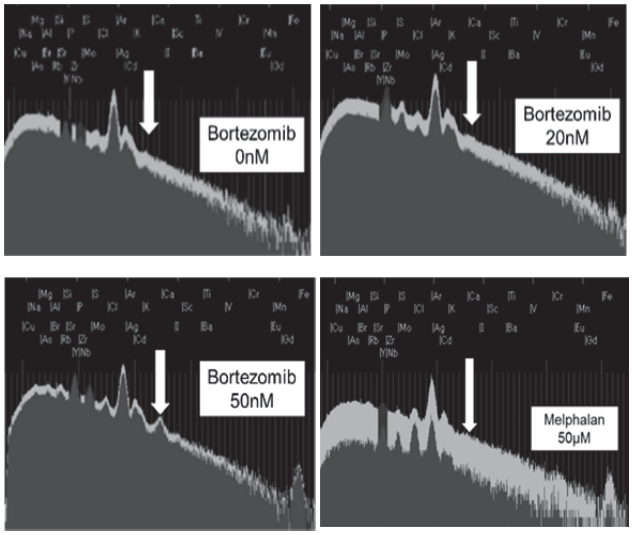

Fig. 1. Representative X-ray spectrum derived from KMS11 after treatment. Dark gray zone means spectrum of single cell.

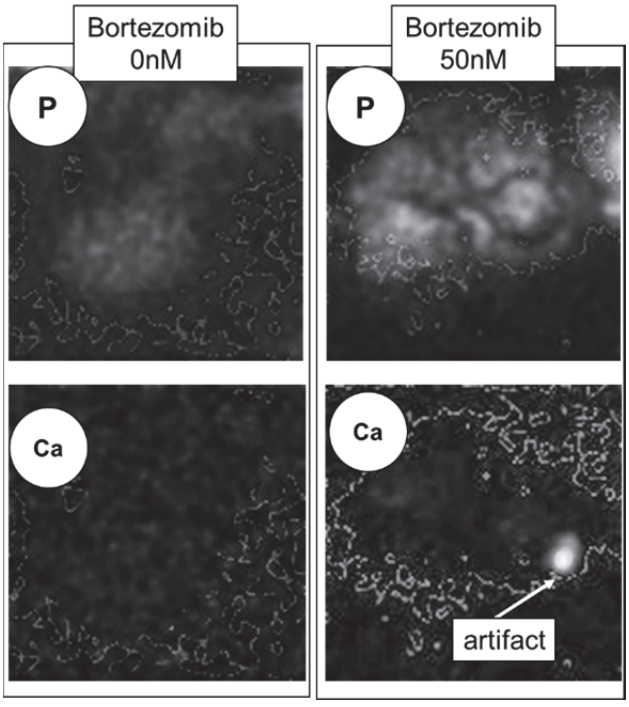

Fig. 2. P and Ca Elemental map of KMS11 after 0 nM and 50 nM bortezomib treatment.

Reference

[1] S. Orrenius *et al.*, Nat. Rev. Mol. Cell Biol. **4**, 552-65, (2003).

2 - 36 Iron Localization in Root Tips of *Lotus japonicus* Using Micro-PIXE

J. Furukawa [a)], Y. Noda [a)], N. Yamada [b)], T. Satoh [b)] and S. Satoh [a)]

[a)] Life and Environmental Sciences, University of Tsukuba,
[b)] Department of Advanced Radiation Technology, TARRI, QST

Plants need various elements for its growth. Not only major elements, such as nitrogen, phosphorous and potassium, but many essential trace elements are needed for plant development. The analysis of trace element content and localization in the focused organ or tissue is important to identify its functions. Especially the localization of trace elements in the tissue level is highly valuable for investigating where the deficiency or toxicity of elements is detected and how to control the mechanisms for keeping homeostasis of plant body. Micro-PIXE (Particle Induced X-ray Emission) method can detect multi-element distributions in the same sample and visualize those localizatons with high-resolution images [1, 2]. In this study, iron (Fe) localization in the roots of *Lotus japonicus* was focused. *L. japonicus* is a model legume and its two experimental lines, MG-20 and B-129, have a diversity in some metal concentrations including Fe in seed [3]. For understanding the mechanisms related to this Fe accumulation variety, the concentration and localization of Fe was investigated.

After the 4-week-cultivation of MG-20 and B-129 with hydroponics using 1/10 Hoagland's solution, above ground shoot part and root were harvested. After the digestion with HNO_3, Fe concentrations of two lines were compared using ICP-AES. The Fe concentrations were indicated in Table 1. Fe concentration in shoot was higher in MG-20, but its concentration in root was obviously higher in B-129. These Fe allocation pattern suggests the Fe translocation activity from root to shoot is low in B-129.

As for the Fe translocation from soil to shoot, some transmembrane steps are needed, such as uptake into the root cell and xylem loading around the vascular bundles. To identify what kind of steps are involved in the suppression of Fe translocation from root to shoot in B-129, Fe localization analysis using Micro-PIXE was carried out. As for the Fe imaging, the samples were embedded in the compound for a freeze section and sliced to 30 μm sections by freezing microtome and then exposed by 3 MeV H^+ beam. In the MG-20 root, the spectrum of Fe was not observed, however, B-129 sample showed the Fe accumulation around the root surface and center of the root (Fig. 1). For indicating the root structure more in detail, potassium (K) image was obtained with the same sample. Comparing the Fe and K localization, it was revealed that the center part where Fe was accumulated was vascular bundles.

These results indicated that the steps of Fe translocation suppressed in B-129 were both in Fe uptake at the root surface and Fe loading around the vascular bundles. In the *Arabidopsis*, it was known that loss of FRD3, which is a citrate xylem loading transporter, was resulted in the Fe deficiency in shoot part [4, 5]. The Fe ion in the xylem vessels are chelated by citrate and this chelate complex is necessary for long distance Fe transport to shoot [5].

Based on the Fe localization within the root tissue, the candidate mechanisms involved in the Fe deficiency in B-129 shoot was obtained. To identify the responsible genes of this suppression, the expression levels and gene structures of some genes including Fe uptake gene, IRT1, Fe xylem loading transporter and citrate xylem loading transporter, FRD3, will be investigated as a next study.

Table 1
Iron concentration in shoot and root of two *L. japonicus* lines, MG-20 and B-129.

Element	Line	Concentration (nmol / g D.W.)			
		Shoot		Root	
		Average	S.D.	Average	S.D.
Fe	MG-20	1293.5	122.2	1905.9	247.1
	B-129	810.8	80.6	3254.2	473.6

D.W. : Dry weight, S.D. : Standard deviation (n = 5).

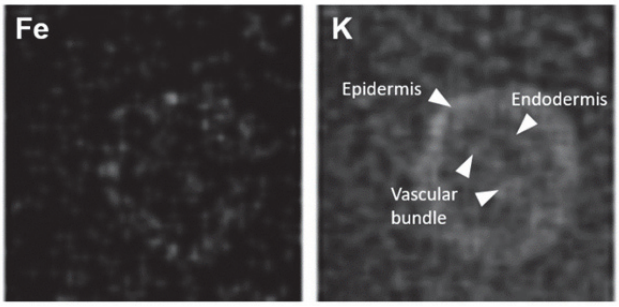

Fig. 1. Iron and potassium localization in root tip of B-129 line with Micro-PIXE.

References

[1] T. Yamamoto *et al.*, JAEA Takasaki Annu. Rep. 2014, JAEA-Review 2015-022, 88 (2016).
[2] Y. Noda *et al.*, QST Takasaki Annu. Rep. 2015, **QST-M-2**, 151 (2017).
[3] M. A. Klein and M. A. Grusak, Genome **52**, 677-91 (2009).
[4] E. Delhaize, Plant Physiol. **111**, 849-55 (1996).
[5] T. P. Durrett *et al.*, Plant Physiol. **144**, 197-205 (2007).

2 - 37 Effects of Chloride Ions on Cadmium Behaviors in Sorghum Plants

S. Nakamura [a)], N. Suzui [b)], Y.-G. Yin [b)], S. Ishii [b)], S. Fujimaki [b)] and N. Kawachi [b)]

[a)] Faculty of Life sciences, Tokyo University of Agriculture,
[b)] Department of Radiation-Applied Biology Research, TARRI, QST

Cadmium (Cd) is one of toxic heavy metals. Cd, taken via foods, has negative effects on our health. So, we need to decrease Cd content in agricultural soils to cultivate farm products with low levels of Cd. Phytoremediation is one of expectable technologies for removing cadmium (Cd) from agricultural soils. To remove Cd from these soils effectively, more Cd should be transported from roots to the shoot organs for later harvest. Sorghum plants (*Sorghum vulgare* L.) have a high shoot biomass. Therefore, sorghum plants are expected to be a clean-up plant to recover more Cd from cultivated soils. In our research, we confirmed effects of chloride ions in the root zone on Cd behaviors in sorghum plants. We tried to elucidate the molecular mechanisms of Cd transport in sorghum plants by analyzing the experimental data which is obtained from Positron Emitting Tracer Imaging System (PETIS) experiments.

^{107}Cd (half-life 6.5 h) was used as a positron emitter in our PETIS experiments. ^{107}Cd was produced as previously described [1, 2]. Purified ^{107}Cd was dissolved in an appropriate volume of culture solution with or without 1 mM KCl. In these PETIS experiments, Two-week-old seedlings, grown hydroponically in a growth chamber which can control plant growth condition completely, were used. After setting test plants in an experimental apparatus, PETIS experiments were started by adding a total of 0.1 μM Cd including ^{107}Cd to each culture solution. Images of the ^{107}Cd distribution in sorghum plants were obtained every 4 minutes for 32 h. Time-activity curves, temporal changes of ^{107}Cd signals in specific regions of interest (leaves, roots and so on) were generated from these PETIS data, following the methods of *Nakamura et al.*, 2013 with a small modification.

We could obtain fine serial images of Cd transport in sorghum plants (Fig. 1). Strong signals of ^{107}Cd were found in the basal region of shoots. These Cd accumulation patterns resemble those in rice plants [2]. ^{107}Cd in KCl treated plants moved to shoots more rapidly than that in control plants (Fig. 1). Time courses of ^{107}Cd signals were established in roots of sorghum plants (Fig. 2). In these roots, ^{107}Cd accumulated following its addition to the culture solution. There was a significant difference in the pattern of ^{107}Cd increase in roots. Accumulation of ^{107}Cd signals in roots of KCl treated plants increased sharply than that of control plants (Fig. 2).

Weggler *et al.* 2004 reported Chloride ions in soil solution have effects on Cd concentration in soil solution and Cd availability for plants. In our PETIS experiments, plants were treated in culture solutions. All Cd in these solutions were available to test plants. These experimental results demonstrated that chloride ions might be working at plant roots for absorbing Cd in roots and transporting Cd to shoots.

References

[1] N. S. Ishioka *et al.*, JAEA Takasaki Annu. Rep. 2005, JAEA-Review 2006-042, 162 (2007).
[2] S. Fujimaki *et al.*, Plant Physiol., **152**, 1796-806 (2010).
[3] S. Nakamura *et al.*, J. Exp. Bot., **64**, 1073-81 (2013).
[4] K. Weggler *et al.*, J. Enviorn. Qual., **33**, 496-504 (2004).

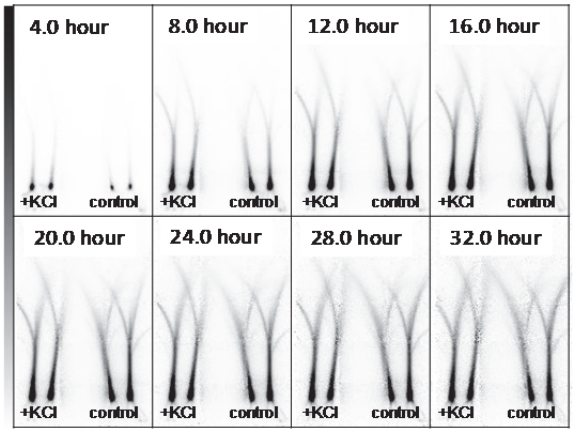

Fig. 1. Time series of PETIS images showing the ^{107}Cd signal (0 - 32 h) after decay correction. All plants are exposed to ^{107}Cd in the root medium. Two plants on the left were treated with 1.0 mM KCl.

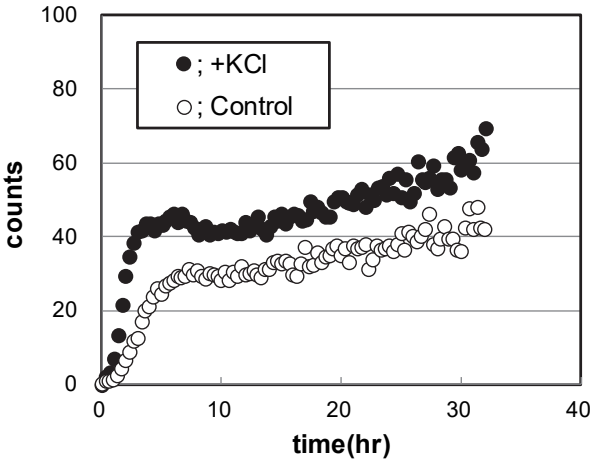

Fig. 2. Time-course analyses of ^{107}Cd signals accumulation in roots of sorghum plants. This graph indicates the intensity of ^{107}Cd signals after decay correction.

2 - 38 A Simulation Study on Imaging of a Proton Beam Using a Pinhole Camera Measuring Low-energy Photons

M. Yamaguchi , Y. Nagao and N. Kawachi

Department of Radiation-Applied Biology Research, TARRI, QST

Noninvasive monitoring techniques of trajectories of incident ions are important to realize precise dose control for particle therapies. Recently, we proposed a new method by measuring low-energy photons, that mainly consist of secondary electron bremsstrahlung (SEB) photons [1, 2]. Although the method was proposed for carbon ion therapy, it might also be useful for proton one. In this work, a Monte Carlo study was performed to evaluate the feasibility of proton-beam imaging using a pinhole camera for X-ray.

Simulations were performed on a supercomputer system at the Japan Atomic Energy Agency (JAEA). The utilized simulation code was the Particle and Heavy Ion Transport code System (PHITS) [3] version 2.82.

Figure 1 shows a three-dimensional view of the simulation geometry. A right-hand system of a Cartesian coordinate was defined in the simulation space. The axis of the proton beam having an infinitesimal diameter was set to the *x*-axis of the system, and the direction of the movement of the incident protons was set to the positive of the *x*-axis. The injection energy of the proton beam was 139 MeV. The *y*-axis was set to be perpendicular to a horizontal plane and the positive of the *y*-axis was set upward.

A water phantom consisted of a ceiling-opened container and water in the container was placed in the simulation space. The container was composed of five 0.5-cm-thick acrylic (polymethyl methacrylate) boards. The length, height and width of the outside of the container were 20, 20, and 10 cm, respectively. The phantom has a 2-fold rotational symmetry around the *y*-axis. The center of gravity of the phantom located along the *y*-axis and the shortest sides of the phantom were parallel to the *z*-axis. The heights of the surface of the water and the beam axis from the base of the container were 10 and 5 cm, respectively.

A pinhole camera consisted of a tungsten shield having a pinhole collimator with an opening angle of 30º and a $2 \times 2 \times 0.1$ cm^3 board of cerium-doped gadolinium aluminum gallium garnet (GAGG) was placed in the simulation space. The camera has a 4-fold symmetry along the *z*-axis. The center of the pinhole was placed 100 cm apart from the center of the phantom. A sensitive volume having the size of $0.687 \times 0.687 \times 0.1$ cm^3 was set to a GAGG region. The volume was partitioned into 28×28 matrix. Distribution of energy deposition in the volume was recorded for each cell of the matrix. The image of the phantom was acquired by recording distribution of energy deposition in each pixel in the matrix of the GAGG board during the beam injection. The field of view (FOV) of the camera at the center of the phantom corresponded to a 13.1×13.1 cm^2 square. The FOV area was divided into 28×28 pixels by the partitioning of the sensitive volume of the GAGG detector.

Figure 2 represents the resultant image by the simulation, where the lower and upper thresholds of the energy deposition were set to 30 and 60 keV, respectively. We found that the beam trajectory, which locates from the beam-injection surface ($x = -10.0$ cm) to the proton-range position ($x = 3.8$ cm) along the *y*-axis, was clearly visible in the image.

In conclusion, we evaluated the feasibility of the proton beam imaging using a pinhole X-ray camera by means of the Monte Carlo simulations. The simulation study showed that the beam trajectory was clearly imaged by SEB observation using a pinhole camera.

References

[1] M. Yamaguchi *et al.*, Phys. Med. Biol, **57**, 2843-56 (2012).

[2] M. Yamaguchi *et al.*, Phys. Med. Biol., **61**, 3638-44 (2016).

[3] T. Sato *et al.*, J. Nucl. Sci. Tech., **50**, 913-23 (2013).

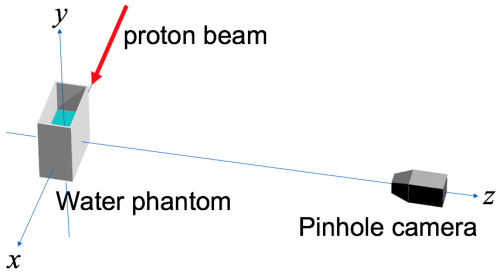

Fig. 1. A three-dimensional view of the simulation geometry.

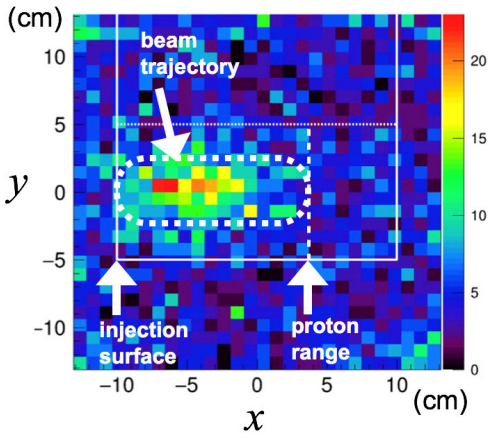

Fig. 2. The resultant image by the simulation. White solid and dotted lines represent the edges of the water phantom and the surface of the water, respectively.

2 - 39 Estimation of the Kinetics of Nutrient Uptake Using Positron Imaging Data

N. Suzui, Y.-G. Yin, S. Ishii and N. Kawachi

Department of Radiation-Applied Biology, TARRI, QST

The kinetics value (*K*m and *V*max) of nutrient uptake is one of the most important information in order to understand the mechanism of nutrient acquisition in plant. To estimate the kinetics value, uptake velosities of numerous plants in various concentrations of nutrient elements should be determined using ICP-MS. In this study, we have attempted to estimate the kinetics of nutrient uptake noninvasively using positron imaging data of few plants.

To experimentally determine the uptake kinetics of zinc, which is one of the essential nutrient elements, the roots of five rice plants were inserted in a transparent acrylic root box specialized for direct root imaging (Fig. 1). Each compartment of the root box was supplied with 14 mL of 0.5 mM $CaCl_2$ containing different concentrations (0.1, 0.25, 0.5, 1 and 2.5 μM) of $ZnSO_4$, labeled with 124 kBq of ^{65}Zn and the ^{65}Zn movement from the solution to the roots was monitored by PETIS for 7 h. The solution was continuously stirred with gentle aeration in order to maintain a uniform composition in each compartment of the root box. The uptake velocities for the various zinc concentrations were calculated every hour using the imaging data acquired from the individual rice plants. The obtained substrate velocity data were fitted with the modified Michaelis-Menten equation according to Claassen and Barber (1974) [1]. *V*max and *K*m value were estimated by least-square regression.

We obtained serial images and quantified zinc uptake in non-dwarf plants for various initial zinc concentrations (0.1 - 2.5 μM; Fig. 2). The corresponding zinc uptake velocities were calculated from the decrease in zinc observed in the solution every hour (six values from each plant). The obtained substrate velocity data (30 values in total) were fitted by the modified Michaelis-Menten model (Fig. 3) and the values of Vmax and Km value were estimated to be 11.4 ± 1.9 nmol (g root fresh weight)$^{-1}$ h^{-1} and 1.1 ± 0.4 μM, respectively (R^2 value: 0.91).

The approach in this study has the advantage of obtaining several substrate-velocity data measurements from one plant without continuous sampling. Principally, the uptake kinetics of a nutrient element can be estimated from the depletion curve of one plant [1]. The development of this analytical method makes it possible to estimate the *K*m and *V*max value from an individual plant.

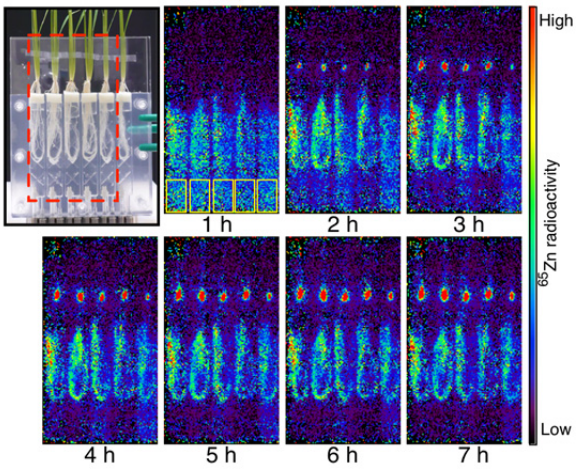

Fig. 1. Serial images of ^{65}Zn uptake by rice plants fed with different initial zinc concentrations. The yellow rectangles indicate the regions examined for the time course analysis.

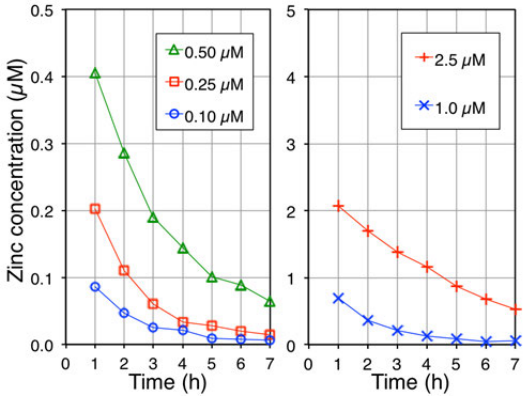

Fig. 2. Time course of the zinc concentration in the solution for the different solutions.

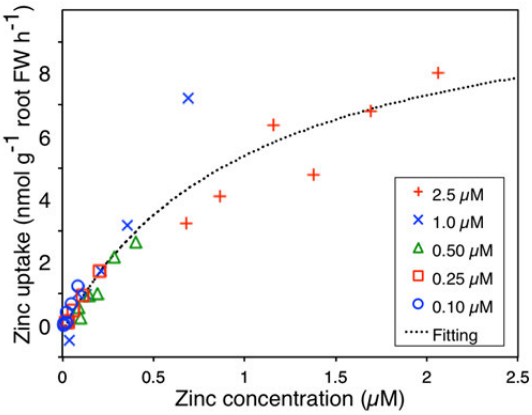

Fig. 3. Scatter plot of the uptake velocity as a function of zinc concentration.

Reference

[1] N. Claassen and SA. Barber, Plant Physiol., **54**, 564-68 (1974).

2 - 40 Application of ^{67}Cu Produced with Accelerator Neutrons to the Biodistribution Study

Y. Sugo [a, b], K. Hashimoto [b], M. Kawabata [c], H. Saeki [c], K. Tsukada [d], Y. Hatsukawa [b] and Y. Nagai [b]

[a] Department of Radiation-Applied Biology Research, TARRI, QST, [b] Tokai Quantum Beam Science Center, TARRI, QST, [c] Chiyoda Technol Corporation, [d] Advanced Science Research Center, JAEA

The radioactive copper ^{64}Cu and ^{67}Cu are promising radionuclides for positron emission tomography (PET) imaging and internal radiotherapy of cancer, respectively. In the previous studies, it was demonstrated that the cancer was successfully visualized on the PET images of tumor-bearing mice using ^{64}Cu ions ($^{64}CuCl_2$) without any labeling process [1]. We also developed a new method to produce a large amount of ^{67}Cu from ^{68}Zn irradiated with fast neutrons, which were obtained by the irradiation of Be with 50 MeV deuterons using AVF cyclotron [2]. In order to apply ^{67}Cu produced via the ^{68}Zn(*n, n'p+d*) ^{67}Cu reaction to the therapeutic radiopharmaceuticals, we investigated the biodistribution of ^{67}Cu ions ($^{67}CuCl_2$) in tumor-bearing mice in this study.

An isotopically enriched ^{68}ZnO (99.94%) pellet was irradiated with accelerator neutrons for 10 h to afford 17 MBq ^{67}Cu at the end of irradiation (EOI). The chemical separation of ^{67}Cu from the irradiated ^{68}Zn target was performed by three steps using a cation-exchange column (AG50W), a chelating ion-exchange column (Chelex-100), and an anion-exchange column (AG-1-X8), which was slightly modified the previous method [3]. The recovery efficiency and radionuclide purity of ^{67}Cu were 91% and 99.8%, respectively. The specific activity of ^{67}Cu was determined to be 4.5 MBq/μg at EOI by the titration method [4] using 1,4,7,10-tetraazacyclododecane-1,4,7, 10-tetraacetic acid.

In the biodistribution study, tumor-bearing mice were prepared by subcutaneous injection of human colon adenocarcinoma (LS180) cells (5×10^6 cells) into the dorsal flank of male nude mice. When the tumors were palpable after 2 w, the mice were intravenously injected with 35 or 50 kBq $^{67}CuCl_2$ dissolved in 100 μL saline via the tail vein. After the mice were sacrificed at 0.5, 1, 4, 8, 24, and 48 h post-injection, their blood, tumors, and other tissues (liver, kidney, intestine without content, etc.) were collected. The collected samples were weighed, and their radioactivities were measured with a well-type NaI(Tl) detector.

It is common in biodistribution studies to express the percentage of accumulation using the parameter of %ID/g, which is percentage of injected dose per weight of each tissue. Results of the biodistribution of $^{67}CuCl_2$ in LS180 tumor-bearing mice are shown in Fig. 1, where each error bar indicates the standard deviation (n=4). High uptake of ^{67}Cu was observed in the tumor as well as in the liver which is the major organ for copper metabolism. Changes in %ID/g as a function of time after injection showed that ^{67}Cu uptake in the liver was gradually reduced with progression of time, whereas accumulation of ^{67}Cu in the tumor was increased.

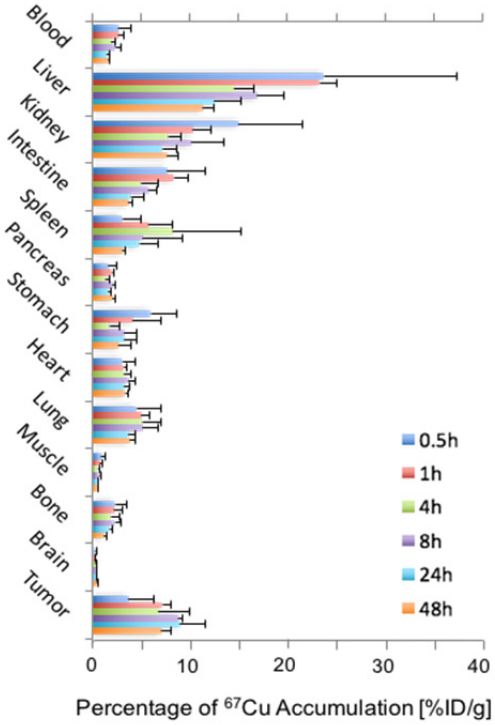

Fig. 1. Biodistribution of $^{67}CuCl_2$ in LS180 tumor-bearing mice.

The result showing high specific uptake of ^{67}Cu in the tumor suggests that $^{67}CuCl_2$ can be a potential radionuclide agent for cancer radiotherapy. It was also confirmed that the quality of ^{67}Cu produced by accelerator neutrons was sufficient for the biodistribution study [5].

Acknowledgements

We would like to gratefully thank all the members of Medical Radioisotope Application Research Project for their continuous support and useful discussions. Acknowledgement is also due to the operating crew of TIARA facility.

References

[1] Y. Sugo *et al.*, QST Takasaki Annu. Rep. 2015, **QST-M-2**, 144 (2017).
[2] K. Tsukada *et al.*, ibid., 146 (2017).
[3] M. Kawabata *et al.*, J. Radioanal. Nucl. Chem. **303**, 1205 (2015).
[4] D. W. McCarthy *et al.*, Nucl. Med. Biol. **24**, 35 (1997).
[5] Y. Sugo *et al.*, J. Phys. Soc. Jpn. **86**, 023201 (2017).

2 - 41 Purification by Resin Method of High Radionuclidic Purity ^{89}Zr Produced by Cyclotron

R. Imura [a)], S. Noda [a)], H. Ida [a)], N. Yukitake [a)], Y. Mizukawa [a)], K. Osaki [a)], S. Watanabe [b)] and N. S. Ishioka [b)]

[a)] JFE Engineering Corporation,
[b)] Department of Radiation-Applied Biology Research, TARRI, QST

There is growing worldwide interest in the production of long-lived positron emitters such as ^{124}I, ^{64}Cu, ^{89}Zr and ^{86}Y for targeted molecular imaging via positron emission tomography (PET). In particular, ^{89}Zr is receiving much attention because its relatively long half-life ($t_{1/2}$ = 3.27 days) is well-suited for immuno-PET systems for tracking and quantification of mAbs by PET *in vivo*. Furthermore, ^{89}Zr emits a low-energy positron ($E_{\beta+}$ = 0.40 MeV) that is favorable for high spatial resolution in PET, with an adequate branching ratio for positron emission (BR = 23%). In this study, we investigate the irradiation conditions and purification methods for the development of immuno-PET systems.

^{89}Zr was produced via the ^{89}Y(p, n)^{89}Zr reaction by proton bombardment of a ^{89}Y foil target (100% natural abundance) on the Takasaki Ion Accelerator for Advanced Radiation Application (TIARA). The irradiation conditions were incident proton beam energy: 20 MeV, beam current: 1 μA, irradiation time: 1 h. In order to prevent generation of byproducts such as ^{88}Zr, the incident energy of the proton beam on the Y targets was adjusted by Al degraders, whose thickness was optimized by the PHITS code [1]. The irradiated Y targets were dissolved in hydrochloric acid, and the radionuclidic purity of the irradiated Y targets was determined by gamma spectroscopy. The dissolved target solution was purified by a resin method.

The experimental cross-sectional data of the ^{89}Y(p,n)^{89}Zr and ^{89}Y(p, 2n)^{88}Zr reactions are shown in Fig. 1, which indicate that only the ^{89}Y(p, n)^{89}Zr reaction occurs when the incident proton energy is 6-13 MeV. The cross-sectional data determined by PHITS supported this result. The thickness of the Al degraders and Y targets optimized by PHITS were 1.2 mm and 0.6 mm, respectively (the proton energy in the Y targets was 6.8-12.4 MeV). Figure 2 shows the attenuation of proton energy in the Al degraders and Y targets under irradiation with a 20 MeV proton beam. After irradiation, the Y targets were dissolved in hydrochloric acid and Ge detector measurements were conducted. The measured spectrum of gamma ray energy is shown in Fig. 3. There were only ^{89}Zr energy peaks, and other radionuclides (^{88}Zr, ^{88}Y etc.) were not observed. Purification of the irradiated Y target was conducted by the resin method reported by Holland *et al*. [3]. In every purification experiment, > 99.5% of the ^{89}Zr activity remained trapped on the resin, and elution of ^{89}Zr was achieved with >98% recovery of the radioactivity.

References

[1] T. Sato *et al.*, J. Nucl. Sci. Tech. **50**, 913-23 (2013).
[2] M. G. Mustafa *et al.*, Phys. Rev. C, **38**, 1624 (1988).
[3] J. Holland *et al.*, Nucl. Med. Biol., **36**, 729-39 (2009).

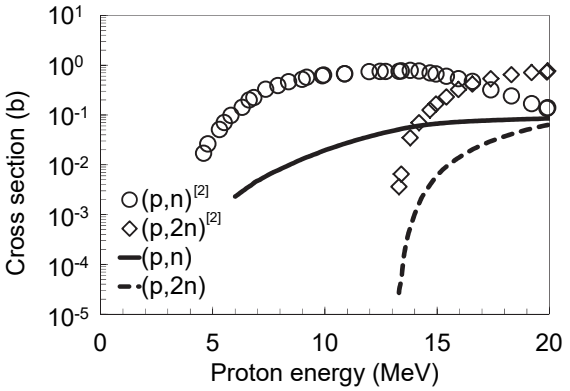

Fig. 1. Cross-sectional data for ^{89}Y(p, n)^{89}Zr and ^{89}Y(p, 2n)^{88}Zr reactions by experiments (plots) and PHITS calculation results (lines).

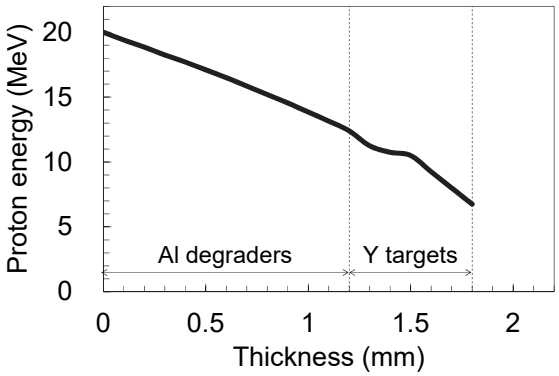

Fig. 2. Penetrating proton energy in Al degraders and Y targets.

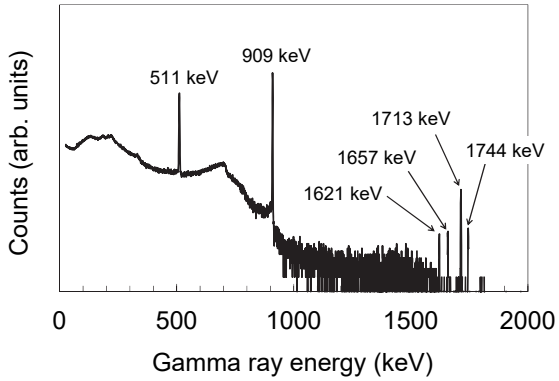

Fig. 3. Energy spectrum of gamma ray emitted from irradiated Y target in hydrochloric acid.

Prat II

3. Advanced Quantum-Beam Technology

3 - 01 Development of Wavelength Dispersive IBIL Detector Based on Multichannel Photomultipliers

W. Kada [a)], S. Kawabata [a)], R. K. Parajuli [b)], T. Satoh [c)], M. Koka [c)], N. Yamada [c)], K. Miura [a)], O. Hanaizumi [a)] and T. Kamiya [a)]

[a)] Faculty of Science and Technology, Gunma University,
[b)] Graduate School of Medicine, Gunma University,
[c)] Department of Advanced Radiation Technology, TARRI, QST

Recently, there has been increasing interest in complimentely analysis techiqnue for particle induced x-ray emission (PIXE). Ion beam induced luminescence (IBIL) analysis is one of these candidate which is useful for determining chemical compositions [1, 2]. However, IBIL spectra of organic compounds rapidly change during irradiation, and most IBIL analytical systems with conventional spectrometer has a typical response speed of several milliseconds. These factors negatively affect and it would be ideal to accompalish wavelength-dispersive IBIL at scan speeds comparable to that of microbeam probes used for micro-PIXE analysis.

In this study, we developed high-speed wavelength-dispersive IBIL detector. Figure 1 shows the picture of developed detector unit. This detector is consist of a 32-channel photomultiplier array, a high-efficiency optical grating, and an integrated electrical circuit based on a field-programmable gate array (FPGA). LVDS signals are generated by incident of individual IBIL photons to the photomultiplier array. Each channels correspond to different wavelength by calibrating the position of grating. Then 32 channel LVDS signals were processed and multiplexed in the FPGA unit and analog pulses with different amplitude corresponding to the channel number of the array was outputed from the unit to conventional signal chain for micro-PIXE analysis. The analog pulse signal had a pulse width of 2 μs in the amplitude range upto 10 V. Newly developed IBIL detector was then evaluated at external proton microbeam setup for in-air micro PIXE analysis on a micro-beam line of the 3 MV single-ended accelerator facility at TIARA, QST.

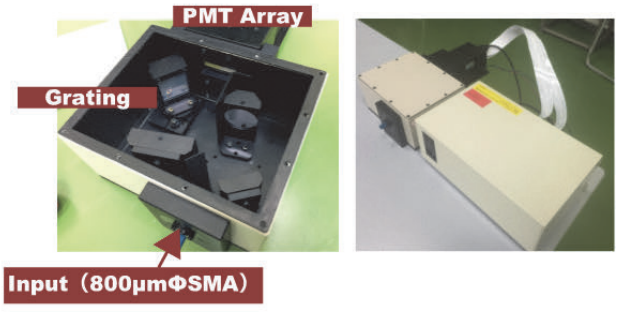

Fig. 1. Pictures of newly developed IBIL detector. Detector consist of visible light grating and 32 channel photoncounting mode photomultiplier array. The signals of 32 indipendent LVDS signals are transferred to FPGA unit to further signal process.

Figure 2 shows a schematic drawing of the micro-IBIL analysis system.Typical beam current up to 100 pA was used for experiment. For IBIL imaigng, typical beam diameter of 1 μm was used.

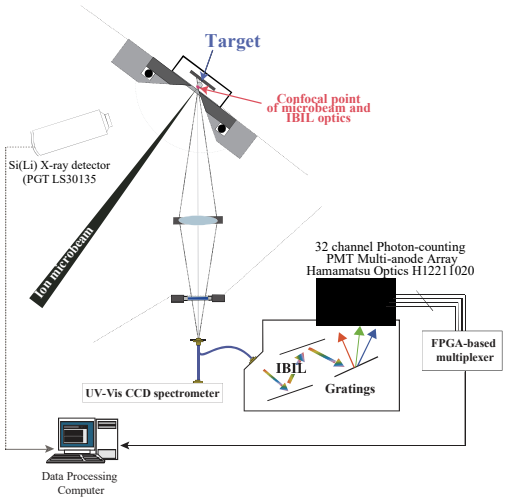

Fig. 2. Schematic illuatration of IBIL detector evaluation system using proton external microbeam.

Example of the multiwavelength imaging of IBIL was shown in Figs. 3. Compared to the conventional system, new detector is capable to obtain IBIL without any delays at the speed of microbem scan. It is not shown in these figure, however, decay of IBIL was also able to be obtained for each wavelegth [3]. These results suggest that the demonstrated IBIL detector can be used to analysis of IBIL of organic targets.

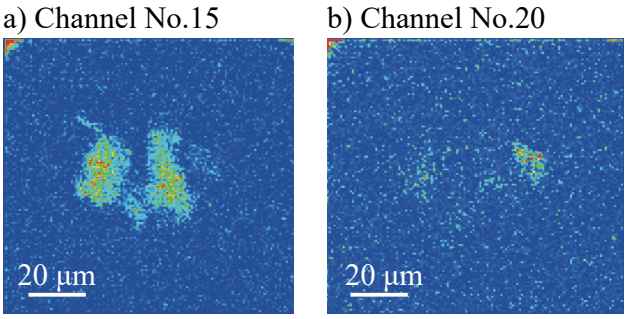

Figs. 3. Comparison of two IBIL images obtained at different wavelength of interest.

References

[1] W. Kada *et al.*, Int. J. PIXE **23**, 47-53 (2013).
[2] W. Kada *et al.*, Nucl. Instrum. Meth. B **332**, 42-45 (2014).
[3] W. Kada *et al.*, Nucl. Instrum. Meth. B, (2016, in press).

3 - 02 RBS and FTIR Studies of Significant Fe Diffusion Assisted by Phase Transition

Y. Maeda [a)], M. Arima [a)], M. Fuchi [a)] and K. Narumi [b)]

[a)] Graduate School of Information Engineering, Kyushu Institute of Technology,
[b)] Department of Advanced Radiation Technology, TARRI, QST

Ion beam synthesis (IBS) using iron ion implantation into Si substrates realizes high-density formation of semiconducting β-$FeSi_2$ in Si [1]. In the IBS process, understanding of thermal annealing is crucial for control of the silicide growth. The distribution of Fe atoms implanted into Si substrates is dominated by both diffusion of Fe atoms and the silicidation rate at the given annealing temperature. In this study, we investigate distribution and diffusion behavior of Fe atoms in the Si substrates annealed at 600-900 ºC by Rutherford backscattering spectrometry (RBS) and formation of β-$FeSi_2$ by Fourier transformation infra-red spectrometry (FTIR).

Mass separated $^{56}Fe^+$ ions were randomly implanted into Si(001) substrates. The three-step implantation was carried out at the energies of 50, 80 and 100 keV and each dose was 3.3×10^{16} ions/cm^2. After the implantation, the samples were annealed at necessary temperatures in vacuum by using a rapid thermal annealing (RTA). Scanning electron microscope (SEM) revealed that this 3 step implantation realized the silicide polycrystalline films after annealing at 800 ºC. For RBS measurements, 2-MeV $^4He^+$ ions were used and the backscattering angle was 165 degrees. The absorbance (ABS) was measured in the wavenumber region of 100-650 cm^{-1} by FTIR.

Figure 1 shows the Fe-RBS spectra of the as-implanted sample and those of the samples annealed at 600-900 ºC for 2 hours. The inset of Fig. 1 shows ABS spectra of the samples annealed at 800 and 900 ºC. In comparison between the spectra of the as-implanted and annealed samples (below 800 ºC), the spectrum width decreased and the yield peak (Fe peak concentration) increased. It is indicated that surface segregation of Fe atoms is caused by radiation enhanced diffusion (RED) due to an asymmetric distribution of implantation damages [2].

In these samples annealed below 800 ºC, silicide film growth was observed by SEM observation. Moreover, we can also confirm the film growth in the ABS spectrum in the bottom of the inset of Fig. 1. The bottom spectrum consists of some polariton peaks observed in the silicide film [3].

It should be noted that the distribution of Fe atom after annealing at 900 ºC was significantly different from other distributions. The RBS spectrum indicates that significant diffusion of Fe atom toward the deep portion of the substrate is caused. The Fe diffusion brings pronounced decrease of Fe concentration near the implantation region. This change observed at 900 ºC can be seen also in the ABS spectrum (the top spectrum of the inset). This ABS spectrum consists of three polariton peaks observed in β-FeS_{i2} nanocrystals (NCs) [3].

These ABS results indicate that the change at 900 ºC is related to change of a crystal morphology from the film to the NC. The lowering of Fe concentration shown in the RBS spectrum makes the film growth impossible because Fe concentration becomes insufficient for film formation. Film growth requires more than 33 at.% Fe in the growing region. In the low concentration region, discontinuous morphologies such as NCs or island-like precipitates grow.

Remaining discussion is the reason that significant diffusion of Fe atoms occurs during annealing at 900 ºC. It is reasonable thought that Fe atoms bound with Si atoms in the silicide lattice and cannot diffuse from the lattice by cutting the covalent bonds. However, when a known transition from the β- to the tetragonal α-lattice phase occurs, Fe atoms can be released from the lattice, then diffuse freely before growth of the α-lattice. The phase transition temperature of bulk β-crystal is 937 ºC, which is consistent with our findings.

From discussions, it is concluded that significant Fe diffusion occurring at 900 ºC is assisted by the β-α phase transition. Moreover, this process can be applied to growth of high grade β-NCs.

References

[1] Y. Maeda *et al.*, Thin Solid Films, **381**, 256-60 (2001).
[2] Y. Maeda *et al.*, Microsc. Semicond. Mater., IOP Ser. No. 157, 511-14 (1997).
[3] Y. Maeda *et al.*, Physics Procedia, **11**, 167-70 (2011).

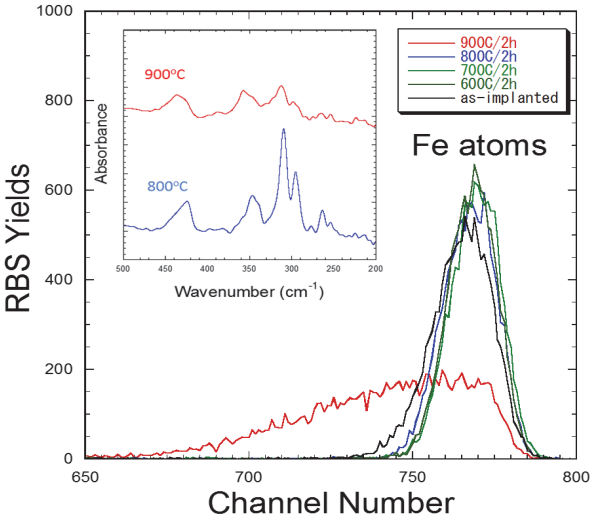

Fig. 1. RBS spectra of Fe channel of the as-implanted sample and the samples annealed at temperatures shown and IR ABS spectra of the samples annealed at 800 and 900 ºC (inset).

3 - 03 Neutron Measurements with the Bonner Sphere Spectrometer for the low Energy Region in the TIARA Neutron Field

T. Matsumoto [a)], A. Masuda [a)], H. Harano [a)], H. Seito [b)] and S. Kurashima [b)]

[a)] National Metrology Institute of Japan,
National Institute of Advanced Industrial Science and Technology (AIST)
[b)] Department of Advanced Radiation Technology, TARRI, QST

Precise measurements for high-energy neutrons are important in studies on neutron dose estimation around large accelerator facilities such as J-PARC, nuclear data, exposure in aircrafts and neutron induced soft error rate in semiconductor devices. High energy quasi-monoenergetic neutron standard fields with peak neutron energies of 45 MeV and 60 MeV at the AVF cyclotron facility of TIARA have been developed to calibrate high energy neutron detectors and dosimeters [1, 2]. In many cases, the high-energy neutron detectors and dosimeters have also sensitivities to low energy neutrons below 1 MeV. The low energy neutrons are slightly produced by scattering process in a collimator and an experimental room. In the present study, neutron energy spectra of the entire energy region in the TIARA high energy neutron field were measured using a Bonner sphere spectrometer (BSS).

Quasi mono-energetic neutrons are produced by the ^{7}Li(p,n)^{7}Be reaction with a proton beam from an AVF cyclotron At first, neutron energy spectrum above 100 keV at 6.5 m from a neutron production target was obtained by the time-of-flight (TOF) method using an organic liquid scintillator (BC501A, diameter: 7.62 cm, thickness: 7.62 cm) and a ^{6}Li glass scintillator (GS20, diameter: 5 cm, thickness: 5 mm). In the TOF measurements, ion pulses with intervals of micro second were obtained by using the S- and P- chopper systems [3]. Second, the BSS was used to measure neutron energy spectra of the entire energy region at 6.5 m and 13 m from the target. The BSS consists of spherical ^{3}He proportional counter (SP9, gas pressure: 0.5 atm.) and polyethylene moderators (diameter from 7.62 cm to 24.13 cm), a copper moderator in polyethylene and a lead moderator in polyethylene.

In the data analysis, the neutron energy spectrum was successfully obtained by unfolding the measured data using the MAXED code in the UMG3.3 package. The default spectrum used in the unfolding process was calculated by the MCNPX code. The neutron energy spectrum obtained by the TOF measurements was used in the calculation of the default spectrum.

Figures 1 and 2 show the neutron energy spectra measured at 6.5 m and 13 m from the target, respectively. Calculated results are also shown in these figures. Figure 2 indicates the thermal neutron contribution at 13 m is relatively large in the TIARA field. The discrepancy between measured and calculated results is found in the thermal neutron region. It is necessary to improve the calculations of the default spectrum.

References

[1] T. Matsumoto *et al.*, J. Nucl. Sci. Tech. **54 (5)**, 529-39 (2017).
[2] A. Masuda *et al.*, IEEE Trans. Nucl. Sci. **62(3)**, 1295-300 (2015).
[3] S. Kurashima *et al.*, Rev. Sci. Instrum. **86**, 073311 (2015).

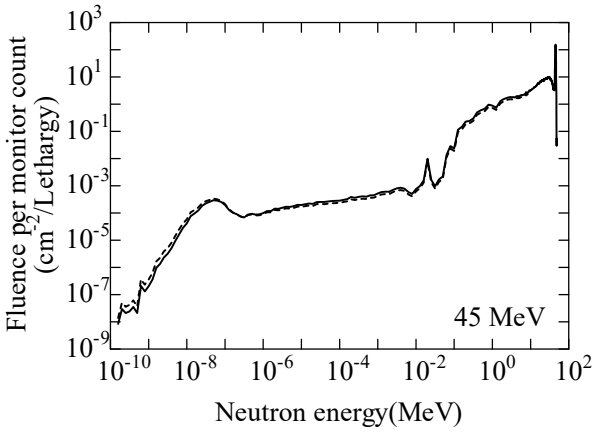

Fig. 1. Neutron spectrum measured by the BSS at 6.5 m from the target. Dashed line shows the default spectrum used in the unfolding process.

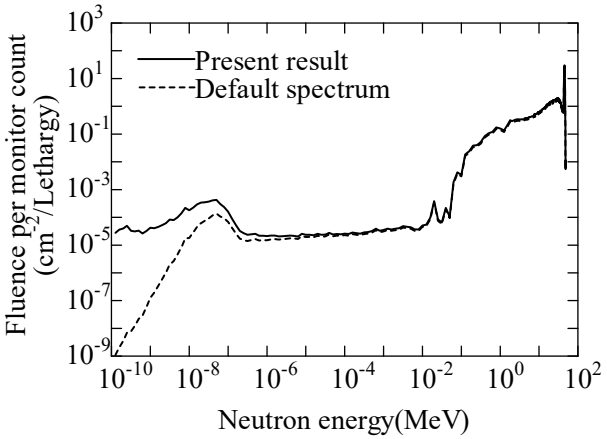

Fig. 2. Neutron spectrum measured by the BSS at 13 m from the target. Dashed line shows the default spectrum used in the unfolding process.

3 - 04 Vacancy-induced Magnetism in GaN Film Probed by Spin-polarized Positron Beam

M. Maekawa, S. Sakai, K. Wada, A. Miyashita and A. Kawasuso

Department of Advanced Functional Materials Research, TARRI, QST,

Some semiconductor materials of metal oxides or nitrides, such as zinc oxide (ZnO) or gallium nitride (GaN), are known to exhibit ferromagnetism without having magnetic elements (d^0 ferromagnetism), which could be induced by lattice defects. *Ab-initio* studies predict that cation vacancies cause the d^0 ferromagnetism [1]. However, conventional measurement techniques cannot relate directly the origin of the ferromagnetism to vacancies, because such techniques have sensitivity only to either magnetism or defects. To clarify the magnetism at vacancies, a new experimental method is required. The spin-polarized positron annihilation spectroscopy (SP-PAS) is the promising method because this method is sensitive to both vacancies and electron spins. Indeed, we already have found that the Magnetic Doppler broadening (MDB) spectrum, which is the residual curve of energy spectra of annihilation gamma rays for the inversion of the external magnetic field polarity, shows certain intensity for the ion-implanted ZnO crystals containing vacancy defects [2]. Since the MDB intensity appears only when the spin-polarized positrons annihilate with the spin-polarized electrons [3] and positrons tend to be trapped to cation vacancies, the MDB intensity indicates that magnetic moments caused by spin-polarized electrons are associated with such vacancies.

In order to obtain stronger ferromagnetism, it is necessary to keep the high spin state of electrons at the vacancies. *Ab-initio* calculations suggest that the charge state of vacancies should be neutral or positive. It is desirable to use p-type crystal to avoid cancelling electron spins by excess electrons [4]. GaN is one of the semiconductor materials showing d^0 ferromagnetism by ion irradiation [5], moreover, it is easy to make p-type crystal unlike the case of ZnO. In this study, we investigated whether the vacancy-induced d^0 ferromagnetism in GaN is affected by the crystal conductivity.

Samples used in this study were undoped (naturally n-type) and p-type MBE-grown GaN films with the thicknesses of 2 μm formed on the sapphire substrates. Nitrogen ions were irradiated to the samples with a dose of 1×10^{17} cm^{-2} at 100 keV to introduce vacancy defects. After the irradiation, MDB spectra were measured using the SP-PAS method in the magnetic field of ± 0.91 T at room temperature. Figure 1(a) shows the MDB spectrum for the unimplanted GaN sample. This spectrum seems to be nearly zero intensity at whole momentum region. This indicates that there are no vacancies accompanying the magnetic moments. Figures 1(b) and (c) show the MDB spectra for the ion-irradiated state. In the case of p-type GaN, the MDB intensity appears (Fig. 1(c)). As in the case of ZnO, this indicates that electron spins having a magnetic moment exists in the cation vacancies where positrons are easily trapped. However, in the case of the undoped sample (Fig. 1(b)), the MDB intensity is almost disappeared. This might be the canceling the electron spin at vacancies by the conduction electrons. These results confirm that the control of the charge state of vacancies is important for the vacancy-induced magnetism, as suggested by the theoretical calculation.

References

[1] O. Volnianska and P. Boguslawski, J. Phys. Conden. Matter, **22**, 073202 (2010).
[2] M. Maekawa *et al.*, Appl. Phys. Lett. **110**, 172402 (2017).
[3] A. Kawasuso *et al.*, Phys. Rev. **B83**, 100406(R) (2010).
[4] O. Volnianska *et al.*, Phys. Rev. **B83**, 205205 (2011).
[5] J. Xu *et al.*, Chem. Phys. Lett., **616-17**, 161-64 (2014).

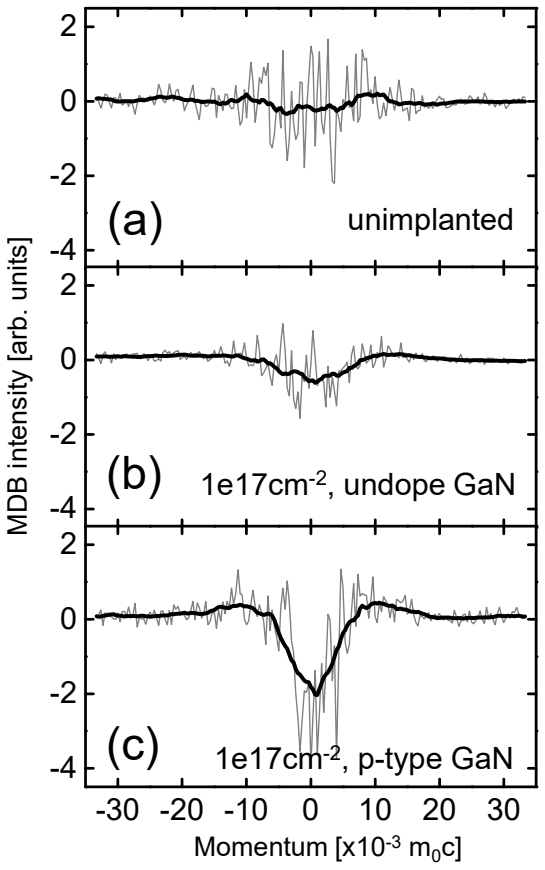

Fig. 1. MDB spectra for (a) unimplanted state, (b) N^+- irradiated undoped GaN and (c) N^+-irradiated p-type GaN samples at room temperature. Irradiation dose was 1×17 cm^{-2}.

3 - 05 Microbeam Formation of a 320 MeV $^{12}C^{6+}$ Using the Focusing Magnet at HX Course

S. Kurashima, N. Miyawaki, H. Kashiwagi, N. Yamada and T. Satoh

Department of Advanced Radiation Technology, TARRI, QST

A microbeam formation system using focusing magnets on the HX course of the TIARA AVF cyclotron [1] is being continuously improved. This system is mainly required for elucidation of radiation biology effect such as a bystander effect on biological cells.

The spot size of the microbeam is usually estimated by analyzing a secondary electron (SE) image of a copper grid with 1,000 lines/in. as described in Ref. 1. The accuracy of the spot size estimation depends on the signal to noise ratio (S/N) of the SE image. In the case of a 320 MeV $^{12}C^{6+}$ microbeam formation, the S/N adequate for the estimation could not be obtained because of poor yields of SE since the linear energy transfer (LET) and the beam intensity of the fully-stripped ion was lower than the other microbeam such as a 260 MeV $^{20}Ne^{7+}$. Therefore, a new system for estimating the beam size was constructed by using an EM-CCD (Electron Multiplying Charge Coupling Device) camera with high detection sensitivity and a gadolinium pyrosilicate $Gd_2Si_2O_7$:Ce (GPS:Ce) scintillator [2]. This system can detect the single-ion hit position, and the beam image is obtained by adding up individual picture images as shown in Fig. 1a. The beam sizes were estimated, by analyzing the intensity distribution of the picture image, to be 6 and 7 μm in full width at half maximum (FWHM) for *x*- and *y*-directions, respectively. To estimate the targeting accuracy of the microbeam, the single-ion hit irradiation on a CR-39 solid-state nuclear track detector was done in a pattern of 5×5 points as shown in Fig. 1b. The CR-39 was placed in the air at a distance of 1 mm from the vacuum window. The targeting accuracy was estimated to be about 8 μm in FWHM by analyzing etch-pit positions [3] shown in Fig. 1b, and there is no great difference compared with the beam size estimated from the picture image shown in Fig. 1a.

To irradiate living cells or microscopic worms, the microbeam is extracted in the atmosphere through a vacuum window made of Si_3N_4 with a thickness of 200 nm. The targeting accuracy (beam size) is deteriorated, compared with that in vacuum, because of scattering in the Si_3N_4 and the atmosphere layers. Figure 2 shows position dependence of the targeting accuracy from the vacuum window. The target sample must be placed as close to the vacuum window as possible.

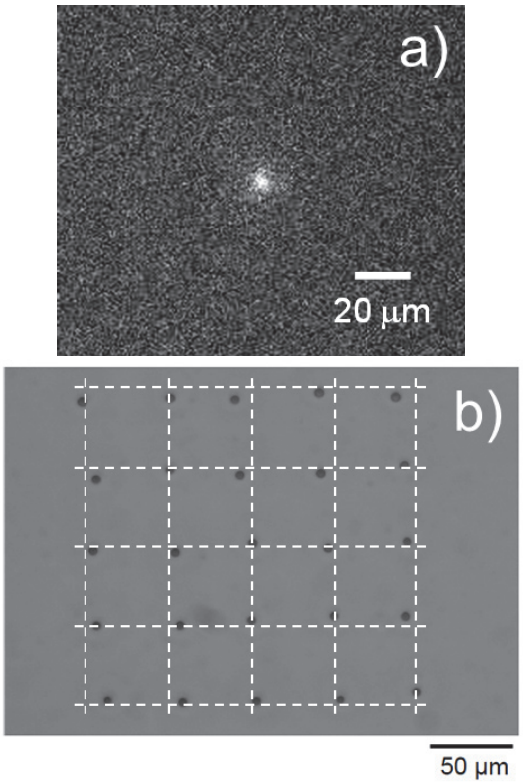

Fig. 1. a) Scintillation image of the 320 MeV $^{12}C^{6+}$ obtained by adding up 100 pictures in which several luminescence points were observed. b) Photomicrograph of the CR-39 detector etched by a solution after 5×5 single-ion hits. The intersections of broken lines show the target points.

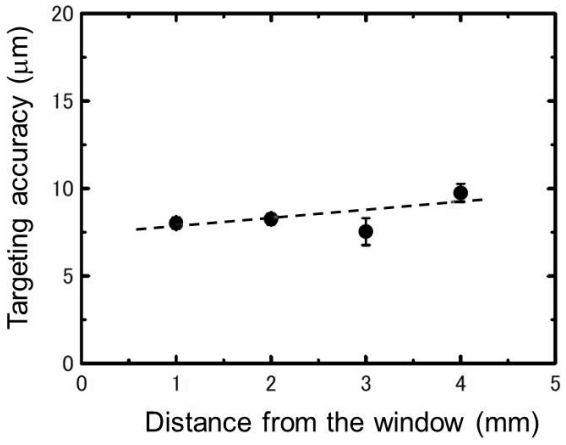

Fig. 2. Position dependence of the targeting accuracy of the 320 MeV $^{12}C^{6+}$ microbeam. The position is a distance from the vacuum window. The targeting accuracy was analyzed from the etch-pit pattern on the CR-39 such as Fig. 1b.

References

[1] M. Oikawa *et al.*, Nucl. Instrum. Meth. B **260**, 85-90 (2007).
[2] Y. Tsubota *et al.*, Prog. Nucl. Sci. Tech. **3**, 97-99 (2012).
[3] T. Satashita *et al.*, Radioisotopes **60**, 47-53 (2011).

3 - 06 Status Report on Technical Developments of the TIARA AVF Cyclotron

N. Miyawaki, H. Kashiwagi and S. Kurashima

Department of Advanced Radiation Technology, TARRI, QST

Estimation of the phase bunching effect for *h*=3

The phase bunching effect for beam conditions of the harmonic number (*h*) 3 in the TIARA AVF cyclotron was estimated by the calculation with the geometric orbit analysis model for investigation of the same effect of narrowing beam phase width as *h*=2 [1]. Figure 1 shows the measured beam phase distribution and the calculated correlation between the relative initial phase and the relative RF phase at each acceleration gaps in a turn for a 120-MeV $^{20}Ne^{6+}$ beam with *h*=3. Phase bunching was observed in the measured result and the calculated correlations at the entrance of No. 1 dee electrode and the exit of No. 2 dee electrode. The positions of the observed phase bunching in the calculation result was corresponding to the measurement position. However, the calculated results at the other positions had no phase bunching. Thus, the phase bunching effect was canceled out for one revolution, and there is no effect of phase bunching in beam conditions for *h*=3. To obtain the phase bunching effect for *h*=3, the electrode shapes in the central region was numerically estimated. The second acceleration gap was shifted 14 degrees to the first acceleration gap, because the beam phase at the second acceleration gap can be bunched into the phase around the top of the acceleration voltage waveform which minimizes the energy gain difference. As a result of the calculation with the model, phase bunching for *h*=3 was sustained to extraction and narrowed the phase width.

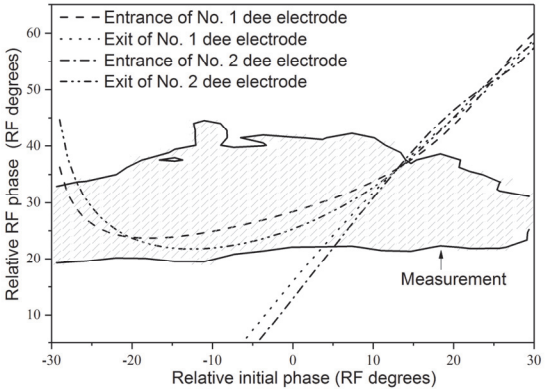

Fig. 1. Measurement results and calculated correlations between the relative initial phase and the relative RF phase for a 120 MeV $^{20}Ne^{6+}$ beam with *h*=3.

Development of a slit-harp emittance measurement system

We are developing an optimization method of beam injection tuning based on measurements of the emittance of the injection beam and acceptance of the cyclotron. The measurements are performed with a double-slit scanning method using two pairs of slits installed in the injection line of the cyclotron [2]. Regarding emittance, the time for horizontal or vertical measurement is almost seven minutes. In order to perform high resolution measurements and repeated measurements in the case of changing operating condition of the ion source or changing conditions of beam transport, long measurement time is required. Therefore, in order to realize rapid emittance measurement, we have developed an emittance measurement system with a slit-harp method.

Figure 2 shows a layout of a slit-harp emittance device, which consists of horizontal or vertical slits and multi-wires, each of which is on a motorized stage. The positions of a beam are defined by the slit and distributions of the beam divergence are measured by the multi-wires. In double-slit method, only one coordinate in a phase-plane can be measured at a time, whereas in the slit-harp method, the coordinates of the number of wires can be measured simultaneously. Therefore, the slit-harp method realizes fast measurement.

The harp units with 48 wires were installed downstream of the position defining slits which were also used in double slit method. The measurement angle range is about ± 20 mrad, and the angular resolution determined from the position of the wire is about 0.9 mrad. The beam intensity detected by each harp is measured by a DAQ device after voltage conversion by 96 channels (48 channels for horizontal direction, 48 channels for vertical direction).

As a result of the measurement using this system, the obtained emittance diagram was almost the same as that by double-slit method. The measurement time was 51 seconds for the slit-harp method and 406 seconds for the double slit method. From the above, it was confirmed that the measurement time in the slit-harp method was shortened to about 1/8 of that in the slit-harp method.

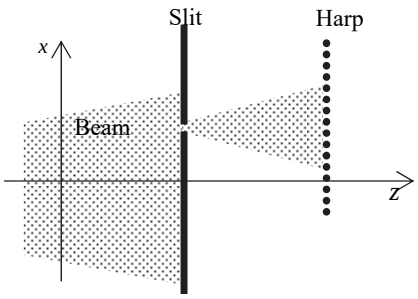

Fig. 2. Layout of a slit-harp device.

References

[1] N. Miyawaki *et al.*, Proc. 13th Annu. Meet. Part. Accel. Soc. Jpn. 617-18 (2016).

[2] H. Kashiwagi *et al.*, Rev. Sci. Instrum., 02A735~1-5 (2014).

3 - 07 Status Report on Technical Developments of Electrostatic Accelerators

Y. Hirano, A. Chiba, K. Yamada, A. Yokoyama, Y. Ishii, T. Satoh, T. Ohkubo and T. Nara

Department of Advanced Radiation Technology, TARRI, QST

Development of negative fullerene ion source

Exponential increase of MeV-energy fullerene ion beam intensity had been achieved through a novel technique of the negative ionization of fullerenes based on a thermal electron attachment process with the use of an existing ion source of 3 MV Tandem Accelerator at TARRI [1]. Although availability of the MeV-energy fullerene beam has improved drastically in recent years, the beam intensity was not enough to be useful for several experiments which need the higher fluence irradiations. Therefore, a new oven-rod equipped with a filament in the oven nozzle was developed. The schematic drawing is shown in Fig. 1. Some of fullerenes sublimated in the oven capture one of thermal electrons emitted from the filament at an electron attachment cell put in the oven nozzle. The electron attachment rate increased due to the high density interaction between electrons and fullerenes in the attachment cell designed as narrow as possible. The beam intensity was more than five times higher than that the new oven-rod previously developed, and reached to the level that means the irradiation with fluence of the order of 10^{14} atom/cm^2 in a few hours is available.

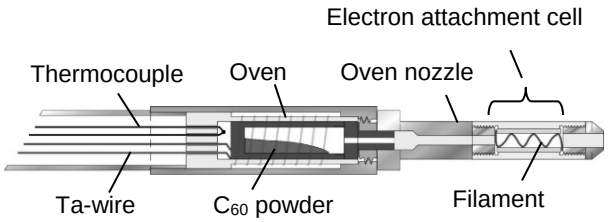

Fig. 1. Schematic drawing of new oven-rod.

Measurement of beam energy shift using resonance nuclear reaction

Beam irradiation time of approximately 70% at 3 MV Single-ended Accelerator, hereafter accelerator, is used for micro-PIXE analysis. The shifts of trace element distribution in a range of a few microns are observed for several hours in the analysis with the spatial resolution of 1 μm. The shift is considered to be caused by voltage drift of the accelerator over time, because the target positions were fixed in the analysis for several hours. The main purpose of this study is to reduce the shift within the spatial resolution for the accurate analysis. As a first step, the range of voltage drift is estimated by comparing the reaction energy experimentally obtained from the nuclear resonance of ^{27}Al(p, γ)^{28}Si and the acceleration voltage displayed in the control device under the accelerator operated to be constant voltage.

In the fiscal 2016, 992 keV proton beam up to current of about 450 nA was used for the measurements. The γ-ray, 1,772 keV, yields of the nuclear reaction of ^{27}Al(p, γ)^{28}Si at 992 keV with the resonance width of 100 eV was measured using a NaI scintillation detector every one hour from 16 p.m. to 21 p.m. The range of the voltage drift was experimentally estimated to be within 0.1 keV during the measurements. The result was almost the same as that in the last year. In the next fiscal year, the variation of the accelerating voltage will be measured to clarify a quantity of the shift during the accelerator's operation hours.

Measurement of a pulse width of a fullerene ion beam

A short-pulsed fullerene ion beam is used in a development of Time-of-Flight (TOF) secondary ion mass spectrometry measurements for surface analysis. In order to measure a mass spectrum more accurately, it is necessary to form the pulse width of the primary beam as narrow as possible, because the time resolution of TOF depends on the pulse width The conventional pulse widths of the fullerene beam with 400 kV Ion Implanter were quite wide, up to a few hundred ns, so the reduction of the pulse width is required. The pulsed ion beam is formed from the direct current beam with a beam pulsing system consists of deflection plates, a high voltage pulse generator, and an aperture slit.

In the fiscal year 2016, the high voltage pulse generator (Matsusada Precision, HEOPT-1B60) was upgraded to one which has a fast rise and fall time (DEI, PVX-4140), and the pulse widths of 120 keV-C_{60}^+ beam were measured by the TOF method at IE beam line. As a result, the pulse width was reduced from 220 ns to 45 ns (FWHM) as shown in Fig. 2.

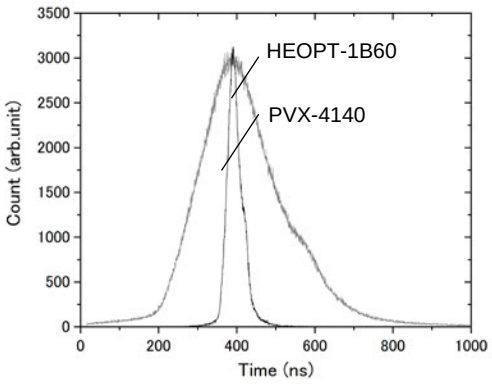

Fig. 2. Measured pulse widths of 120 keV-C_{60}^+.

Reference

[1] A. Chiba *et al.*, JAEA Takasaki Annu. Rep. 2013, JAEA-Review 2014-050, 169 (2015).

3 - 08 Handy Determination of Ion-beam Relative Intensity Distribution Based on Gamma-ray Irradiation Response of Gafchromic Films

T. Ishizaka, Y. Yuri, T. Agematsu, T. Yuyama, H. Seito and S. Okumura

Department of Advanced Radiation Technology, TARRI, QST

Gafchromic films (Ashland) [1] have been widely used for dosimetry in radiation therapy using X-rays and gamma rays, and now applied to the profile measurement of various ion beams. Among several models of Gafchromic films, an HD-V2 film is available to low-energy, i.e., short-range ion beams, since its active layer is not laminated by a surface layer [2]. However, an optical density (OD) response curve of the film to the fluence needs to be determined for each ion species and energy because the OD response is generally unproportional to the fluence in a wide fluence range [2, 3]. This film calibration is a time-consuming process. Therefore, we considered the possibility of the handy determination of the ion-beam relative intensity distribution using a ^{60}Co gamma-ray response curve in place of an ion-irradiation response curve [4].

Gafchromic HD-V2 films, which have a 12-μm-thick active layer on a polyester base, were irradiated uniformly with ^{60}Co gamma rays and three kinds of ion beams (10 MeV ^{1}H, 520 MeV ^{40}Ar, and 450 MeV ^{129}Xe) from the TIARA cyclotron. Then, the coloration of the films was digitized into RGB color values using a flatbed image scanner, ES-10000G (ESPON), for the large-area two-dimensional (2D) measurement. Finally, the ODs were obtained in each component of the RGB color values.

The ion-irradiation results of HD-V2 films are summarized in Fig. 1. The ODs in the three color components are plotted as a function of the gamma-ray dose. The fluence of the ion beams has been scaled to the dose so that the ion-irradiation results are fitted to the gamma-ray response curves using the least-squares method. As highlighted in Fig. 1, the responses of the ion beams are well fitted to the gamma-ray response curve below ODs of about 0.7, 0.5, and 0.4 in the red, green, and blue components, respectively. In other words, the OD responses of various ion beams can be well approximated by the gamma-ray response curve. This result suggests that the gamma-ray response curve can be employed to obtain the relative intensity distribution of the ion beams.

This suggestion has been confirmed in Fig. 2. The 2D OD distribution of a proton-irradiated HD-V2 film is shown in Fig. 2(a). The OD distribution was transformed into the relative intensity using two different response curves; one is the gamma-ray response curve and the other is the proton-irradiation response curve. The relative intensity distributions obtained with the two ways, compared in Fig. 2(b), are almost overlapped each other within the maximum deviation of 5%. This deviation is allowable since it is the same level as uncertainties in ion irradiation and fitting errors of response curves.

In summary, we have investigated the responses of Gafchromic HD-V2 films irradiated with high-energy ion beams and verified that the ion-irradiation responses can be well fitted to the ^{60}Co gamma-ray response within certain OD ranges. From this fact, we have shown that the relative intensity distribution of an ion beam can be determined handily using the gamma-ray response curve in place of the ion-irradiation response curve.

References

[1] A. Niroomand-Rad *et al.*, Med. Phys. **25**, 2093 (1998).
[2] Y. Yuri *et al.*, Nucl. Instrum. Meth. Phys. Res. A, **828**, 15 (2016).
[3] Y. Yuri *et al.*, Nucl. Instrum. Meth. Phys. Res. B, **406**, 221, (2017).
[4] T. Ishizaka *et al.*, Radioisotopes, **66**, 251 (2017) [in Japanese].

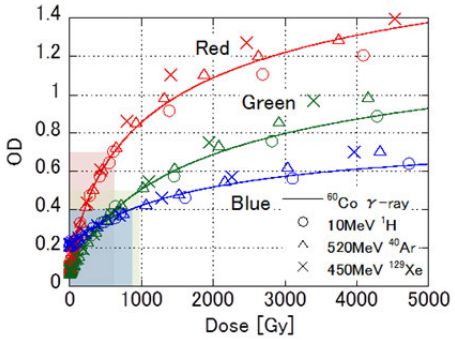

Fig. 1. OD responses of Gafchromic HD-V2 films irradiated with the ion beams (symbols). The ion-irradiation data are fitted to the gamma-ray response curves (solid lines). The curve is defined as follows: OD $= -\log_{10}[(a+bD)/(c+D)]$, where D is a dose and a, b, and c are fitting coefficients.

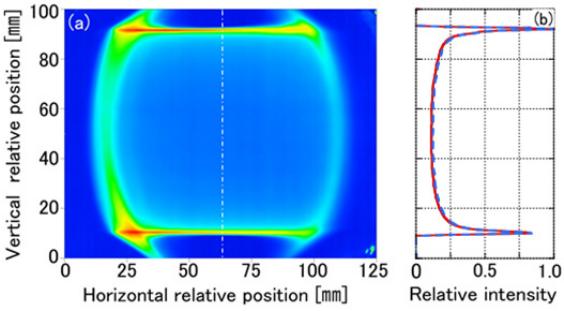

Fig. 2. (a) 2D OD distribution of the Gafchromic film irradiated with 10 MeV H. (b) Relative intensity distributions along the vertical dot-dashed line in (a). The two profiles drawn in the solid and dashed lines are obtained from the H-irradiation response curve and from the gamma-ray response curve, respectively.

3 - 09 Development of PIG Ion Source with Electric Magnet for Compact Ion Microbeam System

Y. Ishii [a)], T. Ohkubo [a)] and Y. Miyake [b)]

[a)] Department of Advanced Radiation Technology, TARRI, QST,
[b)] Beam Seiko Instruments Inc.

An ion microbeam ranging from several hundred keV to several MeV, hereafter microbeam, are mainly used for the visualization of trace elements in a sample and the microfabrication of the 2D or 3D structures with photo-resists by PIXE and proton beam writing (PBW), respectively. The microbeams have, so far, been formed by a large microbeam system with the total length of about 30 m that comprises an accelerator, a beam transport line, and focusing lenses. The installation of the microbeam system in a common experimental room with a size of about $8 \times 6 \times 3$ m^3 is difficult for the large size. A MeV compact ion microbeam system is developed to enable us to install in the experimental room. A 120 keV compact ion microbeam system, hereafter compact microbeam system [1], is constructed using a three-stage acceleration lens and a duoplasmatron-ion source as a prototype of the MeV compact ion microbeam system. A hydrogen ion beam of 2.6 μm in diameter has, so far, been experimentally formed, which is close to our goal.

As a next step, the increase of the beam energy is studied on the basis of developing and improving some elemental technologies. One of the studies is to develop an ion source with small electric power consumption to exchange the present ion source with the large electric one. The present ion source supplies a low energy and high brightness ion beam that are appropriate for the three-stage acceleration lens, whereas it needs the large electric power to heat the filament and frequent exchange its filament. The supply of the large electric power is difficult because of placing it in a small space with high voltage in the MeV compact ion microbeam system. A solution of the difficulty is to use a Penning ionization gauge (PIG) ion source with a cold cathode that is generally low electric power consumption and a compact size. However, the PIG ion source has beam energy over several keVs and small brightness.

In this study, a PIG ion source generating an ion beam with low energy and high brightness, which matches the demand of the three-stage acceleration lens, is developed to enable us to install it in the high voltage space. In this fiscal year, a PIG ion source with electric magnets was designed and constructed to investigate the relationship between magnetic field strength and brightness of ion beam.

The high brightness, especially, is an important parameter for the compact microbeam system to obtain relatively large beam current at a focused point when an ion beam with a smaller diameter is formed. To generate the ion beam with the high brightness, the extraction of ion beam from high density plasma in a small space in a PIG ion source was considered to be effective. The generation of strong magnetic field in the small space is required to realize this consideration. The magnetic field was calculated using a magnetic field calculation code for magnetic circuits with various shapes.

The finally designed PIG ion source with magnetic circuits is represented in Fig. 1. It has two coils placed at the both sides of anode in an iron yoke in the generation point of plasma to obtain the strong magnetic field. The magnetic field over 1.5 T in the small space was numerically obtained by applying 800 AT and 400 AT to up

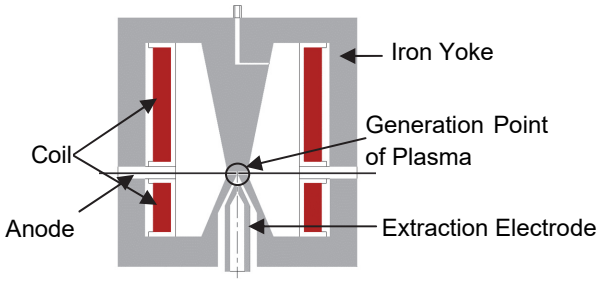

Fig. 1. The finally designed PIG ion source with electric magnets.

and down coils, respectively. The small space for generating plasma is 1.5 mmΦ × 2 mm. The thickness of anode is 0.8 mm. The manufactured PIG ion source is shown in Fig. 2. The coil turns of up and down are 800 and 400. The iron rods around the ion source are used as the return yoke in the magnetic circuit to cool down the coils by air by making spaces. The PIG ion source is placed in a test bench, whose air leaking was checked. There wasn't any air leaking until 1.3×10^{-5} Pa. We will generate hydrogen beams and investigate the relationship between the strength of magnetic field and the brightness of the ion beam in the next fiscal year.

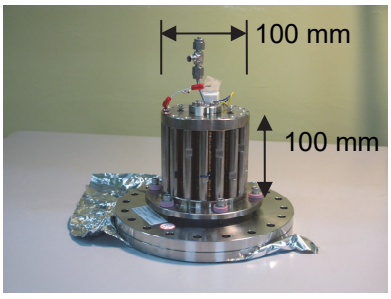

Fig. 2. The manufactured PIG ion source.

Reference

[1] Y. Ishii, T. Ohkubo, *et al.*, Nucl. Instrum. Meth. Phys. Res. B, **332,** 156-59 (2014).

3 - 10 Development of Ion-beam Irradiation Techniques toward Mass Production of Ion-track Polymer Membranes

H. Yamamoto [a)], Y. Yuri [b)], T. Yuyama [b)], K. Yoshida [b)], T. Ishizaka [b)] and I. Ishibori [b)]

[a)] Functional Products Division, Nitto Denko Corporation,
[b)] Department of Advanced Radiation Technology, TARRI, QST

A research and development study is in progress on high-energy heavy-ion irradiation techniques toward the production of track-etched membranes at the TIARA cyclotron. Up to now, we have succeeded in developing the following basic techniques suitable for irradiation of long-scale polymer films; namely, the formation of a ribbon-like beam with a uniform intensity distribution by nonlinear focusing of octupole magnets, and the operation of a roll-to-roll system for continuous irradiation of thin polyethylene terephthalate (PET) films in high vacuum [1].

As a next step, we have considered the efficiency of the operation and irradiation in the roll-to-roll system toward the mass production of track-etched membranes. Therefore, the uniform-beam formation and roll-to-roll irradiation were investigated in low-vacuum environments for reducing the time of vacuum pumping and sample exchange and the cost of a vacuum-pumping system.

For this purpose, a beam duct with a large Ti-foil window has been fabricated to extract an ion beam to an irradiation chamber, in which the vacuum pressure can be changed between 10^{-5} and 10^{5} Pa. Using 385-MeV ^{40}Ar ion beams that can penetrate the foil window, sufficiently uniform intensity distributions were formed even in low vacuum (10^{1} ~ 10^{4} Pa) although the sharpness of the edge in the beam profile was weakened due to multiple Coulomb scattering. The penetration depth of the energy-degraded beam in a sample was checked by stacked PET film pieces. The number of track pores in each film piece was counted with a scanning electron microscope after chemical etching. As shown in Fig. 1, it was confirmed that the penetration depth of the beam in the stacked films was consistent with the calculation result using a software SRIM. No clear difference of the vacuum degree on the pore formation was observed because of a severe etching condition. The present result indicates that it is possible to change the on-target beam energy easily by changing the vacuum pressure in the irradiation chamber or by inserting a degrader material before the target sample. Therefore, the linear energy transfer (LET) can be enhanced quickly so that the Bragg peak can be adjusted to the target sample according to sample conditions (such as thickness and density). This is desirable in that chemical-etching conditions can be made milder in Ar-ion irradiation, in which the LET is relatively low.

The beam current is an important parameter that directly affects the quality of porous membranes. Therefore, the condition of an electron cyclotron resonance ion source is carefully adjusted to reduce the frequency of abrupt changes in beam current. Beam tuning of the ion source is started after outgassing of the vacuum chamber for several hours. Moreover, the variation in ambient temperature of the ion source is kept within ±1 °C by air conditioning. The relative beam current was monitored at several different locations from the exit of the ion source to a beam dump behind the target sample during long-time roll-to-roll irradiation. An example of beam current monitoring is shown in Fig. 2.

The magnitude of radioactivation in volume ion-irradiated samples is also of interest. Therefore, gamma-ray spectrometry was performed with a Ge semiconductor detector system. The dependence of various conditions, such as the Ar-ion beam energy, fluence and sample volume, on the radioactivation was examined to clarify the decay time of samples.

We could get a good prospect for ion irradiation of long-scale polymer membranes at the TIARA cyclotron. We plan to investigate other polymers such as polyimide.

Reference

[1] H. Yamamoto *et al.*, QST Takasaki Annu. Rep. 2015, **QST-M-2**, 169 (2017).

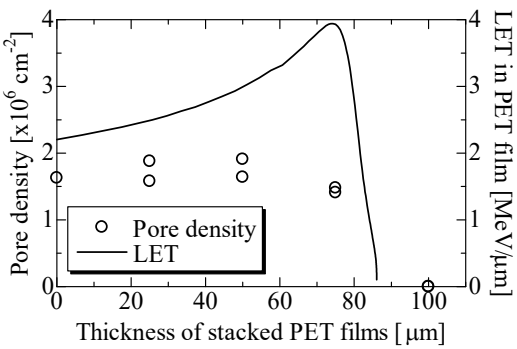

Fig. 1. Pore density in stacked PET films (t25 μm × 4 layers) irradiated with Ar ions at 100 Pa and LET calculated using the SRIM code as a function of the thickness of stacked PET films.

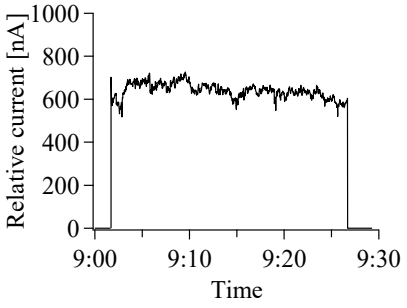

Fig. 2. Relative beam current measured at the beam extraction Ti window during roll-to-roll irradiation of a PET film with Ar ion beam (150 nA) for 25 min.

3 - 11 Development of an Integrated Optical Switch Embedded in Thin PDMS Film Fabricated by Proton Beam Writing

W. Kada [a)], R. Saruya [a)], S. Miura [a)], K. Kasuya [a)], R. K. Parajuli [a)], S. Kawabata [a)], R. Sano [b)], K. Miura [a)], T. Satoh [c)], M. Koka [c)], N. Yamada [c)], Y. Ishii [c)], T. Kamiya [a)], H. Nishikawa [b)] and O. Hanaizumi [a)]

[a)] Faculty of Science and Technology, Gunma University,
[b)] Department of Electrical Engineering, Shibaura Institute of Technology,
[c)] Department of Advanced Radiation Technology, TARRI, QST

Using MeV focused microbeam, it is able to produce micrometer-sized structures with different optical properties in a solid target. So far, our research group has been studying the fabrication of an integrated optical waveguide by the PBW technique. In previous studies, we have successfully fabricated the prototypes of a Mach-Zehnder (MZ) waveguide for integrated fiber telecommunications using poly(methyl methacrylatre) (PMMA) and poly-dimethyl-siloxane (PDMS) [1, 2]. These MZ waveguides are designed to form optical switchs by making a thermal heater on one of the waveguides divided in two. However it was not yet well evaluated for the embedded optical waveguide structure in a PDMS thin film. In this study, we have demonstrated the fabrication of flexible optical switches based on the MZ waveguide drawn by PBW procedure in the film.

The waveguide was drawn in a target thin film by PBW procdure that was performed at a light ion microbeam line connected to 3 MV Single-ended Acceraltator at TIARA. A 750 keV focused proton microbeam with the size of approximately 1 μm^2 was employed in PBW for the drawing. The whole waveguide structure, as shown in Fig. 1(b), was formed by the combination of the usage of the scaning of the microbeam and the sample movement using a samplestage.

The target thin films of PDMS (SYLGARD 184, Toray Dow Corning) were spin-coated on supporting plates of silicon wafers (40 mm × 20 mm × 20.5 mm).

The thickness of thin PDMS film was approximately 40 μm, which was measured by a laser microscope. After removed from the supporting plats and dried in atmoshepere for 1 day at room temperature, the MZ waveguides were drawn in the self-supported PDMS films by PBW as shown in Fig. 1(a) as a mosaic image. In post process of the PBW procedure, a thin film heater electrode of titanium (0.01 mm × 2.5 mm) was formed on the PDMS film by the evapolation. The sufficient adhesive condition of the titanium heater electrode on the PDMS filme was not, so far, obtained from only the procedure of the heater, whereas it was improved by adding the surface plasma treatment to the proceduer. Two aluminum terminal electrodes (0.5 mm × 0.5 mm) were also formed at both ends of the titanium heater electrode to make a contact to an external power supply.

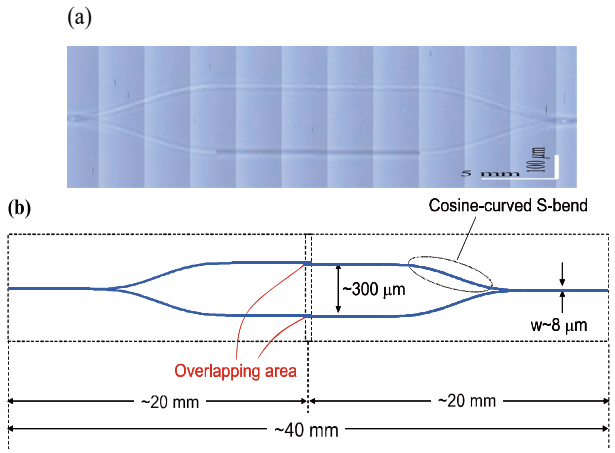

Fig. 1. Schematic illustration of MZ waveguides drawn in PDMS thin films by PBW procedure. The MZ waveguide has core size of approximately 8 μm and a whole length of approximately around 40 mm.

Fundamental characteristics of the optical switch based on the MZ waveguide was evaluated by near field pattern (NFP). The infrared light with the center wavelength λ = 1.55 μm from a fiber laser (ECL-210, Santec) was inputed into the one side of the MZ waveguide to check single-mode optical transmission and the light at the output spot with NFP was observed by a IR vidicon camera (C2741-03, Hamamatsu Photonics). External bias voltage was applied to the titanium electrode from an external voltage supply (Keithley, 2400). Figures 2(a) and (b) show an example of the experimental results of optical switching function obtained by applying bias voltage to the titanium heater electrode. The experimental results suggested that the output light intensity was successfully controlled by the external bias voltage on and off.

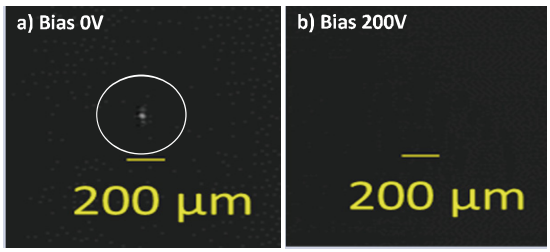

Fig. 2. An example of experimental results of the optical switch function based on the interference effect of thin film MZ waveguide. (a) Bias voltage of 200 V was applied to eliminate optical spot. (b) Light spot was recovered by decreasing bias voltage to 0 V.

References

[1] K. Miura *et al.*, Key Eng. Mater. **497**, 147 (2012).
[2] W. Kada *et al.*, Nucl. Instrum. Meth., B, **348**, 218 (2015).

3 - 12 Effects of Proton Beam Irradiation on Optical Properties of TiO_2/polydimethylsiloxane Composite Material

Y. Kaneko [a)], H. Hayashi [b)], Y. Ishii [c)] and H. Nishikawa [a, b)]

[a)] Department of Electrical Engineering, Shibaura Institute of Technology (SIT),
[b)] SIT Research Laboratories (SRL), SIT,
[c)] Department of Advanced Radiation Technology, TARRI, QST

Composite materials of polymers containing inorganic particles such as ceramics are of considerable importance for electrical, electronics, and optical applications for the superior electrical, thermal, mechanical, and optical properties. It was previously demonstrated that the polydimethylsiloxane (PDMS) can be a platform for flexible light circuit written by proton beam writing [1]. To further exploit the possibility of PDMS as a flexible platform for proton beam writing of composite materials [2], we studied the proton beam irradiation effects of PDMS-based composite materials. The present study reports the irradiation effects by MeV protons on optical properties of a flexible PDMS composite material containing TiO_2 nanoparticles with higher refractive index.

We have prepared TiO_2/PDMS by mixing a commercially available PDMS pre-polymer and curing agent (Sylgard 184, Dow Corning) with TiO_2 nanoparticles (size: 21 nm, 718467, Sigma Aldrich). The mixture of the TiO_2/PDMS was spin-coated to form a film with a thickness of ~ 5 μm on Si substrate. Irradiation of 1.0 MeV protons with a beam size of ~1.0 mm and with a beam current of ~20 nA was performed either using a 1.0 MeV single-ended accelerator at SRL (SIT), or using a 3.0 MeV single-ended accelerator at TIARA (QST). The refractive index increase was observed for the film by spectroscopic ellipsometry.

Figure 1 shows optical absorption spectra obtained for TiO_2/PDMS composites with varied TiO_2 concentration. With increasing concentration of the nanoparticles, optical absorption at 300 - 400 nm associated with the band gap of the TiO_2 increases. The increased loss at 600 - 800 nm possibly due to the scattering by aggregated nanoparticles is significant for the TiO_2 concentration of 3.0 wt.%, while it is not for the concentration lower than 1.0 wt.%.

Figure 2 shows the refractive index change at 600 nm measured by the spectroscopic ellipsometer as a function of the concentration of TiO_2 nanoparticles. Since the refractive index of TiO_2 is relatively higher (~2.3) than that of PDMS (~1.4), the refractive index of the PDMS composite increased by 0.008 for the concentration of 1.0 wt.% TiO_2.

After 1.0-MeV proton beam irradiation, we observed the refractive index increase by 0.012 for the 1.0 wt.% TiO_2/PDMS composite with fluence of 1.0 MeV protons up to 100 nC/mm^2. The optical properties will be further investigated in conjunction with the results of microscopic observation of nanoparticles using SEM and EPMA.

References

[1] W. Kada *et al.*, Nucl. Instrum. Meth. Phys. Res. B, **348**, 218-22 (2015).
[2] R. Sano *et al.*, Nucl. Instrum Meth. Phys. Res. B, **404**, 228-32 (2017).

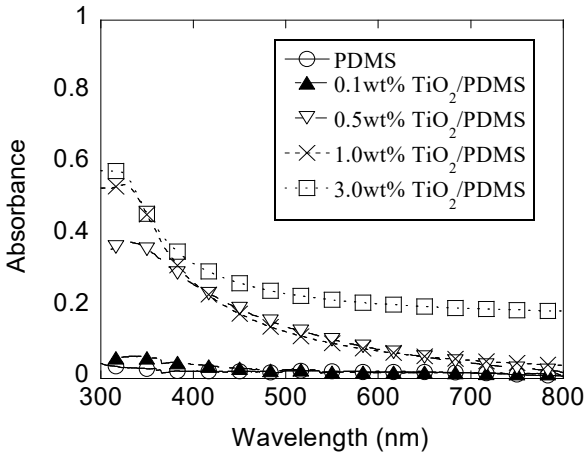

Fig. 1. Visible to ultraviolet absorption spectra of TiO_2/PDMS composite.

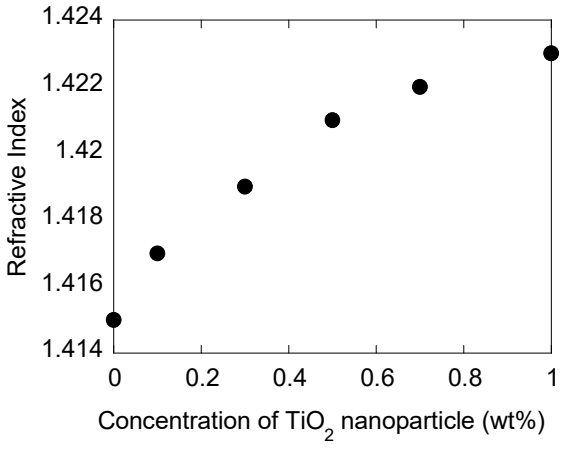

Fig. 2. Refractive index at 600 nm as a function of added TiO_2 particles to PDMS.

3 - 13 Fabrication of Neutron Optical Devices Using PBW Technique

T. Sakai [a)], H. Iikura [a)], N. Yamada [b)], T. Satoh [b)], Y. Ishii [b)] and M. Uchida [c)]

[a)] Neutron Materials Research Division, MSRC, JAEA,
[b)] Department of Advanced Radiation Technology, TARRI, QST,
[c)] Advanced Science Research Laboratory, Saitama Institute of Technology

In this paper, we report on the application of a UV/EB curable resin in proton beam writing (PBW) for the fabrication of fine neutron optical devices. PBW is a unique technique used for the fabrication of micro- and nano-structures with high-aspect-ratios from polymeric and inorganic materials [1]. The UV/EB curable resin is a photo-curable polymer that rapidly cures in three dimensions by radical polymerization. The resin is a liquid at room temperature; therefore, it mixes easily with functional materials, such as neutron absorbers [2]. On the other hand, electron vortex beams were first experimentally observed by M. Uchida and A. Tonomura in 2010 [3]. The electron vortex beam has a helical wavefront not a plane wave. It is expected that neutron vortex beams will be realized by using fine gratings like the electron beam. In case of neutron optics, 20-30 μm thick neutron absorber must be required as the grating materials, because neutron has relatively high transmittance in materials. So PBW is a promising technique to fabricate the neutron devices.

The fabrication process is similar to lithography. The base materials used are UV/EB curable resin and neutron absorber. The utilized resin is Bis-A ethylene oxide modified acrylate (ARAKAWA CHEMICAL INDUSTRIES, LTD.) [4]. The neutron absorber is gadolinium oxide (Gd_2O_3). The mean particle size is approximately 15 nm. The resin is mixed with the absorber at a mass ratio of 2:1. The optimum mixing ratio is still under investigation. The mixture of the base materials is spread on a sample backing film that attached on a sample holder. The film is 10 nm-thick gold coated 3.6 μm-thick PET and also plays the role of a beam exit window. The holder is an annular disk of acrylic resin, and the hole is 2 mm in diameter on the atmospheric side. Pattern exposures are performed using 3 MeV proton beams approximately 1 μm in diameter. The pixel resolution is approximately 0.6 μm. The beam fluence is of the order of 100 pC/mm^2 with a beam current of 1~2 pA. The irradiated areas are quickly cured by polymerization. The samples are developed with mixture of ethanol and 3 N hydrochloric acid. After the chemical process, the samples are treated with supercritical drying.

The fabricated gratings were observed using an optical microscope. The original pattern and the micrograph of the grating are shown in Fig. 1. The microscopic images show that the patterns of the fabricated structures agree well with the original one. In addition, a lateral direction of the sample was observed using the scanning electron microscope (SEM). The SEM image of sample is shown in Fig. 2. The thickness of the sample is approximately 35 μm.

In conclusion, the fabrication of grating structures is successful and the results also proved that the UV/EB curable resin is very promising material for use in PBW micromachining.

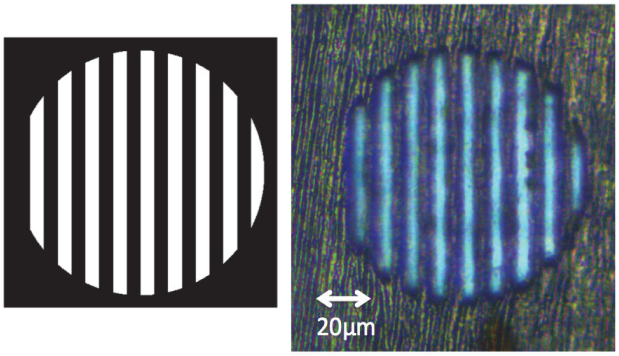

Fig. 1. The original pattern (left) and the micrograph of the fabricated grating structure.

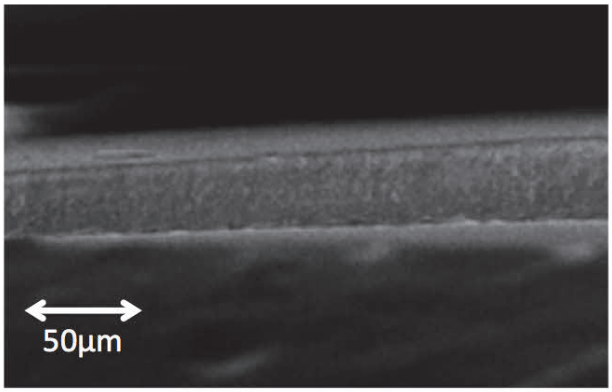

Fig. 2. The SEM image of lateral view of the grating structure.

References

[1] S. V. Springham *et al.*, Nucl. Instrum. Meth. Phys. Res. B, **130**, 155-59, (1997).
[2] T. Sakai *et al.*, Nucl. Instrum. Meth. Phys. Res. B, **332**, 238-41, (2014).
[3] M. Uchida and A. Tonomura, Nature **464**, 737-39, (2010).
[4] ARAKAWA CHEMICAL INDUSTRIES, LTD. website:http://www.arakawachem.co.jp/en/business/photo/03.html.

3 - 14 Formation of Nano-porous Surface Structures by Fast C_{60} Beam Bombardments

H. Tsuchida [a], N. Nitta [b], S. Tomita [c], K. Sasa [d], K. Hirata [e], H. Shibata [f], Y. Saitoh [g], K. Narumi [g], A. Chiba [g], K. Yamada [g] and Y. Hirano [g]

[a] Quantum Science and Engineering Center, Kyoto University, [b] School of Environmental Science and Engineering, Kochi University of Technology, [c] Institute of Applied Physics, University of Tsukuba, [d] Tandem Accelerator Complex, University of Tsukuba, [e] National Institute of Advanced Industrial Science and Technology (AIST), [f] The Institute of Scientific and Industrial Research, Osaka University, [g] Department of Advanced Radiation Technology, TARRI, QST

Ion-induced porous structures in semiconductor surfaces have recently attracted considerable attention as a new bottom-up approach to nanofabrication. In this work, the effect of cluster ion beam irradiation in GaSb surface was investigated by observation of porous structure. The formation of porous structure is dominated by self-assembly of the point defects induced by the cluster ion irradiation. The cluster ion beam has the potential to change of point defect density on cascade collision. We focus on the dependence of projectile energy or target temperature on the nano-porous structure formation in GaSb surfaces. A single crystal GaSb sample was bombarded by fast C_{60} beams with energy of 540-keV or 6-MeV. The formed nano-porous structures were characterized with a high-resolution scanning electron microscope. Comparison of the samples irradiated with monomer (C_1) and cluster (C_{60}) ion beams at the same equivalent fluence showed that the porous structure was observed only for the cluster beam irradiation. This indicates that the formation of the porous structure is due to the high density of point defects induced by cascade collision on the basis of the cluster ion irradiation. The cluster ion irradiation is therefore efficient for surface modifications.

The experiments were performed using two types of ion accelerators (a 400-kV ion implanter and a 3-MV tandem Pelletron accelerator) at TIARA. A well-collimated C_{60} projectile with incident energy of 540-keV or 6-MeV was incident parallel to the surface normal of a sample. A sample was a mirror polished GaSb single crystal wafer with (001) orientation. According to the previous study with low-energy atomic heavy ions [1], the following irradiation condition concerning the amount of defect production must be satisfied for the porous structure formation. The amount of defects produced at the surface layer of 18 nm thickness is more than 1,600 defects per a single projectile impact. Based on this result, we determined the beam fluence required to form porous structures, using a TRIM code [2]. In the present experiments, fluence of C_{60} beam was set to 1×10^{14} - 1×10^{15} ions cm^{-2}. A target was kept at two different temperatures during the irradiation experiment at room temperature (RT) without control, and low temperature (103 K) of liquid-nitrogen cooler. The evaluation of the as-irradiated surface was performed by field-emission scanning electron microscopy (FE-SEM) at Kochi University of Technology.

The surface SEM images of GaSb bombarded by C_{60} ion beam with energy of 540-keV or 6-MeV is shown in Fig. 1. Nanofiber networks are observed in them, whose shapes are different depending on the projectile energy. The growth of fiber networks is more remarkable for 6-MeV C_{60} beams. To compare with them, results for single atomic projectile bombardments (C ions) are also shown, where the fluence is equivalently the same as that of C_{60} beams. The nano-structure was not observed owing to less defect concentration for single atomic projectiles.

In Fig. 2, we demonstrate the temperature dependence on nano-porous structure formation. At the low temperature, the nano-porous structures were not formed, but uneven surface structures were visible. This is due to the prevention of point defect migration under low temperatures.

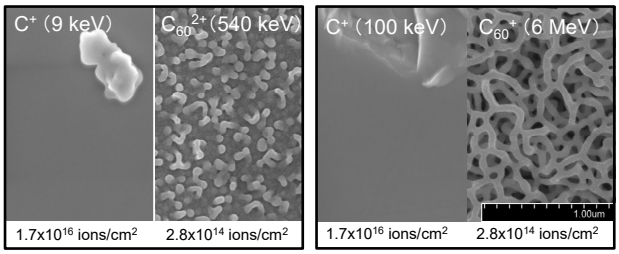

Fig. 1. Comparison of surface SEM images of GaSb irradiated with C_{60} cluster and C atomic beams: Left and right figures denote results obtained under the same irradiation conditions (beam fluence and projectile velocity), respectively.

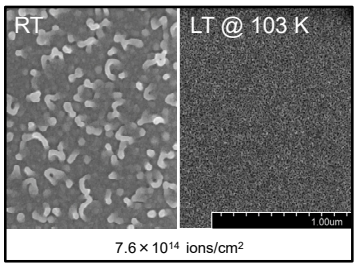

Fig. 2. Surface SEM images of GaSb irradiated with 540-keV C_{60} beams for different sample temperatures.

References

[1] N. Nitta *et al*., J. Appl. Phys. **92** 1799-802 (2002).
[2] J. Zieglar *et al*., SRIM Ver. 2013, www.SRIM.org.

3 - 15 Local Heating Induced by 0.72 MeV C_{60}^{3+} Ion Impacts

H. Hayashi [a], S. Matsuzaki [a], K. Nakajima [a], K. Narumi [b], Y. Saitoh [b], M. Tsujimoto [c], M. Toulemonde [d] and K. Kimura [a]

[a] Department of Micro Engineering, Kyoto University,
[b] Department of Advanced Radiation Technology, TARRI, QST,
[c] Institute for Integrated Cell-Material Sciences, Kyoto University,
[d] CIMAP, Le Grand Accélérateur National d'Ions Lourds (GANIL)

When a swift heavy ion impinges on a solid surface the ion loses its kinetic energy mainly via electronic excitations. The energy of the excited electrons is transferred to the lattice and the temperature rises around the impact position in a short period of ~10^{-11} s. Recently, we have demonstrated that such local heating can be traced by observing desorption of gold nanoparticles (Au-NPs) from the surface upon ion impacts [1]. In this work, we extend our previous work to cluster ion impacts. The temperature of local heating induced by MeV C_{60}^{3+} ions on amorphous silicon nitride (a-SiN) was studied with emphasis on the difference between the entrance and exit surfaces.

Either gold or platinum nanoparticles (Pt-NPs) were deposited on a-SiN films by vacuum evaporation. The prepared Au- and Pt-deposited films were irradiated with 0.72 MeV C_{60}^{3+} ions at normal incidence to a fluence of $3 - 5 \times 10^{10}$ ions/cm^2 using the 400-kV ion implanter of TARRI, QST.

Figure 1(a) shows an example of the TEM bright field images of the Pt-deposited a-SiN film before irradiation. There are many Pt-NPs formed by the vapor deposition. This sample was irradiated with 0.72 MeV C_{60}^{3+} ions. The irradiation was performed on the Pt-deposited side (front surface irradiation). Ion tracks are clearly seen as bright spots with a diameter of about 4 nm (Fig. 1(b)). It is seen that the Pt-NPs disappeared from the surrounding area of the ion tracks. According to the MD simulations [2], this indicates that the temperature of the NP-cleared region surpassed the melting point of NPs during the local heating. A similar results were also observed for Au-NPs deposited films. The NP-cleared region for Au-NPs is much larger than that for Pt-NPs. This is because the melting point of Au-NP (0.4 eV/atom) is lower than that of Pt-NP (0.64 eV/atom).

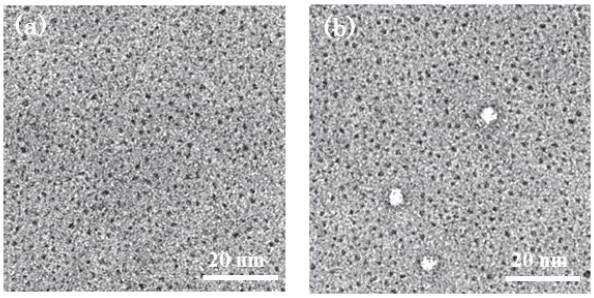

Fig. 1. TEM bright field images of Pt-deposited 20-nm a-SiN films observed (a) before and (b) after irradiation with 0.72 MeV C_{60}.

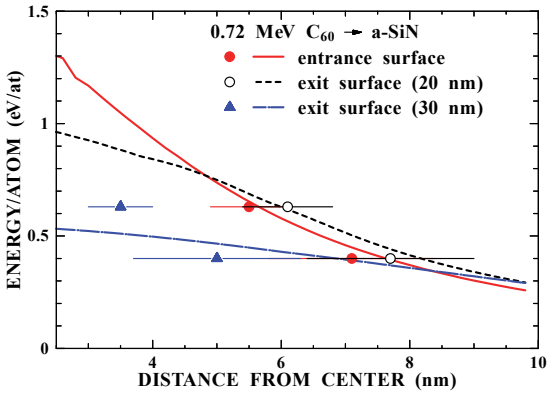

Fig. 2. Observed temperature distributions of local heating upon impact of 0.72 MeV C_{60} ions on a-SiN (symbols). The symbols at 0.4 (0.64) eV/atom correspond to the results with Au- (Pt-) NPs. The results of u-TS calculations are also shown (lines).

Figure 2 shows the observed temperature distributions on the entrance and exit surfaces of a-SiN films. Comparing to the entrance surface, the local heating on the exit surface is enhanced in the case of 20-nm film while it is reduced in the case of 30-nm film. It is noteworthy that the stopping power of the C ion at exit surface (0.27 and 0.26 keV/nm for 20- and 30-nm a-SiN, respectively) is slightly lower than that at the entrance surface (0.29 keV/nm) irrespective of the film thickness. This indicates that the stopping power difference cannot be the origin of the observed complicated behavior of the local heating on the exit surface. A possible origin could be the dissociation of C_{60} ions during penetration.

Taking account of the dissociation of C_{60} ions, the temperature evolution of the local heating induced by C_{60} ion impact was calculated using the unified thermal spike (u-TS) model. The calculated results are shown by lines in Fig. 2. The agreement with the observed results is reasonably good. This indicates that the u-TS model is proper for describing the local heating induced by MeV C_{60} ions and the observed complicated behavior is ascribed to the dissociation of C_{60} ions during penetration.

References

[1] K. Nakajima *et al.*, Sci. Rep., **5**, 13363 (2015).
[2] C. Anders *et al.*, Nucl. Instrum. Meth. Phys. Res. B, **267**, 2503-14 (2009).
[3] M. Toulemonde *et al.*, Phys. Rev. B, **83**, 054106 (2011).

3 - 16 Distribution of the Number of Secondary Ions Emitted by Sub MeV C_{60} Ion Impacts

K. Hirata [a)], K. Yamada [b)], A. Chiba [b)], Y. Hirano [b)], K. Narumi [b)] and Y. Saitoh [b)]

[a)] Research Institute for Material and Chemical Measurement, AIST,
[b)] Department of Advanced Radiation Technology, TARRI, QST

Secondary ions (SIs), produced upon a primary ion impact on a target, are emitted from the target surface with various emission parameters, including the number, energy, and angle. The distribution of the number of SIs emitted for one primary ion should include information on how the SIs are emitted from the target, however, their detailed measurements and analysis have not been performed. One of the reasons is that the mean SI number per impact is too small to obtain the distributions accurately. Cluster ion impacts give different energy transfer from monoatomic ion impacts, which considerably enhances the mean numbers of emitted SIs in comparison with the impact of the corresponding monoatomic ion with the same velocity [1]. Generally, the larger the primary cluster ion is, the larger the enhancement effect is expected to be on the mean SI number. The higher mean number of emitted SIs makes it possible to measure their number distributions accurately. In this paper, we report distributions of the emitted SI number for a series of sub MeV C_{60} ion impacts on an organic target [2].

The experiments were performed using a time-of-flight (TOF) SI mass spectrometer with primary C_{60} ions with energies of the order of sub MeV at QST/Takasaki [3]. A pulsed C_{60} ion beam was incident on a poly methyl methacrylate (PMMA) target at an angle of 45º to the target surface. The number of positive-SIs (P-SIs) for each ion pulse was recorded based on event-by-event counting. The counting data were analyzed using an analytical model that can derive the distributions of the number of emitted SIs from experimental counting data obtained by a TOF SI ion mass spectrometer combined with pulsed primary ion beams [2]. Additionally, I_o and I_p (I_o: incident beam electric current, I_p: P-SI current) were measured as described elsewhere [4]. As major peaks observed in P-SI mass spectra obtained by the TOF SI mass spectrometer can be attributed to singly-charged ions, the qI_p/I_o values (q: incident ion charge number) give the mean numbers of emitted P-SIs per C_{60} ion impact.

As an example, Fig. 1 shows the counting data for 0.54-MeV C_{60}^{2+} together with the distributions reproduced by the analytical model [2]. The dotted, dashed, and dotted and dashed lines in the figure show the results of the least-squares fits of the model to the counting data under the condition that the number distribution of the emitted SIs for each ion pulse follows the (a) Polya, (b) Poisson, and (c) two Poisson distributions, respectively. The line (c) using two Poisson distributions is calculated by taking into consideration of single- and double-impact events for one ion pulse because the double-impact event, containing two primary ions for one pulse, gives a different mean SI number from the single-impact event. A comparison between the lines reveals that the line (c) provides better reproducibility than the other lines.

The fitting parameters obtained in the fits using two Poisson distributions provide the values related to the mean SI number and the probability of the single-impact events, and consistency between each fitting parameter and the corresponding experimental value is observed [2]. This shows that use of two Poisson distributions for single- and double-impact events are appropriate for expressing the emitted SI number distribution. Figure 2 shows the emitted SI number distribution obtained by the fitting parameters of the line (c). Thus, we have the result that the number distribution of the emitted SIs for one impact can be well approximated by the Poisson distribution [2]. Similar results are obtained for the other C_{60} impacts.

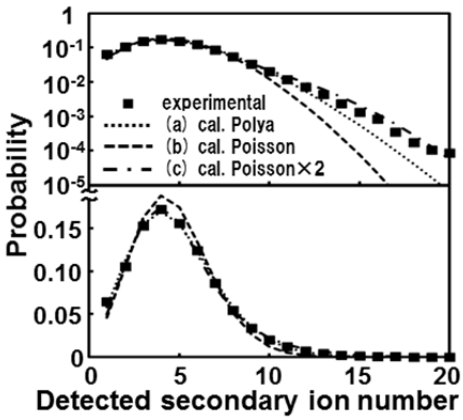

Fig. 1. Probability distribution of the detected secondary ion number for 0.54-MeV C_{60}^{2+} impact.

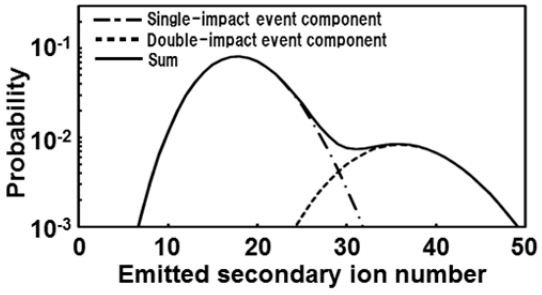

Fig. 2. Probability distribution of the emitted secondary ion number for 0.54-MeV C_{60}^{2+} impact.

References

[1] K. Hirata *et al.*, Appl. Phys. Lett., **81**, 3669 (2002).
[2] K. Hirata *et al.*, J. Chem. Phys., **145**, 234311 (2016).
[3] K. Hirata *et al.*, Nucl. Instrum. Meth. B, **266**, 2450 (2008).
[4] K. Hirata *et al.*, Appl. Phys. Lett., **85**, 044105 (2005).

3 - 17 Thermal Stability of Irradiation-induced Non-equilibrium Lattice Structures of NiTi Intermetallic Compound

M. Ochi [a)], H. Kojima [a)], Y. Kaneno [a)], F. Hori [a)], Y. Saitoh [b)], S. Semboshi [c)] and A. Iwase [a)]

[a)] Department of Materials Science, Osaka Prefecture University,
[b)] Department of Advanced Radiation Technology, TARRI, QST,
[c)] Institute for Materials Research, Tohoku University

In our previous report [1], we have shown that the 16 MeV Au ion irradiation induces the amorphous state and 200 MeV Xe ion irradiation induces the disordered BCC structure (A2 structure) in NiTi intermetallic compounds. Such irradiation-induced lattice structures cannot be found in the phase diagram. Therefore, they are far from the thermal equilibrium states and unstable against the thermal energy. In the present study, we have investigated the thermal stability of the irradiation-induced lattice states in NiTi by using the annealing experiment at elevated temperatures.

NiTi bulk samples with the B19' structure were irradiated with 16 MeV Au ions at QST-Takasaki or with 200 MeV Xe ions at JAEA-Tokai at room temperature. The ion fluence for each irradiation was 5×10^{13} /cm^2. After the irradiation, the thermal annealing was performed at 523 K, 673 K, 823 K and 973 K. The time interval for each annealing was 60 min. Before and after the irradiation and after the thermal annealing, the grazing incidence X-ray diffraction (GIXD) was measured to investigate the effect of annealing on the surface lattice structure.

Figure 1 shows the effect of the thermal annealing on the GIXD spectrum for the Xe ion–irradiated samples. The spectrum for the unirradiated sample shows the B19' structure. The spectrum for the irradiated sample clearly shows that the Xe ion irradiation induces the A2 lattice structure. By the 523 K annealing, the A2 lattice structure remains unchanged. By the annealing at 673 K, however, the lattice structure nearly completely recovers to the intrinsic B19' structure.

Figure 2 shows the effect of the thermal annealing on the GIXD spectrum for the Au ion irradiated samples. The spectrum for the irradiated sample shows only one broad peak, meaning that the Au ion irradiation induces the amorphous state. By the 523 K annealing, the irradiation-induced amorphous state does not change. By the annealing at 673 K, the lattice structure recovers to the intrinsic B19' structure.

The present result confirms that the irradiation induced lattice structure is not the thermal equilibrium state and is unstable against the thermal energy. The present result also shows that even though the irradiation induced lattice state is different (amorphous state or A2 structure), the annealing temperature, at which the lattice structure recovers to the intrinsic structure, is the same.

Reference

[1] M. Ochi *et al.,* QST-Takasaki Annu. Rep. 2015, **QST-M-2**, 62 (2017).

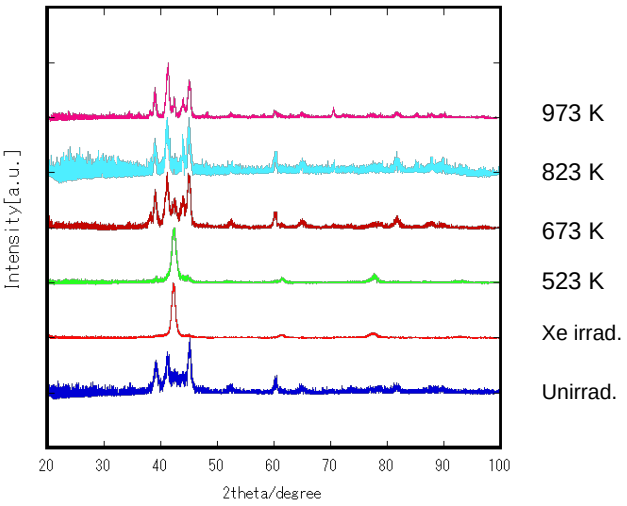

Fig. 1. GIXD spectra for unirradiated NiTi sample, for 200 MeV Xe ion irradiated NiTi sample and thermally annealed NiTi sample.

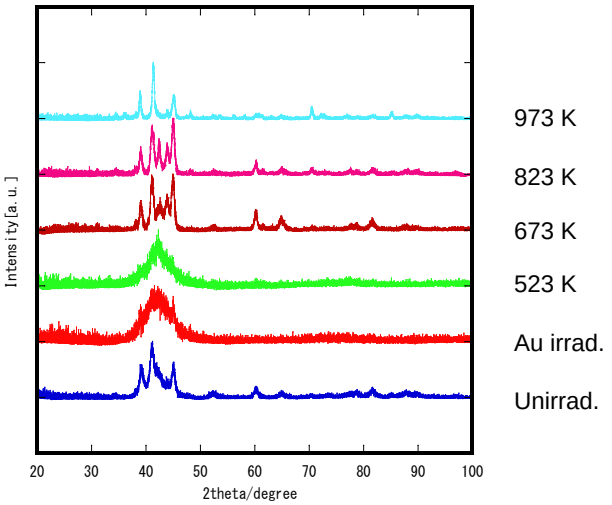

Fig. 2. GIXD spectra for unirradiated NiTi sample, for 16 MeV Au ion irradiated NiTi sample and thermally annealed NiTi sample.

3 - 18 Optical Absorption due to Silver Nano-particles in Silica Glass Produced by 380 keV-Ag Ion Implantation and Subsequent Energetic Heavy Ion Irradiation

K. Fukuda [a)], F. Hori [a)], S. Semboshi [b)], Y. Saitoh [c)] and A. Iwase [a)]

[a)] Department of Materials Science, Osaka Prefecture University,
[b)] Institute for Materials Research, Tohoku University,
[c)] Department of Advanced Radiation Technology, TARRI, QST

Nanocomposite glasses containing metal nanoparticles in a matrix have become an object of interest among many researchers because of their promising photonics materials for the fabrication of optical components. The presence of metal nanoparticles leads to the modification of optical properties of the glass matrix. There are several well-known methods to prepare nanocomposite glasses. The ion implantation is one of the most suitable techniques for the synthesis of metal nanoparticles in solid host matrix. The advantages of the ion implantation are the possibilities to use any matrix, to choose various elements to be implanted, to overcome the solubility limits and to control the depth and distribution of implanted atoms. The optical properties of the nanocomposite glasses depend on the type of implanted ions, the fluence and the energy of the ions. In the present study, we have investigated the effect of Ag ion implantation and the subsequent high energy heavy ion irradiation on the optical absorption of silica glass.

Target samples were silica glass sheets with the dimension of 5 mm × 5 mm × 1 mm. They were implanted with 380 keV Ag ions at room temperature with various fluences. After the ion implantation, some samples were subsequently irradiated with 16 MeV Au ions at room temperature.

The optical absorption measurement shows an absorption band around 400 nm for the Ag ion implanted samples, corresponding to the surface plasmon resonance of the Ag nanoparticles. With increasing the amount of implanted Ag ions, the intensity of 400 nm peak increases and also another peak appears around 600 nm (Fig. 1).

This experimental result shows that Ag nano-particles are produced by the ion implantation, and that the size and density of Ag nanoparticles change gradually during the Ag implantation (Fig. 2). It is suggested that the change cause the appearance of another peak around 600 nm.

The optical absorption spectra are also changed by the subsequent 16 MeV Au ion irradiation (Fig. 3). The positions of 400 nm peak and 600 nm peak shift to lower wavelengths and their intensity decreases.

The present experimental result suggests that the combination of the metal ion implantation and the subsequent high energy ion irradiation is a useful method to control the optical properties of silica glass.

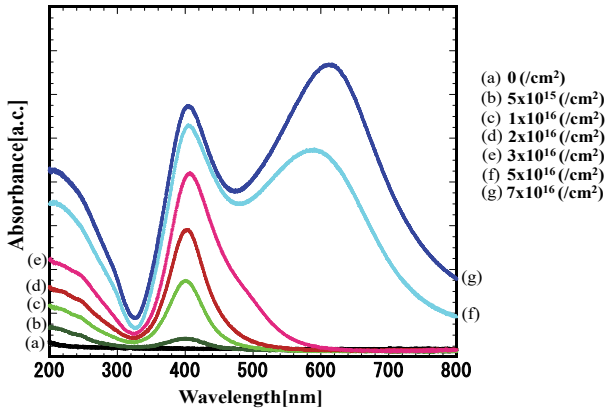

Fig. 1. Optical absorption of SiO_2 implanted with 380 keV-Ag^+.

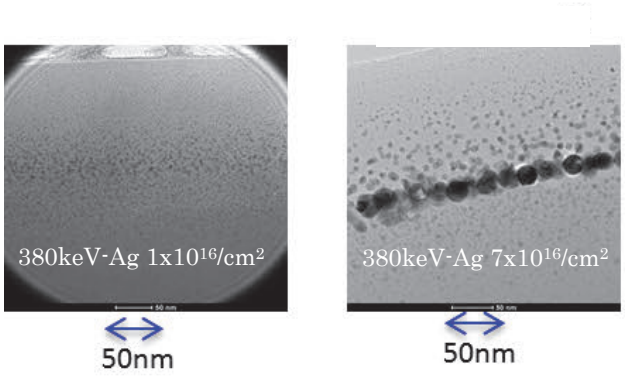

Fig. 2. TEM images of SiO_2 implanted with 380 keV Ag ions.

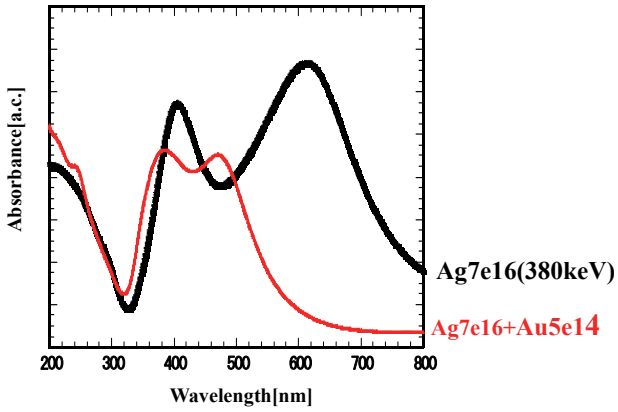

Fig. 3. Optical absorption of Ag-implanted SiO_2 before and after 16 MeV Au ion irradiation.

3 - 19 Change in Magnetic Properties of FeRh by C_{60} Cluster Ion Beam Irradiation

R. Soma [a)], A. Iwase [a)], Y. Saitoh [b)] and T. Matsui [c)]

[a)] Department of Materials Science, Osaka Prefecture University,
[b)] Department of Advanced Radiation Technology, TARRI, QST,
[c)] Research Organization for the 21st Century, Osaka Prefecture University

Iron rhodium is known to exhibit a first order phase transition from anti-ferromagnetic to ferromagnetic near room temperature. We have ever revealed that the energetic ion beam irradiation induces the ferromagnetic state below room temperature. Further irradiation caused the structural phase transition to high temperature phase which resulted in exhibiting paramagnetic nature [1]. In addition, the change in magnetization of ion irradiated FeRh was considered to be mainly dominated by elastic collisions between the ions and the samples, and not by ion fluence or electron excitation [2]. However, in our recent studies, we revealed that the saturation magnetization of the sample irradiated with the Au_3 cluster ions was larger than that of the sample irradiated with the Au single ions even when the same number of Au ions was irradiated with the same rate. In the present study, therefore, we examined the cluster effect by using the C_{60} cluster ions.

The samples were FeRh thin films about 50 nm thick, which were deposited on MgO substrates by the ion beam sputtering equipment. The samples were irradiated with 83 keV C_1 ions. The fluences are 6.75×10^{12} C_1/cm^2, 1.35×10^{13} C_1/cm^2, and 1.35×10^{14} C_1/cm^2. Magnetic properties near the surface of samples were characterized by XMCD method at KEK-Photon Factory.

Figure 1 shows the x-ray magnetic circular dichroism (XMCD) spectra at the Fe L2,3-edge for the unirradiated and irradiated samples. As can be seen in the figure, with the small fluence, the Fe L2,3-edge spectrum for the sample irradiated with C_{60} cluster ions shows a larger XMCD signal than that for the sample irradiated with C_1 ions under the same fluence. On the other hand, with the large fluence, the spectrum for the sample irradiated with C_1 ions shows a larger XMCD signal than that for the sample irradiated with C_{60} cluster ions.

Figure 2 shows the magnetic moment per Fe atom as a function of ion fluence, which was obtained by analyzing the XMCD spectra. As can be seen in Fig. 2, In the case of the sample irradiated with C_{60} cluster ion, the magnetic moment increases with small fluence and then decreases, however, for the C_1 ions, it monotonically increases with increasing ion fluence. These results show that C_{60} cluster ion irradiation is much better than C_1 single ion irradiation for the viewpoint of saturation magnetization, even if the same irradiation energy is deposited in the samples. This is also qualitatively in agreement with the result in the case of Au cluster ion irradiation and clearly denies the conclusion that the deposition energy by elastic collisions dominates the change of magnetization, which has been discussed in the previous reports.

References

[1] M. Fukuzumi *et al.*, Nucl. Instrum. Meth. Phys. Res. B, **230**, 269-73 (2005).
[2] N. Fujita *et al.*, J. Appl. Phys., **107**, 09E302 (2010).

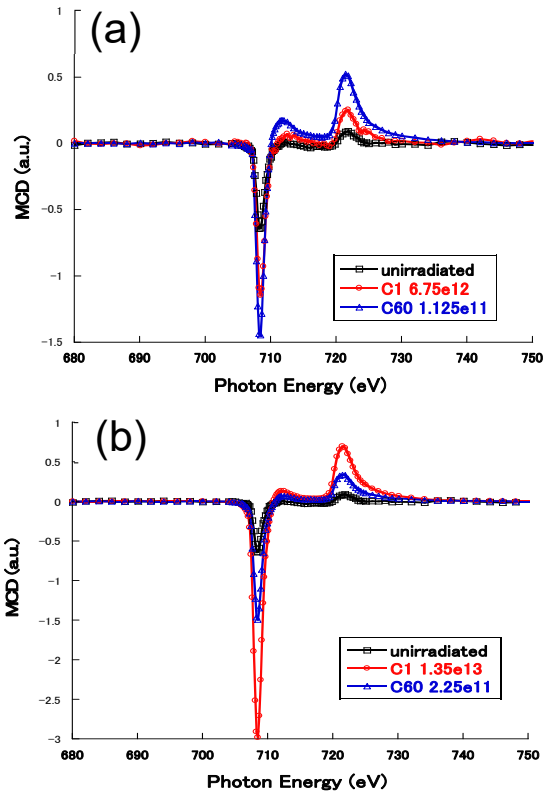

Fig. 1. XMCD spectra for the irradiated samples with the C_1 and C_{60} cluster ion.

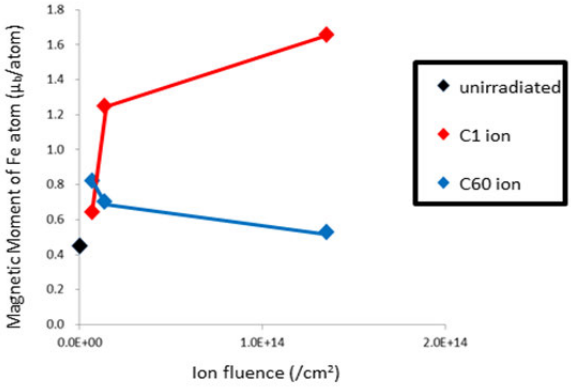

Fig. 2. Magnetic moment per Fe atom for the irradiated samples with C_1 and C_{60} cluster ions, as a function of ion fluence.

3 - 20 Shape Elongation of Embedded Metal Nanoparticles Induced by C_{60} Cluster Ion Irradiation

H. Amekura [a)], Y. Saitoh [b)], A. Chiba [b)], Y. Hirano [b)], A. Usui [c)] and K. Narumi [b)]

[a)] RCAMC, National Institute for Materials Science (NIMS),
[b)] Department of Advanced Radiation Technology, TARRI, QST,
[c)] Health and Safety Department, ORDC, JAEA

Shape elongation of embedded nanoparticles (NPs) induced under swift heavy ion (SHI) irradiation has been extensively studied for this decade [1]. While the mechanism is still under debate, the majority agree with an assumption that large electronic energy deposition plays an important role. However, SHI is primarily defined by its high velocity, *i.e.*, large kinetic energy per nucleon, which is higher than ~0.1 MeV/u.

An arising question is whether the shape elongation of NPs is induced under irradiation with slow ions but high electronic stopping power S_e. We have irradiated Zn NPs with 6 MeV C_{60}^+ ions, which have a slow velocity of 0.008 MeV/u. The S_e value of the C_{60} ions was estimated by the sum of independent 60 pieces of 6 MeV/60 = 0.1 MeV carbon monomer ions. The estimated value was 15.5 keV/nm in silica, which was comparable to S_e of 200 MeV Xe SHIs.

Contrary to SHIs, the cluster ions interact with NPs in shallow depth only. A C_{60} ion injected into a solid can be no longer stable as in a vacuum. The interatomic distances increase with the depth and finally the C_{60} ion is no longer a cluster ion but 60 pieces of C monomer ions. While the ion range of 100 keV C-monomer ion is 315 nm, the cluster effect can be active only much shallower than the ion range of 315 nm. We formed Zn NPs in the surface layer of silica (SiO_2) shallower than 70 nm [2] using 60 keV Zn^+ ion implantation to a fluence of 1×10^{17} ions/cm^2.

The irradiations of C_{60}^+ ions were carried out at TARRI, QST, using a newly developed high-flux C_{60} negative ion source. A 6 MeV C_{60}^+ beam of ~50 pA was utilized through an aperture of 3 mm in diameter in the present experiments, while the flux can be increased further more.

We have developed a sensitive detection method for the elongation of NPs using linearly polarized light [3]. Figure 1 shows optical absorption spectra of Zn NPs embedded in silica irradiated with 6 MeV C_{60}^+ ions to different fluences, monitored by linearly polarized light. Dotted and solid curves denote the polarization parallel (0°) and perpendicular (90°) to the major axes of the NPs. In unirradiated state, the spectra detected in both the polarizations mostly overlapped with each other. A broad peak around 4.8 eV was observed and ascribed to Zn NPs [4]. The independence from the polarization angle indicated the NPs in spherical shapes and no macroscopic anisotropy. However, weak but non-negligible deviation of the spectra was observed between both the polarizations at the fluence of 1×10^{12} ions/cm^2, indicating the elongation of NPs. At the fluence of 1×10^{13} ions/cm^2, the deviation became more pronounced, indicating enhanced elongation. However, at the fluence of 5×10^{13} ions/cm^2, all the absorption due to Zn NPs mostly disappeared. This is ascribed to enhanced sputtering loss. In fact, the 4.8 eV peak due to Zn NPs showed a monotonic decrease with the fluence, which began even at 1×10^{12} ions/cm^2. Since the Zn NPs exist only in the surface layer of ~70 nm thick, the absorption change looks very suddenly.

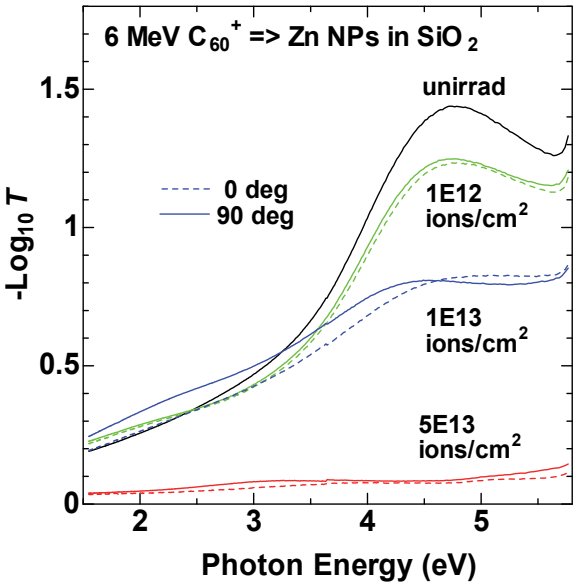

Fig. 1. Optical absorption spectra of Zn NPs in silica irradiated with 6 MeV C_{60}^+ ions, detected by linearly polarized light. Dotted and solid curves denote the polarization parallel (0°) and perpendicular (90°) to the major axes of the NPs, respectively. The deviation between the different polarizations corresponds to the elongation of NPs. A decrease of the 4.8 eV peak with the fluence corresponds to sputtering loss of Zn NPs.

References

[1] G. Rizza and M. C. Ridgway, in *"Ion Beam Modification of Solids"*, ed. W. Wesch and E. Wendler, Chap. 11, [Springer, New York] (2016).
[2] H. Amekura and N. Kishimoto, in *"Lecture Notes in Nanoscale Science and Technology" Vol. 5*, ed. Z. Wang, [Springer, New York], p. 1~75 (2009).
[3] H. Amekura *et al.*, Phys. Rev. B, **83**, 205401 (2011).
[4] H. Amekura *et al.*, Nanotechnology, **18**, 395707 (2007).

3 - 21 Development of Nanomaterials and Visualization of Ion Tracks through Interactions between Cluster Ion Beams and Organic Materials

T. Sakurai [a)], A. Horio [a)], K. Kayama [a)], A. Chiba [b)], Y. Saitoh [b)], K. Narumi [b)] and S. Seki [a)]

[a)] Department of Molecular Engineering, Graduate School of Engineering, Kyoto University,
[b)] Department of Advanced Radiation Technology, TARRI, QST

Since highly accelerated cluster ions with MeV energies serve as new radiation sources useful for future industrial applications, understanding of these ions is strongly demanded. Our research is directed to the visualization of interactions between a series of cluster ions, in particular for C_{60} ions, and organic materials. Related researches reported by other groups include the observation of latent tracks of C_{60} cluster ions irradiated to thin films of C_{60} by transmission electron microscopy (TEM) [1]. Meanwhile, our group has developed a novel method to isolate nanowires on substrates via intra-track cross-linking/ polymerization reactions using high-energy single particles and the following development process using organic solvents [2-4]. So far we have demonstrated this technique by using single ions and cluster beams composed of a couple of ions. Moreover, in the last-year project, we newly used C_{60}^{+} cluster ions and found tadpole-shaped nanostructures that were formed after the irradiation of C_{60}^{+} ions and following development process. Here we further investigated how the C_{60}^{+} ion interacts with an organic thin film by changing the film thickness.

Six MeV C_{60}^{+} ions were generated by a tandem accelerator at TARRI. For the observation of tracks of a single cluster ion, the fluence was set at 1.0×10^{9} cm^{-2} to avoid the overlaps of ion trajectories. 4,4',4''-Tri-9-carbazolyltriphenylamine (**TCTA**) was purchased from TCI Co. and used as received. In this study, the target **TCTA** films with a thickness of 125, 290, and 1,200 nm were prepared on a silicon substrate by spin-coating or dropcasting method, and irradiated with 6.0 MeV C_{60}^{+} under vacuum. Then the films were developed by cyclohexane and observed by atomic force microscopy (AFM). As shown in Fig. 1a, nanowires with a length of ca. 100 nm were observed as similar to the case with single ion irradiations. Thus these nanowires were formed by the polymerization/crosslinking reactions of **TCTA** molecules in solid state and isolated by eluting the non-reacted pristine **TCTA** area with cyclohexane. Of interest, tadpole-shaped nanostructures with a length of 201 ± 17 nm were developed from 290-nm thick films. To our surprise, 194 ± 23 nm length tadpole-shaped nanostructures were isolated by the same procedure with 1,200-nm thick films. If the charged particles penetrate the film and reach up to the silicon substrate, the nanowire length should correspond to the film thickness. Therefore, the quite similar lengths observed for 290 and 1,200-nm thick films indicate that the range of particles was saturated at around 200 nm, where the schematic illustration of ion tracks was drawn as Fig. 1 (bottom). We presumed that a C_{60}^{+} cluster ion was dissociated soon after the penetration into the film surface and gradually become the equilibrium charge state. Then coulomb repulsion among carbon ions was operated to result in the enlarged inter-ion distance. Finally the kinetic energy of the ions was sufficiently decreased to trigger a coulomb expansion, which resulted in the formation of the “head” of the tadpole nanostructure.

References

[1] P. Kumar *et al.*, Appl. Surface Sci., **313**, 102-06 (2014).
[2] Y. Takeshita, T. Sakurai, M. Sugimoto, S. Seki, *et al.*, Adv. Mater. Lett., **6**, 99-103 (2015).
[3] A. Horio, T. Sakurai, G. B. V. S. Lakshmi, D. K. Avasthi, M. Sugimoto, T. Yamaki, S. Seki, Nanoscale, **8**, 14925-31 (2016).
[4] A. Horio, T. Sakurai, K. Kayama, G.B.V.S. Lakshmi, D. V. Avasthi, M. Sugimoto, T. Yamaki, A. Chiba, Y. Saito, S. Seki, Radiat. Phys. Chem., in press. (2017). DOI: 10.1016/j.radphyschem.2017.02.052.

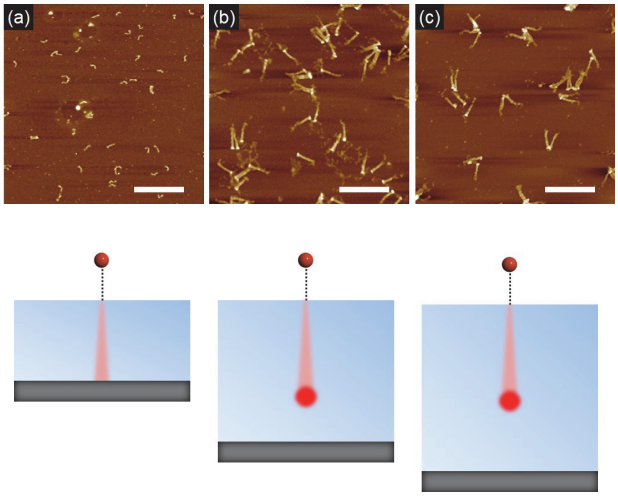

Fig. 1. (top) AFM topographic images of nanowires from thin films of **TCTA**. The film thicknesses are 125, 290 and 1,200 nm for (a–c) respectively. The films were irradiated with 6.0 MeV C_{60}^{+} ions at the fluence of 1×10^{9} ions cm^{-2}, and developed with cyclohexane. Scale bars represent 500 nm. (bottom) Schematic illustrations of possible ion tracks of 6.0 MeV C_{60}^{+} cluster ion in **TCTA** film on Si substrate. The thicknesses of **TCTA** are 125, 290, 1,200 nm (left to right), respectively.

3 - 22 Production Yield of Swift MeV/atom Carbon Cluster Ions as a Function of Charge-changing Gas Pressure

T. Kaneko [a)], D. Miyamoto [a)], S. Fukushima [a)], Y. Yamashita [a)] and Y. Saitoh [b)]

[a)] Graduate School of Science, Okayama University of Science,
[b)] Department of Advanced Radiation Technology, TARRI, QST

Swift cluster ion beams have been utilized to study various phenomena in basic and applied fields [1-6]. With use of tandem accelerator, the charge-changing process from negative to positive charge state and the decay process will govern the intensity of positively charged cluster ions. This theoretical study aims to obtain more intense cluster ion beam and understand elementary processes regarding charge changing and destruction processes, and if possible to find cluster effect in cross sections for those processes. The basic equation here is the rate equation, which describes the charge state fraction $\phi_i(x)$ of a cluster in charge state *i* at penetrating depth *x* in the charge- changing region:

$$\frac{d\phi_i(x)}{N\,dx} = \sum_{j(\neq i)} \sigma_{ji}\phi_j(x) - \left(\sum_{j(\neq i)} \sigma_{ij} + \sigma_{id} \right) \phi_i(x)$$

Here σ_{ij} is the cross section for changing charge from *i* to *j* of a cluster, σ_{id} the destruction cross section for a cluster in charge state *i* in collision with a target gas, and N is the number density of a target gas. Here we considered charge state $i = -1, 0, 1$. Solving the above equation under the initial condition of $\phi_{-1}(0) = 1, \phi_0(0) = 0$, and $\phi_1(0) = 0$, one has the expression of $\phi_1(x)$. Apart from a previous work [6], we took into account charge state difference in destruct cross sections.

We estimated the cross sections of σ_{ij} and σ_{id} in a quantum-mechanical treatment. According to the time-dependent perturbation theory, the destruction and production processes are regarded as the electron stripping from a cluster excited by an incident neutral (target gas) atom, if it is seen in the rest frame of a cluster. In the collision of a C_2 ion with a rare-gas atom, the transition amplitude of an electron from the initial (i) state to a final (j) state is formulated in the framework of impact parameter method, where the target atom is assumed to move on a straight-line trajectory at constant speed. In case of a carbon cluster atom, the initial states of electrons are 1s, 2s, and 2p states, whose Hartree-Fock (HF) wave-functions were tabulated. Here we use only the radial distribution function because the angular distribution is assumed to be averaged. The final ionized state is expressed by a distorted plane wave. Using the single electron ionization probabilities as a function of impact parameter together with the independent-electron model, we estimate the one- and multi-electron ionization cross sections for charge changing process. Destruction cross sections are estimated as those which yield for more than doubly positive charge states of a cluster. As a result, in collision of 2.5 MeV C_2 with Ne target, we obtained in Fig. 1 the singly charged C_2 ion as a function of gas pressure of Ne. These calculated results are found to show a similar profile of the experimental particle yield [7] so that we will refine the present treatment as a next step, and will discuss the cluster effect in charge-changing and destruction cross sections.

References

[1] T. Kaneko, Phys. Rev., **A66**, 052901 (2002).
[2] A. Chiba *et al.*, Phys. Rev., **A76**, 063201 (2007).
[3] A. Chiba *et al.*, Nucl. Instrum. Meth. B, **315**, 81 (2013).
[4] S. Tomita *et al.*, Phys. Rev., **A73**, 060901(R) (2006).
[5] T. Kaneko, Phys. Rev., **A 86**, 012901 (2012).
[6] F. Zappa *et al.*, Phys. Rev., **A 64**, 032701 (2001).
[7] Y. Saitoh *et al.*, private communication.

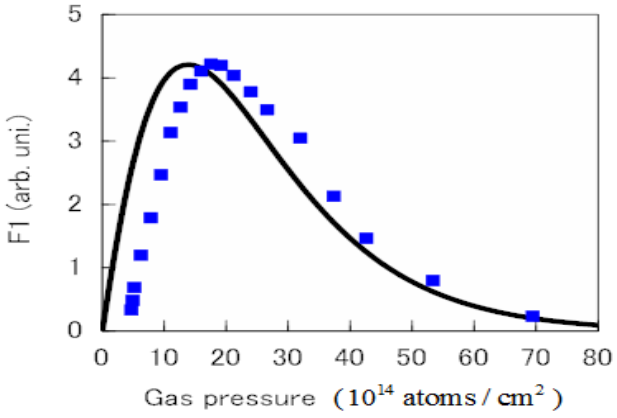

Fig. 1. The yield of singly charged C_2 cluster ions vs gas pressure of Ne. The solid line shows the theoretical result and the solid squares are the experimental data [7]. The theoretical curve is normalized to fit the maximum value of the experimental data.

3 - 23 Study on Interaction of Swift Cluster Ion with Matter

Y. Yuri, Y. Saitoh, A. Chiba, K. Yamada, Y. Hirano and K. Narumi

Department of Advanced Radiation Technology, TARRI, QST

Interaction of high energy cluster ions with matter has attracted considerable attention in fundamental research fields and also in various application fields, because of a massive energy deposition into a very small volume in solid materials introduced by simultaneous multiple collisions of constituent atoms of a cluster ion and an isotropic collision with an atom or a molecule in a gas phase. In the last financial year, the interaction of C_2^- with a helium gas-target and that of C_n^+ (n=1, 3, 4, and 8) and C_{60}^{2+} with Gafchromic films were investigated.

Study on interaction of swift cluster ion with gas phase

Cross sections of a negative cluster ion C_2^- for collision-induced destruction and charge exchange from a negative ion to positive one are investigated by measuring a cluster ion beam transmission as a function of the target gas density at a charge exchange section in a tandem accelerator. That allows us to determine the cross sections [1]. The destruction cross section for C_2^- in 1.25 MeV/atom on the helium gas target is shown in Fig. 1 with those on neon and xenon previously obtained. The cross sections decrease with decreasing physical radius (ex. Van der Waals radius) of target gases, and the tendency qualitatively consists with our previous work [2]. However, the cross section for helium is smaller than that predicted by anisometric collision of C_2^- with helium atom.

Study on the cluster-ion irradiation response of a Gafchromic radiochromic film

It is necessary to measure and evaluate the two-dimensional (2D) spatial profile of MeV cluster ion beams for the utilization of the cluster beams in the TIARA tandem accelerator. Here, a Gafchromic radiochromic film (Ashland) [3] is employed as a possible tool to measure the profile of the cluster ion beams. Therefore, the coloration response of Gafchromic HD-V2 film was investigated using different cluster ion beams.

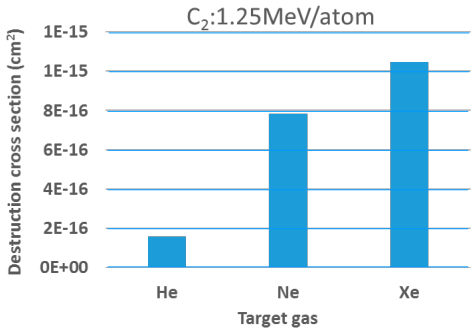

Fig. 1. The destruction cross sections of C_2^- (1.25 MeV/atom) collided with target gases of helium, neon and xenon.

A change in the optical density (OD) was quantified by reading ion-irradiated films with a flatbed optical scanner according to Ref. [4]. The irradiation results of several C cluster ion beams are summarized together with the result of monoatomic ions in Fig. 2 where the net OD is plotted as a function of the atom fluence. No significant difference in the OD responses can be seen among $C_1 \sim C_8$ while the data of C_{60} is slightly shifted toward the high-fluence side. Namely, the sensitivity of the OD change is lowered at low fluence for C_{60} ion irradiation. It is known that the coloration of Gafchromic films is induced from the polymerization of monomers [3]. The sensitivity was reduced probably by local saturation of the polymerization due to high-density energy deposition of fullerene ions. We have experimentally shown that some cluster irradiation effect can occur in the coloration of HD-V2 film when the cluster size is sufficiently large.

As shown in Fig. 2, the OD increases monotonically at relatively low fluences between 10^9 and 10^{11} atoms/cm^2. The 2D profile of a cluster ion beam at around 10 keV/u could be obtained in the above fluence range from the OD distribution of an ion-irradiated film using a fitting function that relates the OD with the fluence.

References

[1] F. Ames *et al.*, Nucl. Instrum. Meth. Phys. Res. B, **112** 64 (1996).
[2] K. Yamada *et al.*, JAEA Takasaki Annu. Rep. 2012, JAEA-Review 2013-059 159 (2014).
[3] A. Niroomand-Rad *et al.*, Med. Phys., 25 (1998) 2093.
[4] Y. Yuri, K. Narumi and T. Yuyama, Nucl. Instrum. Meth. Phys. Res. A, **828** 15 (2016).

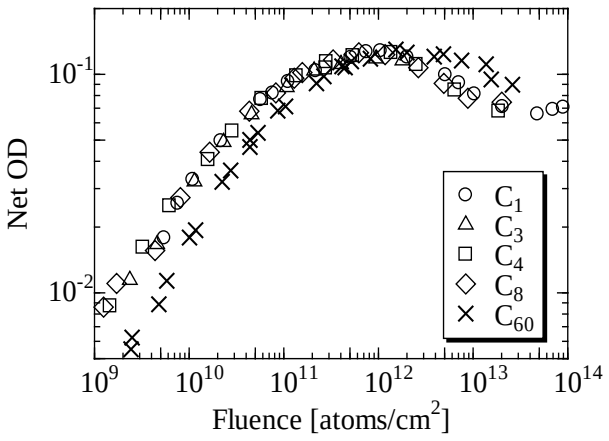

Fig. 2. Net optical density response of HD-V2 films irradiated with monoatomic and cluster C ion beams of 150 keV/atom. The ODs are plotted as a function of the atom fluence.

3 - 24 Transmission Properties of a 6-MeV Fullerene Ion Beam through a Wedge-shaped Glass Channel

K. Motohashi [a)], N. Miyawaki [b)] and Y. Saitoh [b)]

[a)] Department of Biomedical Engineering, Toyo University,
[b)] Department of Advanced Radiation Technology, TARRI, QST

Fullerene ion beam has many attractive features for nanotechnologies, such as high sputtering yields [1], high density surface excitation [2], and encapsulation of other atoms or molecules [3]. Fast fullerene ion beam developed in TARRI, QST, has potential as a powerful tool for nanotechnologies. On one hand, our group has found a guide effect of a 4-MeV carbon ion beam transmitted through a curved glass channel; its transmission at the tilt angle is greater than the geometric limit without significant energy loss [4]. If this effect appears in the transmission of the fast fullerene ion beam, it becomes widely used for the nanotechnology because it is possible to focus the beam without using any costly electromagnetic lenses.

In the present study, we measured the transmission property of a 6-MeV C_{60}^{+} ion beam that entered a wedge-shaped glass channel. The experimental setup is shown in Fig. 1. The wedge-shaped glass channel comprises two planar optical lenses facing each other on the two pairs of two ball bearings with 0.3-mm and 0.6-mm radiuses, and the center-to-center distance between the two pairs is 17.9 mm, hence the taper angle of the planar lens is 0.96° (= $\tan^{-1}((0.6\text{-}0.3)/17.9)$. The wedge-shaped channel can be tilted around the z-axis at the entrance orifice. The count rate and the electric current of particles transmitted through the wedge-shaped channel were measured with a Si surface barrier detector (SBD) and a Faraday cup just behind the 0.8-mm copper slits, respectively. The SBD and the two slits were movable in one body, whereas the Faraday cup was fixed. The observation angle φ was defined as $\tan^{-1}(Y_D/X)$ or $\tan^{-1}(Y_F/X)$. The count rate and the electric current as a function of the observation angle φ were measured at some tilt angle θ. The typical current of C_{60}^{+} ion beam was 10 pA. It was significantly reduced below 1/3,000 using an attenuator and a chopper in the measurement with the SBD. The vacuum was less than 8×10^{-6} Pa.

Figures 2 and 3 display the count rate and the electric current of the transmitted particles as a function of the observation angle φ at several tilt angles θ measured with the SBD and the Faraday cup, respectively. Almost 100% of particles were transmitted through the wedge-shaped channel at $\theta = 0°$ as shown in the two figures. All ions would collide with one side of a planar glass lens at a tilt angle >2° because the taper angle of the wedge-shaped channel was <1°. However, number of ions and current larger than one-third of the maximum at θ = 0° were transmitted at $\theta = 2°$. Note that the negative current was measured with the Faraday cup at $|\varphi| \geq 0.3°$, as shown in Fig. 3. This may correspond to secondary electrons emitted at the edges of the copper slit. Furthermore, no significant change between the pulse height distributions of primary ions and transmitted particles measured by the SBD at $\theta = 2°$ and φ~0° in our preliminary experiment. Therefore, guide effect is being expected at φ ~ 0°, though it is necessary to check whether any fragmentation exists or not.

References

[1] I. L. Bolotin *et al*., Appl. Surf. Sci., **252**, 6533-36 (2006).
[2] G. Jaskierowicz *et al*., Nucl. Instrum. Meth. Phys. Res. B., **222**, 213-27 (2004).
[3] V.N. Popok *et al*., Solid State Comm., **133**, 499-503 (2005).
[4] K. Motohashi *et al*., Jpn. J. Appl. Phys., **56**, 046301-1~6 (2017).

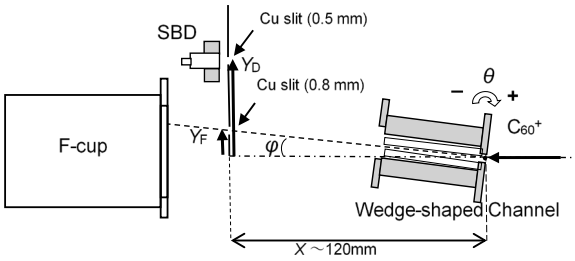

Fig. 1. Experimental setup of the wedge-shaped channel, slits, detector, and Faraday cup.

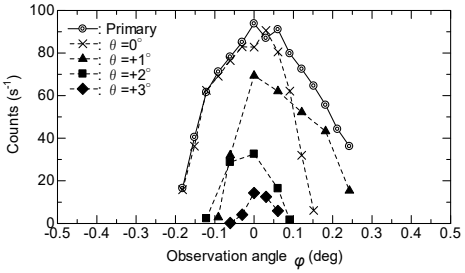

Fig. 2. Count rate of particles exited from the wedge-shaped channel at an incidence of a 6-MeV C_{60}^{+} ion beam.

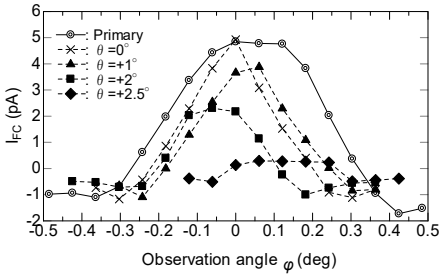

Fig. 3. Electric current of charged particles exited from the wedge-shaped channel at an incidence of a 6-MeV C_{60}^{+} ion beam.

3 - 25 Analysis of Linear Energy Transfer Effects on the Scintillation Properties of a $Bi_4Ge_3O_{12}$ Crystal

M. Koshimizu [a)], S. Kurashima [b)], A. Kimura [c)], M. Taguchi [c)], T. Yanagida [d)], Y. Fujimoto [a)] and K. Asai [a)]

[a)] Graduate School of Engineering, Tohoku University,
[b)] Department of Advanced Radiation Technology, TARRI, QST,
[c)] Department of Advanced Functional Materials Research, TARRI, QST,
[d)] Graduate School of Materials Science, Nara Institute of Science and Technology

Dense electronic excitation in scintillators leads to LET-dependent response. Recently, we began investigating the excited state dynamics in scintillators. Thus far, we have shown the LET effects on the energy transfer process, i.e., the dependence of the rise in the scintillation temporal profiles on LET [1–3]. These LET effects are attributed to a competition between the quenching caused by the interaction of the excited states, and the energy transfer.

In this study, we focused on a scintillator in practical use, $Bi_4Ge_3O_{12}$ (BGO). It should be noted that self-activated-type scintillation occurs in BGO, *i.e.*, the luminescence occurs in the entire crystal of BGO, in contrast to the impurity-doped scintillators, in which the concentration of the luminescence centers is several mol% at most. Thus, at high LET, we expected a dependence of the decay and the rise in the scintillation temporal profiles on LET, because the closely located excited states at the luminescence sites can be achieved in the self-activated scintillator at high excitation density. In this study, we report the dependence of the rise and decay of the scintillation temporal profiles of BGO on LET.

Scintillation temporal profiles at different LETs were obtained using pulsed ion beams from the AVF cyclotron at TIARA, QST, Japan. The samples were irradiated with pulsed beams of 20-MeV H^+, 50-MeV He^{2+}, and 220-MeV C^{5+}, which were obtained using two types of timing filters. The details of the pulsed beam generation system are described elsewhere [4]. A BGO crystal (1 cm × 1 cm × 1 mm) was irradiated in air. The scintillation from the sample was detected with a photomultiplier tube (PMT; Hamamatsu R7400U). The detection signal from the PMT was delivered to a digital storagescope (DSO; Tektronix DPO 7104) and the DSO was triggered with timing signals supplied from the accelerator. Further details of the measurement system are described in our previous paper [5].

Figures 1 and 2 show rise and the decay parts of the scintillation temporal profiles under irradiations of 20-MeV H^+, 50-MeV He^{2+}, and 220-MeV C^{5+} in the rise and decay regions. Firstly, it is evident that the rise is faster at higher LET. This same trend has been observed with a Li-glass scintillator [1], Ce-doped $LiCaAlF_6$ [2], and Ce-doped Gd_2SiO_5 [3]. Secondly, it can be observed that the decay is also faster at higher LET. In particular, for the irradiation of 220-MeV C^{5+}, a fast component appears, and the decay at longer than 200 ns is similar to that of the other ions. This is in contrast to the case of the Li-glass scintillator and Ce-doped $LiCaAlF_6$, for which no significant LET dependence was observed in the decay region. This can be attributed to the difference in the concentration of luminescence sites: scintillation occurs at doped Ce^{3+} ions in the Li-glass scintillator and Ce-doped $LiCaAlF_6$, whereas scintillation occurs in the entire crystal of BGO.

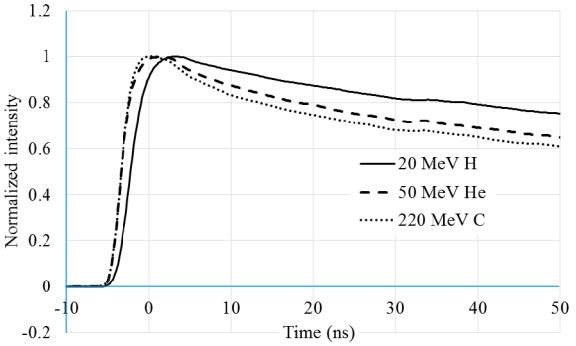

Fig. 1. Rise in the scintillation temporal profiles.

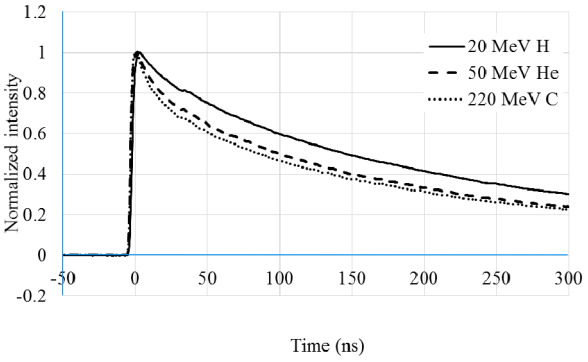

Fig. 2. Decay in the scintillation temporal profiles.

References

[1] M. Koshimizu *et al.*, J. Lumin., **169**, 678 (2016).
[2] T. Yanagida *et al.*, Nucl. Instrum. Meth. Phys. Res. B, **365**, 529 (2015).
[3] T. Yanagida *et al.*, Nucl. Instrum. Meth. Phys. Res. B, in press.
[4] S. Kurashima *et al.*, Rev. Sci. Instrum., **86**, 073311 (2015).
[5] M. Koshimizu et al., Rev. Sci. Instrum., **86**, 013101 (2015).

3 - 26 An Evaluation of Microbicidal Effectiveness of Low Energy Electron Beam with *Dμ* Approach

S. Todoriki [a)], H. Kameya [a)], K. Kimura [a)], H. Seito [b)] and T. Kojima [b)]

[a)] Food Research Institute, NARO
[b)] Department of Advanced Radiation Technology, TARRI, QST

Electrons of 300 keV or lower have a potential to decontaminate the surface of various kinds of cereals and grains with minimal quality deterioration. To confirm that the lethal effect of electron beam (EB) on foodborne microorganisms is comparable at energies below 300 keV, we examined bactericidal effects of the low energy EB employing *Dμ* approach [1].

Spores of *Bacillus pumilus* ATCC27142 were used as model organisms. An aliquot of spore suspension was diluted serially with sterile water and filtrated through a sterile membrane filter disc (47 mm φ, pore size 0.2 μm, PALL Corp.). Spores on the membrane filters (10^3-10^8 CFU/disc) were irradiated with EB at acceleration voltage of 150 keV. The details of irradiation conditions are shown in Table 1. Alanine film dosimeters (130 μm thickness, Biomax film, Kodak) calibrated for ^{60}Co gamma rays were parallelly irradiated with spore samples to measure apparent absorbed dose (D_{app}). After irradiation, the membrane filters were put on agar plates and incubated for 24 h at 37 ºC, and number of the colonies formed on the membrane were counted to determine the survival rate.

The poor penetration ability of low-energy EB makes the precise dose measurement difficult due to the dose gradient created across the thickness of the film dosimeter (Fig. 1). Therefore, apparent doses absorbed by alanine film dosimeter, D_{app}, were lower than the expected dose estimated from spore inactivation curve (Fig. 2 and Table 2). To solve this problem, the concept of *Dμ*, the surface dose (average dose in the first micrometer), has been proposed [1].

We deduced *Dμ* values from the depth-dose profile of stacked B3 film dosimeters (18 μm thickness, Gex Corp.) that were irradiated with 150-keV EB. Figure 1 shows normalized depth-dose profile of the Alanine dosimeter cretaed by the depth-dose profile of B3 films and density correction of dosimeter materials (ρ=1.120 for B3 and ρ = 1.482 for Alanine). The polynomial equation for 150 keV depth-dose profile were obtained as $P'(x) = 1.719E\text{-}06x^3 - 3.225E\text{-}04x^2 + 5.528E\text{-}03x + 1.000E+00$ ($R^2 = 9.975E\text{-}01$). Using this equation and dose-response calibration curve for alanine film dosimeter, D_{app} were converted to *Dμ*, according to the procedure of Helt-Hansen [1].

Table 2 shows the *Dμ* values that correspond to D_{app} measured in the spore irradiation experiments. The spore inactivation curve fitted and adjusted by the *Dμ* value gave D10 of 1.69 kGy for spore inactivation, which was in a good agreement with earlier studies (1.65 kGy) [2]. Considering the spore cell size and population on the membrane, it was expected that the spores were spread as monolayer on plain surface. Under this ideal condition, 150-keV EB showed the lethal effect that was equivalent to those of gamma and high-energy EB reported in previous studies [2].

References

[1] J. Helt-Hansen *et al.*, Radiat. Phys. Chem., **79**, 68-74 (2010).
[2] A. Tallentire *et al.*, Radiat. Phys. Chem., **79**, 701-04 (2010).

Table 1
Irradiation conditions for 150-keV EB.

No	Voltage (keV)	Ti foil thickness (μm)	Air gap (mm)	Current (mA)	Conveyer speed (m/min)
1	150	10	48	1.2	30
2				1.2	22
3				1.2	18
4				1.2	15

Equipment: Model EC250/15/10 mA, Iwasaki Electric, Co. Ltd.

Table 2
Dμ values for measured doses (D_{app}, by Alanine film).

No	D_{app} (kGy)	*Dμ* (kGy)
1	2.47	5.17
2	3.08	7.75
3	4.48	9.47
4	5.82	11.4

uncertainty : 6.67% (k=2).

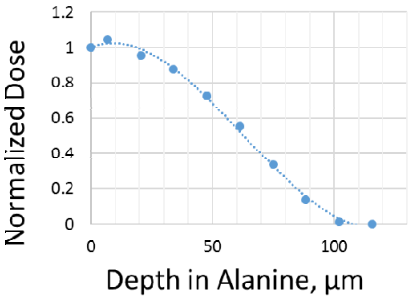

Fig. 1. Normalized depth dose profile of Alanine dosimeter.

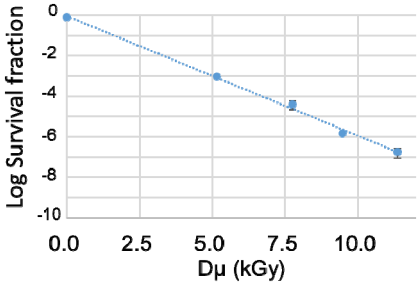

Fig. 2. Survival fraction of spore of *B. pumilus* irradiated with 150-keV EB.

3 - 27 Optical Property of Tb-doped G9 Glass Material

A. Yokoyama [a, b], W. Kada [b], S. Kawabata [b], K. Miura [b] and O. Hanaizumi [b]

[a] Department of Advanced Radiation Technology, TARRI, QST,
[b] Graduate School of Science and Technology, Gunma University

In heavy-particle therapy, carbon beams with an energy of the order of hundreds of MeV/n are used to damage DNA in the malignant tumor cell. The cell is merely annihilated by such beam irradiation because the radiation sensitivity of the tissue in a tumor is higher than that of a normal tissue. An energy-controlled beam is irradiated to the tumor to impart the largest energy transfer in the ion-beam range (Bragg peak). To irradiate the normal tissue around the tumor, collimators and various filters are set to adjust the Bragg peak and the irradiation area. Currently, ionization chambers are used to measure the dose distribution in the tumor at 10 points along the beam direction during radiation-therapy planning. Therefore, it is necessary to obtain three-dimensional dose-distribution images within a few minutes so that patients can be treated efficiently and the damage of normal tissue on them can be reduced.

To this end, scintillators were tested to obtain dose-distribution images in real time. However, detailed images could not be obtained owing to scintillation saturation [1]. Wherein the photostimulated luminescence (PSL) material is focused, PSL materials are read out by exposing visible light after the irradiation. If the PSL glass material having a dynamic dose range from mGy to Gy is made by adjusting the amount of activator and the kind of elements, the granted total dose will be known by the PSL intensity. In addition, unlike imaging plates, PSL glass materials prepared in Sumita Optical Inc. are transparent enable us to observe three-dimensional beam trajectories, although the observation is not in real time. A three-dimensional dose distribution can be obtained using stereo image measurements, in which two-dimensional luminescence-distribution images are taken in different directions.

The following two activities were conducted in fiscal 2016: (1) G9, a glass material having potential applications in PSL, was characterized by photoluminescence (PL) measurement and (2) PSL was read from the G9 irradiated ^{60}Co g-rays.

PL measurements were performed at room temperature using a He–Cd laser at a wavelength of 325 nm with a 20-mW excitation light. The light spot on the sample was approximately 1 mm in diameter. The PL values of G9 and G2000 were obtained using a high-sensitive spectrometer and an electrically-cooled charge coupled device camera. The number of camera pixel was 1,340 × 100, and the pixel size was 20 × 20 μm^2. A filter was placed in front of the spectrometer to cut off the excitation wavelength. PL was observed for wavelengths from 490 to 650 nm, as shown in Fig. 1. The peaks at 497, 550, 592, and 628 nm were attributed to the interlevel transitions in the electronic energy levels of Tb^{3+}. The PL intensity of G9 at 550 nm was approximately 437 times greater than that of G2000.

PSL was measured using the PSL detection system constructed in the last fiscal [2]. ^{60}Co g-rays were irradiated on each G9 sample in a range from 100 mGy to 100 Gy. PSL was read out by exposing the sample to He–Ne laser with a 1-mm diameter after g-ray irradiation. A photomultiplier tube was used to detect the induced photons at an interval of 1 s of exposure time. The detected signals were counted using a data acquisition device and averaged for 60 s. As a result, the PSL intensity of G9 was linear for the total dose of the g-rays and was almost the same as that of G2000. The linearity of PSL was observed in the irradiated samples in a range from 100 mGy to 100 Gy, which were kept at room temperature, even after one month. The radiation induced damage was recovered via annealing at 70 ºC for 30 min. This result indicates that G9 may be utilized as a detector in heavy-ion therapy.

Measurements to read the dose obtained by irradiating ion beams used in heavy-ion therapy to glass materials will be conducted in next stage.

Acknowledgment

This work was supported by KAKENHI, Grant-in-Aid for Young Scientists (B) JP15K18321.

References

[1] J. M. Schippers *et al.*, Nucl. Instrum. Meth. Phys. Res. A **477**, 480 (2002).

[2] A. Yokoyama *et al.*, QST Takasaki Annu. Rep. 2015, **QST-M-2**, 185 (2017).

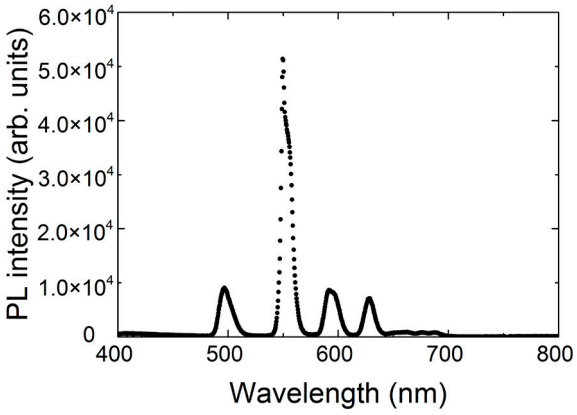

Fig. 1. PL spectrum of G9. The peaks were attributed to the interlevel transitions for the electronic energy levels of Tb^{3+}. The maximum PL peak of G9 at 550 nm was approximately 437 times greater than that of G2000.

3 - 28 Three-dimensional Elemental Analysis of Soil Sample by Particle Induced X-ray Emission-computed Tomography

Y. Ueki [a)], T. Hatakeyama [a)], K. Ishii [a)], S. Matsuyama [a)], A. Terakawa [a)], M. Fujiwara [a)], H. Oikawa [a)], T. Satoh [b)], M. Koka [b)], N. Yamada [b)] and T. Kamiya [c)]

[a)] Department of Quantum Science and Energy Engineering, Tohoku University,
[b)] Department of Advanced Radiation Technology, TARRI, QST,
[c)] Faculty of Science and Technology, Gunma University

A serious accident occurred in Fukushima Daiichi nuclear power plant due to The Great East Japan Earthquake in 2011. After this, radioactive substances, for example ^{137}Cs, were released into the environment and polluted the large area [1]. Since ^{137}Cs has long half-lives of about 30 years, the radioactive substances from the soil at disaster area should be removed. Recently, it has been researched to remove Cs from clay sample. In addition, it has been revealed that Cs atoms are absorbed strongly in clay particles and form complicated chemical bond with soil atoms. Since the soil including the clay particles is treated as radioactive waste, the volume reduction is also an important issue.

For analysis of these samples, we developed a way to investigate Cs distribution in the clay particles including inside of a particle by particle induced X-ray emission-computed tomography (PIXE-CT) based on micro-PIXE because it is a nondestructive, multi-elemental, high efficient and 3D analysis. Because of these advantages, analysis of biological samples has been carried out in many studies [2].

To prepare the samples of the soil, we added water to some soil, mixed it and filtered to remove large particles and impurities. This filtered muddy water was mixed with non-radioactive Cs_2CO_3 and dried for 24 hours and was attached on a small carbon fiber using glue, which was inserted into a tip of a needle. Subsequently, the micro-PIXE analysis was carried out using the microbeam system connected to the single-ended accelerator at TIARA. Energy of the proton microbeam was 3 MeV, and the beam spot size was 1.0×1.0 μm^2. The average amount of charge was 0.017 μC. The distance and angle of lithium-drifted silicone detector (PGTLS30135) for X-rays were 22 mm from the target and 140º to the beam axis, respectively. A sample was automatically rotated with a step of 9º in vacuum. The measurement area was 150 μm × 150 μm corresponding to 128 × 128 pixels of projection images. The measuring time of micro-PIXE analysis at each angle was 5 minutes.

When we get the PIXE image, it occurs the changes of X-ray emission cross section by beam energy loss and absorption of X-rays. To correct these effects, we assume the soil samples have almost spherical shape. Figure 1 shows Cs distribution over the particle reconstructed by GeoPIXEII [3] before/after the correction. The distribution of Cs inside of the clay particle was obtained by the micro-PIXE analysis and an image reconstruction algorithm based on maximum likelihood-expectation maximization. These results show small and equable amount of Cs in soil particles. It is assumed that the soil absorbed these Cs finely while drying sample. Figure 2 shows pixel value profiles in Fig 1. These profiles show distribution of pixel values. We successfully observed the distribution images of Cs in soils quantitatively and unbiasedly in bilateral sides.

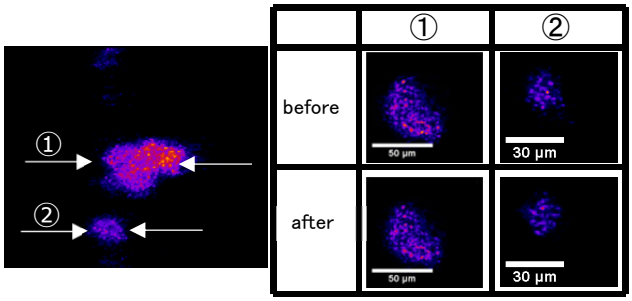

Fig. 1. Micro-PIXE and Micro-PIXE-CT images of Cs in soil sample before/after correction.

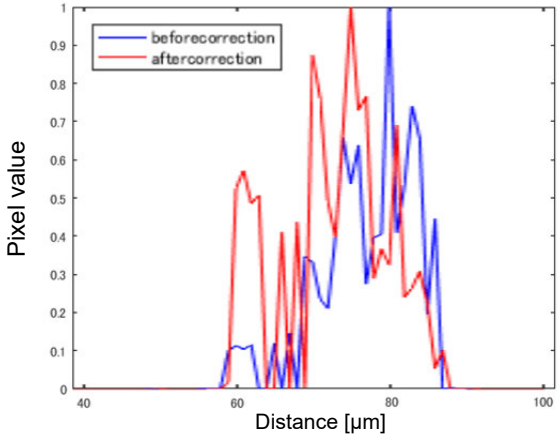

Fig. 2. Pixel value profiles indicated by white allows in Fig. 1.

References

[1] K. Ishii *et al.*, Nucl. Instrum. Meth. Phys. Res. B, **318**, 70-75 (2014).
[2] Y. Kawamura *et al.*, Int. J. PIXE **17**, 41-46 (2007).
[3] C. G. Ryan, Int. J. Imaging Syst. Tech. **11**, 219-30 (2000).
[4] T. Satoh *et al.*, Int. J. PIXE **22**, 73 (2012).

3 - 29 In-situ Measurement of Li Distribution in All Solid-state Li-ion Battery

K. Mima [a)], K. Fujita [a)], Y. Kato [a)], A. Yamazaki [b)], T. Satoh [c)], K. Yoshino [d)], K. Suzuki [d)], T. Kamiya [e)] and M. Finsterbusch [f)]

[a)] The Graduate School for the Creation of New Photonics Industries,
[b)] Research Facility Center for Science and Technology, Tsukuba University,
[c)] Department of Advanced Radiation Technology, TARRI, QST,
[d)] Department of Chemical Science and Engineering, School of Materials and Chemical Technology, Tokyo Institute of Technology,
[e)] Graduate School of Science Technology, Gunma University,
[f)] IEK-1, Forschungszentrum Jülich, GmbH

Lithium distributions in charged all solid-state Li-ion batteries (ASSLIB), which are provided by Forschungszentrum Jülich, Germany, were analyzed with a micro-PIXE/PIGE analyzer in a new experimental setup. A reduction of Li was seen in the interface between a cathode and a solid electrolyte probably due to the localized electrochemical reaction. This result indicates that local mobility of Li can be measured by the micro-PIXE and micro-PIXE.

はじめに

リチウムイオン電池(LIB)の開発においては、電池の性能に直結する電極面の Li の挙動を電気化学反応下で測定する“その場計測”手法の開発が不可欠である。本研究では、ドイツのユーリヒ総合研究機構で製作された全固体リチウムイオン電池(ASSLIB)[$Li_7La_3Zr_2O_{12}$(LLZ) + $LiCoO_2$(LCO)]について、分析用試料と専用の試料ホルダーを製作し、イオンマイクロビームを用いた微量元素分布分析法であるマイクロ PIGE とマイクロ PIXE により、充放電時の Li 濃度の時間変化に関する“その場計測”を実施した。

方法

マイクロ PIXE とマイクロ PIGE は、TIARA の 3MV シングルエンド加速器からの 3.0 MeV の $^1H^+$ビームを用いて行った。ビーム径は約 1 μm、ビーム電流は約 100 pA、測定範囲は 100 μm × 100 μm である。Figure 1 に測定した ASSLIB の概要を示す。今回は ASSLIB の断面の cathode 部分を中心に測定を行った。cathode は LLZ + LCO で構成されており Co を含んでいるので、試料から発生する Co の特性 X 線(PIXE)で cathode の形状を把握し、Li から発生するガンマ線(PIGE)で Li の分布を測定した。

これまでの研究によって、液体電解質を用いた LIB の Li 分布の時間変化を測定することに成功している [1]。今回はその知見に基づいて、ASSLIB のその場計測が可能な新しいサンプルホルダーを設計製作し、Fig. 2 のようなセットアップで分析した。

結果

充電状態の測定結果を Fig. 3 に示す。ここで、左図は Co の 2 次元分布であり、cathode の形状を表している。右図は 2 次元分布から得た Co と Li の濃度のプロファイルである。固体電解質と cathode の境界近傍で Li 濃度が減少しているのは、電気化学反応(充電反応)が電極表面からバルクに侵入しなかったためと考えられる。現在データ解析を引き続き進めており、今後シミュレーション結果との比較により、反応領域の時間変化の計測が可能になると期待される。

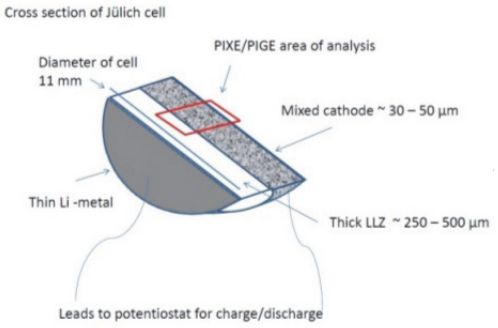

Fig. 1. Schematic view of an ASSLIB sample. A frame indicated with “PIXE/PIGE area of analysis” was a measurement area.

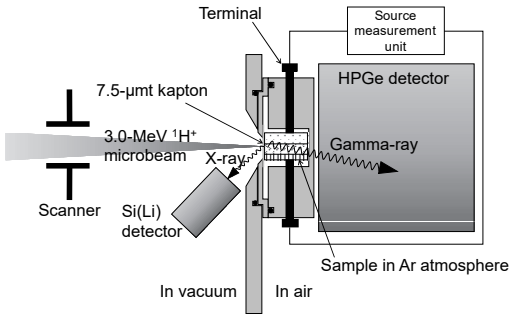

Fig. 2. Experimental setup for micro-PIXE/PIGE analysis.

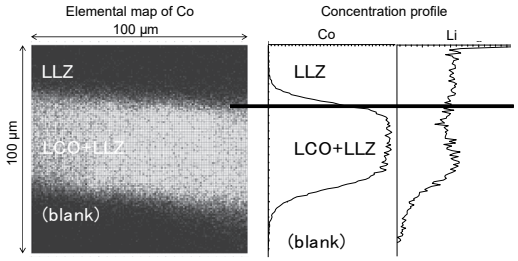

Fig. 3. Distribution of Co (PIXE) and Li (PIGE) in ASSLIB after charging. Left map: two-dimensional distribution of Co, and right profile: relative concentration of Co and Li.

Reference

[1] A. Yamazaki *et al.*, Nucl. Instrum. Meth. Phys. Res. B, **371**, 298-302 (2016).

3 - 30 Dynamic Behavior of Elements with Low Atomic Numbers in Lithium Oxide Ceramics under Irradiation

B. Tsuchiya [a)], S. Yamamoto [b)], K. Takahiro [c)] and S. Nagata [d)]

[a)] Department of General Education, Faculty of Science and Technology, Meijo University,
[b)] Department of Advanced Functional Materials Research, TARRI, QST,
[c)] Materials Science and Engineering, Kyoto Institute of Technology,
[d)] Institute for Materials Research, Tohoku University

Lithium oxides (Li_2TiO_3, Li_2ZrO_3, Li_4SiO_4, $LiAlO_2$, $LiCoO_2$, and so on) are potential candidates as tritium breeding materials in fusion devices [1]. It is of significant importance to investigate the relationship of radiation damage processes and dynamic behaviors of hydrogen as well as lithium atoms in lithium oxides under charging and heating by combining in situ radiation measurements with post-irradiation examinations.

Figure 1 shows the SEM images of the unirradiated Li_2ZrO_3 ((a) and (c)) and irradiated Li_2ZrO_3 ((b) and (d)) with 10 keV D_2^+ ions of up to ~5.0×10^{17} ions/cm^2 at room temperature. The grains on the surface of Li_2ZrO_3 exhibit a diameter of ~5 μm and are activated by ion bombardments.

Figure 2(a) shows the typical elastic recoil detection (ERD) spectra of H obtained with the as-prepared Li_2ZrO_3 before and after heating the sample at 623 K in vacuum, which were measured using 2.8-MeV He^{2+} ion-probe beams from the tandem accelerator. The horizontal axis of the ERD spectra corresponds to the energies of the recoiled H^+ and represents the depth from the topmost surface. The vertical axis (Counts) provides the counts per energy in the ERD spectra corresponding to the areal density of H retained in the Li_2ZrO_3 bulk. The residual H concentration, N_{H/Li_2ZrO_3}, indicative of the ratio of H to Li_2ZrO_3, reduced from ~2.0 to 0.08 on heating the sample at 623 K for 10 min in vacuum. However, it is not possible to distinguish the formations of atomic or molecular H, hydroxide (-OH), and H_2O from the spectra.

Figure 2(b) shows the typical ERD spectra of H and D recoiled from Li_2ZrO_3, which was irradiated with 10 keV D_2^+ ions of up to ~5.0×10^{17} ions/cm^2 after heating the sample at 623 K in vacuum and subsequently exposing to air for 290 h at ~299 K and relative humidity of ~40%. The ERD results revealed the exchange of D implanted in the near surfaces with H. The elementary processes such as the absorption of H produced from H_2O splitting at the formed defects on the surface, diffusion of H into the bulk, exchange of the diffused H with the implanted D, trapping of the diffused H into the vacant traps, local molecular recombinations (HD and H_2) of the diffused H with the implanted D, detrapped D, and trapped H were taken into account.

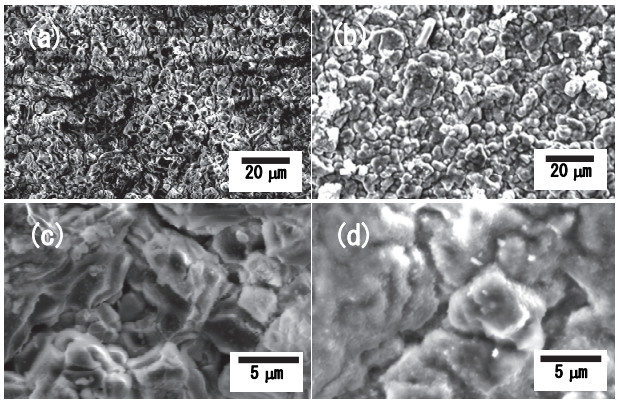

Fig. 1. SEM micrographs of unirradiated Li_2ZrO_3 ((a) and (c)) as well as D_2^+ ion irradiated Li_2ZrO_3 ((b) and (d)).

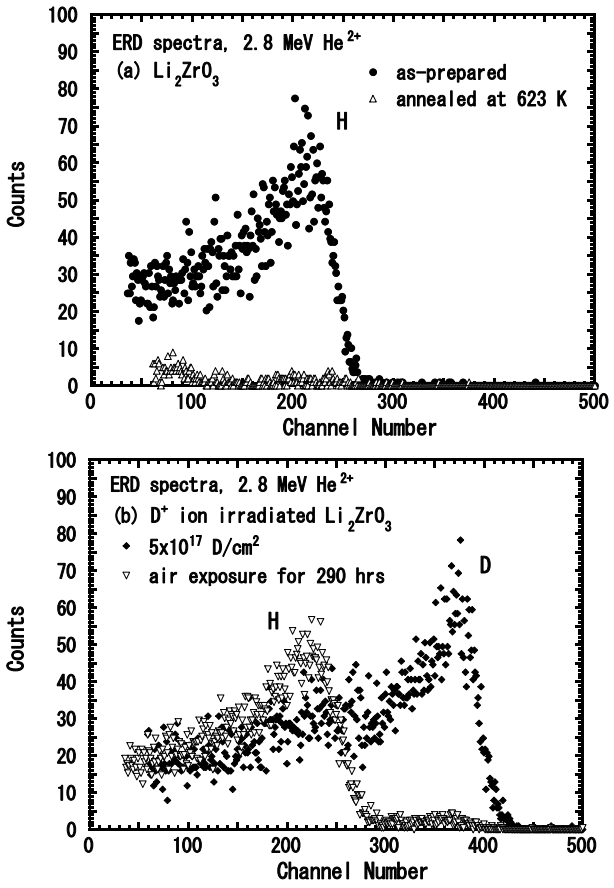

Fig. 2. Typical ERD spectra of recoiled H^+ and D^+ ions from Li_2ZrO_3 for (a) as-prepared and annealed at 623 K in vacuum and (b) irradiated with 10 keV D_2^+ ions of up to 5×10^{17} ions/cm^2 for the sample exposed to air at room temperature for 290 h.

Reference

[1] C. E. Johnson, K. Noda, N. Roux, J. Nucl. Mater. **258-63**, 140-48 (1998).

3 - 31 Improvement of Sample Holder for PIXE Tomography

T. Satoh [a)], M. Koka [b)], N. Yamada [a)], A. Yokoyama [a)], T. Ohkubo [a)] and Y. Ishii [a)]

[a)] Department of Advanced Radiation Technology, TARRI, QST,
[b)] Beam Operation Co., Ltd

In this study, particle-induced X-ray emission (PIXE) tomography system has been developed, combining micro-PIXE, scanning transmission ion microscopy (STIM) tomography [1], and image reconstruction based on maximum likelihood-expectation maximization (ML-EM) algorithm [2]. Because it is necessary to rotate a micro target in the present system, the target had to adhered to the tip of a thin diagonal-cut polyimide tube [3]. This preparation was hard since micro-manipulation under the microscope is required. Therefore, in this study, new preparation method has been developed. In new method, a number of micro samples are easily picked by a thin carbon fiber coated with adhesive as shown in Fig. 1. The uncondensed and isolated sample can be chosen by a two-dimensional stage in a vacuum chamber.

If the target prepared with the new method is used for the PIXE tomography, the carbon fiber is included in the projection maps. Therefore, a new computer program was also developed to manage these maps. In this program, the areas of the samples and the carbon fiber are first discriminated by the values of the STIM tomography, then X-ray absorption and beam energy attenuation in each area are corrected. Finally, 3-dimensional elemental maps are reconstructed by the ML-EM algorithm. As a practical test, 3-dimensional elemental distributions of Eu in a porous silica adsorbent were analyzed with the PIXE tomography by using the new sample preparation and the new program.

The experiment of the PIXE tomography was carried out with a microbeam of 3-MeV $^{1}H^{+}$. The beam size was approximately 1 μm in diameter, and the beam current was less than 100 pA. The scan area was 150 μm × 150 μm (128 pixels × 128 pixels). An X-ray detector was sit at a 140-degree angle with respect to the beam axis. The target was rotated by 9 degrees each time, and the 10-minute measurement of projection map was performed 40 times. The experiment of STIM tomography was carried out with the beam intensity of less than 100 cps in the same way as PIXE tomography. Figure 2 shows a 3-dimensional density map in the target measured by the STIM tomography. Using this result, the corrections in the PIXE tomography was performed.

Figure 3 shows the 3-dimensional relative distribution of Eu measured by PIXE tomography. Without being distracted by the fiber, the required elemental distribution was successfully obtained. The new sample preparation method and the new image reconstruction program developed in this study make the PIXE tomography easy to use. Therefore, the PIXE tomography system will contribute to the improvement of the internal microstructure in the porous silica adsorbent and so on.

References

[1] G. Bench *et al.*, Nucl. Instrum. Meth. Phys. Res. B **68**, 481 (1992).
[2] L. A. Shepp *et al.*, J. Comput. Assist. Tomogr. **7**, 571 (1983).
[3] T. Satoh *et al.*, Nucl. Instrum. Meth. Phys. Res. B **371**, 419 (2016).

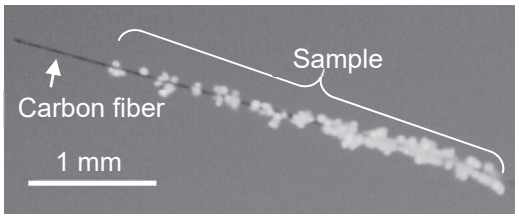

Fig. 1. Microphotograph of a target for PIXE tomography. Porous silica particles were stuck to a carbon fiber with adhesive.

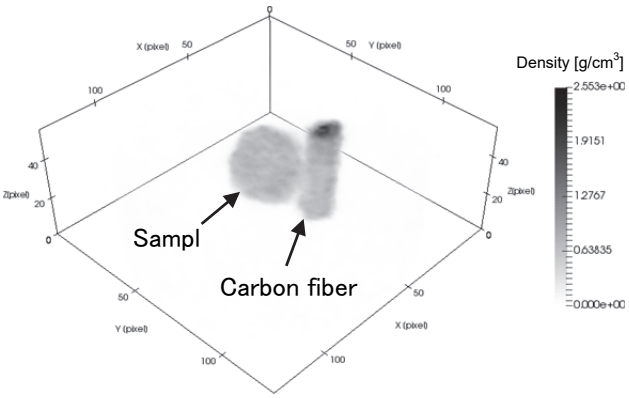

Fig. 2. Three-dimensional density map measured by STIM tomography.

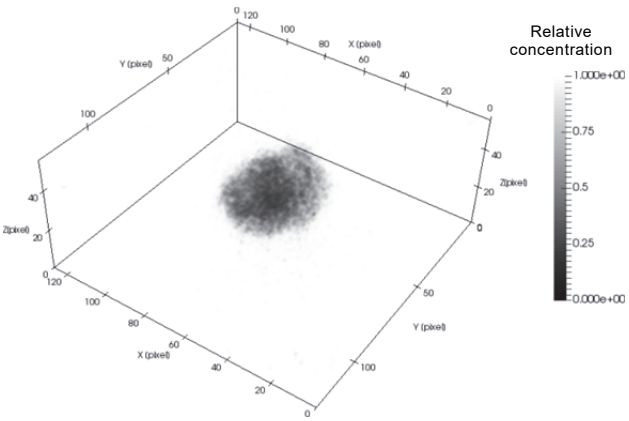

Fig. 3. Three-dimensional relative distribution of Eu measured by PIXE tomography.

3 - 32 Mapping Analysis of Putative Microbial Fossils in Olivine Using Micro-PIXE

H. Sugawara [a] and M. Sakakibara [b]

[a] Curatorial Division, Gunma Museum of Natural History,
[b] Faculty of Collaborative Regional Innovation, Ehime University

1. Introduction

The objective of this study is to elucidate the elemental distribution at the putative microbial fossils occurred in olivine pseudomorph of Earth basalt as the analog study of searching life on Mars. Our team has preliminary discovered filamentous textures in olivine of Mesozoic basalt obtained from Southern Chichibu Belt, Tokushima, Japan. Filamentous textures unlike banded, weathered textures, also known as abiotic iddingsite, have not been reported except only a few studies [1, 2]. These filamentous textures would not be the primary textures on the point of mineral composition with iron and clay minerals. Also, olivines in the sample are totally weathered into mainly chlorite. The goal of this study is to show the distribution of trace elements over the area including filamentous textures and the matrix of olivine pseudomorph so that it could contribute astrobiology by petrographical approach.

2. Experimental

The thin section of basalt with the thickness of approximately 30 μm was finished with 1 μm grained polishing paste and carbon coated. The sample was mounted on the sample stage inserted into the vacuum condition. PET filter with 60 μm in thickness was applied to the PGT detector. The sample was irradiated with 3 MeV protons with both x and y beam diameter of 1.1 μm, the beam current of 30 - 40 pA, and the working distance of 22 mm by micro-PIXE1 housed at TIARA. The elemental mapping analyses were performed over the area of a) 800 μm square, b) 400 μm square, and c) 100 μm square.

3. Results

The elements of Al, Si, K, Ca, Ti, Cr, Mn, Fe, Ni, and Zn are detected over the mapping areas; however, the trace elements such as Rare Earth Elements in filamentous textures were not obtained caused by the strong peak intensity of Fe covering the peaks of those trace elements. The relative concentration of Fe and Mn are wholly higher over olivine pseudomorphs than the matrix of basalt based on the result of (a) (Fig. 1). The heterogeneous relative concentrations of K and Ti in olivine pseudomorphs are revealed. The mapping analysis of non-filamentous iron minerals shows partial distribution of Zn and Mn whereas correlated negatively with Ti, Ca, and K. Based on the experiment (b), on the other hand, the elemental maps of filamentous textures composed mainly of iron minerals show the partially positive correlations with Ti but not with other detected elements (Fig. 2).

4. Discussion

This study shows the elemental correlation over the area including the filamentous textures in olivine pseudomorphs and abiotic iron minerals in ppm for the first time. The comparison of elemental correlations between abiotic non-filamentous textures and filamentous textures in olivine pseudomorph suggests that these different textures are not formed in the identical secondary mineralization. Local higher concentrations of Ti over filamentous textures imply the presence of minute Fe-Ti oxides.

References

[1] L. M. White *et al.*, Astrobio., **14**, 170-81 (2014).
[2] M. Fisk and N. McLoughlin, Geosph., **9**, 317-41 (2013).

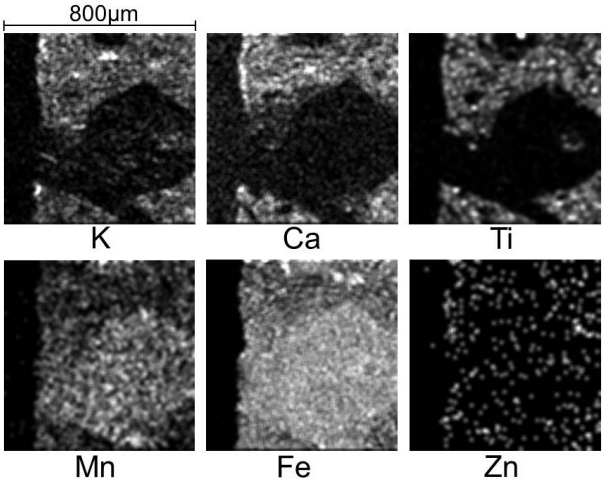

Fig. 1. Elemental maps of K, Ca, Ti, Mn, and Fe obtained from an olivine pseudomorph including filamentous textures and the matrix of basalt.

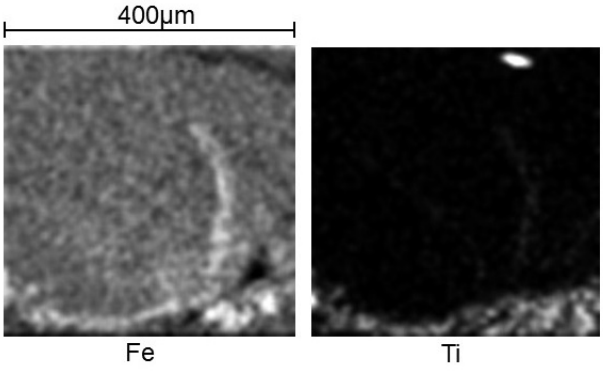

Fig. 2. Elemental maps of a filamentous texture showing the partial distribution of Ti on the Fe-rich filament.

3 - 33 Quantitative Valuation of Radiation-induced Defects in Mineral: The Alpha Effectiveness of the Dating ESR Signal in Hydrothermal Barite by He^+-ion Implantation Experiments

T. Fujiwara [a)], S. Toyoda [a)], H. Nishido [a)] and J. Ishibashi [b)]

[a)] Graduate School of Science, Okayama University of Science,
[b)] Department of Earth and Planetary Sciences, Kyushu University

Barite ($BaSO_4$) is a mineral recently found to be practically useful for electron spin resonance (ESR) dating [1], especially for those occurring in submarine hydrothermal sulfide deposits. As the hydrothermal fluid contains large amount of Ra, it incorporates in barite replacing Ba in the crystal lattice. In the hydrothermal sulfide deposits containing barite, most of the natural radiation is from ^{226}Ra, ^{228}Ra and their daughter radioactive nuclei where other radioactive elements such as U, Th, and K in sulfide minerals give negligible contribution to the dose rates [2]. When estimating the dose rate to barite crystals, which is a necessary procedure for ESR dating, therefore, internal radiation, especially, that of alpha particles is significant for total dose rates up to 60% [*e.g.*, 1]. The ratio, k, is the alpha effectiveness, which is the signal formation rate in the dose response by alpha particles relative to that by gamma rays, has to be used to correct this difference to estimate the "effective" dose rates. Therefore, the experiments of He^+ ion implantation should be required to determine the precise alpha effectiveness. We implanted He^+ ions accelerated by a Tandem accelerator into two series of barite samples, one synthetic and the other hydrothermal extracted from a sea-floor hydrothermal sulfide deposit. The alpha effectiveness of the SO_3^- is determined as the slope in the dose response to He^+ ion implantation relative to that to gamma ray irradiation.

A Tandem accelerator at Takasaki Ion Accelerators for Advanced Radiation Application (TIARA) of QST was used to implant He^+ ions into the deposited samples where the aluminum plates were attached on a copper plate. The He^+ ions with energy of 4 MeV was implanted with a current of about 200 nA in duration of 2 to 80 seconds to an area of about 2 cm^2. The samples were peeled from an aluminum plate for ESR measurements. The doses given to the samples were calculated by dividing the total energy of He^+ ions, that have passed the surface of the barite samples deposited on an aluminum plates, by the mass of barite sample on the aluminum plate, the surface of which He^+ ions passed, and in the volume of which He^+ ions reached down to 10 μm from the surface. The implanted samples were measured at room temperature with an ESR spectrometer (JES-PX2300) with a microwave power of 1 mW and the magnetic field modulation amplitude of 0.1 mT.

The ESR signals assigned to SO_3^- radical by their g-values have been observed in samples implanted with He^+ ions. The signal intensities were enhanced by He^+ ion implantation where single saturating exponential curves were fitted to the dose responses for natural samples and exponential with linear functions were for the synthetic sample, suggesting that the k values estimated from the dose response curves of He^+ ion implantation may change with dose. In this case, the range of the equivalent doses in the actual dating samples is quite low, typically up to about 400 Gy [*e.g.*, 3].

Tentatively, based on the present results, the k-value, 0.053 ± 0.006, obtained for the young natural sample should be adopted for young barite samples (typically up to 1500 years). This value is 19% higher than the previously reported value of 0.043 ± 0.018 [4]. With this value, the ESR ages will typically become about 10% younger than the ones with the old k-values where currently, this difference will not affect the geological interpretations. This k-value would be much more realistic than the previous value in the sense that the present value was obtained with using the natural barite extracted from a hydrothermal sulfide deposit which is actually used in dating while examined the barite crystal occurring on land [4]. This value is very similar with the value, 0.052, for calcite speleothem obtained [5], and in the same order with those for mollusk shells, 0.07 to 0.10 [6] and with those for corals, 0.05 to 0.15 [*e.g.*, 7].

Conclusively, the value of alpha effectiveness was evaluated by the experiments with 4 MeV He^+ ion implantation and gamma ray irradiation to three barite samples. However, the present study also found that the value is sample dependent possibly on the age, therefore, the value should be used for young samples up to 1,500 years. Further studies on the k value are still necessary.

References

[1] T. Okumura *et al.*, Geochronometria, **37,** 57-61 (2010).
[2] S. Toyoda *et al.*, Radiat. Meas., **47**, 900-02 (2012).
[3] T. Fujiwara *et al.*, TAIGA Concept, Springer, Tokyo, 369-86 (2015).
[4] S. Toyoda *et al.*, Radiat. Protect. Dosim. **159**, 203-11 (2014).
[5] R. Lyons. & G. Brennan, Nucl. Tracks Radiat. Meas., **18**, 223-27 (1991).
[6] R. Grün and O. Katzenberger-Apel, Ancient TL, **12**, 35-38 (1994).
[7] M. Ikeya & K. Ohmura, Earth Planet. Sci. Lett., **65**, 34-38 (2012).

3 - 34 The Change in the Environment and Tectonics during Late Paleocene to Early Miocene in the Northeastern Tibetan Plateau

A. Sakuma [a)], R. Tada [a)], T. Kanzaki [a)], S. Kurokawa [a)] and H. Zheng [b)]

[a)] Graduate School of Science, The University of Tokyo, [b)] Yunnan University

The first rapid cooling step in the Cenozoic occurred at the Eocene-Oligocene boundary, but the cause of this cooling remains unproven. One possibility is that the uplift of the Tibetan Plateau caused the intensification of weathering, drawdown of the atmospheric CO_2 and the global cooling. To test this hypothesis, we examined the provenance of quartz in the terrestrial sediments of the Lanzhou Basin to detect the signal of uplift using the Electron Spin Resonance (ESR).

新生代は長期的寒冷化によって特徴付けられ、寒冷化はいくつかのステップで進行したことが知られている。始新世/漸新世境界(EOB)はその中で最初かつ最大のものであり、EOB で安定した南極氷床が出現したことが知られている。Raymo and Ruddiman [1]はヒマラヤ山脈・チベット高原の隆起が風化・侵食速度を増大させ、大気中の二酸化炭素を減少させたことにより寒冷化が起きたという仮説を提唱したが、チベット高原の隆起時期及び様式については未だに正確には解っていない。そこで本研究では、チベット高原北東部蘭州盆地の新生代堆積物に含まれる砕屑性石英のESR強度から供給源におけるテクトニックな変化を、層相や鉱物組成、粒度分布から周辺地域の環境変化を推定し、テクトニクスと環境変化の関係を調べた。

分析試料は 2016 年 9 月にチベット高原北東部、中国甘粛省蘭州市皐蘭県対亭溝付近の対亭溝セクションで採取した。このセクションでは Zhang [2]により古地磁気層序が確立されており、後期暁新世(~60 Ma)から前期中新世(~18 Ma)までの地層を連続して観察出来る。最初に乾燥・粗砕した試料約 0.1 g から炭酸塩、鉄・マンガン酸化物、有機物を除去した後、篩を用いて 64 μm よりも大きい画分と 64 μm 以下の画分の 2 つに分割し、それぞれの画分について石英のESR信号強度と結晶化度(CI)の測定を行った。自然放射線により酸素が欠落することで生じる石英中の格子欠陥は E_1'中心と呼ばれ、ESR 信号強度の測定によりその量を推定出来る[3]。格子欠陥量は石英が受ける総放射線量に依存しており、母岩年代が古いほど ESR 信号強度は大きくなる[3]。

64 μm 以上の画分は国立研究開発法人量子科学技術研究開発機構高崎量子応用研究所において ^{60}Co を線源とする総線量 2.5 kGy の γ 線照射を行った後、300 ºC で 15 分加熱した。そして、東京大学理学系研究科の X-band ESR spectrometer(JEOL, JES-FA100)を用いて ESR 信号強度の測定を行った。測定条件はマイクロ波: 0.01 mW、磁場強度: 0.1 mT、magnetic field modulation: 100 kHz、測定範囲: 5 mT、測定時間: 2 min、Time constant: 0.03 sec、走査回数: 20 回とした。64 μm 以上の画分を用いたのは、風成塵の影響を排除し、河川により上流から運搬された粒子に分析対象を限定するためである。

砂岩試料の 64 μm 以上の画分のESR信号強度測定の時代変化は Fig. 1 のようになった。約 52~24 Ma において徐々に ESR 信号強度が大きくなるのは、後背地で隆起が起こり、浸食により次第に下位の古い年代の地層が露出、浸食される現象が起きたためと推定される。この現象は少なくとも約 24 Ma まで継続したと考えられる。

約 24 Ma に ESR 信号強度が急激に減少することについては、供給源の位置に変化はなかったが、侵食の継続により 200 ºC 以上の温度に到達して ESR 信号強度がリセットされた地層が約 24 Ma に露出し始めた可能性、供給源が突然変わったことにより、新たに石英の ESR 強度が低い地層の露出域が供給源に加わった可能性が考えられる。

以上の結果から、チベット北東部での隆起は約 52 Ma 頃に開始した可能性があるが、急激な隆起と侵食速度の増加が起こったとすれば約 32~20 Ma にかけてであり、少なくとも蘭州盆地後背地においては急激な CO_2 濃度の低下と全球的寒冷化が起こったと言われる EOB よりも後であることが示された。

References

[1] M. E Raymo & W. F. Ruddiman, Nature, **359**, 117-22 (1992). https://doi.org/10.1038/359117a0

[2] P. Zhang., "Magnetostratigraphy and paleo-environmental evolution of the Middle Eocene-Early Miocene deposits in the Lanzhou Basin", northwest China (2015).

[3] S. Toyoda *et al*., Geochem. J., **26**, 111-15 (1992).

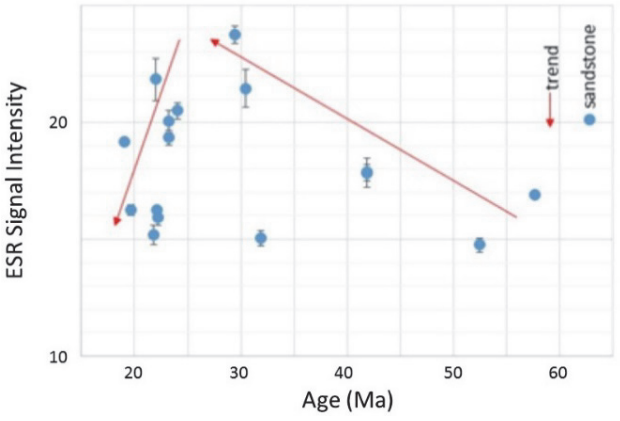

Fig. 1. Changes in ESR intensity of quartz in > 64 μm fraction of sandstones.

3 - 35 ESR Dating of the Gomura Fault Distributed on Tango Peninsula Using Radiation Defect Radical Centers

T. Fukuchi

Graduate Faculty of Interdisciplinary Research, University of Yamanashi

It is difficult to assess the activity of unrecognized active faults in the region with unclear tectonic landform or without Quaternary overlying sediments, so that we have no way of the assessment but to determine the age of fault rocks such as fault gouge produced by faulting using absolute dating techniques. The ESR (Electron Spin Resonance) dating method is a technique to estimate the age of fault movement by determining the age of fault rocks using radiation defect radical centers derived from fault-rock-forming minerals.

In ESR dating, we assume that ESR signals detected from fault rocks have been once reset by frictional heating [1]. Then, the ESR age (T) is calculated by dividing the total radiation dose (TD) to which the fault rocks have been subjected since the resetting of the ESR signals by the annual radiation dose (D); $T = TD / D$. The TD is obtained by extrapolating the growth line or curve calculated from the ESR signal intensities before and after artificial γ-irradiation.

If the ESR signals have been completely reset at the time of the latest fault movement, they may give the actual age (T_a) of the latest fault movement. However, they are not always reset completely near the Earth's surface because frictional heat hardly rises. When the ESR signals are incompletely reset, the TDs obtained are overestimated, and then the ESR ages obtained are older than the actual age of the latest fault movement. Therefore, the ESR ages (T_{esr}) theoretically give the upper limit of the actual age ($T_a \leq T_{esr}$).

In this study, I carry out ESR dating of the fault gouge collected from the Gomura fault located in Kyotango city on Tango Peninsula, which caused the 1927 Kita Tango earthquake. The artificial γ-irradiation for determining the TDs was carried out with a ^{60}Co source at 2 cell irradiation facility in the food irradiation building, Takasaki Advanced Radiation Research Institute, QST. The irradiation dose rate is 390.2 Gy/h.

ESR measurements reveal that the quartet signals (A, B, C and D signals) derived from montmorillonite and the E', Al and Ti centers in quartz are detected from the Gomura fault gouge just on the fault plane, which moved in the 1927 Kita Tango earthquake [1]. Moreover, the γ-irradiation shows that they regularly increase with increasing radiation dose (Fig. 1). This means that these radical centers probably give precise TD values.

As a result, the ESR age of $0.36 \sim 0.56 \pm 0.11$ Ma is obtained from the Gomura fault gouge using multiple radical centers derived from montmorillonite and quartz. Therefore, the age (T_a) of the latest fault movement along the Gomura fault is estimated as $T_a \leq 0.36 \sim 0.56 \pm 0.11$ Ma.

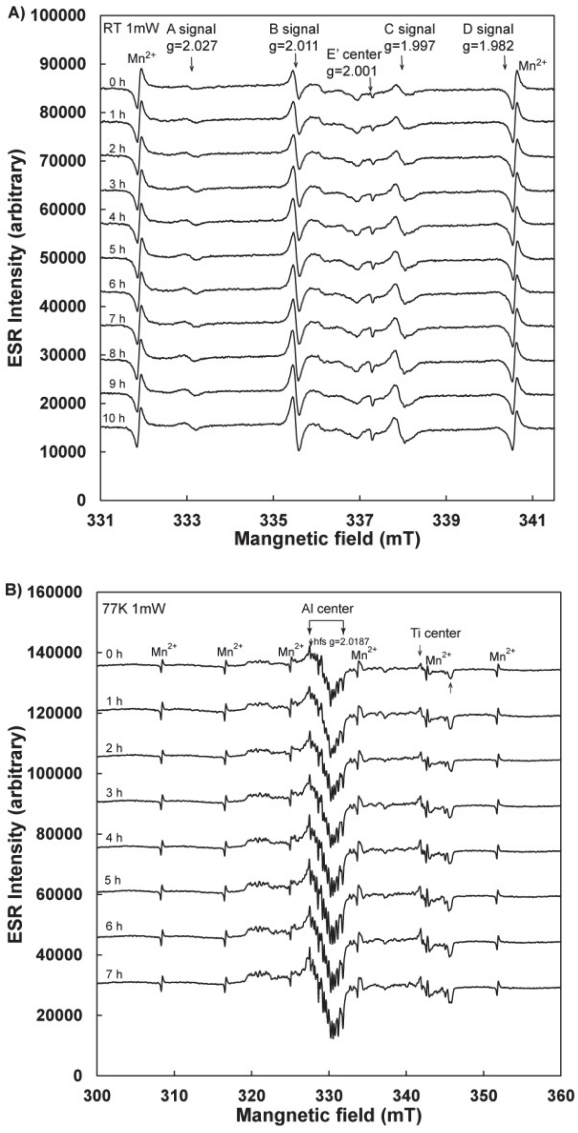

Fig. 1. A) Gamma-irradiation effect on the quartet signals derived from montmorillonite and E' center in quartz in the Gomura fault gouge. B) Gamma-irradiation effect on the Al and Ti centers in quartz in the Gomura fault gouge. The irradiation dose rate is 390.2 Gy/h and the irradiation time is 0-10 hours.

This result supports that the principle of ESR dating of fault movement is effective. Thus I conclude that the ESR dating technique is available for the assessment of fault activity of unrecognized active faults that have moved in the Middle Pleistocene.

Reference

[1] T. Fukuchi, "ESR dating of fault movement- Its principle and practice", Fukadaken Library 63, 45pp (2004).

Prat Ⅱ

4. Status of Quantum-Beam Facilities

4 - 01 Utilization Status at TIARA Facility

H. Hanaya [a)], S. Watanabe [a)], H. Takizawa [a)],
H. Kaneko [b)], S. Kaneya [b)], M. Kawabata [b)], K. Saga [b)] and Y. Nakamura [b)]

[a)] Department of Advanced Radiation Technology, TARRI, QST,
[b)] Takasaski Establishment, Radiation Application Development Association

1. Research & Industrial Use

There are four accelerators, a cyclotron and three electrostatic accelerators (a tandem, a single-ended accelerator and an ion implanter) at the TIARA facility to meet various research needs. Research activities for the cyclotron for the past 5 years are shown in Fig. 1. Total utilization time of each fiscal year (FY) was in the range of 2,200 to 2,300 hours. However, the utilization time of FY 2016 was reduced to about 1,400 hours because of the remodelling of a cooling system of the cyclotron facility. The trend of research activities using the cyclotron changed in FY 2016. The utilization time of “Base of Quantum Beam” in FY 2016 extremely decreased, in comparison with the other three research fields.

When we see the research activities for the three electrostatic accelerators, the profile of total utilization time is different from that of the cyclotron, as shown in Fig. 2. The utilization time of “Material Science” and “Base of Quantum Beam” accounts for more than about 80% of the total time. The utilization time of “Facility use program” increased in FY 2016, because the classification of JAEA users was changed from “Internal use” to “Facility use program”.

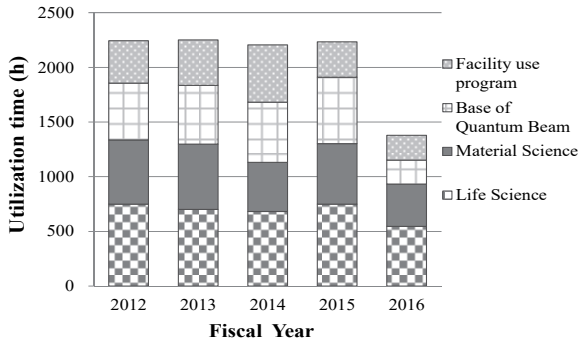

Fig. 1. Status of research activities for cyclotron for the past 5 years.

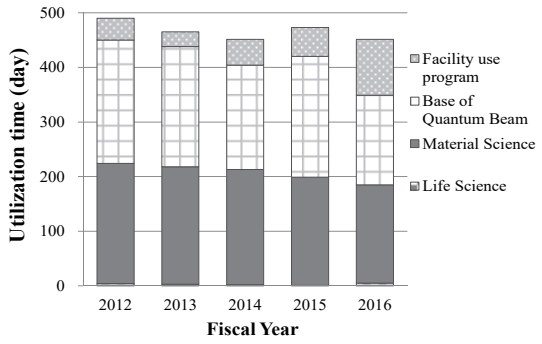

Fig. 2. Status of research activities for the three electrostatic accelerators for the past 5 years.

The trend of the number of users in the past 5 years is shown in Fig. 3. The total number of users has increased year by year from FY2012 to FY2014. However, it decreased from FY 2015. The trend of the number of project category in the past 5 years is shown in Fig. 4. The number of projects was in the range of 120 to 140 per year until FY 2015. In FY 2016, the number of projects decreased, because a new system was introduced and projects of “Cooperation priority research”, “Joint research” and “Internal use” were consolidated.

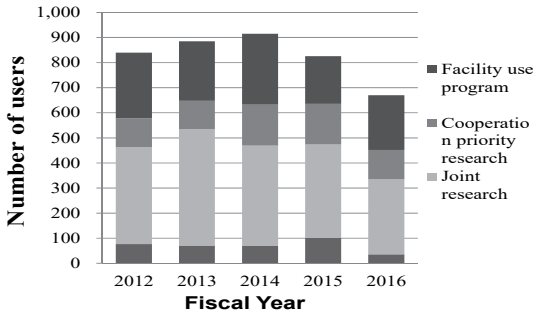

Fig. 3. The number of users for the past 5 years.

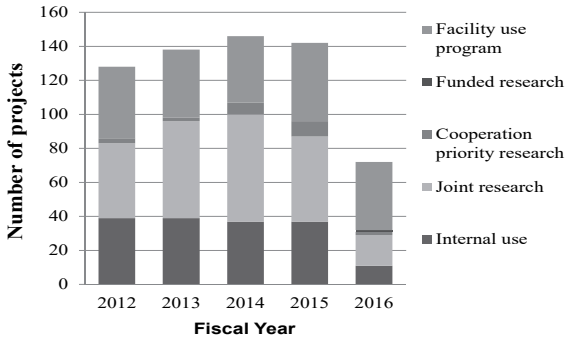

Fig. 4. The number of projects for the past 5 years.

2. The others

First QST Takasaki Research Symposium was held successfully in January 26 and 27, 2017 at Takasaki Advanced Radiation Research Institute. The number of oral presentations and poster sessions was 13 and 141, respectively. The number of participants of the symposium was 315, and decreased by 165 in comparison with last meeting.

The QST Takasaki annual report 2015 including 155 research papers was issued as usual. About 610 books were mainly distributed to domestic relevant departments. In addition, 50 English letters which described the URL about an electric version of the annual report, were also sent abroad.

4 - 02 Operation of the AVF Cyclotron

I. Ishibori [a)], S. Kurashima [a)], K. Yoshida [a)], T. Yuyama [a)], T. Ishizaka [a)], N. Miyawaki [a)], H. Kashiwagi [a)], Y. Yuri [a)], S. Okumura [a)], T. Nara [a)], To. Yoshida [b)], Tu. Yoshida [b)], S. Ishiro [b)], S. Kanou [b)], K. Takano [b)], H. Saitoh [b)], T. Atobe [b)] and K. Akaiwa [b)]

[a)] Department of Advanced Radiation Technology, TARRI, QST,
[b)] Beam Operation Service, Co., Ltd.

Operation

Operation time of the AVF cyclotron in fiscal year 2016 was reduced because of some troubles and the previously scheduled remodeling of a cooling system of the cyclotron facility.

Table 1 shows the statistics of the cyclotron operation of FY2016. It includes the data in FY2015 for comparison. The total operation time amounted to 1,953 hours, and monthly operation times are shown in Fig. 1.

Table 1
Statistics for cyclotron operation.

	FY2015	FY2016
Beam service time (h)	2304	1407
Machine tuning (h)	732	535
Beam development (h)	53	11
Total operation time (h)	3089	1953
Change of particle and/or energy	248 times	165 times
Change of beam course	328 times	199 times
Change of harmonic number	86 times	75 times
The number of experiments	514	339
Cancellation due to machine trouble	5	11

The percentages of operation time of the year used for regular experiments, facility use program and promotion of shared use program, beam tuning, and beam development are 62.7%, 9.3%, 27.4%, and 0.6%, respectively. Eleven experiments were canceled due to troubles as follows, shield doors 6, main coils 4 and the other 1. Consequently, the accumulative operation time was 80,117 hours and the total number of experiments was 11,693 from the first beam extraction in 1991 to March 2017.

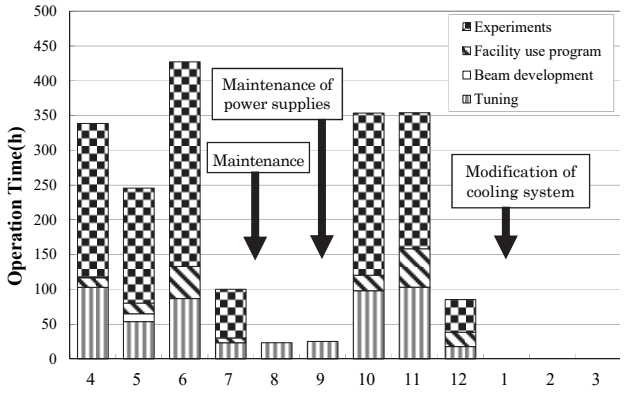

Fig. 1. Monthly operation times in fiscal 2016.

Maintenance

The regular yearly overhaul and maintenance were carried out. The major items were as follows: 1) Replacement of the “Bebeo” fitting O-ring used for the cyclotron cooling water line. 2) Routine maintenance of the power supplies. 3) Replacement of the turbo molecular pumps of the cyclotron vacuum system.

Water leaks due to aging of the cyclotron cooling system frequently occurred for these years. The cooling water that might contain radioactive contaminations circulates through the power supply room. There is a risk of contamination outside of the power supply room when the large leakage occurs, because the power supply room has no drainage conduit. The water lines circulating in the power supply room were therefore separated from the cyclotron and the beam transport lines and were connected to the contamination free line used for ion sources. Furthermore, cooling water tubes of the power supplies were replaced and the flow switches for interlock were added to the cooling water line for the beam transport system.

For the first time since the installation, maintenance of the shield door of the No.5 heavy ion room was carried out. The axle bearings were replaced and aligned.

A vacuum leak occurred in the RF cavity of the cyclotron. As a result of the investigation, the compressed air leaked from the contact finger. Heavy ions beams such as 560 MeV $^{129}Xe^{26+}$ and 490 MeV $^{192}Os^{30+}$ could not be accelerated due to the air leak. Therefore unscheduled maintenance was carried out. A degraded O-ring used at the piping of the finger was also replaced.

Trouble with the main coil

The main coil of the cyclotron consists of two coils for the upper and lower poles of the magnet yoke. The each coil is composed of 5 layers of hollow conductor pancakes. The total number of turns of the main coil is 480. In December 2016, it was found that the voltage between the main coil terminals suddenly decreased by about 5% compared with the previous value when the coil was excited to 820 A. An electrical short between two pancakes of the upper coil was found. The short was occurred at the innermost part of the coil, and the damaged part could be identified visually. However, it was quite difficult to repair the upper coil immediately since heavy components such as the vacuum chamber and the magnet poles have to be uninstalled from the cyclotron. The damaged two pancakes of the upper coil were bypassed. Moreover, two pancakes of the lower coil were bypassed to obtain a vertically symmetric magnetic field at the median plane. As a result, the total number of turns of the main coil and the maximum energy of the cyclotron (K-value) were reduced to 60%. We are planning to replace the upper and lower coils as soon as possible.

4 - 03 Operation of Electrostatic Accelerators in TIARA

A. Chiba [a)], K. Yamada [a)], A. Yokoyama [a)], Y. Hirano [a)], T. Satoh [a)], T. Ohkubo [a)], T. Nara [a)], T. Takayama [b)], S. Kanai [b)],Y. Aoki [b)], M. Hashizume [b)], Y. Takahashi [b)] and M. Hasegawa [b)]

[a)] Department of Advanced Radiation Technology, TARRI, QST,
[b)] Beam Operation Service, Co., Ltd

1. Operation and Status

In fiscal year 2016, operating rate of 100% had been achieved in the tandem accelerator and the ion implanter; meanwhile a serious trouble which is hard to identify its causes was encountered in the single-ended accelerator. Some experiments using the single-ended accelerator were forced to cancel due to the trouble for over two months. The annual operating times including the conditioning operations of the tandem accelerator, the single-ended accelerator and the ion implanter were 1,971, 2,068 and 1,817 hours, respectively. The monthly operating times of these accelerators are shown in Fig. 1.

2. New Beam

In the ion implanter, a Pr ion beam became available using a Freeman type ion source with the oven method. In this method, PrCl powder is useable as a sample. The Pr ion beam was required for the experiments on a formation of the single-photon sources in a semi-conductor. Figure 2 shows the ion mass spectrum of the beam extracted from the ion source. The Pr ion beam of 800 nA was accelerated with a total voltage of 350 kV.

3. Maintenance

A serious trouble in the single-ended accelerator happened on December 2016. It became difficult to form the focusing beams required for micro-PIXE analysis and PBW technique because of deteriorations of the energy stability of a proton and a helium beam. Moreover, the maximum applied voltage to an acceleration tube became far below the rated value of 3 MV due to unexpected electrical loads generated somewhere in a multiple voltage-boosting circuit. In consequence of our detailed survey on almost all components of the voltage-boosting circuit (*e.g.*, a Schenkel-type main circuit, a 200-kV RF transformer, a ripple regulator, a RF generator, and a high-stability 10-kV DC power supply), it was revealed that one of two cylindrical shielding-plates to suppress the leakage of magnetic-fields of the RF transformer coils generates an abnormal heating. It was concluded that the quantity of the heating caused by the magnetic-induced current increased drastically with the increase of electrical contact resistance at the overlapping surface at the connection of the shielding plate due to sulfurization under high pressure of SF_6 gas. The images of the connection and connecting screws of the shielding plate damaged by the abnormal heating are shown in Fig. 3. Therefore, as the temporary repairs on the shielding plate, the surface polishing and the addition of the connecting screws were carried out rapidly. As a result of these measures, it was confirmed that the single-ended accelerator is able to operate as usual.

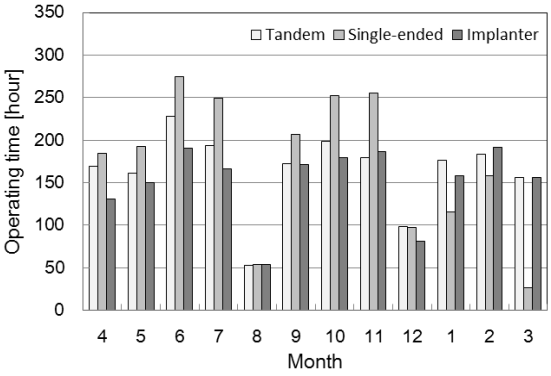

Fig. 1. Monthly operating times in FY 2016.

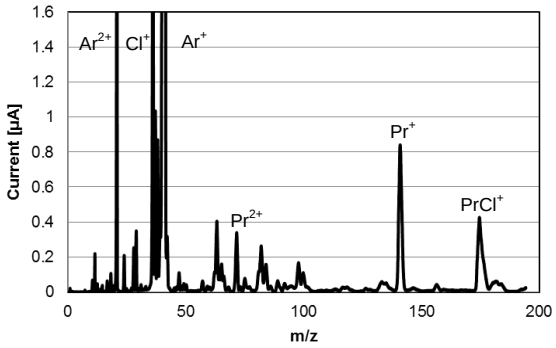

Fig. 2. Ion mass spectrum of the beam generated by the Freeman type ion source using a PrCl powder sample.

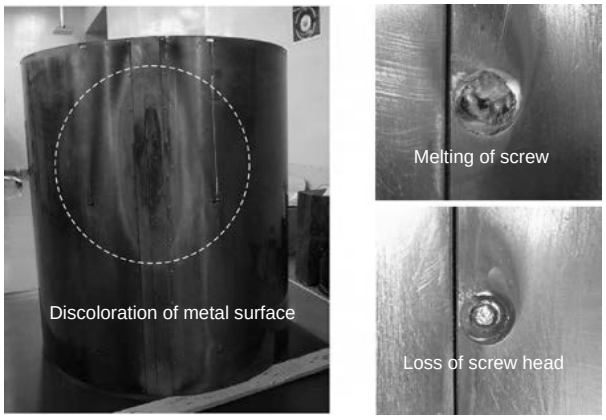

Fig. 3. Images of the connection and screws of the shielding plate damaged by the abnormal heating.

4 - 04 Operation of the Electron Accelerator and the Gamma-ray Irradiation Facilities

T. Agematsu [a)], S. Uno [a)], R. Yamagata [a)], H. Seito [a)], Y. Nagao [a)], S. Yamasaki [a)], N. Yagi [b)], M. Takagi [b)], K. Nagai [b)] and T. Asai [b)]

[a)] Department of Advanced Radiation Technology, TARRI, QST,
[b)] Takasaki Establishment, Radiation Application Development Association

1. Operation

The electron accelerator and the ^{60}Co gamma-ray irradiation facilities were operated approximately smoothly in FY 2016.

The annual operation time of the electron accelerator in this FY was 766 h, including 89 h of conditioning operation. The operation time in recent-years is shown in Fig. 1. The annual operation time decreased in FY 2014 because the operation time was changed from 8:30-23:00 to 9:00-17:30 for effective operation. Furthermore, there were a lot of troubles in FY 2014 and FY 2015, and the operation time decreased. The annual irradiation time in FY 2016 increased due to smooth operation.

The ^{60}Co gamma-ray irradiation facilities consisting of three buildings with eight irradiation rooms cover a wide dose-rate range from 10^{-1} Gy/h to 10^{4} Gy/h as of January 2017. The annual operation times of the first and the second cobalt irradiation facilities and the food irradiation facility were 17,835 h, 15,276 h and 13,656 h, respectively, as shown in Fig. 2.

2. Maintenance

2.1 Electron accelerator

The operation of the vertical beam line at 0.5 MV was impossible in FY 2014 and FY 2015 by the heat trouble of the beam duct near the beam scanner. We designed a magnetic pole of the steering magnet to improve the beam optics. It was installed, and adjustment of beam optics, which included adjustment of position, angle and coil currents for the magnet, was finished. Therefore, 0.5-MV operation was available for irradiation service from May 2016. The maintenance in the accelerator vessel was carried out in October 2016.

2.2 Gamma-ray irradiation facilities

The periodical maintenance check mainly on mechanical systems for radiation source transportation is performed every year on one of the three gamma-ray irradiation facilities in turn. The maintenance check of the food irradiation facility was done in September and October 2016 with suspension of operation for nineteen days. The wall repaint of the pool in the food irradiation facility was carried out in March 2017.

The new ^{60}Co sources, whose total radioactivity was 2.22 PBq, were loaded into the irradiation room No.2 in the first irradiation facility to increase the area of high-dose-rate fields. Old twenty pencil sources of ^{60}Co were disposed of to Japan Radioisotope Association (JRIA). Total ^{60}Co sources of all the facilities at the Takasaki Institute of QST have decreased year by year because purchase quantity of new ^{60}Co sources in recent years was not enough to compensate quantity of isotope decay and disposal quantity of old ^{60}Co sources. Therefore, the maximum dose rate has decreased gradually year by year.

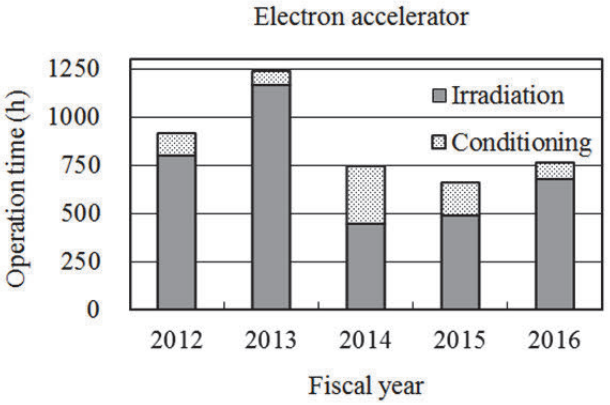

Fig. 1. Annual operation time of the electron accelerator.

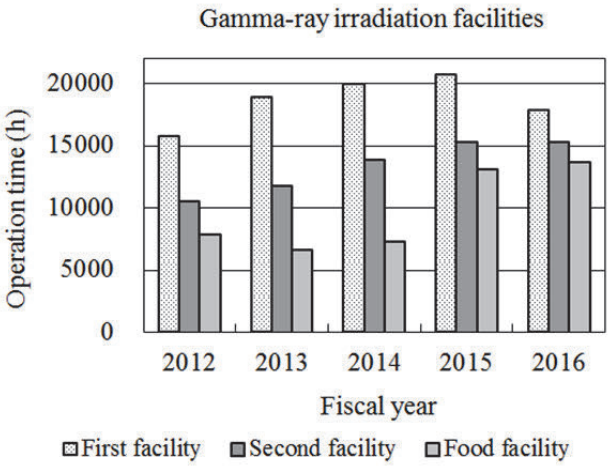

Fig. 2. Annual operation times of the ^{60}Co gamma-ray irradiation facilities.

4 - 05 Utilization Status of the Electron Accelerator and the Gamma-ray Irradiation Facilities

T. Agematsu [a)], S. Uno [a)], R. Yamagata [a)], H. Seito [a)], Y. Nagao [a)], S. Yamasaki [a)], N. Yagi [b)], M. Takagi [b)], K. Nagai [b)] and T. Asai [b)]

[a)] Department of Advanced Radiation Technology, TARRI, QST,
[b)] Takasaki Establishment, Radiation Application Development Association

The electron accelerator and the three gamma-ray irradiation facilities were operated for various research subjects according to the operation plans in FY 2016. Figure 1 shows the number of irradiation experiments in each old research field in FY 2012-2016. The number of irradiation experiments at the accelerator decreased from FY 2014 by following two causes. The first cause was the change of the operation time from 8:30-23:00 to 9:00-17:30 for efficient operation in FY 2014. The second cause was that many troubles happened in FY 2014-2015. The accelerator mainly served for graft-polymerization in new material development, radiation effect studies on semiconductors and various experiments by visiting users. The first cobalt irradiation facility mainly served for long-term radiation resistance testing of cables used in nuclear power plants and nuclear reactor facilities. The second cobalt irradiation facility, including the irradiation room No.6 operated on hourly schedule, mainly served for development of new functional materials and other research subjects of visiting users. The food irradiation facility having a lower-dose-rate field served for radiation resistance testing at wide dose-rate range.

QST was established in April 2016, and the research fields at JAEA were reclassified in QST. “Materials for space”, “Nuclear facilities”, “Material processing”, “Heat-resistant materials” and “Environment” were combined into “Materials science”. “Resources & Bio-technology” and “Basic technology” were relabelled to “Life science” and “Quantum beam science”, respectively. Figure 2 shows the irradiation time of experiments in each old research field in FY 2012-2016. The classification of the users who remained in JAEA was changed from “internal users” to “external users” from FY 2016. Therefore, at the gamma-ray facilities, the irradiation time of “Nuclear facilities” decreased, and that of “Facility use program” increased. Furthermore, because of the delay of procedure for transfer from JAEA to QST, the irradiation time decreased in FY 2016 compared to FY 2015. On the other hand, at the accelerator, the irradiation time increased due to smooth operation in FY 2016 compared to FY 2014-2015 which had many troubles. Irradiation experiments for recovery from the accident at the Fukushima Daiichi Nuclear Power Station of Tokyo Electric Power Company were carried out as “Facility use program” by external users.

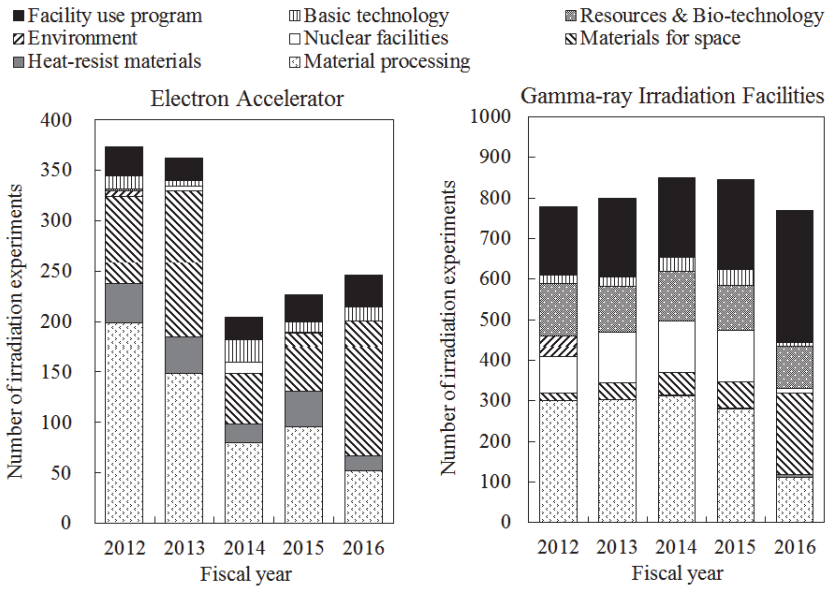

Fig. 1. The number of irradiation experiments (FY 2012-2016).

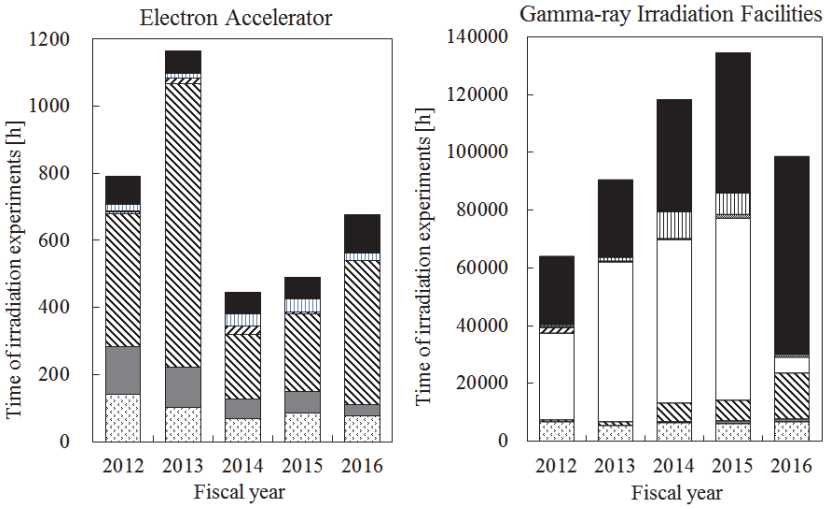

Fig. 2. The time of irradiation experiments (FY 2012-2016).

4 - 06 Radiation Monitoring in TIARA

Safety Management Section

Department of Administrative Services, TARRI, QST

1. Individual monitoring

(1) Individual monitoring for the radiation workers

Table 1 shows a distribution of effective dose of the radiation workers in FY 2016. The effective dose values of almost all radiation workers were below the detection limit of 0.1 mSv.

The maximum dose of the radiation workers was 1.0 mSv/y due to being exposed to radiation by exchanging some radioactive parts of the TIARA AVF cyclotron during the overhaul time.

Table 1

Distributions of the effective dose of the radiation workers in FY 2016.

Items		Number of persons in each periods				
		1st quarter	2nd quarter	3rd quarter	4th quarter	Annual
Distribution range of effective dose HE:Effective dose*1 (mSv)	HE < 0.1	389	429	442	448	552
	0.1 ≦ HE ≦ 1.0	1	8	3	7	14
	1.0 < HE ≦ 5.0	0	0	0	0	0
	5.0 < HE ≦ 15.0	0	0	0	0	0
	15.0 < HE	0	0	0	0	0
Total number of persons (A)		390	437	445	455	566
Exposure above 1 mSv	Number of persons (B)	0	0	0	0	0
	(B)/(A)×100(%)	0	0	0	0	0
Mass effective dose (Person･mSv)		0.2	1.6	0.4	1.0	3.2
Mean dose (mSv)		0.00	0.00	0.00	0.00	0.01
Maximum dose (mSv)		0.1	0.6	0.2	0.4	1.0

*1 The dose by the internal exposure was not detected.

(2) Individual monitoring for the visitors and others

Table 2 shows the number of people who temporarily entered the radiation controlled areas. The effective doses of all people were less than 0.1 mSv.

Table 2

The number of people who temporarily entered the radiation controlled areas in FY 2016.

Periods	1st quarter	2nd quarter	3rd quarter	4th quarter	Total
Number of persons	812	1209	1341	1482	4844

2. Monitoring of radioactive gases and dusts

Table 3 shows the maximum radioactive concentrations and total activities for radioactive gases released from the stack of TIARA, during each quarter of FY 2016.

Small amounts of ^{41}Ar, ^{11}C, ^{13}N and ^{131}I were detected occasionally during the operation of the cyclotron or experiments, but the particulate substances (^{65}Zn, etc.) were not detected.

Table 3

Monitoring results of released radioactive gases and dust in FY 2016.

Nuclide	Periods / Items	1st quarter	2nd quarter	3rd quarter	4th quarter	Total
^{41}Ar	Maximum concentratio	3.3×10^{-4}	$<1.4\times10^{-4}$	1.7×10^{-4}	$<1.4\times10^{-4}$	
	Activity	1.5×10^{9}	0	1.1×10^{9}	0	2.6×10^{9}
^{11}C	Maximum concentratio	$<1.4\times10^{-4}$	——	$<1.4\times10^{-4}$	——	
	Activity	6.0×10^{7}	——	3.8×10^{7}	——	9.8×10^{7}
^{13}N	Maximum concentratio	$<1.4\times10^{-4}$	——	$<1.4\times10^{-4}$	——	
	Activity	7.5×10^{7}	——	2.3×10^{8}	——	3.1×10^{8}
^{131}I	Maximum concentratio	3.9×10^{-9}	——	——	——	
	Activity	6.6×10^{4}	——	——	——	6.6×10^{4}
^{65}Zn	Maximum concentratio	$<5.0\times10^{-10}$	$<4.8\times10^{-10}$	$<5.0\times10^{-10}$	$<4.3\times10^{-10}$	
	Activity	0	0	0	0	0

Unit : Bq/cm^3 for Maximum concentration, Bq for Activity.

3. Monitoring for external radiation and surface contamination

The monitoring for external radiation and surface contamination was routinely performed in/around the radiation controlled areas. Neither anomalous value of dose equivalent rate nor surface contamination was detected.

Figure 1 shows a typical example of distribution of the dose equivalent rate in the radiation controlled area of the cyclotron building.

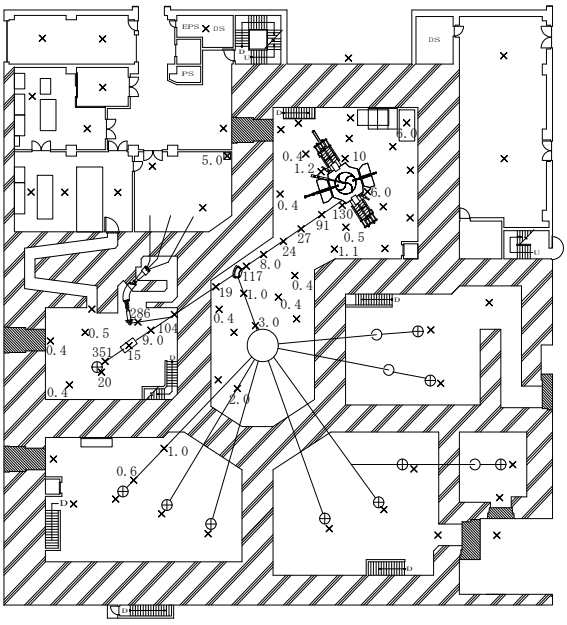

Fig. 1. Dose equivalent rate distribution in the radiation controlled area of the cyclotron building. Measurement date: 15th and 29th March 2016, Measuring position: Indicated with × (1 m above floor), Unit : μSv/h. (The values are not indicated if less than 0.2 μSv/h.)

4 - 07 Radioactive Waste Management in TIARA

N. Higuchi

Department of Administrative Services, TARRI, QST

1. Radioactive wastes management

The radioactive wastes generated in TIARA are managed by Utilities and Maintenance Section. The main radioactive wastes are the solid wastes generated from research experiments and the maintenance of the cyclotron. Other radioactive wastes are the liquid wastes such as inorganic waste fluids generated from research experiments and the air-conditioning machines in controlled area. These wastes are managed according to their properties. Radioactive waste is stored in a storage facility and handed over to the RI Association for disposal.

2. Solid radioactive waste

Table 1 shows the amounts of solid wastes at various properties and kinds generated in each quarter of FY 2016. Combustible wastes are papers and clothes, etc. Flame-retardant wastes are rubber gloves, plastic articles, and polyethylene articles. Incombustible wastes are pieces of metal, the glasses, and contaminated parts. Solid waste emitting α, β, and γ is classified according to the properties.

3. Liquid radioactive waste

Table 2 shows the amounts of liquid wastes generated in each quarter of FY 2016. Most of liquid waste was inorganic waste water generated from chemical experiments and condensed water from operation of air conditioning units installed in each room of the radiation controlled area. The largest quantity of waste water in summer season (2nd quarter) is mainly due to the condensed water. After treatment by evaporation, inorganic water is reused in the radiation controlled area. Only small amounts of concentrated liquid are generated from the evaporation.

Table 1
Radioactive solid wastes generated in FY 2016.

Items \ Amounts	Amounts of generation in each period (m^3)					Number of package /drum
	1st quarter	2nd quarter	3rd quarter	4th quarter	Total	
Category β, γ*	0.10	0.36	0.00	0.71	1.17	20
Combustible	0	0.04	0	0.08	0.12	3
Flame-retardant	0	0.24	0	0.24	0.48	12
Incombustible(Compressible)	0	0.08	0	0.04	0.12	3
〃 (Incompressible)	0	0	0	0.05	0.05	1
Laboratory animal	0	0	0	0.04	0.04	1
Filters	0.10	0	0	0.26	0.36	-
Category α*	0	0	0	0.20	0.20	4
Combustible	0	0	0	0.02	0.02	-
Flame-retardant	0	0	0	0.14	0.14	3
Incombustible(Compressible)	0	0	0	0	0	-
〃 (Incompressible)	0	0	0	0	0	-
Laboratory animal	0	0	0	0.04	0.04	1
Filters	0	0	0	0	0	-

* defined by amount in Bq (β, γ): < 2 GBq , (α) : (A) < 37 MBq (B) ≤ 37 MBq
** 50-liter drum

Table 2
Radioactive liquid waste generated in FY 2016.

Items \ Amounts	Amounts of generation in each period (m^3)					Number of package /drum
	1st quarter	2nd quarter	3rd quarter	4th quarter	Total	
Category β,γ*	10.51	24.43	6.33	5.81	47.08	-
1)Inorganic	10.51	24.43	6.33	5.79	47.06	-
Inorganic	10.51	24.43	6.28	5.71	46.93	treatment
Sludge, Evaporation residue	0	0	0.05	0.075	0.125	5 **
2)Organic	0	0	0	0.025	0.025	1 **
Organic	0	0	0	0.025	0.025	0
Oil	0	0	0	0	0	0
Category α*	0	0	0	0	0	0

* defined by concentrations in Bq/mL (β, γ Inorganic) : < 200 kBq, (Organic) : < 2 kBq, (α) : ≤ 1.85 kBq
** 50-liter container

4 - 08 Facility Use Program in Takasaki Advanced Radiation Research Institute (TARRI)

S. Nozawa, H. Hanaya and R. Nakahara

Research Planning and Promotion Office, QuBS, QST

1. Introduction

The usage of the facilities in QST is widely allowed for many users in universities, public institutes, R&D divisions of companies, and so on (hereafter 'outside users'). FACILITY USE PROGRAM is for users' service on the basis of fee-charging in the usage. The users can use the irradiation fields of Co-60 gamma-rays, electron beams, and various ion beams that are produced by the facilities of Co-60 gamma-ray, an electron accelerator, and TIARA's four ion accelerators, respectively, and some of off-line analysis instruments. In this program, the research proposals from the outside users are reviewed every half a year, from the points of the availability and the validity of the experimental plans by the expert committee member. The confirmed research proposals had been carried out under the facility use program.

2. Classification of Facility Use Program

Charging system for the Facility Use Program is classified by the purpose of irradiation and intending to publication of results, as shown in Table 1. The amount of charging fee had been calculated from handling, irradiation, and expendable fees, in addition to radioactive waste disposal expenses, and additional labor charges. For research and development (R&D) users who will intend to disclose the results of experiment by publication, partially exempted charges were applied for irradiation. For Except R&D using, such as commercial irradiation, the depreciation cost for irradiation facilities were charged.

Table 1
Charging system for Facility Use Program.

Classification	R&D Intended for Publication	R&D Not Intended for Public disclosure	Commercial
Purpose	Research and Development		Except R&D
Belonging of Results	Non-proprietary	Proprietary	
Duty for publishing	Yes	No need to public disclose	
Charging fees*	A	B	C

*A = handling fees + expendables fee (other charges are exempted)
B = handling fees + expendables fee + irradiation fee + radioactive waste disposal expenses
C = handling fees + expendables fee + irradiation fee + radioactive waste disposal expenses + depreciation cost for irradiation facilities

3. Numbers of irradiation experiments in FY2016

The frequencies of irradiation experiments for each facility in FY2016 are shown in Table 2.

Table 2
Frequency of irradiation experiments at each facility in this program in FY2016.

Facility \ User		University	Institute	Company	Total
TIARA	AVF cyclotron	14	11	20	45
	3 MV tandem accelerator	13	16	6	35
	3 MV single-ended accelerator	3	11	0	14
	400 kV ion implanter	11	12	0	23
Co-60 gamma-ray irradiation facilities		29	97	202	328
Electron accelerator		18	2	10	30
Total		88	149	238	475

In Table 2, the irradiation experiments of more than three hundred times were carried out at the Co-60 gamma-ray irradiation facilities. Of them, the irradiation experiments of two hundred times and more were carried out by the outside users of private companies. It is also that the largest part of irradiation experiments at the AVF cyclotron had been carried out by users from private companies.

The irradiation experiments for private companys' users are increasing year by year. Many of the users were not experts for irradiation experiments, and they needed the more information about the irradiation facilities and the related techniques. Practical information about how to use the facilities; the application of proposals, the time table of experiments, the performance of equipment, the arrangement of samples, charging system, and so on, were required. And we also provide the basic information for the users, *i.e.* access to facilities, method for payment, duties of users, and etc.

The other detailed information about this program is available on QST website as follows:
http://www.qubs.qst.go.jp/kyoyo/index.html.

Appendices

Appendix 1 Publication list

Items in gray show the works in collaboration with other projects of QST.
Bold letters and **numbers** at the last of each item mean as follows.
Letter : Accelerators or irradiation facilities used for the work.
C : Cyclotron, **T** : Tandem accelerator, **S** : Single-ended accelerator, **I** : Ion implanter,
E : Electron accelerator, **G** : Gamma-ray irradiation facilities, **N** : Not used.
Number that contains hyphen: Serial number of the related paper in Part II.

Functional Polymer Research Project（P1-1）

Papers

1) T. Hamada, H. Fukasawa, S. Hasegawa, A. Miyashita and Y. Maekawa, "Graft-type Polymer Electrolyte Membranes Based on Poly(ether ether ketone)/Nanosilica Hybrid Films for Fuel Cell Applications", Int. J. Hydrogen Energy, **41**, 18621-30 (2016). **G, 1-19**

2) Y. Zhao, M. Yoshida, T. Oshima, S. Koizumi, M. Rikukawa, N. Szekely, A. Radulescu, D. Richter, "Elucidation of the morphology of the hydrocarbon multi-block copolymer electrolyte membranes for proton exchange fuel cells", Polymer, **86,** 157-67 (2016). **N, 1-17**

3) Y. Zhao, M. Yoshida, T. Oshima, S. Koizumi, M. Rikukawa, N. Szekely, A. Radulescu, D. Richter, "Hard-sphere model analysis on the morphology of polymer electrolyte membranes partially swollen in water", Data in Brief, **7**, 599-603 (2016). **N, 1-17**

4) 澤田 真一, 小平 岳秀, 田中 伸幸, 久保 真治, 野村 幹弘, "熱化学水素製造ISプロセスに向けた陽イオン交換膜の開発", 放射線と産業, **141,** 12-15 (2016). **G, 1-18**

5) S. Sawada, S. Hasegawa, Y. Zhao, and Y. Maekawa, "Block-type proton exchange membranes prepared by a combination of radiation-induced grafting and atom-transfer radical polymerization", J. Membr. Sci., **532**, 105-14 (2017). **G, 1-18**

6) K. Shimasaki, T. Yamaki, S. Sawada, A. Hiroki, Y. Maekawa and N. Miyamoto, "Synthesis of Anisotropic Poly(N-isorpopylacrylamide)/Inorganic-Nanosheets Composite Gels by γ-Radiation-Induced Polymerization and Crosslinking", J. Nanosci. Nanotech., **16**, 9231-37 (2016). **G**

7) M. Higa, M. Goto, T. Yamaki, S. Sawada, H. Koshikawa, A. Kitamura, "Characterization of Cation-exchange Membranes Prepared by Ion-track Graft Polymerization", Bull. Soc. Sea Water Sci. Jpn., **71**, 37-38 (2017). **C**

8) 八巻 徹也, 小平 岳秀, 澤田 真一, 田中 伸幸, 久保 真治, "放射線グラフト重合法による膜ブンゼン反応用カチオン交換膜の開発", 膜(MEMBRANE), **41**, 114-20 (2016). **G, 1-09**

9) S. Yamashita, J. Ma, J.-L. Marignier, A. Hiroki, M. Taguchi, M. Mostafavi and Y. Katsumura, "Radiation-Induced Chemical Reactions in Hydrogel of Hydroxypropyl Cellulose (HPC): A Pulse Radiolysis Study", Radiat. Res., **186**, 650-58 (2016). **G, E**

Proceedings

1) Y. Zhao, K. Yoshimura, H. Shishitani, S. Yamaguchi, H. Tanaka and Y. Maekawa, "Elucidation of the morphology of imidazolium-based anion exchange membranes for alkaline anion fuel cells", Abstr. ECS Meet. **38**, 2534, [San Diego, USA] (2016/05-06). **G, 1-17**

2) Y. Maekawa, "Mechanistic Study of Radiation-Induced Graft-Polymerization for Application in Fuel Cells", Abstr. 12th Meet. Ionizing Radiat. Polymers Symp., P37, [Les Criques, France] (2016/09). **G**

3) K. Yoshimura, S. Watanabe, H. Shishitani, S. Yamaguchi, H. Tanaka, and Y. Maekawa, "Synthesis, Characterization, and Alkaline Stabilities of 4-Vinylimidazolium-Based Anion Conducting Polymer Electrolyte Membranes Prepared by Radiation-Induced Grafting for Alkaline Fuel Cell Applications", Abstr. 230th ECS Meet., #2525, [Honolulu, USA] (2016/10). **G**

4) Y. Zhao, K. Yoshimura, and Y. Maekawa, "Morphology and interplay between morphology and properties of imidazolium-based anion exchange membranes", Abstr. 230th ECS Meet., #2534, [Honolulu, USA] (2016/10). **G, 1-17**

5) Y. Maekawa, "New Aspects of Radiation-induced Graft-polymerization and its Application to Fuel Cell Polymer Electrolyte Membranes", Abstr. 14th Int. Conf. Radiat. Curing, [Tokyo, Japan] (2016/10). **G**

6) ザオ ユエ, 吉村 公男, 猪谷 秀幸, 山口 進, 田中 裕久, 小泉 智, 前川 康成, "Elucidation of the morphology and interplay between morphology and properties of imidazolium-based anion exchange membranes for alkaline anion fuel cells", 第 65 回高分子学会年次大会, 要旨集 1K15, [神戸国際会議場・神戸] (2016/05). **G, 1-17**

7) 濱田 崇, 吉村 公男, 廣木 章博, 前川 康成, "放射線グラフト重合によるアニリン型アニオン伝導電解質膜の合成と特性評価", 第 65 回高分子学会年次大会, 要旨集 3Pc067, [神戸国際会議場・神戸] (2016/05). **G, 1-19**

8) 前川 康成, 吉村 公男, ザオ ユエ, 廣木 章博, 猪谷 秀幸, 岸山 佳央, 山口 進, 田中 裕久, "イミダゾリウム基を含むグラフト型アニオン伝導高分子電解質膜の構造と特性", 第 65 回高分子討論会, 要旨集 3X05, [神奈川大・横浜] (2016/09). **G**

9) 吉村 公男, 廣木 章博, ザオ ユエ, 猪谷 秀幸, 岸山 佳央, 山口 進, 田中 裕久, 前川 康成, "放射線グラフト重合により合成したアルカリ耐性アニオン伝導電解質膜", 第 65 回高分子討論会, 要旨集 3Pc043, [神奈川大・横浜] (2016/09). **G**

10) 澤田 真一, 前川 康成, "新しい放射線グラフト重合法による非対称構造膜の創製", 第 59 回放射線化学討論会, 要旨集 2O03, [量研高崎・高崎] (2016/09). **G, 1-18**

11) 吉村 公男, 廣木 章博, 猪谷 秀幸, 山口 進, 田中 裕久, 前川 康成, "放射線グラフト型アニオン伝導電解質膜の開発と水加ヒドラジン燃料電池自動車への応用", 第 59 回放射線化学討論会, 要旨集 2O04, [量研高崎・高崎] (2016/09). **G**

12) 長谷川 伸, 廣木 章博, 前川 康成, "放射線グラフト重合法による芳香族炭化水素燃料電池膜の高温低加湿下における耐久性", 第59回放射線化学討論会, 要旨集 P-17, [量研高崎・高崎] (2016/09). **G, 1-16**

13) ザオ ユエ, 吉村 公男, 長谷川 伸, 廣木 章博, 猪谷 秀幸, 山口 進, 田中 裕久, 前川 康成, "Imidazolium-Based Anion

Exchange Membranes for Alkaline Anion Fuel Cells: Elucidation of the Distribution of ions and its Impact on the Ion Conductivity", 第 59 回放射線化学討論会, 要旨集 P-19, [量研高崎・高崎] (2016/09). **G, 1-17**

14) 濱田 崇, 長谷川 伸, 前川 康成, "放射線リビンググラフト重合による高分子電解質膜の合成と燃料電池への応用", 第 59 回放射線化学討論会, 要旨集 P-20, [量研高崎・高崎] (2016/09). **G, 1-19**

15) 竹内 航太, 吉村 公男, 廣木 章博, 前川 康成, "放射線グラフト重合により作製したアニオン伝導電解質膜のアルカリ溶液中での物性変化", 第59回放射線化学討論会, 要旨集 P-37, [量研高崎・高崎] (2016/09). **E, G**

16) 竹内 航太, 吉村 公男, 廣木 章博, 前川 康成, "放射線グラフト重合により作製したアニオン伝導電解質膜のアルカリ溶液中での物性変化", 日本化学会関東支部群馬地区研究交流発表会, 要旨集 P-02, [量研高崎・高崎] (2016/12). **G**

17) 濱田 崇, 吉村 公男, 廣木 章博, 前川 康成, "アニリン型アニオン伝導電解質膜の合成と特性評価", 第 26 回日本 MRS 年次大会, 要旨集 B3-P19-014, [横浜市開港記念会館・横浜] (2016/12). **G, 1-19**

18) 澤田 真一, 前川 康成, "放射線非対称グラフト重合法による新規バイポーラ膜の作製", 膜シンポジウム 2016, 要旨集 206, [関西大学100周年記念会館・大阪] (2016/12). **G, 1-18**

19) 八巻 徹也, ヌリヤンティ ヌヌン, 喜多村 茜, 越川 博, 吉村 公男, 澤田 真一, 寺井 隆幸, "高エネルギー重イオンビームによる燃料電池用ナノ構造制御電解質膜の開発", 日本膜学会第 38 年会, 要旨集 1A-6, [早稲田大・東京] (2016/05). **C, G, 1-09**

20) M. Nomura, T. Kodaira, K. Oura, A. Ikeda, Y. Naka, H. Nishijima, S. Imabayashi, S. Sawada, T. Yamaki, N. Tanaka and S. Kubo, "Radiation-grafted ion exchange membranes for the thermochemical hydrogen production IS process", Proc. 10th Conf. Aseanian Membrane Soc. (AMS10), PO1-034, [Nara, Japan] (2016/07). **E, G**

21) M. Goto, M. Omori, T. Yamaki, S. Sawada, H. Koshikawa, A. Kitamura and M. Higa, "Characterization of cation-exchange membranes prepared by ion beam irradiation graft polymerization", Proc. 10th Conf. Aseanian Membrane Soc. (AMS10), PO4-009, [Nara, Japan] (2016/07). **C**

22) M. Omori, M. Goto, T. Yamaki, S. Sawada, H. Koshikawa, A. Kitamura and M. Higa, "Preparation and characterization anion-exchange membranes (AEM) by heavy ion track graft polymerization method", Proc. 10th Conf. Aseanian Membrane Soc. (AMS10), PO3-075, [Nara, Japan] (2016/07). **C**

23) 越川 博, 佐藤 裕真, 山本 春也, 杉本 雅樹, 澤田 真一, 八巻 徹也, "イオン穿孔膜をテンプレートとした白金ナノコーンアレイの作製", 第 77 回応用物理学会秋季学術講演会, 要旨集 15a-B5-9, [朱鷺メッセ・新潟] (2016/09). **C, G, 1-06**

24) 廣木 章博, 小曽根 雄介, 山下 真一, 木村 敦, 長澤 尚胤, 田口 光正, 村上 健, "電子線架橋ヒドロキシプロピルセルロースゲルを用いて作製したポリマーゲル線量計材料の高感度化", 第 59 回放射線化学討論会, 要旨集 1O08, [量研高崎・高崎] (2016/09). **E, G**

25) 廣木 章博, 小曽根 雄介, 山下 真一, 木村 敦, 長澤 尚胤, 田口 光正, "放射線架橋ゲルを母材とするポリマーゲル線量計材料の高感度化", 第 5 回 3Dゲル線量計研究会, 要旨集, [京大宇治キャンパスおうばくぷらざ・宇治] (2016/12). **E, G**

26) 佐藤 裕真, 越川 博, 山本 春也, 杉本 雅樹, 澤田 真一, 八巻 徹也, "イオン穿孔膜を鋳型とした白金ナノコーン構造の形成", 電気化学会第 84 回大会, 要旨集 PS88, [首都大東京・八王子] (2017/03). **C, G, 1-07**

Books

1) 前川 康成, "重合・グラフト重合", EB 技術を利用した材料創製と応用展開, シーエムシー出版, 15-23, (2016). **G, 1-16~19**

2) 廣木 章博、吉村 公男, "燃料電池用高分子電解質膜の開発", EB 技術を利用した材料創製と応用展開, シーエムシー出版, 161-69, (2016). **G, 1-16~19**

Patents

1) 吉村 公男, 越川 博, 八巻 徹也, 浅野 雅春, 前川 康成, 三瓶 文寛, 猪谷 秀幸, 朝澤 浩一郎, 山口 進, 田中 裕久, "Anion conductive electrolyte membrane and producing method thereof" 米国特許登録 9379402 (2016.06.28). **E, G**

2) 吉村 公男, 越川 博, 八巻 徹也, 浅野 雅春, 前川 康成, 猪谷 秀幸, 田中 裕久, 山口 進, 朝澤 浩一郎, 山本 和矢, 三瓶 文寛, "Anion conducting electrolyte membrane and method for producing the same", 米国特許登録 5959046 (2016.07.01). **E, G**

3) 吉村 公男, 越川 博, 八巻 徹也, 浅野 雅春, 前川 康成, 三瓶 文寛, 猪谷 秀幸, 朝澤 浩一郎, 山口 進, 田中 裕久, "Anion conductive electrolyte membrane and producing method thereof" 米国特許登録 6028312 (2016.10.28). **E, G**

4) 百合 庸介, 石堀 郁夫, 湯山 貴裕, 石坂 知久, 奥村 進, 前川 康成, 越川 博, 八巻 徹也, 浅野 雅春, "Porous polymer membrane and method for producing the same" 米国特許登録 6044895 (2016.11.25). **C**

5) 澤田 真一, 前川 康成, "バイポーラ膜及びその製造方法、電気透析装置並びに燃料電池" 出願 2017-053424 (2017.03.17). **G, 1-18**

Press・TV

1) 芝浦工業大学・量研機構・科学技術振興機構, "高効率な水素製造を可能にするイオン交換膜型ブンゼン反応器を開発ー高温熱を利用し CO_2フリー水素を製造する膜分離新 IS プロセス実用化の第一歩ー", プレス発表:化学工業日報、日本経済新聞(Web 版)、財経新聞(Web 版)、徳島新聞(Web 版)に掲載, (2017.03.02). **G**

Advanced Catalyst Research Project（P1-2）

Papers

1) T. Kimata, S. Kato, T. Yamaki, S. Yamamoto, T. Kobayashi and T. Terai, "Platinum nanoparticles on the glassy carbon surface irradiated with argon ions", Surf. Coat. Tech., **306**, 123-26 (2016). **S, I**

2) S. Tsukuda, R. Takahashi, S. Seki, M. Sugimoto, A. Idesaki, M. Yoshikawa and S. Tanaka, "Fabrication of Pt nanoparticle incorporated polymer nanowire by high energy ion and electron beam irradiation", Radiat. Phys. Chem., **118**, 16-20 (2016). **C**

3) 八巻 徹也, 小平 岳秀, 澤田 真一, 田中 伸幸, 久保 真治, 野村 幹弘, "放射線グラフト重合法による膜ブンゼン反応用カチオン交換膜の開発", 膜(MEMBRANE), **41**, 114-20 (2016). **E, G, 1-09**

4) T. Wasin, K. Enomoto, T. Sakurai, V. S. Padalkar, H. L. Cheng, M. T. Tang, A. Horio, D. Sakamaki, M. Omichi, A. Saeki, K. Kikuchi, Y. Hori, A. Chiba, Y. Saito, T. Kamiya, M. Sugimoto and S. Seki, "Fabrication of "clickable" polyfluorene nanowires with high aspect ratio as biological sensing platforms," ACS Sens., **1**, 766-74 (2016). **C, 3-21**

5) A. Horio, T. Sakurai, V. S. Padalkar, D. Sakamaki, T. Yamaki,

M. Sugimoto and S. Seki, “Fabrication of fluorescent nanowires via high-energy-particles-triggered polymerization reactions”, J. Photopolym. Sci. Tech., **29**, 373-77 (2016). **C, 3-21**

6) A. Horio, T. Sakurai, G. B. V. S. Lakshmi, D. K. Avasthi, M. Sugimoto, T. Yamaki and S. Seki, “Formation of nanowires via single particle triggered linear polymerization of solid-state aromatic molecules”, Nanoscale, **8**, 14925-31 (2016). **C, 3-21**

7) A. Horio, T. Sakurai, K. Kayama, G. B. V. S. Lakshmi, D. V. Avasthi, M. Sugimoto, T. Yamaki, A. Chiba, Y. Saito and S. Seki, “Remarkable Effect of Halogenation of Aromatic Compounds on Efficiency of Nanowire Formation through Polymerization/Crosslinking by High-Energy Single Particle Irradiation”, Radiat. Phys. Chem., **142**, 100-06 (2018). **C, T, 3-21**

8) S. Tsukuda, M. Omichi, M. Sugimoto, A. Idesaki, V. Padalkar and S. Seki, “Anisotropic swelling of hydrogel nanowires based on poly(vinylpyrrolidone) fabricated by single-particle nanofabrication technique”, J. Polymer Sci. B Polymer Phys., **54**, 1950-56 (2016). **C**

9) K. Shimasaki, T. Yamaki, S. Sawada, A. Hiroki, Y. Maekawa, and N. Miyamoto, “Synthesis of Anisotropic Poly(N-isorpopylacrylamide)/Inorganic-Nanosheets Composite Gels by γ-Radiation-Induced Polymerization and Crosslinking”, J. Nanosci. Nanotech., **16**, 9231-37 (2016). **G**

10) T. Taguchi, R. Tsubakiyama, K. Miyajima, S. Yamamoto and H. Ohba, “Effect of surface treatment on photoluminescence of silicon carbide nanotubes”, Appl. Surf. Sci., **403**, 308-13 (2017). **T, I, 1-24**

11) M. Higa, M. Goto, T. Yamaki, S. Sawada, H. Koshikawa and A. Kitamura, “Characterization of cation-exchange membranes prepared by ion-track graft polymerization”, Bull. Soc. Sea Water Sci. Jpn., **71**, 37-38 (2017). **C**

12) 垣谷 健太, 木全 哲也, 八巻 徹也, 寺井 隆幸, “炭素担体におけるイオン照射欠陥を利用した白金ナノ微粒子の特性制御”, 放射線と産業, **141**, 29-32 (2016). **S, I, 1-10**

13) 小林 知洋, 森 利之, 山本 春也, “液相中プロトンビーム照射による金属ナノ粒子生成”, 放射線と産業, **141**, 25-28 (2016). **N**

14) 澤田 真一, 小平 岳秀, 田中 伸幸, 久保 真治, 野村 幹弘, “熱化学水素製造ISプロセスに向けた陽イオン交換膜の開発”, 放射線と産業, **141**, 12-15 (2016). **E, G, 1-18**

15) 佃 諭志, 杉本 雅樹, “高エネルギーイオンビームを利用したナノワイヤー状複合触媒の開発”, 放射線と産業, **141**, 16-19 (2016). **C**

Proceedings

1) 八巻 徹也, ヌリヤンティ ヌヌン, 喜多村 茜, 越川 博, 吉村 公男, 澤田 真一, 寺井 隆幸, “高エネルギー重イオンビームによる燃料電池用ナノ構造制御電解質膜の開発:アニオン交換膜の作製と特性”, 日本膜学会第 38 年会, 1A-6, [早稲田大・東京] (2016/05). **C, 1-09**

2) 大森 理之, 後藤 光暁, 八巻 徹也, 澤田 真一, 越川 博, 喜多村 茜, 比嘉 充, “イオン照射グラフト重合法による陰イオン交換膜の作製及び特製評価”, 2016 年度日本海水学会第 67 年会, P-22S, [登別グランドホテル・登別] (2016/06). **C**

3) 高橋 研一, 森 利之, 鈴木 彰, チャウハン シプラ, 前川 康成, 山本 春也, 廣木 章博, 吉村 公男, “放射線グラフト重合法による固体高分子形燃料電池膜電極複合体中の電極構造ならびに三相界面数の変化”, 第 32 回日本セラミックス協会関東支部研究発表会, 1A-16, [富士 緑の休暇村・鳴沢] (2016/09). **E, G**

4) 高橋 研一, 森 利之, 鈴木 彰, チャウハン シプラ, 前川 康成, 山本 春也, 廣木 章博, 吉村 公男, “固体高分子形燃料電池電極層中における高分子の放射線グラフト重合による三相界面数増加に寄与する電極活物質/アイオノマー界面の設計”, 第 65 回高分子討論会, 要旨集 3Pd044, [神奈川大・横浜] (2016/09). **E, G**

5) 高橋 研一, 森 利之, 鈴木 彰, チャウハン シプラ, 前川 康成, 廣木 章博, 吉村 公男, 山本 春也, “150 ℃及び 70 ℃の温度で動作する固体高分子形燃料電池膜電極複合体内のバインダー/電極活物質界面設計による三相界面の変化”, 日本セラミックス協会 第 29 回秋季シンポジウム, 1PV09, [広島大・東広島] (2016/09). **E, G**

6) 森 利之, レドニク アンドリー, 山本 春也, 鈴木 彰, 伊藤 滋啓, 伊坂 紀子, 丹司 敬義, 大久保 弘, Shipra Chauhan, “中温作動酸化物形燃料電池の性能改善に及ぼす極微少量白金ドープ効果”, 日本セラミックス協会 第 29 回秋季シンポジウム, 1V08, [広島大・東広島] (2016/09). **S**

7) S. Chauhan, T. Mori, A. Suzuki, S. Yamamoto, A. Rednyk and H. Okubo, “Design of yttria stabilized zirconia fibre network fabricated by sol-gel method for IT-SOFC”, 日本セラミックス協会 第 29 回秋季シンポジウム, 1PV04, [広島大・東広島] (2016/09). **S**

8) 越川 博, 佐藤 裕真, 山本 春也, 杉本 雅樹, 澤田 真一, 八巻 徹也, “イオン穿孔膜をテンプレートとした白金ナノコーンアレイの作製”, 第 77 回応用物理学会秋季学術講演会, 要旨集 15a-B5-8, [朱鷺メッセ・新潟] (2016/09). **C, 1-06**

9) 出崎 亮, 杉本 雅樹, 山本 春也, 田口 光正, 八巻 徹也, “イオン注入法を利用した前駆体高分子からの窒素含有カーボン材料の合成”, 日本セラミックス協会 第 29 回秋季シンポジウム, 1K07, [広島大・東広島] (2016/09). **I, 1-21**

10) 垣谷 健太, 木全 哲也, 八巻 徹也, 山本 春也, 毛 偉, 寺井 隆幸, 小林 知洋, “イオンビーム照射グラッシーカーボンに担持した白金ナノ微粒子触媒:密度汎関数理論計算による電子構造解析”, 日本原子力学会 2016 年秋の大会, 1K07, [久留米シティプラザ・久留米] (2016/09). **S, I, 1-10**

11) 垣谷 健太, 木全 哲也, 八巻 徹也, 山本 春也, 毛 偉, 寺井 隆幸, 小林 知洋, “イオンビーム照射した炭素担体と白金ナノ微粒子との界面電子構造”, 第 77 回応用物理学会秋季学術講演会, 要旨集 14a-D62-9, [朱鷺メッセ・新潟] (2016/09). **S, I, 1-10**

12) S. Yamamoto, M. Sugimoto, H. Koshikawa, T. Hakoda and T. Yamaki, “Orientational control of CeO_2 films on sapphire substrates grown by magnetron sputtering”, Proc. 18th Int. Conf. Crystal Growth & Epitaxy (ICCGE-18), MoP-G04-10, [Nagoya, Japan] (2016/08). **S, 1-22**

13) 田口 富嗣, 山本 春也, 大場 弘則, “SiC ナノチューブ内の新奇構造を有する多層カーボンナノチューブの創製”, 第 51 回フラーレン・ナノチューブ・グラフェン総合シンポジウム, 1P-16, [道民活動センター・札幌] (2016/09). **T, I, 1-24**

14) 関 修平, 堀尾 明史, 香山 一登, 竹下 友輝, 榎本 一之, 櫻井 庸明, 大道 正明, D. K. Avasthi, G. B. V. S. Lakshmi, 杉本 雅樹, 八巻 徹也, “単一粒子反応:高分子架橋と重合によるアプローチ”, 第 59 回放射線化学討論会, 3O11, [量研高崎・高崎] (2016/09). **C, 3-21**

15) 竹内 夕桐子, 中村 俊介, 杉本 雅樹, 長澤 尚胤, 島田 明彦, 箱田 照幸, 田口 光正, “高温・高線量放射線照射システムの構築と耐熱耐放射線性エラストマーの開発”, 第 59 回放射線化学討論会, 要旨集 P-13, [量研高崎・高崎] (2016/09). **G**

16) 越川 博, 佐藤 裕真, 山本 春也, 杉本 雅樹, 澤田 真一, 八巻 徹也, “イオン穿孔膜により作製した白金ナノコーンの構造”, 第59回放射線化学討論会, 要旨集 P-38, [量研高崎・高崎] (2016/09). **C, 1-06**

17) A. Idesaki, M. Sugimoto, S. Yamamoto, M. Taguchi and T. Yamaki, "Fabrication of nitrogen-doped carbon material from precursor polymer by ion implantation technique", Proc. 6th Int. Congr. Ceramics (ICC6), L-02, [Dresden, Germany] (2016/08). **I, 1-21**

18) M. Nomura, T. Kodaira, K. Oura, A. Ikeda, Y. Naka, H. Nishijima, S. Imabayashi, S. Sawada, T. Yamaki, N. Tanaka and S. Kubo, "Radiation-grafted ion exchange membranes for the thermochemical hydrogen production IS process", Proc. 10th Conf. Aseanian Membrane Soc. (AMS10), PO1-034, [Nara, Japan] (2016/07). **E, G**

19) M. Goto, M. Omori, T. Yamaki, S. Sawada, H.Koshikawa, A. Kitamura and M. Higa, "Characterization of cation-exchange membranes prepared by ion beam irradiation graft polymerization", Proc. 10th Conf. Aseanian Membrane Soc. (AMS10), PO4-009, [Nara, Japan] (2016/07). **C**

20) M. Omori, M. Goto, T. Yamaki, S. Sawada, H. Koshikawa, A. Kitamura and M. Higa, "Preparation and characterization anion-exchange membranes (AEM) by heavy ion track graft polymerization method", Proc. 10th Conf. Aseanian Membrane Soc. (AMS10), PO3-075, [Nara, Japan] (2016/07). **C**

21) 大森 理之, 後藤 光暁, 八巻 徹也, 澤田 真一, 越川 博, 比嘉 充, "イオン照射グラフト重合法を用いた陰イオン交換膜の作成と膜特性評価", 2016 年度第 10 回中四国若手 CE 合宿, PS-44, [ホテル常盤・山口] (2016/09). **C**

22) T. Yamaki, N. Nuryanthi, T. Kimata, S. Kato, S. Yamamoto, M. Sugimoto, H. Koshikawa and T. Terai, "Quantum beam technology: nanomaterials prepared by ion-beam irradiation for fuel cell applications"【**Invited talk**】, Proc. Energy Mater. Nanotech. Meet. Fuel Cells, C02, [Jeju, Korea] (2016). **C, S, I, 1-09**

23) T. Yamaki, "Fluoropolymer-based nanostructures created by swift-heavy-ion irradiation"【**Invited talk**】, Semin. Korea Inst. Sci. Tech., (KIST), [Seoul, Korea] (2016). **C, 1-09**

24) 杉本 雅樹, "タンパク質やフラーレンのナノワイヤーをイオンビームで創る", 第 6 回 CSJ 化学フェスタ 2016 量研機構特別企画: 量子ビームでなんでも操れる ～細胞, 分子, 原子, スピンを制御するモノづくりの最前線～, G3-02, [タワーホール船堀・東京] (2016/11). **C**

25) T. Yamaki, Quantum beam technology, "Metallic nanostructures prepared by ion beam irradiation for electrochemical devices"【**Invited talk**】, 12th Workshop Reactive Metal Process., [Cambridge, USA] (2017). **C, I, S, 1-09**

26) T. Yamaki, "Quantum beam technology for creating new polymeric membranes toward a hydrogen society"【**Invited talk**】, Proc. Int. Conf. Innovat. Polym. Sci. Tech., 2016 (IPST 2016), KS4-04, [Medan, Indonesia] (2016/11). **C, E, G, 1-09**

27) T. Yamaki, "Recent emerging technology for materials development with different radiations"【**Invited talk**】, Semin. BATAN-Jakarta, [Jakarta, Indonesia] (2016). **C, E, G, 1-09**

28) 八巻 徹也, ヌリヤンティ ヌヌン, 吉村 公男, 喜多村 茜, 越川 博, 澤田 真一, 寺井 隆幸, "高エネルギー重イオンビームによるナノ構造制御アニオン交換膜の開発 ー膜特性と燃料電池性能ー", 膜シンポジウム 2016, 要旨集 207, [関西大・吹田] (2016/12). **C, 1-09**

29) 小川 達彦, 八巻 徹也, 佐藤 達彦, "凝縮相における低エネルギー電子の微視的放射線作用の研究 ～NE102 シンチレータの発光・消光の再現～", 2017 年第 64 回応用物理学会春季学術講演会, 要旨集 14p-E204-8, [パシフィコ横浜・横浜] (2017/03). **N, 1-08**

30) 山本 春也, 垣谷 健太, 佐藤 裕真, 越川 博, 田口 富嗣, 八巻 徹也, "放射線還元法によるセリア膜上の Pt 微粒子形成", 電気化学会第 84 回大会, 要旨集 1D23, [首都大東京・八王子] (2017/03). **S, E, 1-22**

31) 越川 博, 佐藤 裕真, 山本 春也, 杉本 雅樹, 澤田 真一, 八巻 徹也, 臼井 博明, "イオン穿孔膜を用いた酸化チタンナノコーンの作製", 2017 年第 64 回応用物理学会春季学術講演会, 要旨集 14a-313-7, [パシフィコ横浜・横浜] (2017/03). **C, 1-06**

32) 越川 博, 佐藤 裕真, 山本 春也, 杉本 雅樹, 澤田 真一, 八巻 徹也, "イオンビームを用いた酸化チタンナノコーンの作製", 電気化学会第 84 回大会, 要旨集 1F28, [首都大東京・八王子] (2017/03). **C, 1-06**

33) 後藤 光暁, 大森 理之, 八巻 徹也, 澤田 真一, 越川 博, 喜多村 茜, 比嘉 充, "重イオンビームによるナノ構造制御陽イオン交換膜の開発", 化学工学会中国四国支部大会, C8, [山口大・宇部] (2016/12). **C**

34) K. Kakitani, T. Kimata, T. Yamaki, S. Yamamoto, W. Mao, T. Terai, I. Shimoyama, D. Matsumura, T. Taguchi, A. Iwase and T. Kobayashi, "The interface between Pt nanoparticles and the Ar^+ irradiated glassy carbon substrate", 26th Annu. Meet. Mater. Res. Soc. Jpn. (MRS-J), D3-O20-004, [Yokohama, Japan] (2016/12). **S, I, 1-10**

35) 垣谷 健太, 木全 哲也, 八巻 徹也, 山本 春也, 田口 富嗣, 下山 巖, 松村 大樹, 岩瀬 彰宏, 小林 知洋, 毛 偉, 寺井 隆幸, "イオンビームによる炭素担体の格子欠陥を利用した Pt ナノ微粒子触媒の作製:密度汎関数理論に基づく電子構造解析", 電気化学会第 84 回大会, 要旨集 1D25, [首都大東京・八王子] (2017/03). **S, I, 1-10**

36) 大森 理之, 後藤 光暁, 八巻 徹也, 越川 博, 澤田 真一, 安川 政宏, 比嘉 充, "イオン照射グラフト重合法により作製したモザイク荷電膜を用いた圧透析による脱塩特性", 化学工学会中国四国支部大会, C9, [山口大・宇部] (2016/12). **C**

37) 大森 理之, 八巻 徹也, 越川 博, 澤田 真一, 安川 政宏, 比嘉 充, "イオン照射グラフト重合法により作製したモザイク荷電膜の圧透析による脱塩特性評価", 日本海水学会若手会第 8 回学生研究発表会, G-6(O), [海峡メッセ下関・下関] (2017/03). **C**

38) 佐藤 裕真, 越川 博, 山本 春也, 杉本 雅樹, 澤田 真一, 八巻 徹也, "イオン穿孔膜を鋳型とした白金ナノコーンの作製と触媒性能評価", 日本化学会 第 97 春季年会, 2E1-29, [慶応大・横浜] (2017/03). **C, 1-07**

39) 鹿沼 裕貴, 毒島 梨那, 出崎 亮, 杉本 雅樹, 山本 春也, 越川 博, 八巻 徹也, "NH_3 中電子線照射を利用した窒素添加炭素系触媒の作製 ～窒素添加量の制御～", 電気化学会第 84 回大会, 要旨集 3D22, [首都大東京・八王子] (2017/03). **E, 1-20**

40) T. Yamaki, N. Nuryanthi, K. Yoshimura, S. Sawada, A. Kitamura, H. Koshikawa and T. Terai, "Fuel cell performance of anion exchange membranes prepared by ion-track grafting", 26th Annu. Meet. Mater. Res. Soc. Jpn. (MRS-J), D3-P21-015, [Yokohama, Japan] (2016/12). **C, 1-09**

41) N. Nuryanthi, T. Yamaki, K. Yoshimura, S. Sawada, A. Kitamura, H. Koshikawa and T. Terai, "Anion exchange membranes prepared by the ion-track grafting polymerization for fuel cell applications", Proc. Int. Conf. Innovat. Polym. Sci. Tech. 2016 (IPST 2016), PP4-06, [Medan, Indonesia] (2016/11). **C**

42) 山本 春也, 杉本 雅樹, 越川 博, 箱田 照幸, 八巻 徹也, "放射線還元法による酸化セリウム薄膜上の白金ナノ粒子形成", 第 16 回放射線プロセスシンポジウム, P2-14, 要旨集 71, [東京大・東京] (2016/11). **S, E, 1-22**

43) S. Yamamoto, M. Sugimoto, H. Koshikawa, T. Taguchi, T. Hakoda and T. Yamaki, "Effect of thermal annealing on the

structural properties of CeO_2 films investigated by RBS/channeling", 26th Annu. Meet. Mater. Res. Soc. Jpn. (MRS-J), D3-P21-013, [Yokohama, Japan] (2016/12). **S, 1-22**

44) 山本 春也, 杉本 雅樹, 越川 博, 田口 富嗣, 箱田 照幸, 八巻 徹也, 森 利之, "マグネトロンスパッタリング法により作製した酸化セリウム薄膜の表面形態", 第 26 回日本 MRS 年次大会, B3-P19-007, [横浜市開港記念会館・横浜] (2016/12). **S, 1-22**

45) 田口 富嗣, 山本 春也, 大場 弘則, "電子線照射法による Pt 微粒子担持 SiC ナノチューブの創製とキャラクタリゼーション", 第 26 回日本 MRS 年次大会, B3-P19-015, [横浜市開港記念会館・横浜] (2016/12). **E, 1-24**

46) T. Taguchi, S. Yamamoto and H. Ohba, "Synthesis of heterostructured SiC nanotubes and newstructured multi-walled carbon nanotubes by ion irradiation-induced changes", 26th Annu. Meet. Mater. Res. Soc. Jpn. (MRS-J), D3-P21-014, [Yokohama, Japan] (2016/12). **I, S, 1-24**

47) チャウハン シプラ, 森 利之, 伊坂 紀子, 山本 春也, 小林 知洋, "プロトンビーム照射技術を用いた高いORR活性をもつ超低白金担持 CeOx ナノワイヤー/C 電極触媒の設計", 第 26 回日本 MRS 年次大会, B3-P19-003, [横浜市開港記念会館・横浜] (2016/12). **S, 1-24**

48) チャウハン シプラ, 森 利之, 鈴木 彰, 山本 春也, レドニク アンドリー, 大久保 弘, "ヅルゲル法による中温域動作 SOFC 用イットリア安定化ジルコニアファイバーの合成", 第 26 回日本 MRS 年次大会, B3-P19-004, [横浜市開港記念会館・横浜] (2016/12). **N**

49) 森 利之, レドニク アンドリー, 伊藤 滋啓, 鈴木 彰, 大久保 弘, 山本 春也, 山本 悠太, 石田 高史, 伊坂 紀子, 丹司 敬義, "高性能中温動作 SOFC 作成に資する微細構造観察結果を基にした極微小量白金とアノード間界面の設計", 第 26 回日本 MRS 年次大会, B3-P19-005, [横浜市開港記念会館・横浜] (2016/12). **N**

50) レドニク アンドリー, 森 利之, チャウハン シプラ, 鈴木 彰, 山本 春也, 伊藤 滋啓, 伊坂 紀子, 山本 悠太, 石田 高史, 丹司 敬義, "PtO_x 薄膜スパッタによる酸化物型燃料電池デバイス内高性能アノード層の設計", 第 26 回日本 MRS 年次大会, B3-P19-006, [横浜市開港記念会館・横浜] (2016/12). **S**

51) 出崎 亮, 毒島 梨那, 鹿沼 裕貴, 山本 春也, 杉本 雅樹, 有谷博文, 八巻 徹也, "窒素添加カーボン系触媒の作製における量子ビーム利用の可能性", 第16回放射線プロセスシンポジウム, 要旨集 P2-2, [東京大・東京] (2016/11). **I, 1-21**

52) 越川 博, 佐藤 裕真, 山本 春也, 杉本 雅樹, 澤田 真一, 八巻 徹也, "イオン穿孔膜を用いた白金ナノコーンの作製", 第 16 回放射線プロセスシンポジウム, P2-8, 要旨集 65, [東京大・東京] (2016/11). **C, 1-06**

53) 越川 博, 佐藤 裕真, 山本 春也, 杉本 雅樹, 澤田 真一, 八巻 徹也, "イオンビーム照射による高分子多孔膜への導電層形成:電気メッキ用テンプレートとしての活用", 平成 28 年度日本化学会関東支部群馬地区研究交流発表会, P-81, [量研高崎・高崎] (2016/12). **C, S, I, 1-06**

54) H. Koshikawa, Y. Sato, S. Yamamoto, M. Sugimoto, S. Sawada and T. Yamaki, "Morphology of platinum nanocone arrays prepared using ion-track membranes", 26th Annu. Meet. Mater. Res. Soc. Jpn. (MRS-J), D3-P21-016, [Yokohama, Japan] (2016/12). **C, 1-06**

55) 雨宮 邦招, 越川 博, 八巻 徹也, 井邊 真俊, 蔀 洋司, 座間 達也, "イオンビームマイクロ加工に基づく完全黒色平板の開発", 2016 年度産業技術総合研究所計量標準総合センター成果発表会, 38, [産総研・つくば] (2017/01). **C, 1-14**

56) 後藤 光暁, 大森 理之, 八巻 徹也, 澤田 真一, 越川 博, 喜多村 茜, 比嘉 充, "イオン照射グラフト重合法により作製した陽イオン交換膜のイオン輸送特性評価", 膜シンポジウム 2016, P-56S, [関西大・吹田] (2016/12). **C**

57) K. Kakitani, T. Kimata, T. Yamaki, S. Yamamoto, W. Mao, T. Terai, T. Kobayashi, "Activity enhancement of platinum nanoparticle catalysts by ion-beam induced lattice defects: density functional theory calculation clarifies localized quantum structures", 日本原子力学会関東・甲越支部第15回若手研究者発表討論会, A-06, [東京工業大・東京] (2016/11). **S, I, 1-10**

58) 垣谷 健太, 木全 哲也, 毛 偉, 寺井 隆幸, 八巻 徹也, 山本 春也, 田口 富嗣, 下山 巖, 松村 大樹, 岩瀬 彰宏, 小林 知洋, "イオンビーム照射した炭素担体と白金ナノ微粒子触媒の界面状態分析", 第 16 回放射線プロセスシンポジウム, P3-1, 要旨集 73, [東京大・東京] (2016/11). **S, I, 1-10**

59) 垣谷 健太, 木全 哲也, 八巻 徹也, 山本 春也, 毛 偉, 寺井 隆幸, 下山 巖, 田口 富嗣, 岩瀬 彰宏, 松村 大樹, 小林 知洋, "イオンビームによる燃料電池用白金触媒の高活性化～X線吸収端近傍構造と密度汎関数理論計算による高活性化メカニズムの解明～", 平成 28 年度日本化学会関東支部群馬地区研究交流発表会, P-27, [量研高崎・高崎] (2016/12). **S, I, 1-10**

60) 木全 哲也, 垣谷 健太, 山本 春也, 田口 富嗣, 松村大樹, 下山 巖, 岩瀬 彰宏, 小林 知洋, 八巻 徹也, 寺井 隆幸, "Ar イオン照射グラッシーカーボンを担体とした Pt ナノ微粒子の XAFS 解析", 2017 年第 64 回応用物理学会春季学術講演会, 要旨集 15p-P11-4, [パシフィコ横浜・横浜] (2017/03). **S, I**

61) 大森 理之, 後藤 光暁, 八巻 徹也, 越川 博, 澤田 真一, 安川 政宏, 比嘉 充, "イオン照射グラフト重合法によるモザイク荷電膜の作成及び圧透析評価", 膜シンポジウム 2016, P-59S, [関西大・吹田] (2016/12). **C**

62) 佐藤 裕真, 越川 博, 山本 春也, 杉本 雅樹, 澤田 真一, 八巻 徹也, "イオン穿孔膜を鋳型とした白金ナノコーンの作製:形状制御を目指した試み", 平成 28 年度日本化学会関東支部群馬地区研究交流発表会, P-28, [量研高崎・高崎] (2016/12). **C, 1-07**

63) 佐藤 裕真, 越川 博, 山本 春也, 杉本 雅樹, 澤田 真一, 八巻 徹也, "イオン穿孔膜を鋳型とした白金ナノコーン構造の形成", 電気化学会第 84 回大会, 要旨集 PS88, [首都大東京・八王子] (2017/03). **C, 1-07**

64) 毒島 梨那, 鹿沼 裕貴, 出崎 亮, 山本 春也, 杉本 雅樹, 越川 博, 八巻 徹也, 有谷 博文, "電子線照射を利用した窒素ドープ炭素触媒の開発", 平成 28 年度日本化学会関東支部群馬地区研究交流発表会, P-35, [量研高崎・高崎] (2016/12). **E, 1-20**

65) 木村 壮宏, 池田 歩, 野村 幹弘, 西嶋 陽之, 今林 慎一郎, 澤田 真一, 八巻 徹也, 田中 伸幸, 久保 真治, "水素製造 IS プロセス中酸化還元反応用イオン交換膜の開発", 化学工学会第 82 年会, PD307, [芝浦工大・東京] (2017/03). **E, G, 1-13**

66) M. Nomura, T. Kodaira, K. Oura, A. Ikeda, Y. Naka, H. Nishijima, S. Imabayashi, S. Sawada, T. Yamaki, N. Tanaka, S. Kubo, "Development of ion exchange membranes for the redox reaction of the thermochemical hydrogen production IS process" Proc. 5th Asian Conf. Innovative Energy & Environ. Chem. Eng. (5th ASCON-IEEChE), S2-1, [Yokohama, Japan] (2016/11). **E, G**

67) 木村 壮宏, 小平 岳秀, 池田 歩, 名嘉 泰史, 西嶋 陽之, 今林 慎一郎, 野村 幹弘, 澤田 真一, 八巻 徹也, 田中 伸幸, 久保 真治, "熱化学水素製造 IS プロセス中ブンゼン反応用イオン交換膜の開発", 分離技術会 年会 2016, S7-P8, [日本大・習志野] (2016/05). **E, G, 1-13**

68) 木村 壮宏, 池田 歩, 野村 幹弘, 西嶋 陽之, 今林 慎一郎,

澤田 真一, 八巻 徹也, 田中 伸幸, 久保 真治, “放射線グラフト膜による熱化学水素製造ISプロセスの改善”, 第36回水素エネルギー協会大会, P05, [タワーホール船堀・東京] (2016/11). **E, G, 1-13**

Patents

1) K. Yoshimura, H. Koshikawa, T. Yamaki, M. Asano, Y. Maekawa, H. Shishitani, H. Tanaka, S. Yamaguchi, K. Asazawa, K. Yamamoto and F. Sanpei, “Anion conducting electrolyte membrane and manufacturing method thereof”, U.S. Patent No. 9379402, (2016.6.28). **E, G**
2) 吉村 公男, 越川 博, 八巻 徹也, 浅野 雅春, 前川 康成, “アニオン伝導電解質膜およびその製造方法”, 登録 5959046 (2016.07.01). **E, G**
3) 百合 庸介, 石堀 郁夫, 湯山 貴裕, 石坂 知久, 奥村 進, 前川 康成, 越川 博, 八巻 徹也, 浅野 雅春, “多孔性高分子フィルムの製造方法および多孔性高分子フィルム”, 登録 6044895 (2016.11.25). **C**

Press・TV

1) 芝浦工業大学・量研機構・科学技術振興機構, “高効率な水素製造を可能にするイオン交換膜型ブンゼン反応器を開発 ～高温熱を利用し CO_2 フリー水素を製造する膜分離 IS プロセス実用化の第一歩～”, 2017.03.02, プレス発表: 日本経済新聞 Web 版, YOMIURI ONLINE, 化学工業日報, 徳島新聞 Web 版, SankeiBiz, 財経新聞 Web 版に掲載. **E, G**
2) “航空機に日本の新素材 米 GE 採用 軽量で燃費改善”, 2017.01.11, メディア掲載: 日本経済新聞に掲載. **E**
3) “新製品フラッシュ 配管内の水素ガス検知”, 2017.01.19, メディア掲載: 日刊工業新聞に掲載.

Positron Nano-Science Research Project（P1-3）

Papers

1) M. Maekawa, H. Abe, A. Miyashita, S. Sakai, S. Yamamoto and A. Kawasuso, “Vacancy-induced ferromagnetism in ZnO probed by spin-polarized positron annihilation spectroscopy”, Appl. Phys. Lett., **110**, 172402-1~5 (2017). **C, 3-04**
2) D. D. Wang, B. Zhao, N. Qi, Z. Q. Chen and A. Kawasuso, “Vacancy-mediated ferromagnetism in Co-implanted ZnO studied using a slow positron beam”, J. Mater. Sci, **52**, 7067-76 (2017). **C**
3) H. Li, M. Maekawa, A. Miyashita, A. Kawasuso, “Spin-Polarized Positron Annihilation Study on Some Ferromagnets”, Defect and Diffusion Forum, **373**, 65-70 (2017). **C**
4) M. Maekawa, K. Wada, A. Miyashita and A. Kawasuso, “Construction of a surface positronium lifetime spectroscopy apparatus with a spin-polarized low energy positron beam”, J. Phys. Conf. Ser. **791**, 021009 (2017). **C, 3-04**

Proceedings

1) A. Kawasuso, “Spin-polarized positron annihilation on ferromagnets, vacancies and surfaces”【**Invited talk**】, 14th Int. Workshop Slow Positron Beam Tech. & Appl., [Matsue, Japan] (2016/05). **C**
2) M. Maekawa, K. Wada, H. Abe, A. Miyashita, A. Kawasuso, “Construction of a spin-polarized positronium time-of-flight apparatus”, 14th Int. Workshop Slow Positron Beam Tech. & Appl., [Matsue, Japan] (2016/05). **C, 3-04**
3) A. Kawasuso, “Application of spin-polarized positron spectroscopy to current-induced surface spin-polarization”【**Invited talk**】, Spin Orbit Coupling and Topology in Low Dimensions 2016, [Spetses, Greece] (2016/06-07). **C**
4) 阿部 浩之, 前川 雅樹, 境 誠司, 宮下 敦巳, 河裾 厚男, “スピン偏極陽電子ビームを用いたイオン照射酸化亜鉛による空孔誘起強磁性効果”, 第 53 回アイソトープ・放射線研究発表会, 要旨集 2p-Ⅱ-12, [東京大・東京] (2016/07). **C, 1-26**
5) 前川 雅樹, 和田 健, 阿部 浩之, 宮下 敦巳, 河裾 厚男, “スピン偏極陽電子ビームによるポジトロニウム放出エネルギー測定装置の開発”, 第 53 回アイソトープ・放射線研究発表会, 要旨集 2p-Ⅱ-13, [東京大・東京] (201 6/07). **C, 3-04**
6) 前川 雅樹, 和田 健, 阿部 浩之, 宮下 敦巳, 河裾 厚男, “スピン偏極陽電子ビームによる表面ポジトロニウム寿命測定”, 日本物理学会 2016 年秋季大会, [金沢大・金沢] (2016/09). **C, 3-04**
7) 前川 雅樹, 圓谷 志郎, 境 誠司, 河裾 厚男, “窒素イオン照射 GaN 膜の空孔誘起磁性評価”, 平成 28 年度京都大学原子炉実験所専門研究会「陽電子科学とその理工学への応用」, [京都大・熊取] (2016/12). **C, 3-04**
8) 和田 健, 前川 雅樹, 望月 出海, 河裾 厚男, 木村 正雄, 兵頭 俊夫, “KEK 低速陽電子実験施設パルスストレッチングセクションの建設と動作試験 II”, 平成 28 年度京都大学原子炉実験所専門研究会「陽電子科学とその理工学への応用」, [京都大・熊取] (2016/12). **N**
9) 兵頭 俊夫, 和田 健, 望月 出海, 木村 正雄, 一宮 彪彦, 峠 陽一, 設楽 哲夫, 深谷 有喜, 前川 雅樹, 河裾 厚男, 飯田 進平, 満汐 孝治, 長嶋 泰之, “KEK 物構研低速陽電子実験施設の最近の成果”, 平成 28 年度京都大学原子炉実験所専門研究会「陽電子科学とその理工学への応用」, [京都大・熊取] (2016/12). **N**
10) 和田 健, 白澤 徹郎, 望月 出海, 藤浪 真紀, 前川 雅樹, 河裾 厚男, 兵頭 俊夫, “加速器ベース低速陽電子ビームを用いた低速陽電子回折(LEPD)実験装置の開発状況”, KEK 物構研 PF 低速陽電子実験施設 陽電子回折研究会, [KEK・つくば] (2017/01). **N**
11) 兵頭 俊夫, 望月 出海, 和田 健, “KEK 物質構造科学研究所低速陽電子実験施設の低速陽電子ビームと陽電子回折ステーション”, KEK 物構研 PF 低速陽電子実験施設 陽電子回折研究会, [KEK・つくば] (2017/01). **N**
12) 三木 一司, 一宮 彪彦, 望月 出海, 和田 健, 深谷 有喜, 兵頭 俊夫, “Si(001)表面上の Mn 鎖状一次元構造の TRHEPD の測定”, KEK 物構研 PF 低速陽電子実験施設 陽電子回折研究会, [KEK・つくば] (2017/01). **N**
13) 兵頭 俊夫, 和田 健, 望月 出海, 一宮 彪彦, 小菅 隆, 採用 裕樹, 濁川 和幸, 峠 暢一, 大沢 哲, 池田 光男, 白川 明広, 古川 和郎, 本間 博幸, 設楽 哲夫, 岩瀬 広, 深谷 有喜, 前川 雅樹, 河裾 厚男, 長嶋 泰之, 満汐 幸治, 藤浪 真紀, 白澤 徹朗, 高橋 敏男, “低速陽電子実験施設報告”, 2016 年度量子ビームサイエンスフェスタ, [つくば国際会議場・つくば] (2017/03). **N**
14) 兵頭 俊夫, 和田 健, 白澤 徹朗, 望月 出海, 藤浪 真紀, 前川 雅樹, 河裾 厚男, “低速陽電子回折法による表面構造解析”, 2016 年度量子ビームサイエンスフェスタ, [つくば国際会議場・つくば] (2017/03). **N**

Semiconductor Analysis and Radiation Effects Research Project（P1-4）

Papers

1) K. Fox, P. A. Tran, D. W. M. Lau, T. Ohshima, A. D. Greentree, B. C. Gibson, "Nanodiamond- polycaprolactone composite: A new material for tissue engineering with sub-dermal imaging capabilities", Mater. Lett., **185**, 185-88 (2016). **E**

2) A. Takeyama, T. Matsuda, T. Yokoseki, S. Mitomo, K. Murata, T. Makino, S. Onoda, S. Okubo, Y. Tanaka, M. Kandori, T. Yoshie, Y. Hijikata, T. Ohshima, "Improvement of radiation response of SiC MOSFETs under high temperature and humidity circumstance", Jpn. J. Appl. Phys., **55**, 104101-1~4 (2016). **G, 1-28**

3) S.-i. Sato, K. J. Schmieder, S. M. Hubbard, D. V. Forbes, J. H. Warner, T. Ohshima, R. J. Walters, "Defect characterization of proton irradiated GaAs pn-junction diodes with layers of InAs quantum dots", J. Appl. Phys., **119,** 185702-1~8 (2016). **N**

4) N. Skukan, V. Grilj, I. Sudić, M. Pomorski, W. Kada, T. Makino, Y. Kambayashi, Y. Andoh, S. Onoda, S. Sato, T. Ohshima, T. Kamiya, M. Jakšić, "Charge multiplication effect in thin diamond films", Appl. Phys. Lett., **109**, 043502-1~5 (2016). **N**

5) T. Miyazaki, T. Makino, A. Takeyama, S. Onoda, T. Ohshima, Y. Tanaka, M. Kandori, T. Yoshie, Y. Hijikata, "Effect of gamma-ray irradiation on the device process-induced defects in 4H-SiC epilayers", Superlattices and Microstructures, **99**, 197-201 (2016). **G**

6) A. Angerer, T. Astner, D. Wirtitsch, H. Sumiya, S. Onoda, J. Isoya, S. Putz, J. Majer, "Collective strong coupling with homogeneous Rabi frequencies using a 3D lumped element microwave resonator", Appl. Phys. Lett., **109**, 089901 (2016). **E, 1-05**

7) C. Grezes, Y. Kubo, B. Julsgaard, T. Umeda, J. Isoya, H. Sumiya, H. Abe, S. Onoda, T. Ohshima, K. Nakamura, I. Diniz, A. Auffeves, V. Jacques, J. Roch, D. Vion, D. Esteve, K. Moelmer, P. Bertet, "Towards a spin-ensemble quantum memory for superconducting qubits", Comptes Rendus Physique, **17**, 693-704 (2016). **E, 1-05**

8) M. Niethammer, M. Widmann, S.-Y. Lee, P. Stenberg, O. Kordina, T. Ohshima, N. T. Son, E. Janzén, J. Wrachtrup, "Vector Magnetometry Using Silicon Vacancies in 4H-SiC Under Ambient Conditions", Phys. Rev. Appl., **6**, 034001-1~8 (2016). **E**

9) J. Jeske, D. Lau, X. Vidal, L. McGuinness, P. Reineck, B. Johnson, M. Doherty, J. McCallum, S. Onoda, F. Jelezko, T. Ohshima, T. Volz, J. Cole, B. Gibson, A. Greentree, "Stimulated emission from nitrogen-vacancy centers in diamond", Nat. Comm. **8**, 14000-1~8 (2017). **E**

10) M. Imaizumi, T. Nakamura, T. Takamoto, T. Ohshima, M. Tajima, "Radiation degradation characteristics of component subcells in inverted metamorphic triple-junction solar cells irradiated with electrons and protons", Progr. Photovoltaics: Res. & Appl. **25**, 161-74 (2017). **C, T, I, E, 1-03**

11) S. Castelletto, A. F. M. Almutairi, G. Thalassinos, A. Lohrmann, R. Buividas, D. W. M. Lau, P. Reineck, S. Juodkazis, T. Ohshima, B. C. Gibson, B. C. Johnson, "Fluorescent color centers in laser ablated 4H-SiC nanoparticles", Optics Lett., **42**, 1297-300 (2017). **E**

12) K. Murata, S. Mitomo, T. Matsuda, T. Yokoseki, T. Makino, S. Onoda, A. Takeyama, T. Ohshima, S. Okubo, Y. Tanaka, M. Kandori, T. Yoshie, Y. Hijikata, "Impacts of gate bias and its variation on gamma-ray irradiation resistance of SiC MOSFETs", Phys. Status Solidi A, **214**, 1600446-1~7 (2017). **G**

13) S. Mitomo, T. Matsuda, K. Murata, T. Yokoseki, T. Makino, A. Takeyama, S. Onoda, T. Ohshima, S. Okubo, Y. Tanaka, M. Kandori, T. Yoshie, Y. Hijikata, "Optimum structures for gamma-ray radiation resistant SiC-MOSFETs", Phys. Status Solidi A, **214**, 1600425-1~7 (2017). **G**

14) H. Kraus, D. Simin, C. Kasper, Y. Suda, S. Kawabata, W. Kada, T. Honda, Y. Hijikata, T. Ohshima, V. Dyakonov and G. V. Astakhov, "Three-Dimensional Proton Beam Writing of Optically Active Coherent Vacancy Spins in Silicon Carbide", Nano Letters, **17**, 2865-70 (2017). **S**

15) D. Simin, H. Kraus, A. Sperlich, T. Ohshima, G. V. Astakhov and V. Dyakonov, "Locking of electron spin coherence above 20 ms in natural silicon carbide", Phys. Rev. B, **95**, 161201(R)-1~5 (2017). **E**

16) M. Radulaski, M. Widmann, M. Niethammer, J. L. Zhang, S.-Y. Lee, T. Rendler, K. G. Lagoudakis, N. T. Son, E. Janzén, T. Ohshima, J. Wrachtrup and J. Vučković, "Scalable Quantum Photonics with Single Color Centers in Silicon Carbide", Nano Letters, **17**, 1782-86 (2017). **E**

17) T. Ohshima, T. Honda, S. Onoda, T. Makino, M. Haruyama, T. Kamiya, T. Satoh, Y. Hijikata, W. Kada, O. Hanaizumi, A. Lohrmann, J. R. Klein, B. C. Johnson, J. C. McCallum, S. Castelletto, B. C. Gibson, H. Kraus, V. Dyakonov, G. V. Astakhov, "Creation and Functionalization of Defects in SiC by Proton Beam Writing", Mater. Sci. Forum, **897**, 233-37 (2017). **S**

18) S-I. Kuroki, T. Kurose, H. Nagatsuma, S. Ishikawa, T. Maeda, H. Sezaki, T. Kikkawa, T. Makino, T. Ohshima, M. Östling and C.-M. Zetterling, "4H-SiC Pseudo-CMOS Logic Inverters for Harsh Environment Electronics", Mater. Sci. Forum, **897**, 669-72 (2017). **G**

19) D. M. Tex, T. Nakamura, M. Imaizumi, T. Ohshima, Y. Kanemitsu, "Direct evaluation of influence of electron damage on the subcell performance in triple-junction solar cells using photoluminescence decays", Sci. Rep. **7**, 1985-1~8 (2017). **E, 1-03**

20) P. Reineck, M. Capelli, D. W. M. Lau, J. Jeske, M. R. Field, T. Ohshima, A. D. Greentree and B. C. Gibson, "Bright and photostable nitrogen-vacancy fluorescence from unprocessed detonation nanodiamond", Nanoscale, **9**, 497-502 (2017). **E**

21) M. S. J. Barson, P. Peddibhotla, P. Ovartchaiyapong, K. Ganesa R. L. Taylor, M. Gebert, Z. Mielens, B. Koslowski, D. A. Simpson, L. P. McGuinness, J. McCallum, S. Prawer, S. Onoda, T. Ohshima, A. C. B. Jayich, F. Jelezko, N. B. Manson, and M. W. Doherty, "Nanomechanical Sensing Using Spins in Diamond", Nano Letters, **17**, 1496-503 (2017). **E**

22) S.-I Sato, T. Makino, T. Ohshima, T. Kamiya, W. Kada, O. Hanaizumi, V. Grilj, N. Skukan, M. Pomorski, G. Vizkelethy, "Transient current induced in thin film diamonds by swift heavy ions", Diam. Relat. Mater., **75**, 161-68 (2017). **G**

23) F. Dong, S. Maganty, S. J. Meschter, S. Nozaki, T. Ohshima, T. Makino, J. Cho, "Electron beam irradiation effect on the mechanical properties of nanosilica-filled polyurethane films", Polymer Degrad. Stabil., **141**, 45-53 (2017). **E**

24) S. Onoda, K. Tatsumi, M. Haruyama, T. Teraji, J. Isoya, W. Kada, T. Ohshima, O. Hanaizumi, "Diffusion of vacancies created by high energy heavy ion strike into diamond", Physica Status Solidi, A, **214**, 1700160-1~6 (2017). **C, 1-04**

25) J. Choi, S. Choi, G. Kucsko, P. C. Maurer, B. J. Shields, H. Sumiya, S. Onoda, J. Isoya, E. Demler, F. Jelezko, N. Y. Yao, and M. D. Lukin, "Depolarization dynamics in a strongly

interacting solid-state spin ensemble", Phys. Rev. Lett., **118**, 093601 (2017). **E, 1-05**

26) S. Choi, J. Choi, R. Landig, G. Kucsko, H. Zhou, J. Isoya, F. Jelezko, S. Onoda, H. Sumiya, V. Khemani, C. V. Keyserlingk, N. Y. Yao, E. Demler and M. D. Lukin, "Observation of discrete time-crystalline order in a disordered dipolar many-body system", Nature, **543**, 221-25 (2017). **E, 1-05**

Proceedings

1) S. Kawakita, M. Imaizumi, K. Makita, J. Nishinaga, T. Sugaya, H. Shibata, S.-i. Sato and T. Ohshima, "High efficiency and radiation resistant InGaP/GaAs//CIGS stacked solar cells for space applications", Proc. 43th IEEE Photovoltaic Specialists Conf. (PVSC43), [Portland, USA] (2016/06). IEEE, DOI: 10.1109/PVSC.2016.7750113. **C, T, I, E, 1-03**

2) M. Imaizumi, T. Takamoto, and T. Ohshima, "Analysis on degradation characteristics of component subcells in IMM triple-junction solar cells", Proc. 43th IEEE Photovoltaic Specialists Conf. (PVSC43), [Portland, USA], 3396-400 (2016/06). IEEE, DOI: 10.1109/PVSC.2016.7750297. **C, T, I, E, 1-03**

3) M. Imaizumi, T. Takamoto, N. Kaneko, Y. Nozaki and T. Ohshima, "Qualification Test Results of IMM Triple-Junction Solar Cells, Space Solar Sheets, and Lightweight & Compact Solar Paddle" Proc. 11th Euro. Space Power Conf., CD Paper #G024, ESA, [Thessaloniki, Greece] (2016/10). **C, T, I, E, 1-03**

4) K. Tatsumi, M. Haruyama, S. Onoda, T. Teraji, J. Isoya, W. Kada, T. Ohshima, O. Hanaizumi, "Dependence of Annealing Conditions on Creation Efficiency of NV Center in Single C-crystalline Diamond", Proc. 12th Int. Workshop Ionizing Radiat. Monit. (IWIRM), [Oarai, Japan] (2016/12). **C**

5) K. Takeuchi, M. Tada, T. Sakamoto, H. Shindo, S. Kuboyama, A. Takeyama, T. Ohshima and K. Suzuki, "Research of semiconductor technology for the normally-off computing", Proc. 29th Microelectron. Workshop (MEWS29), [Tsukuba, Japan] (2016/10). **C, 1-02**

6) K. Takeuchi, M. Tada, T. Sakamoto, H. Shindo, S. Kuboyama, A. Takeyama, T. Ohshima and K. Suzuki, "SEE Sensitivity Evaluation Results of Atom Switch ROM/FPGA", Proc. 31st Int. Symp. Space Tech. Sci., ISTS, [Matsuyama, Japan] (2017/06). **C, 1-02**

7) 阿部 浩之, 前川 雅樹, 境 誠司, 宮下 敦巳, 河裾 厚男, "スピン偏極陽電子ビームを用いたイオン照射酸化亜鉛による空孔誘起強磁性効果", 第 53 回アイソトープ・放射線研究発表会, [東京大・東京] (2016/07). **C, 1-26**

Press・TV

1) 筑波大学, 量研機構, "世界最高濃度の室温量子スピンを有するダイヤモンド結晶の作製により、理論的に存在が予測されていた「時間結晶」の室温観測に成功", (2016.03.08), プレス発表: 日経新聞電子版に掲載. **E, 1-05**

2) 日本電気株式会社, [国研]産業技術総合研究所, "NEC と産総研、宇宙環境での利用に向け、優れた放射線耐性の「NanoBridge(R)」技術を搭載した LSI を開発～高放射線耐性と超低消費電力を両立～", 2017.03.07, プレスリリース, NEC の HP に掲載. http://jpn.nec.com/press/201703 /20170307_03.html. **C**

Biocompatible Materials Research Project（P1-5）

Papers

1) T. G. Oyama, A. Oshima and S. Tagawa, "Estimation of resist sensitivity for extreme ultraviolet lithography using an electron beam", AIP Advances **6**, 085210 (2016). **E**

2) S. Yamashita, J. Ma, J.-L. Marignier, A. Hiroki, M. Taguchi, M. Mostafavi and Y. Katsumura, "Radiation-induced Chemical Reactions in Hydrogel of Hydroxypropyl Cellulose (HPC): A Pulse Radiolysis Study", Radiat. Res., **186**, 650-58 (2016). **E**

3) Y. Yamahara, N. Nagasawa, M. Taguchi, A. Oshima, M. Washio, "Fabrication of thermo-responsive PNIPAAm-g-ETFE for medical devices by pre-irradiation grafting", Radiat. Phys. Chem., **142**, 88-93 (2018). **E, 1-50**

4) N. Nagasawa, T. Tago, H. Kudo and M. Taguchi, "Radiation-induced crosslinking of polyamide11 in presence of triallylisocyanurate", Polym. Degrad. Stab., **136**, 98-102 (2017). **E, 1-50**

5) N. Nagasawa, A. Kimura, A. Idesaki, N. Yamada, T. Satoh, Y. Ishii, M. Taguchi, "Microfabrication of biocompatible hydrogels by proton beam writing", Nucl. Instrum. Meth. Phys. Res. B, **409**, 102-06 (2017). **S, 1-50**

6) A. Idesaki, T. Nakamoto, M. Yoshida, A. Shimada, M. Iio, K. Sasaki, M. Sugano, Y. Makida, T. Ogitsu, "Development of high radiation-resistant glass fiber reinforced plastics with cyanate-based resin for superconducting magnet systems", Fusion Eng. Design, **112**, 418-24 (2016). **G, 1-21**

7) 山下 真一, 村上 健太, 田口 光正, "イオンビーム放射線化学", RADIOISOTOPES, **66**(10), 497-505 (2017). **N**

Proceedings

1) A. Idesaki, M. Sugimoto, S. Yamamoto, M. Taguchi and T. Yamaki, "Fabrication of nitrogen-doped carbon material from precursor polymer by ion implantation technique", Proc. 6th Int. Congr. Ceramics (ICC6), L-02, [Dresden, Germany] (2016/08). **I, 1-21**

2) 出崎 亮, 杉本 雅樹, 山本 春也, 田口 光正, 八巻 徹也, "イオン注入法を利用した前駆体高分子からの窒素含有カーボン材料の合成", 日本セラミックス協会 第 29 回秋季シンポジウム, 1K07, [広島大・東広島] (2016/09). **I, 1-21**

3) 出崎 亮, 毒島 梨那, 鹿沼 裕貴, 山本 春也, 杉本 雅樹, 有谷博文, 八巻 徹也, "窒素添加カーボン系触媒の作製における量子ビーム利用の可能性", 第16回放射線プロセスシンポジウム, P2-2, 要旨集 59, [東京大・東京] (2016/11). **I, 1-21**

4) 大山 智子, 木村 敦, 田口 光正, 大山 廣太郎, "量子ビーム技術を駆使した機能性バイオデバイスの開発", 第 16 回放射線プロセスシンポジウム, P2-3, 要旨集 60, [東京大・東京] (2016/11). **G**

5) 長澤 尚胤, 木村 敦, 出崎 亮, 山田 尚人, 江夏 昌志, 佐藤 隆博, 石井 保行, 田口 光正, "プロトンビームライティング法によるゲルの微細加工体の創製", 第 16 回放射線プロセスシンポジウム, P2-10, 要旨集 67, [東京大・東京] (2016/11). **S, 1-50**

6) 大山 智子, 大山 廣太郎, 木村 敦, 田口 光正, "放射線架橋ゼラチンハイドロゲルの開発と機能性足場材料への応用", 第 59 回放射線化学討論会, 要旨集, 1O04, [量研高崎・高崎] (2016/09). **E, G**

7) 山原 有未, 日名田 暢, 長澤 尚胤, 田口 光正, 大島 明博, 鷲尾 方一, "医療デバイス応用に向けた温度応答性膜の放射線滅菌適性評価", 第 59 回放射線化学討論会, 要旨集, 1O05, [量研高崎・高崎] (2016/09). **E, G**

8) 砂川 武義, 青木 祐太郎, 梅田 昌幸, G. Harvel, 速水 醇一, 榊原 和久, 五東 弘昭, 蛯名 武雄, 田口 光正, 長澤 尚胤, 吉橋 幸子, 畑下 昌範, 久米 恭, 佐倉 俊治, "PVA-KI 系に

おけるゲルインジケータの開発", 第 59 回放射線化学討論会, 要旨集, 1O07, [量研高崎・高崎] (2016/09). **E, G**

9) 廣木 章博, 小曽根 雄介, 山下 真一, 木村 敦, 長澤 尚胤, 田口 光正, 村上 健, "電子線架橋ヒドロキシプロピルセルロースゲルを用いて作製したポリマーゲル線量計材料の高感度化", 第 59 回放射線化学討論会, 要旨集 1O08, [量研高崎・高崎] (2016/09). **E, G**

10) 小山 雄大, 高岡 登仁人, 田口 光正, 廣木 章博, 黒岩 広樹, "放射線治療におけるポリマーゲル線量計の実用化に向けた開発", 第 59 回放射線化学討論会, 要旨集 1O09, [量研高崎・高崎] (2016/09). **E, G**

11) L. D. Barr, A. Idesaki, M. Taguchi, T. Yamaguchi, "Radiolytic degradation of high density polyethylene used for storage of water treatment waste from Fukushima Daiichi NPS", 第 59 回放射線化学討論会, 要旨集 2O01, [量研高崎・高崎] (2016/09). **G**

12) 中川 清子, 長澤 尚胤, 田口 光正, "電子線照射による CYPMPO-HO2 生成条件の検討", 第 59 回放射線化学討論会, 要旨集 P-1, [量研高崎・高崎] (2016/09). **E**

13) 竹内 夕桐子, 中村 俊介, 杉本 雅樹, 長澤 尚胤, 島田 明彦, 箱田 照幸, 田口 光正, "高温・高線量放射線照射システムの構築と耐熱耐放射線性エラストマーの開発", 第 59 回放射線化学討論会, 要旨集 P-13, [量研高崎・高崎] (2016/09). **G**

14) 池谷 建了, 河井 貴彦, 黒田 真一, 長澤 尚胤, "量子ビームを利用した架橋化ポリ乳酸の構造形成に関する研究", 第 59 回放射線化学討論会, 要旨集 P-21, [量研高崎・高崎] (2016/09). **E, G**

15) 山下 真一, 藤枝 美菜, 木村 敦, 田口 光正, 村上 健, 勝村 庸介, "重粒子線による水分解における水素のプライマリ収量", 第 59 回放射線化学討論会, 要旨集 P-23, [量研高崎・高崎] (2016/09). **N**

16) 田中 恒夫, 高橋 駿平, 菅原 思織, 杉本 匠, 長澤 尚胤, 田口 光正, "放射線架橋 HPC ゲルの刺激応答性", 第 59 回放射線化学討論会, P-25, [量研高崎・高崎] (2016/09). **G**

17) 長澤 尚胤, 木村 敦, 出崎 亮, 山田 尚人, 江夏 昌志, 島田 明彦, 佐藤 隆博, 石井 保行, 田口 光正, "プロトンビームライティング法による高分子ヒドロゲルの微細加工", 第 59 回放射線化学討論会, P-30, [量研高崎・高崎] (2016/09). **S, 1-50**

18) 木村 敦, 島田 明彦, 長澤 尚胤, 田口 光正, "放射線架橋反応を利用したイオン液体中天然多糖類ゲルの作製", 第 59 回放射線化学討論会, P-39, [量研高崎・高崎] (2016/09). **C**

19) 廣木 章博, 小曽根 雄介, 山下 真一, 木村 敦, 長澤 尚胤, 田口 光正, "放射線架橋ゲルを母材とするポリマーゲル線量計材料の高感度化", 第 5 回 3Dゲル線量計研究会, 要旨集, [京大宇治キャンパスおうばくぷらざ・宇治] (2016/12). **E, G**

Books

1) 田口 光正, "架橋反応について", 第 3 章, EB 技術を利用した材料創製と応用展開, シーエムシー出版, 24-33 (2016). **E**

2) 大山 智子, "量子ビームナノインプリント」による高分子の改質と微細加工", 第 19 章, EB 技術を利用した材料創製と応用展開, シーエムシー出版, 189-98 (2016). **E**

3) 長澤 尚胤, "電子線照射による生分解性・生体適合性ヒドロゲルの創製とその応用", 第 20 章, EB 技術を利用した材料創製と応用展開, シーエムシー出版, 199-212 (2016). **E, 1-50**

Patent

1) 田口 光正, 廣木 章博, 長澤 尚胤, 吉井 文男, 森 謙二, 光宗 倫彦, "擬似心筋およびその製造方法、焼灼性能評価用検体、ならびに焼灼性能の評価装置", 特願 2016-0077531 (2016.04.07). **E, G**

Environmental Polymer Research Project（P1-6）

Papers

1) T. Shibata, N. Seko, H. Amada, N. Kasai, S. Saiki, H. Hoshina and Y. Ueki, "Evaluation of a cesium adsorbent grafted with ammonium 12-molybdophosphate", Radiat. Phys. Chem., **119**, 247-52 (2016). **E, G**

2) P. A. Kavaklı, C. Kavaklı, N. Seko, M. Tamada and O. Güven, "Radiation induced emulsion graft polymerization of 4-vinylpyridine onto PE/PP nonwoven fabric for As(V) adsorption", Radiat. Phys. Chem., **127**, 13-20 (2016). **E**

3) J. F. Madrid, L. V. Abad, T. Yamanobe and N. Seko, "Effects of chain transfer agent on the electron beam-induced graft polymerization of glycidyl methacrylate in emulsion phase", Colloid Polym. Sci., **295**, 1007-16 (2017). **E**

4) J. F. Madrid, Y. Ueki, L. V. Abad, T. Yamanobe and N. Seko, "RAFT-mediated graft polymerization of glycidyl methacrylate in emulsion from polyethylene/polypropylene initiated with γ-radiation", J. Appl. Polymer. Sci., DOI:10.1002/app. 45270 (2017) **G, 1-51**

Proceedings

1) N. Seko, H. Hoshina, N. Kasai, Y. Ueki, S. Saiki, K. Tanaka and M. Takahashi, "Development of Scandium Recovery Adsorbent by Radiation Grafting Technique from Acidic Solution", Proc. Rare Earths 2016, 1P-14, [Sapporo, Japan] (2016/06). **E, G, 1-52**

2) S. Saiki and N. Seko, "Synthesis of Aminocarboxylic Acid Type Adsorbents for Rare Earth Recovery by Radiation-induced Grafting Technique", Proc. Rare Earths 2016, 1P-15, [Sapporo, Japan] (2016/06). **E**

3) H. Hoshina, Y. Ueki, S. Saiki and N. Seko, "Evaluation of Fibrous Grafted Adsorbent for Dysprosium Separation", Proc. Rare Earths 2016, 1P-16, [Sapporo, Japan] (2016/06). **E, 1-52**

4) Y. Ueki, H. Hoshina, N. Kasai, S. Saiki, K. Tanaka, M. Takahashi and N. Seko, "Recovery of Scandium from Hot Spring Water using Fibrous Grafted adsorbent with Phosphoric Groups", Proc. Rare Earths 2016, 1P-30, [Sapporo, Japan] (2016/06). **E, G, 1-51**

5) 陳 進華, 林 菜月, 瀬古 典明, "RAFT 重合による ETFE 膜への単分散性放射線グラフト鎖の構築", 第 65 回高分子討論会, 要旨集 2Pb002, [神奈川大・横浜] (2016/09). **G, 1-55**

6) 陳 進華, 笠井 昇, 林 菜月, 瀬古 典明, "ガンマ線照射によるクロロメチルスチレンの RAFT 重合の検討", 第 59 回放射線化学討論会, 要旨集 P-34, [量研高崎・高崎] (2016/09). **G, 1-55**

7) 佐伯 誠一, 瀬古 典明, "放射線グラフト重合反応におけるテトラヒドロキシメチルホスホニウムクロリドの添加効果", 第 59 回放射線化学討論会, 要旨集 P-40, [量研高崎・高崎] (2016/09). **E**

8) 大道 正明, 高橋 憲司, 杉本 雅樹, 櫻井 庸明, 関 修平, "高分子架橋反応を利用したイオントラックの可視化", 第 59 回放射線化学討論会, 3O13, [量研高崎・高崎] (2016/09). **C, 3-21**

9) 林 菜月, 保科 宏行, 陳 進華, 瀬古 典明, "3 価、6 価クロムを除去可能な繊維状電子線グラフト吸着材の作製", 平成 28 年度繊維学会秋季研究発表会, 要旨集 2C04, [山形大・米沢] (2016/09). **E, 1-54**

10) S. Saiki, K. Okaya, N. Seko and H. Kudo, "A study on radical decays and radiation-induced grafting of irradiated polyethylene

nonwoven fabric at various storage conditions", Proc. IRap 2016, [Hyères, France] (2016/09). **E**

11) S. Saiki and N. Seko, "Radiation-induced grafting method with an addition of organophosphorous compounds", Proc. IRap 2016, [Hyères, France] (2016/09). **E**

12) N. Hayashi, Y. Ueki and N. Seko, "Development of Radiation-Grafted Fibrous Adsorbents for Trivalent and Hexavalent Chromium Removal", Proc. RadTech Asia 2016, P-08, [Tokyo, Japan] (2016/10). **E, 1-54**

13) Y. Ueki, S. Saiki, H. Hoshina and N. Seko, "Synthesis of Fibrous Grafted Polymer as Heterogeneous Acidic Catalyst for Biodiesel Fuel Production from Free Fatty Acids", Proc. RadTech Asia 2016, P-12, [Tokyo, Japan] (2016/10). **E, 1-51**

14) S. Saiki, N. Kasai, N. Seko, T. Oida, K. Yamagishi, M. Matsuhisa and T. Kawashima, "Vanadium Recovery from Seawater by Radiation Grafted Adsorbents Based on Polyethylene Terephthalate Fiber", Proc. RadTech Asia 2016, P-22, [Tokyo, Japan] (2016/10). **E**

15) H. Hoshina, N. Kasai, T. Shibata, Y. Ueki, S. Saiki, N. Hayashi and N. Seko, "New approach for mass production procedure of fibrous adsorbent using continuous pre-irradiation grafting system", Proc. IMRP 2016, #2.2, [Vancouver, Canada] (2016/11). **E, 1-52**

16) Y. Ueki, S. Saiki, H. Hoshina and N. Seko, "Biodiesel fuel production from waste cooking oil using radiation-grafted fibrous catalysts", Proc. IMRP 2016, #2.5, [Vancouver, Canada] (2016/11). **E, 1-51**

17) N. Seko, T. Shibata, S. Saiki, Y. Ueki, H. Hoshina and N. Kasai, "Removal of radioactive cesium from contaminated natural water by radiation-grafted fibrous adsorbent", Proc. IMRP 2016, #10.3, [Vancouver, Canada] (2016/11). **E**

Books

1) 中野 正憲, 見上 隆志, 柴田 卓弥, 笠井 昇, 瀬古 典明, "放射線グラフト重合によるセシウム捕集材の開発", EB 技術を利用した材料創製と応用展開, シーエムシー出版, 109-19 (2016). **E**

2) 瀬古 典明, 植木 悠二, "電子線エマルショングラフト重合及びこれを利用したバイオディーゼル燃料転換用触媒の開発", 第 15 章, EB 技術を利用した材料創製と応用展開, シーエムシー出版, 150-60 (2016). **E, 1-51**

3) 瀬古 典明, "シリーズ. 海のすべて 第 3 回 期待高まる海洋資源 ー石油, ガス, 鉱物資源が大量に海に眠っているー", 「海水中の資源」, 月刊科学雑誌 Newton, 株式会社ニュートンプレス, 37(1), 80-81 (2017).

4) 瀬古 典明, "6 期待高まる海洋資源 ー海水中の資源ー", Newton 別冊 "海のすべて", 株式会社ニュートンプレス, 154-55 (2017).

Patents

1) 馬 紅娟, 保科 宏行, 瀬古 典明, "金属吸着材とその製造方法及び金属吸着材を用いた金属捕集方法", 特許第 5979712 号 (2016.08.05).

2) 瀬古 典明, 保科 宏行, "金属吸着材とその製造方法及び金属吸着材を用いた金属捕集方法", 登録 5979713 (2016.08.05). **E**

3) 瀬古 典明, 植木 悠二, "重合性モノマーがグラフト重合されたグラフト重合高分子繊維の製造方法, 機能性材料, 並びに金属捕集材", 登録 6025164 (2016.10.21). **E**

4) 瀬古 典明, 笠井 昇, 植木 悠二, 佐伯 誠一, 保科 宏行, "セシウム除去用フィルターカートリッジの製造方法", 登録 6089179 (2017.02.17). **E, G**

Press・TV

1) "電力を問う「改革の行方」4 -六ケ所、核燃サイクル 再処理工場、膨れる建設費-", (2017.04.23), 朝日新聞に掲載. **E, G**

Element Separation and Analysis Research Project（P1-7）

Papers

1) Y. Kurosaki, K. Yokoyama, "Quantum optimal control of the isotope-selective rovibrational excitation of diatomic molecules", Chem. Phys., **493**, 183-93 (2017). **N**

2) A. Ruas, A. Matsumoto, H. Ohba, K. Akaoka, I. Wakaida, "Application of laser-induced breakdown spectroscopy to zirconium in aqueous solution", Spectrochim. Acta B, **131**, 99-106 (2017). **N**

3) T. Taguchi, R. Tsubakiyama, K. Miyajima, S. Yamamoto, H. Ohba, "Effect of surface treatment on photoluminescence of silicon carbide nanotubes", Appl. Surf. Sci., **403**, 308-13 (2017). **I, 1-24**

4) K. Tamura, S. Toyama, "Laser cutting performances for thick steel specimens studied by molten metal removal conditions", J. Nucl. Sci. Tech. **54**, 1011-17 (2017). **N**

5) K. Tamura, R. Yamagishi, "Observation of the molten metal behaviors during the laser cutting of thick steel specimens using attenuated process images", J. Nucl. Sci. Tech., **54**, 655-61 (2017). **N**

6) S. Asai, T. Yomogida, M. Saeki, H. Ohba, Y. Hanzawa, T. Horita, A. Kitatsuji, "Determination of ^{107}Pd in Pd Recovered by Laser-Induced Photoreduction for Inductively Coupled Plasma Mass Spectrometry", Anal. Chem., **88**, 12227-33 (2016). **N**

7) N. Nakashima, K. Yamanaka, M. Saeki, H. Ohba, S. Taniguchi, T. Yatsuhashi, "Metal ion reductions by femtosecond laser pulses with micro-Joule energy and their efficiencies", J. Photochem. Photobiol. A, **319**, 70-77 (2016). **N**

8) Y. Kurosaki, T. S. Ho, H. Rabitz, "The role of dissociation channels of excited electronic states in quantum optimal control of ozone isomerization: a three-state dynamical model", Chem. Phys., **469-470**, 115-22 (2016). **N**

9) K. Tamura, and R. Yamagishi, "Laser cutting conditions for steel plates having a thickness of more than 100 mm using a 30 kW fiber laser for nuclear decommissioning", Mech. Eng. J., **3**, 15-00590 (2016). **N**

10) K. Tamura, R. Ishigami and R. Yamagishi, "Laser cutting of thick steel plates and simulated steel components with a 30 kW fiber laser", J. Nucl. Sci. Tech., **53**, 916-20 (2016). **N**

11) E. Minehara, S. Toyama, K. Tamura and H. Nakamura, "Radioisotope decontamination and cutting of structural objects using laser for the decommissioning of nuclear power plants", Kinzoku, **86**, 590-95 (2016) (Review) (in Japanese). **N**

Proceedings

1) 田口 富嗣, 山本 春也, 大場 弘則, "SiC ナノチューブ内の新奇構造を有する多層カーボンナノチューブの創製", 第 51 回 フラーレン・ナノチューブ・グラフェン総合シンポジウム, 1P-16, [道民活動センター・札幌] (2016/09). **T, I, 1-24**

2) T. Taguchi, S. Yamamoto and H. Ohba, "Synthesis of heterostructured SiC nanotubes and newstructured multi-walled carbon nanotubes by ion irradiation-induced changes", 26th Annu.

Meet. Mater. Res. Soc. Jpn. (MRS-J), D3-P21-014, [Yokohama, Japan] (2016/12). **S, I, 1-24**

3) 田口 富嗣, 山本 春也, 大場 弘則, "電子線照射法による Pt 微粒子担持 SiC ナノチューブの創製とキャラクタリゼーション", 第 26 回日本 MRS 年次大会, B3-P19-015, [横浜市開港記念会館・横浜] (2016/12). **E, 1-24**

4) 山本 春也, 垣谷 健太, 佐藤 裕真, 越川 博, 田口 富嗣, 八巻 徹也, "放射線還元法によるセリア膜上の Pt 微粒子形成", 電気化学会第 84 回大会, 要旨集 1D23, [首都大東京・八王子] (2017/03). **S, E, 1-22**

5) 垣谷 健太, 木全 哲也, 毛 偉, 寺井 隆幸, 八巻 徹也, 山本 春也, 田口 富嗣, 下山 巖, 松村 大樹, 岩瀬 彰宏, 小林 知洋, "イオンビーム照射した炭素担体と白金ナノ微粒子触媒の界面状態分析", 第 16 回放射線プロセスシンポジウム, P3-1, 要旨集 73, [東京大・東京] (2016/11). **S, I, 1-10**

6) 垣谷 健太, 木全 哲也, 八巻 徹也, 山本 春也, 毛 偉, 寺井 隆幸, 下山 巖, 田口 富嗣, 岩瀬 彰宏, 松村 大樹, 小林 知洋, "イオンビームによる燃料電池用白金触媒の高活性化～X線吸収端近傍構造と密度汎関数理論計算による高活性化メカニズムの解明～", 平成 28 年度日本化学会関東支部群馬地区研究交流発表会, P-27, [量研高崎・高崎] (2016/12). **S, I, 1-10**

7) 木全 哲也, 垣谷 健太, 山本 春也, 田口 富嗣, 松村 大樹, 下山 巖, 岩瀬 彰宏, 小林 知洋, 八巻 徹也, 寺井 隆幸, "Ar イオン照射グラッシーカーボンを担体とした Pt ナノ微粒子の XAFS 解析", 2017 年第 64 回応用物理学会春季学術講演会, 要旨集 15p-P11-4, [パシフィコ横浜・横浜] (2017/03). **S, I**

Press・TV

1) 浅井 志保(JAEA), 佐伯 盛久, 大場 弘則, "使用済燃料中パラジウム-107 の存在量を世界で初めて実測 ～試料に近づかずに高純度パラジウムを分離し正確に測定～", 2017.02.03, プレス発表:福井新聞, 福島民友, 福島民報に掲載.

Ion Beam Mutagenesis Research Project（P2-1）

Papers

1) M. Takahashi, K. Umetsu, Y. Oono, T. Higaki, E. B. Blancaflor and A. Rahman, "SMALL ACIDIC PROTEIN 1 (SMAP1) and SCF^{TIR1} ubiquitin proteasome pathway act in concert to induce 2,4-dichlorophenoxyacetic acid-mediated alteration of actin in Arabidopsis roots", Plant J., **89**, 940-56 (2017). **C, 2-10**

2) Y. Hase, A. Nozawa, I. Narumi and Y. Oono, "Effects of ion beam irradiation on size of mutant sector and genetic damage in Arabidopsis" Nucl. Instrum. Meth. Phys. Res. B, **391**, 14-19 (2017). **C, 2-18**

3) 浅見 逸夫, 鈴木 良地, 長谷川 徹, 辻 孝子, 大野 徹, 長谷 純宏, 野澤 樹, "イオンビーム照射による新規花弁型キク突然変異系統の作出", 愛知県農業総合試験場研究報告, **48**, 1-8 (2017). **C**

4) 北村 智, "イオンビーム照射による色素蓄積が異常な植物の作出とその応用" 放射線と産業, **140**, 32-35 (2016). **C**

Proceedings

1) 宮城 敦子, 西丸 拓也, 針谷 のぞみ, 尾﨑 莉沙子, 大野 豊, 長谷 純宏, 長野 稔, 石川 寿樹, 山口 雅利, "イネにおけるシュウ酸蓄積機構の解析", 第 58 回日本植物生理学会年会, 要旨集 2aF05, [鹿児島大・鹿児島] (2017/03). **C**

2) 宮城 敦子, 西丸 拓也, 大野 豊, 長谷 純宏, 川合 真紀, "イオンビーム照射イネ系統におけるメタボローム解析", 第 34 回日本植物細胞分子生物学会大会 , 要旨集 1Ca-02, [信州大・上田] (2016/09). **C**

3) 大野 豊, 長谷 純宏, "戦略的イノベーション創造プログラム(次世代農林水産業創造技術)におけるイオンビーム育種技術の高度化研究", 第 16 回放射線プロセスシンポジウム, P6-2, 要旨集 83, [東京大・東京] (2016/11). **C, 2-10**

4) 大野 豊, 平田 翔也, 鳴海 一成, 北村 智, "イオンビーム変異体解析による植物色素アントシアニンの液胞輸送機構に関与する遺伝子の解明", 第 16 回放射線プロセスシンポジウム, P6-3, 要旨集 84, [東京大・東京] (2016/11). **C, 2-10**

5) M. Takahashi, K. Umetsu, T. Higaki, Y. Oono, E. B. Blancaflor and A. Rahman, "SMALL ACIDIC PROTEIN 1 (SMAP1) and SCF^{TIR1} ubiquitin proteasome pathway act in concert to regulate 2,4-dichlorophenoxyacetic acid-mediated alteration of actin in Arabidopsis root", Abstr. 22nd Int. Plant Growth Substances Assoc. (IPGSA) Conf., Book #133, [Toronto, Canada] (2016). **C, 2-10**

6) 柳澤 昌臣, 浅水 俊平, 菅井 佳宣, 佐藤 勝也, 尾仲 宏康, "複合培養における放線菌の二次代謝活性化に関与する遺伝子のイオンビームを用いた逆遺伝学的解析", 日本農芸化学会 2017 年度大会, [京都女子大・京都] (2017/03). **C, 2-14**

7) 柳澤 昌臣, 浅水 俊平, 菅井 佳宣, 佐藤 勝也, 尾仲 宏康, "重イオンビーム遺伝子変異導入法を用いた複合培養による放線菌の二次代謝活性化に関与する遺伝子の探索", 2016 年度日本放線菌学会大会, [東京大・東京] (2016/09). **C, 2-14**

8) 渡部 貴史, 佐藤 勝也, 林 秀謙, 高橋 仁恵, 増渕 隆, "吟醸用群馬 KAZE 酵母のイオンビーム照射による尿素非生産化の検討", 日本農芸化学会 2017 年度大会, [京都女子大・京都] (2017/03). **C, 2-24**

9) 小松原 芙未, 池永 裕, 佐藤 勝也, 鳴海 一成, 渡部 貴史, 増渕 隆, 林 秀謙, "清酒酵母によるガラクトース代謝能の解析", 日本農芸化学会 2017 年度大会, [京都女子大・京都] (2017/03). **C, 2-24**

10) 面曽 宏太, 佐藤 勝也, 鳴海 一成, "Involvement of mutagenesis promoting gene dnaE2 of *Deinococcus grandis* in repair of UV-induced DNA damage", Proc. Extremophiles 2016 -, 11th Int. Congr. Extremophiles, [Kyoto, Japan] (2016/09). **N, 2-23**

11) 面曽 宏太, 佐藤 勝也, 鳴海 一成, "*Deinococcus grandis* カナマイシン耐性変異株の特徴解析", 変異機構研究会・第 29 回夏の学校, [京都府立ゼミナールハウス・京都] (2016/09). **N, 2-23**

12) 島田 岳, 小林 桃歌, 佐藤 勝也, 鳴海 一成, "放射線抵抗性細菌 *Deinococcus geothermalis* における DNA 修復促進遺伝子 *pprA* の破壊効果", 極限環境生物学会 2016 年度(第 17 回)年会, [東京工業大・横浜] (2016/11). **N, 2-23**

13) 黒澤 飛翔, 佐藤 勝也, 鳴海 一成, "放射線抵抗性細菌 *Deinococcus grandis* の DNA 修復応答制御タンパク質 PprI の機能解析", 極限環境生物学会 2016 年度(第 17 回)年会, [東京工業大・横浜] (2016/11). **N, 2-23**

14) 黒澤 飛翔, 面曽 宏太, 竹島 創, 佐藤 勝也, 鳴海 一成, "In silico identification of radiation/desiccation response regulon in *Deinococcus grandis*", Proc. Extremophiles 2016-, 11th Int. Congr. Extremophiles, [Kyoto, Japan] (2016/09). **N, 2-23**

15) 島田 岳, 小林 桃歌, 佐藤 勝也, 鳴海 一成, "Disruption of DNA repair promoting gene *pprA* in the moderate thermophile *Deinococcus geothermalis* and expression of the gene in the extreme thermophile *Thermus thermophiles*", Proc.

Extremophiles 2016-, 11th Int. Congr. Extremophiles, Int. Soc. Extremophiles, [Kyoto, Japan] (2016/09). **N, 2-23**

16) 佐藤 勝也, "量子ビームを用いた有用微生物資源の創成に関する研究", 第 61 回放射線科学研究会, [住友クラブ・大阪] (2016/10). **N, 2-22**

17) A. Sakamoto, M. Akita, H. Yamaguchi and M. Teranishi, "Deletion of TLS polymerases promotes UV- or IR-induced homologous recombination in Arabidopsis", Proc. Plant Genome Stability and Change 2016, [Hayama, Japan] (2016). **C, G**

18) 長谷 純宏, "粒子線を用いた植物育種研究", 日本放射線影響学会第 59 回大会, 要旨集 W8-5, [JMS アステールプラザ・広島] (2016/10). **C, 2-18, 2-20**

19) 納富 麻子, 松尾 洋一, 長谷 純宏, 竹下 大樹, 岡部 春菜, "放射線育種を利用した機能性成分高含有カンキツの育成（第 2 報）実生胚軸上カルスへ重イオンビーム照射後再分化した個体の生育特性", 第 79 回九州農業研究発表会, 要旨集 16 (2016). **C**

Book

1) Y. Hase, "Creation of flower color mutants using ion beams and a comprehensive analysis of anthocyanin composition and genetic background", K. Yoshida, V. Cheynier and S. Quideau (Eds), Recent Advances in Polyphenol Research, 5, 127-42 (2017). **C, 2-18**

Patent

1) 木村 亮祐, 長谷 純宏, 野澤 樹, "つたばゼラニウム「フリンジェ フィオーレローザ」", 品種登録 25726 (2017.2.24).

Microbeam Radiation Biology Research Project（P2-2）

Papers

1) K. Nagata, C. Hashimoto, T. Watanabe-Asaka, K. Itoh, T. Yasuda, K. Ohta, H. Oonishi, K. Igarashi, M. Suzuki, T. Funayama, Y. Kobayashi, T. Nishimaki, T. Katsumura, H. Oota, M. Ogawa, A. Oga, K. Ikemoto, H. Itoh, N. Kutsuna, S. Oda and H. Mitani. "*In vivo* 3D analysis of systemic effects after local heavy-ion beam irradiation in an animal model", Sci. Rep. **6**, 28691 (2016); doi: 10.1038/srep28691. **C, 2-09**

2) 冨田 雅典, 松本 英樹, 舟山 知夫, "重イオン線によるバイスタンダー応答の特徴", 放射線生物研究, **51**, 324-35 (2016). **C, 2-04**

3) 舟山 知夫, 横田 裕一郎, 鈴木 芳代, "量研機構・高崎の重イオンマイクロビーム", 放射線生物研究, **51**, 336-56 (2016). **C, 2-01**

4) M. Kikuchi, "Detection of radicals induced in raw bovine livers irradiated in frozen condition", Food Irradiation, Japan, **51**, 3-10 (2016) (in Japanese). **G, 2-06**

5) E. Chiba, T. Iizuka, M. Ichikawa, M. Ukai, M. Kikuchi and Y. Kobayashi, "Study on sensory test of irradiated spices", Food Irradiation, Japan, **51**, 23-36 (2016) (in Japanese). **G, 2-06**

Proceedings

1) Z. Soh, M. Suzuki, T. Tsuji, "An estimation method for environmental friction based on body dynamic model of *Caenorhabditis elegans*", Proc. 2017 Int. Conf. Artificial Life & Robotics (ICAROB2017), 511-19, [Prague, Czech Republic] (2017/05). **N, 2-26**

2) 菊地 正博, "牛レバ刺しにおける照射誘導ラジカルの ESR 測定", 第 16 回放射線プロセスシンポジウム, P4-1, 要旨集 77, [東京大・東京] (2016/11). **G, 2-06**

Medical Radioisotope Application Research Project（P2-3）

Papers

1) Y. Ohshima, K. Kaira, A. Yamaguchi, N. Oriuchi, H. Tominaga, S. Nagamori, Y. Kanai, T. Yokobori, T. Miyazaki, T. Asao, Y. Tsushima, H. Kuwano and N. S. Ishioka, "Efficacy of system L amino acid transporter 1 inhibition as a therapeutic target in esophageal squamous cell carcinoma", Cancer Sci., **107**, 1499-505 (2016). **C**

2) K. Yamada, S. Watanabe, Sh. Watanabe, T. Takahashi, T. Moriguchi, H. Oku, N. S. Ishioka and K. Shinozuka, "Synthesis and Properties of Silylated Phenylalanine Derivatives" Peptide Science 2015, 93-94 (2016/3). **C**

Proceedings

1) 石岡 典子, "価値ある RI を創り出す～がん診断用アミノ酸トレーサーの開発～", 第 33 回日本核医学技術学会下咽頭地方会総会, 要旨集 11-12, [量研高崎・高崎] (2016). **C**

2) 花岡 宏史, 山口 藍子, 渡辺 智, 上原 知也, 石岡 典子, 対馬 義人, 荒野 泰, "非標的臓器への放射能集積を低減した ^{76}Br 標識抗体の開発", 第 11 回日本分子イメージング学会総会・学術集会, 要旨集 P-026, [神戸国際会議場・神戸] (2016/05). **C**

3) Y. Ohshima, S. Watanabe, A. Tsuji, K. Nagatsu, T. Sakashita, A. Sugiyama, Y. Harada, A. Waki, K. Yoshinaga and N. S. Ishioka, "Therapeutic efficacy of α-emitter meta-^{211}At-astato-benzylguanidine (MABG) in a pheochromocytoma model", SNMMI 2016 Annu. Meet., [San Diego, USA] (2016/06), J. Nucl. Med., **57**, 468 (2016). **C**

4) K. Tsukada, S. Watanabe, N. S. Ishioka, Y. Hatsukawa, K. Hashimoto, Y. Sugo, N. Sato, T. Kin, M. Kawabata, H. Saeki, Y. Nagai, "Medical use radioisotope production with accelerator neutrons by deuterons", Abstr. 9th Int. Conf. Nucl. Radiochem., (NRC9), [Helsinki, Finland] (2016/08-09). **C**

5) 佐々木 一郎, 渡辺 茂樹, 大島 康宏, 須郷 由美, 山田 圭一, 花岡 宏史, 石岡 典子, "^{131}I標識ペプチドの医学的応用－HER2を標的としたF(*p*-^{131}I)KCCYSLの合成と*in vitro*評価－", 第53回アイソトープ・放射線研究発表会, 要旨集 1a-III-07, [東京大・東京] (2016/07). **C**

6) 鈴木 博元, 大島 康宏, 渡辺 茂樹, 佐々木 一郎, 坂下 哲哉, 須郷 由美, 上原 知也, 石岡 典子, 荒野 泰, "抗体フラグメントの非特異的な腎集積を低減する^{211}At標識薬剤の開発", 第56回日本核医学会学術総会, 要旨集 M2ⅦA3, [名古屋国際会議場・名古屋] (2016/11). **C**

7) 永津 弘太郎, 峯岸 克行, 辻 厚至, 石岡 典子, 大島 康宏, 渡辺 茂樹, 脇 厚生, 吉永 恵一郎, 東 達也, 張 明栄, "^{211}At-MABGの遠隔製造に関する検討", 第56回日本核医学会学術総会, 要旨集 M1ⅨF6 [名古屋国際会議場・名古屋] (2016/11). **N**

8) 石岡 典子, "アルファ放射体、アスタチン211のがん治療への応用", 第16回放射線プロセスシンポジウム, S7-4, 要旨集 41-42, [東京大・東京] (2016/11). **C**

9) 渡辺 茂樹, 渡辺 智, 島田 明彦, 石岡 典子, "TIARAにおけるAt-211新規大量製造法の開発", 第16回放射線プロセスシンポジウム, P5-3, 要旨集 81, [東京大・東京] (2016/11). **C**

10) Sh. Watanabe, "Isolation of ^{211}At using "wet chemistry approach"

based on column method", 第3回核医学治療 国際シンポジウム, 要旨集, [東京コンベンションホール・東京] (2017/02). **C**

11) 須郷 由美, 大島 康宏, 山口 藍子, 花岡 宏史, 塚田 和明, 橋本 和幸, 川端 方子, 佐伯秀也, 永井 泰樹, 石岡 典子, "サイクロトロンで製造する放射性銅のがんの診断・治療への応用", 第 59 回放射線化学討論会, 要旨集 P-41, [量研高崎・高崎] (2016/09). **C, 2-40**

Books

1) 石岡 典子, 大島 康宏, "放射性物質とは何か？", シリーズ元素と周期表 第 4 回, Newton 10 月号, ニュートンプレス, 64-65 (2016). **C**

2) 坂下 哲哉, 大島 康宏, 渡辺 茂樹, 石岡 典子, "MABG の生物半減期と Free 成分の検討", 群馬県核医学研究会会誌 **31**(1), 11-13 (2016). **C**

Patent

1) 山口 充孝, 長尾 悠人, 河地 有木, 石岡 典子, "放射線検出方法", 特願2017-16048(2017.1.31). **C**

Press・TV

1) "がん細胞を狙い撃ちするα線放出核種を標識した新しい治療薬剤を開発ーアスタチン**-211** がん治療薬剤による褐色細胞腫の大幅な縮小に成功ー", 2016.06.13, プレス発表:NHK シブ 5 時, ニュースチェック 11(TV 放映), NHK ニュースで英会話(ラジオ放送), 同収録テキスト 2016 年 9 月号, 日経新聞, 千葉日報, 上毛新聞, 共同通信社47NEWS他ネットニュース23件(掲載). **C**

Accelerator-Neutron-Generated Radioisotope Research Project（P2-4）

Papers

1) Y. Sugo, K. Hashimoto, M. Kawabata, H. Saeki, S. Sato, K. Tsukada and Y. Nagai, "Application of ^{67}Cu Produced by ^{68}Zn($n,n'p+d$)^{67}Cu to Biodistribution Study in Tumor-Bearing Mice", J. Phys. Soc. Jpn., **86**, 023201-1~3 (2017). **C, 2-40**

2) S. Q. Yan, Z. H. Li, Y. B. Wang, K. Nishio, H. Makii, J. Su, Y. Li, I. Nishinaka, K. Hirose, Y. L. Ham, R. Orlandi, Y. P. Shen, B. Guo, S. Zeng, G. Lian, Y. S. Chen, X. X. Bai, L. H. Qiao, W. P. Liu, "Examination of the surrogate ratio method for the determination of the ^{93}Zr(n,γ)^{94}Zr cross section with ^{90,92}Zr(^{18}O, ^{16}O)^{92,94}Zr reactions", Phys. Rev. C, 94, 015804-1~4 (2016). **N**

3) R. Leguillon, K. Nishio, K. Hirose, H. Makii, I. Nishinaka, R. Orlandi, K. Tsukada, J. Smallcombe, S. Chiba, Y. Aritomo, T. Ohtsuki, R. Tatsuzawa, N. Takaki, N. Tamura, S. Goto, I. Tsekhanovich, C. M. Patrache and A. N. Andreyev, "Fission fragments mass distributions of nuclei populated by the multinucleon transfer channels of the ^{18}O + ^{232}Th reaction", Phys. Lett. B, **761**, 125-30 (2016). **N**

4) K. Hirose, K. Nishio, H. Makii, I. Nishinaka, S. Ohta, T. Nagayama, N. Tamura, S. Goto, A. N. Andreyev, M. J. Vermeulen, S. Gillespie, C. Barton, A. Kimura, H. Harada, S. Meigo, S. Chiba and T. Ohtsuki, "Simultaneous measurement of neutron-induced fission and capture cross sections for ^{241}Am at neutron energies below fission threshold", Nucl. Instrum. Meth. Phys. Res. A, **856**, 133-38 (2017). **N**

Proceedings

1) Y. Nagai, "^{99}Mo-^{99m}Tc Production: Solution for its Shortage ?", Proc. Annu. Meet. Soc. Nucl. Med. Mol. Imag., [San Diego, USA] (2016). **C**

2) K. Tsukada, S. Watanabe, N. S. Ishioka, Y. Hatsukawa, K. Hashimoto, Y. Sugo, N. Sato, T. Kin, M. Kawabata, H. Saeki and Y. Nagai, "Medical use radioisotope production with accelerator neutrons by deuterons", Proc. 9th Int. Conf. Nucl. Radiochem. (NRC9), [Helsinki, Finland] (2016). **C**

3) M. Kawabata, K. Tsukada, S. Watanabe, N. Ishioka, Y. Hatsukawa, K. Hashimoto, Y. Sugo, N. Sato, T. Kin, M. Kawabata, H. Saeki and Y. Nagai, "^{99}Mo generation by accelerator-driven neutrons and thermo-separation of ^{99m}Tc", Proc. 9th Int. Conf. Nucl. Radiochem. (NRC9), [Helsinki, Finland] (2016). **C**

4) I. Nishinaka, K. Washiyama, E. Maeda, T. Taniguchi, A. Yokoyama and K. Hashimoto, "Production and utilization of astatine and iodine radioisotopes using ^{7}Li ion beams at the JAEA tandem accelerator", Abstr. 16th Int. Workshop Targetry & Target Chem. (WTTC16), P98, [Santa Fe, USA] (2016/08-09). **N**

5) K. Washiyama, E. Maeda, I. Nishinaka, K. Hashimoto, H. Makii and A. Yokoyama, "Measurement of the ^{209}Bi(^{7}Li, 5n)^{211}Rn, ^{209}Bi(^{7}Li,6n)^{210}Rn reaction cross sections towards the development of ^{211}Rn/^{211}At generator", Abstr. 16th Int. Workshop Targetry & Target Chem. (WTTC16), P140, [Santa Fe, USA] (2016/08-09). **N**

6) Y. Hatsukawa, "Production of Technetium Isotopes for Compton Camera Imaging", Proc. 62nd Conf. Radiobioassay & Radiochem. Meas. (RRMC2017), [Honolulu, USA] (2017/02). **N**

7) 橋本 和幸, 川端 方子, 佐伯 秀也, 佐藤 俊一, 塚田 和明, 須郷 由美, 永井 泰樹, 初川 雄一, 渡辺 智, 石岡 典子, "重陽子照射で発生する加速器中性子によって製造するがん治療用 ^{67}Cu の高純度化に関する検討", 2016 放射化学会年会・第 60 回放射化学討論会, 要旨集 P33, [新潟大・新潟] (2016/09). **C**

8) 塚田 和明, 橋本 和幸, 初川 雄一, 川端 方子, 佐伯 秀也, 湊 太志, 岩本 信之, 永井 泰樹, 須郷 由美, 渡辺 智, 石岡 典子, "50 MeV 重陽子照射で発生する高速中性子による医療用放射性核種の合成研究", 2016 放射化学会年会・第 60 回放射化学討論会, 要旨集 1B05, [新潟大・新潟] (2016/09). **C**

9) 川端 方子, 本石 章司, 佐伯 秀也, 竹内 宣博, 橋本 和幸, 初川 雄一, 永井 泰樹, "加速器中性子利用 ^{99}Mo 製造における濃縮 $^{100}MoO_3$ 試料の回収と再利用", 2016 放射化学会年会・第 60 回放射化学討論会, 要旨集 2A04, [新潟大・新潟] (2016/09). **C**

10) 初川 雄一, 塚田 和明, 橋本 和幸, 佐藤 哲也, 浅井 雅人, 豊嶋 厚史, 永井 泰樹, 谷森 達, 園田 伸也, 株木 重人, 木村 寛之, 高田 敦史, 水本 哲也, 早川 岳人, "コンプトンカメライメージング用 Tc-95m 及び Tc-96 の生成研究", 2016 放射化学会年会・第 60 回放射化学討論会, 要旨集 2A03, [新潟大・新潟] (2016/09). **N**

11) 西中 一朗, 鷲山幸信, 前田 英太, 谷口 拓海, 横山 明彦, 橋本 和幸, "原子力機構タンデム加速器での ^{7}Li イオンビームを用いたアスタチンとヨウ素放射性同位体の製造と利用", 2016 放射化学会年会・第 60 回放射化学討論会, 要旨集 2A01, [新潟大・新潟] (2016/09). **N**

12) 山田 記大, 新 裕喜, 大江 崇太, 村上 拳冬, 橋本 和幸, 西中 一朗, 鷲山 幸信, 横山 明彦, "^{211}Rn–^{211}At ジェネレーター開発を目的としたシリンジ密封抽出系の At/Rn 分離係数の研究", 2016 放射化学会年会・第 60 回放射化学討論会, 要旨集 P34, [新潟大・新潟] (2016/09). **N**

13) 秋山 和彦, 宮下 由香, 初川 雄一, 久冨木 志郎, "高速中性子照射による核反跳効果を用いた放射性 Sr@C60 の生成", 2016 放射化学会年会・第 60 回放射化学討論会, 要旨集

2B01, [新潟大・新潟] (2016/09). **N**

14) 西中 一朗, "ハロゲン元素アスタチンの核医学利用のための新規合成法", 第16回放射性医薬品、画像診断薬研究会, B-2 プログラム&要旨集 P10, [京都勧業館・京都] (2016/10). **N**

15) 永井 泰樹, "日本におけるモリブデン/テクネチウムの安定供給の現状ー中型加速器による製造法ー", 第 44 回日本放射線技術学会秋季学術大会 合同シンポジウム, [ソニックシティー・さいたま] (2016/10). **C**

16) 永井 泰樹, "加速器中性子による $^{99}Mo/^{99m}Tc$ 及び治療用 ^{67}Cu の製造研究", 第 56 回日本核医学会学術総会 合同シンポジウム, [名古屋国際会議場・名古屋] (2016/11). **C**

17) 西中 一朗, 橋本 和幸, 牧井 宏之, "α 放射性同位体の核医学利用のための $^{211}Rn/^{211}At$ ジェネレータ開発", 第16回放射線プロセスシンポジウム, P5-1, 要旨集 79, [東京大・東京] (2016/11). **N**

18) 須郷 由美, 大島 康宏, 山口 藍子, 花岡 宏史, 塚田 和明, 橋本 和幸, 川端 方子, 佐伯秀也, 永井 泰樹, 石岡 典子, "サイクロトロンで製造する放射性銅のがんの診断・治療への応用", 第59回放射線化学討論会, 要旨集 P-41, [量研高崎・高崎] (2016/09). **C, 2-40**

Press・TV

1) 量研機構・千代田テクノル(共同研究者), "がん診断と治療の両方に適した放射性銅 67 の大量・高品質製造法の開発に成功ー加速器で作る中性子が新たな診断・治療薬開発に道を拓くー", 2016.12.28 プレス発表: 上毛新聞, 日刊工業新聞, 科学新聞, ネットニュース(時事通信, ニュースイッチ)に掲載. **C, 2-40**

Radiotracer Imaging Research Project (P2-5)

Papers

1) M. Yamaguchi, Y. Nagao, T. Satoh, H. Sugai, M. Sakai, K. Arakawa and N. Kawachi, "Monte Carlo simulation of photon emission below a few hundred kiloelectronvolts for beam monitoring in carbon ion therapy", Rev. Sci. Instrum., **88**, 014301-1~8 (2017). **N, 2-38**

2) M. Yamaguchi, Y. Nagao, N. kawachi, T. Satoh, S. Fujimaki, T. Kamiya, K. Torikai, H. Shimada, H. Sugai, M. Sakai, K. Arakawa and T. Nakano, "Detection of a gas region in a human body across a therapeutic carbon beam by measuring low-energy photons", Int. J. PIXE, **26**, 61-72 (2016). **N, 2-38**

3) M. Yamaguchi, Y. Nagao, K. Ando, S. Yamamoto, T. Toshito, J. Kataoka and N. Kawachi, "Secondary-electron-bremsstrahlung imaging for proton therapy", Nucl. Instrum. Meth. Phys. Res. A, **833**, 199-207 (2016). **N, 2-38**

4) M. Yamaguchi, K. Torikai, N. Kawachi, H. Shimada, T. Satoh, Y. Nagao, S. Fujimaki, M. Kokubun, S. Watanabe, T. Takahashi, K. Arakawa, T. Kamiya and T. Nakano, "Corrigendum: Beam range estimation by measuring bremsstrahlung (2012 Phys. Med. Biol. 57 2843)", Phys. Med. Biol., **61**, 3638-44 (2016). **N, 2-38**

5) L. Fontanili, C. Lancilli, N. Suzui, B. Dendena, Y.-G. Yin, A. Ferri, S. Ishii, N. Kawachi, G. Lucchini, S. Fujimaki, G. A. Sacchi and F. F. Nocito, "Kinetic Analysis of Zinc/Cadmium Reciprocal Competitions Suggests a Possible Zn-Insensitive Pathway for Root-to-Shoot Cadmium Translocation in Rice", Rice, **9**, 1-13 (2016). **C, 2-39**

6) S. Nakamura, N. Suzui, S. Ito-Tanabata, S. Ishii, N. Kawachi, H. Rai, H. Hattori and S. Fujimaki, "Application of glutathione and dithiothreitol to oil seed rape (Brassica napus L.) roots affects cadmium distribution in roots and inhibits Cd translocation to shoots", Soil Sci. Plant Nutr., **62**, 379-85 (2016). **C, 2-37**

7) M. Kihira, K. Taniguchi, C. Kaneko, Y. Ishii, H. Aoki, A. Koyanagi, H. Kusano, N. Suzui, Y.-G. Yin, N. Kawachi, S. Fujimaki and H. Shimada, "Arabidopsis thaliana FLO2 is Involved in Efficiency of Photoassimilate Translocation, Which is Associated with Leaf Growth and Aging, Yield of Seeds and Seed Quality", Plant Cell Physiol., **58**, 440-50 (2017). **C**

8) 山口 充孝, 長尾 悠人, 酒井 真理, 菅井 裕之, "電子制動輻射を用いた粒子線モニタリング手法", 放射線と産業, **140**, 23-27 (2016). **N, 2-38**

Proceedings

1) 酒井 真理, 菅井 裕之, 菊地 美貴子, 鳥飼 幸太, 荒川 和夫, 山口 充孝, 長尾 悠人, 河地 有木, 小高 裕和, 国分 紀秀, 武田 伸一郎, 渡辺 伸, 高橋 忠幸, 取越 正巳, 中野 隆史, "Y-90 Bremsstrahlung Imaging using Compton Camera", 第 111 回日本医学物理学会学術大会, [パシフィコ横浜・横浜] (2016/04). **N**

2) 尹 永根, 鈴井 伸郎, 石井 里美, 栗田 圭輔, 信濃 卓郎, 河地 有木, "異なる培地条件における根の分泌物のポジトロンイメージング技術による可視化", アグリ・バイオ公開シンポジウム, [東京理科大・東京] (2016/07). **C**

3) 石井 里美, 鈴井 伸郎, 尹 永根, 栗田 圭輔, 藤巻 秀, 日髙 功太, 三好 悠太, 河地 有木, "ポジトロンイメージング技術によるイチゴ果実への光合成産物の転流の可視化", アグリ・バイオ公開シンポジウム, [東京理科大・東京] (2016/07). **C**

4) 栗田 圭輔, 鈴井 伸郎, 尹 永根, 石井 里美, 渡部 浩司, 山本 誠一, 河地 有木, "植物チェレンコフイメージング技術によるダイズ体内のセシウム動態撮影", アグリ・バイオ公開シンポジウム, [東京理科大・東京] (2016/07). **C**

5) 鈴井 伸郎, 尹 永根, 石井 里美, 河地 有木, "ラジオアイソトープを用いて複数の元素吸収速度を同時に定量化する", アグリ・バイオ公開シンポジウム, [東京理科大・東京] (2016/07). **C, 2-39**

6) 日高 功太, 三好 悠太, 石井 里美, 鈴井 伸郎, 尹 永根, 栗田 圭輔, 安武 大輔, 北野 雅治, 河地 有木, "「PETIS」ライブイメージング解析を援用したイチゴ果実への同化産物転流に対する果実生育ステージの影響の評価", 日本生物環境工学会2016年金沢大会, [金沢工大・金沢] (2016/09). **C**

7) 三好 悠太, 日高 智美, 日高 功太, 石井 里美, 鈴井 伸郎, 尹 永根, 栗田 圭輔, 安武 大輔, 河地 有木, 北野 雅治, "イチゴシンク果実における光合成産物のアンローディング動態モデルの構築", 日本生物環境工学会 2016 年金沢大会, [金沢工大・金沢] (2016/09). **C**

8) N. Suzui, Y.-G. Yin, S. Ishii and N. Kawachi, "Noninvasive imaging of zinc movement in an intact plant using 65Zn", Proc. 18th Int. Conf. Heavy Metals Environ., [Ghent, Belgium] (2016/09). **C, 2-39**

9) 栗田 圭輔, 山口 充孝, 長尾 悠人, 鈴井 伸郎, 尹 永根, 吉原 利一, 河地 有木, "簡易型個人線量計を用いた樹体内放射能モニタリング手法の開発", 日本土壌肥料学会 2016 年度佐賀大会, [佐賀大・佐賀] (2016/09). **N**

10) 尹 永根, 鈴井 伸郎, 石井 里美, 栗田 圭輔, 信濃 卓郎, 河地 有木, "ダイズ根が根圏土壌へ分泌した有機物の可視化と定量解析(3) 水耕培地への分泌物のリアルタイムイメージング", 日本土壌肥料学会 2016 年度佐賀大会, [佐賀大・佐賀] (2016/09). **C**

11) 石井 里美, 鈴井 伸郎, 尹 永根, 栗田 圭輔, 藤巻 秀, 日髙 功太, 三好 悠太, 河地 有木, “イチゴ果実への光合成産物の転流を可視化するポジトロンイメージング技術の開発”, 日本土壌肥料学会 2016 年度佐賀大会, [佐賀大・佐賀] (2016/09). **C**

12) 鈴井 伸郎, 尹 永根, 石井 里美, 藤巻 秀, 河地 有木, “γ線スペクトロメーターを用いた多元素輸送速度の同時モニタリングシステムの開発”, 日本土壌肥料学会 2016 年度佐賀大会, [佐賀大・佐賀] (2016/09). **C, 2-39**

13) 栗田 圭輔, 鈴井 伸郎, 尹 永根, 石井 里美, 渡部 浩司, 山本 誠一, 河地 有木, “植物チェレンコフイメージング技術で見る植物体内の放射性セシウム動態”, 日本土壌肥料学会 2016年度佐賀大会, [佐賀大・佐賀] (2016/09). **C**

14) M. Yamaguchi, Y. Nagao, T. Satoh, T. Kamiya, M. Sakai, H. Sugai, K. Arakawa and N. Kawachi, “A simulation study on detection of a cavity across a therapeutic carbon beam using secondary electron bremsstrahlung”, 2016 IEEE Nucl. Sci. Symp. (**NSS**) & Med. Imaging Conf. (**MIC**), [Strasbourg, France] (2016/11). **N, 2-38**

15) K. Kurita, N. Suzui, Y.-G. Yin, S. Ishii, K. Watanabe, S. Yamamoto and N. Kawachi, “Development of Cherenkov Light Imaging System for Studies of Radiocesium Dynamics in Plant”, 2016 IEEE Nucl. Sci. Symp. (NSS) & Med. Imaging Conf. (MIC), [Strasbourg, France] (2016/11). **C**

16) 石井 里美, 鈴井 伸郎, 尹 永根, 栗田 圭輔, 藤巻 秀, 日髙 功太, 三好 悠太, 河地 有木, “イチゴ果実への光合成産物の転流を可視化するポジトロンイメージング技術の開発”, 第 16 回放射線プロセスシンポジウム, P6-1, 要旨集 82, [東京大・東京] (2016/11). **C**

17) 栗田 圭輔, 鈴井 伸郎, 尹 永根, 石井 里美, 渡部 浩司, 山本 誠一, 河地 有木, “チェレンコフ光で植物体内の放射性セシウム動態を見る”, 第 16 回放射線プロセスシンポジウム, P6-4, 要旨集 85, [東京大・東京] (2016/11). **C**

18) 鈴井 伸郎, 尹 永根, 石井 里美, 栗田 圭輔, 河地 有木, “市販のラジオアイソトープを用いたナトリウムと亜鉛の非破壊イメージング”, 2016 年度日本土壌肥料学会関東支部大会, [宇都宮大・宇都宮] (2016/12). **N, 2-39**

19) 尹 永根, 鈴井 伸郎, 石井 里美, 栗田 圭輔, 河地 有木, “ダイズ体内におけるセシウムの移行様式の解析”, 2016 年度日本土壌肥料学会関東支部大会, [宇都宮大・宇都宮] (2016/12). **C**

20) 栗田 圭輔, 鈴井 伸郎, 尹 永根, 石井 里美, 渡部 浩司, 山本 誠一, 河地 有木, “チェレンコフ光で見る植物体内の放射性セシウム動態”, 2016 年度日本土壌肥料学会関東支部大会, [宇都宮大・宇都宮] (2016/12). **C**

21) 栗田 圭輔, 山口 充孝, 長尾 悠人, 鈴井 伸郎, 平野 裕之, 福井 久智, 太田 裕士, 秦野 歳久, 河地 有木, “モンテカルロ法による排水全量放射能モニタリング装置の特性評価”, 日本原子力学会「2017年春の年会」, [東海大・平塚] (2017/03). **N**

22) 山口 充孝, 長尾 悠人, “炭素線治療におけるビーム上ガス領域検出手法のシミュレーション”, JAEA-Review 2016-024 (平成 27 年度 大型計算機システム利用による研究成果報告集), 139-40 (2017). **N, 2-38**

Patents

1) 山口 充孝, 長尾 悠人, 河地 有木, 石岡 典子, “放射線検出方法”, 出願 2017-16048 (2017.01.31). **N, 2-38**

2) 中野 隆史, 荒川 和夫, 酒井 真理, 菅井 裕之, 菊地 美貴子, 山口 充孝, 長尾 悠人, 河地 有木, 神谷 富裕, “情報処理装置、イメージング方法、及び、イメージングプログラム”, 出願 2016-172263 (2016.09.02). **N**

Press・TV

1) 量研・名古屋大学・名古屋陽子線治療センター・早稲田大学・群馬大学, “粒子線の“リアルタイム見える化”を実現する新手法～飛跡に沿って発生する制動放射線に着目～”, 2016.03.28, プレス発表: 毎日新聞, 上毛新聞に掲載. **N, 2-38**

Radiation and Biomolecular Science Research Project（P2-6）

Papers

1) 甲斐 健師, 横谷 明徳, 藤井 健太郎, 渡辺 立子, “高エネルギー電子線により水中で生成された 2 次電子の動的挙動”, 陽電子科学, **8**, 11-17 (2017). **N**

2) T. Kai, A. Yokoya, M. Ukai, K. Fujii and R. Watanabe, “Dynamic Behavior of Secondary Electrons in Liquid Water at the Earliest Stage upon Irradiation: Implications for DNA Damage Localization Mechanism”, J. Phys. Chem. A, **120**, 8228-33 (2016). **N**

3) I. Shiraishi, N. Shikazono, K. Fujii and A. Yokoya, “Efficiency of radiation-induced base lesion excision and the order of enzymatic treatment”, Int. J. Radiat. Biol., **93**, 295-302 (2017). **C**

4) A. Yokoya, “The 8th Auger Symposium: Preface”, Int. J. Radiat. Biol., **92**, 614-15 (2016). **N**

5) K. Kaminaga, M. Noguchi, A. Narita, Y. Hattori, N. Usami and A. Yokoya, “Cell cycle tracking for irradiated and unirradiated bystander cells in a single colony with exposure to a soft X-ray microbeam”, Int. J. Radiat. Biol., **92**, 739-44 (2016). **N**

6) A. Narita, K. Fujii, Y. Baba and I. Shimoyama, “Use of a DNA film on a self-assembled monolayer for investigating the physical process of DNA damage induced by core electron ionization”, Int. J. Radiat. Biol., **92**, 733-38 (2016). **N**

7) H. Fukunaga, A. Yokoya and Y. Taki, “Now is the time to consider personalized effective dose”, Int. J. Radiat. Oncol., Biol., Phys., **96**, 479-80 (2016). **N**

8) Y. Izumi, K. Fujii, F. Wien, C. Houée-Lévin, S. Lacombe, D. Salado-Leza, E. Porcel, R. Masoud, S. Yamamoto, M. Réfrégiers, M. -A. Hervé du Penhoat and A. Yokoya, “Structural transition from β-strand and turn to α-helix in histone H2A-H2B induced by DNA damage response”, Biophys. J., **111**, 69-78 (2016). **N**

9) T. Kai, A. Yokoya, M. Ukai, K. Fujii and R. Watanabe, “Deceleration processes of secondary electrons produced by a high-energy Auger electron in a biological circumstance”, Int. J. Radiat. Biol., **92,** 654-59 (2016). **N**

10) 横谷 明徳, 藤井 健太郎, “2-6. 放射線ストレスに対する量子効果に基づくゲノム安定化機構の解明”, KEK 放射光 Conceptual Design Report (CDR), **Ver. 1**, 85-88 (2016). **N**

11) 甲斐 健師, 横谷 明徳, 藤井 健太郎, 渡邊 立子, “放射線物理化学過程に関する最近の進展（中編）”, 放射線化学, **102**, 49-56 (2016). **N**

12) M. Tomita, M. Maeda, N. Usami, A. Yokoya, R. Watanabe and K. Kobayashi, “Enhancement of DNA double-strand break induction and cell killing by K-shell absorption of phosphorus in human cell lines”, Int. J. Radiat. Biol., **92,** 724-32 (2016). **N**

13) 島田 紘行, 横谷 明徳, 鵜飼 正敏, “水溶液環境下における生体分子放射線損傷の分光研究”, 日本物理学会誌, **71**, 736-45 (2016). **N**

14) H. Fukunaga and A. Yokoya, “Low-dose radiation risk and individual variations in radiation sensitivity in Fukushima”,

J. Radiat. Res., **57**, 98-100 (2016). **N**

15) 泉 雄大, 山本 悟史, 藤井 健太郎, 横谷 明徳, “放射線DNA損傷の修復応答を開始させる染色体タンパク質ヒストンの構造変化”, Isotope News, **746**, 2-5(2016). **N**

16) Y. Sakamoto, K. Kaminaga, Y. Kanari, N. Usami, M. Noguchi and A. Yokoya, “Live-cell imaging study of radiation effect on cell cycles of three-dimensional cultured cells exposed to synchrotron soft X-ray microbeam”, 乳癌基礎研究, **24**, 21-27 (2015). **N**

Proceedings

1) 藤井 健太郎, “X線分光を用いた放射線生物研究と今後の展望”, PF研究会「PF挿入光源ビームラインBL-19の戦略的利用に関する研究会」, 要旨集 P3, [KEK・つくば] (2017/01). **N**

2) S. Yamamoto, Y. Izumi, K. Nishikubo, K. Matsuo, K. Fujii and A. Yokoya, “Study of structural alteration of chromosomal proteins induced by post-translational modification after ionizing irradiation”, 21st Hiroshima Int. Symp. Synchrotron Radiat., Abstr. Book P30S, [Higashi-Hiroshima, Japan] (2017). **N**

3) 横谷 明徳, 神長 輝一, 濱田 涼, 宇佐美 徳子, 鈴木 啓司, “X線マイクロビーム照射後の細胞運命とミトコンドリア活性変化”, 茨城大学公開シンポジウム(第10回Quantum Medicine研究会)ー茨城大学重点研究「がん放射線治療のための基礎生命科学研究」講演会ー「組織や個体の環境から発がん・がん放射線治療を考える」, 要旨集 P2, [茨城大・水戸] (2017/02). **N**

4) 神長 輝一, 宇佐美 徳子, 横谷 明徳, “X線マイクロビームを用いたDNA損傷に開始される細胞細胞周期変調のライブセルイメージング”, 2016年度量子ビームサイエンスフェスタ, 要旨集 P2015T001, [つくば国際会議場・つくば] (2017/03). **N**

5) 藤井 健太郎, “キラリティー科学から低エネルギー回折限界光源への期待”, 第30回日本放射光学会年会・放射光科学合同シンポジウム, 要旨集 企画講演 3-1, [神戸芸術センター・神戸] (2017/01). **N**

6) 泉 雄大, 山本 悟史, 藤井 健太郎, 松尾 光一, 横谷 明徳, “放射光円二色性分光によるDNA損傷誘起ヒストン二次構造変化の観測”, 第30回日本放射光学会年会・放射光科学シンポジウム, 要旨集 8P106, [神戸芸術センター・神戸] (2017/01). **N**

7) 島田 紘行, 武田 泰明, 三浦 亮介, 篠澤 柚衣, 柏田 拓臣, 村井 龍司, 鵜飼 正敏, 横谷 明徳, 藤井 健太郎, 福田 義博, 斎藤 祐児, A. Knie, C. Ozga, A. Ehresmann, “水溶液中ピリミジン塩基の軟X線光電子およびオージェ電子スペクトル”, 第30回日本放射光学会年会・放射光科学シンポジウム, 要旨集 5C004, [神戸芸術センター・神戸] (2017/01). **N**

8) 米谷 佳晃, “水和イオン対解離過程の多次元自由エネルギー地形解析”, 第30回分子シミュレーション討論会, 要旨集 P222, [大阪大・豊中] (2016/11-12). **N**

9) 島田 紘行, 武田 泰明, 三浦 亮介, 篠澤 柚衣, 柏田 拓臣, 村井 龍司, 鵜飼 正敏, 横谷 明徳, 藤井 健太郎, 福田 義博, 斎藤 祐児, A. Knie, C. Ozga, A. Ehresmann, “水和ヌクレオチドに対する軟X線電子分光実験”, 原子衝突学会第41回年会, 要旨集 P82, [富山大・富山] (2016/12). **N**

10) K. Fujii, M.-A. Hervé du Penhoat, M.-F. Politis and A. Yokoya, “Spectroscopic Study for Physical Process of DNA Strand Breakage by Ionizing Radiations using Soft X-rays”, Hiroshima Int. Workshop on Circular Dichroism Spectros. 2017, Abstr. Book P9, [Higashi-Hiroshima, Japan] (2017). **N**

11) 米谷 佳晃, 中川 洋, 藤井 健太郎, 横谷 明徳, “DNAの水和構造と放射線損傷サイトの関係”, 第39回溶液化学シンポジウム, 要旨集 P02, [産総研・つくば] (2016/11). **N**

12) 神長 輝一, 宇佐美 徳子, 鈴木 啓司, 横谷 明徳, “X線マイクロビームを用いた細胞質への放射線生物影響研究”, 第39回日本分子生物学会年会, 要旨集 3P-0307, [横浜パシフィコ・横浜] (2016/11-12). **N**

13) K. Fujii, M.-F. Politis, M.-A. Hervé du Penhoat and A. Yokoya, “Roles of Oxygen for Inducing DNA Strand Breakages by Ionizing Radiation”, Oxygenalia 2016, Abstr. Book P54, [Krakow, Poland] (2016/11). **N**

14) 神長 輝一, 宇佐美 徳子, 鈴木 啓司, 横谷 明徳, “X線マイクロビームを使用した細胞質への放射線影響の研究”, 日本放射線影響学会第59回大会, 要旨集 P032, [JMSアステールプラザ・広島] (2016/10). **N**

15) 渡辺 立子, “DNA損傷・飛跡構造解析に関する研究”, 放射線影響学会第59回大会, 要旨集 W5-1, [JMSアステール プラザ・広島] (2016/10). **N**

16) 服部 佑哉, 横谷 明徳, 渡辺 立子, “バイスタンダー効果による DNA 二本鎖切断生成数の数理解析”, 日本放射線影響学会第59回大会, 要旨集 P044, [JMSアステール プラザ・広島] (2016/10). **N**

17) 島田 紘行, 柏田 拓臣, 篠澤 柚衣, 村井 龍司, 小田島 嘉孝, 槇島 熙, 鵜飼 正敏, 横谷 明徳, 藤井 健太郎, 福田 義博, 斎藤 祐児, “内殻励起された水溶液中ヌクレオチドからの発光の観測”, 日本物理学会 2016 年秋季年会, 要旨集 14pKK7, [金沢大・金沢] (2016/09). **N**

18) H. Shimada, A. Yokoya, K. Fujii, M. Ukai, “Selective energy deposition to nucleotides in the primary radiation interaction using a soft X-ray synchrotron radiation”, Proc. 12th Asian Int. Semin. Atom. Mol. Phys., [Changchun, China] (2016). **N**

19) 横谷 明徳, “生体の放射線ストレス応答と生体分子内の電荷輸送”**【招待講演】**, 新学術領域研究「ハイブリッド量子科学」, 量子生物研究会, [東京] (2016). **N**

20) 甲斐 健師, 横谷 明徳, 鵜飼 正敏, 藤井 健太郎, 渡辺 立子, 米谷 佳晃, 樋川 智洋 , 佐藤 達彦, “電子線トラックエンドの放射線最初期過程の研究”, 第59回放射線化学討論会, 要旨集 3O04, [量研高崎・高崎] (2016/09). **N**

21) 泉 雄大, 山本 悟史, 藤井 健太郎, 松尾 光一, 横谷 明徳, “DNA損傷により誘起されるヒストンタンパク質の二次構造変化”, 第59回放射線化学討論会, 要旨集 1O02, [量研高崎・高崎] (2016/09). **N**

22) 横谷 明徳, 神長 輝一, 渡辺 立子, 服部 佑哉, 福永 久典, 鈴木 啓司, 泉 雄大, 藤井 健太郎, “放射線生体影響のメカニズム解明に向けた放射光利用研究”, PF 研究会「福島環境回復を目指した放射光研究の現状と今後の課題」, 要旨集 P14-19, [KEK・つくば] (2016). **N**

23) 渡辺 立子, “低線量放射線影響の初期過程のシミュレーション”**【招待講演】**, 自然科学研究機構核融合科学研究所, 低線量放射線とその影響に関するシンポジウム, [核融合科学研・土岐] (2016). **N**

24) 神長 輝一, 宇佐美 徳子, 鈴木 啓司, 横谷 明徳, “X線マイクロビームとライブセルイメージングを用いた細胞質への放射線影響研究”, 平成29年度若手放射線生物学研究会専門研究会, 要旨集 P18, [東京大・東京] (2016/09). **N**

25) 濱田 涼, 神長 輝一, 横谷 明徳, “照射細胞における ATP 産生及びDNA修復との相関”, 平成28年度若手放射線生物学研究会専門研究会, 要旨集 P19, [東京大・東京] (2016/09). **N**

26) 西久保 開, 山本 悟史, 神長 輝一, 泉 雄大, 横谷 明徳, “DNA損傷タンパク質のリン酸によっておこる立体構造の変化の測定”, 平成 28 年度若手放射線生物学研究会専門研究会, 要旨集 P20, [東京大・東京] (2016/09). **N**

27) 鬼澤 美智, 芳賀 芳範, 横谷 明徳, “放射線増感剤としてのブロモウラシル(BrU)の電子物性の研究”, 平成 28 年度若手放射線生物学研究会専門研究会, 要旨集 P22, [東京大・東

京］(2016/09). **N**

28) 杉本 理峻, 神長 輝一, 服部 佑哉, 渡辺 立子, 立花 章, 横谷 明徳, "低線量X線による放射線適応応答誘導経路のモデル化の試み", 平成 28 年度若手放射線生物学研究会専門研究会, 要旨集 P23, ［東京大・東京］(2016/09). **N**

29) 横谷 明徳, "量子技術と生命科学(話題提供)", (第 5 回)量子科学技術委員会, 配布資料, ［文部科学省・東京］(2016/08). **N**

30) 藤井 健太郎,"シンクロトロン放射光を用いた分光学的手法による DNA 損傷生成の物理過程に関する研究" **【招待講演】**, 平成 28 年東京 RBC 特別放談会, ［産業・情報プラザ・東海］(2016/07). **N**

31) 藤井 健太郎, "シンクロトロン放射光を用いた放射線生物研究" **【招待講演】**, 第 6 回群馬大学 Genome Damage Discussion Group 公開セミナー, ［群馬大・前橋］(2016/07). **N**

32) 横谷 明徳, "生物学・光源・物性研究者による量子生物学合宿勉強会: Workshop on Quantum Biology for scientists in biology, optics and physic", 生物学・光源・物性研究者による量子生物学合宿勉強会, 要旨集 P1, ［量研関西・佐用］(2016/07). **N**

Biomolecular Function Research Project（P2-7）

Papers

1) S. Arai, C, Shibazaki, M. Adachi, E, Honjo, T, Tamada, Y. Maeda, T. Tahara, T. Kato, H. Miyazaki, M. Blaber, R. Kuroki, "An insight into the thermodynamic characteristics of human thrombopoietin complexation with TN1 antibody", Protein Sci. **25**, 1786-96 (2016). **N**

2) M. Shigehisa, N. Amaba, S. Arai, C. Higashi, R. Kawanabe, A. Matsunaga, F. A. Laksmi, M. Tokunaga, M. Ishibashi, "Stabilization of luciferase from Renilla reniformis using random mutations", Protein Eng. Des. Sel. **30**, 7-13 (2017). **N**

Proceedings

1) S. Arai, C. Shibazaki, R. Shimizu, M. Adachi, H. Tokunaga, M. Ishibashi, M. Tokunaga, "X-ray crystallographic analysis of the highly acidic thioredoxin from an extreme halophile Halobacterium sp. NRC-1", Photon Factory Activity Report 2015, #33 (2016). **N**

2) M. Adachi, C. Shibazaki, S. Arai, R. Kuroki, "Structure analysis of drug target protein CK2 by high resolution X-ray and neutron crystallography", Photon Factory Activity Rep. 2015, #33 (2016). **N**

3) M. Adachi, Y. Matsuzawa, R. Kuroki, Y. Saito, K. Maekawa, "Crystal structure analysis of human drug metabolizing enzyme CYP2C9 complexed with medicinal compound Losartan", Photon Factory Activity Rep. 2015, #33 (2016). **N**

4) 柴崎 千枝, 村川 武志, 安達 基泰, 清水 瑠美, 栗原 和男, 日下 勝弘, 岡島 俊英, "中性子結晶構造解析を目指したアポ型銅アミン酸化酵素の大型結晶作製", 第 16 回日本蛋白質学会, Poster 2P-031, ［福岡国際会議場・福岡］(2016/06). **N**

5) 南畑 孝介, 安達 基泰, 清水 瑠美, 黒木 良太, 長棟 輝行, "静電相互作用を駆動力とした迅速なストレプトアビジンの結晶化", 第 68 回日本生物工学会大会, ポスター, ［ANA クラウンホテルプラザ・富山］(2016/09). **N**

6) 塚本 啓介, 南畑 孝介, 安達 基泰, 清水 瑠美, 黒木 良太, 長棟 輝行, "静電相互作用による小分子-タンパク質共結晶の作製", 第 68 回日本生物工学会大会, ポスター, ［ANA クラウンホテルプラザ・富山］(2016/09). **N**

7) M. Shah, K. Maekawa, Y. Matsuzawa, Y. Saito, M. Adachi, R. Kuroki, "Crystal Structures of CYP2C9, CYP2C9*3 and CYP2C9*30 in Complex with Multiple Losartan Molecules Reveal a Peripheral Binding Site and Alternate Active Site Orientations", Proc. 21st Int. Symp. Microsomes and Drug Oxidations, Microsomes and Drug Oxidations, Poster, [Davis, USA] (2016/10). **N**

8) M. Shah, K. Maekawa, Y. Matsuzawa, Y. Saito, M. Adachi, R. Kuroki, "Crystal Structures of CYP2C9, CYP2C9*3 and CYP2C9*30 in Complex with Multiple Losartan Molecules Reveal a Peripheral Binding Site and Alternate Active Site Orientations", Proc. 21st Int. Symp. Microsomes & Drug Oxidations, Microsomes and Drug Oxidations, Oral, [Davis, USA] (2016/10). **N**

9) 新井 栄揮, 柴崎 千枝, 安達 基泰, 玉田 太郎, 前田 宜丈, "中和抗体結合反応におけるヒト・トロンボポエチンの構造学的・熱力学的変化", 日本結晶学会平成 28 年度年会, Poster PC-08, ［県民文化センター・水戸］(2016/11). **N**

Book

1) 新井 栄揮, 安達 基泰, "人工改変タンパク質を利用したセシウム回収技術の開発", ファインケミカル, シーエムシー出版, **46**(2), 33-40 (2017).

Biomolecular Structure and Dynamics Research Project（P2-8）

Papers

1) S. Fujiwara, K. Araki, T. Matsuo, H. Yagi, T. Yamada, K. Shibata, H. Mochizuki, "Dynamical behavior of human α-synuclein studied by quasielastic neutron scattering", PLoS ONE, **11**, e0151447 (2016). **N**

2) Y. Hirano, K. Takeda and K. Miki, "Charge-density analysis of an iron-sulfur protein at an ultra-high resolution of 0.48 Å", Nature, **534**, 281-84 (2016). **N**

3) T. Matsuo, T. Arata, T. Oda, K. Nakajima, S. Ohira-Karamura, T. Kikuchi and S. Fujiwara, "Difference in the hydration water mobility around F-actin and myosin subfragment-1 studied by quasielastic neutron scattering", Biochem. Biophys. Rep., **6**, 220-25 (2016). **N**

4) 海野 昌喜, 日下 勝弘, 玉田 太郎, 杉島 正一, 和田 啓, 萩原 義徳, 福山 恵一, "ビリン還元酵素PcyAと基質ビリベルジン複合体の中性子結晶構造解析で見えてきたもの", 波紋, **26**, 130-34 (2016). **N**

5) 松尾 龍人, 藤原 悟, "蛋白質水和水の多様性ー中性子・X線散乱による水和構造・ダイナミクス解析ー", 波紋, **26**, 135-38 (2016). **N**

6) 玉田 太郎, "抗がん剤の作用メカニズムの『鍵』を原子レベルで解明", ATOMOΣ, **58**, 51-54 (2016). **N**

7) S. Arai, C. Shibazaki, M. Adachi, E. Honjo, T. Tamada, Y. Maeda, T. Tahara, T. Kato, H. Miyazaki, M. Blaber and R. Kuroki, "An insight into the thermodynamic characteristics of human thrombopoietin complexation with TN1 antibody", Protein Sci., **25**, 1786-96 (2016). **N**

8) K. Tomoyori and T. Tamada, "New data reduction protocol for Bragg reflections observed by TOF single-crystal neutron diffractometry for protein crystals with large unit cells", J. Phys. Conf. Ser., **762**, 012040 (2016). **N**

9) 竹田 一旗, 三木 邦夫, 平野 優, "高電位鉄硫黄タンパク質HiPIPの超高分解能結晶構造と電荷密度解析", 日本結晶学会誌, **58**, 267-72 (2016). **N**

10) S. Waz, T. Nakamura, K. Hirata, Y. K. Ogawa, M. Chifune, T. Arimori, T. Tamada, S. Ikemizu, Y. Nakabeppu and Y. Yamagara, "Structural and kinetic studies of the human nudix hydrolase MTH1 reveal the mechanism for its broad substrate specificity", J. Biol. Chem., **292**, 2785-94 (2017). **N**

11) K. Takaba, K. Takeda, M. Kosugi, T. Tamada and K. Miki, "Distribution of valence electrons of the flavin cofactor in NADH-cytochrome b_5 reductase", Sci. Rep., **7**, 43162 (2017). **N**

12) 玉田 太郎, "放射光X線により明らかとなった抗体医薬品の作用メカニズム", Isotope News, **749**, 2-6 (2017). **N**

Proceedings

1) T. Matsuo, T. Arata, T. Oda and S. Fujiwara, "Neutron scattering studies on the dynamics of F-actin, myosin subfragment-1, and their hydration water", Proc. 4th Awaji Int. Workshop electron Spin Sci. & Tech.: Biological and Material Science Oriented Applications, [Awaji, Japan] (2016). **N**

2) 平野 優, 木村 成伸, 玉田 太郎, "ブタ肝臓由来シトクロム b5 ヘム結合ドメインの高分解能結晶構造", 第 16 回日本蛋白質科学会年会, 要旨集 3P-036, [福岡国際会議場・福岡] (2016/06). **N**

3) 玉田 太郎, 新見 大輔, 池田 昌弘, 森 英治, 元木 一宏, "モノクローナル完全ヒトアゴニスト抗体 KMTR2 により惹起されるTRAIL-R2の超重合状態", 第16回日本蛋白質科学会年会, 要旨集 3P-057, [福岡国際会議場・福岡] (2016/06). **N**

4) T. Tamada, "High-resolution neutron crystal structural studies of electron transfer proteins", Proc. IPR Int. Symp., 2016 Taiwan-Japan Joint Symp. Crystallography, [Sapporo, Japan] (2016). **N**

5) T. Tamada, D. Shinmi, M. Ikeda, E. Mori and K. Motoki, "TRAIL-R2 Superoligomerization Induced by Human Monoclonal Agonistic Antibody KMTR2", Proc. 5th Int. Symp. Diffraction Struct. Biol. (ISDSB2016), [Knoxville, USA] (2016/08). **N**

6) Y. Hirano, S. Kimura and T. Tamada, "High-resolution crystal structures of the heme-binding domain of cytochrome b5 from porcine liver", Proc. 5th Int. Symp. Diffraction Struct. Biol. (ISDSB2016), [Knoxville, USA] (2016/08). **N**

7) K. Kurihara, K. Tomoyori, Y. Hirano and T. Tamada, "Neutron diffractometer for protein crystallography covering crystals with large unit cell volume at J-PARC", Proc. 5th Int. Symp. Diffraction Struct. Biol. (ISDSB2016), [Knoxville, USA] (2016/08). **N**

8) T. Matsuo, T. Arata, T. Oda and S. Fujiwara, "Picosecond dynamics of F-actin, myosin subfragment-1, and their hydration water studied by quasielastic neutron scattering" Proc. 14th Int. Conf. Appl. Quasielastic Neutron Scattering, [Potsdam, Germany] (2016/09). **N**

9) 平野 優, 福原 宏章, 有木 真吾, 上田 光宏, 玉田 太郎, "シマミミズ由来 α-アミラーゼと β-マンナナーゼの結晶構造解析", 平成 28 年度日本結晶学会年会, 要旨集 PC-40, [県民文化センター・水戸] (2016/11). **N**

10) 栗原 和男, 友寄 克亮, 平野 優, 玉田 太郎, "生体高分子専用高分解能単結晶中性子回折装置の設計～大型単位胞結晶からの回折データ収集の実現に向けて～", 平成 28 年度日本結晶学会年会, 要旨集 PC-74, [県民文化センター・水戸] (2016/11). **N**

11) 友寄 克亮, 栗原 和男, 平野 優, 玉田 太郎, "生体高分子専用高分解能単結晶中性子回折装置の設計～高効率かつ低バックグラウンドの回折データ収集の実現に向けて～", 平成 28 年度日本結晶学会年会, 要旨集 PC-82, [県民文化センター・水戸] (2016/11). **N**

12) 新井 栄揮, 柴崎 千枝, 安達 基泰, 玉田 太郎, 前田 宜丈, "中和抗体結合反応におけるヒト・トロンボポエチンの構造学的・熱力学的変化", 日本結晶学会平成 28 年度年会, Poster PC-08, [県民文化センター・水戸] (2016/11). **N**

13) F. Kono, T. Matsuo, T. Tomioka, K. Shibata, K. Araki, H. Mochizuki and S. Fujiwara, "Relationship between the dynamics of human α-synuclein and its propensity to form amyloid fibrils", 第 54 回日本生物物理学会年会, 要旨集 1pos059, [つくば国際会議場・つくば] (2016/11). **N**

14) S. Fujiwara, T. Chatake, T. Matsuo, F. Kono, T. Tominaga, K. Shibata, A. Sato and N. Shibayama, "Changes in the picosecond dynamics of hemoglobin related to the structural states", 第 54 回日本生物物理学会年会, 要旨集 3pos077, [つくば国際会議場・つくば] (2016/11). **N**

15) T. Matsuo, T. Tominaga, K. Shibata and S. Fujiwara, "Effects of a cardiomyopathy-causing mutation on the internal dynamics of troponin revealed by quasielastic neutron scattering", 第 54 回日本生物物理学会年会, 要旨集 3pos123, [つくば国際会議場・つくば] (2016/11). **N**

16) 平野 優, 玉田 太郎, "シマミミズ由来 α-アミラーゼと β-マンナナーゼの X 線結晶構造解析", 第 1 回次世代生物研究会, [大阪府立大・大阪] (2016/11). **N**

17) 友寄 克亮, 木下 誉富, 山田 貢, 栗原 和男, 黒木 良太, 多田 俊治, 玉田 太郎, "セリンプロテアーゼ静止状態の中性子結晶構造解析", 日本中性子科学会第 16 回年会, 要旨集 P1-19, [名古屋大・名古屋] (2016/12). **N**

18) 松尾 龍人, 富永 大輝, 河野 史明, 柴田 薫, 藤原 悟, "心筋症原因変異によるトロポニン蛋白質のピコ秒ダイナミクス変化", 日本中性子科学会第 16 回年会, 要旨集 P2-20, [名古屋大・名古屋] (2016/12). **N**

19) 栗原 和男, 友寄 克亮, 玉田 太郎, "タンパク質大型単位胞結晶を測定可能な J-PARC 単結晶中性子回折装置", 日本中性子科学会第 16 回年会, 要旨集 P2-22, [名古屋大・名古屋] (2016/12). **N**

20) 松尾 龍人, 荒田 敏昭, 小田 俊郎, 中島 健次, 河村 聖子, 菊地 龍弥, 藤原 悟, "中性子準弾性散乱で観る筋収縮蛋白質と水和水のピコ秒ダイナミクス", 第 6 回量子ビームサイエンスフェスタ, [つくば国際会議場・つくば] (2017/03). **N**

21) S. Fujiwara, "Hydration water around F-actin studied by neutron scattering", Proc. Okazaki Conf. 2017 Mol. Syst. Sci.: Grand Challenges in Small-angle Scattering, [Okazaki, Japan] (2017/03). **N**

22) T. Tamada, "Neutron Protein Crystallography in Japan", Neutron Biology for Next Generation 2017, [Tokai, Japan] (2017/03). **N**

23) T. Matsuo, T. Arata, T. Oda, K. Nakajima, S. Kawamura, T. Kikuchi, K. Shibata, D. Tominaga, F. Kono and S. Fujiwara, "Picosecond dynamics of proteins and hydration water studied by quasi-elastic neutron scattering", Neutron Biology for Next Generation 2017, [Tokai, Japan] (2017/03). **N**

Press・TV

1) "パーキンソン病発症につながる「病態」タンパク質分子の異常なふるまいを発見ー発症のカギとなるタンパク質の線維状集合状態の形成過程解明の手がかりにー", 2016.04.21, プレス発表: 日経産業新聞, 日本経済新聞等に掲載. **N**

Laser Compton Scattering γ-ray Research Project（P3-1）

Papers

1) T. Hayakawa, T. Shizuma, S. Miyamoto, S. Amano, A. Takemoto, M. Yamaguchi, K. Horikawa, H. Akimune, S. Chiba, K. Ogata and M. Fujiwara, "Spatial anisotropy of neutrons emitted from the $^{56}Fe(\gamma,n)^{55}Fe$ reaction with a linearly polarized γ-ray beam", Phys. Rev. C, **93**, 044313 (2016). **N**

2) T. Hayakawa, S. Miyamoto, R. Hajima, T. Shizuma, S. Amano, S. Hashimoto, T. Misawa, "Proposal for selective isotope transmutation of long-lived fission products using quasi-monochromatic γ-ray beams", J. Nucl. Sci. Tech., **53**, 2064-71 (2016). **N**

3) J. K. Koga and T. Hayakawa, "Precision Measurement of Delbrück Scattering via Laser Compton Scattered γ-rays", J. Phys.: Conf. Ser., **688**, No.1, 012050 (2016). **N**

4) H. Zen, Y. Taira, T. Konomi, T. Hayakawa, T. Shizuma, J. Yamazaki, T. Kii, H. Toyokawa, M. Katoh, H. Ohgaki,. "Generation of High Energy Gamma-ray by Laser Compton Scattering of 1.94-μm Fiber Laser in UVSOR-III Electron Storage Ring", Energy Procedia, **89**, 335-45 (2016). **N**

5) M. Mori, A. Kosuge, H. Kiriyama, R. Hajima and K. Kondo, "Simple synchronization technique of a mode-locked laser for Laser-Compton scattering γ-ray source", Rev. Sci. Instrum. **87**, 063307 (2016). **N**

6) M. Yamamoto and N. Nishimori, "High voltage threshold for stable operation in a dc electron gun", Appl. Phys. Lett. **109**, 014103 (2016). **N**

7) S. Matsuba, T. Hayakawa, T. Shizuma, N. Nishimori, R. Nagai, M. Sawamura, C. T. Angell, M. Fujiwara and R. Hajima, "Enhanced diffraction of MeV γ rays by mosaic crystals", Jpn. J. Appl. Phys. **55**, 112402 (2016). **N**

8) C. T. Angell, R. Hajima, T. Shizuma, B. Ludewigt and B. J. Quiter, "Branching and fragmentation of dipole strength in ^{181}Ta in the region of the scissors mode", Phys. Rev. Lett. **117**, 142501 (2016). **N**

9) T. Hayakawa, Y. Toh, M. Huang, T. Shizuma, A. Kimura, S. Nakamura, H. Harada, N. Iwamoto, S. Chiba and T. Kajino, "Measurement of the isomer production ratio for the 112Cd(n,γ)113Cd reaction using neutron beams at J-PARC", Phys. Rev. C, **94**, 055803 (2016). **N**

10) T. Nakamura and T. Hayakawa, "Quasi-monoenergetic positron beam generation from ultra-intense laser-matter interactions", Physics of Plasmas **23**, 103109 (2016). **N**

11) T. Akagi, A. Kosuge, S. Araki, R. Hajima, Y. Honda, T. Miyajima, M. Mori, R. Nagai, N. Nakamura, M. Shimada, T. Shizuma, N. Terunuma and J. Urakawa, "Narrow-band photon beam via laser Compton scattering in an Energy Recovery Linac", Phys. Rev. Accel. Beams, **19**, 114701 (2016). **N**

12) R. Hajima, "Status and Perspectives of Compton Sources", Physics Procedia, **84**, 35-39 (2016). **N**

13) 羽島 良一,「会議報告:Nuclear Photonics 2016 国際会議報告」,「加速器」, **13**, (4), 270-71 (2016). **N**

Proceedings

1) R. Hajima, M. Fujiwara, "Generation of GeV Photons from X-ray Free Electron Laser Oscillators", Proc. 2016 Int. Part. Accel. Conf. (IPAC-16), 751-53, [Busan, Korea] (2016/05). **N**

2) T. Kubo, T. Saeki, E. Cenni, R. Hajima, M. Sawamura, H. Hokonohara, Y. Iwashita, H. Tongu, "Multipactor Simulations in 650 MHz Superconducting Spoke Cavity for an Electron Accelerator", Proc. 2016 Int. Part. Accel. Conf. (IPAC-16), 2161-63, [Busan, Korea] (2016/05). **N**

3) H. Tongu, H. Hokonohara, Y. Iwashita, R. Hajima, M. Sawamura, H. Hayano, T. Kubo, T. Saeki, Y. Yamamoto, "Study on Nondestructive Inspections for Super-conducting Cavity", Proc. 2016 Int. Part. Accel. Conf. (IPAC-16), 2174-76, [Busan, Korea] (2016/05). **N**

4) M. Shimada, K. Yokoya, R. Hajima, M. Tecimer, "Proposal of 6 GeV Energy Recovery Linac Hybrid Machine", Proc. 2016 Int. Part. Accel. Conf. (IPAC-16), 3254-56, [Busan, Korea] (2016/05). **N**

5) N. Nishimori, R. Hajima, R. Nagai, Y. Honda, T. Miyajima, T. Uchiyama, M. Yamamoto, M. Mori, "DC Photoemission Gun Upgrade at the Compact ERL", Proc. 2016 Int. Part. Accel. Conf. (IPAC-16), 3944-46, [Busan, Korea] (2016/05). **N**

6) T. Obina, R. Hajima, M. Mori, R. Nagai, N. Nishimori, M. Sawamura, T. Shizuma, et al. "Recent Developments and Operational Status of the Compact ERL at KEK", Proc. 2016 Int. Part. Accel. Conf. (IPAC-16), 1835-37, [Busan, Korea] (2016/05). **N**

7) M. Sawamura, R. Hajima, H. Hokonohara, Y. Iwashita, H. Tongu, T. Kubo, T. Saeki, "Fabrication of Superconducting Spoke Cavity for Laser Compton Scattered Photon Sources", Proc. 2016 Int. Part. Accel. Conf. (IPAC-16), 2177-79, [Busan, Korea] (2016/05). **N**

8) M. Omer, R. Hajima, C. T. Angell, T. Shizuma, T. Hayakawa, M. Seya and M. Koizumi, "Simulation of the Elastic Scattering Contributions to the NRF-Based Nondestructive Assay of Nuclear Materials", Proc. Institute Nucl. Mater. Manage. Annu. Meet. 2016. [Atlanta, USA] (2016). **N**

9) M. Sawamura, R. Hajima, H. Hokonohara, Y. Iwashita, H. Tongu, T. Kubo, T. Saeki, "Fabrication of Superconducting Spoke Cavity for Compact Photon Source", Proc. 28th Linear Accel. Conf. (LINAC2016), 212-14, [Michigan, USA] (2016/09). **N**

10) 坂中 章悟, 芳賀 開一, 本田 洋介, 松村 宏, 宮島 司, 野上 隆史, 帯名 崇, 下ヶ橋 秀典, 島田 美帆, 山本 将博, 中村 典雄, 高井 良太, 田中 オリガ, 原田 健太郎, 許斐 太郎, 阪井 寛志, 梅森 健成, 河田 洋, 小林 幸則, 羽島 良一, 西森 信行, "コンパクトERLにおけるビーム電流約1 mAの運転", 第13回日本加速器学会年会プロシーディングス, 291-95, [幕張メッセ・千葉] (2016/08). **N**

11) 羽島 良一, 藤原 守, "共振器型X線自由電子レーザーにおけるコンプトン散乱ガンマ線の発生", 第13回日本加速器学会年会プロシーディングス, 300-03, [幕張メッセ・千葉] (2016/08). **N**

12) 西森 信行, 永井 良治, 沢村 勝, 羽島 良一, "アルカリアンチモン光陰極高電圧電子銃からのビーム生成", 第13回日本加速器学会年会プロシーディングス, 464-67, [幕張メッセ・千葉] (2016/08). **N**

13) 西森 信行, 山本 将博, 羽島 良一, 森 道昭, 永井 良治, 宮島 司, 内山 隆司, 本田 洋介, "コンパクトERL電子銃の高性能化", 第13回日本加速器学会年会プロシーディングス, 468-72, [幕張メッセ・千葉] (2016/08). **N**

14) 羽島 良一, 永井 良治, "赤外自由電子レーザーによるアト秒・ゼプト秒X線発生"、第13回日本加速器学会年会プロシーディングス, 551-55, [幕張メッセ・千葉] (2016/08). **N**

15) 羽島 良一, 宮島 司, 松葉 俊哉, "レーザー・コンプトン光源における短パルスX線の発生", 第13回日本加速器学会年会プロシーディングス, 556-59, [幕張メッセ・千葉] (2016/08). **N**

16) 永井 良治, 羽島 良一, “アト秒・ゼプト秒 X 線パルス発生のための共振器型赤外 FEL の 3 次元シミュレーション”, 第 13 回日本加速器学会年会プロシーディングス, 563-66, [幕張メッセ・千葉] (2016/08). **N**

17) 沢村 勝, 羽島 良一, 佐伯 学行, 久保 毅幸, 岩下 芳久, 頓宮 拓, 鉾之原 久雄, “超伝導スポーク空洞のプレス成型試験”, 第 13 回日本加速器学会年会プロシーディングス, 889-92, [幕張メッセ・千葉] (2016/08). **N**

18) 羽島 良一, “高出力 ERL-FEL における RF 安定性”, 第 13 回日本加速器学会年会プロシーディングス, 1181-85, [幕張メッセ・千葉] (2016/08). **N**

19) 永井 良治, 宮島 司, “加速器パラメータ最適化のための GUI ツール開発”, 第 13 回日本加速器学会年会プロシーディングス, 1186-88, [幕張メッセ・千葉] (2016/08). **N**

20) 許斐 太郎, 梅森 健成, 加古 永治, 阪井 寛志, 久保 毅幸, 太田 智子, 沢村 勝, “EUV 光源加速器に適した 9 セル超伝導空洞の RF 設計”, 第 13 回日本加速器学会年会プロシーディングス, 263-67, [幕張メッセ・千葉] (2016/08). **N**

21) 太田 智子, 高崎 正浩, 山田 正博, 宮本 篤, 佐藤 潔和, 許斐 太郎, 梅森 健成, 加古 永治, 阪井 寛志, 沢村 勝, “超伝導加速空洞用 HOM ダンパーの開発”, 第 13 回日本加速器学会年会プロシーディングス, 377-79, [幕張メッセ・千葉] (2016/08). **N**

22) 江木 昌史, 梅森 健成, 江並 和宏, 阪井 寛志, 沢村 勝, 篠江 憲治, 古屋 貴章, “cERL 主空洞のマイクロフォニックス原因調査”, 第 13 回日本加速器学会年会プロシーディングス, 383-86, [幕張メッセ・千葉] (2016/08). **N**

23) 沢村 勝, “C 形導波管の高周波特性”, 第 13 回日本加速器学会年会プロシーディングス, 885-88, [幕張メッセ・千葉] (2016/08). **N**

24) 山本 将博, 西森 信行, “超高真空における電子刺激脱離と直流放電現象の関係”, 第 13 回日本加速器学会年会プロシーディングス, 47-51, [幕張メッセ・千葉] (2016/08). **N**

25) 山本 将博, 金 秀光, 西森 信行, 本田 洋介, 宮島 司, 帯名 崇, 亀田 吉郎, 川崎 泰介, “大電流 CW ビーム運転前後の半導体フォトカソード量子効率分布測定”, 第 13 回日本加速器学会年会プロシーディングス, 453-57, [幕張メッセ・千葉] (2016/08). **N**

26) 亀田 吉郎, 山本 将博, 帯名 崇, 金 秀光, 宮島 司, 西森 信行, “光陰極の 2 次元高解像度 QE 分布測定装置の開発”, 第 13 回日本加速器学会年会プロシーディングス, 1163-67, [幕張メッセ・千葉] (2016/08). **N**

Beam Engineering Section（P3-2）

Papers

1) H. Kojima, H. Yoshizaki, Y. Kaneno, S. Semboshi, F. Hori, Y. Saitoh, Y. Okamoto, A. Iwase, “Lattice structure transformation and change in surface hardness of Ni_3Nb and Ni_3Ta intermetallic compounds induced by energetic ion beam irradiation”, Nucl. Instrum. Meth. Phys. Res. B, **372**, 72-77 (2016). **T, S, I, 1-29, 3-17~19**

2) Y. Fujimura, S. Semboshi, Y. Okamoto, Y. Saitoh, T. Matsui, A. Iwase, “Magnetic states of cobalt atoms in copper metal after cobalt-implantation and effects of subsequent annealing”, Trans. Mater. Res. Soc. Jpn., **41**, 209-12 (2016). **T, S, I, 1-29, 3-17~19**

3) R. Mayumi, S. Semboshi, Y. Okamoto, Y. Saitoh, T. Yoshiie, A. Iwase, “Radiation enhanced precipitation of solute atoms in AlCu binary alloys - energetic ion irradiation experiment and computer simulation -”, Trans. Mater. Res. Soc. Jpn., **42,** 9-14 (2017). **T, S, I, 1-29, 3-17~19**

4) S. Watanabe, Y. Sano, H. Shiwaku, T. Yaita, S. Ohno, T. Arai, H. Matsuura, M. Koka and T. Satoh, “Local structure and distribution of remaining elements inside extraction chromatography adsorbents”, Nucl. Instrum. Meth. Phys. Res. B, **404**, 202-06 (2017). **S, 1-34**

5) R. Abe, K. Nagoshi, T. Arai, S. Watanabe, Y. Sano, H. Matsuura, H. Takagi, N. Shimizu, M. Koka and T. Satoh, “Microscopic analyses of complexes formed in adsorbent for Mo and Zr separation chromatography”, Nucl. Instrum. Meth. Phys. Res. B, **404**, 173-78 (2017). **S, 1-34**

6) N. Nagasawa, A. Kimura, A. Idesaki, N. Yamada, T. Satoh, Y. Ishii, M. Taguchi, “Microfabrication of biocompatible hydrogels by proton beam writing”, Nucl. Instrum. Meth. Phys. Res. B, **409**, 102-06 (2017). **S, 1-50**

7) M. Yamaguchi, Y. Nagao, T. Satoh, H. Sugai, M. Sakai, K. Arakawa and N. Kawachi, “Monte Carlo simulation of photon emission below a few hundred kiloelectronvolts for beam monitoring in carbon ion therapy”, Rev. Sci. Instrum., **88**, 014301-1~8 (2017). **N, 2-30**

8) M. Yamaguchi, Y. Nagao, N. kawachi, T. Satoh, S. Fujimaki, T. Kamiya, K. Torikai, H. Shimada, H. Sugai, M. Sakai, K. Arakawa and T. Nakano, “Detection of a gas region in a human body across a therapeutic carbon beam by measuring low-energy photons”, Int. J. PIXE, **26**, 61-72 (2016). **N, 2-30**

9) M. Yamaguchi, K. Torikai, N. Kawachi, H. Shimada, T. Satoh, Y. Nagao, S. Fujimaki, M. Kokubun, S. Watanabe, T. Takahashi, K. Arakawa, T. Kamiya and T. Nakano, “Corrigendum: Beam range estimation by measuring bremsstrahlung (2012 Phys. Med. Biol. 57 2843)”, Phys. Med. Biol., **61**, 3638-44 (2016). **N, 2-30**

10) 金井 敬海, 笠松 哲光, 栗田 真彩, 村田 佳祐, 長嶋 友海, 山田 尚人, 喜多村 茜, 佐藤 隆博, 江夏 昌志, 神谷 富裕, 長嶺 竹明, 村上 博和, “大気 Micro-PIXE 法を用いた多発性骨髄腫細胞内微量元素の動態解析”, 北関東医学, **66**, 253 (2016). **S, 2-36**

11) Y. Koga, T. Satoh, K. Kaira, M. Koka, T. Hisada, J. Hirato, B. Altan, M. Yatomi, A. Ono, Y. Kamide, Y. Shimizu, H. Aoki-Saito, H. Tsurumaki, K. Shimizu, A. Mogi, T. Ishizuka, M. Yamada and K. Dobashi, “Elemental and immunohisto-chemical analysis of the lungs and hilar lymph node in a patient with asbestos exposure, a pilot study”, Environ. Health Prev. Med., **21**, 492-500 (2016). **S, 2-37**

12) S. Harada, S. Ehara, T. Segawa, K. Ishii, T. Satoh, T. Kamiya, K. Sera and S. Goto, “Innovation of hyaluronic acid-protamine microparticles and their kinetics *in vivo*”, Int. J. PIXE, **26**, 45-51, (2016). **S, 2-41**

13) T. Nagamine, K. Sato, S. Kakizaki, T. Satoh, M. Koka, T. Kamiya, “Analysis of Erythrocyte Elements in Chronic Hepatitis C Patients Received PegIFN MOnotheraph, Dual Therapy, and Triple Therapy using in-air MicroPIXE”. Kitakanto Med. J., **66**, 91-102 (2016) (Review). **S**

14) S. Kawabata, W. Kada, R. K. Parajuli, Y. Matsubara, M. Sakai, K. Miura, T. Satoh, M. Koka, N. Yamada, T. Kamiya and O. Hanaizumi, “In situ ion-beam-induced luminescence analysis for evaluating a micrometer-scale radio-photoluminescence glass dosimeter”, Jpn. J. Appl. Phys., **55**, 06GD03 (2016). **S, 3-01**

15) R. K. Parajuli, W. Kada, S. Kawabata, Y. Matsubara, K. Miura, A. Yokoyama, M. Haruyama, M. Sakai and O. Hanaizumi, “Evaluation of Radio-Photoluminescence Spectra of Copper-

Doped Phosphate Glass Dosimeter Irradiated with Ionized Particles", Key Eng. Mater., **698**, 163-70 (2016). **S, 3-01**

16) R. K. Parajuli, W. Kada, S. Kawabata, Y. Matsubara, M. Sakai, K. Miura, T. Satoh, M. Koka, N. Yamada, T. Kamiya, O. Hanaizumi, "Ion-Beam-Induced Luminescence Analysis of β-SiAlON:Eu Scintillator under Focused Microbeam Irradiation". Sensors and Materials 2016, **28**, 837-44, (2016). **S, 3-01**

17) W. Kada, S. Kawabata, T. Satoh, M. Sakai, R. K. Parajuli, N. Yamada, M. Koka, K. Miura, O. Hanaizumi and T. Kamiya, "Observation of changes in ion beam induced luminescence spectra from organics during focused microbeam irradiation", Nucl. Instrum. Meth. Phys. Res. B, **404**, 100-05 (2017). **S, 3-01**

18) T. Matsumoto, A. Masuda, H. Harano, Y, Shikaze, Y. Tanimura, H. Seito, S. Kurashima, S. Nishino, H. Yoshitomi, J. Nishiyama, M. Hagiwara, Y. Unno, M. Yashizawa, "Development of high-energy neutron fluence rate standard field in Japan with a energy of 45 MeV using the ^{7}Li(p,n)^{7}Be reaction at TIARA", J. Nucl. Sci. Tech. **54** (5), 529-39 (2017). **C, 3-03**

19) S. Kurashima, T. Satoh, Y. Saito and W. Yokota, "Irradiation Facilities of the Takasaki Advanced Radiation Research Institute", Quantum Beam Sci. **1**(1), 2 (2017). **C, T, S, I, 3-05**

20) H. Kashiwagi, K. Yamada, S. Kurashima, "Development of a laser ion source for production of high-intensity heavy-ion beams", Nucl. Instrum. Meth. Phys. Res. B, **406**, 256-59 (2017). **C**

21) 石坂 知久, 百合 庸介, 上松 敬, 清藤 一, 湯山 貴裕, 奥村 進, "ガフクロミックフィルム HD-V2 のガンマ線応答曲線を用いたイオンビームの相対強度分布測定法", RADIOISOTOPES, **66**, (7), 251-58 (2017). **C, T, G, 3-08, 3-23**

22) Y. Ishii, T. Ohkubo, T. Kamiya, "Reduction of a beam diameter by decreasing the divergence angle of an incident beam in a compact ion microbeam system producing several-hundred-keV beam", Nucl. Instrum. Meth. Phys. Res. B, **404**, 65-68 (2017). **N, 3-09**

23) R. K. Parajuli, R. Saruya, N. Akutzu, S. Miura, W. Kada, S. Kawabata, Y. Matsubara, T. Satoh, M. Koka, N. Yamada, T. Kamiya, K. Miura, and O. Hanaizumi, "Fabrication and evaluation of flexible Mach-Zehnder waveguide structure embedded in a poly(dimethylsiloxane) thin film using a proton microbeam", Jpn. J. Appl. Phys., 55(6S1), 06GD01 (2016). **S, 3-11**

24) R. Sano, S. Hayakawa, H. Hayashi, Y. Ishii, H. Nishikawa, "Micro-structuring of epoxy resists containing nanoparticles by proton beam writing", Nucl. Instrum. Meth. Phys. Res. B, **404**, 228-32 (2017). **S, 3-12**

25) H. Hayashi, S. Matsuzaki, K. Nakajima, K. Narumi, Y. Saitoh, M. Tsujimoto, M. Toulemonde, and K. Kimura, "Local heating induced by single MeV C_{60} ion impacts", Nucl. Instrum. Meth. Phys. Res. B, **406**, 591-95 (2017). **I, 3-15**

26) K. Hirata, K. Yamada, A. Chiba, K. Narumi, and Y. Saitoh, "Characterization of secondary ion emission processes of sub-MeV C_{60} ion impacts via analysis of statistical distributions of the emitted ion number", J. Chem. Phys. **145**, 234311 (2016). **T, I, 3-16**

27) T. Wasin, K. Enomoto, T. Sakurai, V. S. Padalkar, H. L. Cheng, M. T. Tang, A. Horio, D. Sakamaki, M. Omichi, A. Saeki, K. Kikuchi, Y. Hori, A. Chiba, Y. Saito, T. Kamiya, M. Sugimoto and S. Seki, "Fabrication of "clickable" polyfluorene nanowires with high aspect ratio as biological sensing platforms," ACS Sens., **1**, 766-74 (2016). **C, 3-21**

28) A. Horio, T. Sakurai, K. Kayama, G. B. V. S. Lakshmi, D. V. Avasthi, M. Sugimoto, T. Yamaki, A. Chiba, Y. Saito and S. Seki, "Remarkable Effect of Halogenation of Aromatic Compounds on Efficiency of Nanowire Formation through Polymerization/Crosslinking by High-Energy Single Particle Irradiation", Radiat. Phys. Chem., **142**, 100-06 (2018). **C, T, 3-21**

29) Y. Yuri, K. Narumi, and T. Yuyama, "Characterization of a Gafchromic film for the two-dimensional profile measurement of low-energy heavy-ion beams", Nucl. Instrum. Meth. Phys. Res. A, **828** 15-21 (2016). **C, T, I, 3-23**

30) Y. Yuri, T. Ishizaka, T. Agematsu, T. Yuyama, H. Seito, S. Okumura, "Use of a Gafchromic film HD-V2 for the profile measurement of energetic ion beams", Nucl. Instrum. Meth. Phys. Res. B, **406**, 221-24 (2017). **C, T, I, 3-23, 3-08**

31) 百合 庸介, 「TOPICS」"イオンビームの非走査式大面積均一照射技術の開発", 放射線と産業, **141**, 47-50 (2016). **C, T, I, 3-23**

32) K. Motohashi, N. Miyawaki, Y. Saitoh, K. Narumi and S. Matoba, "Guiding of 4 MeV C^{+} and C^{4+} ion beams using cylindrical glass channel", Jpn. J. Appl. Phys., **56**, 046301-1~6 (2017). **T, 3-24**

33) 小嶋 拓治, 「特別寄稿」"水素社会の実現に向けた放射線利用研究の新しい芽", 放射線と産業, **141**, 4-6, (2016). **N**

34) 小嶋 拓治, "放射線プロセスにおける線量の標準化", JAPI ニューズレター, **19**(3), 2-7 (2016). **E, G**

Proceedings

1) 長澤 尚胤, 木村 敦, 出崎 亮, 山田 尚人, 江夏 昌志, 島田 明彦, 佐藤 隆博, 石井 保行, 田口 光正, "プロトンビームライティング法による高分子ヒドロゲルの微細加工", 第 59 回放射線化学討論会, P-30, [量研高崎・高崎] (2016/09). **S, 1-50**

2) M. Fuchi, M. Arima, K. Narumi, Y. Terai, and Y. Maeda, "Ion channeling measurements of β-$FeSi_2$ films epitaxially grown on Si(111) and their analysis by multiple scattering theory", Proc. Asia-Pacific Conf. Semicond. Silicides & Related Mater. 2016, [Fukuoka, Japan] (2016/07), JJAP Conf. Proc. **5**, 011104 (2017). **S, 3-02**

3) M. Arima, M. Fuchi, K. Narumi, and Y. Maeda, "Analysis of oxidation behavior in nanocrystal β-$FeSi_2$/Si composites by Rutherford backscattering spectrometry and computation of diffusion flux", Proc. Asia-Pacific Conf. Semicond. Silicides & Related Mater. 2016, [Fukuoka, Japan] (2016/07), JJAP Conf. Proc. **5**, 011105 (2017). **S, 3-02**

4) S. Kurashima, N. Miyawaki, S. Okumura, T. Satoh, H. Kashiwagi, K. Yoshida, T. Yuyama and M. Fukuda, "Cyclotron technology and beam dynamics for microbeam appications", Proc. 21st Int. Conf. Cyclo. Their Appl., MOB01, 16-20, [Zürich, Switzerland] (2016/09). **C, 3-05, 3-06**

5) 倉島 俊, 宮脇 信正, "サイクロトロンにおけるパルスビーム開発", 第 16 回放射線プロセスシンポジウム, P1-4, 要旨集 54, [東京大・東京] (2016/11). **T, I, 3-05**

6) N. Miyawaki, M. Fukuda, S. Kurashima and H. Kashiwagi, "Comparison of phase bunching in the TIARA AVF cyclotoron", Proc. 13th Annu. Meet. Part. Accel. Soc. Jpn., 617-18, [Chiba, Japan] (2016/08) (in Japanese). **C, 3-06**

7) H. Kashiwagi, N. Miyawaki and S. Kurashima, "Development of a fast emittance measurement system with the slit-harp method", Proc. 13th Annu. Meet. Part. Accel. Soc. Jpn., 619-21, [Chiba, Japan] (2016/08) (in Japanese). **C, 3-06**

8) 千葉 敦也, 平野 貴美, 山田 圭介, "フラーレンビームの高強度化", 第29回タンデム加速器及びその周辺技術の研究会, 要旨集 138, [筑波大・筑波] (2016/06). **T, I, 3-07**

9) 平野 貴美, 千葉 敦也, 山田 圭介, 横山 彰人, 高山 輝充,

金井 信二, 青木 勇希, 橋爪 将司, 高橋 悠人, 長谷川 雅人, 佐藤 隆博, 大久保 猛, 奈良 孝幸, “TIARA 静電加速器の現状”, 第29回「タンデム加速器及びその周辺技術の研究会」, 報告集 134-37, [筑波大・筑波] (2016/06). **T, S, I, 3-07, 4-03**

10) 千葉 敦也, 平野 貴美, 山田 圭介, “既存イオン源の革新的活用法によるフラーレンビームの高強度化”, 第59回放射線化学討論会, 要旨集 3O03, [量研高崎・高崎] (2016/09).
T, I, 3-07

11) 山田 圭介, 柏木 啓次, “レーザーイオン源用静電アナライザー電極の製作”, 第 13 回日本加速器学会年会プロシーディングス, 978-80, [幕張メッセ・千葉] (2016/08). **C, T**

12) 山田 圭介, 千葉 敦也, 横山 彰人, 鳴海 一雅, 齋藤 勇一, “フラーレン負イオン源の開発”, 第 13 回日本加速器学会年会プロシーディングス, 981-82, [幕張メッセ・千葉] (2016/08).
T, I, 3-07

13) 平野 貴美, 千葉 敦也, 山田 圭介, 薄井 絢, “MeV 級 C_{60} ビームの生成”, 第 16 回放射線プロセスシンポジウム, P1-5, 要旨集 55, [東京大・東京] (2016/11). **T, I, 3-07**

14) 鳴海 一雅, 千葉 敦也, 山田 圭介, 平野 貴美, 齋藤 勇一, “Research and Development in Cluster-Ion Beams at QST/Takasaki” **【招待講演】**, D3-O20-008, 日本MRS年次大会, [横浜市開港記念会館・横浜] (2016/12). **T, I, 3-07**

15) 石坂 知久, 百合 庸介, 上松 敬, 湯山 貴裕, 清藤 一, 奥村 進, “ガフクロミックフィルムを用いたイオンビーム強度分布測定法”, 第16回放射線プロセスシンポジウム, P1-1, 要旨集 51, [東京大・東京] (2016/11). **C, G, 3-08**

16) 加田 渉, 三浦 聡, 猿谷 良太, 佐藤 隆博, R. K. Parajuli, 川端 駿介, 三浦 健太, 江夏 昌志, 神谷 富裕, 花泉 修, “集束陽子線微細加工技術による高分子薄膜内包型 Mach-Zehnder 光導波路・光スイッチの開発”, 第 59 回放射線化学討論会, P-22, [量研高崎・高崎] (2016/09). **S, 3-11**

17) 三浦 聡, 猿谷 良太, 川端 駿介, 三浦 健太, 加田 渉, 江夏 昌志, 佐藤 隆博, 神谷 富裕, 花泉 修, “集束陽子マイクロビームにより PDMS 薄膜内部に埋め込み加工された Mach-Zehnder 導波路型光スイッチング素子の開発”, 第 77 回応用物理学会秋季学術講演会, [朱鷺メッセ・新潟] (2016/09). **S, 3-11**

18) 高橋 龍平, 三浦 聡, 猿谷 良太, 川端 駿介, 三浦 健太, 加田 渉, 江夏 昌志, 佐藤 隆博, 神谷 富裕, 花泉 修, “集束陽子線微細加工技術によるフレキシブル電子回路基板内部への光導波路構造の埋込形成”, 第 77 回応用物理学会秋季学術講演会, [朱鷺メッセ・新潟] (2016/09). **S, 3-11**

19) 金子 優斗, 林 秀臣, 佐藤 隆博, 石井 保行, 加田 渉, 三浦 健太, 花泉 修, 西川 宏之, “集束陽子線描画による TiO2/PDMS 製光導波路作製の検討”, 第 30 回 エレクトロニクス実装学会 春季講演大会, 6P1-2, [東京工業大・東京] (2017/03). **S, 3-12**

20) 澁谷 泰一, 林 秀臣, 石井 保行, 佐藤 隆博, 中河原 僚介, 内田 諭, 西川 宏之, “誘電泳動を用いた PMMA マイクロピットアレイへの金ナノ粒子捕集における周波数依存性”, 第 30 回 エレクトロニクス実装学会 春季講演大会, 6P1-3, [東京工業大・東京] (2017/03). **S, 3-12**

21) 澁谷 泰一, 林 秀臣, 石井 保行, 片岡 良介, 中河原 僚介, 内田 諭, 西川 宏之, “誘電泳動による金属ナノ粒子の捕集および三次元マイクロ構造体作製”, 平成 28 年度電気学会 基礎・材料・共通部門大会, 5-P-53, [九州工業大・北九州] (2016/09). **S, 3-12**

22) 百合 庸介, 鳴海 一雅, 湯山 貴裕, “ガフクロミックフィルムの低エネルギーイオンビーム強度分布計測への適用”, Proc. 13th Annu. Meet. Part. Accel. Soc. Jpn., (TUP130) 1277-80, [幕張メッセ・千葉] (2016/08). **C, T, I, 3-23**

23) 湯山 貴裕, 百合 庸介, 石坂 知久, 石堀 郁夫, 奥村 進, “TIARA における蛍光体を用いたリアルタイムビーム分布計測システムの特性評価”, Proc. 13th Annu. Meet. Part. Accel. Soc. Jpn., (MOP089) 622-25, [幕張メッセ・千葉] (2016/08).
C, 3-23, 3-08

24) 百合 庸介, 鳴海 一雅, 千葉 敦也, 齋藤 勇一, “ガフクロミックフィルムの高速単原子・クラスターイオン照射応答の比較”, 第 59 回放射線化学討論会, 講演要旨集 P-16, [量研高崎・高崎] (2016/09). **T, I, 3-23**

25) Y. Yuri, T. Ishizaka, T. Yuyama, T. Agematsu, H. Seito, S. Okumura and K. Narumi, “Transverse Intensity Distribution Measurement of Ion Beams Using Gafchromic Films”, Proc. 7th Int. Part. Accel. Conf., IPAC16, 130-32, [Busan, Korea] (2016/05). **C, 3-23, 3-08**

26) K. Takayama, M. Wake, Y. Iwata, Y. Yuri, T. Adachi and K. Okamura, “A Racetrack-Shape Fixed Filed Induction Accelerator for Giant Cluster Ions”, Proc. 7th Int. Part. Accel. Conf., IPAC16, 1278-80, [Busan, Korea] (2016/05). **N**

27) 加田 渉, 三浦 聡, 猿谷 良太, 佐藤 隆博, R. K. Parajuli, 川端 駿介, 三浦 健太, 江夏 昌志, 神谷 富裕, 花泉 修, “集束陽子線微細加工技術による高分子薄膜内包型 Mach-Zehnder 光導波路・光スイッチの開発”, 第 59 回放射線化学討論会, 講演要旨集 P-22, [量研高崎・高崎] (2016/09).
S, 3-11

28) T. Satoh, “IAEA/RCA Regional Workshop on Identification Trans-boundary Air Pollution Events across Asia-Pacific”, [Philippines] (2016/06-07). **S, 3-31**

29) 佐藤 隆博, “目に見えない微粒子をイオンビームで視る ～イオンビーム分析の環境科学への貢献～”, 群馬大学公開講座, [群馬大・桐生] (2016/09). **S, 3-31**

30) T. Satoh, “Development and Application of Micro-Particle-Induced X/Gamma-ray Emission”, Rad Tech Asia 2016, [Tokyo, Japan] (2016/10). **S, 3-31**

31) 佐藤 隆博, “IAEA/RCA 2016 年度第 1 回国内対応委員会資料”, [外務省・東京] (2016/11).

Books

1) 小嶋 拓治, “電子線の計測技術”, 第 9 章, EB 技術を利用した材料創製と応用展開, シーエムシー出版社 (2016/07). **E**

2) 薄井 絢, 千葉 敦也, 山田 圭介, “セシウムスパッターイオン源を利用した電子付着による C_{60} 負イオン生成技術の開発”, QST-R-1 (27p) (2017/03). **T, I, 3-07**

Patents

1) 加田 渉, 三浦 健太, 花泉 修, 神谷 富裕, 佐藤 隆博, 須崎 純一, 山田 鈴弥, “荷電粒子放射線計測方法および荷電粒子放射線計測装置”, 国際出願番号:PCT/JP2016/074813 (2016.8.25), 台湾出願番号:105127462, (2016.08.26). 出願: 電気化学工業株式会社. **S, 3-01**

2) 加田 渉, 三浦 健太, 花泉 修, 神谷 富裕, 佐藤 隆博, 須崎 純一, 山田 鈴弥, ”荷電粒子放射線計測方法および荷電粒子放射線計測装置”, 特願 2017-036154 (2017.02.27). 出願: 電気化学工業株式会社. **S, 3-01**

3) 古山 了, 森山 順一, 長井 陽三, 百合 庸介, 石堀 郁夫, 湯山 貴裕, 石坂 知久, 奥村 進, 前川 康成, 越川 博, 八巻 徹也, 浅野 雅春, “多孔性高分子フィルムの製造方法および多孔性高分子フィルム”、特許第6044895号(2016.11.25登録). **C**

4) 百合 庸介, 石堀 郁夫, 湯山 貴裕, 石坂 知久, 奥村 進, 前川 康成, 越川 博, 八巻 徹也, 浅野 雅春, “Porous polymer membrane and method for producing the same” 米国特許登録 6044895 (2016.11.25). **C**

External Research Groups Except for Takasaki Advanced Radiation Research Institute

Papers

1) K. Irisawa and Y. Meguro, "Swelling pressure and leaching behaviors of synthetic bituminized waste products with various salt contents under a constant-volume condition", J. Nucl. Sci. Tech., **54**, (3), 365-72 (2017). **G, 1-37**

2) Y. Oya, Y. Hatano, M. Shimada, D. Buchenauer, R. Kolasinski, B. Merrill, S. Kondo, T. Hinoki, V. K. Alimov, "Recent progress of hydrogen isotope behavior studies for neutron or heavy ion damaged W", Fusion Eng. Design, **113**, 211-15 (2016). **T, 1-38**

3) S. Sakurada, K. Yuyama, Y. Uemura, H. Fujita, C. Hu, T. Toyama, N. Yoshida, T. Hinoki, S. Kondo, M. Shimada, D. Buchenauer, T. Chikada, Y. Oya, "Annealing effects on deuterium retention behavior in damaged tungsten", Nucl. Mater. Energy, **9**, 141-44 (2016). **T, 1-38**

4) H. Fujita, K. Yuyama, X. Li, Y. Hatano, T. Toyama, M. Ohta, K. Ochiai, N. Yoshida, T. Chikada and Y. Oya, "Effect of neutron energy and fluence on deuterium retention behaviour in neutron irradiated tungsten", Physica Scripta, T167 014067 (2016). **T, 1-38**

5) Y. Oya, X. Li, M. Sato, K. Yuyama, M. Oyaidzu, T. Hayashi, T. Yamanishi and K. Okuno, "Deuterium permeation behavior for damaged tungsten by ion implantation", J. Nucl. Sci. Tech., **53**, (3), 402-05 (2016). **T, 1-38**

6) M. Saito, K. Anzai, T. Maruyama, Y. Noguchi, K. Ueno, N. Takeda, S. Kakudate, "Development of radiation hard components for ITER blanket remote handling system", Fusion Eng. Design, **109-11** 1502-06 (2016). **G, 1-40**

7) 熊谷 友多, "固体と水との界面での放射線化学", RADIOISOTOPES, to be accepted (2016). **G, 1-49**

8) M. Takahashi, K. Akamatsu, N. Shikazono, "A polymerization-based method to construct a plasmid containing clustered DNA damage and a mismatch", Anal. Biochem. **510**, 129-35 (2016). **C, G, 2-07**

9) E Sage and N. Shikazono, "Radiation-induced clustered DNA lesions: Repair and mutagenesis", Free Radical Biol. Med. **107**, 125-35 (2017). **C, G, 2-07**

10) S. Habibi, A. G, Ayubi, N. Ohkama-Ohtsu, H. Sekimoto, T. Yokoyama, "Genetic Characterization of Soybean Rhizobia Isolated from Different Ecological Zones in North-Eastern Afghanistan", Microbes Environ. **32**, 71-79 (2017). **C, 2-23**

11) 横山 正,「TOPICS」"バイオ肥料微生物と除去植物を利用した福島での農耕地復興の試み", 放射線と産業, **141**, 41-46 (2016). **C, 2-23**

12) Y. Ueda, Y. Shinmyouzu, H. Nakayama, T. Tanino, E. Sakurai and E. Sakurai, "Claudin-1 Leads to Strong Formation of Tight Junction in Cultured Mouse Lung Microvascular Endothelial Cells", Pharmacology & Pharmacy, **7**, 133 (2016). **S, 2-34**

13) K. Okuyama, Y. Kadowaki, Y. Matsuda, N. Hashimoto, S. Oki, H. Yamamoto, Y. Tamaki and H. Sano, "Efficacy of a new filler-containing root coating material for dentin remineralization", Ame. J. Dent., **29**, 213-18, (2016). **S, 2-38**

14) S. Miyata, S. Tanaka, Y. Matsuda, N. Hashimoto, H. Sano and M. Kawanami, "Caries Prevention After Surface Reaction-Type Prereacted Glass Ionomer Filler-Containing Coating Resin Removal from Root Surfaces", J. Nanosci. Nanotech., **16**, 12996-3000 (2016). **S, 2-40**

15) S. Ushimura, K. Nakamura, Y. Matsuda, H. Minamikawa, S. Abe and Y. Yawaka, "Assessment of the inhibitory effects of fissure sealants on the demineralization of primary teeth using an automatic pH-cycling system", Dent. Mater. J., **35**, 316-24 (2016). **S, 2-40**

16) 大木 彩子, 松田 康裕, 橋本 直樹, 奥山 克史, 船戸 良基, 川本 千春, 小松 久憲, 佐野 英彦, "フッ化物徐放性材料の象牙質表面への塗布による脱灰抑制効果", 日本歯科保存学雑誌, **59**, 359-69 (2016). **S, 2-40**

17) H. Hayashi, S. Hayakawa, H. Nishikawa, "Micro structure processing on plastics by accelerated hydrogen molecular ions", Nucl. Instrum. Meth. Phys. Res. B, **404**, 233-37 (2017). **S, 3-12**

18) B. Tsuchiya, T. Yamamoto, K. Ohsawa and G. R. Odette, "First-principles Calculation of Formation Energies and Electronic Structures of Hydrogen Defects at Tetrahedral and Octahedral Interstitial Sites in Pyrochlore-type $Y_2Ti_2O_7$ Oxide", J. Alloys Comp., **678**, 153-59 (2016). **G, 3-30**

19) T. Fujiwara, S. Toyoda, A. Uchida, H. Nishido and J. Ishibashi, "The alpha effectiveness of the dating ESR signal in barite: possible dependence with age", Geochronometria, **43**, 174-78 (2016). **T, 3-33**

20) Y. Tsuchiya, M. Kayama, H. Nishido and Y. Noumi, "Cathodoluminescence of synthetic zircon implanted by He^+ ion", Geochronometria, **44**, 129-35 (2017). **T, 3-33**

21) S. Ohgo, M. Mishima, K. Ninagawa and H. Nishido, "Cathodoluminescence color zonation in the Antarctic meteorite (enstatite chondrite) of Yamato 86004", Geochronometria, **44**, 136-41 (2017). **T, 3-33**

22) S. Nakano, S. Kojima, K. Makino, M. Kayama, H. Nishido and J. Akai, "Cryptoperthitic and replacive intergrowths with iridescence in monzonitic rocks from Cerro Colorado, northern Chile", Euro. J. Mineral., **28**, 355-74 (2016). **T, 3-33**

23) A. Gucsik, I. Gyollai, H. Nishido, K. Ninagawa, M. Izawa, C. Jäger, I. Simonia, U. Ott, C. Szaniszló and M. Kayama, "Cathodoluminescence and Raman Spectromicroscopy of Forsterite in Tagish Lake Meteorite, Implications for Astromineralogy", Int. J. Spectroscopy, doi.org/10.1155/2016/1751730, 1-8 (2016). **T, 3-33**

24) S. Maki, S. Ohgo and H. Nishido, "Cathodoluminescence characterization of feldspar minerals from granite- syenite rocks in Iwagijima Island, Ehime Prefecture, Japan", Naturalistae, **20**, 13-18 (2016). **T, 3-33**

Proceedings

1) 野村 幹弘, "熱化学水素製造 IS プロセスによる水素製造の最前線", スマートエンジニアリング TOKYO 2016,［東京ビッグサイト・東京］(2016/10). **E, G, 1-13**

2) M. Ando, H, Tanigawa, H, Kurotaki, "Void swelling behavior of multi-ion irradiated F82H", Proc. 4th Nucl. Mater. Conf. (NuMAT2016), P3.37, [Montpellier, France] (2016/11). **C, T, S, 1-30**

3) M. Saito, H. Kozaka, T. Maruyama, Y. Noguchi, N. Takeda, S. Kakudate, "Irradiation tests of radiation hard materials for ITER blanket remote handling system", Proc. 29th Symp. Fusion Tech. (SOFT 2016), [Prague, Czech Republic] (2016/09). **G, 1-40**

4) S. Meigo, M. Ooi, K. Ikezaki, T. Kawasaki, H. Kinoshita, A. Akutsu, M. Nishikawa and S. Fukuta, "High Power Target Instrumentation at J-PARC for Neutron and Muon Sources", Proc. 57th ICFA Advanced Beam Dynamics Workshop on High-Intensity and High-Brightness Hadron Beams (HB2016), WEPM2X01, [Malmo, Sweden] (2016/07). **C, 1-41**

5) 本岡 隆文, “希釈人工海水中での炭素鋼の腐食速度と吸収線量率の関係”, 材料と環境2016 講演集, A-306, [つくば国際会議場・つくば] (2016/05). **G, 1-47**

6) Y. Matuo, Y. Izumi and K. Shimizu, “Dosimetric application of biological technique by evaluating DNA lesions induced with various LET ion beams exposure”, Proc. 12th Int. Workshop Individual Monit. Ionizing Radiat., P-67, [Oarai, Japan] (2016). **C, 2-20**

7) 松尾 陽一郎, 泉 佳伸, 清水 喜久雄, “放射線による DNA 損傷の定量評価に関する検討及び線量評価への応用”, 日本放射線安全管理学会第 15 回学術大会, P23, [岡山大・岡山] (2016/11). **C, 2-20**

8) 加田 渉, “集束イオンビームを利用した光材料開発とその場分析技術の開発”, 荷電粒子の工業への応用第 132 委員会, 第 223 回研究会, [森戸記念会館(東京理科大)・東京] (2016/12). **S, 3-01, 3-11**

9) H. Hayashi and H. Nishikawa, “Fabrications of Fluorinated Polymer-Based Microstructures by Proton Beam Writing and its Applications”, Proc. Adv. Appl. Ion Beams Mater. Sci., IUMRS-ICEM2016, K-2 ICEM16-A-1119, [Singapore] (2016/07). **S, 3-12**

10) 早川 志文, 林 秀臣, 小池 義和, 西川 宏之, “陽子線照射した P(VDF/TrFE)膜のウェットエッチング特性の照射量依存性”, 第 77 回応用物理学会, No.14p-B6-3, [朱鷺メッセ・新潟] (2016/09). **S, 3-12**

11) 金子 優斗, 林 秀臣, 西川 宏之, “PDMS 系コンポジット材料の陽子線による改質”, 電気学会,第 47 回電気電子絶縁材料システムシンポジウム, MVP-18, [岐阜大・岐阜] (2016/09). **S, 3-12**

12) H. Amekura, “Shape elongation of embedded metal nanoparticles induced by irradiation with swift heavy ions/cluster ions”, Proc. 2016 IEEE Nanotech. Mater. Devices Conf. (IEEE-NMDC 2016), #7777110, [Toulouse, France] (2016/10). **T, 3-20**

13) T. Fujiwara, S. Toyoda, A. Uchida, J. Ishibashi, S. Totsuka, K. Shimada and S. Nakai, “Dating of barite and anhydrite in sea-floor hydrothermal deposits in the Okinawa Trough”, 2016 AGU Fall Meet., [San Francisco, USA] (2016/12). **T, 3-33**

14) T. Fujiwara, S. Toyoda, A. Uchida, J. Ishibashi, S. Totsuka, K. Shimada and S. Nakai, “Radioactive disequilibrium and ESR dating of barite in sea-floor hydrothermal deposits of the Okinawa Trough”, Goldschmidt 2016, [Yokohama, Japan] (2016/06). **T, 3-33**

15) S. Toyoda, T. Fujiwara, A. Uchida and J. Ishibashi, “ESR dating of barite in see-floor hydrothermal deposits a new dating technique”, Goldschmidt 2016, [Yokohama, Japan] (2016/06). **T, 3-33**

16) S. Noumi, N. Kusano and H. Nishido, “CL emission mechanism of Pb-bearing carbonates”, Goldschmidt 2016, [Yokohama, Japan] (2016/06). **T, 3-33**

17) K. Nagashima, H. Nishido and M. Kayama, “Provenance study of Asian dust using cathodoluminescence spectrum of single quartz grain”, Goldschmidt 2016, [Yokohama, Japan] (2016/06). **T, 3-33**

18) R. Kanamaru, H. Nishido and A. Yamaguchi, “Cathodo-luminescence study of silica minerals in eucrites”, Goldschmidt 2016, [Yokohama, Japan] (2016/06). **T, 3-33**

19) H. Asai, M. Saneyoshi, H. Nishido, S. Toyoda, K. Tsogtbaatar and B. Mainbayar, “Stratigraphic assignment of eolian sediments in the Central Gobi Desert, Mongolia using an indicator of defect centers in quartz composed of sand particles”, ASAI 2016, [Ulan Bator, Mongolia] (2016). **T, 3-33**

20) S. Kobayashi, T. Nimura, M. Nakata, R. Nakamura, H. Chihara, C. Koike and H. Nishido, “In-situ polarimetric analysis of organic materials in Allende and Murchison meteorites”, AGU 2016 Fall Meet., [San Francisco, USA] (2016/12). **T, 3-33**

21) N. Kusano, H. Nishido and S. Noumi, “Temperature effects on CL emissions in Mn-activated carbonates”, AGU 2016 Fall Meet., [San Francisco, USA] (2016/12). **T, 3-33**

22) S. Noumi, N. Kusano and H. Nishido, “ns^2 type luminescence in Pb-bearing carbonates using cathodoluminescence”, AGU 2016 Fall Meet., [San Francisco, USA] (2016/12). **T, 3-33**

23) R. Kanamaru, A. Yamaguchi and H. Nishido, “Cathodoluminescence study of secondary minerals in basaltic eucrites”, Proc. 7th Symp. Polar Sci., OA_Kanemaru_00239_01.pdf, [Tachikawa, Japan] (2016/11). **T, 3-33**

24) S. Nagy, S. Józsa and H. Nishido, “Heating Experiments of sideritic sedimentary rock as a possible Martian sediment: Can this rock survive a flash heating when it enters the earth’s atmosphere?”, Proc. 7th Symp. Polar Sci., OA_Nagy_00035_01.pdf, [Tachikawa, Japan] (2016/11). **T, 3-33**

25) 藤原 泰誠, 豊田 新, 内田 乃, 石橋 純一郎, 野崎 達生, “伊豆・小笠原弧から採取された熱水性鉱石に含まれる重晶石の年代測定”, 2016 年度日本地球化学会第 63 回年会, 3P 30, [大阪市立大・大阪] (2016/09). **T, 3-33**

26) 常 昱, 鹿山 雅裕, 田近 英一, 関根 康人, 関根 利守, 西戸 裕嗣, 小林 隆道, “石英の衝撃誘起ガラス化とカソードルミネッセンスの系統的変化:新しい衝撃圧力計としての可能性”, 日本地球惑星連合学会 2016 年年会, [幕張メッセ・千葉] (2016/05). **T, 3-33**

27) 土屋 裕太, 鹿山 雅裕, 西戸 裕嗣, 能美 洋介, “ジルコンのカソードルミネッセンスに及ぼす放射線損傷の評価”, 日本地質学会2016年年会, T6-P-1, [日本大・東京] (2016/09). **T, 3-33**

28) 金丸 礼, 山口 亮, 西戸 裕嗣, “玄武岩質ユークライトに見られる石英の成因”, 日本鉱物科学会 2016 年年会, R5-11, [金沢大・金沢] (2016/09). **T, 3-33**

29) 小林 優, 二村 徳宏, 田中 真人, 中村 良介, 茅原 弘毅, 小池 千代枝, 中嶋 悟, 西戸 裕嗣, “マーチンソン隕石およびアエンデ隕石に産する有機物のその場観察”, 日本惑星科学会 2016 年秋期講演会, P1-10, [ノートルダム清心女子大・岡山] (2016/09). **T, 3-33**

Books

1) 友岡 憲彦, 横山 正, “耐塩性ダイズのスクリーニングと耐塩性根粒菌の利用による津波塩害地でのダイズ 栽培技術の開発”, 「福島農業復興支援バイオ肥料プロジェクト最終報告書」(ISBN 978-4-9906944-3-2-C3045-＼00000E)”, 出版社名:東京農工大学 農学部文科省特別経費プロ バイオ肥料, 出版者記号:9906944, 119-22 (2017). **N**

2) 金丸 礼, 蜷川 清隆, 西戸 裕嗣, 豊田 新, “普通コンドライトの TL 測定における nanoGrayTL/OSL 一体型装置と岡山理科大学 TL 装置の比較”, 岡山理科大学自然科学研究所報告, **41**, 21-26 (2016). **T, 3-33**

3) 内田 乃, “海洋性熱水重晶石の放射非平衡年代測定”, 岡山理科大学・理学研究科, 博士論文 (2017/01). **T**

4) 草野 展弘, “炭酸塩鉱物におけるカソードルミネッセンス発現メカニズムの解明”, 岡山理科大学・理学研究科, 博士論文 (2017/01). **T**

Patent

1) 加田 渉, 春山 盛善, 須田 義規, 三浦 健太, 花泉 修, 村尾 智, “マーキング方法, マーキング装置, およびマーキングされた物品”, 特願 2017-036566, (2017.02.28), 出願: 産業技術総合研究所. **S, 3-11**

Appendix 2 Type of Research Collaboration and Facilities Used for Research

Paper No.	Type of Research Collaboration*1					Irradiation Facilities*2						Paper No.	Type of Research Collaboration*1					Irradiation Facilities*2					
	Joint Res.	Entr. Res.	Coop. Res.	Inter. Use	Ext. Use	C	T	S	I	E	G		Joint Res.	Entr. Res.	Coop. Res.	Inter. Use	Ext. Use	C	T	S	I	E	G
1-01	●					◎					◎	1-46					●						◎
1-02	●					◎						1-47					●		◎				◎
1-03	●					◎	◎		◎	◎		1-48					●						◎
1-04				●		◎			◎			1-49	●									◎	
1-05	●						◎		◎	◎		1-50				●						◎	
1-06				●		◎		◎	◎			1-51				●						◎	
1-07				●		◎						1-52	●									◎	
1-08				●N								1-53				●						◎	
1-09				●		◎						1-54				●							◎
1-10				●				◎	◎														
1-11				●			◎		◎			2-01				●		◎					
1-12				●						◎	◎	2-02				●		◎					◎
1-13				●						◎	◎	2-03	●					◎					◎
1-14					●	◎						2-04	●					◎					
1-15					●				◎			2-05	●					◎					
1-16				●		◎					◎	2-06				●							◎
1-17	●										◎	2-07	●					◎					
1-18	●										◎	2-08	●					◎					
1-19				●							◎	2-09	●					◎					
1-20				●						◎		2-10	●					◎					
1-21				●					◎			2-11	●					◎					
1-22				●				◎				2-12	●					◎					
1-23				●							◎	2-13	●					◎					
1-24	●										◎	2-14	●					◎					
1-25				●			◎		◎			2-15	●					◎					
1-26	●						◎					2-16	●					◎					
1-27	●								◎			2-17					●	◎					
1-28				●						◎		2-18				●							◎
1-29					●		◎					2-19	●					◎					
1-30				●			◎	◎	◎			2-20				●			◎				
1-31					●		◎	◎	◎			2-21	●					◎					
1-32					●						◎	2-22				●		◎					◎
1-33					●		◎					2-23	●										◎
1-34			●					◎				2-24	●					◎					
1-35					●			◎				2-25	●					◎					
1-36					●						◎	2-26	●					◎					
1-37					●						◎	2-27	●										◎
1-38					●		◎					2-28				●			◎				
1-39				●							◎	2-29			●					◎			
1-40				●							◎	2-30			●					◎			
1-41	●					◎						2-31			●					◎			
1-42					●						◎	2-32			●					◎			
1-43					●						◎	2-33			●					◎			
1-44					●						◎	2-34			●					◎			
1-45					●						◎	2-35			●					◎			

Paper No.	Type of Research Collaboration*1					Irradiation Facilities*2						Paper No.	Type of Research Collaboration*1					Irradiation Facilities*2					
	Joint Res.	Entr. Res.	Coop. Res.	Inter. Use	Ext. Use	C	T	S	I	E	G		Joint Res.	Entr. Res.	Coop. Res.	Inter. Use	Ext. Use	C	T	S	I	E	G
2-36			●					◎				3-29	●							◎			
2-37	●					◎						3-30					●						◎
2-38				●							◎	3-31			●					◎			
2-39	●					◎						3-32					●			◎			
2-40	●					◎						3-33					●		◎				
2-41	●					◎						3-34					●						◎
												3-35					●						◎
3-01	●							◎															
3-02	●							◎				4-01						◎	◎	◎	◎		
3-03	●					◎						4-02						◎					
3-04				●					◎			4-03							◎	◎	◎		
3-05				●		◎						4-04										◎	◎
3-06				●		◎						4-05										◎	◎
3-07				●			◎	◎	◎			4-06						◎	◎	◎	◎		
3-08				●		◎					◎	4-07						◎	◎	◎	◎		
3-09				●N								4-08						◎	◎	◎	◎	◎	◎
3-10	●					◎																	
3-11	●							◎															
3-12	●							◎															
3-13	●																						
3-14			●						◎														
3-15			●						◎														
3-16			●				◎		◎														
3-17	●						◎																
3-18			●				◎																
3-19			●				◎		◎														
3-20			●				◎																
3-21			●				◎																
3-22			●				◎																
3-23			●				◎		◎														
3-24	●						◎																
3-25					●	◎																	
3-26	●										◎												
3-27				●							◎												
3-28			●					◎				Total	47	0	20	39	24	47	29	29	24	14	39

*1 Type of Research Collaboration

Joint Res. : Joint research with external users

Entr. Res. : Research entrusted to QST

Coop. Res. : Cooperative research with plural universities through The University of Tokyo

Inter. Use : Internal use

Ext. Use : Common use based on two programs of "QST-facility-use" and "Creation of Research Platforms and Sharing of Advanced Research Infrastructure" supported from MEXT

*2 Utilization of Irradiation Facilities

C : AVF Cyclotron

T : 3 MV Tandem Electrostatic Accelerator

S : 3 MV Single-ended Electrostatic Accelerator

I : 400 kV Ion Implanter

E : 2 MV Electron Accelerator

G : Co-60 Gamma-ray Irradiation Facilities

N : Non-use of irradiation facilities at TARRI

Appendix 3 Examples of Typical Abbreviation Name for Organizations in National Institutes for Quantum and Radiological Science and Technology, and Japan Atomic Energy Agency

◆Institute, Center, Laboratory etc.

TARRI	**（高崎量子応用研究所）**	:	Takasaki Advanced Radiation Research Institute
NFI	**（那珂核融合研究所）**	:	Naka Fusion Institute
RFI	**（六ヶ所核融合研究所）**	:	Rokkasho Fusion Institute
KPSI	**（関西光科学研究所 ）**	:	Kansai Photon Science Institute
NIRS	**（放射線医学総合研究所）**	:	National Institute of Radiological Sciences
NSEC	**（原子力基礎工学研究センター）**	:	Nuclear Sciences and Engineering Center
MSRC	**（物質科学研究センター）**	:	Materials Sciences Research Center
NERCC	**（原子力エネルギー基盤連携センター）**	:	Nuclear Engineering Research Collaboration Center
AFRC	**（次世代高速炉サイクル研究開発センター）**	:	Advanced Fast Reactor Cycle System Research and Development Center
NHARC	**（原子力水素・熱利用研究センター）**	:	Nuclear Hydrogen and Heat Application Research Center
NSRI	**（原子力科学研究所）**	:	Nuclear Science Research Institute
NFCEL	**（核燃料サイクル工学研究所）**	:	Nuclear Fuel Cycle Engineering Laboratories
ORDC	**（大洗研究開発センター）**	:	Oarai Research and Development Center
J-PARC	**（**J-PARC**センター）**	:	J-PARC Center
CLADS	**（廃炉国際共同研究センター）**	:	Collaborative Laboratories for Advanced Decommissioning Science

◆Department, Division, Center etc.

- **量子ビーム科学研究部門、高崎量子応用研究所、先端機能材料研究部**
  ⇒ Department of Advanced Functional Materials Research, TARRI, QST
- **量子ビーム科学研究部門、高崎量子応用研究所、放射線生物応用研究部**
  ⇒ Department of Radiation-Applied Biology Research, TARRI, QST
- **量子ビーム科学研究部門、高崎量子応用研究所、放射線高度利用施設部**
  ⇒ Department of Advanced Radiation Technology, TARRI, QST
- **量子ビーム科学研究部門、高崎量子応用研究所、東海量子ビーム応用研究センター**
  ⇒ Tokai Quantum Beam Science Center, TARRI, QST
- **量子ビーム科学研究部門、関西光科学研究所、量子生命科学研究部**
  ⇒ Department of Quantum Beam Life Science, KPSI, QST
- **核融合エネルギー研究開発部門、那珂核融合研究所、トカマクシステム技術開発部**
  ⇒ Department of Tokamak System Technology, NFI, QST
- **核融合エネルギー研究開発部門、六ヶ所核融合研究所、核融合炉システム研究開発部**
  ⇒ Department of Fusion Reactor Systems Research, RFI, QST
- **核融合エネルギー研究開発部門、六ヶ所核融合研究所、核融合炉材料研究開発部**
  ⇒ Department of Fusion Reactor Materials Research, RFI, QST
- **放射線医学総合研究所、放射線障害治療研究部**
  ⇒ Department of Basic Medical Sciences for Radiation Damages, NIRS, QST

・原子力基礎工学研究センター、原子力化学ディビジョン
⇒ Nuclear Chemistry Division, NSEC, JAEA

・原子力基礎工学研究センター、環境・放射線科学ディビジョン
⇒ Environment and Radiation Sciences Division, NSEC, JAEA

・原子力基礎工学研究センター、燃料・材料工学ディビジョン
⇒ Fuels and Materials Engineering Division, NSEC, JAEA

・原子力基礎工学研究センター、軽水炉基盤技術開発ディビジョン
⇒ LWR Key Technology Development Division, NSEC, JAEA

・先端基礎研究センター
⇒ Advanced Science Research Center, JAEA

・物質科学研究センター、放射光エネルギー材料研究ディビジョン
⇒ Energy and Environment Materials Science Division, MSRC, JAEA

・物質科学研究センター、中性子材料解析研究ディビジョン
⇒ Neutron Materials Research Division, MSRC, JAEA

・大洗研究開発センター、福島燃料材料試験部
⇒ Fukushima Fuels and Materials Department, ORDC, JAEA

・大洗研究開発センター、照射試験炉センター
⇒ Neutron Irradiation and Testing Reactor Center, ORDC, JAEA

・原子力水素・熱利用研究センター、水素利用研究開発ディビジョン
⇒ Hydrogen Application Research and Development Division, NHARC, JAEA

・J-PARC センター、加速器ディビジョン
⇒ Accelerator Division, J-PARC, JAEA

・核燃料サイクル工学研究所、再処理技術開発センター
⇒ Tokai Reprocessing Technology Development Center, NFCEL, JAEA

・核燃料サイクル工学研究所、環境技術開発センター
⇒ Nuclear Backend Technology Center, NFCEL,JAEA

・核燃料サイクル工学研究所、福島技術開発試験部
⇒ Department of Fukushima Technology Development, NFCEL, JAEA

・次世代高速炉サイクル研究開発センター、燃料サイクル技術開発部
⇒ Fast Reactor Fuel Cycle Technology Development Department, AFRC, JAEA

・廃炉国際共同研究センター、廃棄物処理処分ディビジョン
⇒ Waste Management Division, CLADS, JAEA

・敦賀連携推進センター、レーザー共同研究所
⇒ Applied Laser Technology Institute, JAEA

・東濃地科学センター、地層科学研究部
⇒ Geoscientific Research Department, Tono Geoscience Center, JAEA

・楢葉遠隔技術開発センター
⇒ Naraha Remote Technology Development Center, JAEA

QST Takasaki Annual Report 2016

(Ed) Watalu YOKOTA

Date of Publishing: March 2018

Editorial committee : Watalu YOKOTA, Hiroyuki YAMAMOTO, Yasunari MAEKAWA,
Yasuhiko KOBAYASHI, Yuichi SAITOH, Kazumasa NARUMI,
Takehisa SUZUKI, Kenji YAMAGUCHI and Satoshi WATANABE

Publication : Takasaki Advanced Radiation Research Institute
National Institutes for Quantum and Radiological Science and Technology
1233 Watanuki, Takasaki, Gunma Japan 370-1292

Tel : +81-27-346-9610

E-mail : taka-tiaraplan@qst.go.jp

Homepage：http://www.taka.qst.go.jp

Printed in Japan

QST-M-8

http://www.qst.go.jp